John T. Yates Jr.

Experimental Innovations in Surface Science

A Guide to Practical Laboratory Methods and Instruments

Second Edition

Experimental Innovations in Surface Science

John T. Yates Jr.

Experimental Innovations in Surface Science

A Guide to Practical Laboratory Methods and Instruments

Second Edition

Springer

John T. Yates Jr.
Department of Chemistry
University of Virginia
Charlottesville, VA
USA

ISBN 978-3-319-17667-3 ISBN 978-3-319-17668-0 (eBook)
DOI 10.1007/978-3-319-17668-0

Library of Congress Control Number: 2015941351

Springer Cham Heidelberg New York Dordrecht London
© Springer International Publishing Switzerland 1998, 2015
This work is subject to copyright. All rights are reserved by the Publisher, whether the whole or part of the material is concerned, specifically the rights of translation, reprinting, reuse of illustrations, recitation, broadcasting, reproduction on microfilms or in any other physical way, and transmission or information storage and retrieval, electronic adaptation, computer software, or by similar or dissimilar methodology now known or hereafter developed.
The use of general descriptive names, registered names, trademarks, service marks, etc. in this publication does not imply, even in the absence of a specific statement, that such names are exempt from the relevant protective laws and regulations and therefore free for general use.
The publisher, the authors and the editors are safe to assume that the advice and information in this book are believed to be true and accurate at the date of publication. Neither the publisher nor the authors or the editors give a warranty, express or implied, with respect to the material contained herein or for any errors or omissions that may have been made.

Printed on acid-free paper

Springer International Publishing AG Switzerland is part of Springer Science+Business Media
(www.springer.com)

Preface to the Second Edition

A number of new experimental innovations have been added in over 50 new chapters. I thank each of the innovators for their contributions which are acknowledged in the text. I very much appreciated the graphical work of Dr. Ana Stevanovic who skillfully converted hand drawings to computer graphics. I also deeply appreciate the assistance of Dr. Zhen Zhang in assembling the new and former material to produce a well-organized second edition. And finally, I wish to thank Dr. Winfried Heichler and his son Jan Heichler for important high-resolution optical scanning of the first edition, allowing its fusion with new material in the second edition. I also thank the Department of Chemistry at the University of Virginia for financial support of the graphics effort. And finally, as in the first edition, I thank my loving and caring wife, Kerin Yates, for her continued support and constructive criticism of the new book.

Virginia John T. Yates Jr.

Preface to the First Edition

The modern era of surface science, developed in the last 30 years, features hundreds of new physical and chemical measurement methods such as low-energy electron diffraction and Auger electron spectroscopy, which form a vital foundation for the field. These measurement methods constitute the basis for a number of books used by beginning students as their introduction to experimental research.

This book is not about this particular experimental core of the field. Instead, it is about those practical laboratory methods used throughout the field, but seldom communicated coherently in writing and drawings to beginning students. These practical methods of design, construction, and measurement also form their own foundation for making possible significant research. They constitute a gold mine of clever ideas and "tricks of the trade" about how to use basic materials and components effectively for research and measurement in surface science. Approximately 250 practical methods are described in the book in enough detail that one could design a new experimental device from the book alone.

This book will be useful to beginning research workers in surface science as well as to those who work with similar methods in fields such as semiconductor technology, materials science, and physical electronics.

The contents of the book have been selected from unpublished information supplied by more than 100 workers in the field as well as from the literature, dating back to the mid-1960s. I have attempted to communicate the core ideas from published and unpublished accounts of research in easy-to-comprehend pictorial form, believing that pictures are the most effective mode for communication of information of this type. Thus, the reader can learn much just by looking at the pictures. The text associated with each drawing gives more details. In many cases, the text and its citations indicate the originators and subsequent contributors to the innovation, but in other cases the origin of the key ideas is unknown, making accurate historical citations impossible.

There are some topics that have not been addressed in the book, primarily because they are currently highly specialized and fast-moving activities that are best learned by advanced research students who have previously mastered some of the topics covered in this book. Untreated topics include many details of the scanning

tunneling microscope (STM), complex molecular beam techniques, and complex laser-based measurements.

Updated information on United States and international suppliers of materials and components used in surface science research is featured at the end of the book. Here the reader will find a guide to product sources as well as addresses and other communications information for all companies mentioned in the text footnotes as well as many other company listings. I thank Dr. Jun Yoshinobu and Dr. Joachim Ahner for help with these compilations.

I very much appreciate the involvement of many friends and colleagues who have contributed to this book by sending me accounts of their innovative methods. This includes many of my own students and postdoctoral who have developed some of the experimental methods described here. I also thank the publishers of the Journal of Vacuum Science and Technology for permission to use many published contributions dating back to 1964. These were organized for me by Professor Michael Bozack and Mr. Kenneth W. Bryant at Auburn University, to whom I am greatly indebted, and were invaluable in writing a portion of this book. I thank Dr. Fred Dylla and Mrs. Maria Taylor for their encouragement during work with AIP and with Springer-Verlag as the book progressed. Mrs. Marge Augenstein and Mrs. Mary Beth Merenick supplied accurate assistance in organizing the collection and verification of information for the book at the University of Pittsburgh, and in checking the accuracy of the citations. Ms. Hana Novak took my hand-drawn mechanical drawings and skillfully converted them to computer graphics. The book would not have been produced without the financial assistance of the Alexander von Humboldt Stiftung, which made possible my stay in the Department of Physics, Philipps University, Marburg, Germany. I am indebted also to the University of Pittsburgh for a coincident sabbatical leave to write the book. I wish to thank my many German friends for their hospitality, particularly Dr. Heinz J. Jaensch and Professor Dieter Fick for their friendship during my seven months in Marburg. I also thank my parents, Mr. and Mrs. J. Thomas Yates, Sr., for their hospitality in Hagerstown, Maryland, during the completion of the book. And finally, and most importantly, I thank my wife, Kerin, for all of her support. Without her understanding and constructive criticism, writing and illustrating the book would have been impossible.

March 1997

John T. Yates, Jr.
R.K. Mellon Professor
Department of Chemistry
and Department of Physics and Astronomy
Director, Surface Science Center
University of Pittsburgh

Contents

Part I Vacuum System Technology

1 Motion in Vacuum 3
1.1 Crystal Manipulator with Six Degrees of Motional Freedom 3
1.2 Rotation in Ultrahigh Vacuum 6
1.3 Crystal Positioning Using Capacitance 11
1.4 UHV Rotary Manipulator with Arcsec Resolution 13
1.5 Solenoid Driven Linear Motion Device 15
1.6 An Inexpensive Linear Motion Device 15
1.7 Translating Auger Spectrometer 16
1.8 Simple Multiple Motion Manipulator 18
1.9 Simple Device for Small Rotations in Ultrahigh Vacuum—Grating Application 18
1.10 Turntable Rotation in Ultrahigh Vacuum 20
1.11 Small Motions in UHV Systems Using Shape Memory Effect Alloys 20
1.12 Rotary Shutter Device Driven by Magnetic Eddy Current . . . 22
1.13 High-Speed Ultrahigh Vacuum Motor 24
1.14 High-Speed Rotary Feedthrough for UHV Operation 25
1.15 Self-lubricating Bearings in UHV 26
1.16 Lubrication for Heavy Sliding Loads in Ultrahigh Vacuum 27
1.17 Simple UHV Bearing for High-Speed Shafts 29
1.18 Flange-Mounted UHV Variable Aperture 30
1.19 Linear Motion Platform (LMP) 31
1.20 Vacuum Trolley Transport System 33
1.21 Thermally Compensated STM with Repeatable Sample Positioning 34
References 36

2 Sample Transfer 39
2.1 Sample Transfer from High Pressure to Ultrahigh Vacuum 39
2.2 Novel Sample Transfer from UHV Chamber to External Cell 45
2.3 UHV Sample Transfer Device with Low-Temperature Capability 45
2.4 Internal Cup High-Pressure Cell 49
2.5 High-Pressure Transfer Cell 50
2.6 Sample Transfer with Disconnect-I 52
2.6.1 Transfer in Standard UHV Systems 52
2.6.2 Transfer in STM Systems 54
2.7 Sample Transfer with Disconnect-II 54
2.8 Vibration-Free Translatable Device 55
2.9 Mirror Port for Enhanced Sample Transfer 56
2.10 UHV Access Port 56
References 58

3 Electrical Connections 61
3.1 Tungsten Ribbon—Attachment to Power Leads 61
3.2 Wrap Connection—Tungsten to Tungsten 62
3.3 Cold-Formed Wire Connector 64
3.4 Ultrahigh Resistance Vacuum Feedthroughs 64
3.5 Sliding Metal Electrical Contact 66
3.6 Low-Profile Electrical Lead Clamp 67
References 68

4 Pumping and Trapping 69
4.1 Water Aspirator/Sorption Pump Combination for Efficient UHV System Evacuation 69
4.2 Ballast Pumping—Vibration Free 71
4.3 The Use of Appendage Titanium Sublimation Pumps for Pumping Low Gas Loads in Ultrahigh Vacuum 72
4.4 Pressure-Equalizing Device in Complex Systems 72
4.5 Diode Ion Pump Performance in He Pumping 75
4.6 Vacuum Applications of Metal Foams 75
4.7 Cleaning of Ion Pumps by Chemical Etching 78
4.8 An Efficient Liquid Nitrogen Trap 79
References 80

5 Bakeout 83
5.1 Bakeout of Metal Ultrahigh Vacuum Systems 83
References 85

6 Behavior of UHV Systems 87
6.1 Wall Passivation in Stainless Steel Ultrahigh Vacuum Systems 87
6.2 Minimizing Wall Reactions in Ultrahigh Vacuum Systems—Gas Dosers 89
References. . . . 91

7 Mechanical Action on Samples 93
7.1 Simple UHV Crystal Cleaver 93
7.2 Piezoelectric Fatigue Apparatus for UHV Operation 95
References. . . . 97

8 Gasket Seals 99
8.1 Gasket Seals for Ultrahigh Vacuum Systems 99
8.2 Cryogenic Gasket Seals 101
8.3 Copper Gasket Removal Devices 102
8.4 Unconventional Compression Seals for Ultrahigh Vacuum . . . 103
References. . . . 105

9 Leak Repairs and Detection 107
9.1 Coaxial Pumped He Leak Detection Probe 107
9.2 Temporary Leak Sealing of Welded Bellows 108
9.3 Atmospheric Permeation—Viton O-Ring 108
References. . . . 110

10 Specialized UHV Systems 113
10.1 Aluminum Ultrahigh Vacuum System 113
10.2 Surface Electrochemistry Apparatus. . . . 114
References. . . . 116

Part II Mechanical Fabrication Techniques

11 Grids 119
11.1 Hemispherical Grids—Formation and Piercing 119
11.2 Making Flat Mesh Grids of Large Size 120
11.3 Grid Fabrication Techniques—Conical Grid 121
References. . . . 122

12 Conductive Coatings 123
12.1 Deposition of Electrically Conductive SnO_2 Films. . . . 123
References. . . . 125

13 Phosphor Screens 127
13.1 Sedimentation Method for Depositing Phosphor Screens 127
13.2 Dusting Method for Coating Phosphor Screens 129
References 131

14 Thermionic Emitters 133
14.1 Thoriated Thermionic Emitters 133
14.2 Lanthanum Hexaboride Thermionic Emitters—Deposition on Metals 135
14.3 Directly Heated Lanthanum Hexaboride Thermionic Emitters 137
14.4 Thermionic Emitter Mounting 139
14.5 Indirectly Heated Cathodes for High-Temperature Operation 141
14.6 Filament Power Supply Tester 141
14.7 Bayard-Alpert Ionization Gauge with Corrections for External Radiation and External Electron Flux Effects . . . 142
14.8 Replacing Filaments in Glass Bayard-Alpert Gauges 145
References 146

15 Shielding 149
15.1 Magnetic Shielding in Ultrahigh Vacuum 149
15.2 Electrical Isolation of UHV Components 151
References 152

16 Single Crystal Fabrication/Orientation 155
16.1 Making Small Au Single Crystals from Au Wire for STM and Other Studies 155
16.2 Single Crystal Orientation, Grinding, and Polishing 156
16.3 A Simple Goniometer for Cutting Single Crystals 159
16.4 Ion Beam Polishing of Crystals to Subnanometer Roughness 160
16.5 Crystal Optical Alignment 161
16.6 Measurement of the Angles of Incidence in a LEED Experiment 162
16.7 Measurement of Angle of Incidence of an Electron Beam on a Single Crystal 163
References 165

17 Tip Fabrication 167
17.1 Fabrication of Metal Tips Using Zone Electropolishing 167
17.2 Etching STM Tips Reproducibly 168
17.3 STM Tip Flasher 170

17.4 Reverse Bias Method for Sharp Tip Etching 170
17.5 Sharpening Single Crystal Metal Tips by Ion Bombardment 173
References 174

18 Spot-Welding 175
18.1 Spot-Welding Difficult Junctions 175
References 177

19 Mechanical Procedures 179
19.1 Stretching Thin Metal Foils to a Wrinkle-Free Condition 179
19.2 Making Micron-Size Holes for Supersonic Nozzles 180
19.2.1 Method I—Fig. 19.2a 180
19.2.2 Method II—Fig. 19.2b 182
19.3 Straightening and Braiding Wires 183
References 183

Part III Measurement Methods

20 Electrons 187
20.1 Electron Gun Design and Behavior 187
20.2 Low-Energy Electron Gun for Broad-Beam Irradiation 189
20.3 Low-Energy Electron Gun for Broad-Beam Irradiation—Cylindrical Symmetry 190
20.4 Electron Energy Analyzers 191
20.5 Electron Spectrometer Calibration Using Graphite 196
20.6 Measurement of Electron Beam Angular Divergence 198
20.7 Measuring Anisotropy of Electrical Conductivity of a Single Crystal—Four Point Probe 200
20.8 Spot Photometer for LEED Intensity Measurements 201
20.9 Modified Faraday Cup for Electron Current Measurement . . . 202
20.10 HREELS-Discrimination Between Single and Multiple Electron Scattering Events 205
20.11 Rejuvenation of Cu/Be Electron Multipliers 205
20.12 Geiger-Müller Counter for Inverse Photoemission 206
References 208

21 Ions 211
21.1 Ion Sputter Gun with Low Gas Emission 211
21.2 Alternate Ion Bombardment Sources 213
21.3 Ion Gun Based on Bayard-Alpert Gauge 214
21.4 Sputter Ion Gun—Cold Cathode 216
21.5 Broad Ion Sources—Improved Stability with Oxygen 218

21.6 Focusing of Low-Energy Ions by Magnetic Field 220
21.7 Low Energy Ion Gun—Construction and Performance 220
21.8 Measuring Ion Beam Dimensions 223
21.9 Beam Position Monitor—Charged Particles 224
21.10 Pulse-Counting LEED/ESDIAD Analyzer—Using MicroChannel Plate Detection. 225
21.11 Time-of-Flight Measurements for Ions Generated in ESDIAD 227
21.12 Ion Detection with Kinetic Energy and Mass Resolution Using a Hemispherical Energy Analyzer 229
21.13 Time-of-Flight Detection for Laser-Ionized Neutrals 231
References. 232

22 Photons (UV) 235
22.1 Hollow Cathode Resonance Lamp for He(II) (40.8 eV) Photoemission 235
22.2 He(I) and He(II) Ultraviolet Resonance Source 236
22.3 Photochemistry on Surfaces Using an Ultraviolet Lamp 238
22.4 Use of Polarized Ultraviolet Light for Photochemistry 240
22.5 Photoreduction of Ag on Doped TiO_2—Making Enhanced Photoactivity Visible. 242
22.6 Reducing Radiation Damage in Raman Spectroscopy of Solids 243
22.7 Lyman-α Lamp Calibration Using a Chemical Actinometer 245
22.8 Pulsed Vacuum UV Light Source 247
22.9 Grazing Incidence X-Ray Photoemission Spectroscopy (GIXPS): Enhanced Surface Sensitivity 247
References. 250

23 Kinetics of Adsorption/Adsorbate Coverages 253
23.1 Absolute Adsorption Uptake Measurements from a Calibrated Effusive Molecular Beam 253
23.2 Measurement of Absolute Sticking Coefficient at Desorption Temperature 255
References. 257

24 Mass Spectrometry 259
24.1 Shielded Quadrupole Mass Spectrometers—Temperature-Programmed Desorption. 259
24.2 Enhanced Signal-to-Noise in Quadrupole Mass Spectrometers. 262
24.3 Elimination of Spurious Electron Emission from a Quadrupole Mass Spectrometer 265

24.4 Ta Mass Spectrometer Filament 265
24.5 Modulated QMS Ion Source for Enhanced Sensitivity 267
24.6 Line-of-Sight Mass Spectrometry for Thermal Desorption . . . 269
24.7 Mass Spectrometer Calibration by Molecular Decomposition 270
References. 272

25 Temperature-Programmed Desorption/Reaction 273
25.1 Thermal Desorption—Angular Resolved 273
25.2 Magic-Angle Thermal Desorption Mass Spectroscopy 275
25.3 High-Temperature Thermal Desorption Spectroscopy. 277
25.4 Automated Temperature Programmed Desorption (TPD) Apparatus. 278
25.5 Scanning Kinetic Spectroscopy—A Survey Method for Investigation of Surface Reaction Processes. 280
25.6 Temperature-Programmed Reaction Spectroscopy (TPRS) . . . 282
References. 284

26 Gas Chromatography—Enhanced Sensitivity 287
26.1 Gas Chromatography—Sensitivity Enhancement 287
Reference 288

27 Work Function, Tunneling Spectroscopy and Ellipsometry 289
27.1 Work Function Changes Using Retarding Diode Method 289
27.2 Work Function Measurements Using an Electron Gun 291
27.3 Work Function and Electron Reflection Coefficient Measurements with the Shelton Diode 293
27.4 Improved Piezoelectric Drive Kelvin Probe 295
27.5 Improved Electromagnetic Drive Kelvin Probe 297
27.6 Kelvin Probe—High Temperature Flow Reactor 299
27.7 Scanning Tunneling Spectroscopy (STS)—Compensation for Density of States of the Tip. 300
27.8 Ellipsometry as a Tool for Studying Adsorption 302
References. 303

28 Radioactive Adsorbates. 305
28.1 Radiotracer Techniques for Surface Studies 305
References. 307

29 Thin Film Deposition 309
29.1 Thin Film Deposition to Absolute Surface Coverages 309
29.2 Gold Evaporation Source 312
29.3 Ionization Gauge Measurement of Film Evaporation Rate . . . 314

29.4 Reusable Quartz Crystals for Film Thickness Measurement 314
29.5 Hybrid Thin Film Deposition Processes—Stable and Metastable Films 317
29.6 Sputter-Coating Inner Walls of Tubes 317
References 319

30 Infrared Spectroscopy 321
30.1 Infrared Reflection Absorption Spectrometer 321
30.2 IRAS Measurements at High Pressure 323
30.3 Internal Reflection IR Spectroscopy—Silicon 324
30.4 Internal Reflection IR Spectroscopy—Gallium Arsenide 327
30.5 Infrared Spectroscopy—Continuous Pumping of Detector Dewar 328
30.6 Rapid IR Spectrometer Purge After Cell Transfer—Using Rubber Sleeves 329
References 331

31 Calorimetric Heats of Adsorption—Single Crystals 333
31.1 Measurement of the Calorimetric Heat of Adsorption on Ultrathin Metal Single Crystals 333
31.2 Improved Adsorption Calorimeter for Single Crystals at 100–350 K 334
References 336

32 Surface Debye Temperature 337
32.1 Measuring the Surface Debye Temperature of a Single Crystal 337
References 339

33 Friction and Fracture 341
33.1 UHV Tribometer for Measuring the Coefficient of Friction 341
33.2 Pin-on-Disk Measurement—UHV 343
33.3 UHV Fracture Stage for Surface Analysis After Fracture 343
References 345

Part IV Thermal Control

34 Heating Samples 349
34.1 Electronic Temperature Programmer—Metal Crystals 349
34.2 Temperature Programming of Metal and Semiconductor Crystals 351

34.3 Mounting Nonweldable Crystals for Resistive Heating and Cooling 354
34.4 Strain-Free Single Crystal Mounting Azimuthal Motion 355
34.5 Heating Silicon Crystals and Temperature Measurements 356
34.6 Avoiding Extraneous Electrical Effects Owing to Heating Crystals 359
34.7 Electron Bombardment Crystal Heating 361
34.8 Indirect Sample Heating 363
34.9 Indirect Heating of Compound Semiconductors 365
34.10 Heating Design—Insulator Crystals 366
34.11 Cement Mounting—Semiconductor Crystals 368
34.12 Low-Stress Mount for Fragile Semiconductor Crystals 369
34.13 Radiation Heating of Crystals Through Glass Windows 371
34.14 Pyrolytic Graphite Heating Element for UHV 372
34.15 Heater—Paint-on Type 374
34.16 Mounting High-Temperature Tungsten Filaments 375
34.17 Rotatable Single Crystal 375
34.18 Radiation-Heated Evaporator 378
References 378

35 Cooling Samples 381
35.1 6 K—Cryogenic Crystal Holder 381
35.2 Cooling Crystals by Contact with a Thermal Reservoir 383
35.3 Cooling Samples on Manipulators—Thermal Conductivity Issues 383
35.4 Vacuum-Jacketed Cryogenic Manipulator Rod 386
35.5 Manipulator Component with Cryogenic Azimuthal Rotation 388
35.6 Cooling Using Direct Contact 389
35.7 Cooling Reservoir—Horizontal Manipulator 390
35.8 Cryogenic Connections 392
35.9 Sample Cooling Using Thermal Braid 392
35.10 Flexible Cooling Reservoir 394
35.11 Enhanced Cooling Using Liquid Nitrogen 394
35.12 Level Alarm-Liquid Nitrogen 396
35.13 Liquid Nitrogen Reservoir—Non-leaking 398
35.14 Cryogenic Cooling to Below 4 K—Photon Stimulated Desorption of Adsorbed He 399
35.15 Static Temperature Control by Mixing Gas Streams 401
35.16 Gas Thermal Switch 401
References 404

36 Temperature Measurements 405
36.1 Tungsten-Rhenium Thermocouples—Calibration Over a Wide Temperature Range 405
36.2 Measuring Temperatures of Hot Filaments 407
36.3 Pyrometric Measurement of Temperatures 409
36.4 Pyrometer Measurements Through Windows Coated Inadvertently with Variable-Thickness Thin Films 411
36.5 Calibration Point for Optical Pyrometer Used for Silicon 413
36.6 Control of Silicon Temperature Using Resistivity 415
References 417

Part V Delivery of Adsorbates to Surfaces

37 Gases 421
37.1 Design and Performance of Microcapillary Array Beam Doser 421
37.2 Gas Handling System for Array Beam Doser 423
37.3 Calibration and Use of Array Beam Doser 425
37.4 Sticking Coefficient and Surface Reactivity 426
37.5 Beam Doser Shutoff—Condensable Gases 428
37.6 Neutral Beam Intensity Measurement Using a Stagnation Detector 429
37.7 Low Deadspace Aperture Valve for Repetitive Gas Dosing 430
37.8 Gas Flow Regulation—Squeeze Valve 433
37.9 Retractable Beam Doser with Convenient On-Off Control . . . 434
References 435

38 Evaporation Sources 437
38.1 Degassing Evaporation Sources 437
38.2 Metal Evaporation Sources for Downward Evaporation 439
38.3 Ultralow Coverage Metal Evaporation 440
38.4 Congruent Evaporation of Multicomponent Materials 442
38.5 Evaporator for Eutectic-Forming Metals 444
38.6 Simple Lithium Metal Evaporation Source 444
38.7 Aluminum Evaporation Sources—Long Lived 446
38.8 Cr Evaporator Sources of Compact Design 448
38.9 Electron Beam Evaporator for Refractory Materials 449
38.10 Small Electron Beam Evaporator for Refractory Metals 451
38.11 Electron Beam Evaporator 453
38.12 Break-Seal Ampoule Doser 455
38.13 Cadmium Sulfide Evaporation Source 456
38.14 Arsenic Atom Source 456

38.15 Portable Microevaporator for Depositing Low Coverages of Single Atoms . . . 459
38.16 Nanoscale Templating of Close-Packed C_{60} Nanostructures . . . 460
38.17 Quantitative Molecular Beam Dosing of Slightly Volatile Organics . . . 460
38.18 Organic Doser . . . 464
38.19 Vapor Deposition of Organic Thin Films . . . 464
38.20 Evaporator for Organic Film Deposition . . . 465
References . . . 468

39 Ions . . . 471
39.1 Solid State Cesium Ion Gun Source . . . 471
39.2 Alkaline Earth Metal Ion Sources . . . 473
References . . . 475

40 Active Gases and Species . . . 477
40.1 High Flux Atomic Hydrogen Sources—Thermal . . . 477
40.2 Atomic Hydrogen Beam Source—Radio Frequency Driven . . . 480
40.3 Atomic Fluorine Source . . . 481
40.4 Alkali Metal Sources . . . 483
40.5 Thermal Source of Methyl Free Radicals . . . 485
40.6 Production, Storage, and Use of Ozone . . . 486
40.7 Ozone Generator and Molecular Beam Doser Source . . . 488
40.8 Detection of Ozone or Atomic Oxygen by Oxidation of Silver Films . . . 490
40.9 Purity of Ir and Pt Hot Filament Sources for Atomic Oxygen Production . . . 491
40.10 Pure Hydrogen Peroxide Doser for Ultrahigh Vacuum . . . 493
References . . . 494

41 Electrochemical Sources and Devices . . . 497
41.1 Electrochemical Sulfur Source . . . 497
41.2 Electrochemical Halogen Sources . . . 498
41.3 Electrochemical I_2 Doser . . . 501
41.4 Electrochemical Device Working in UHV . . . 502
References . . . 504

42 Gas Purification . . . 505
42.1 Gas Purification for Experiments at High Pressures . . . 505
42.2 Production and Purity Measurement for Extremely Pure He . . . 507
42.3 Purification of Gases by Cryogenic or Gettering Methods . . . 509

42.4 Gas Purification by Permeation Through Metals 511
42.5 O_2 Source—Solid State 513
42.6 Reusable Sample Holder for Hydrogen Permeation Studies 513
References. 514

43 Liquid Handling in UHV 517
43.1 Adding Liquid to Atomically Clean Surfaces 517
Reference 518

Part VI UHV Windows

44 Spectroscopic Windows. 521
44.1 Mounting Infrared Windows on UHV Systems 521
44.2 Windows for Vacuum UV Transmission into Ultrahigh Vacuum Systems 524
44.3 Construction of Be Windows for Ultrahigh Vacuum Use 526
44.4 Bakeable Aluminum Ultrahigh Vacuum Window 528
44.5 Metal Thin Foil Windows—Welding. 529
44.6 Preparation of Large-Area Si Single Crystal Windows 529
44.7 Strain-Free Optical Window Mounting. 532
References. 533

45 Observation Windows. 535
45.1 Shielded Observation Window 535
45.2 Heated Internal Window for Prevention of Film Deposition 536
45.3 UHV Glass Window Seal—Low Optical Distortion. 537
45.4 Zero-Length Window Assembly 539
References. 540

Part VII Surface Preparation Methods

46 Cleaning Metal and Semiconductor Crystals—Examples 543
46.1 Surface Segregation and the Cleaning of Metal Single Crystals. 543
46.2 Chemical Method to Measure and Remove Carbon from Pd 546
46.3 Surface Cleaning Procedures—Silicon 548
46.4 Preparation of Atomically Clean Tungsten Single Crystals . . . 551
References. 551

Part VIII High-Area Solids

47 Infrared Cells 555
47.1 Infrared Cell for Adsorption Studies on Supported Catalysts 555
47.2 Wide-Temperature-Range IR Cell for High-Area Solids 557
47.3 Measurements of Diffusion Through Powders Using Transmission Infrared Spectroscopy 560
47.4 Using Transmission Infrared Spectroscopy to Witness Diffusion into Core-Shell Structures 562
47.5 Diffusion in Powders as Measured by Transmission IR Spectroscopy 562
47.6 Transmission IR Spectroscopy Through Opaque Materials . . . 564
References 567

48 Adsorption/Desorption—Thermal 569
48.1 Adsorption and Desorption from High-Area Solids 569
48.2 Thermal Desorption from High Area Materials 571
48.3 Microcalorimetric Studies of Adsorption Heat on Powders . . . 574
48.4 Chemical Vapor Synthesis of Oxide Nanoparticles 576
References 577

Part IX Safety

49 Protecting the Vacuum System 581
49.1 Delay Circuit for Turbopumping Protection Against Vacuum Loss from Power Interruptions 581
49.2 Fast-Closing Beam Valve for UHV Chamber Protection 583
49.3 Safety System for Oil Diffusion-Pumped UHV Systems 584
49.4 Folding Linear Magnetic Translator 586
References 587

50 Protecting Personnel 589
50.1 Electrical Shocks in the Laboratory 589
50.2 Accidental Electrical Charging from Ionization Gauge 590
Reference 592

Appendix A 593

Appendix B 597

Index 643

Part I
Vacuum System Technology

Chapter 1
Motion in Vacuum

1.1 Crystal Manipulator with Six Degrees of Motional Freedom

This design [1] is shown in two parts to separate the azimuthal motion (Fig. 1.1) device from the tilt motion device (Fig. 1.2). A central rod extends from a typical *x*, *y*, *z*-plus rotary motion manipulator. The azimuthal and tilt motion (pushing and pulling) devices are connected to the same central rod and are free to slide up and down on this rod. The central rod is slotted to keep the crystal mount linking fittings from rotating with respect to the rod. The two push-and-pull actuators permit the central rod that passes through them to rotate in two ball-bearing (BB) mounts. Azimuthal crystal motion is transmitted by the push-and-pull actuator, which, through two coupled universal joints, turns the crystal mounting platform on its own ball bearing mount behind. Tilt motion is transmitted by the push-and-pull actuator, which tilts the crystal mounting platform about the axis of the hexagonal nut shown in the Tilt Motion diagram. The degrees of freedom for motion at various points are shown by double-headed arrows. This design does not result in a decoupling of tilt motion from other degrees of freedom, which is a disadvantage in some cases, but the design has been used for more than ten years with success. A more recent design uses a circular slot to guide a pin in the crystal tilt mechanism that eliminates the crystal translational motion associated with the tilt motion. It is of interest to note that in this design, ordinary unlubricated ball bearings are used in ultrahigh vacuum with success and without seizure or binding.

The crystal is mounted on electrical and thermal isolation standoffs on the crystal mounting platform and may be heated by electron bombardment or by ohmic heating. Various thermocouples may be connected to the crystal, and cooling to about 40 K is achieved using a copper braid connected between the crystal mounting assembly and a liquid He cryostat. Appropriate provisions are made to shield the mounting assembly from emitted radiation generated during crystal heating so that the desorption of impurities from the mounting is minimized.

© Springer International Publishing Switzerland 2015

J.T. Yates Jr., *Experimental Innovations in Surface Science*,
DOI 10.1007/978-3-319-17668-0_1

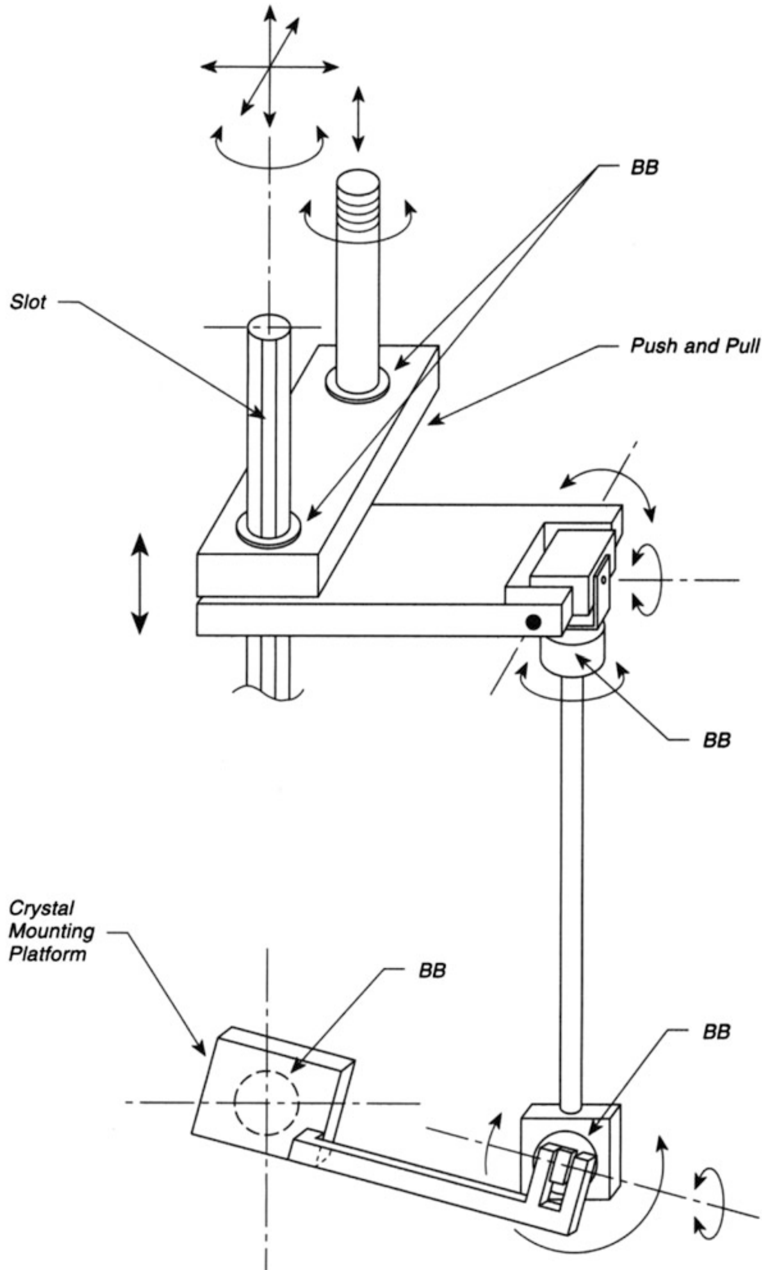

Fig. 1.1 Azimuthal motion

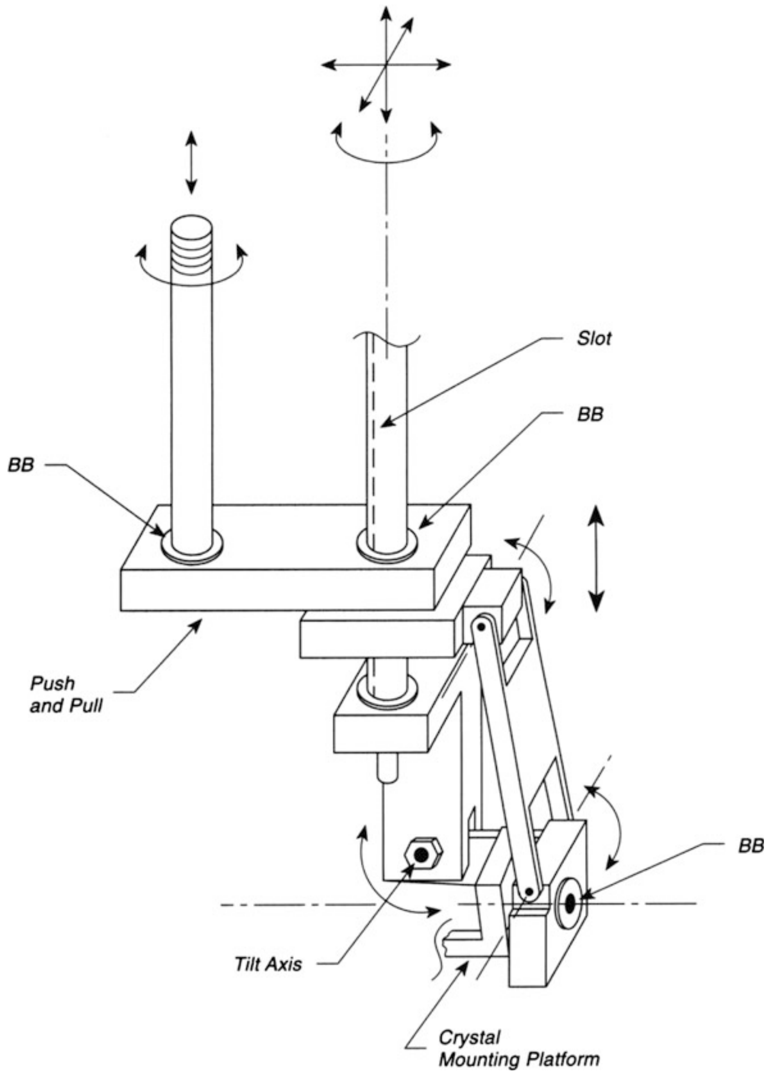

Fig. 1.2 Tilt motion

Because of the complexity of the design of a device of this sort, it is recommended that a working model first be constructed before final design parameters are set.

Many other designs allowing cooled crystals to be azimuthally rotated in ultrahigh vacuum have been published [2–12] and some are treated in this book.

1.2 Rotation in Ultrahigh Vacuum

The provision for rotation of samples in ultrahigh vacuum (UHV) is centrally import ant in most investigations, since the analytical facilities in most research chambers are located on different azimuths from the center line of the vacuum chamber. It is often desired to provide other motions, as well as heating and cooling of the crystal, but this section is concerned only with axial rotation. Historically, the problem was addressed in the first sixty inch cyclotron by Wilson [13], long before ultrahigh vacuum was achieved in metal systems. It is of interest to note that the differential pumping method employed by Wilson is still fundamentally important to UHV technology.

Figure 1.3 shows the Wilson seal as currently used in ultrahigh vacuum to rotate a long cylindrical cryostat on which the crystal is mounted using ceramic feed-throughs [14]. Two Viton gaskets, with a hole cut smaller than the rotary seal tube, are held in place in a brass housing that bolts onto a specially shaped lower Conflat flange having an upward-facing conical section to push the Viton gasket upward as shown. An assembly plate, below the upper Viton seal, also has an upward-directed conical support section. These two Viton seals make a strained contact with the polished-mirror-finished (600 grit) outer portion of the rotary seal, and provide the vacuum tight joint. To prevent significant leakage through the lower Viton seal gasket, the region between the two gaskets is differentially pumped with a rotary pump or a small ion pump. The cryostat tube, welded to a mini-Conflat flange is bolted to a mini-Conflat knife-edge sealing surface on top of the rotary seal. Two stabilizer bearings prevent wobbling of the central components; these may be made of phosphor bronze [14], Teflon, or they may even be ball bearings. Wires for heating the sample electrically, and thermocouple wires conveniently thread down the cryostat tube and exit from the bottom. As is obvious from the drawing, the bottom Con-flat flange must be bolted on from below, meaning that a flanged extension tube from the chamber flange must be employed under the device. A handle added to the flange of the rotary seal (not shown) is helpful in applying torque, and the upper section of the brass housing is divided into degrees of arc for accurate angular positioning, using the pointer. Bakeout temperatures of 150 °C are nondamaging to the Viton seals. For higher temperature bakeout, KALREZ per-fluoro elastomer might be used [15]. The gaskets can most conveniently be made by use of a homemade punching jig to accurately locate and cut the center hole to size as well as to place the six radial holes through which pass the bolts clamping the assembly plates down on the Viton. A pressure rise of about 1×10^{-10} Torr was observed on slow rotation.

The seal in Fig. 1.3 is designed for liquid nitrogen cooling, and in order to achieve long cryogenic storage time, a 1-L storage Dewar with a hole in its bottom was fabricated [16]. To make a liquid nitrogen seal each day with the cryostat tube, a platform support for the Dewar is covered with some cotton wool that is saturated with water; sufficient ice forms to make an excellent seal. Ice formation under the support platform by condensation from the atmosphere is a problem that can be

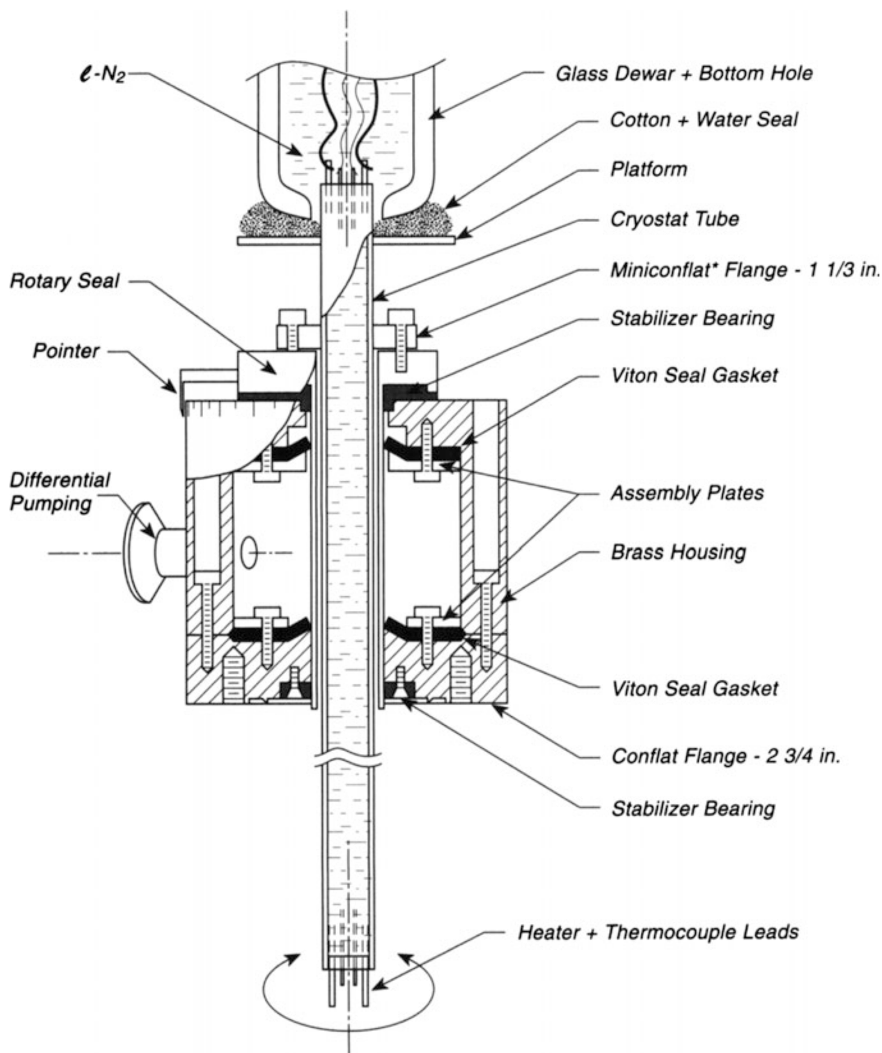

Fig. 1.3 Differentially pumped rotary seal—flat Viton gaskets

reduced by using a heater tape around the brass housing and possibly a fan to evaporate liquid water runoff. The apparatus can be inefficiently used with the gaseous discharge from a liquid He Dewar to achieve temperatures near 30 K, and the momentary transfer of liquid He brings the temperature to 15 K [14, 16]. Another rotary seal based on this principle has been reported [17].

Figure 1.4 shows a second design for a rotary seal in which O-rings are employed as the sealing elements, with one stage of differential pumping between the O-rings [18]. A polished rotary-seal tube rotates against the slightly compressed

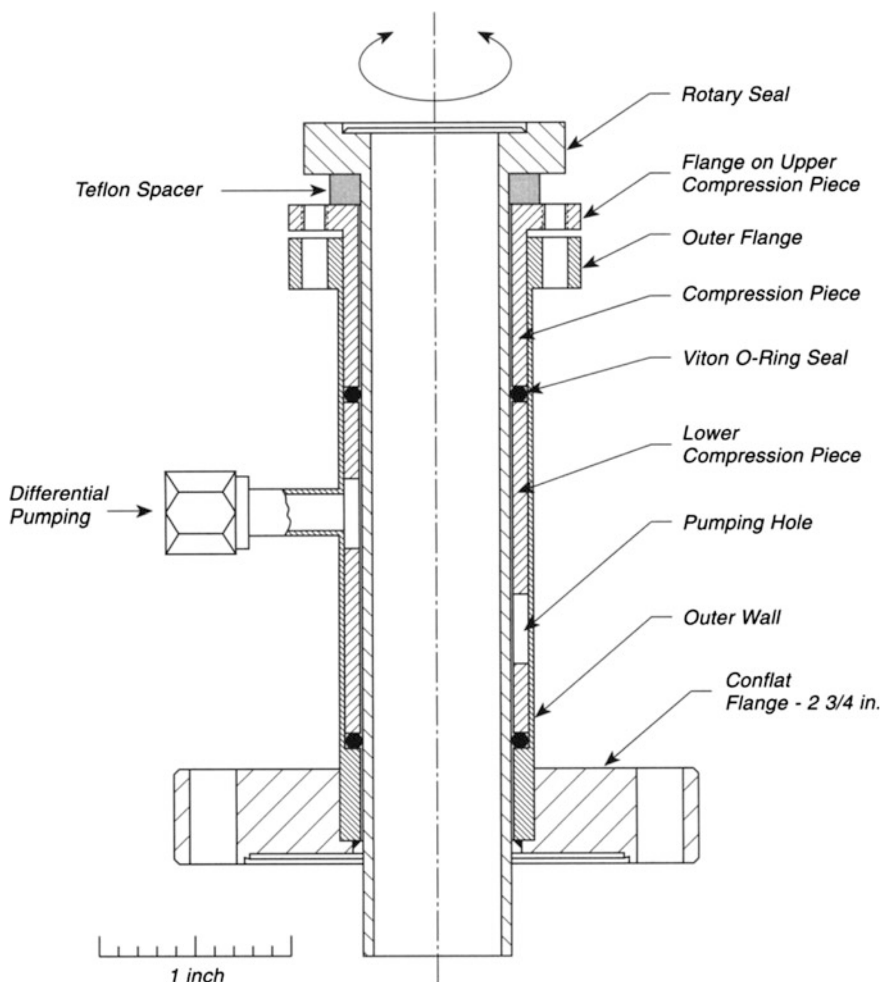

Fig. 1.4 Differentially pumped rotary seal—Viton O-ring

Viton O-rings, which are held in place by tightening the flange on the compression pieces, which are made of copper and which slide in between the outer wall and the rotary seal. These two compression pieces contain a number of holes to provide a pumping opportunity between the inside and outside of the cylindrical pieces. The O-rings are lubricated with a trace of graphite powder. A different lubricant reported to be satisfactory for Viton O-rings consists of a mixture of graphite powder and Santovac 5 diffusion pump oil (a polyfluo-roether) [19]. Differential pumping with a rotary pump or a small ion pump is used for the inner section holding the lower compression piece. A Teflon spacer at the top supplies a bearing surface for the rotary seal. Inside the rotary seal, a cryostat tube similar to that in Fig. 1.3 may be inserted. A pressure rise of about 3×10^{-11} Torr was observed on rotation [18].

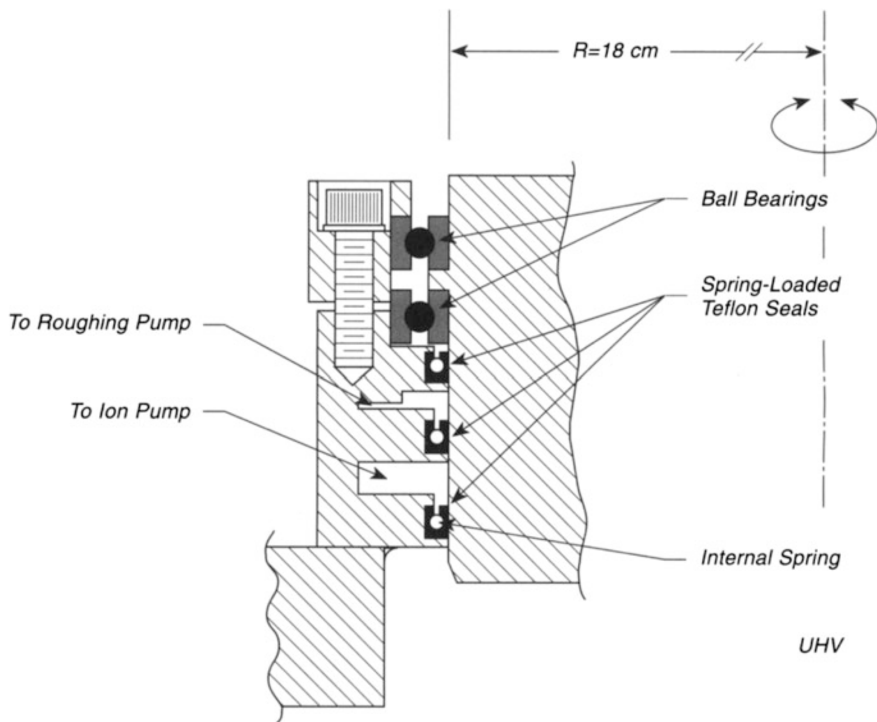

Fig. 1.5 Differentially pumped rotary seal—spring-loaded Teflon seals spring-loaded Teflon

Rotation using large differentially pumped seals is often employed to move heavy instruments inside the vacuum system, with a large-diameter rotating plate being moved through 360°. Auerbach [20] and his colleagues first reported the use of spring-loaded Teflon seals in this role in ultrahigh vacuum systems. Ordinary Teflon has a high thermal expansion coefficient, poor creep characteristics, and high permeability in static systems, so that differential pumping is required, along with a mechanical trick in which a spring is embedded inside the Teflon ring [21] to compensate for creep. These seals can also be obtained with Teflon filled with MoS2 lubricant particles for ultimate lubrication of an already lubricious material [20]. However, the filled polymer has a higher gas permeability than pure Teflon. In Fig. 1.5, a diagram of a double-stage differentially pumped Teflon seal is shown [20]. The large-diameter rotating plate is centered with two ball bearings, which have been split at the inner and outer races to prevent distortion and binding owing to differences in expansion coefficient between the bearings and the stainless steel. Beneath the ball bearings are three spring-loaded Teflon seals. The space between the upper two seals is pumped with a rotary pump, while a small ion pump [11 L/s]

pumps the space above the inner seal and the center seal. The system is baked to 200 °C, and the pressure rise upon rotation is less than 10^{-10} Torr and usually unobservable. The pressure at the small ion pump is in the 10^{-8} Torr range. The estimated gas leakage under static conditions is 10^{-13} Torr L/s [20]. Seals based on this principle are now commercially available. Others have reported the use of this type of seal for rotary manipulators [22–24].

Sometimes rapid rotation in ultrahigh vacuum is desired, where rather massive components must turn in bearings. Figure 1.6 shows a magnetically driven rotation

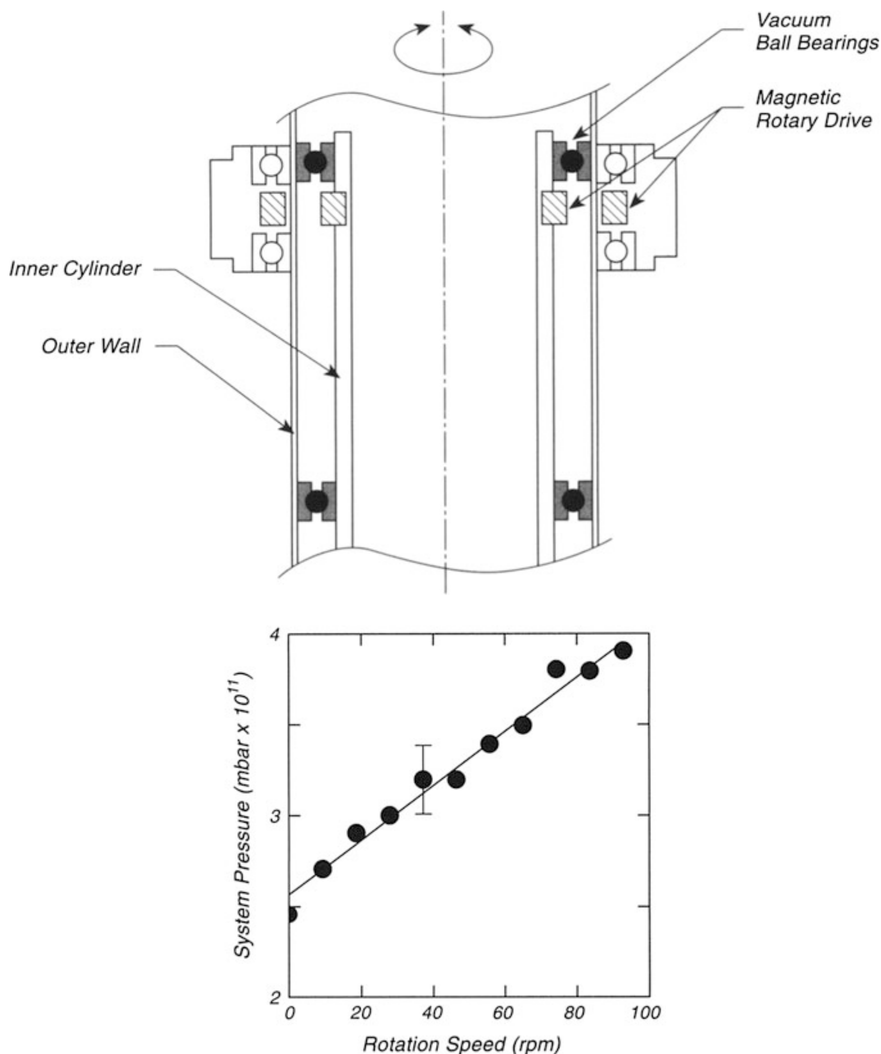

Fig. 1.6 Internal ball bearings

device that drives an inner cylinder suspended in vacuum. Two vacuum ball bearings are used at either end of the inner cylinder. These are ordinary ball bearings that are unlubricated, and they contain large cross section ball races. These bearings are routinely baked at 220 °C, and proved satisfactory for 18 months, having undergone 5×10^6 rotations without any degradation in performance. The evolution of gases is proportional to the rotation speed as shown in the lower part of Fig. 1.6, and the rise in total pressure is about 2×10^{-11} mbar at 100 rpm. Most of the gas evolution was due to H_2O and H_2 liberation [25].

Other designs for achieving independent rotational motions around two axes are described in the literature [26–28]. Reference [26] describes an electrical readout for the angular motions accurate to 0.5° and based on motion of a wire-wound potentiometer.

1.3 Crystal Positioning Using Capacitance

The ability to position a single crystal precisely can be useful in many measurement procedures in ultrahigh vacuum. This is a problem when the positioning must be done at accuracies beyond the capability of micrometer drives on manipulators. Factors such as thermal expansion effects, backlash in precision screw drives, and vibration interfere with accurate positioning methods.

The topic of capacitive positioning of a single crystal is treated in the context of locating the crystal accurately in front of a mass spectrometer that is housed in an apertured shield for accurate and reproducible temperature programmed desorption measurements [29]. This connects to the topic on p. 259.

Figure 1.7a shows a glass shield [29, 30] mounted over a quadrupole mass spectrometer ionization source. A Ta ring is rigidly supported near the aperture of the shield and acts as the capacitive pickup terminal. The capacitance is of the order of 0.1 pF for a 1-mm spacing between the Ta ring and the crystal. The capacitance measuring circuit, to be described below, can measure capacitance changes in the range of 0.1 %, meaning that the crystal can be positioned to 1 μm reproducibility, corresponding to an error in the measurement of the desorption rate from the crystal of only about 0.05 %. Small tilting of the crystal will reduce this reproducibility, and the demonstrated reproducibility of actual measurements was better than 1 % [30].

Figure 1.7b shows a slight variation on the design. Here, an Ag ring is employed as the capacitance pickup terminal, and it is fixed on the end of the glass shield as shown. The Ag plate, (12 mm OD; 6 mm ID, 1 mm thick) is held in place by use of 3 Ta wires that are spotwelded to the plate and wound around three glass eyelets on the shield. The Ag plate is connected through a Kapton-insulated and shielded lead to a BNC connector that exits the vacuum system. To avoid static charging, the glass shield is surrounded by a very thin grounded metal mesh [31]. An Aquadag [32] (colloidal graphite) coating can also be used for this purpose, or a metal shield like that shown on p. 260 may be used. The spacing employed between the crystal

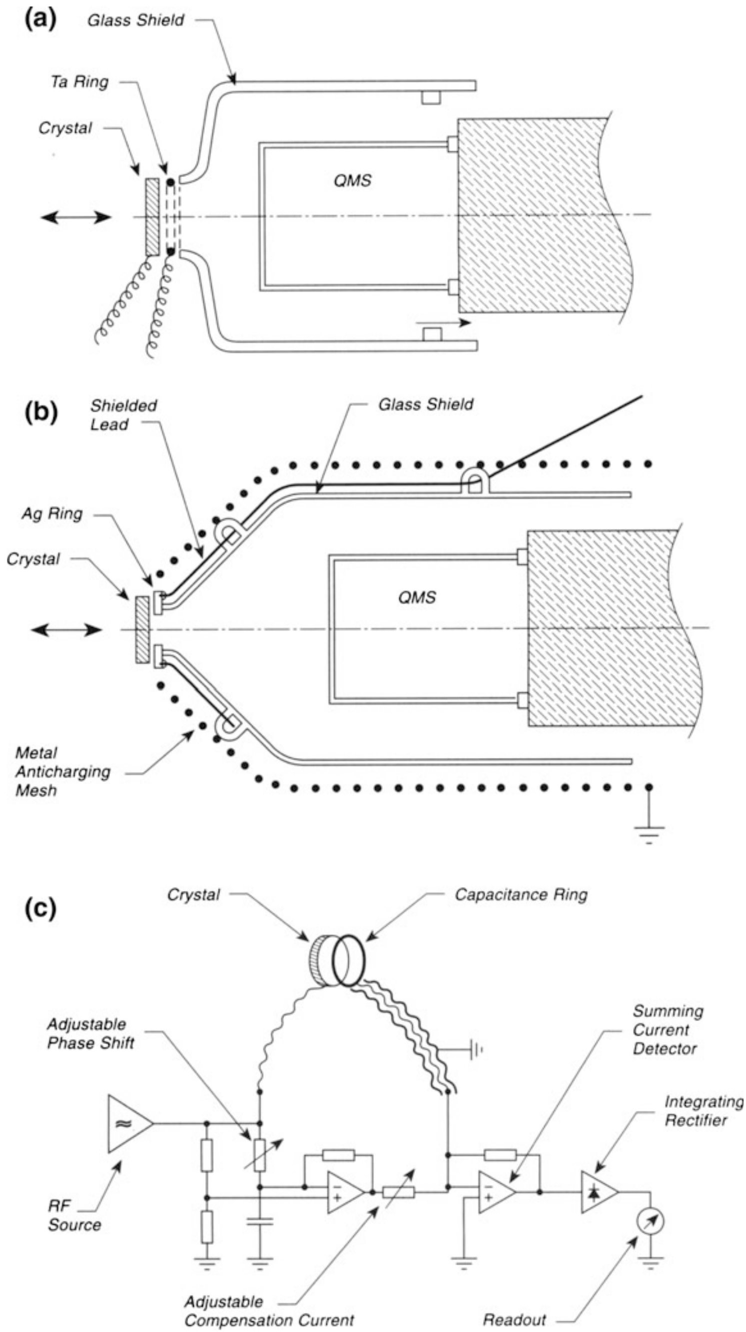

Fig. 1.7 Crystal positioning using capacitance. **a** Ring capacitance. **b** Affixed capacitance. **c** Capacitance measurement—block diagram

and the aperture is reported to be only 10 μm in this design, and this maybe reproduced to 1 μm [31].

The capacitance measuring circuit [30, 31] is shown in schematic block diagram form in Fig. 1.7c. It is a phase-shifted bridge circuit, working at 20 kHz [30]. A sinusoidal signal (20 Vpp) is applied to the crystal and the capacitive pickup is made to the ring aperture, since the crystal is often connected to unshielded leads and electronics outside of the vacuum system. The detection system is used as a simple lock-in amplifier.

1.4 UHV Rotary Manipulator with Arcsec Resolution

In some cases, the use of a commercial crystal manipulator is inappropriate because of the poor resolution and reproducibility inherent in these designs. For certain cases, such as in X-ray standing wave spectroscopy (XSW), a high-precision rotary stage is needed [33].

Figure 1.8a shows a side view of an ultrahigh vacuum system containing both a coarse and a fine adjustment for rotating a single crystal about the horizontal axis. The crystal holder is mounted on a platform such that its surface is in a plane that contains the axis of the shaft that holds the crystal holder. This shaft, made of precision-ground 304 stainless steel, rotates and translates inside of two linear/rotary ball bearings that are mounted on the top flange. With a conventional rotary feedthrough and rotary manipulator contacted to the shaft by a U-joint, coarse sample manipulation in 7 arcsec increments can be achieved with a stepping motor/speed reducer.

Figure 1.8b shows the principle of the high-precision rotary device, where the shaft may be engaged by a lever, and where precise variations in the position of the top of the shaft may be used to make azimuthal rotations to better than arcsec accuracy and precision.

Figure 1.8c shows the detailed structure of the high-precision rotary device coupled to the upper flange by a bellows. The rotary feedthrough drives an actuating lever that pushes a pushrod and the lower clutch body against two springs. When the force on the pushrod is released, the upper and lower clutch bodies grab the shaft. The rotation of the shaft about its axis is determined by the setting of the upper micrometer which is driven by a stepping motor. A weight is used to maintain tension and contact between the upper micrometer and the movable flange, and incremental motion of 0.88 arcsec is achieved with a lever arm of 292 mm length and a micrometer displacement of 1.25×10^{-3} mm [33].

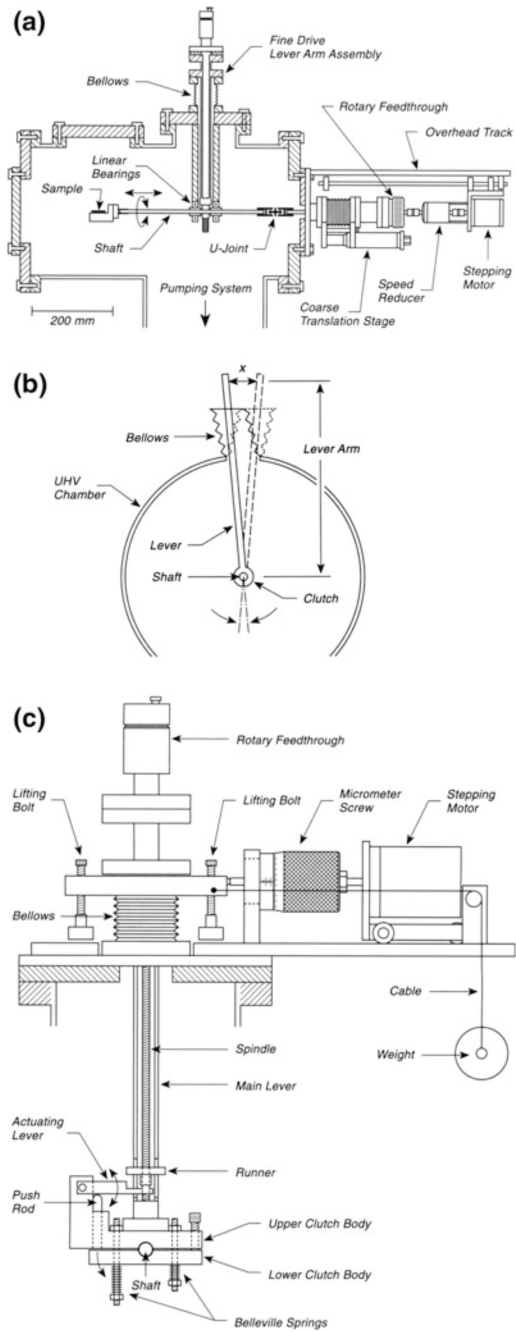

Fig. 1.8 Rotary motion—arcsec resolution. **a** Side view—coarse and fine adjustments. **b** Schematic—fine angular adjustment. **c** Detail—fine angular adjustment

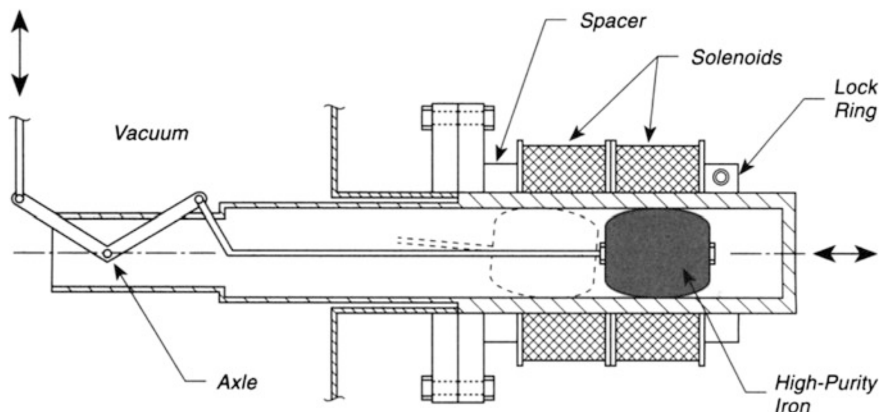

Fig. 1.9 Linear motion actuator

1.5 Solenoid Driven Linear Motion Device

A rapid linear motion inside an ultrahigh vacuum system may be achieved by using a solenoid-power-driven actuator like that shown in Fig. 1.9. All moving parts are inside the vacuum system, and the external solenoids do not require vacuum encapsulation. The actuator is a barrel-shaped plunger made of high-purity iron sized to make a loose fit inside the stainless steel tube. In this device a stroke of 3 cm was achieved. Each solenoid consists of 1400 turns of #24 magnet wire wound on an aluminum spool and giving a dc resistance of 14 Ω. Short electrical pulses are used on either solenoid to move the actuator in or out; the current is then turned off to prevent overheating or stray magnetic fields. In operation, the actuator will tilt as shown in the drawing when it moves inward. Measurements made on the actuator show that a torque of 500 g cm can be achieved at the internal pivot point. The closing time was measured to be 50 ms. The original paper [34] also provides a design for either an automatic or manual actuator circuit.

The solenoids are removed for system bakeout by releasing the lock ring on the back end. A similar magnetically driven shutter assembly using a Nd Fe-B magnetic encapsulated slug and an external ceramic-ring magnet has also been described [35].

1.6 An Inexpensive Linear Motion Device

A homemade linear motion device may be constructed quite easily from an inexpensive machinist's device as shown in Fig. 1.10. The vise is made of high-grade gray iron and the jaws as received from the manufacturer are precision ground for squareness and parallelism to ±0.0001 cm per cm. The hardened jaw pieces are

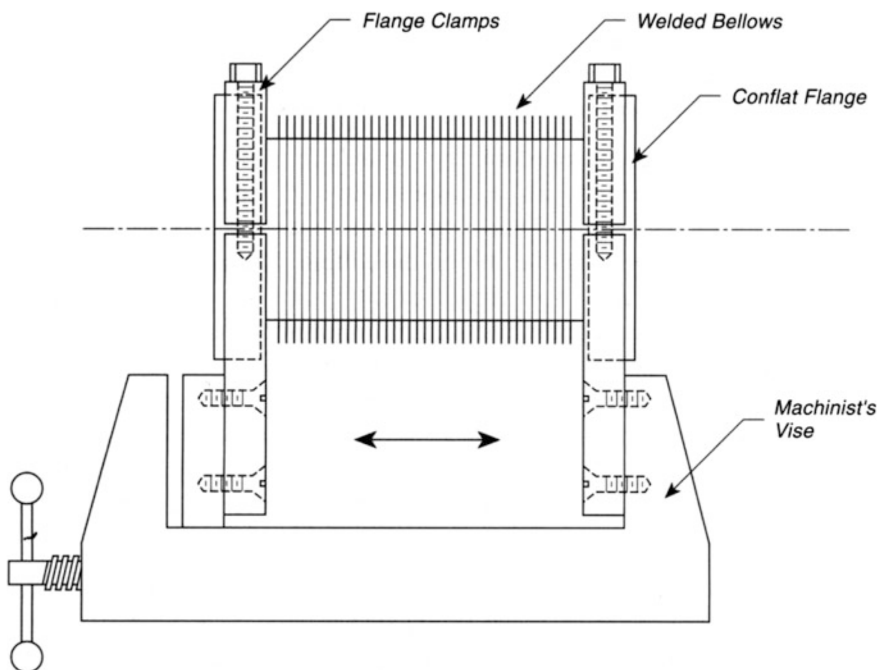

Fig. 1.10 Linear translation device

removed from the vise and replaced with aluminum clamps that have an inner lip machined in them to prevent the Conflat flanges from slipping through. These clamps are mounted on the vise and then tightened around the flanges holding the welded bellows. Machinist's vises giving up to 7.5 cm linear travel are available [36] at a cost of about $200–$300, and this device, while heavy, gives smooth and repeatable translation. The precise position can be determined using a vernier caliper between the clamps, or repeatable positions can be established by using simple spacer bars. The overall price is about a quarter that of a comparable commercial bellows manipulator [37].

1.7 Translating Auger Spectrometer

It is sometimes appropriate to move an Auger spectrometer or other large instrument over a large distance. This may be done in a conventional fashion by using a large-bellows translation device, which is both heavy and expensive. An alternate method for achieving the same result is to employ internal linear ball bearings and to translate with a small bellows-type linear translator. This requires that the electrical connections to the instrument be flexible over rather long extension distances.

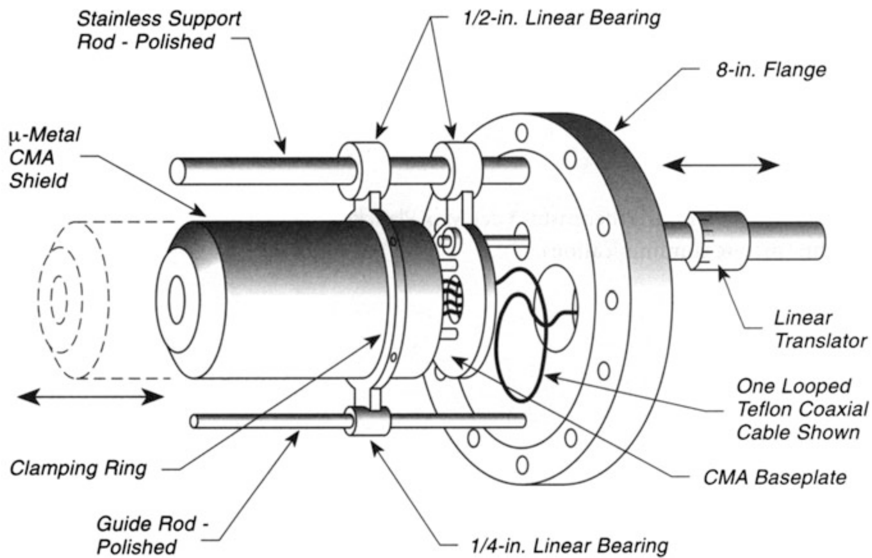

Fig. 1.11 Translating CMA auger spectrometer

Figure 1.11 shows a design [38] for translating a cylindrical mirror analyzer (CMA) Auger spectrometer over a 14-cm distance. This is done using a l/2-in.-diameter linear ball bearing [39] that slides on a polished stainless support rod at the top, and is guided along a 1/4-in.-diameter rod-linear bearing assembly on the bottom. The use of the smaller rod on the bottom allows the system to have a little flexibility to prevent seizure due to slight misalignment. The first upper support bushing is clamped with a stainless steel ring to the μ-metal shield of the CMA spectrometer using three set screws at 120° to each other. The second support bearing is attached to a baseplate that rigidly supports the CMA by rods. The entire assembly is mounted on an 8-in.-diameter Conflat flange. Translation is achieved using a small linear translator, mounted on a small flange, which pushes and pulls on the baseplate at a point close to the upper support rod to avoid torque on the upper bushing during motion.

The flexible electrical connecting wires are looped to give the needed extension and are made of Teflon-coated coaxial cable [40]. The coaxial cable is made UHV compatible by stripping off the outer cover, leaving the cable shield, and contributes no significant outgassing problem.

Another design for a translating Auger spectrometer may be found in [41]. In this case, the miniature instrument (electron optics 30 mm diameter; 45 mm length) is held on a single linear translator mounted on a 2 3/4-in.-diameter Conflat flange. The resolution of this instrument is $R = AE/E_o = 1.5\ \%$ [41].

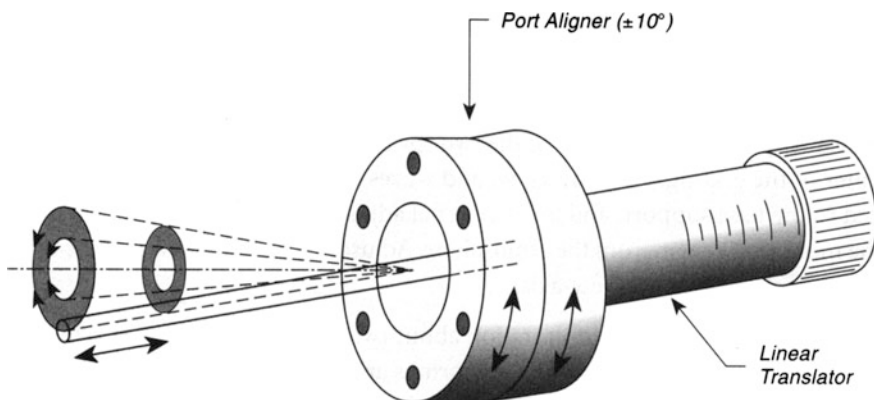

Fig. 1.12 Simple multiple motion

1.8 Simple Multiple Motion Manipulator

The provision of various degrees of motional freedom for samples, apertures, etc., in ultrahigh vacuum systems is often accomplished with complex manipulators such as that shown on p. 3. When complex motion is required and the measurement of the position of the sample is not required, more simple devices are possible. In Fig. 1.12, a device involving the combination of a port aligner and a linear translator is used to give multiple degrees of freedom for a rod. The port aligner allows ±10° motion within a solid cone, which is schematically shaded. The linear translator permits motion back and forth within this solid cone [42].

1.9 Simple Device for Small Rotations in Ultrahigh Vacuum—Grating Application

The rotation of gratings and other optical components through small angles in ultra high vacuum for the purpose of alignment is not straightforward. This device permits the adjustment of a grating through an angular range of less than 1° with ease [43]. Adjustments in one direction or in two are possible, depending on the structure used.

Figure 1.13a shows a side view of a device permitting one-dimensional rotation about the x-axis. Two planar broad-leaf springs are connected to a base support, and to a movable platform. A plane extrapolation of the two springs intercepts at the origin, *o,* which is the center of the grating. Here the *x*-, *y*-, and z-axes are defined. An adjustment rod is connected to the base support, and to an external adjustment screw. Bellows, as shown, isolate the mounting system from the atmosphere. Adjustment of the screw in the z-direction rotates the grating about the x-axis.

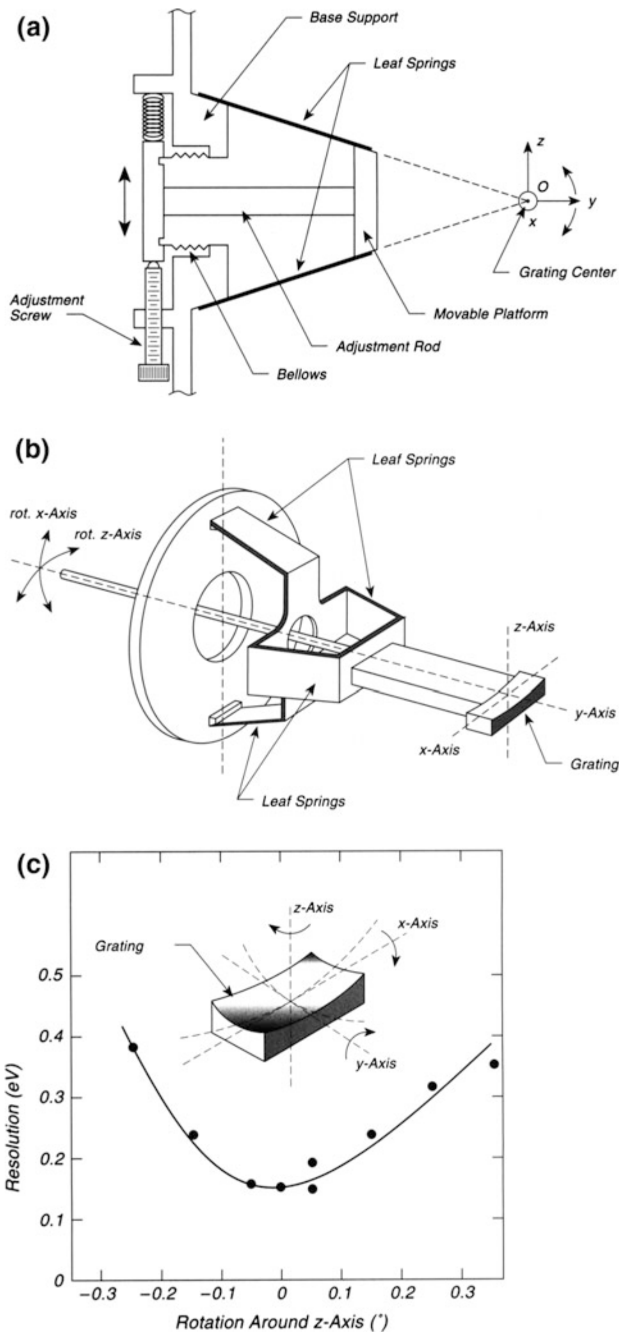

Fig. 1.13 Small rotations in UHV. **a** One-axis device. **b** Two-axis device. **c** Result—Z rotation

The principle can be extended to rotation about two axes, as shown in the schematic (Fig. 1.13b). Here, two sets of orthogonal leaf springs are used, and screws for rotation of the adjustment rod operate in the z- and x-directions, leading to grating rotation about the x- and z-axis.

Figure 1.13c shows the use of the two-axis device for optimization of the resolution of a UHV spectrometer. In this case, an angular resolution of less than 0.1° was achieved for optimum spectrometer resolution adjustment [43].

1.10 Turntable Rotation in Ultrahigh Vacuum

Figure 1.14 shows a turntable for the rotation of heavy equipment in UHV with high angular precision and repeatability, and without the need for coated or lubricated bearings. Rotation is achieved using a rotary feedthrough to move the axle of the turntable. The flat bottom of the turntable rests on three spheres made of a metal carbide mounted in a V-groove. The spheres are of 10-mm diameter and the three define the plane on which the turnable rotates. The mechanical stability is excellent, and several tens of kilograms may be supported. In addition, friction is low in ultrahigh vacuum. The danger of the spheres coming close to each other is small, especially when forward and backward motion is used alternatively. The system is uninfluenced by bakeouts at 200 °C [44].

1.11 Small Motions in UHV Systems Using Shape Memory Effect Alloys

An unusual phenomenon present in certain alloys may be used to make small motions in ultrahigh vacuum systems by the application of a small heating current to a helix of the alloy material. The shape memory effect (SME) is so named

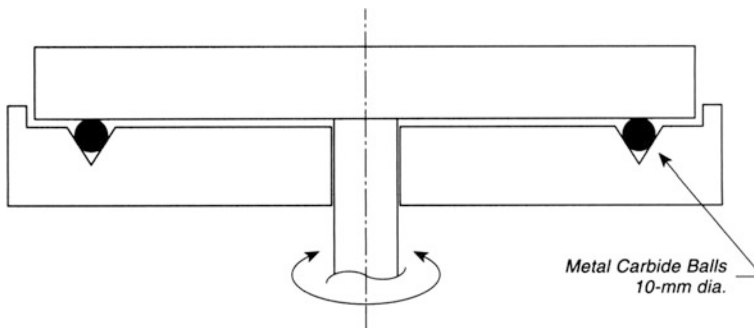

Fig. 1.14 Rotary platform

because shape memory alloy (SMA) wire helixes can be made to change from the "deformed" cold shape to the "preferred" hot shape reversibly. The restoring force. is quite large and may be used to achieve small motions as illustrated in the two examples shown here. There are numerous alloys that exhibit the SME, and a favorite SMA for UHV applications is NiTi. This material is easily formed into the hot shape and has a convenient transformation temperature. The shape change is caused by a transformation from a martensitic to an austenitic phase, with the high temperature austenitic material being produced at about 60 °C, while the reverse transformation occurs at about 30 °C. Deformations producing less that 2 % local strain in the martensitic state can be reversed by heating through the transformation temperature. By setting the hot shape in a helical wire it is possible to get extensions of several hundred percent without exceeding this strain limit.

Figure 1.15a shows a shutter arrangement made with a 0.45-mm-diameter NiTi wire [45]. The hot shape of the left-hand helix was set by winding it on a cylindrical mandrel and then heating to 500 °C for 1 h in a vacuum annealing oven to prevent oxidation. The helix was then stretched between two stainless steel posts and pinch clamped to each. The helix was therefore stretched from its preferred hot shape. Upon heating with a current of 2.5 A, the left segment of the helix contracts to its preferred hot shape, moving the attached shutter to the left in a period of less than 0.5 s. This operation stretches the right-hand cold helix beyond its plastic limit, which means that it has little restoring force. Thus, the heating current can be turned off after the shutter has moved to the left. To restore the shutter to its original position, one heats the right-hand portion of the helix.

The effect of bakeouts at 215 °C on a severely stretched (300 %) helix was tested over a 24-h period, and it was found that this treatment did not affect the hot shape memory [45].

A second example in which the SME is used to open and close a clamp on a manipulator is shown in Fig. 1.15b [46]. Here, the jaws of the clamp are opened when the NiTi SMA wire is heated. The particular wire [47] used here is of small diameter (0.15 mm) and has been treated in manufacture to exhibit a shorter length at high temperature and a longer length at low temperature. For strong clamping, four such wires were braided together and connected to a copper wire by a simple overhand knot above the ceramic insulator tube, which passes through the back end of the stationary upper jaw. The other end of the wire bundle is grounded through the jaw. A restoring force to close the jaws when the heating current is off is supplied by a spring mounted on a screw that is fixed in the upper jaw but that does not touch the lower jaw. When the lower jaw opens, this spring is compressed. Electrical heating to a wire temperature of 115 °C causes the jaws of the clamp to open up by about 2 mm when 0.21 A is passed through the four wires in vacuum. If the current is taken too high (0.23 A in vacuum), the annealing temperature will be exceeded, and the SMA wires will lose their pulling ability. The reader is referred to texts on the SME for more details [48, 49]. Also engineering studies of SME test structures are described in [50].

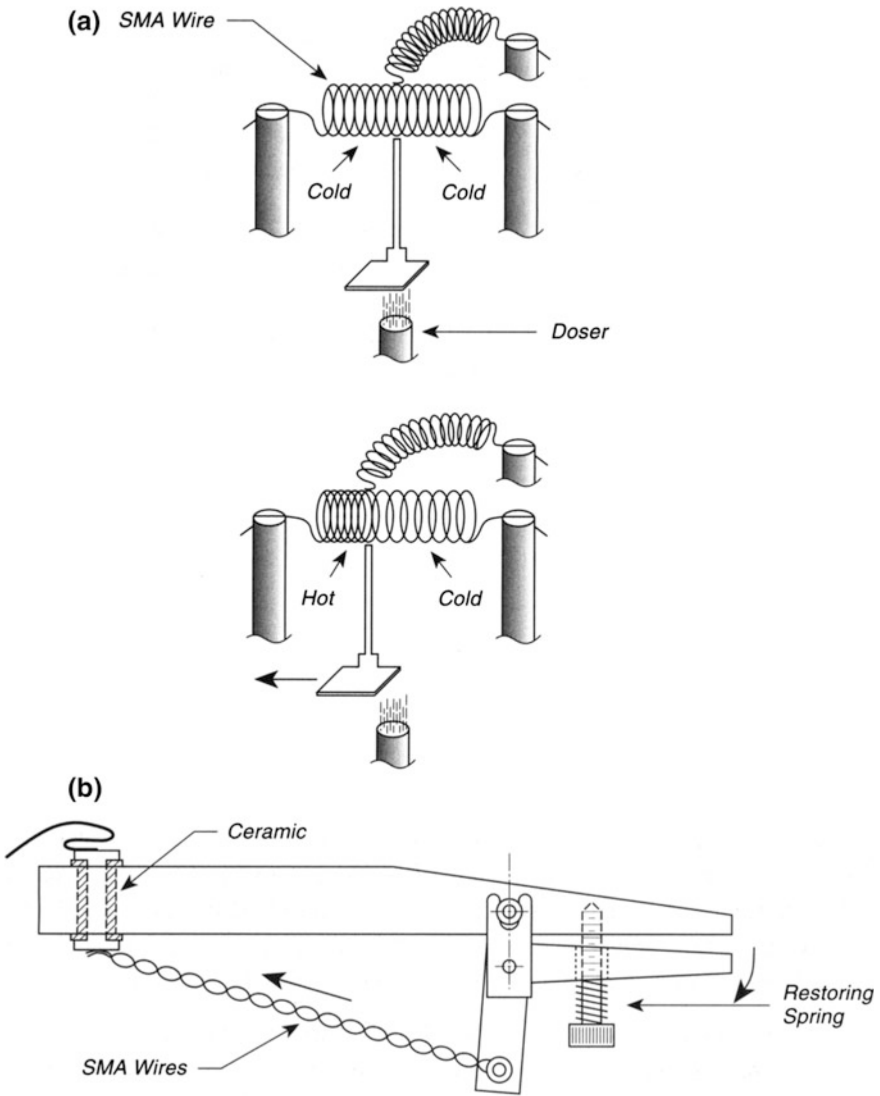

Fig. 1.15 Small motions using shape memory effect. **a** Shape Memory effect—Shutter. **b** shape memory effect—Clamp

1.12 Rotary Shutter Device Driven by Magnetic Eddy Current

The use of magnetic eddy currents in an ultrahigh vacuum system to drive a low friction shutter is illustrated in Fig. 1.16. The eddy current magnet, shown without its housing in the upper part of the Figure, drives the stepped copper rotor at

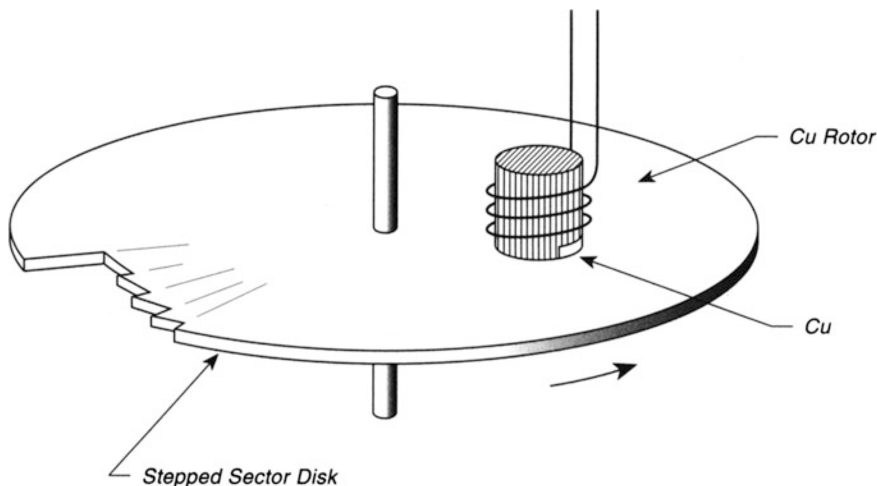

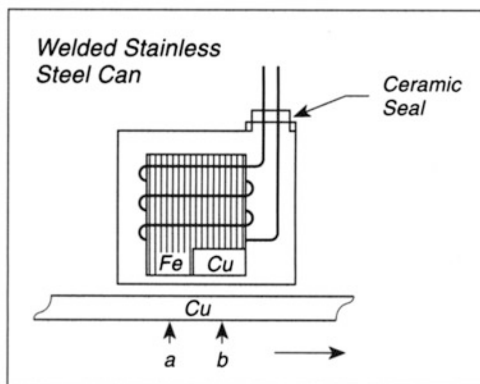

Fig. 1.16 Eddy current rotor

300 rpm when ball bearings are used, and 60-Hz power is applied to the coil. The copper disk is 0.8 mm in thickness. The stepped openings on the perimeter permit the operator to vary the open duty cycle for evaporations through the openings from an evaporation source mounted above the disk; operation near the perimeter gives larger fractional transmission than with the substrate placed more toward the axis.

The lower end of the iron cylinder (5 cm dia. × 7.5 cm long) contains a semi-circular piece of high-purity copper, 0.6 cm thick. It is wrapped with 150 turns of #14 (1.6 mm dia.) magnet wire with Formvar insulation. This is housed in a stainless steel can to prevent outgassing, and the can is welded shut using the ceramic feedthrough for electrical contact to the coil inside.

The device works on the basis of the lag of the magnetic field at position b from that at position a. This means that when the magnetic field is maximized during the

cycle at a, the eddy currents centered at b will also be maximized. A force on the volume element of the copper disk near *a* will be in the direction from *a* to *b*, and the disk will move. One quarter cycle later, the magnetic field at *b* will interact with the eddy currents centered at *a* and the force is again in the direction from *a* to *b*. During the next half cycle, both the magnetic field and eddy current directions are reversed, again giving a force in the same direction. A mechanical brake is employed to stop the rotation.

The shutter device is used to reduce the flux of evaporating material arriving at the substrate by a precise geometrical method involving only the dimensions of the transmission slots relative to the circumference of the sector disk. Thus, thick films deposited near the outer edge of the disk are proportionately reduced to thinner films deposited at a known radius under the disk. Measurements of the film thickness deposited above the shutter can be converted to sector thicknesses below the shutter [51]. A similar device, driven conventionally, for extending the range of a quartz microbalance has been described previously [52].

1.13 High-Speed Ultrahigh Vacuum Motor

A modified hysteresis-synchronous motor was designed to eliminate most of the outgassing that occurs during motor operation [53]. There are two sources of gas evolution in motors working in vacuum. The first is outgassing of the bearings. The second is outgassing of the stator winding insulation owing to heating during operation.

The design shown in Fig. 1.17 eliminates both of these effects to a high degree. The bearings [54] in the motor [55] were lubricated with a dry lubricant. The stator was isolated from the vacuum system and the rotor by a container sealed with two O-ring seals at either end. This container is filled with nitrogen to 1 atm to facilitate heat conduction away from the motor. Cooling coils that are brazed to the outside of the isolation container maintain low temperatures at the motor.

The main modification in the motor involved increasing the gap between rotor and stator to allow the isolation container wall (0.010 in. thick) to fit. This may be done in two ways. Either the inside diameter of the stator is increased, in which case the isolation container wall must be of magnetic stainless steel (this was done), or if the outer diameter of the rotor is decreased, the isolation container wall between rotor and stator must by made of nonmagnetic stainless steel.

Motors modified in this way have been working for more than one year at 200 Hz and exhibit a pressure rise of less than 1×10^{-9} Torr [53].

To reduce the loss of gas still further, the motor housing could be filled with nitrogen gas at about 1 Torr pressure, which is still adequate for heat transfer. Alternatively, UHV sealants might be used to seal the motor [56].

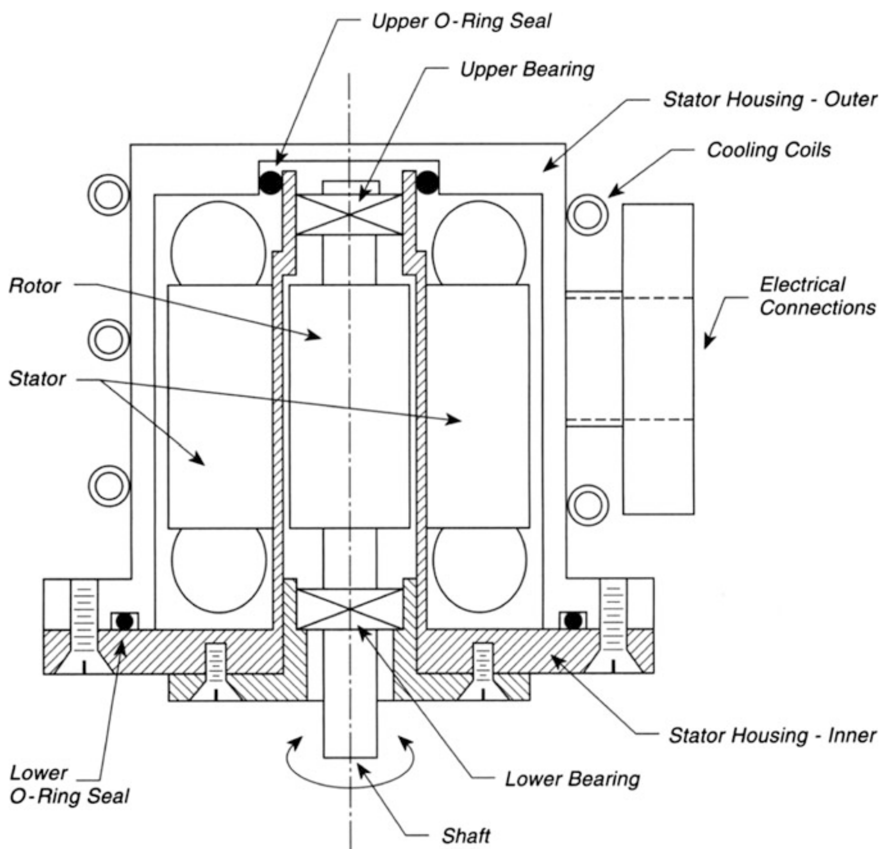

Fig. 1.17 High-speed UHV Motor

1.14 High-Speed Rotary Feedthrough for UHV Operation

A simple rotary feedthrough, suitable for high-speed rotation in an ultrahigh vacuum system, is shown in Fig. 1.18. The device uses a hysteresis motor, in which the stator is externally mounted, for driving a shaft at speeds from 1200 to 15,000 rpm [57]. The pressure rise during operation is less than 1×10^{-10} Torr, since the stator, which generates gas on heating, is isolated from the vacuum system.

In the Figure, a shaft, held between two unlubricated bearings [58], is attached to a rotor and both pieces are ground together to assure good dynamic balance. Two spring washers eliminate axial play. The stator is held in place by plastic supports. The torque delivered is limited by the motor size chosen [59] and by the gap between stator and rotor, which is 1.5 mm here. After 1200 h of intermittent operation, no need for bearing replacement was encountered.

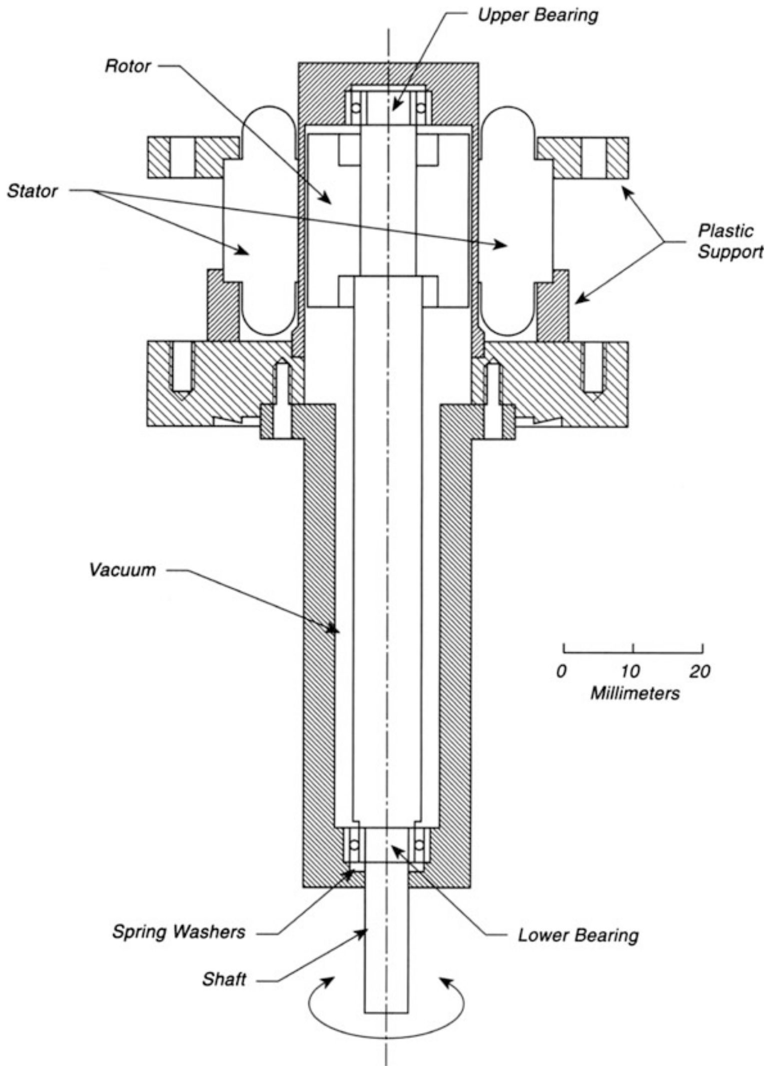

Fig. 1.18 Very high speed UHV motor

1.15 Self-lubricating Bearings in UHV

The use of boron nitride, BN, as a bearing lubricant has been demonstrated for light loads in a combination rotary-translator bearing [60]. This is especially convenient for magnetically driven shafts where only small forces may be applied.

Figure 1.19 shows an exploded view of the bearing assembly. The rotary and translation shaft, made of stainless steel, is supported at some distance from the

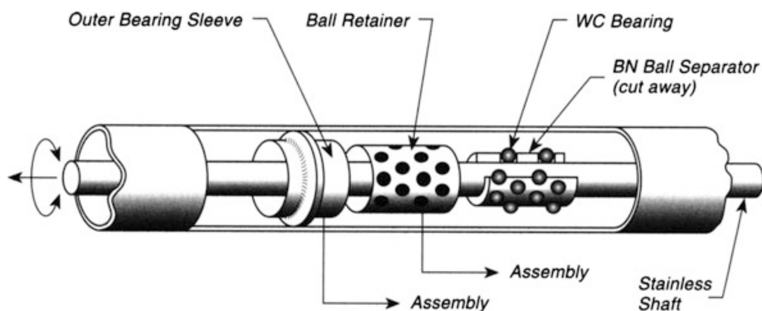

Fig. 1.19 Exploded view—self-lubricating translation-rotation bearing

bearing by V-blocks that can be moved into contact with the shaft, and these are not shown here. The shaft is held by WC bearings (0.48 cm diameter) which themselves are held in a BN ball separator cylinder containing holes that accommodate the WC balls. This BN ball separator provides continuous lubrication to the WC balls and the rod, since BN is a dry lubricant. The balls are held in their place by a type 6061 Al alloy retainer which slips over the top of the balls keeping them from touching each other. An outer-bearing sleeve then slips over all of the components and is stabilized by contact with the inside of the vacuum wall tubulation. The bearing assembly is loosely retained between the magnetic drive mechanism and a stop on its other end, not shown.

The system can be repeatedly baked at 275 °C. Since BN is hygroscopic, when the chamber is open to atmosphere, the bearing is kept at 80–100 °C using heating tape on the outside of the tubulation. No contamination of samples by BN has been detected using various surface analysis methods.

1.16 Lubrication for Heavy Sliding Loads in Ultrahigh Vacuum

The lubrication of metal/metal interfaces for sliding motion in ultrahigh vacuum is a special problem related to the fact that practical surfaces that often slide together with low friction in air will seize in vacuum because of the absence of adsorbed molecular layers of water lubricant or other materials.

Figure 1.20a shows a test device used to evaluate the lifetime of a special coating on stainless steel surfaces that was able to lubricate bearing surfaces successfully for over 200,000 cycles. The comparable unlubricated surfaces failed after 1740 cycles [61].

A ballscrew that translates over spherical bearings in a race was installed, along with a parallel identical partner ballscrew behind the device plane (not shown), in a device which drove a 2-kg mass up and down in ultrahigh vacuum of the order of

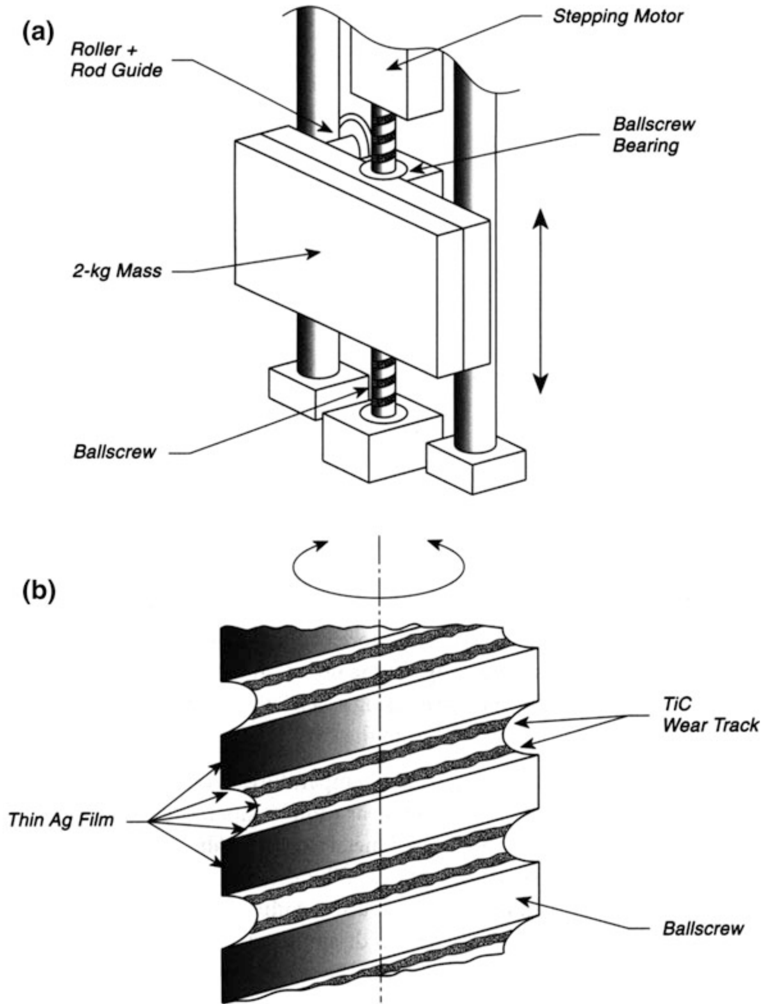

Fig. 1.20 Heavy load lubrication in UHV. **a** Ballscrew test device. **b** Wear track patterns

10^{-10} Torr. The vacuum condition was achieved after a bakeout at 140 °C. The motion drove the mass upward and downward 45 mm, at a speed of 2.25 mm/s. The screws and nuts of the ballscrews are made of 440C stainless steel, finished using electrochemical buffing to a roughness of about 0.1 µm, and then coated as described below.

The ballscrew was coated with a TiC film, 1.5 µm in thickness, and with a micro-Vickers hardness of about Hv 1100. An Ag coating of 0.3-µm thickness was then applied. The ball bearings mating to the ballscrew were also made of 440C stainless steel, coated with an Ag film of 0.3-µm thickness. The unlubricated surface, used as a control, was not treated with either TiC or Ag.

Figure 1.20b shows the wear track observed visually after 200,000 cycles. The thin-film Ag coating is still retained on sections of the screw that did not undergo contact with the balls. The TiC underlayer is visible in the contact regions and was not worn through. Surprisingly, when the device was operated in air, the untreated ballscrew performed well but the coated ballscrew did not move smoothly.

Plasma-coated Ag films on stainless steel screws for use in UHV have been found to resist cold welding [62]. Also, ordinary Ag plating of either the bolt threads or the nut threads of stainless steel bolts used internally or externally in baked UHV systems is reported to be an excellent lubricant using coatings of 10-μm thickness [63]. It has been found that coating metals such as Ta, Cu, Mo, and stainless steel with an oxide film, by heating to redness in air, will provide protection against galling during motion in UHV [64].

A good review on tribology and lubrication in the vacuum environment in space is found in [65].

1.17 Simple UHV Bearing for High-Speed Shafts

Steel ball bearings are often used unlubricated in ultrahigh vacuum. At high rotational speeds, over time, these bearings tend to become sticky before final seizure. The development shown in Fig. 1.21 uses polytetrafluoroethylene (PTFE or Teflon) as a bearing material for continuous rotation at 10–1000 rpm. The bearing is machined using sharp oil-free tools, and care is taken not to introduce metallic particles into the PTFE. Cleaning is carried out in organic solvents, and traces of metal and oil may be removed by use of hot nitric acid solution, followed by soaking in distilled water.

The design has three essential components. The first is the use of relief slots made by a small, round file at 90° intervals around the inside of the bearing. Removal of about one-third of the contact area was found to be essential. The second feature is the placing of pumping holes in the PTFE bearing, and more of these can be supplied on the upper housing. The third feature of the design is the use of an 0.25–0.50-mm-diameter wire squeezed between the bearing and the housing as a friction point to prevent the bearing from rotating when torque is supplied from the shaft.

Bakeout below 200 °C is appropriate, and temperatures above about 250 °C are to be avoided. The bearing should be operated near room temperature and the mechanical admission to the bearing surface of flakes of metal from thin film deposition in the chamber should be avoided. Small partial pressures of fluorine and chlorine were seen initially, and these decreased with time. Initial use also produced small partial pressures of methane and carbon monoxide which soon disappeared. The rotary bearing was used with a 400 rpm shaft for a million rotations without any apparent degradation [66].

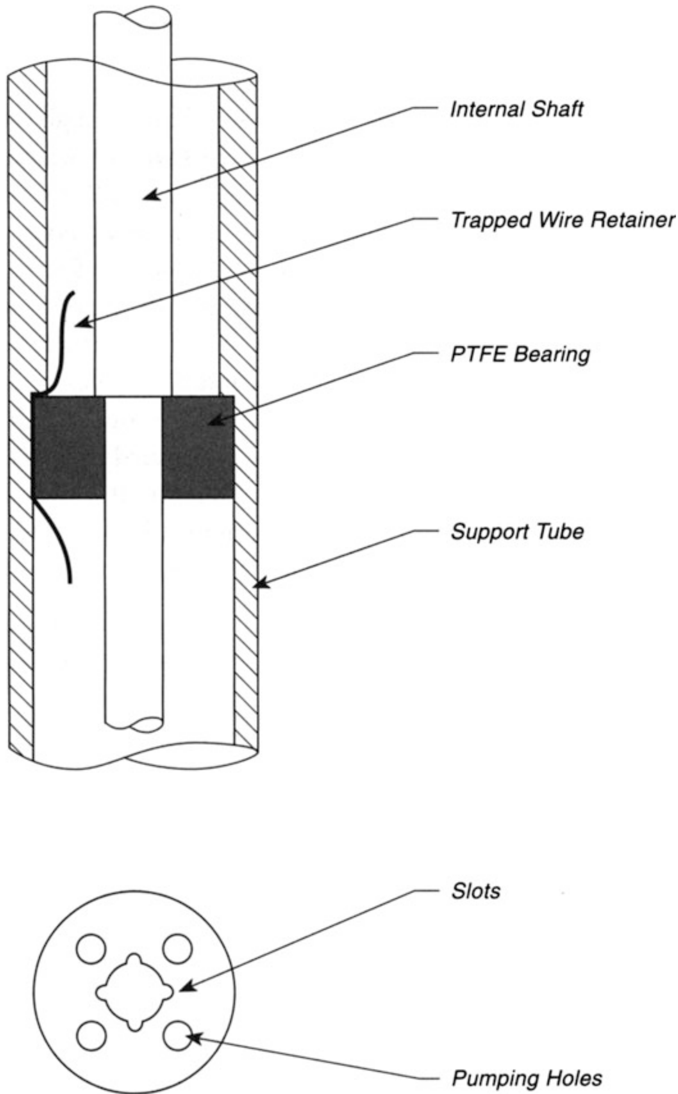

Fig. 1.21 Internal rotary bearing

1.18 Flange-Mounted UHV Variable Aperture

The need for an internal aperture that can be adjusted in ultrahigh vacuum exists both in optical experiments and also in vacuum systems where variable pumping speed control is desired. An inexpensive aperture device is shown in Fig. 1.22. It consists of a variable iris aperture [67] that may be purchased as a component, mounted inside a 2 3/4-in.-diameter Conflat flange. The aperture is mounted on an

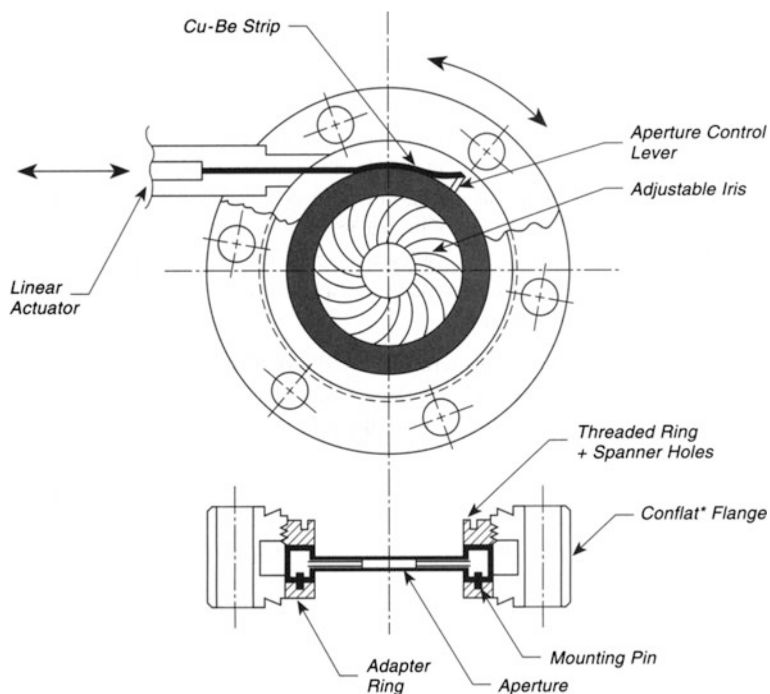

Fig. 1.22 Adjustable UHV Aperture

adapter ring that is tack welded into the flange to avoid distortion. The aperture is fixed from rotation by mounting pins that fit into the adapter ring and through the wall of the aperture housing. The aperture is tightened into place by a threaded ring containing holes for a spanner wrench. The original Conflat flange has had an inside slot milled around its inner circumference for the motion of the aperture control. This is accomplished by a linear actuator coupled to the aperture control lever by a Cu-Be strip (0.3 mm thick) that extends around the aperture housing inside the milled slot. The aperture is degreased before use and relubricated with a tiny amount of MoS_2 applied lightly with a cloth.

The iris opening ranges from 1 to 25 mm and can be reproduced to a precision of 2 % if one is careful to avoid backlash by moving always in the same direction for final adjustment [68].

1.19 Linear Motion Platform (LMP)

A clever mechanical design to convert a linear screw motion into a linear platform motion with reduced amplitude has been described by Dr. H.P. Rust and Mr. L. Cramer [69]. The design is used as an approach mechanism for an STM tip in a low-temperature instrument [70].

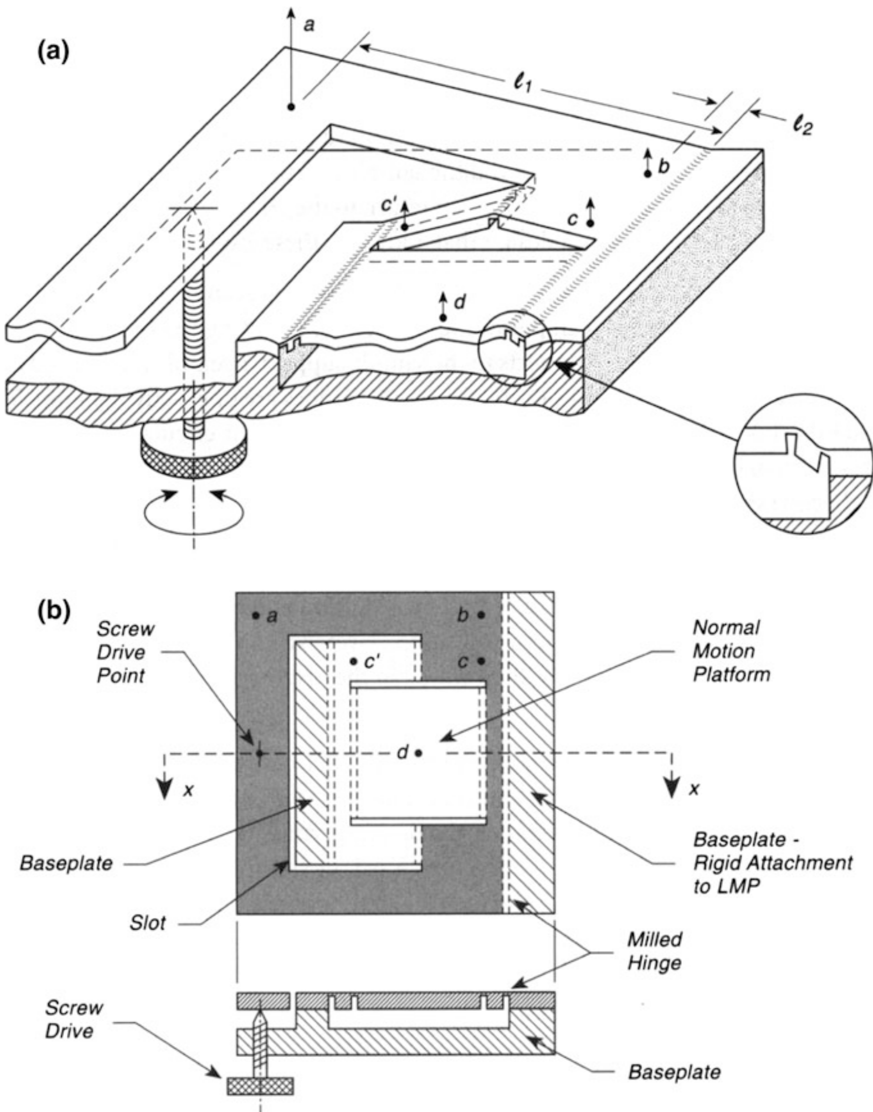

Fig. 1.23 Linear movable platform. **a** 3D-sectional view of portion of LMP. **b** Top and sectional view (x–x)

The device shown in Fig. 1.23a, b is made entirely from a single piece of bronze, which, after fabrication, is rigidly attached to a base plate also made of bronze. The active LMP part is milled with three orthogonal slots in the form of a C, and then 6 "milled hinge" cavities are also produced as shown in Fig. 1.23b by dashed lines. These milled hinge cavities have only a thin section of bronze remaining at the top

of each cavity, giving excellent bending response through a few degrees. The LMP is then rigidly attached to the two projecting flats from the baseplate, and a screw motion, schematically shown as a thumbscrew, is added on the left.

The device works as follows. As the screw is moved up or down, the plate section above it moves up or down, and we will assign a length of motion a as shown in Fig. 1.23a. This motion is reduced at point *b* by virtue of the relative length of the arms involved as the milled hinge is bent near the point *b*. The section of the LMP device labeled *c* is rigidly connected to the outer plate section containing the *a* and *b* motions, and there is therefore an equivalent *c* motion as shown, i.e., $b = c$. As section *c* moves up, a milled hinge, midway between *c* and *c'* flexes as a result of the forces it experiences. This causes a symmetrical distortion in the bridged section *c–c'* and leads to equal angular displacement on both ends of the platform, which occurs as a result of distortions in the region of the pair of milled hinges on each end of the platform. The small motion of the platform is schematically indicated by *d*. Because of the symmetry, the motion of the platform up and down will be in the normal direction without any tilting, which is the desired result.

The function of the device can best be understood by remembering that the light gray region, shown in Fig. 1.23b, and containing *a*, *b*, and *c* and the symmetrically similar regions, is rigid and undergoes identical angular distortion away from the baseplate when the screw is advanced. The mechanical advantage is given by the ratio of the lever arms, l_1 and l_2.

1.20 Vacuum Trolley Transport System

The transport of samples from one vacuum system to another, where different preparation and measurement methods are used, is a common necessity in UHV measurements, as only so many techniques may be used in a single vacuum chamber. A trolley system can be used to make this transport, and the system shown has the capacity to transport 4 samples at one time, dropping them off amongst 5 vacuum systems. Magnetic transfer is used to insert a sample holder into the trolley system from the loading chamber at the third position from the left. A screw advance mechanism moves the samples laterally in 4 special sample holders which are designed as locking devices. The locking sample holders, shown schematically on the trolley in the insert to Fig. 1.24, are used to hold the samples. Engagement of each sample holder by the magnetic transfer device allows the sample holder to be inserted and locked by rotation on centrally-located sample stages in each system. While this device has maximum versatility for simple analysis at various locations, heating of the samples inside the vacuum chambers will require reversible electrical connections for both electrical heating power and thermocouples as described elsewhere in this book [71].

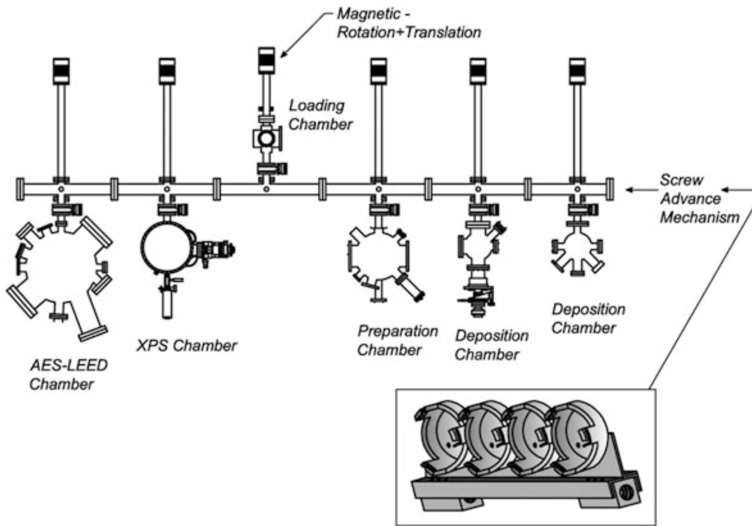

Fig. 1.24 Vacuum trolley transport system—4 samples

1.21 Thermally Compensated STM with Repeatable Sample Positioning

Two problems common to most STM designs have to do with the thermal drift of the relative position of the STM tip and the sample and the inability to replace a sample in the same position so that the STM tip can return to the same image point. Both of these problems have been solved by a design that addresses these issues [72].

Figure 1.25a shows a side view of the STM design. Two piezotubes are mounted on the same base. The inner tube (scan piezotube) is used for scanning the tip, while the outer tube (translation piezotube) connects to the sample support assembly and is used to support and translate this assembly. Both of these piezotubes are of exactly the same length, so that thermal drifts are compensated in the z-direction; their circular symmetry eliminates thermal drifts in the x, y-directions. The outer translation piezotube is surrounded by a thermal shield, made of oxygen-free high conductivity (OFHC) Cu to eliminate temperature gradients, which would defeat the principle of having two identical-length piezotubes for compensation of thermal drift effects. The outer tube is connected to the sample holder through a quartz mounting assembly that consists of an outer quartz tube and a quartz or metal/ceramic sample holder. The sample holder slides (by means of five spherical bearing contacts) on two metallized quartz rails that are mounted inside the outer quartz tube as shown in Fig. 1.25b. Operation of the translator piezodrive causes the sample to jump toward the tip as a result of the friction and inertia effects in the sample holder, and adjustment of the piezo activation waveform can be used to

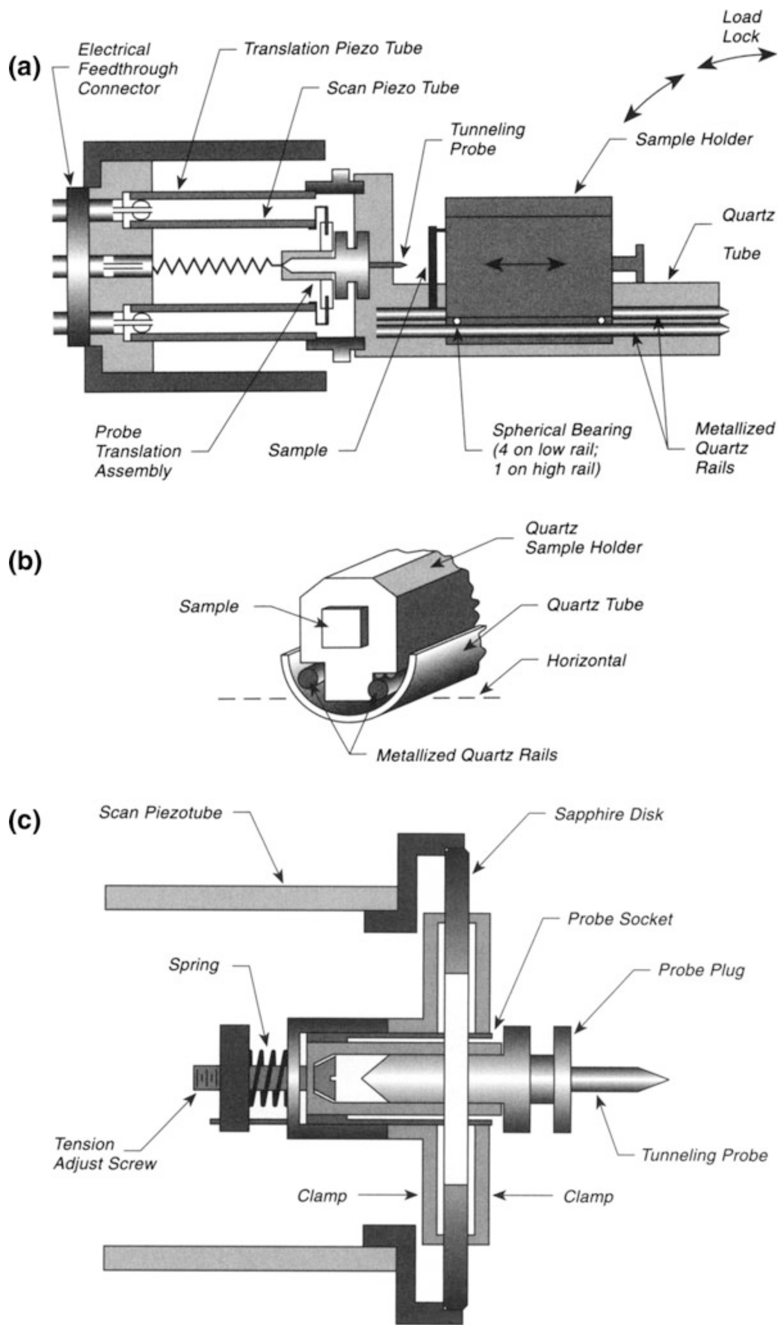

Fig. 1.25 Thermally compensated STM—repeatable sample positioning. **a** Side view. **b** Sample holder. **c** Detail, probe translator

produce jumps from about 10^4 Å to less than 5 Å. By working in the kHz frequency domain, translation rates up to 1 mm/s are possible.

The sample holder may be removed from the outer quartz tube containing the rods and the sample may be transferred and heated in a furnace or in a load lock. Upon return of the sample holder to the quartz rods, the design permits repositioning to an accuracy of several thousand Å, depending upon how much the sample is bumped during transfer. This is accomplished by using gravity to align the sample on the rails, which are tilted with respect to the horizontal plane. The repositioning scheme, using gravity to set the sample on the rails in the same position, is based on kinematic design principles that are well described elsewhere [73].

The details of the construction of the probe translator are shown in Fig. 1.25c. The thermal drift experienced by this design is about 1 Å/h.

A piezo-driven translator for the tip, which moves in the *x*, *y*-directions over several millimeters by a stepping and gripping action, thereby eliminating mechanical positioning devices, has been described as a modification of this device [74].

References

1. P. Toennies, Max Planck Institut Stroemungsf, Bunsenstr. 20, D-37073 Göttingen, Germany (private communication)
2. D. Venus, Rev. Sci. Instrum. **62**, 1361 (1991)
3. Y. Dai, H. Li, F. Jona, Rev. Sci. Instrum. **61**, 1724 (1990)
4. T. Engel, D. Braid, E.H. Conrad, Rev. Sci. Instrum. **57**, 487 (1986)
5. J.J. Zinck, W.H. Weinberg, Rev. Sci. Instrum. **56**, 1285 (1985)
6. K.D. Jamison, F.B. Dunning, Rev. Sci. Instrum. **55**, 1509 (1984)
7. N.J. Wu, A. Ignatiev, Rev. Sci. Instrum. **56**, 752 (1985)
8. J.A. Stroscio, W. Ho, Rev. Sci. Instrum. **55**, 1672 (1984)
9. J. Larscheid, J. Kirschner, Rev. Sci. Instrum. **49**, 1486 (1978)
10. K.D. Jamison, F.B. Dunning, Rev. Sci. Instrum. **55**, 1509 (1984)
11. H. Durr, Th Fauster, R. Schneider, J. Vac. Sci. Technol. **A8**, 145 (1990)
12. M. Michaud, P. Cloutier, L. Sanche, Rev. Sci. Instrum. **66**, 2661 (1995)
13. R.R. Wilson, Rev. Sci. Inst. **12**, 91 (1941)
14. V.R. Unwin, K. Horn, P. Geng, Vakuum Tek **29**, 149 (1980)
15. M.F. Zabielski, R.R. Blaszuk, J. Vac. Sci. Tech. **13**, 644 (1976)
16. J.T. Yates, Jr. (unpublished)
17. J.J. Zinck, W.H. Weinberg, Rev. Sci. Inst. **56**, 1285 (1985)
18. A. Pararas, S.T. Ceyer, J.T. Yates Jr, J. Vac. Sci. Tech. **21**, 1031 (1982)
19. E. Puckrin, J.K. Fowler, A.J. Slavin, J. Vac. Sci. Tech. **A7**, 2818 (1989)
20. D.J. Auerbach, C.A. Becker, J.P. Cowin, L. Wharton, Rev. Sci. Inst. **49**, 1518 (1978)
21. The spring-loaded Teflon seals are available in many sizes from the Fluorocarbon Corporation, 10871 Kyle Street, P.O. Box 520, Los Alamitos, CA 90720. Their descriptive literature gives many details about the seals and the preparation of the metal surfaces on which they ride
22. S.M. George, J. Vac. Sci. Tech. **A4**, 2394 (1986)
23. J.A. Stroscio, W. Ho, Rev. Sci. Inst. **55**, 1672 (1984)
24. P.A. Thiel, J.W. Anderegg, Rev. Sci. Instrum. **55**, 1669 (1984) (A particularly nice design of a manipulator with an easily demountable cold finger end for crystal replacement can be found)

25. R.A. Kubiak, P. Stonestreet, S.M. Newstead, E.H.C. Parker, T. Whall, N. Naylor, J. Vac. Sci. Technol. **A9**, 2797 (1991)
26. J. Larscheid, J. Kirschner, Rev. Sci. Instrum. **49**, 1486 (1978)
27. K.D. Jamison, F.B. Dunning, Rev. Sci. Instrum. **55**, 1509 (1984)
28. H. Durr, Th Fauster, R. Schneider, J. Vac. Sci. Technol. **A8**, 145 (1990)
29. P. Feulner, D. Menzel, J. Vac. Sci. Technol. **17**, 662 (1980)
30. H. Schlichting, D. Menzel, Surface Sci. **285**, 209 (1993)
31. H. Schlichting (private communication)
32. Obtainable from Acheson Colloids, 1607 Washington Avenue, P.O. Drawer 611747, Port Huron, MI 48061-1747
33. T. Gog, S.M. Durbin, Rev. Sci. Instrum. **60**, 3030 (1989)
34. R.W. Bertram, J. Vac. Sci. Tech. **7**, 612 (1970)
35. C.M. Rouleau, R.M. Park, J. Vac. Sci. Tech. **A11**, 464 (1993)
36. MSC, 151 Sunnyside Boulevard, Plainview, Long Island, New York, 11803
37. H. Gutleben, J.T. Yates Jr, J. Vac. Sci. Tech. **A9**, 170 (1991)
38. M.C. Reuter, R.M. Tromp, J. Vac. Sci. Technol. **A6**, 2575 (1988)
39. 1/2 in. -Thompson A-81420-SS; 1/4 in.—Thompson A-4812-SS
40. Custom Cable Corp., 242 Butler Street, P.O. 1050, Westbury, NY 11590-3193. Cable type: RG 316/V
41. D.N. Mcllroy, P.A. Dowben, A. Knop, E. Rühl, J. Vac. Sci. Technol. **B13**, 2142 (1995)
42. Dr. Oliver Schaff, Fritz Haber Institut der Max Planck Gessellschaft, Faraday Weg 4-6, D-14195 Berlin (private communication)
43. W.A.M. van Bers, A.J.J. Franken, P.K. Larsen, Rev. Sci. Instrum. **54**, 637 (1983)
44. W. Stocker, K.H. Rieder, J. Vac. Sci. Tech. **A2**, 1606 (1984)
45. A.P. Jardine, M. Ahmad, R.J. McClelland, J.M. Blakely, J. Vac. Sci. Tech. **A6**, 3017 (1988); This idea is based on an earlier paper which also characterizes the behavior of a similar device as a function of repeated cycling; see B.J. Mulder, Vacuum **26**, 31 (1976)
46. W.F. Smith, E.E. Ehrichs, A.L. de Lozanne, J. Vac. Sci. Tech. **A10**, 576 (1992) (This article contains additional references to other devices constructed with SME alloys)
47. The thicker SME wire used in Figure 11A was obtained from RayChem, 300 Constitution Drive, Menlo Park, CA 94025
48. J. Perkins (ed.) *Shape Memory Effects in Alloys* (Plenum, New York, 1975)
49. T.W. Duerig, K.N. Melton, Proc. Mater. Res. Soc, Int. Meet. Adv. Mater. **9**, 581 (1989)
50. M. Nishikawa, M. Kawai, T. Yokoyama, T. Hoshiya, M. Naganuma, M. Kondo, K. Yoshikawa, K. Watanabe, J. Nucl. Matls. **179–181**, 1115 (1991)
51. J.S. Brooks, R. Meservey, R.K. MacNabb, J. Vac. Sci. Tech. **20**, 243 (1982)
52. F.C. Wilson, D.B. Sandstrom, H.B. Serreze, Rev. Sci. Instrum. **46**, 1593 (1975)
53. T. Engel, D. Braid, Rev. Sci. Instrum. **56**, 1668 (1985)
54. Barden Bartemp bearings, SR 188 SSTB
55. Globe motor, model 75 A 1003-2
56. Professor Thomas Engel, Department of Chemistry, BG-10 University of Washington, Seattle, WA 98195 (private communication)
57. T. Engel, Rev. Sci. Instrum. **52**, 301 (1981)
58. The bearings were from Barden Bartemp, Type SR 188 SSTB
59. The rotor and stator were obtained from KaVo Electrotechnisches Werk GmbH D-7970 Leutkirch, Germany, Type EV 48-15
60. G.J. Collet, E.L. Garwin, R.E. Kirby, Rev. Sci. Instrum. **58**, 479 (1987)
61. H. Saeki, J. Ikeda, I. Kohzu, H. Ishimaru, J. Vac. Sci. Technol. **A8**, 3360 (1990)
62. R.A. MacGill, R.A. Castro, X.Y. Yao, I.G. Brown, J. Vac. Sci. Technol. **A12**, 601 (1994)
63. A. Contaldo, Rev. Sci. Instrum. **36**, 1510 (1965)
64. W.F. Egelhoff, National Institute of Standards and Technology, Gaithersburg, MD 20899-0001 (private communication)
65. E.W. Roberts, M.J. Todd, Wear **136**, 157 (1990)
66. R.A.A. Kubiak, P. Driscoll, V. Manning, R. Houghton, J. Vac. Sci. Tech. **A4**, 1951 (1986)

67. Edmund Scientific Company, 101 East Gloucester Pike, Barrington, NJ 08007-1380
68. F. Homan, J. Vac. Sci. Tech. **17**, 664 (1980)
69. Registered design: H.-P. Rust, L. Cramer, Deutsches Patentamt Gebrauchsmuster No. G94 12 112.5, (27 July 1994)
70. H.-P. Rust, J. Buisset, E.K. Schweizer, L. Cramer, Rev. Sci. Instrum. **68**(1), Jan 1997
71. J. Szuber, private communication
72. J.W. Lyding, S. Skala, J.S. Hubacek, R. Brockenbrough, G. Gammie, Rev. Sci. Instrum. **59**, 1897 (1988); also, U.S. Patent 4,841,148
73. E.B. Wilson, *An Introduction to Scientific Research*, 1st edn. (McGraw Hill, NY, 1952)
74. R.T. Brockenbrough, J.W. Lyding, Rev. Sci. Instrum. **64**, 2225 (1993)

Chapter 2
Sample Transfer

2.1 Sample Transfer from High Pressure to Ultrahigh Vacuum

The ability to transfer samples from high-pressure reaction conditions into ultrahigh vacuum for surface analysis or for crystal preparation has its origin in the work of the Somorjai group at Berkeley [1], who devised apparatus to do this for studies of the kinetics of catalytic reactions on metal single crystal surfaces. Figure 2.1 shows an early version of this scheme. A single crystal mounted on a flange is surrounded by a movable reactor cup that seals the crystal into a small cavity capable of being pressurized. The reactor cup is sealed under strong force by a drive rod that operates inside a stainless steel welded bellows. Because of the strong sealing forces involved, the body of the ultrahigh vacuum chamber, shown cross-hatched in Fig. 2.1, is made of extra thick stainless steel to avoid significant distortion when the sealing force is applied. The crystal can be heated electrically in the reactor cup and its temperature measured with a thermocouple welded to the crystal edge. In some cases the inside of the high-pressure chamber is coated with a gold film to reduce wall reactivity. Gas circulation pumps cause mixing of the high-pressure gas in order to mimic stirred flow conditions. The design shown in Fig. 2.1 would not permit Auger analysis of the crystal surface because of its fixed geometry, but later work permitted the crystal itself to be moved inside the ultrahigh vacuum system after the reactor cup was retracted [2–5].

Figure 2.2 shows an alternate design that has been widely used [6]. The crystal is mounted on a ceramic feedthrough at the end of a transfer tube housed inside a welded stainless steel bellows. The bellows conveniently moves on an external translation carriage containing two parallel stainless rods that accommodate linear bearings connected to the outer flange (not shown) of the retraction device. When retracted, the crystal sits in a reaction chamber which can be pressurized to about two atmospheres. The reaction chamber is closed off by two all metal sealed valves, one leading to the surface analysis/preparation chamber, and the second leading to

© Springer International Publishing Switzerland 2015

J.T. Yates Jr., *Experimental Innovations in Surface Science*,
DOI 10.1007/978-3-319-17668-0_2

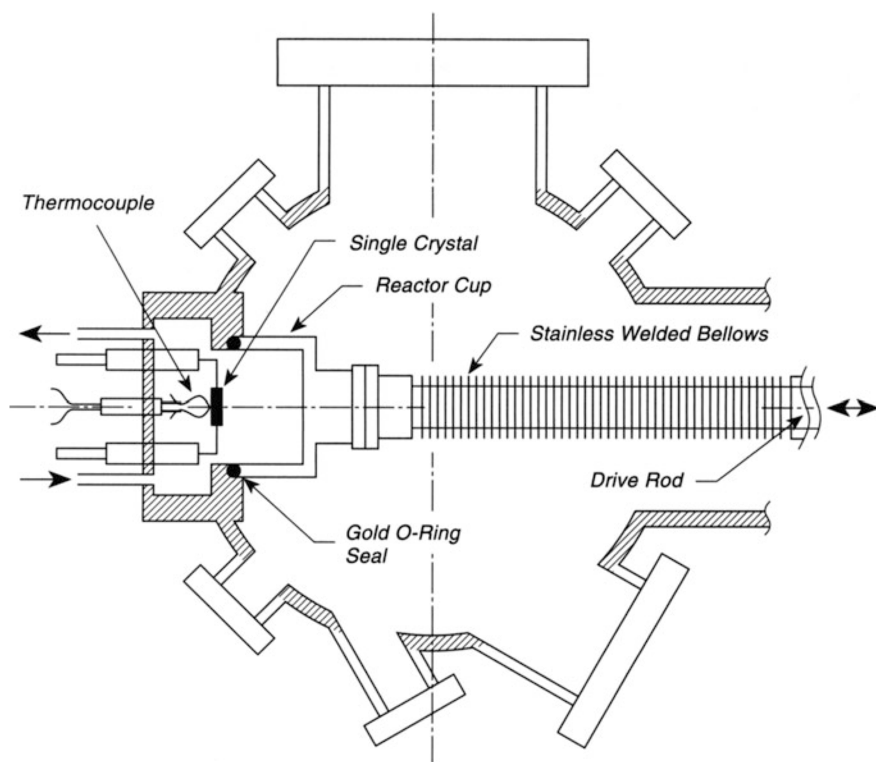

Fig. 2.1 Movable reactor cup—stationary crystal

the high-pressure chamber pumps. As in Fig. 2.1, the entire apparatus can be brought into ultrahigh vacuum condition by means of bakeout. The crystal can be translated into the analysis/surface preparation chamber where surface analysis and gas dosing can be carried out under well-controlled conditions. In the high-pressure reactor chamber, gas analysis is made by extraction of a small quantity of the gas either into the sampling loop of a flame ionization gas chromatograph, or into the mass spectrometer of the main ultrahigh vacuum chamber. For many analyses, the gas chromatograph is superior in sensitivity and selectivity to the mass spectrometer. Compared to the reactor cup design, the internal volume of the high-pressure cell shown in Fig. 2.2 is large and wall effects may in principle be larger. For certain reactions, the wall effect has been measured and found to be small [7]. Viton O-ring sealing valves are likely to give poorer results because of absorption and liberation of gases from the Viton. Often, wall cooling is necessary when the single crystal operates at high pressure and at elevated temperature because of efficient heat transport to the s through the dense gas. It may be necessary to cool the outer wall of the reactor chamber in these cases. Such cooling is not easy to achieve in the reactor cup design of Fig. 2.1. High-pressure chambers are often useful in chemical

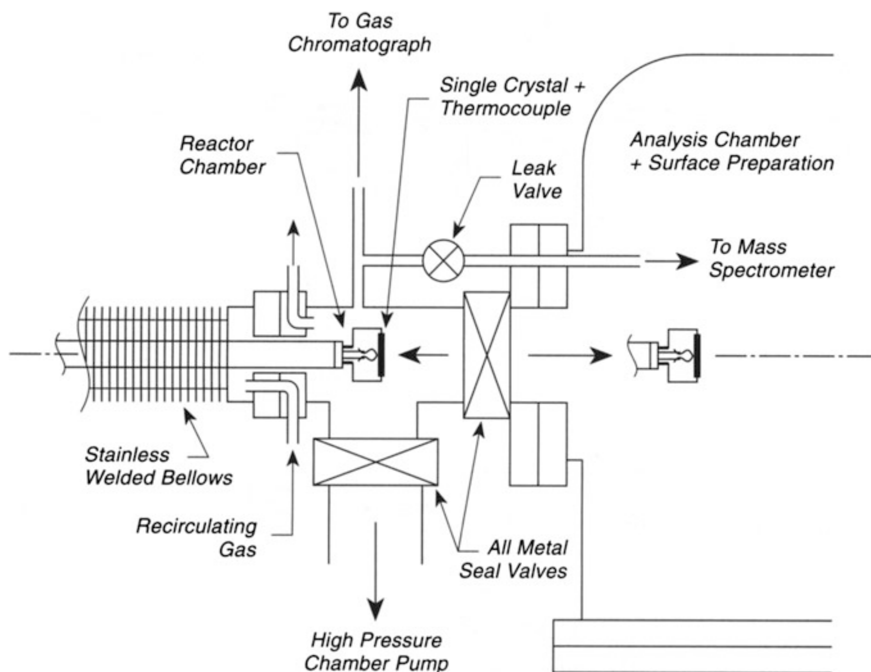

Fig. 2.2 High pressure cell—movable crystal

cleaning of crystals because of the high gas density achievable, let us say for oxygen or hydrogen treatment of a metal single crystal. There is a danger with all stainless steel reactor chambers when operated at high pressure with carbon monoxide gas. The carbon monoxide will produce nickel and iron carbonyls from the stainless walls that transfer their metal atoms to the hot metal surface (see pp. 89 and 505).

Another type of sample transfer device was marketed by Leybold-Heraeus and is schematically shown in Fig. 2.3. A 2-cm-diameter polished stainless steel rod is arranged to move laterally by sliding through a number of differentially pumped O-ring seals that permit rod translation rapidly from a high-pressure reactor into the ultrahigh vacuum system. Differential pumping occurs by means of a mechanical pump in the first stage between the reactor cell and the ultrahigh vacuum system, and high-pressure gases used in the reactor cell would be carried away here. The second stage is pumped with a turbomolecular pump, and achieves a pressure of the order of 10^{-8} mbar [8, 9]. This design was used by others [10, 11] with minor modifications, and in the lower section of Fig. 2.3 can be seen the manner in which a metal single crystal is mounted [10]. The high-pressure reactor is only a few cubic centimeters in volume and was entirely made of stainless steel and gold-plated pan bronze, except for Viton/Teflon seals. The small volume allows an enhanced sensitivity for product gases evolved in catalytic reactions at high pressures [10, 11].

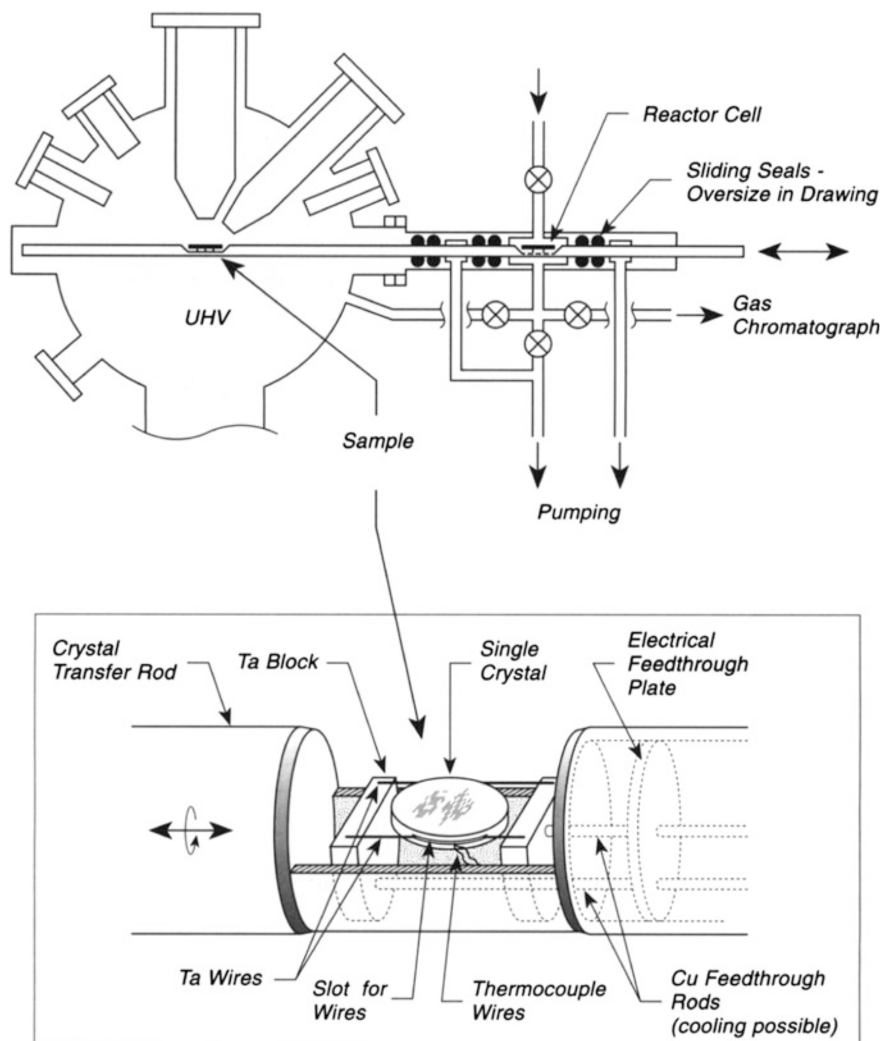

Fig. 2.3 Sliding rod seal

Leaks due to poor O-ring lubrication or to scratching of the stainless rod is avoided to some degree by providing Teflon liners, in the form of tubes which slide on the rod between the O-rings [12].

A more recent type of arrangement for sample transfer between an ultrahigh vacuum system and a high-pressure chamber is called the "rod-through-chamber" geometry. As shown in Fig. 2.4, a single crystal is mounted on a long feedthrough that contains a special conical shoulder that mates to a Teflon gasket when the crystal has been advanced into the high-pressure chamber. The conical contour shoulder is polished to a mirror finish, and acts like a plunger when closing the

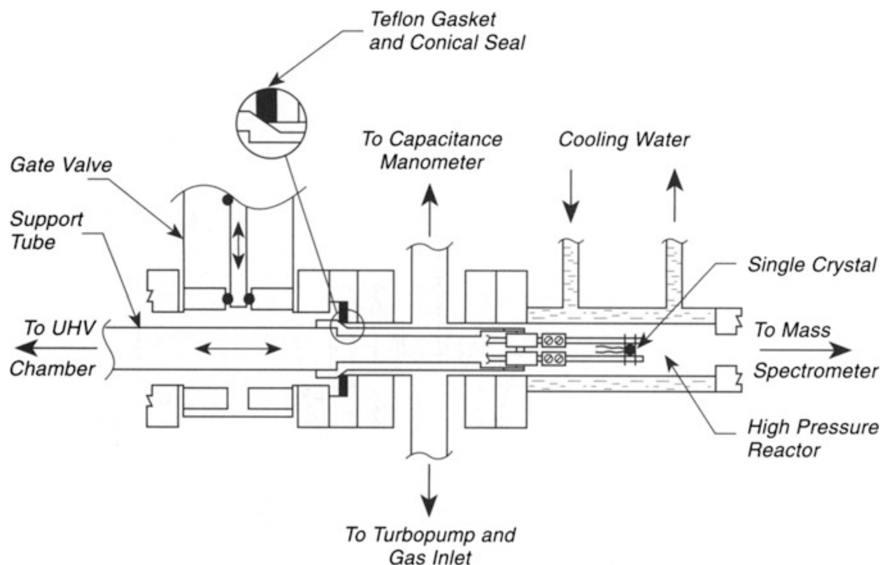

Fig. 2.4 Rod-through chamber

apparatus to isolate the two sections. This Teflon closure can seal against 1 atm pressure with a leak rate less than 10^{-9} Torr L/s. When the high-pressure chamber is evacuated and the probe is withdrawn, a gate valve is closed to completely isolate the ultrahigh vacuum system from the high-pressure chamber. While bakeout temperature limits are not specified in the original paper [13], temperatures in the 150–200 °C range would not be expected to disturb the Teflon. This type of seal requires that a rather large force be applied to the rod in order to make a gas tight junction with the Teflon gasket.

In some cases, it is not appropriate to employ high forces along the rod to make a metal-to-Teflon seal. Fig. 2.5 shows a method for making a high-force seal using another approach, on a crystal holder that moves vertically and that is not so robust as that shown in Fig. 2.4. Here the crystal is mounted on electrical leads that are cooled in a reservoir containing liquid nitrogen supplied through a tube entering from the left-hand side. The gas tight seal is again made by contact between a polished stainless steel surface on the bottom of the plunger, which is of spherical contour mating up with a square-edge Teflon gasket. The upper portion of the plunger is also of spherical contour, and when the plunger is seated properly on the Teflon gasket, tapered steel wedges are able to be brought in from the side to mate with the upper spherical surface. This gives a strong downward force, making the lower Teflon-stainless steel junction gas tight. The steel wedges are driven laterally by two separate linear motion feedthroughs. They enter through heavy guide blocks to provide strength needed to make the compression seal. In order to provide the nonrigid character needed to accommodate the downward motion produced by the

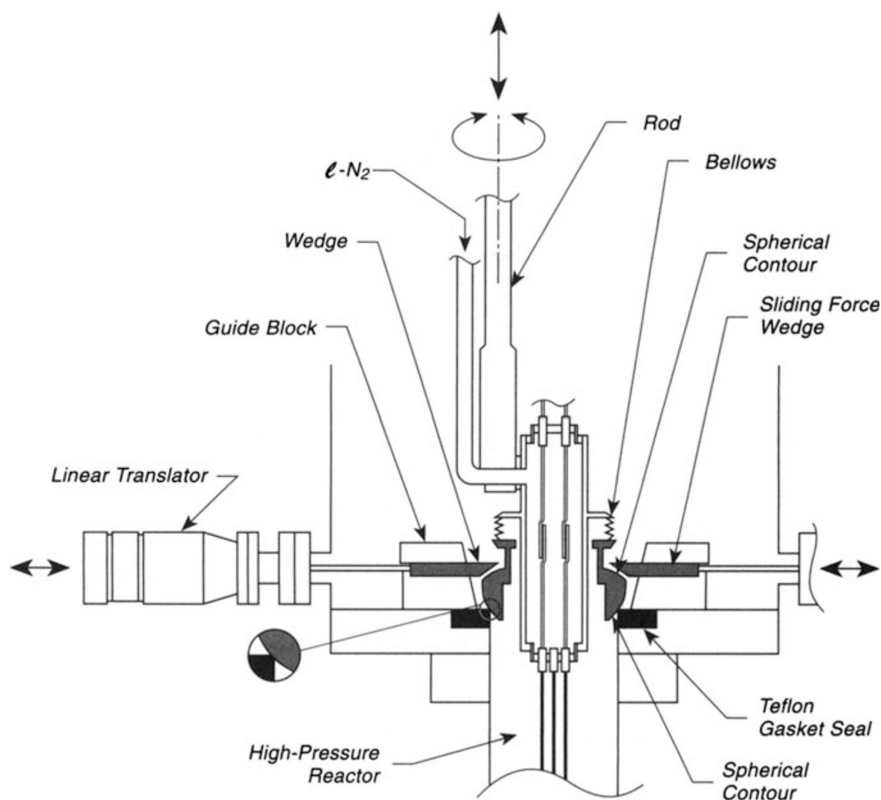

Fig. 2.5 Rod-through chamber seal—local sealing Force

tapered wedges, the plunger assembly is coupled to the liquid nitrogen reservoir by means of an internal bellows. This seal also has a leak rate less that 10^{-9} Torr L/s [13].

A number of other designs for transferring samples between vacuum systems have been devised and are discussed in [14–19].

A novel design for a continuous stirred flow reactor for use in studying surface reaction kinetics at high pressure, but which cannot be used for placing the catalyst surface in a position for surface analysis, is discussed in [20]. The criteria for deter-mining that the reactor is behaving as a stirred flow reactor are given in [20]. Another catalytic reactor, which permits the measurement of the spatial distribution of reactant and product gases, has been described in [21]. This reactor also does not permit the analysis of the catalyst surface composition by electron spectroscopies. In this design, by measuring the leak rate for the reactor through a capillary, the temperature of the gas in the vicinity of the catalyst surface can be measured [21, 22].

2.2 Novel Sample Transfer from UHV Chamber to External Cell

A novel design of an ultrahigh vacuum system permitting the rotation of a manipulator containing a single crystal sample to several analytical ports, while also conveniently allowing sample access to an external cell, has been described [23]. In Fig. 2.6a, an octagonal UHV chamber is shown in side view. The different ports on the octagonal faces contain analytical capabilities of various sorts. The manipulator is mounted on a doubly differentially pumped rotary seal on a 14-in.-diameter flange (see p. 9 for one design), and its center line is 5 in. off center, allowing the sample manipulator to be rotated through 360° on a 5-in. radius circle to face the various analytical probes mounted on the octagonal faces of the chamber. The bellows manipulator has 18 in. of motion in the vertical direction, and is attached to a standard *x, y, z*-translating stage. The hollow tube holding the crystal may be rotated through 360° also, allowing axial rotation of the sample, and this rotational motion is achieved with a differentially pumped rotary seal at the top of the translating stage (see pp. 7 and 8).

The unique access to an external chamber occurs by pushing the sample through three spring-loaded Teflon seals [24] that are doubly differentially pumped and that act as a sliding seal, as in the design shown on Fig. 2.3c. Accurate adjustment of the position of the vertical manipulator with the *x*-*y*-stage allows this to be done without strain. The Teflon seal section is separated from the large chamber above it with a small gate valve. The external cell is located below the sliding seal section and has a small volume. In various cells, high-pressure surface reactions, infrared reflection absorption spectroscopy, and electrochemistry [25] maybe carried out, or if the cell is removed, repairs to the exposed crystal and its mounting maybe made. This permits insertion of new crystal samples into the UHV chamber without requiring bakeout of the chamber, and the design is therefore a tremendous time saver.

The bottom portion of the feedthrough is polished to allow easy motion through the spring-loaded Teflon seals and the achievement of a vacuum seal as shown in Fig. 2.6b. When the sample has been translated back into the UHV chamber, the gate valve may be closed to prevent outgassing from the external cell. A pressure of 2 atm in the external cell causes no measurable degradation of vacuum in the UHV chamber (typical pressure = 2×10^{-10} Torr).

2.3 UHV Sample Transfer Device with Low-Temperature Capability

The transfer of a sample from a manipulator in a preparation chamber to a manipulator in an ultrahigh vacuum is a classic problem, and this has been dealt with on pp. 52 and 54. However, when excellent cooling is required to temperatures below about 100 K, special designs must be used to permit rapid heat transfer

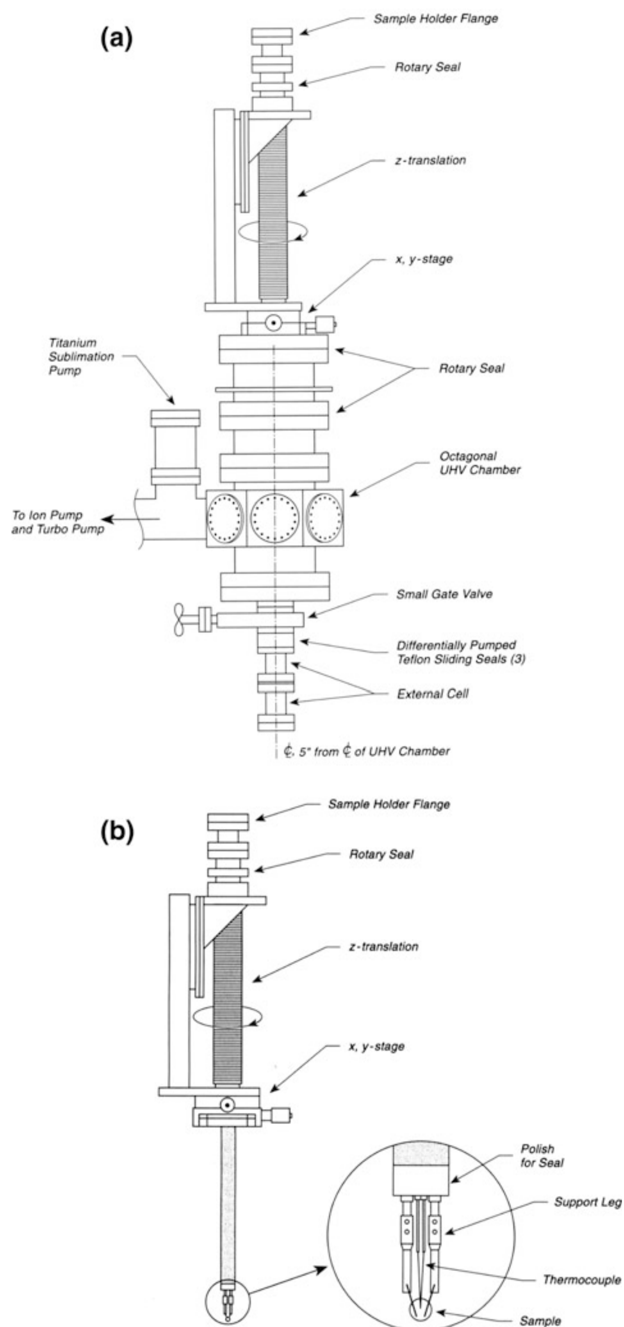

Fig. 2.6 Novel sample transfer to external cell. **a** UHV chamber. **b** Sample transport device

through a demountable joint. Various designs to do this are found starting on p. 383. A particularly appealing design, because of its simplicity, is shown in Fig. 2.7 [26].

Figure 2.7a shows the basic vacuum system with a sample preparation chamber separated from the UHV chamber by a straight-through valve. The sample, initially held at the end of a horizontal manipulator in the sample preparation chamber, can be moved through the valve into the ultrahigh vacuum chamber, where it is transferred to the vertically oriented manipulator. This is done by transfer of a sample slide wedge, shown in Fig. 2.7b. This wedge is made of Mo and is highly polished on its bottom contact surface to avoid cold welding when assembled. The sample is attached to a flat pad (0.3×0.4 in.^{2}) on the top, using spring clips, screws, or welding. A long Mo screw, fixed in the sample slide wedge, and rounded on the threaded end, is tightened by rotation of the transfer rod drawing the wedge shaped surfaces on the slide and the base together. The base is also made of Mo to avoid differential thermal expansion, and its upper surface facing out of the drawing is also polished to receive the slide wedge contact surface. Two screws at the top and bottom of the heating/cooling base act as stops for the sample slide wedge. With the correct adjustment of dimensions, there is actually no sliding of the wedge against the base contact surface; i.e., when the surfaces come together there is no room left for any sliding.

The heating/cooling base is connected by three screws to a copper cooling finger, which may be refrigerated with liquid He. A pancake radiation heater (see p. 364) is attached by a Mo screw to the back of the base [27]. The pancake heater is surrounded by a radiation shield for maximum efficiency in heating. The cutout section of the base between the sample region and the copper block provides sufficiently poor thermal contact when heating to allow a high temperature to be reached, yet also sufficient thermal conduction for cooling the sample.

Transfer of the sample slide wedge is carried out using the inverted screwdriver, which rotates the Mo screw, drawing the slide wedge to the base. Two retaining pins help to align the sample slide wedge and then disengage when the screw is tightened and the transfer rod is retracted. A clutch spring permits rotation of the inverted screwdriver while the pins are engaged with the slide wedge.

The temperature range available was shown to be from 32 K to about 1270 K using 100 W of indirect heating. It was found that Aquadag [28] was needed to prevent galling of the contact surfaces other than the polished Mo wedge contact surfaces. A disadvantage of this design is that attachment of a thermocouple to the sample and transfer of the thermocouple is not provided.

Other transfer systems incorporating low-temperature capabilities for work at cryogenic temperatures are given in [29, 30].

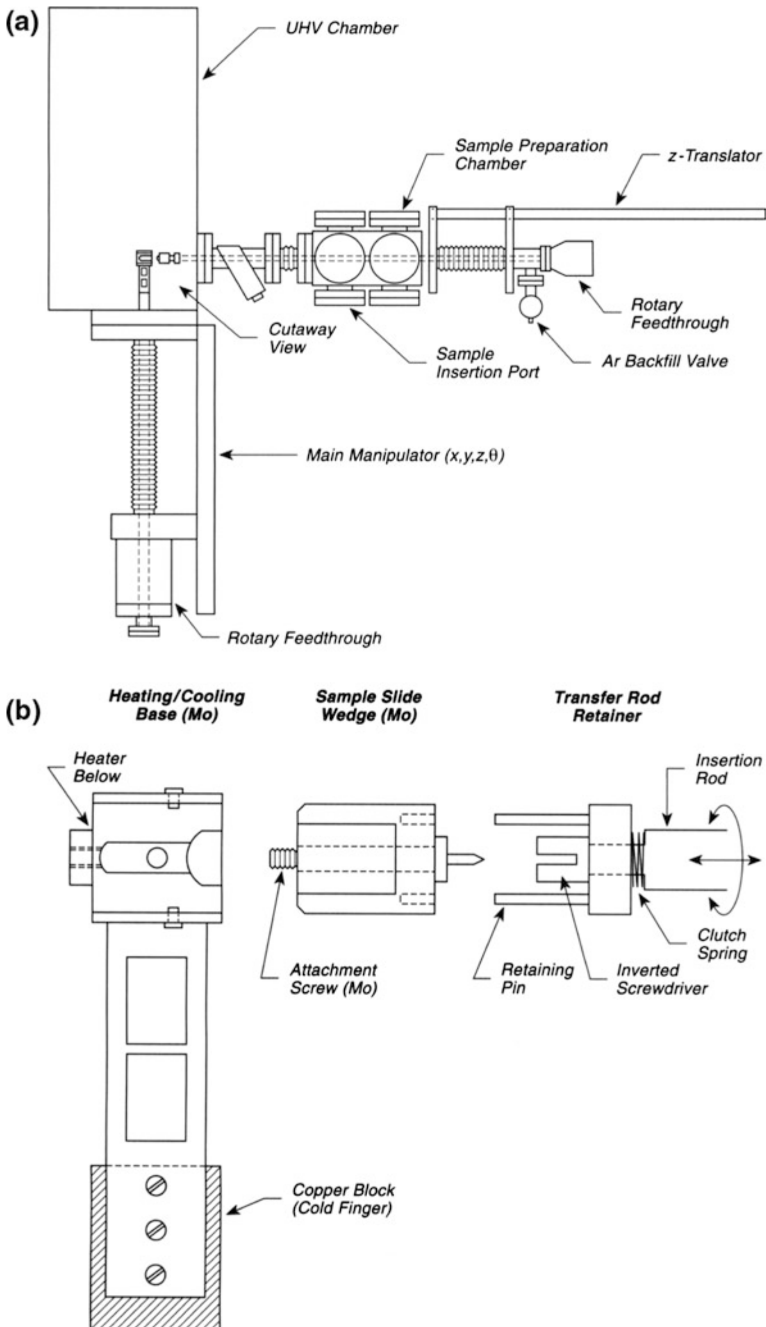

Fig. 2.7 UHV transfer—low-temperature capability. **a** System configuration. **b** Transfer devices

2.4 Internal Cup High-Pressure Cell

Here is described the provision of an internal cup high-pressure cell that accommodates a sample mounted to move in a normal fashion to various analytical ports in an ultrahigh vacuum chamber [31]. A schematic diagram of the apparatus is shown in Fig. 2.8a, where a sample, mounted in a special cup, can rotate to various analytical ports. One of its positions is opposite a reactor cup assembly that can be

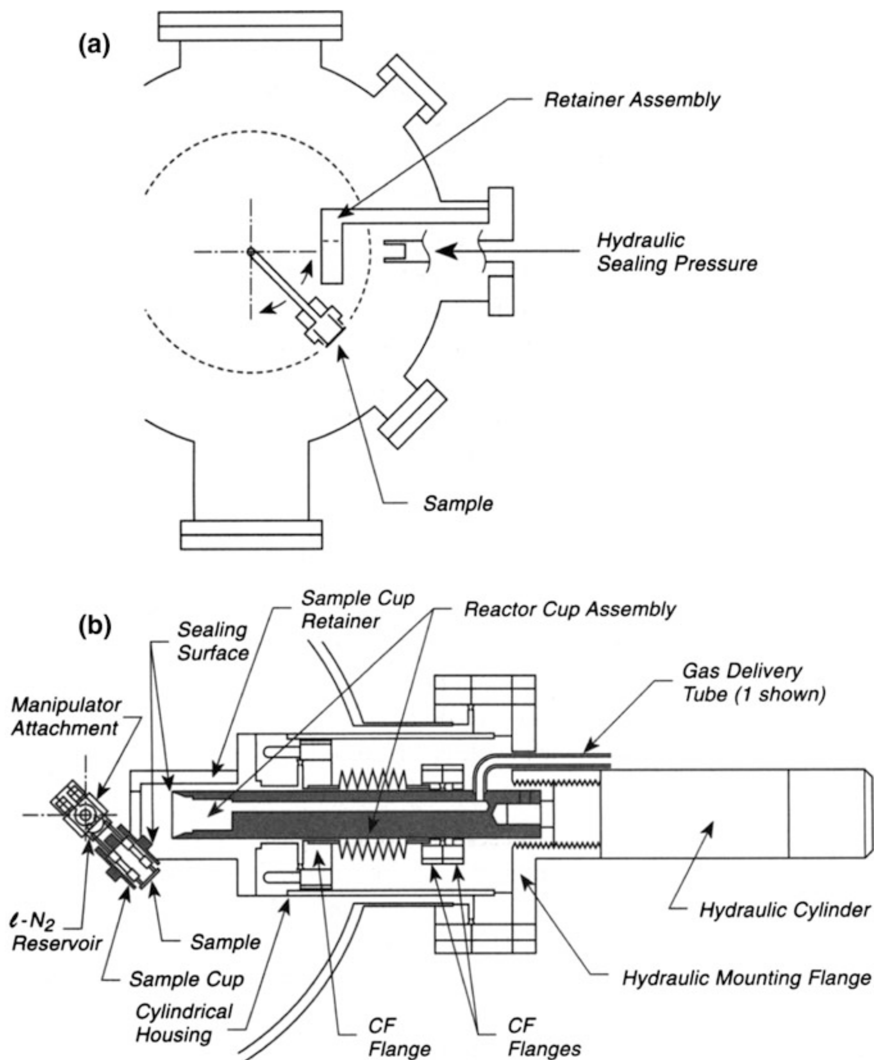

Fig. 2.8 Internal cup high-pressure cell. **a** Schematic of rotating sample + cup assembly. **b** Schematic of high-pressure reaction cell

moved laterally by hydraulic pressure. The sample cup is rigidly held by a retainer assembly, connected to the reactor cup assembly, which prevents the application of large forces to the manipulator shaft when the seal is made using hydraulic pressure. Figure 2.8b shows an enlarged schematic view of the reactor cup assembly and its hydraulic cylinder. When the sample has been rotated into its retainer assembly, the reactor cup assembly is pressed against the sample cup, and an annealed Cu gasket produces the seal at a mini-Conflat sealing surface. This operation is assisted by an internally tapered guiding surface on the outer section of the reactor cup assembly. This method of sealing allows repetitive use of the same annealed gasket. The background pressure in the UHV system was found to rise into the low 10^{-9} Torr range when the cell was pressurized to 100–2500 Torr. The reactor cell (volume 45 cm^3), could be evacuated through gas lines passing through the heavy stainless steel reactor cup assembly, or more rapid evacuation could be achieved by opening the pressurized cell inside the UHV system, causing a pressure surge that decreased into the 10^{-9} Torr range in 1–2 min. The original paper [31] contains a brief review of other methods for building high-pressure cells.

A different design, permitting a single crystal catalyst sample to be moved into a small reactor cup, sealed with a Viton O-ring, has been described previously [32–34]. In this design also, the single crystal may be moved in an ordinary fashion to various positions to face different analytical probes mounted radially in an ultrahigh vacuum system. The design in [33] cleverly permits the reactor cup to be sealed off from the UHV system when the sample is removed, preventing outgassing effects from the inner walls from contaminating the UHV system.

2.5 High-Pressure Transfer Cell

A high-pressure transfer cell that is designed to have a small (30 cm^3) volume and provision for sample cooling is shown in Figs. 2.9a and b. Pressures as high as 15 bar are able to be sustained in the high-pressure cell. Sealing is accomplished by a stainless steel/Teflon seat. Impurities on the crystal that might possibly come from the Teflon under compression are eliminated in this design [35].

Figure 2.9a shows a schematic design for the transfer rod. The sample is electrically mounted on Mo connector rods with W, Ta, or Mo wires. A thermocouple is also welded to the sample. The transfer rod enters the chamber through differentially pumped spring loaded Teflon seals (not shown) such as those mentioned on pp. 6–11 [36]. These seals permit both translation and rotation of the sample when it is in the UHV chamber. The transfer rod is self aligning as it enters the Teflon sealing position. The compression of a spring permits the force on the Teflon seal to be measured and reproduced at about 400 lb. Heating of the sample in vacuum to 1300 K is possible by resistive heating. Heating of the sample to about 700 K is possible in 10 bar of H_2 if cooling is achieved by using flowing air rather than liquid nitrogen. Cooling to about 130 K can be achieved with liquid nitrogen coolant. In order to prevent extreme cooling of the transfer rod when liquid nitrogen is used, a

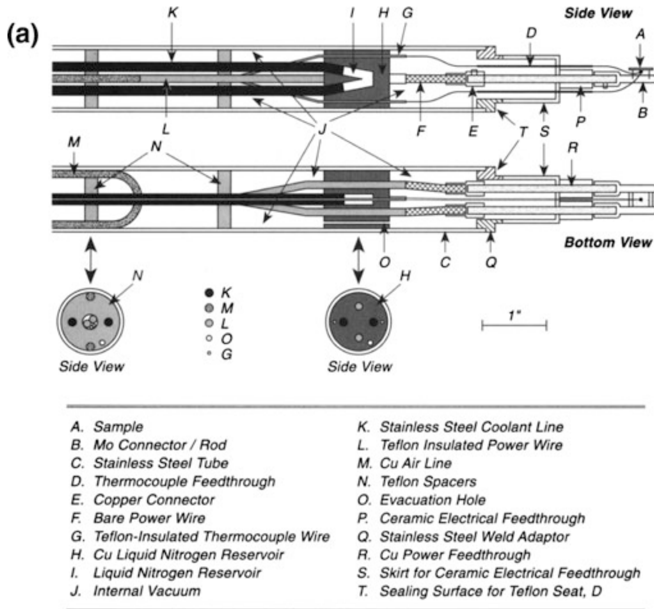

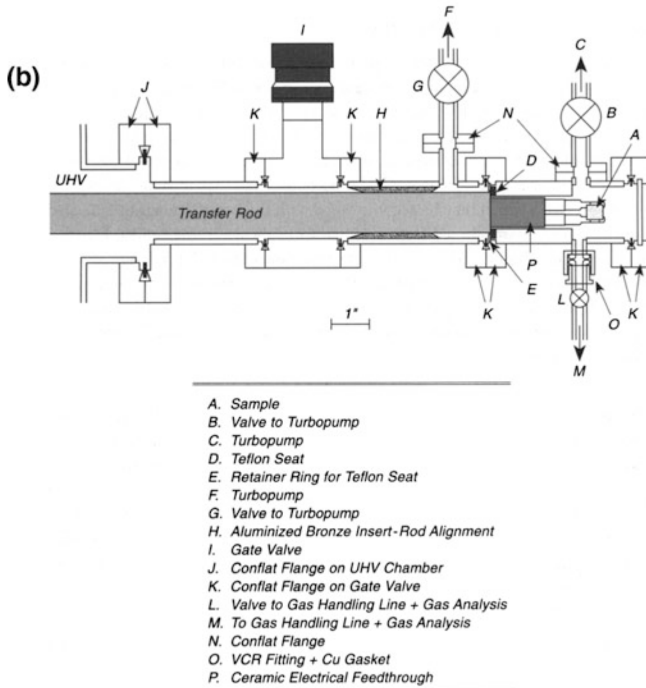

Fig. 2.9 High-pressure transfer-cell. **a** Transfer rod for UHV. **b** High-pressure cell

U-shaped Cu tube is inserted inside the transfer rod wall so that it is held compressively against the inner wall, and warm, dry air is continuously circulated through this tube when liquid nitrogen is used. This prevents failure of the sliding seal mechanism owing to cooling. Teflon spacers are inserted equidistantly inside the transfer rod using a pusher rod with calibrated markings. The outside of the transfer rod is polished to the correct rms roughness following the directions of the spring-loaded Teflon seal manufacturer [36]. The inside of the transfer rod is evacuated with a dual-stage mechanical pump when liquid nitrogen cooling is employed. The outside of the rod is protected with a hypalon/nylon bellows [37] and this bellows is purged continuously with nitrogen gas.

Figure 2.9b shows the transfer rod sealed into the high-pressure chamber. An alignment insert, H, is brazed between the vacuum housing and the high-pressure cell. It is made of a bakeable and UHV-compatible soft aluminized bronze [38] so that it does not scratch or damage the transfer rod. The annular space between the Teflon seat and the high-pressure chamber is of the order of 0.05 cm, and its length is of the order of 2.5 cm. Thus, at high pressure, possible diffusion of impurities from the Teflon to the sample is minimized by the long diffusion time. Calculations of the diffusion time indicate that at 10 bar of gas pressure, diffusion times of greater than 30 min are involved over the 6.5 cm distance from the Teflon to the sample.

The high-pressure cell is directly attached to a gas handling manifold that serves to introduce gases as well as to extract them for gas chromatographic analysis. In addition, direct pumping of the high-pressure cell by a small turbopump may be carried out.

Proof of the performance was made in two ways. First it was shown that a pressure of 10 bar of H_2 led to an increase of pressure of only 1×10^{-9} Torr in the UHV chamber. Secondly, storage of an atomically clean Cu crystal for up to 30 min in the evacuated high-pressure cell does not lead to measurable contamination as measured by XPS or TPD methods. Also, long reaction periods at high pressure occur with constant reaction kinetics on a Cu single crystal surface [35].

2.6 Sample Transfer with Disconnect-I

2.6.1 Transfer in Standard UHV Systems

Often it may be desirable to transfer a sample from one chamber to another and to disconnect the sample from the transfer device after transfer. In Fig. 2.10 one may see that transfer from a reaction chamber to an ultrahigh vacuum chamber is accomplished by use of a magnetic transfer rod, which is commercially available. The sample, mounted on a ceramic sample holder ring at the end of the transfer rod, sits between three tines on the fork at the end of the transfer arm. The hooks of the tines lock into the sample holder ring by a slight twist, which may be accomplished

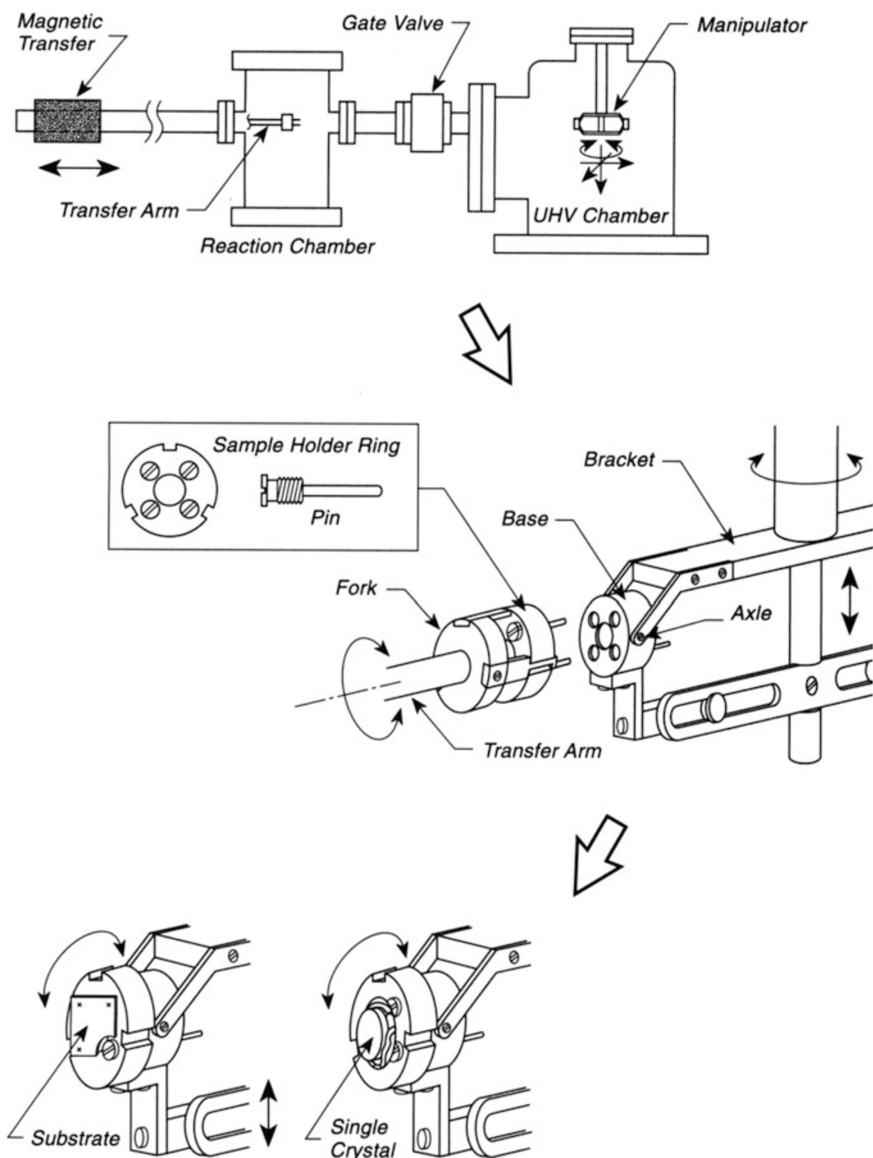

Fig. 2.10 Longitudinal sample transfer—disconnect

with the transfer magnet. The electrical connecting pins are machined from 6–32 screws as shown in the central Figure, and these pins insert into homemade sockets made if necessary from alloys designed for thermocouple connections, etc. It is stated that the electrical connections do not have to be particularly tight and that ordinary misalignments in the pins supply the friction level needed [39]. The

ceramic in this case was cast from machinable ceramic [40] and fired in a hobbyist's ceramic kiln.

The sample is transferred to a manipulator that has a central translating rod used to drive the tilt mechanism. This tilting action is carried out by moving the central manipulator rod up and down, causing the base holding the sample to tilt backward and forward as desired. A locking nut on this rod prevents overdriving the tilting mechanism. In the bottom portion of Fig. 2.10, two types of samples are shown. On the left, a metallic foil substrate is welded to the screwhead ends of the mounting pins in the base. On the right, a single crystal of a metal is welded to a circular piece of foil which is welded to the mounting pins. A circular hole in the backing foil will permit electron bombardment of the back of the crystal. One might provide a radiation shield between the emitter filament and the ceramic base to reduce heating of the ceramic and outgassing.

The proper location of viewports for monitoring the sample transfer is recommended, or else two persons may be needed to transfer the sample.

2.6.2 Transfer in STM Systems

The special considerations needed for the transfer of samples being used for scanning tunneling microscopy (STM) studies as well as other more conventional surface science studies have been reported by Sullivan and Kummel [41]. Here, a design coupling the STM sample to a cold bath, electron beam heating, two degrees of rotation, and electrical isolation, along with sample transfer are described, and a review of other manipulator designs is given [41]. Noteworthy is a simple design for transferring sample holders between forklike manipulators [42]. (See also p. 45.)

2.7 Sample Transfer with Disconnect-II

A simple and inexpensive method to transfer a sample with disconnect [43] is shown in Fig. 2.11. The sample is mounted on stainless steel or other metal posts using Ta clamps that bolt into the base of the holder as shown. This assembly is placed on a transfer screw rod in the the loadlock chamber, and then, after loadlock chamber evacuation, the valve between chambers is opened and the sample assembly is passed into the UHV chamber and plugged into the female banana plug receptacles. These receptacles are mounted on a rod that is connected to the rotary manipulator in the UHV chamber. Electrical power is supplied through Cu braid (see p. 392) as shown. The sample transfer screw rod is then unscrewed and withdrawn. The UHV banana plugs [44] tend to allow the sample to sag a little, and

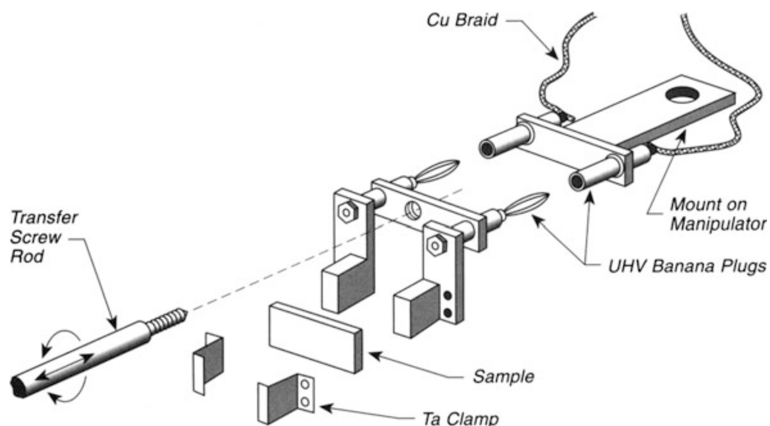

Fig. 2.11 Sample transfer with disconnect

if this is unacceptable, then a mechanical modification to the design near the banana plugs can be added.

In cases where ohmic heating of the sample is inappropriate, it may be backed with a section of a Si wafer (approximately 0.1 Ω cm) for indirect resistive heating.

2.8 Vibration-Free Translatable Device

It is often necessary to perform a delicate translation under conditions where, after adjustment, the translated device is vibrationally decoupled from the UHV system. The example shown in Fig. 2.12 is used to make mechanical/thermal contact of a

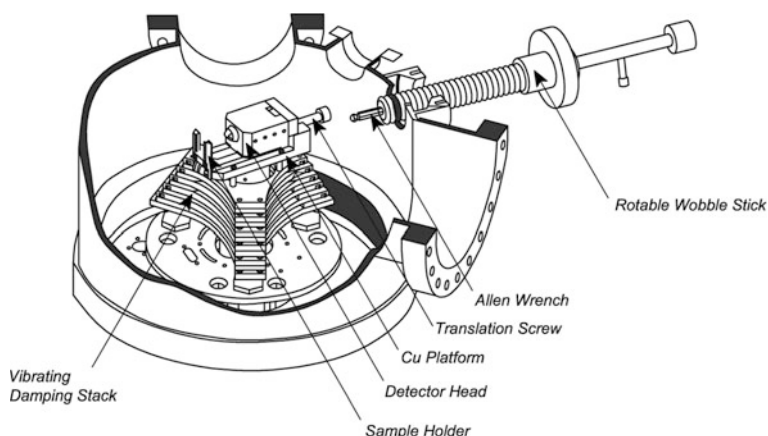

Fig. 2.12 Vibration-free translatable device

detector head (consisting of a polymer pyroelectric foil material) to the back side of a sample experiencing adsorption from a molecular beam, as for example in a microcalorimeter as described in Chap. 163. The sample is held in an electrically-isolated Mo sample holder and the movable detector head may be adjusted on a Cu platform to make contact with the back of the sample, using an Allen wrench to engage a translation screw. The Allen wrench can be rotated using a rotatable wobble stick. The entire assembly is mounted on a vibration damping stack which rests on a plate on the bottom of the chamber. Thus, when the translation has been achieved and the Allen wrench is disengaged, the detector and the attached sample is free of vibration [45].

2.9 Mirror Port for Enhanced Sample Transfer

Often sample transfer from one manipulator to another must be achieved in a loadlock chamber in order to pass the sample through a gate valve and on to another chamber for study. The transfer process can be improved by having a mirror mounted on an external viewport which gives a wide angle view throughout the chamber when one looks through small viewports in the load lock chamber [46] (Fig. 2.13).

2.10 UHV Access Port

The entry into an ultrahigh vacuum chamber can often be achieved through a flanged entry port that contains a standard copper gasket. For large ports that permit access to the entire chamber, one wall of the system may be designed to be reversibly removable without a need for gasket replacement [47].

The design for a removable wall for a rectangular access port is shown in Fig. 2.14. The port contains spring-loaded Teflon [48] seals in separate wells. The regions between the Teflon seals are differentially pumped to prevent small leakage from influencing the vacuum conditions in the chamber. Thus, an ion pump is used on the pumping region closest to the chamber, and a roughing pump is used on the pumping region closest to the atmosphere. The access port is arranged, by means of a recessed section, to be pulled down tightly against the mating surface, providing some further sealing at the very inner section of the seal.

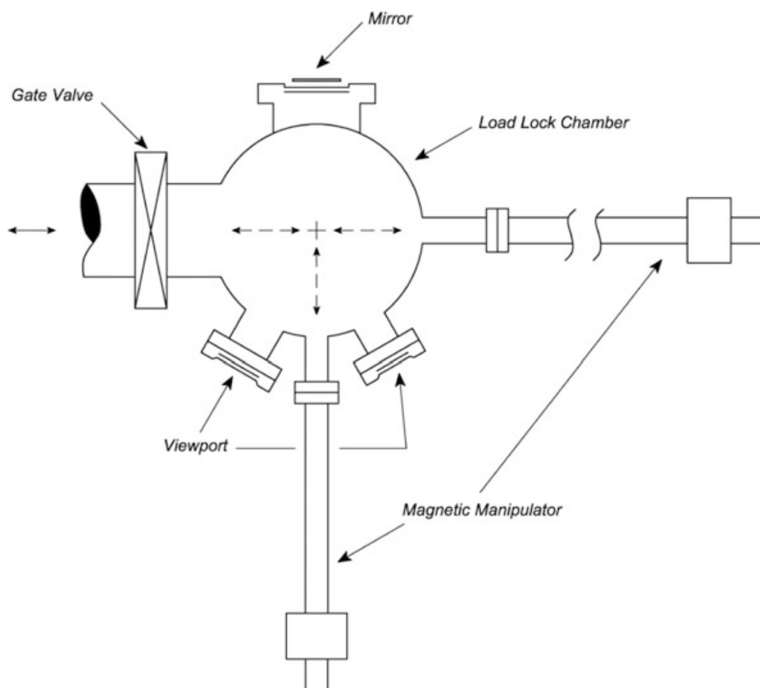

Fig. 2.13 Mirror port for enhanced sample transfer

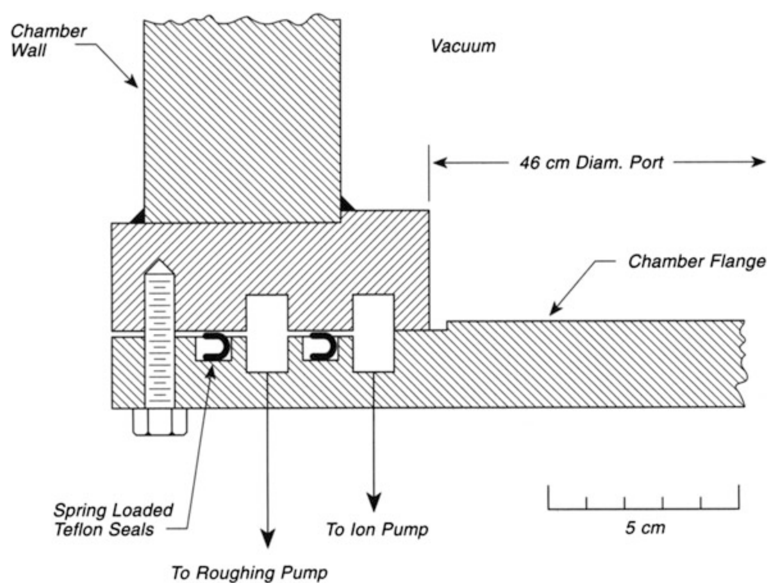

Fig. 2.14 UHV access port

References

1. D.R. Kahn, E.E. Petersen, G.A. Somorjai, J. Catal. **34**, 294 (1974)
2. D.W. Blakely, E.I. Kozak, B.A. Sexton, G.A. Somorjai, J. Vac. Sci. Tech. **13**, 1091 (1976)
3. G.A. Somorjai, Surf. Sci., **89**, 496 (1979)
4. A.L. Cabrera, N.D. Spencer, E. Kozak, P.W Davies, G.A. Somorjai, Rev. Sci. Instrum. **53**, 1888 (1982)
5. T.G. Rucker, K. Franck, D. Colomb, M.A. Logan, G.A. Somorjai, Rev. Sci. Instrum. **58**, 2292 (1987)
6. D.W. Goodman, R.D. Kelley, T.E. Madey, J.T. Yates, Jr., J. Catal. **63**,226 (1980); see also, D. W. Goodman, J. Vac. Sci. Technol. **20**,522 (1982)
7. D.W. Goodman, J.T. Yates Jr, J. Catal. **82**, 255 (1983)
8. H.J. Krebs, H.P. Bonzel, G. Gamer, Surf. Sci. **88**, 269 (1979)
9. H.P. Bonzel, G. Broden, H.J. Krebs, Appl. Surf. Sci. **16**, 373 (1983)
10. C.T. Campbell, M.T. Paffett, Surf. Sci. **139**, 396 (1984)
11. C.T. Campbell, J. Vac. Sci. Tech. **A2**, 1024 (1984)
12. Dr. Renato Zenobi, Analytical Chemistry, Universitätstr. 16, ETH Zentrum CHN C59, CH-8092 Zurich, Switzerland (private communication)
13. T. Yamada, T. Misono, K.I. Tanaka, Y. Murata, J. Vac. Sci. Tech. **A7**, 2808 (1989)
14. C.A. Crider, G. Cisneros, P. Mark, J.D. Levine, J. Vac. Sci. Technol. **13**, 1202 (1976)
15. J.P. Hobson, E.V. Kornelsen, J. Vac. Sci. Technol. **16**, 701 (1979)
16. R.E. Clausing, L. Heatherly, L.C. Emerson, J. Vac. Sci. Technol. **16**, 708 (1979)
17. J. Klebanoff, V.H. Ritz, R.E. Thomas, J. Vac. Sci. Technol. **A2**, 1396 (1984)
18. G.S. Chottiner, W.D. Jennings, K.I. Pandya, J. Vac. Sci. Technol. **A5**, 2970 (1987)
19. R. Raval, M.A. Harrison, D.A. King, G. Caine, J. Vac. Sci. Technol. **A9**, 345 (1991)
20. J.J. Vajo, W. Tsai, W.H. Weinberg, Rev. Sci. Instrum. **56**, 1439 (1985)
21. S. Lundgren, K.E. Keck, B. Kasemo, Rev. Sci. Instrum. **65**, 2696 (1994)
22. B. Kasemo, Rev. Sci. Instrum. **50**, 1602 (1979)
23. (a) R.A. Campbell and D.W. Goodman, Rev. Sci. Instrum. **63**, 172 (1992). (b) J. Szanyi and D.W. Goodman, Rev. Sci. Instrum. **64**, 2350 (1993). These articles also contain useful references to other external high-pressure cell designs
24. Furon Co., 3336 E. Lapaima Ave., Anaheim, CA 92806
25. L.-W.H. Leung, T.W. Gregg, D.W. Goodman, Rev. Sci. Instrum. **62**, 1857 (1991)
26. N.J. DiNardo, J.E. Demuth, W.A. Thompson, P.G. Ledermann, Rev. Sci. Instrum. **55**, 1492 (1984)
27. Custom as well as standard heaters are available from Spectra-Mat, Inc., 100 Westgate Drive, Watsonville, CA 95076. The version used here has W/Re alloy wires embedded in an alumina matrix and housed in a Mo can
28. Aquadag is a colloidal graphite paint, which can be brushed onto a surface and then outgassed by bakeout. It provides lubrication and is electrically conductive. Obtain Dag 154 from Ache-son Colloids, 1607 Washington Avenue, P.O. Drawer 611747, Port Huron, MI 48061-1747
29. G.S. Chottiner, W.D. Jennings, K.I. Pandya, J. Vac. Sci. Technol. **A5**, 2970 (1987)
30. R. Raval, M.A. Harrison, D.A. King, G. Caine, J. Vac. Sci. Technol. **A9**, 345 (1991)
31. Y.-N. Wang, R. McAllister, R.G. Herman, G.W. Simmons, K. Klier, Rev. Sci. Instrum. **63**, 5767 (1992)
32. J.J. Weimer, F.A. Putnam, Rev. Sci. Instrum. **55**, 238 (1984)
33. K.-E. Keck, B. Kasemo, A. Hoglund, Rev. Sci. Instrum. **54**, 574 (1983)
34. M.J. Mummey, L.D. Schmidt, Surf. Sci. **91**, 301 (1980)
35. A. Ludviksson, J. Yoshihara, C.T. Campbell, Rev. Sci. Instrum. **66**, 4370 (1995). This paper also contains references to many other transfer devices in the literature
36. Obtained from: Fluorocarbon Co., 10871 Kyle Street, P.O. Box 520, Los Alamitos, CA 90720
37. Gortiflex Protector Bellows

38. No. UNS C95400, Copper and Brass Sales, 17401 Ten Mile, East Detroit, MI 48021
39. A. Garcia, M.E. Kordesch, J. Vac. Sci. Tech. **A11**, 461 (1993)
40. Aremco, P.O. Box 429,23 Snowden Avenue, Ossining, NY 10562-0429
41. D.J.D. Sullivan, A.C. Kummel, Rev. Sci. Instrum. **63**, 4285 (1992)
42. B.J. Mulder, J. Phys. **E12**, 908 (1979)
43. Dr. Ray Kaplan, Mail Code 6863, Naval Research Laboratory, Washington, DC 20375 (private communication)
44. UHV banana plugs (Model Nos. BPBPM and BPBPF) can be obtained from: Surface/Interface Inc., 110 Pioneer Way, Suite H, Mountain View, CA 94041
45. S. Schauermann, private communication
46. Kejing Li, private communication
47. D.J. Auerbach, C.A. Becker, J.P. Cowin, L. Wharton, Rev. Sci. Instrum. **49**, 1518 (1978)
48. The spring-loaded Teflon seals are available from the Fluorocarbon Co., 10871 Kyle Street, RO. Box 520, Los Alamitos, CA 90720. Many sizes of the seals are available, and instructions for their use are given by the company

Chapter 3
Electrical Connections

3.1 Tungsten Ribbon—Attachment to Power Leads

Heated tungsten ribbons are used in many experiments as radiation sources, metal deposition sources, electron bombardment sources, and molecular cracking sources. Most commonly, the ribbons are attached to heating leads by spot welding. This method requires that the mounted power leads be removed from the vacuum system for ribbon replacement, a time-consuming procedure. An alternative method for ribbon attachment shown in Fig. 3.1 may be carried out inside the vacuum system without welding [1].

A Ta feedthrough lead has a slot milled into it as shown in Fig. 3.1a. The length of the slot is about 1.5 times the ribbon width, and the width of the slot is about 1.5 times the ribbon thickness. A small cap is machined from Ta, for example, as shown in Fig. 3.1b. The inside diameter of the cap is larger than that of the feedthrough lead by one thickness of the ribbon. The cap length is three to four times that of the ribbon width, and the depth of the bore is 2.5 times the ribbon width, leaving plenty of material in the slotted upper region. The cutout on the cap is centered on the cap so as to allow the ribbon to pass as shown in Fig. 3.1c. The end of the lead extends internally above the cutout by about 0.5 mm, as shown by the dotted lines in Fig. 3.1c, preventing the cap from tilting when rotated.

To assemble the device, the ribbon is passed through the slot in the lead with the cap in place, and extends about one-half the lead diameter beyond the cap. To secure the ribbon, the cap is rotated one-half turn as shown, wrapping the ribbon around the lead under the cap, and locking it in place.

This method will work on very thin W ribbon and has been extended to 0.010-mm-thick ribbon material, 1.2 mm wide; this particular mounting was done on 1.5-mm-diameter Ta leads. To keep the ribbon straight after it has been used, it is common to strain the two leads toward each other before making the second cap attachment. The strain in the two supporting leads will place tension on the ribbon and keep it straight.

© Springer International Publishing Switzerland 2015

J.T. Yates Jr., *Experimental Innovations in Surface Science*,
DOI 10.1007/978-3-319-17668-0_3

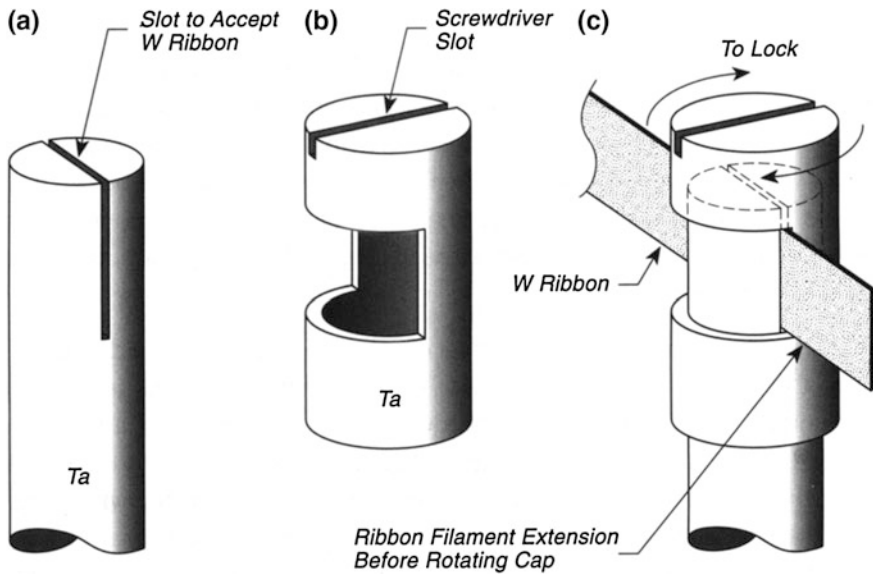

Fig. 3.1 Tungsten ribbon—attachment to power leads

3.2 Wrap Connection—Tungsten to Tungsten

Tungsten is a brittle metal that is difficult to bend or wrap. In addition, tungsten is also difficult to weld. The method shown in Fig. 3.2 involves a wrapping technique that produces tungsten coils that fit onto tungsten wires tightly without welding. Such coils can be used as a friction support or locator in high-temperature applications [2].

Splintering or breakage during fabrication of tungsten wire above about 0.25 mm diameter is a common occurrence owing to its inherent brittle character. While this may be avoided by bending tungsten wire while it is being heated to redness in a flame, heavy oxidation will occur and also intricate bends are difficult to achieve before the tungsten cools. The method shown here prevents splintering of 0.5-mm-diameter W wire when it is bent into a tight coil. Such coils maybe used to make strong friction contacts to 0.5-mm W wire as will be shown.

A hand drill is mounted in a vise, and a core wire of W, 0.5 mm in diameter, is held in the jaws of the chuck. The second piece of similar W wire to be wrapped is also inserted into the chuck between the edges of the jaw pieces as shown so that it will be prevented from slipping when the wrapping begins. About two revolutions of the chuck are carried out, giving preliminary contact between the core wire and the wrapping wire; the wrapping wire does not start out directed normally from the

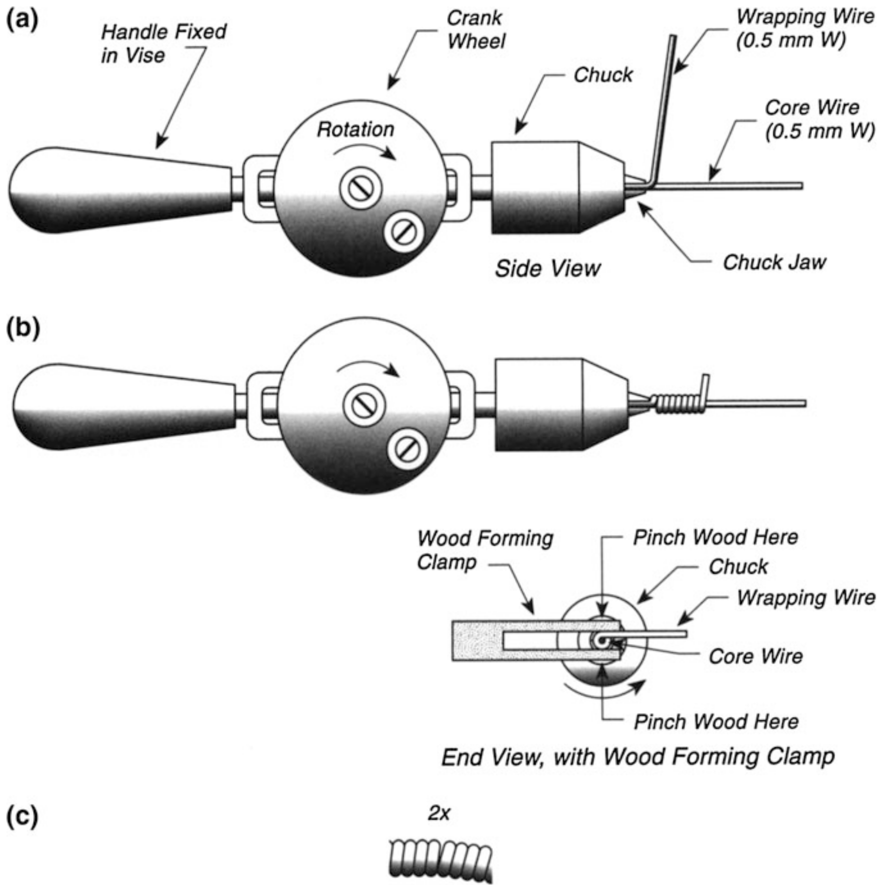

Fig. 3.2 Wrap connection—Tungsten to Tungsten. **a** Starting coil. **b** During winding. **c** Final coil —slightly bent in *middle*

axis of rotation. A wood-forming clamp is next placed on the wrapping wire coil, and while under pressure, the coil is formed to the desired length. The friction between the wood and the W will prevent fracture. The ends of the wrap wire coil can now be cut to the desired length using tungsten carbide end nippers and dressing on a grinding wheel if necessary.

The coil is removed from the core wire, and a slight bend is placed in the center of the coil, using either two pairs of pliers or a knife blade inserted partially into the coil. This slight bend allows the coil to be forced onto a 0.5 mm W wire and to remain fixed owing to the strain induced in the coil as it is straightened by the inner wire. The coil will not move at high temperature either during ohmic heating or bakeout.

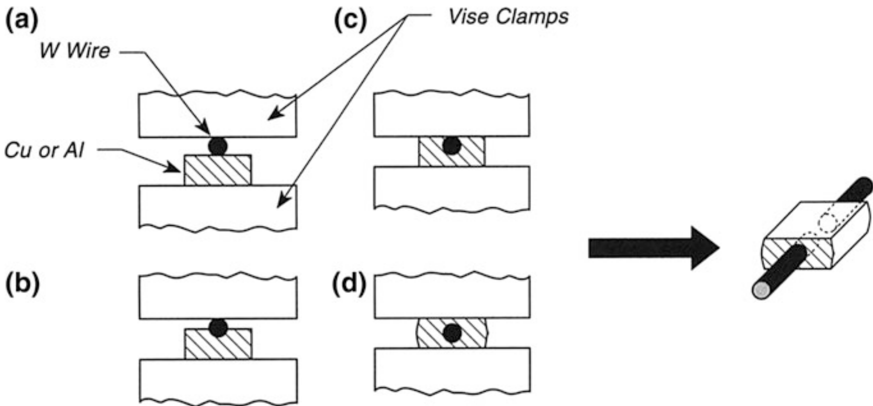

Fig. 3.3 Cold-formed wire connector

3.3 Cold-Formed Wire Connector

The fabrication of electrical connections that are conductive for both electricity and heat may be carried out using silver soldering, welding, or screw-type connectors. Another method, involving a press fit of a hard wire into a soft material such as Cu or Al, is shown in Fig. 3.3. Here a vise is used to press the junction, and the various stages of compression are illustrated. The last stage (d) involves deformation of the soft metal and enclosure of the hard wire. The resistance of these junctions between tungsten and copper is typically about 0.05 Ω [3].

3.4 Ultrahigh Resistance Vacuum Feedthroughs

The measurement of the electrical conductivity of materials with a very high resistance can be plagued by lower-resistance pathways to ground that interfere with the electrical measurements. In particular, Al_2O_3 ceramic insulators exhibit resistances of about 10^{12} Ω, and these may deteriorate in their resistance with time due to the adsorption of water on the alumina or to the deposition of thin metal films on the vacuum side of the insulator surface. Such problems are termed electrical leakage problems, and prevent measurements into the 10^{16} Ω range, which are often needed [4]. In some cases, using an enclosure containing drying agent on the outside of the feedthrough will help, and the more complicated use of forepump evacuation of this region will prevent water adsorption there. For the highest resistivity feedthroughs, other methods must be employed, as shown in Fig. 3.4.

The Figure shows the construction principles of a doubly insulated and guarded design that permits measurements down to the 10^{16} Ω range. A special crystalline sapphire-metal feedthrough [5] is employed, and this is brazed into an ordinary Cu

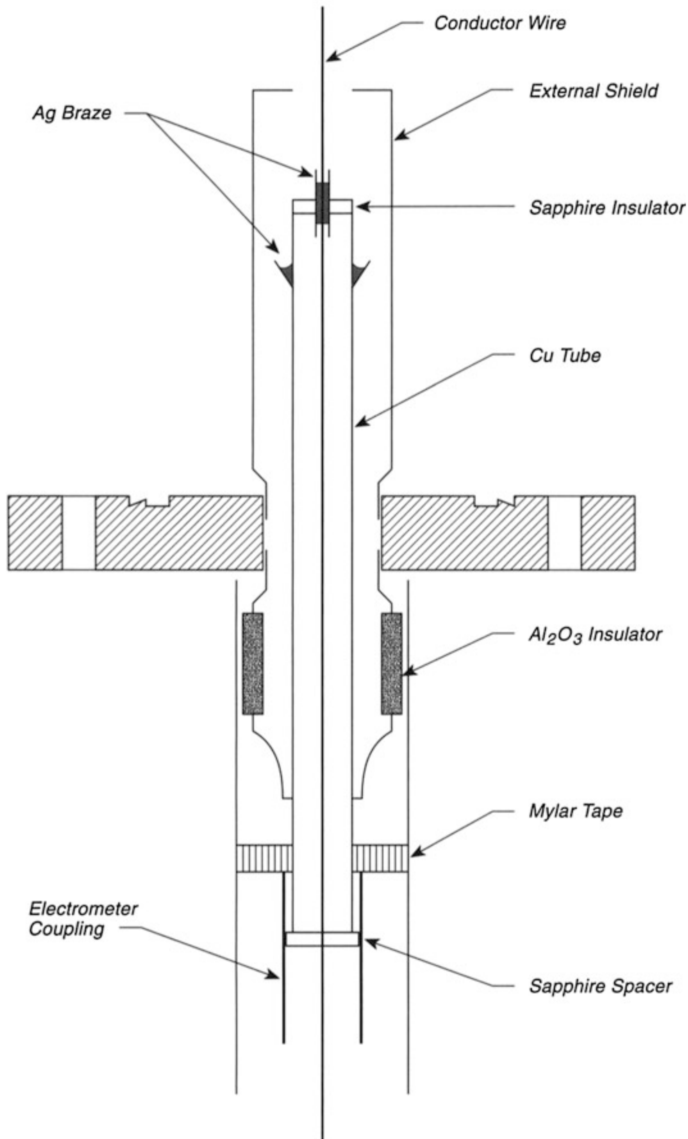

Fig. 3.4 Ultrahigh resistance vacuum feedthrough

tubing feedthrough mounted on a flange by means of an alumina ceramic insulator. The sapphire feedthrough contains a hollow tube. Into this tube is placed either a Ni or Cu conductor wire, which is silver brazed under hydrogen into the hollow tube. At the same time the brazing of the sapphire thimble and the flared Cu tubing is carried out. Great care must be taken to avoid extreme thermal shocks at the

sapphire. The assembly on the vacuum side is provided with a second shield as shown, and also shielding of the outer air side of the feedthrough is carried out as shown.

The impedance to ground of the sapphire insulator approached 10^{16} Ω when the sapphire was thoroughly cleaned [4]. Spectroscopic grade alcohol, followed by distilled water spraying through a fine glass nozzle, is recommended, followed by blotting the excess water and drying in an oven.

3.5 Sliding Metal Electrical Contact

A need for a sliding electrical contact can occur when flexible coils of ceramic bead-insulated wire are unsatisfactory, perhaps because of the formation of ceramic dust as motion occurs. Figure 3.5 shows a sliding stainless steel rod that moves through a Teflon bearing that is mounted inside a re-entrant stainless tube connected to a vacuum linear drive of the bellows or magnetic type. Electrical contact to the rod is made by a phosphor bronze spring contact rigidly mounted on a stainless support assembly, and electrically isolated by ceramic insulator cylinders that contain small bolts for holding the spring contact strip. The phosphor bronze spring strip is electrically connected to an electrical feedthrough as shown. The holes drilled in the Teflon-bearing should be about 5 % larger than the sliding rod to allow for deformation of the Teflon as well as for its large thermal expansion coefficient. The contact can pass a 2-A current. The stainless steel rod can be moved

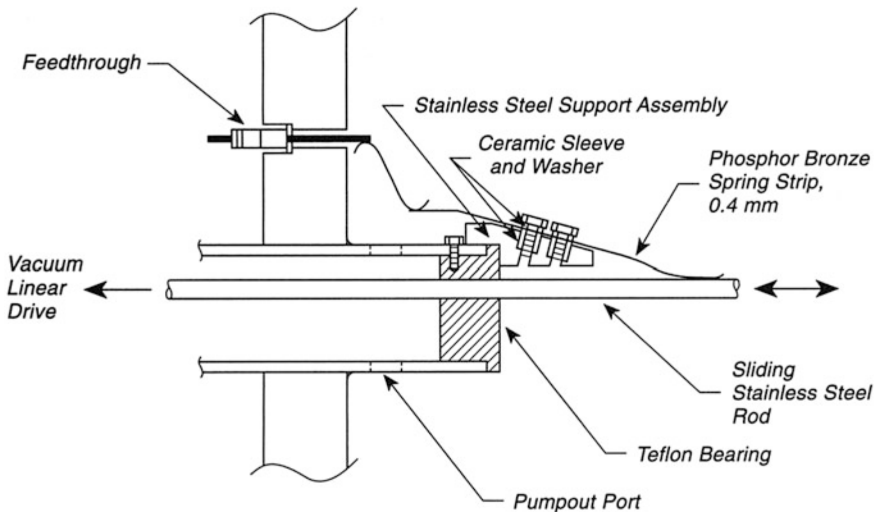

Fig. 3.5 Sliding metal electrical contact

in and out at 5 cm/s without difficulty, and cold welding in ultrahigh vacuum does not occur [1]. The authors also report that a Ta wire spring may be used successfully against a Mo slider in a rotary device [6].

3.6 Low-Profile Electrical Lead Clamp

There is often a need for a band clamp arrangement to anchor electrical leads to a manipulator rod or other structure. Often, narrow clearance spacing is available around the rod so that the binding on the electrical leads to the rod must be achieved in a limited annular space. Figure 3.6 illustrates one solution to this problem, using half-hard Cu-Be spring stock. This material is formed as desired by using steel-forming wires of the correct diameter to produce the rounded grooves in the Cu-Be stock by hammering the forming wire into the stock with the forming jig as a guide to fabrication. An extra channel is provided as an additional spring expansion channel to give the band extra elasticity. The tabs at the end of the band are each about 3–4 mm in length. To install, the ceramic insulated wires are placed into

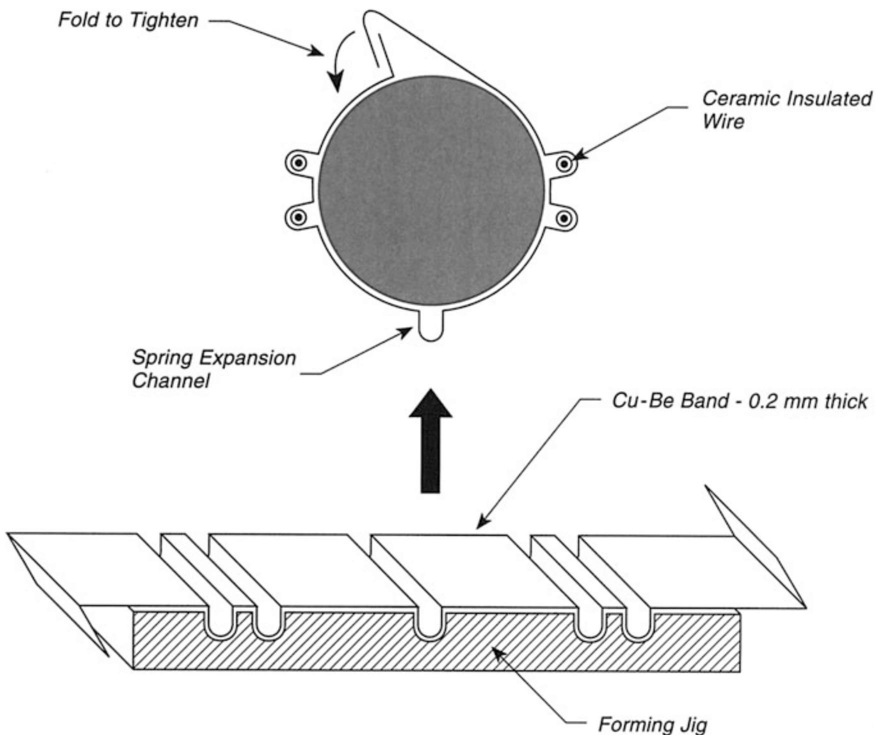

Fig. 3.6 Band clamp for electrical leads

position on the rod and temporarily anchored. Overlapping the Cu-Be tabs and folding them into each other will result in a tension holding the band and the ceramic insulated wires in place. The band will not soften or lose its spring quality from −200 °C to bakeout temperatures [7].

References

1. Mr. Gerald L. Fowler, 6816 Kelly Ave., N.E., Albuquerque, NM 87109 (private communication)
2. Mr. G.L. Fowler, 6816 Kelly Ave., N.E., Albuquerque, NM 87109 (private communication)
3. D. Edwards Jr, J. Vac. Sci. Tech. **16**, 970 (1979)
4. A.H. Madjid, J.M. Martinez, A.A. Vaala, Rev. Sci. Instrum. **43**, 1049 (1972)
5. Obtained from: Cory Lab, Inc., 823 5th Street, Menominee, MI 49858
6. S.M. Newstead, R.A.A. Kubiak, E.H.C. Parker, J. Vac. Sci. Tech. **A2**, 1603 (1984)
7. G.L. Fowler, J. Vac. Sci. Tech. **A5**, 2978 (1987)

Chapter 4
Pumping and Trapping

4.1 Water Aspirator/Sorption Pump Combination for Efficient UHV System Evacuation

On ion-pumped UHV systems, it is of course necessary to bring the system pressure down from atmospheric to about 10^{-2} Torr before starting the ion pumps. This may be done in several ways, including the use of zeolite sorption pumps that are cooled to liquid nitrogen temperatures in order to physically adsorb all of the atmospheric gases. Because of the large quantity of air that must be removed by the zeolite, the process of reaching the limiting pressure sometimes exceeds 1 h. A method to remove the majority of the atmospheric gas has been reported that is free from the possibility of causing oil contamination [1]. The use of a rotary pump does not exclude this possibility.

Figure 4.1 shows a schematic diagram of the use of a water aspirator for removing the majority of the atmospheric gas. The aspirator is prevented from admitting water to the system (equilibrium vapor pressure of water = 24 Torr at 25 °C) by interposing a liquid nitrogen trap. After this aspirator evacuation, which takes about 1–2 min, the aspirator is isolated from the pumping system by closing valves V_1 and V_2. The sorption pump is then cooled with liquid nitrogen, and valve V_2 is opened. It is observed that the pressure in the vacuum system is reduced to about 5×10^{-3} Torr in only about 10 min, since the capacity of the zeolite is much greater than the quantity of air that remains to be pumped after the aspirator evacuation. Several hours of pumping with the zeolite trap used alone would be required to go to this pressure range.

Following the initial pumpout of the system, valves V_4 and V_3 are closed, and the bake-out processing of the system is carried out to reach UHV conditions, as discussed on p. 83. This procedure allows the sorption pump to be cycled several times without the need for warmup and vaporization of the sorbed gases.

© Springer International Publishing Switzerland 2015
J.T. Yates Jr., *Experimental Innovations in Surface Science*,
DOI 10.1007/978-3-319-17668-0_4

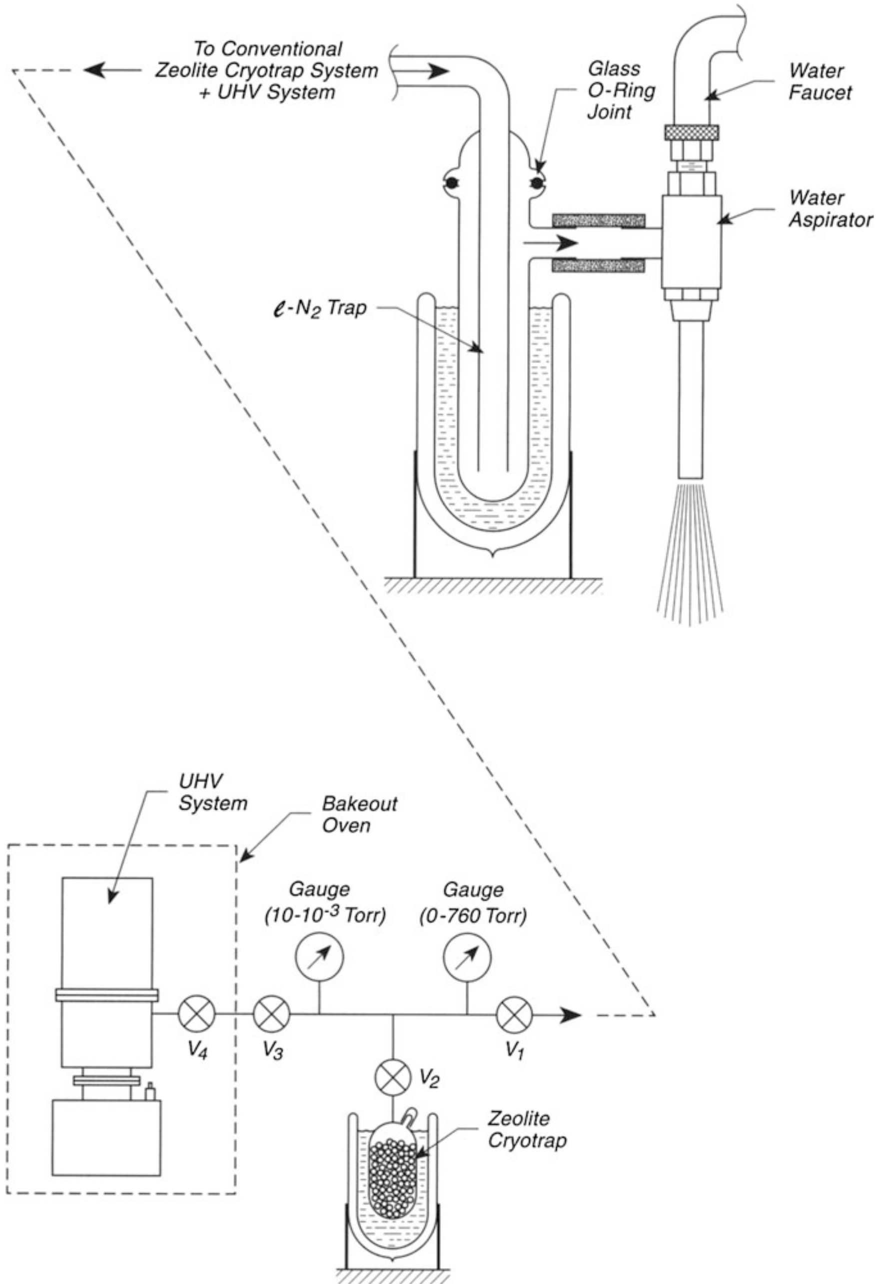

Fig. 4.1 Water aspirator/sorption pump combination

4.2 Ballast Pumping—Vibration Free

There are often situations in which the elimination of mechanical vibrations in an ultrahigh vacuum system would require turning off the mechanical forepump. This is feasible using the method to be described [2], since the gas load being pumped from the system is very low if ultrahigh vacuum conditions exist there. The system is fore-pumped by a large ballast volume of the order of 50 L, which is isolated from the mechanical pump by a valve as shown in Fig. 4.2. The ballast will pump for several days without significant degradation of the turbopump's ability to pump. It can be evacuated in minutes after several days' operation where the forepump has been turned off.

This arrangement is also useful for maintenance of the forepump, since it may be disconnected from the ballast after the isolation valve is closed.

The same idea may be applied to diffusion pumps where large gas loads are not being handled.

A variation on this idea is to back a turbopump with an ion pump over evenings and the weekend. If the power should fail, problems with oil sucking back into the system from the forepump will be avoided [3].

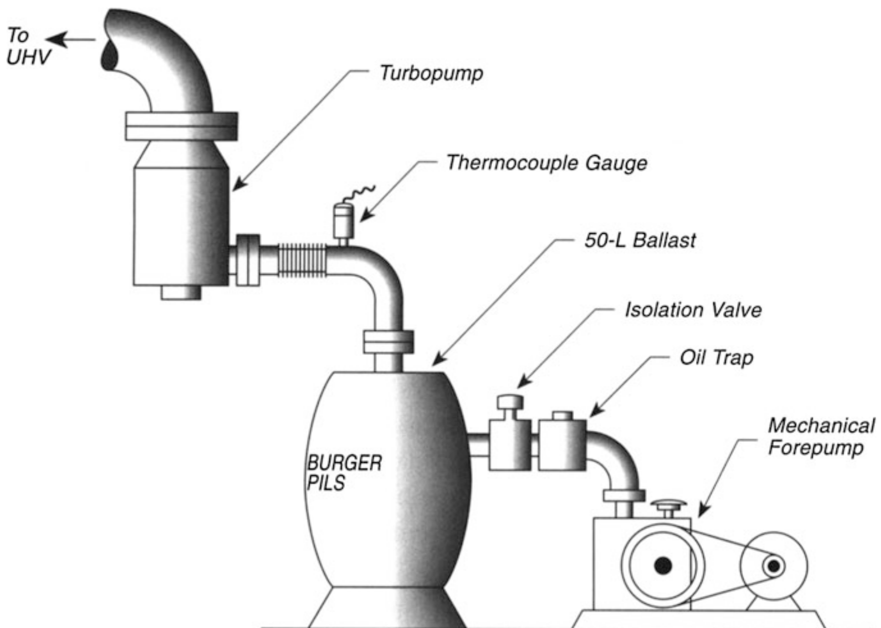

Fig. 4.2 Ballast pumping—vibration free

4.3 The Use of Appendage Titanium Sublimation Pumps for Pumping Low Gas Loads in Ultrahigh Vacuum

Getter films of active metals have been used for many years in ultrahigh vacuum technology, especially in the days when work was carried out in glass vacuum systems that were sealed off from dynamic pumping [4]. This method of pumping chemically active gases is superior to all other methods insofar as secondary effects are concerned. The principle of getter film pumping is the strong irreversible chemisorption of chemically active gases by clean active metal surfaces. Simple considerations of monolayer capacity indicate that 1 cm^2 of a getter surface will pump of the order of $1–3 \times 10^{-5}$ Torr L of an active gas. Film roughness factors of 2 or 3 will increase the gettering capacity accordingly.

One example of the use of a Ti sublimation pump (TSP) for pumping low flux gases from a differentially pumped mass spectrometer is shown in Fig. 4.3. Here, a thin film of Ti is deposited on the stainless steel wall of a cylindrical appendage each morning before beginning work. The Ti film is kept at 77 K to maintain its pumping efficiency to the highest level. A single Ti film will remain active all day during use of the mass spectrometer at low gas loads. This particular apparatus also contains a 60-L/s diode ion pump for maintenance of vacuum quality in the mass spectrometer overnight when the titanium pump is not being used [5].

Careful studies, in which the Ti getter film pump has been compared with ion pumping, show that regurgitation effects [6] involving methane liberation from the ion pump are completely eliminated when the Ti pump is employed [5]. This may be seen by looking at the thermal desorption spectra of methyl chloride from an inert surface. The use of the TSP eliminates the CH_4 evolution originating in the ion pump. However, wall displacement effects caused by molecules entering the mass spectrometer region from the single crystal when it is heated in thermal desorption experiments can still be detected. These displaced molecules were H_2, CO, and H_2O in the particular experiments carried out [5].

The detailed behavior of the residual gases in a liquid nitrogen-cooled titanium sublimation pumping system has been reported [7].

4.4 Pressure-Equalizing Device in Complex Systems

Often in systems such as those used in molecular beam research, it is undesirable for large pressure differences to exist during either pumpdown or during vacuum failure in one section of the apparatus. Large pressure differences, and the associated flow of gas, can damage fragile parts such as thin walls, skimmers, and orifices.

The device shown in Fig. 4.4 is designed to relieve large pressure differences between sections of a vacuum system that are pumped in parallel [8]. Thin metal pressure-release sheets are designed to open in either direction if a large pressure difference occurs. The thin metal sheets are mounted inside flanges that accept

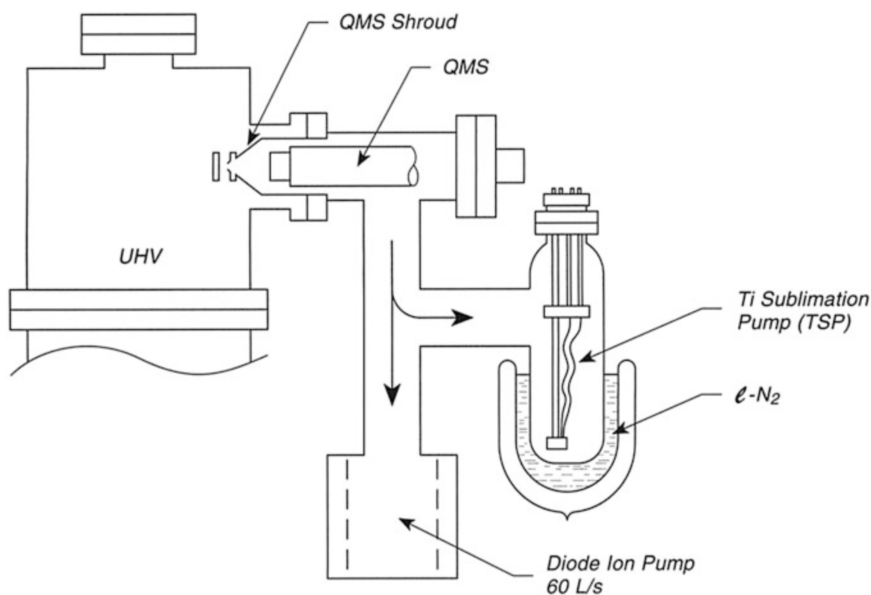

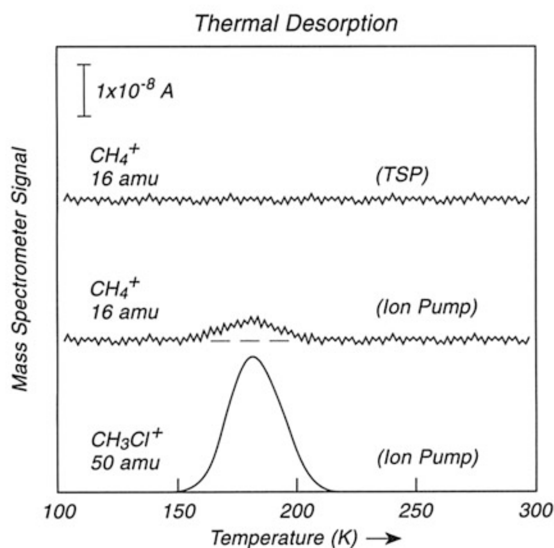

Fig. 4.3 Appendage titanium sublimation pump

Viton O-ring seal rings. The O-ring seal ring is brazed to a disk containing two holes, and the thin metal sheets are mounted on opposite sides of the disk in order to relieve pressure differences in either direction.

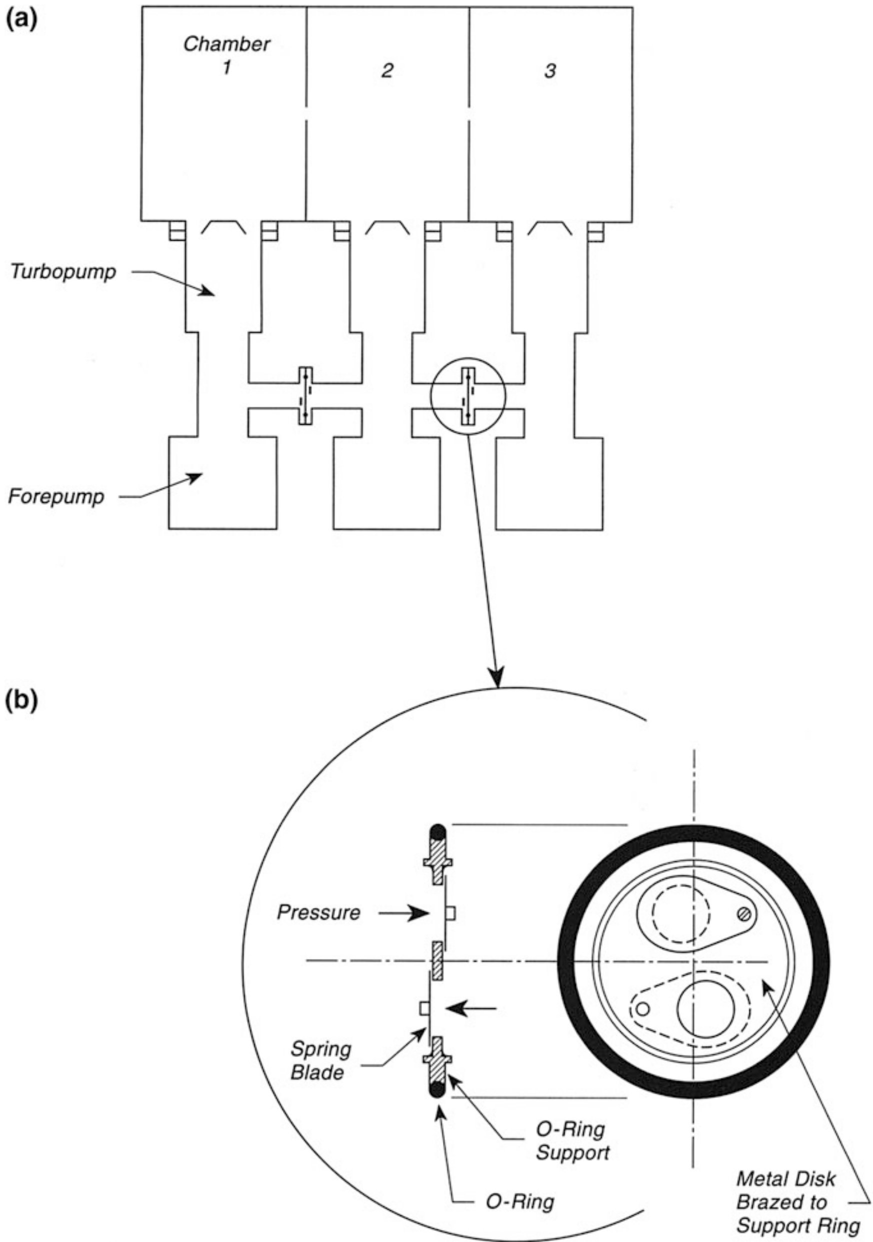

Fig. 4.4 Pressure-equalizing device. **a** Chambers/pumps in parallel. **b** pressure-release device

4.5 Diode Ion Pump Performance in He Pumping

There is sometimes a need to fill a vacuum system with a high-pressure inert purge gas, and then to recover ultrahigh vacuum. Diode ion pumps have only a limited pumping speed for inert gases such as He, and their performance is of interest in this application; triode ion pumps are designed to have good pumping speed for inert gases at a small sacrifice in total pumping speed.

In Fig. 4.5, a series of pumping tests were performed on an ultrahigh vacuum system that could be filled with high-purity He at 1 atm pressure. The He was pumped out with a trapped mechanical pump to about 1×10^{-5} Torr, and then the diode ion pump was employed. Figure 4.5 shows selected pumping performance curves after the first He filling and the fifth. The performance degrades in successive tests because of traces of water vapor admitted with the high-purity He and also because of a drop in efficiency of the diode ion pump owing to the regurgitation effect in which previously pumped gas is partially evolved in successive pumping periods. Baking out (BO) the ion pump (IP) only for 4 h at 250 °C restores some of the original pumping speed; baking out the ion pump plus the vacuum system restores all of the original performance seen in the first test.

The behavior shown in Fig. 4.5 indicates that He can be pumped well by a diode ion pump from ultrahigh vacuum systems made of stainless steel using highly purified He as a purge gas, and that short bakeouts at 250 °C restore system pumping performance. It was suspected that residual water in the He (1.9 ppm) was partially responsible for degradation of the pumping behavior in successive tests [9].

4.6 Vacuum Applications of Metal Foams

Copper [10], nickel [10] and aluminum [11] foams are commercially available and may be used in a number of vacuum applications [12]. The foams are highly porous, they are easily shaped and machined, and they have some inherent strength. They also can be easily brazed or soldered.

Four vacuum applications of foamed metals are illustrated in Fig. 4.6. In panel A, a plug of foamed Cu is used as a hydrocarbon trap between a forepump and a vacuum system. The high surface area and the torturous pathways in the foam impede hydrocarbon passage through the trap. In panel B, a zeolite trap is retained between porous Cu plugs, and serves also as a hydrocarbon trap. The zeolite must be baked out prior to becoming active and acts as a molecular sieve for hydrocarbon molecules. Panel C shows a plug of Cu foam used as a conductance limiter under molecular flow conditions. To adjust the conductance accurately, additional Cu foam segments can be added as needed. Finally, in panel D, a cylindrical piece of metal foam is used as a diffuser for injection of gases in random directions into a vacuum system.

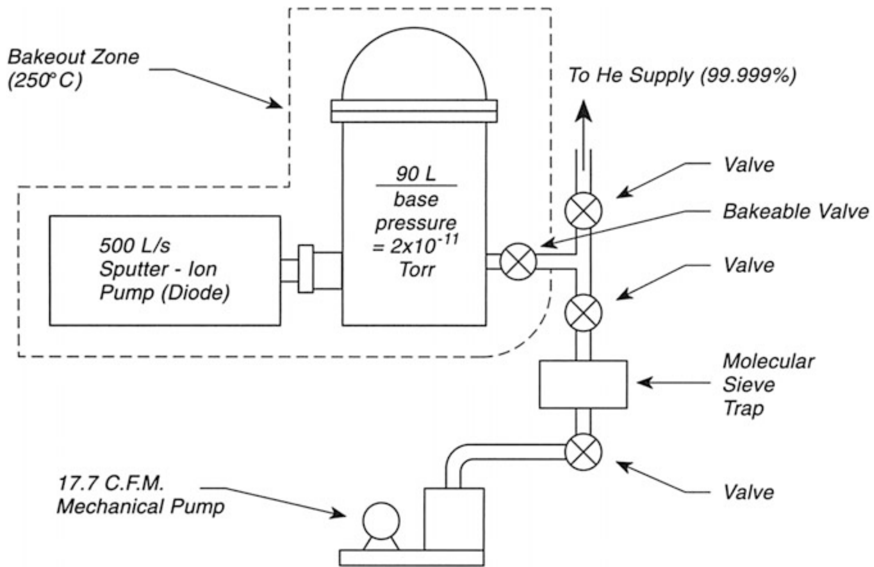

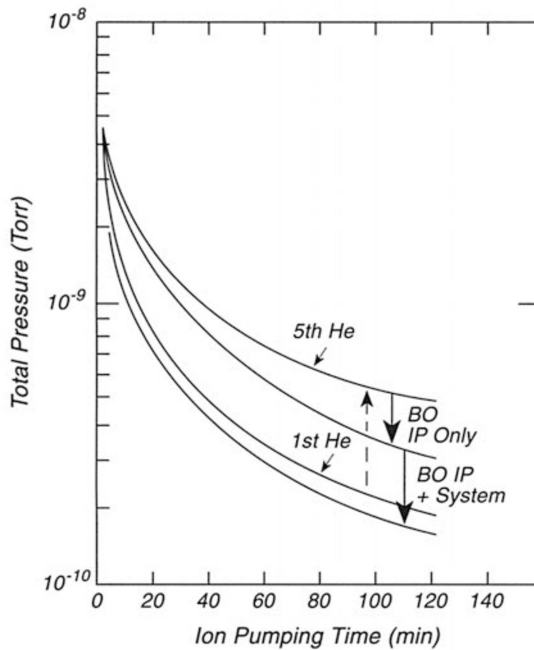

Fig. 4.5 Test chamber and pumping behavior after He purge (1 atm)

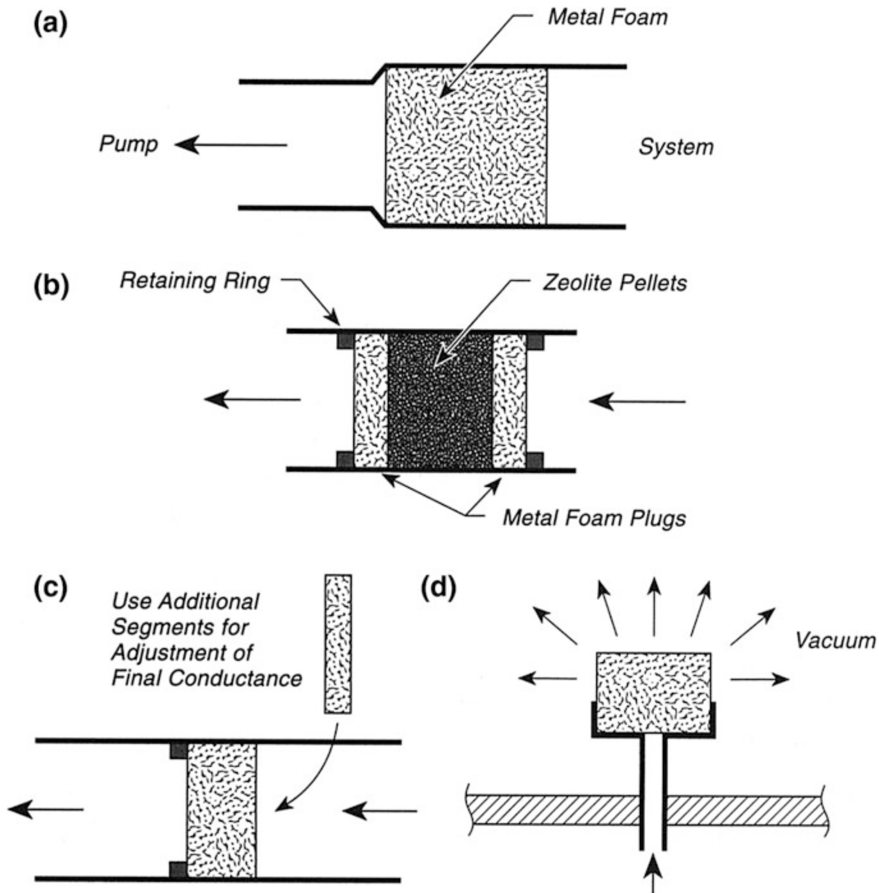

Fig. 4.6 Vacuum applications of metal foams. **a** Foreline hydrocarbon trap. b Foreline zeolite trap. **c** Molecular flow conductance limiter. **d** Gas diffuser

Metal foam has a cellular internal structure. Low-density foam has cell diameters in the range 0.5–1.5 μm, whereas high density foam has cell diameters from 9 to 40 μm. Typical surface areas range from 0.025 to 0.038 m^2/g. For low-density foam the density is typically from 2 to 5.5 % of that of the parent metal. For high-density foam, the density ranges from 20 to 60 % of the bulk metal. Low-density foam can be compressed by up to a factor of 7.

Measurements of the conductance of 2.4 mm thick disks of 5 % density Cu foams made by compression of 1.9 % density foam gave a conductance (for air?) of 3.2 L/s cm^2.

4.7 Cleaning of Ion Pumps by Chemical Etching

There are a number of companies that will take in used ion pumps for reconditioning at a fraction of the cost of purchasing a new ion pump [13]. In cases where the pump is a large one, this may be done by disassembly and cleaning or replacement of the individual components. In the case of small ion pumps, it may be necessary to open the pump casing to get at the inner components, and then to reweld the reconditioned components back into the cleaned casing.

The reconditioning of a dirty ion pump can also be done by controlled chemical etching procedures as described for two cases below.

Case A: Chemical Etching After Disassembly

The pump casing is separated from the Ti cathode assembly as shown in Fig. 4.7. The surface region of the Ti containing implanted impurities is removed by etching the assembly, containing electrode connectors and supports, in a water solution containing 9 % HNO_3, 12 % HF(aq), and 0.4 % H_2O_2 by weight. A 3-s dip, followed by repeated rinsing in deionized water, should produce shiny Ti surfaces. The pump casing is etched in a standard solution (Varian) containing 30 %

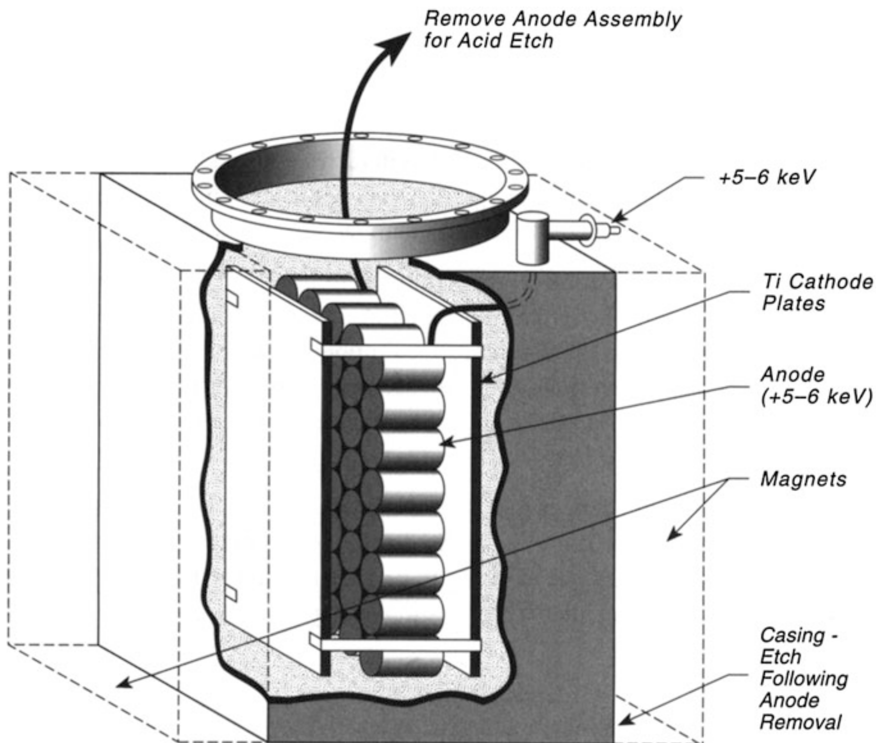

Fig. 4.7 Chemical cleaning—Ion pump

HNO_3(aq), and 3 % HF(aq) by volume. The carbon deposit must be removed mechanically by fine abrasive paper; or, alternatively, it may float off with the Ti film during etching. The pump elements are dried in warm air, assembled, and pumped into a second ion pump while baking at 200 °C [14].

Case B: Chemical Etching Without Disassembly
In this situation, the fact that the acid attacks the Ti more readily than the ceramic-metal seal is employed. First the pump is rinsed in deionized water. This is reported [14] to seal the ceramic partially against the acid. A water solution of 30 % HNO_3(aq) and 3 % HF(aq) by volume is added and quickly rinsed away with deionized water. The pump is dried by warm air and baked and pumped as in Case A.

The original report indicates that the hydrogen background pressure from an acid-cleaned pump will be somewhat higher than from one reassembled using new elements [14].

4.8 An Efficient Liquid Nitrogen Trap

Liquid nitrogen traps are highly inefficient because of the discharge of liquid nitrogen out of the trap when the trap is being refilled periodically. A design, shown made of glass in Fig. 4.8, eliminates this problem [15], and reduces liquid nitrogen consumption by severalfold, resulting in great economies over long periods of time. The basic concept embodied in this small glass trap is transferable to large metal traps.

The trap consists of an inner trap of conventional design, labeled the inner chamber, surrounded by a second outer chamber, which is in turn surrounded by a silvered Dewar flask. All of these are sealed together by glassblowing in this design. A resistance temperature sensor is immersed in the second outer chamber.

When the trap is at a condition where refilling is to occur, all liquid nitrogen in the Dewar has been lost, and the level of nitrogen in the outer chamber has dropped to a level causing the sensor to turn on the liquid nitrogen supply, which is driven by compressed nitrogen gas. Liquid nitrogen flows into the Dewar and spills into the outer chamber through the lower hole; it then fills the outer chamber until the sensor delivers a shutoff signal.

The avoidance of liquid nitrogen loss is attributed to the fact that the Dewar does not contain liquid nitrogen at the time of filling, so that the burst of nitrogen gas at the beginning of the fill sequence does not eject liquid nitrogen from the trap. In addition, ice buildup does not occur at the inlet and outlet to the trap [15].

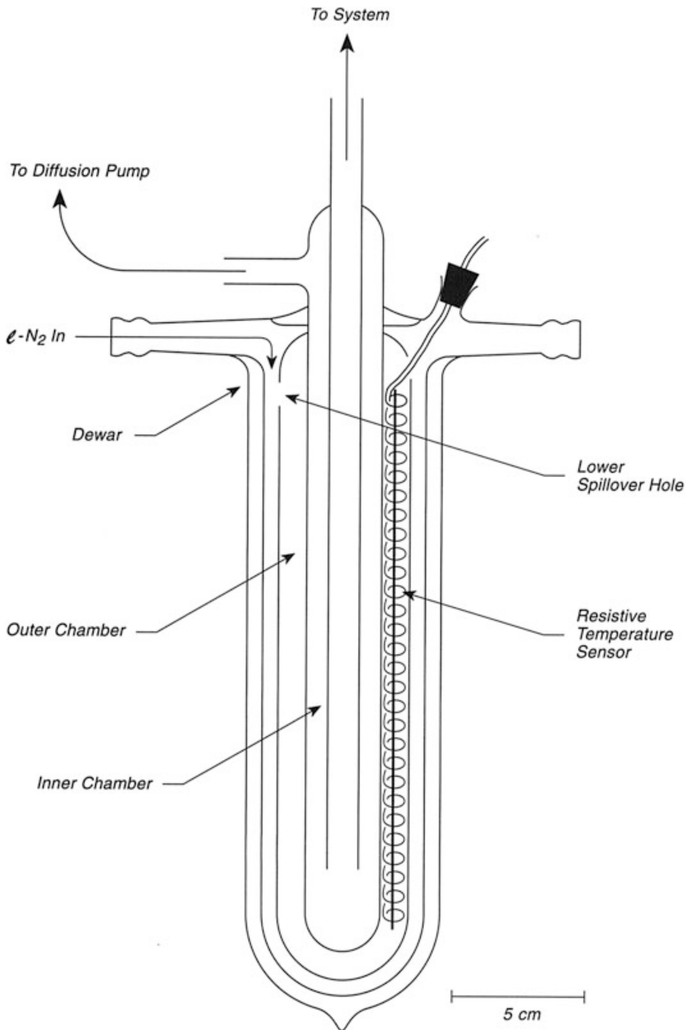

Fig. 4.8 Efficient liquid N_2 trap

References

1. A.M. Russell, Rev. Sci. Instrum. **36**, 854 (1965)
2. Dr. Oliver Schaff, Fritz Haber Institut der Max Planck Gessellschaft, Faradayweg 4–6, D-14195, Berlin (private communication)
3. Dr. W. F. Egelhoff, National Institute of Standards and Technology, Gaithersburg, MD 20899-0001 (private communication)
4. P.A. Redhead, E.V. Kornelsen, J.P. Hobson, Can. J. Phys. **40**, 1814 (1962)
5. G. Lu, A.L. Linsebigler, J.T. Yates Jr, J. Vac. Sci. Technol. **A12**, 384 (1994)

6. P.A. Redhead, J.P. Hobson, E.V. Kornelsen, *The Physical Basis of Ultrahigh Vacuum* (AIP, New York, 1993), pp. 403–406
7. L.Y.L. Shen, Rev. Sci. Instrum. **43**, 1301 (1972)
8. Dr. R. David, Institut fur Grenzflächenforschung und Vakuum physik, Forschungszentrum Jülich GmbH, Postfach 1913, D-52425 Jülich, Germany (private communication)
9. P.M. Danielson, J. Vac. Sci. Technol. **5**, 89 (1968)
10. Foametal, Inc., 37645 Vine Street, Willoughby, OH 44904
11. Energy Research and Generation, Inc., 900 Stanford Avenue, Oakland, CA 94608
12. B.R.F. Kendall, J. Vac. Sci. Technol. **17**, 1385 (1980)
13. One company offering this service: Duniway Stockroom, Inc., 1600 N. Shoreline Boulevard, Mountain View, CA 94043
14. P.H. Schmidt, L.Y.L. Shen, Rev. Sci. Instrum. **44**, 1788 (1973)
15. R.S. Timsit, A.K.C. Kiang, Rev. Sci. Instrum. **44**, 770 (1973)

Chapter 5
Bakeout

5.1 Bakeout of Metal Ultrahigh Vacuum Systems

The removal of adsorbed impurities from the walls of an ultrahigh, vacuum system is carried out by heating the walls uniformly while pumping the system. Generally, for stainless steel systems this is done in the temperature range 150–200 °C. For preservation of effective ion pumping, bakeout into a turbopump is recommended to avoid introducing a high gas load into the ion pump. Ion pumps have only a finite capacity, and also suffer from regurgitation effects in which previously pumped gas is evolved when another gas is being pumped-as would occur in an experiment in which gas is admitted to the chamber.

Many methods are used to bake out metal systems. Heating tapes, IR radiation heaters on the outside, clamp-on band heaters, glue-on rubberized heaters, and internal light-bulb heaters have all been used. In order to lose as little heat as possible, it is appropriate to surround the system with some sort of reflective bakeout shield [1]. Figure 5.1 shows a schematic system in which aluminized fiberglass [2] is used to shield the main system. The fiberglass tent is supported internally by temporary metal supports. Radiative heaters are uniformly distributed over the system inside the reflective shield, and for appendages such as the bellows on the top, lightweight reflective metal cylinders may be used for radiation capture. The system should be monitored over many positions with thermocouples to assure uniform heating, and the wattage output of the various radiative heaters may be varied to achieve uniformity. Experience in monitoring the pressure during bakeout will supply information about the bakeout time needed to reach the ultimate low pressure [3]. It is reported that external IR lamps bring the vacuum system to bakeout temperatures much faster than other methods [1].

Quite nice tents made, of the aluminized fiberglass may be constructed, and a convenient method for joining the sections is to use a poprivet device to make excellent lap seams. The aluminum surface is placed on the inside of the tent. Even nonaluminized fiber glass curtain material may be used by sandwiching aluminum

© Springer International Publishing Switzerland 2015

J.T. Yates Jr., *Experimental Innovations in Surface Science*,
DOI 10.1007/978-3-319-17668-0_5

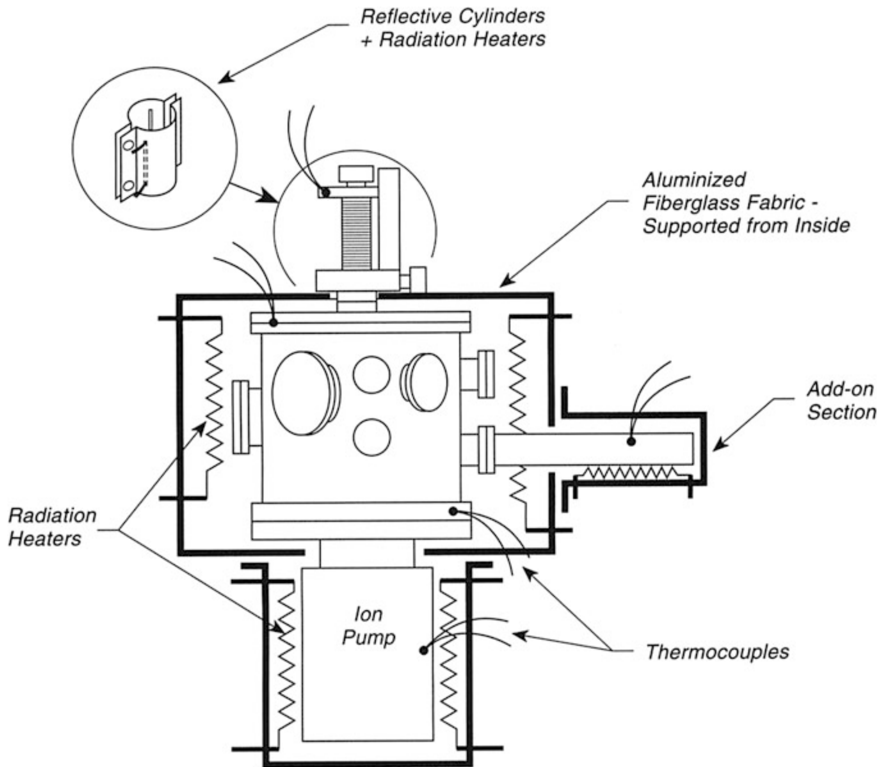

Fig. 5.1 Schematic bakeout assembly

foil between the layers. A small internal circulating fan inside the oven will lead to improved temperature uniformity.

Experience indicates that clamp-on band heaters applied to metal flanges can thermally shock the flanges to a point where a leak develops. In the event that these heaters are used, a gradual increase in the applied voltage over time is recommended. Internal lamp heaters, working inside the vacuum system, would seem to be ideal for bakeout because of efficient radiation capture by the system walls, but if breakage of the glass envelope occurs, the system will have to be completely cleaned of glass slivers before continued use. Such slivers are very detrimental to welded bellows and to the sealing surfaces of valves.

Turbopumps should be baked at the end of the bakeout period (for about 4 h). Titanium sublimation pumps should be outgassed until the pressure reading reaches a maximum; long outgassing at high temperature will oxidize the components near the hot Ti. It has been found that cooling the room during measurements will cause a substantial improvement in the limiting pressure under ultrahigh vacuum conditions owing to the reduction in the outgassing rate from the system walls [4].

Often it is appropriate to bake, out a new system, with all heat sensitive components removed, to temperatures between 300 and 450 °C to remove impurities left from chemical cleaning procedures.

References

1. B.V. Hess, T.E. Felter, J. Vac. Sci. Tech. **A3**, 2218 (1985)
2. Fyrepel, P.O. Box 518, Newark, OH 43055
3. R. David, Institut fur Grenzflächenforschung und Vakuum-physik, Forschungszentrum Jülich GmbH, Postfach 1913, D-5170 Jülich, Germany (private communication)
4. Pittsburgh Surface Science Center

Chapter 6
Behavior of UHV Systems

6.1 Wall Passivation in Stainless Steel Ultrahigh Vacuum Systems

To achieve the limiting pressure in an ultrahigh vacuum system, it is necessary to reduce the rate of desorption of molecules from the stainless steel walls to the lowest possible limit. These surface impurities originate from exposure of the walls to impurities during opening and processing of the system. They also result from the diffusion of impurities in the bulk of the stainless steel to the wall surface, especially for the case of dissolved hydrogen [1].

Bakeout in the presence of traces of oxygen or water may result in further oxidation of the walls, leading to some passivation. However, a more effective technique involves the oxidative passivation of the stainless steel walls with a strong gaseous oxidizing agent. The oxidation of the walls and the oxidizable surface impurities is kinetically accelerated using a strong oxidizing molecule. In Fig. 6.1, an energy level diagram (Gibbs free energy) is shown. It may be seen that the nitric oxide molecule is more energetic than a mixture of O_2 and N_2 to which its energy is referenced. The excess energy is 0.9 eV/NO at 300 K. This excess chemical energy may be sufficient to allow the NO molecule to produce a rapid surface oxidation process that proceeds only slowly over an activation barrier when O_2 is the oxidizing agent. The oxidation process on the surface is schematically shown as the formation of a chemisorbed O atom (O(a)), but the formation of CO_2 or H_2O from surface carbon or from surface hydrogen could also be the end result of the oxidation process.

These ideas have been used to clean up the walls of an ultrahigh vacuum system during bakeout, achieving lower base pressure [2]. The bakeout at 200 °C was carried out in a background pressure of NO of 5×10^{-7} mbar achieved by flowing NO through the hot system. Initially, during the first phase of the treatment, high levels of N_2, H_2O, and CO_2 are detected as the NO acts to oxidize the surface and the oxidizable impurities. After 30–180 min, a continuous increase of the partial

© Springer International Publishing Switzerland 2015

J.T. Yates Jr., *Experimental Innovations in Surface Science*,
DOI 10.1007/978-3-319-17668-0_6

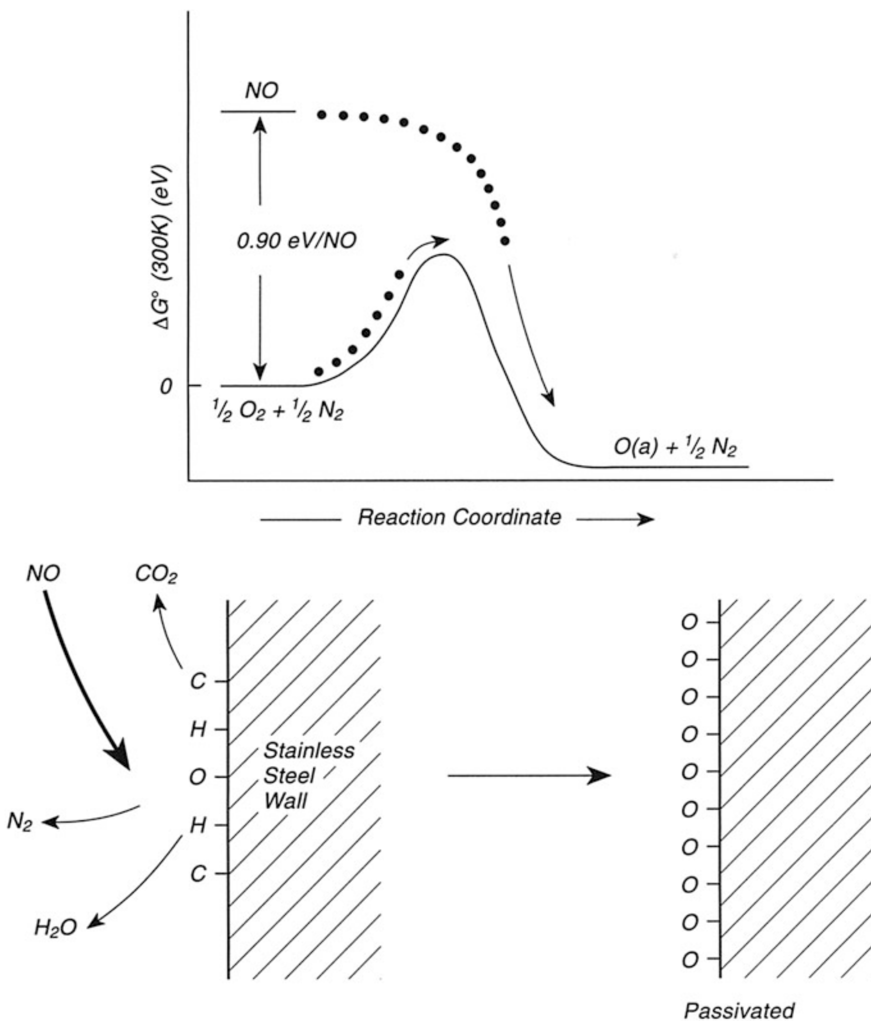

Fig. 6.1 Nitric oxide surface reactivity for passivation of vacuum system walls

pressure of NO occurs, and the oxidation of the surface approaches completion. This treatment is particularly good for reducing the displacement of surface impurities from the walls during subsequent adsorption experiments. A simple equilibrium thermodynamics calculation shows that the use of the energetic NO molecule at 5×10^{-7} mbar is equivalent to the use of O_2 gas for the same purpose at a pressure of about 10^6 atm!

6.2 Minimizing Wall Reactions in Ultrahigh Vacuum Systems—Gas Dosers

The purity of gases used in surface science adsorption and surface reaction studies is of paramount concern just as the production of ultrahigh vacuum is directed toward the same end. Often gas dosers are employed to deliver pure gases to surfaces, and for some gases, the displacement of adsorbed impurities, or the reaction of the dosing gas with the internal surfaces of the gas dosing system itself can be a problem. In the case of a surface reaction, it is sometimes possible to passivate the internal surface of a gas doser to reduce the rate of the surface reaction. Figure 6.2a shows a typical gas doser made mainly of stainless steel. The construction of this doser and its calibration are discussed elsewhere (p. 421); however, it may be seen that the conductance is controlled by a laser-drilled aperture, and collimation of the exiting gas is achieved using a microcapillary array made of glass. Both the internal metal surface and the internal surface of the microcapillary array (which is many tens of cm^2) provide reactive surface area that can evolve impurities by displacement or reaction [3], Displacement processes, such as the exchange of surface OH groups with OD groups in deuterated alcohols, can often best be handled by overnight flushing of the doser with the isotopic gas. In extreme cases of reaction with acid sites on the internal surfaces of the capillaries [3], one must remove the glass microcapillary array from the doser [3, 4]. Reaction processes with the stainless steel walls of the doser system can sometimes be reduced in magnitude by passivation of the internal surfaces. This is vividly seen in the behavior of the metal carbonyls, where decomposition of $Fe(CO)_5$ on the inner stainless steel walls has been shown to produce CO(g), leaving iron on the wall [4]. The surface reaction was studied, and it was found that predosing the doser and its stainless steel delivery system with high fluxes of molecular oxygen resulted in significant reduction of the decomposition reaction, as judged by mass spectrometric studies of the gas exiting the doser, line-of-sight, into the mass spectrometer [4]. The internal walls of the ultrahigh vacuum system were found to have little effect on the metal carbonyl, probably because it was exposed to oxygen each day [4]. For the experiments, it was found that the glass microcapillary usually employed with this design of gas doser had to be removed because of deleterious effects on $Fe(CO)_5$.

Another solution to this problem is to make the doser system from materials other than stainless steel [5]. Figure 6.2b shows such a system, in which the glass tube doser contains a capillary for the control of the flow rate from the connecting tube into the ultrahigh vacuum system through the Pyrex doser tube. The high-pressure (several Torr) section beyond the Teflon-glass valve is made of PFA (polyfluoroalkoxy) plastic and fittings are readily available commercially [6]. The paper describing this system indicates that the capillary tube was produced by hand and was drawn down to a fine diameter. This particular design was used for the delivery of hydrazine (N_2H_4). Thermometer tubing, made generally of lead glass, has a ~100–150-μm diameter capillary for sensitive thermometers (1 K/3.8 cm

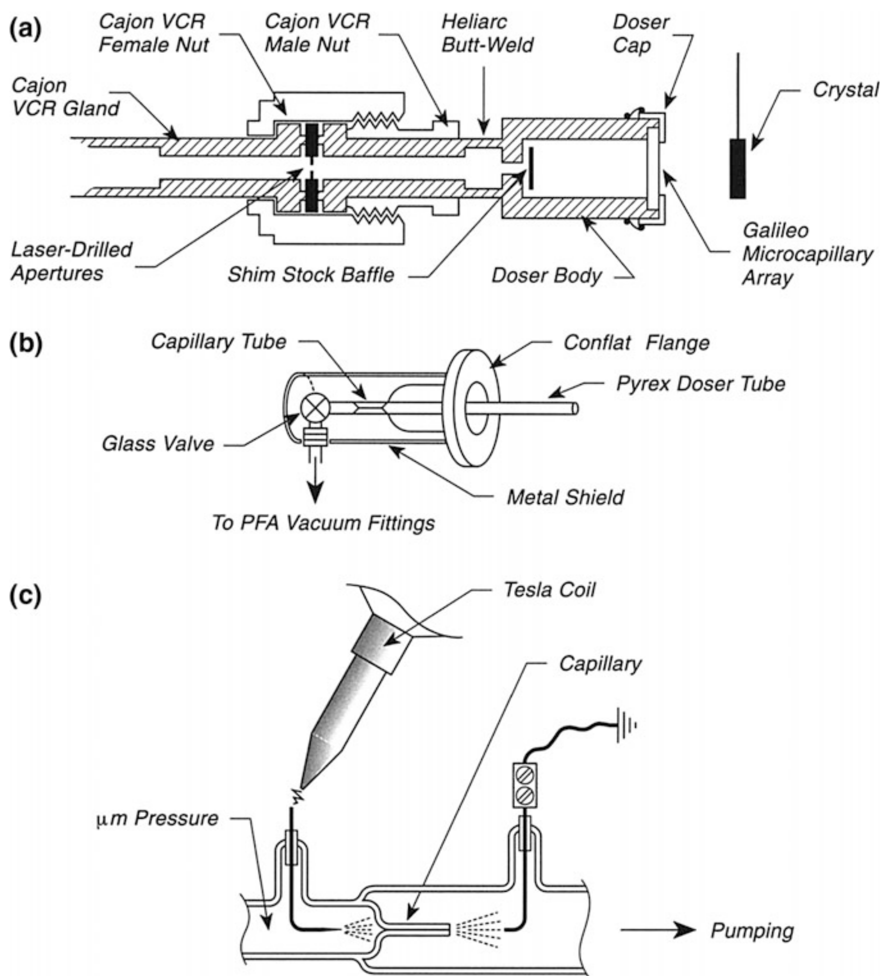

Fig. 6.2 Gas doser designs. **a** Stainless doser+microcapillary array collimator. **b** Pyrex—plastic doser. **c** Cleaning clogged glass capillaries

capillary length) and may be used if a lead glass to Pyrex glass graded seal is employed. A Teflon doser for ultrahigh vacuum use also has been described [7], as well as a heatable glass and Teflon doser for admission of organometallics of low vapor pressure [8].

It is unfortunate that glass capillaries often clog up with traces of dust or grease that are present within the vacuum system. A clever method to restore the capillary to a clean, unblocked condition is shown in Fig. 6.2c [9]. Here, the capillary section is surrounded on both ends of the capillary with pointed tungsten electrodes, easily installed by the glassblower. When the capillary becomes blocked, micron pressures are established on the high-pressure side of the capillary, and the vacuum-side

electrode is electrically grounded. The application of a Tesla coil to the high-pressure tungsten electrode produces an internal plasma discharge, and the plasma usually cleans out the obstruction in the capillary within seconds. We have found that this harsh internal treatment changes the conductance of the glass capillary slightly, and recalibration after cleaning is suggested.

A third solution that has been used to minimize reactions inside a gas doser is to dilute the reactant gas with an inert diluent such as He or Ar [10]. This may be done in a gas handling line that is dynamically pumped, causing the gas mixture to be replenished rapidly, and removing products of reaction [10]. This method also permits small doses of the reactive gas to be quantitatively monitored since pressure measurements of the mixture may be converted to partial pressure measurements of the active gas. One must remember that the composition of the gas mixture will change under dynamic pumping conditions owing to different rates of pumping for the gas components [10].

Reports of the use of a Teflon coating for passivation of the stainless steel walls of an ultrahigh vacuum system are available [11, 12]. Briefly, a weak acid priming treatment was used to remove oxide films to promote adhesion of the Teflon. A Teflon suspension [13] was painted on the walls and cured in the air for several days. The coating was then baked in vacuum at 200 °C. Small parts were cured using a heat gun before assembly. This coating was effective in preventing $TiCl_4$ decomposition on the walls. However, the Teflon adsorbs water from the air when the system is opened, and longer bakeout is required to get to a base pressure in the mid 10^{-9} Torr range than would be required with an uncoated vacuum chamber [12].

References

1. P.A. Redhead, J.R. Hobson, E.V. Kornelsen, *The Physical Basis of Ultrahigh Vacuum* (AIP, New York, 1993)
2. M. Grunze, G. Strasser, O. Eishazly, J. Vac. Sci. Technol. **A4**, 2396 (1986)
3. P.K. Leavitt, P.A. Thiel, J. Vac. Sci. Technol. **A8**, 148 (1990)
4. M.A. Henderson, R.D. Ramsier, J.T. Yates Jr, J. Vac. Sci. Technol. **A9**, 2785 (1991)
5. E. Apen, R. Wentz, F. Pompei, J.L. Gland, J. Vac. Sci. Technol. **A12**, 2946 (1994)
6. Swagelok fittings are available from Swagelok, 31400 Aurora Road, Solon, OH 44139
7. M.A. Mendicino, E.G. Seebauer, J. Vac. Sci. Technol. **A10**, 3590 (1992)
8. L.A. Jones, F.-X. Wei, D.F. Thomas, Rev. Sci. Instrum. **66**, 4981 (1995)
9. D.A. King, (1970) (private communication)
10. E.C. Henn, M.E. Bussell, C.T. Campbell, J. Vac. Sci. Technol. **A9**, 10 (1991)
11. W. Muller-Markgraf, M.J. Rossi, Rev. Sci. Instrum. **61**, 1217 (1990)
12. Professor E.G. Seebauer, Department of Chemical Engineering, University of Illinois, Urbana, IL 61801. From thesis by M.A. Mendicino, Ph.D (1994) (private communication)
13. Teflon or PTFE suspension is obtainable from: Intek Services, Inc., 7 McMillan Way, Suite 101, Newark, DE 19713

Chapter 7
Mechanical Action on Samples

7.1 Simple UHV Crystal Cleaver

Often one of the best ways to produce an atomically clean surface is to expose an inner cleavage plane by cleaving the crystal in ultrahigh vacuum. A simple mechanical cleaver design is shown in Fig. 7.1a [1]. Here, a MgO single crystal is mounted on a coolable manipulator inside a small rectangular compartment, held by a screw that presses on an internal plate that distributes the screw pressure over the side of the crystal. A portion of the crystal projects upward, ready for the cleaver blade.

The cleaver is a spring-loaded tungsten carbide blade (25° cutter angle) that slides in a stainless steel channel. Two springs are compressed by turning a pair of screws prior to attaching the cleaver to the manipulator. The manipulator/cleaver assembly is loaded into the vacuum system, and after system processing, the trigger holding the blade back is released by moving the manipulator against the side of the manipulator port. The blade cleaves the crystal, and caution should be exercised not to allow the cleaved-off portion of the crystal to enter fragile apparatus as it bounces around the chamber.

Using a closed cycle He cryocooler, this assembly can reach 44 K. Studies on the freshly cleaved MgO(100) surface, involving Kr adsorption, are shown in Fig. 7.1b, and the results are compared to MgO that has been cleaved outside the vacuum system, transferred, and thermally processed. The sharp vertical step indicating a 2D gas → 2D solid transformation, as studied by LEED, is characteristic of the UHV-cleaved crystal; a less distinct transition is seen on the externally cleaved crystal because of defects produced by water adsorption that cannot be removed by thermal processing. Indeed, after days of storage in UHV, the UHV-cleaved crystal begins to yield an isotherm resembling that of the defective crystal because of slow impurity adsorption.

© Springer International Publishing Switzerland 2015

J.T. Yates Jr., *Experimental Innovations in Surface Science*,
DOI 10.1007/978-3-319-17668-0_7

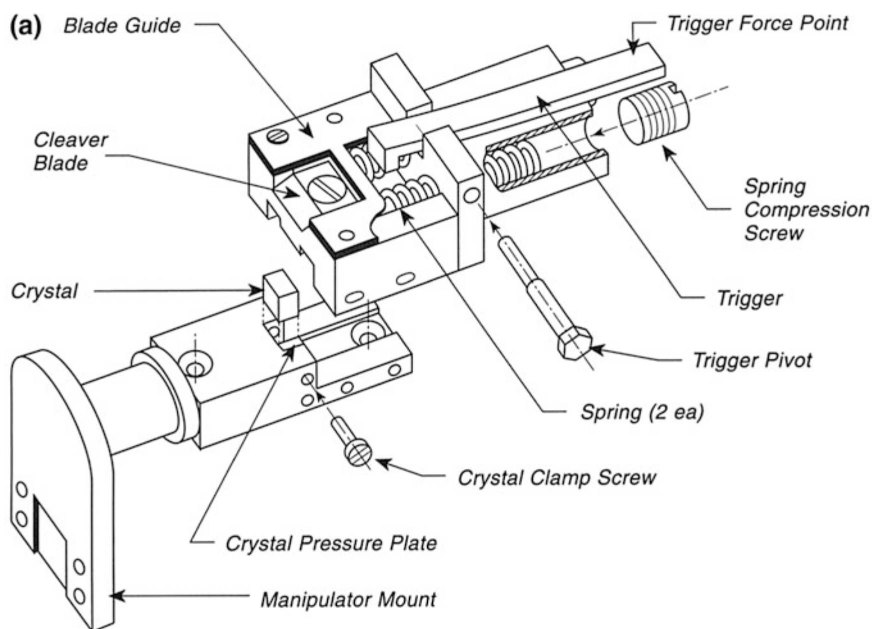

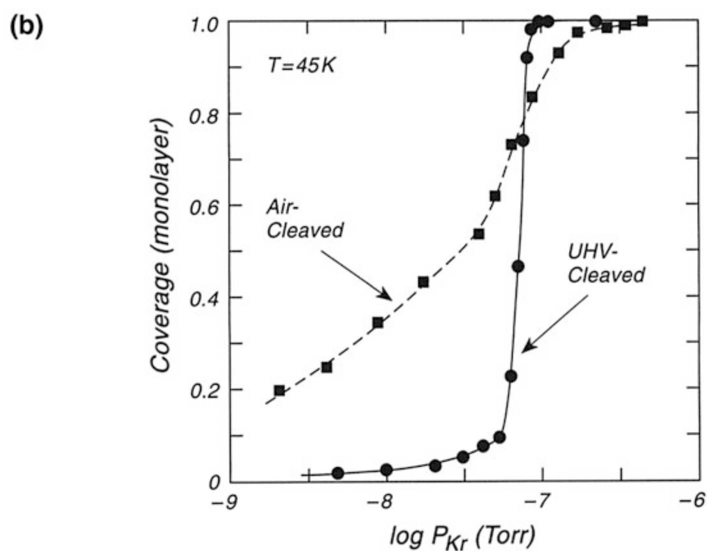

Fig. 7.1 Simple UHV cleaver. **a** Cleaver design. **b** Comparison of Kr isotherms on MgO(100) using LEED

The authors report that the only disadvantage of this design is that only one cleave can be achieved per loading into the vacuum system because of the necessity to compress the springs outside the vacuum system.

A cleavage device for mica has been described that can be used in ultrahigh vacuum [2].

7.2 Piezoelectric Fatigue Apparatus for UHV Operation

There is much interest in the role of adsorption on the rate of fatigue of metals undergoing periodic stress conditions. Usually these measurements are performed under cycle rates of about 1 Hz. Hydraulic cycling methods often impart noise to the stress-strain measurement system. A piezoelectric drive mechanism, capable of working at 100 Hz frequency in UHV, is described below [3].

Figure 7.2a shows a schematic drawing of the apparatus. The specimen, coupled to an extensomer, is clamped between two grips that have serrated clamping surfaces to prevent misalignment during testing. A load cell is placed above the moving grip and below the piezoelectric actuator. The translator used has a capacity of 10 kN in compression, and 3.5 kN in tension [4]. It is capable of translation through about 40 μm over an applied voltage range of 0–1500 V. The load is measured with a load cell having a range of 0–2000 N [5]. A strain of about 0.3 % may be measured using an extensometer [6] in a gauge section of 5 mm, and the specimen tested in this case was polycrystalline Ag. The control electronics are described in [7]. Figure 7.2b shows a hysteresis curve measured for Ag in which the stress and strain are measured during compression and expansion. The hysteresis loop changes as the number of cycles increases, and is a measure of the specimen fatigue. The data obtained with the piezodriver exhibits a better signal-to-noise ratio than data taken with hydraulic devices.

The main disadvantage of the device is the small translation range of the driver. The device must account for all of the translations taken up by the components along the axis of the load. This limits the machine to small specimens, and for high-strength materials, smaller gauge lengths and more narrow cross sections would be needed to obtain sufficient strains for accurate measurement [3].

Another design, providing fatigue to a thin metal specimen in ultrahigh vacuum, has been described [8]. It was found that clean Al(111) single crystals exhibited changes in their ultraviolet photoelectron spectrum after 1000 fatigue cycles at 0.2 % strain. The involvement of chemisorbed species containing oxygen was eliminated on the basis of the absence of O(2p) emission in the photoelectron spectrum, and no explanation was given for this effect [8].

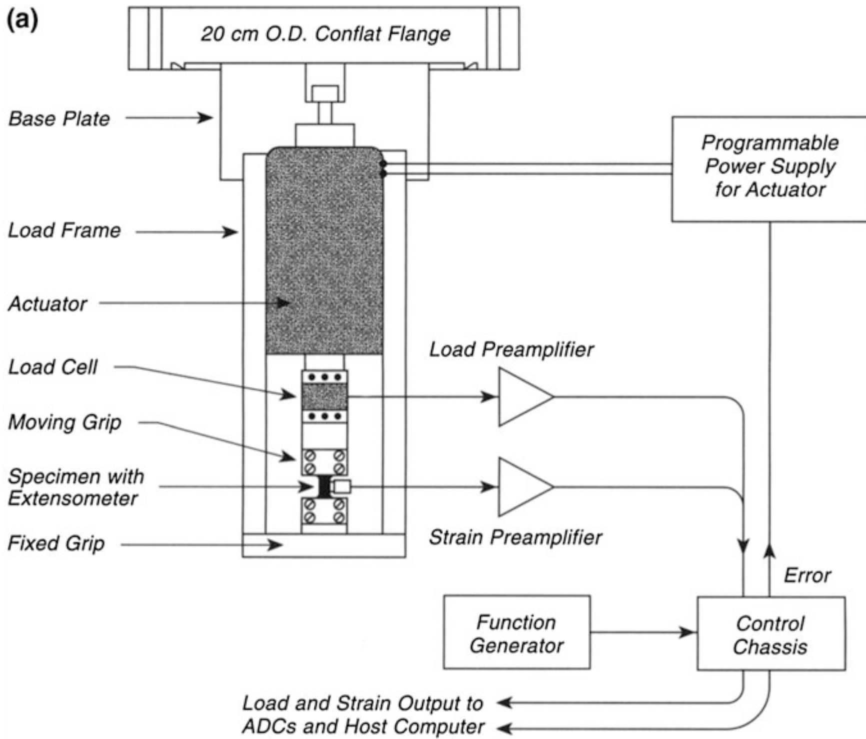

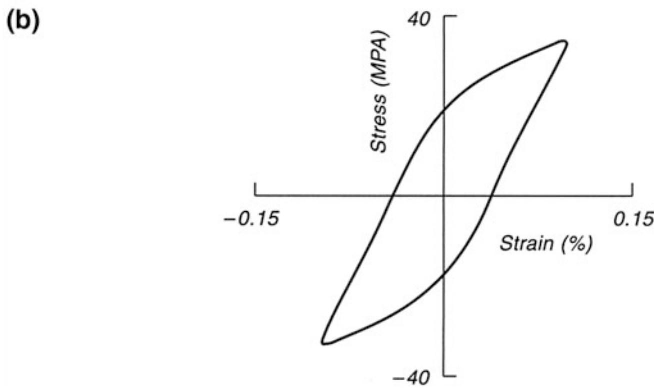

Fig. 7.2 Piezoelectric fatigue apparatus—UHV. **a** Schematic design. **b** Typical stress-strain curve —polycrystalline Ag

References

1. T. Angot, J. Suzanne, J.Y. Hoarau, Rev. Sci. Instrum. **62**, 1865 (1991)
2. K. Reichelt, Rev. Sci. Instrum. **44**, 243 (1973)
3. T.S. Sriram, M.E. Fine, Y.-W. Chung, Rev. Sci. Instrum. **62**, 2008 (1991)
4. Physik Instrumente, Model 243.37, Option 703.20, sold by PolyTec Optronics, 3001 Redhill Ave., Costa Mesa, CA 92626
5. Model 31, SENSOTE Inc., 1202 Chesapeake Ave., Columbus, OH 43212
6. Model 632.29C, Option 011, MTS Systems Corporation, Box 24012, Minneapolis, MN 55424
7. W.J. Lee, Y.-W. Chung, M.E. Fine, J.P. Baker, Rev. Sci. Instrum. **57**, 2854 (1986)
8. T.K.G. Swami, Y.W. Chung, Rev. Sci. Instrum. **51**, 842 (1980)

Chapter 8
Gasket Seals

8.1 Gasket Seals for Ultrahigh Vacuum Systems

The primary ultrahigh vacuum flange design used universally is the stainless steel Conflat sexless flange, which operates with two opposed knife edges that seal a metallic gasket by deformation when the flange is tightened. A cross-sectional view of the flange and a confined gasket is shown in Fig. 8.1.

In many cases where it may be difficult to seal the gasket by applying the necessary torque to the flange bolts, or where tightening down to the maximum force level is not desired, it is useful to use annealed copper gaskets. These maybe purchased from the suppliers, but they can be made quite simply in the laboratory beginning with a nonannealed gasket. The gasket is heated while rotating it around its circumference in an oxygen-gas torch (cool flame) until dull red color is emitted by the hot copper. The gasket is then quenched in water quickly, resulting in softening to almost the softness of lead or tin. This gasket will deform in the seal region with less torque on the bolts and also with less deformation of the flange during tightening. Often, gaskets of this type are needed for spectroscopic windows mounted in stainless steel flanges in order to prevent window cracking during tightening owing to flange flexure.

The annealing process results in considerable oxidation of the copper gasket, and this oxide layer must be removed before use. Two methods are available to do this. In the first, the hot gasket, immediately after annealing, is dropped into methanol instead of water. The methanol, a reducing agent, immediately strips off the oxide from the hot metal, leaving a clean copper surface. Care should be exercised to avoid damage if the methanol should ignite. The second method involves dropping the cool gasket into an aqueous solution of citric acid. Here the citric acid forms a soluble complex with the copper ions in the oxide film, and again clean copper surfaces are produced.

Certain coatings are employed to prevent the oxidation of copper gaskets following relatively high temperature bakeouts. Heavy amounts of copper oxide can

© Springer International Publishing Switzerland 2015

J.T. Yates Jr., *Experimental Innovations in Surface Science*,
DOI 10.1007/978-3-319-17668-0_8

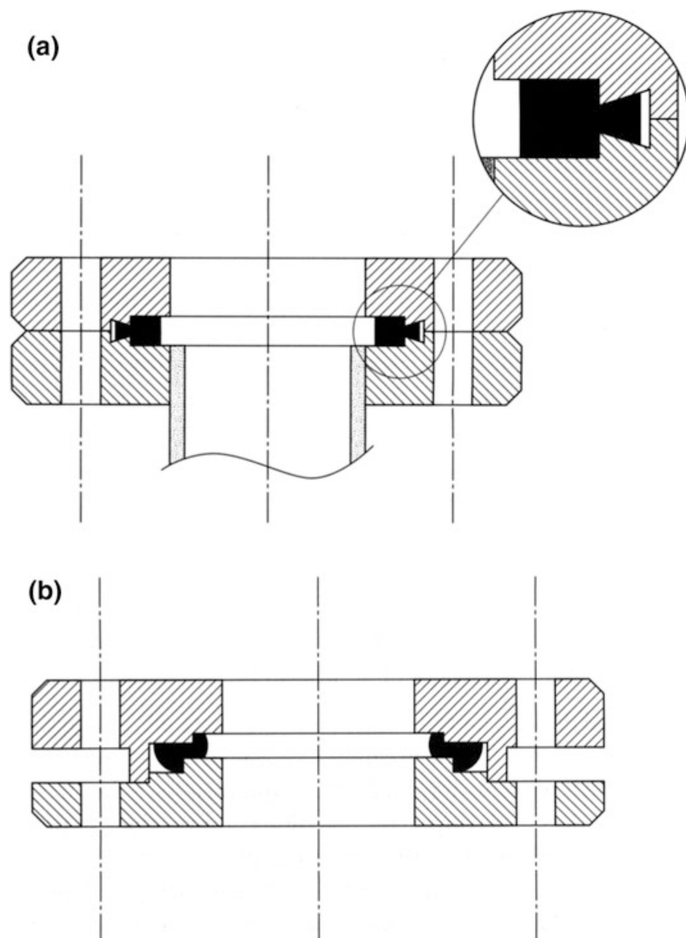

Fig. 8.1 Gasket designs. **a** Conflat flange + Cu gasket. **b** Gold wire—shear seal

fall into the vacuum system when the flange is opened, and also seizure of the gasket in its recess in the stainless steel flanges can occur. Silver plating has been used to prevent this effect [1]. A minimum 5-μm-thick silver film, made by plating, is required. The silver will stand repeated bakeouts at 300–350 °C. Contamination of the silver film by sulfur from either the gasket or from sulfur-containing lubricants is to be avoided as this causes discoloration and peeling of the silver film. Thus, bolt lubricants such as molybdenum disulfide cannot be used and graphite or other lubricants must be employed.

Another useful copper gasket coating is titanium nitride, TiN [2]. Using reactive magnetron sputtering from a Ti target in an N_2 + Ar mixture (20 % N_2), films from 50 to 150 Å were deposited on copper gaskets. In tests, ten flanges were baked at 550 °C in a vacuum of 10^{-5} Torr for up to 200 h, and were then tested for leak

tightness with a He leak detector, finding no leaks. The flanges could then be disassembled without seizure. Without the TiN film, separation must be done with jacking screws and copper is left on the sealing surfaces, requiring abrasives for removal. A similar coating has also been prepared using diamondlike carbon coatings prepared by RF discharge techniques in methane gas [3].

One of the early methods of sealing stainless steel flanges employed gold wire gaskets [4]. For flat flanges without a knife edge or for a stepped seal used for crushing a metal gasket, gold wire will make an excellent seal. The wire, of about 0.25–0.5 mm diameter, is made into a circular loop on a forming mandrel; then a microtorch is used to butt weld the ends together when the loop is removed from the mandrel. This process is best accomplished by gently clamping together the squared off ends of the gold wire and slowly melting the gold so that surface tension causes liquid gold flow to even out the diameter of the heated region. Too much heating will result in separation of the gold wires with the formation of balls of gold on the ends of each. Practice is, therefore, necessary. The wire once formed is placed between two smooth flange faces, and the bolts are tightened, making an ultrahigh vacuum seal. A stepped seal may also be used with either gold or copper, and here the seal produces a shear seal within the gasket as shown in Fig. 8.1. In the case of gold wire shear flanges, the wire must be butt-welded to fairly exact dimensions using a mandrel of the same size as the male flange for accurately cutting the gold wire to appropriate length. A nice description of the method to make custom copper wire gaskets is given in [5].

The reuse of large Cu gaskets for many cycles has been described [6]. Here, a "feeler gauge" such as that used to measure spark plug gaps is employed, and successive seals with the original gasket are made by diminishing the flange-to-flange clearance in a systematic manner.

8.2 Cryogenic Gasket Seals

Stainless steel Conflat flanges are guaranteed to be vacuum tight from 77 K up to their normal bakeout temperature limits. However, there are special situations where vacuum components made of different metals are to be joined by flanges, and in these cases cooling to 77 K may disrupt the vacuum seal because of differences in thermal expansion coefficients.

This problem has been solved for 18-mm-diameter junctions between stainless steel flanges and aluminum Conflat 34 flanges using a gold wire seal (Fig. 8.2). In this design, the mismatch in expansion/contraction occurs in a radial direction along the sealing plane, and this stress can be absorbed by the plastic deformation of the gold wire. The seal is maintained through many cycles as a result of the gold ductility and its good adherence against stainless steel and aluminum surfaces [7].

A cross sectional drawing of the seal is shown in Fig. 8.2. The gold wire ring was 1 mm in diameter, prepared by butt-welding. The screws were 4 mm diameter, made of stainless steel which prevents the need for retorquing after a thermal cycle.

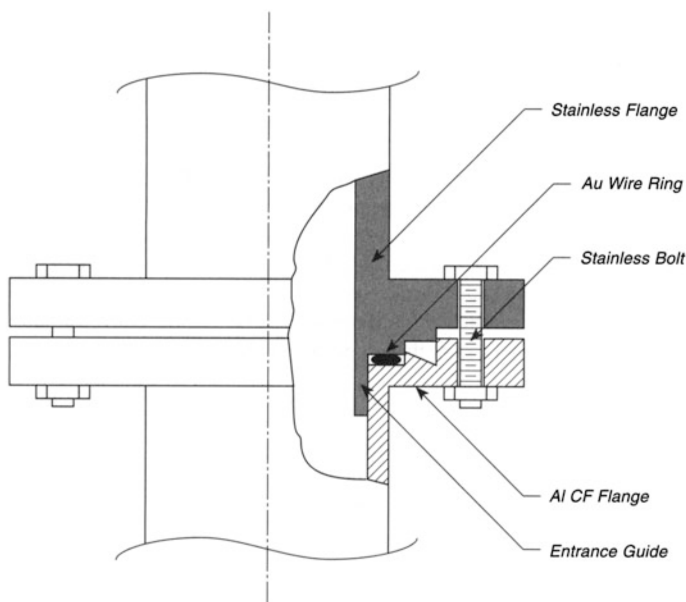

Fig. 8.2 Gold wire seal—cryogenic design

The specially designed stainless steel flange has a precision entrance guide to prevent damage to the aluminum knife edge and it is also machined to be very smooth on its sealing surface. In the particular case shown here, the stainless steel, exhibiting poor heat conduction, was needed to reduce the thermal conduction of heat to the aluminum section therefore preserving liquid nitrogen which was housed in the aluminum section.

8.3 Copper Gasket Removal Devices

There are three published methods that are directed toward easy removal of copper gaskets from Conflat flanges after disassembly [8–10]. These methods are all designed to prevent damage to the sharp sealing knife edges by tools being used to pry up the gaskets. The first of these [8], shown in Fig. 8.3a, employs Conflat flanges that have two opposed slots machined on the inside of the flange. A screwdriver blade can be inserted into the slot and rotated to pop out the gasket and the boundary of the slot prevents the blade from coming into contact with the knife edge. The disadvantage of this design is that one must machine every flange with the two slots [9]. A second design [9] (Fig. 8.3b), uses the leak-check groove as a slot to control the motion of a specially wedge-shaped and hardened steel blade, shown. The third design (Fig. 8.3c), shows a modified "parrot-nose" set of

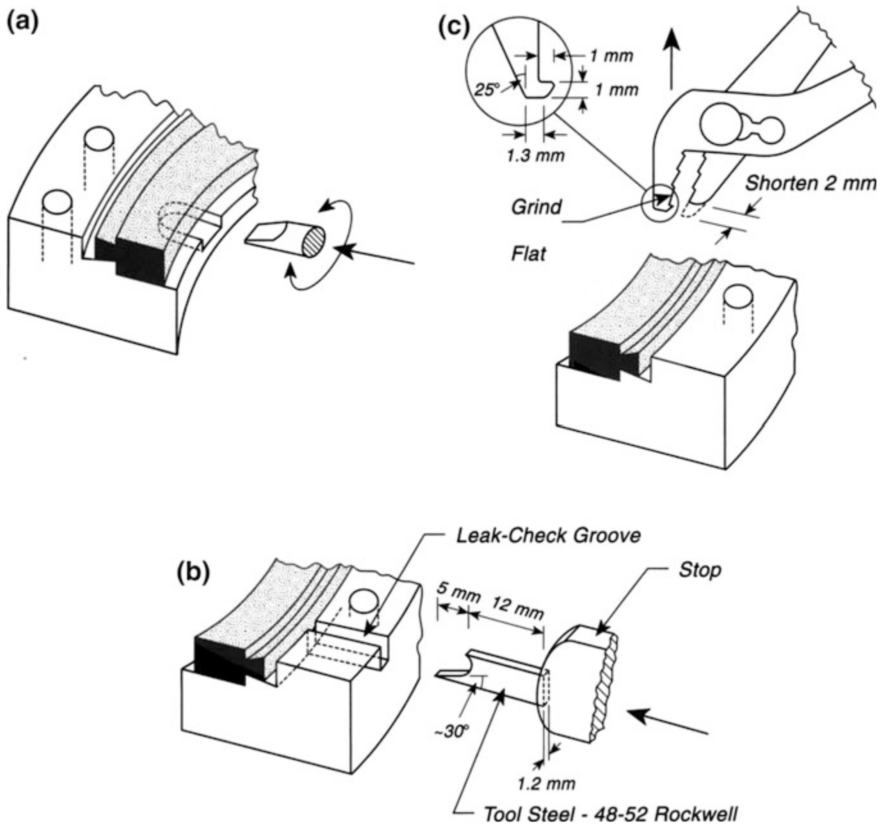

Fig. 8.3 Tools for copper gasket removal. **a** Inside slot design. **b** Leak-check groove tool. **c** Custom pliers

ignition pliers that can safely grip the gasket [10]. This design allows only upward force on the gasket and also grips the gasket during removal to prevent it from falling. In certain instances where there is insufficient clearance for the pliers on the outside of the copper gasket, one must resort to a tool of the second design [9, 10].

8.4 Unconventional Compression Seals for Ultrahigh Vacuum

Several unconventional compression seals have been designed for ultrahigh vacuum systems where flange mounting was inappropriate. These seals all have in common the use of a material softer than stainless steel that is deformed under pressure supplied by screwing down the re-entrant seal from the outside of the vacuum system. This forms the vacuum seal, which is always on the inside of the

vacuum system. Figure 8.4a is a seal involving oxygen-free high conductivity (OFHC) copper that is deformed, at the edge of a hole drilled into the vacuum system wall. A stainless steel bolt, with a hole drilled axially through its length, is machined to present a hemispherical surface under the head. Copper tubing is spun down on a lathe to closely fit over the bolt. The bolt is inserted from the vacuum side of the hole and tightened with the nut from the outside. Such seals can be cycled between 873 and 77 K many times, remaining He-leak tight. The seals may be loosened and used repeatedly for five to ten times. Ultimately, the copper becomes thin and hardened as a result of the mechanical deformation. New copper fittings may be used to replace the original used fitting [11].

A second re-entrant bakeable all-metal vacuum seal is shown in Fig. 8.4b. Here a conventional Conflat flange design is used for the sealing surface and the force to

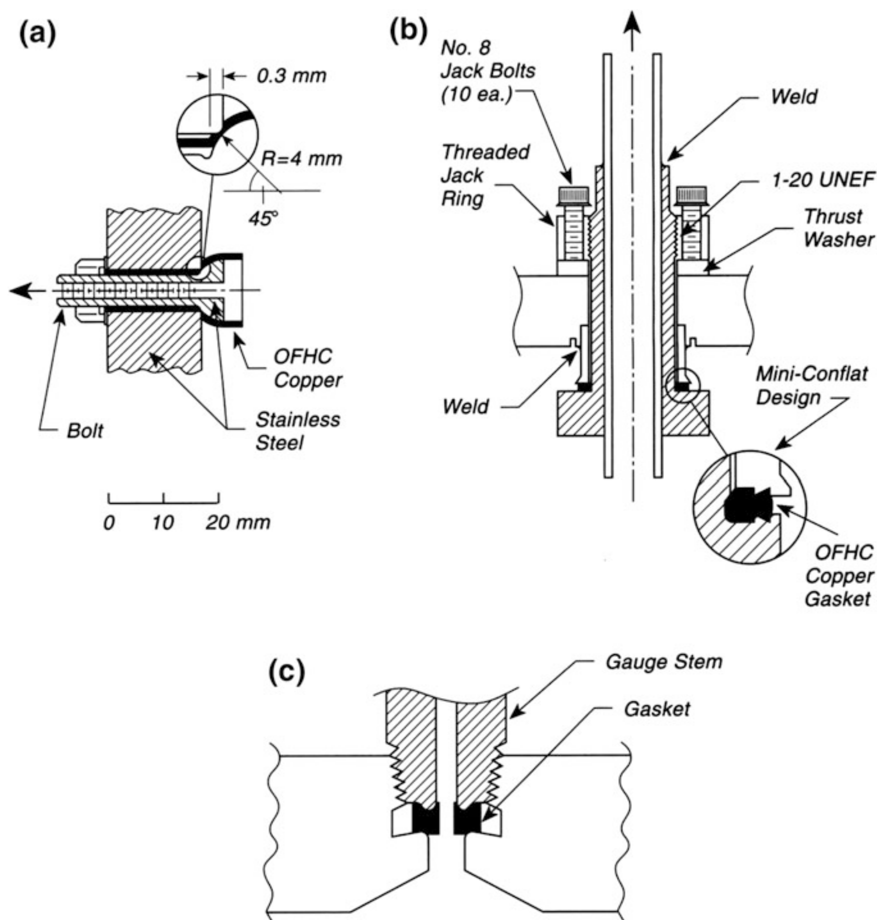

Fig. 8.4 Unconventional compression seals. **a** Hollow bolt seal. **b** Mini-Conflat seal. **c** Gauge tube seal

produce the seal at the copper gasket is applied externally by means of jacking screws. The assembled seal was designed to apply 2000 lb/in. along the copper gasket seal path. The seal is assembled from inside and initially tightened using the threaded jack ring, which pushes down on a chrome plated thrust washer needed to prevent distortion of the main sealing flange that contains the hole and also to prevent galling of the jackbolts under torque. First torquing of ten bolts to 20 in. lb resulted in a leak tight seal. Further torquing to 40 in. lb reached the plastic-flow limited torque for the No. 8 stainless bolts. Disassembly and reassembly at 40 in. lb torque produced a He-leak-tight seal, which withstood baking to 250 °C [12].

A third design, solving a major vacuum problem for sealing thermocouple gauges into ultrahigh vacuum systems, is shown in Fig. 8.4c. For most applications under non-stringent vacuum conditions, thermocouple gauges are sealed at the pipe thread joint by use of Teflon tape, vacuum cements, etc. This is unacceptable for ultrahigh vacuum operation owing to the possibility of gas trapping in the pipe thread or cement. The design shown in Fig. 8.1c uses the pipe thread to compress either a Teflon or aluminum or OFHC copper gasket at the bottom of the tubulation. The end of the stainless steel gauge stem must be smoothed with 600-grit paper, using a removable plug inside the tubulation to prevent entry of debris. Similarly, the sealing surface in the receptor hole must also be polished. This method permits thermocouple gauges to be used on ultrahigh vacuum systems and to withstand normal bakeout temperatures [13].

References

1. T. Wikberg, J. Vac. Sci. Tech. **5**, 205 (1968)
2. E.L. Garwin, E.W. Hoyt, A.R. Nyaiesh, J. Vac. Sci. Tech. **A4**, 2537 (1986)
3. A.R. Nyaiesh, E.L. Garwin, E.W. Hoyt, J. Vac. Sci. Tech. **A5**, 2977 (1987)
4. A. Roth, *Vacuum Sealing Techniques* (Pergamon, Oxford, 1966), p. 380
5. E.M. Beaver, Rev. Sci. Instrum. **51**, 254 (1980)
6. L.Y.L. Shen, J.E. Rowe, E.E. Chaban, Rev. Sci. Instrum. **44**, 1747 (1973)
7. F. Shimoshikiryo, Y. Takakuwa, N. Oyama, N. Miyamoto, J. Vac. Sci. Tech. **A11**, 2874 (1993)
8. J.J. Donelon, J.M. Baker, J. Vac. Sci. Tech. **10**, 894 (1973)
9. E.E. Chaban, J. Vac. Sci. Tech. **12**, 654 (1975)
10. B.J. Waclawski, J. Vac. Sci. Tech. **Al**, 99 (1983)
11. N. Raeuber, K. Stadler, M.J.O. Strutt, J. Vac. Sci. Tech. **8**, 662 (1971)
12. P.H. Edmonds, W.D. Shipley, J. Vac. Sci. Tech. **A6**, 165 (1988)
13. F.N. Rabarchik, J. Vac. Sci. Tech. **16**, 2116 (1979)

Chapter 9
Leak Repairs and Detection

9.1 Coaxial Pumped He Leak Detection Probe

He-leak checking is commonly used, either in the shop with a portable leak detector, or in the laboratory where a mass spectrometer inside the vacuum system is used for detection. A common problem involves the detection of a small leak at some point, where subsequent investigation will show that there is really no leak at that point. This confusing result is caused by the diffusion through the atmosphere of He from the suspect point to the real leak, which is some distance away. The device shown in Fig. 9.1 eliminates this effect by sweeping He away from the test point using a coaxial vacuum sleeve.

Figure 9.1 shows the device, and the reader is referred to the original publication for construction and assembly instructions [1]. The He flow rate is adjusted to one or two bubbles of He per second as determined by placing the probe under water with the valve-controlled vacuum pump turned off. The rate of pumping should be adjusted so that the sensitivity for He is not diminished by too rapid pumping. A pump with a displacement of 5–10 L/min is satisfactory, with a throttle valve for pumping speed adjustment.

Once a leak is noted, a second test should be performed to verify its general location. This consists of placing a plastic bag around the suspected part, sealing the bag with tape, and then filling the bag with He, and observing the leak again. Using this coaxial probe and then using the bag verification test will eliminate carrying non-leaking components to the shop for repair.

In the event that leak sealing compounds are used for temporary repairs, only very small quantities of the sealer should be applied at the leak location, and a tag should be placed on the affected component telling the location of the leak and the date of temporary repair. The leak should be repaired correctly as soon as possible after the temporary repair. The tag is a guide for the memory when the vacuum system is ready to be disassembled.

© Springer International Publishing Switzerland 2015

J.T. Yates Jr., *Experimental Innovations in Surface Science*,
DOI 10.1007/978-3-319-17668-0_9

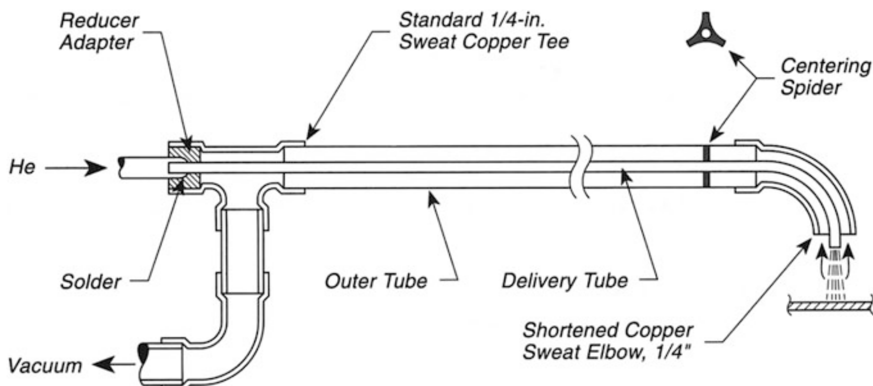

Fig. 9.1 Coaxial pumped he leak detection probe

9.2 Temporary Leak Sealing of Welded Bellows

Welded bellows often develop small leaks at times when it is inconvenient to interrupt the work going on in the vacuum system. These leaks are most likely located on the inner welded seal of the bellows and are difficult to locate precisely.

For small leaks a temporary seal may often be established by using a leak sealer diluted with a solvent to reduce its viscosity and then spraying tiny amounts of the liquid onto the leak region. However, continued flexure of the seal after drying can cause the leak to reappear. Therefore, a clever trick [2] was devised in order to extend the lifetime of the bellows while a new one was being ordered. This involves immobilizing the small section affected by the leak. This is done by squeezing gently several 0.5-mm-thick stainless steel clips around the bellows region of interest immediately after spraying the diluted sealant on the bellows, as shown in Fig. 9.2. Since one leak in a bellows is generally a signal of more to come, this procedure should not be employed as a long-term solution to the leaking bellows problem.

A variety of liquid leak sealers are commercially available, and the reader is referred to the catalogs or to the original reference for a description of a silicone sealer [2].

9.3 Atmospheric Permeation—Viton O-Ring

Viton [3] seals are used in ultrahigh vacuum applications where deformable metalseals cannot be used. Viton seals may be baked out at 200 °C and after a 24 h bake-out an outgassing rate of the order of 2×10^{-9} Torr L/s cm^2 (nitrogen equivalent) has been reported [4]. After bakeout, the main gas evolved was water.

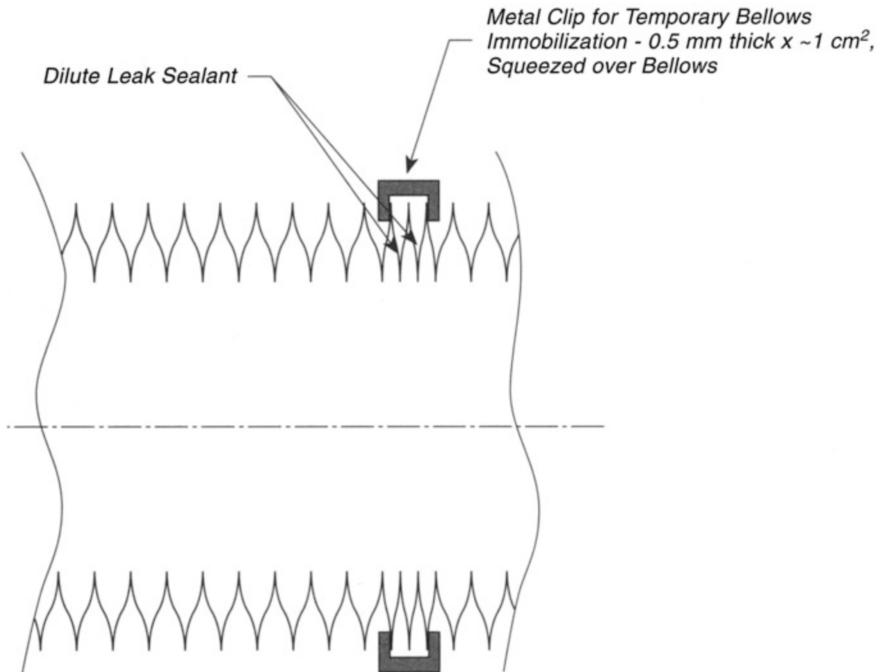

Fig. 9.2 Temporary welded bellows repair

Bakeout eliminates hydrocarbons initially detected upon installation of a fresh Viton seal [4].

A significant property of Viton seals is their ability to allow water from the atmosphere to permeate slowly through the outgassed Viton into the ultrahigh vacuum system, causing the partial pressure of water to rise for many days after bakeout. Figure 9.3a shows an apparatus where atmospheric gas permeation through a Viton O-ring was investigated [5]. A stainless steel vacuum system, equipped with a mass spectrometer and trapped diffusion pumping facilities, contained a test Viton O-ring [4]. The top of the vacuum chamber was baked at about 100 °C, while it was estimated that the section containing the O-ring was baked at 50 °C. A base pressure of about 5×10^{-9} Torr was achieved after 3 days' baking. Following 2 days' cooling, the mass spectrum of the residual gases in the chamber was measured for an additional 30 days, as shown in the test schedule (Fig. 9.3b).

It was found that the major effect was a continuous rise in the partial pressure of water during the 30-day period, with a decreasing rate after about 20 days. Figure 9.3c, d schematically show these tests for conditions of low atmospheric humidity and high atmospheric humidity. The rate of water permeation increases for the humid conditions. There is no detectable amount of permeation of other atmospheric gases such as N_2, Ar, or CO_2 during the 30-day test, although some O_2 permeation was reported [5].

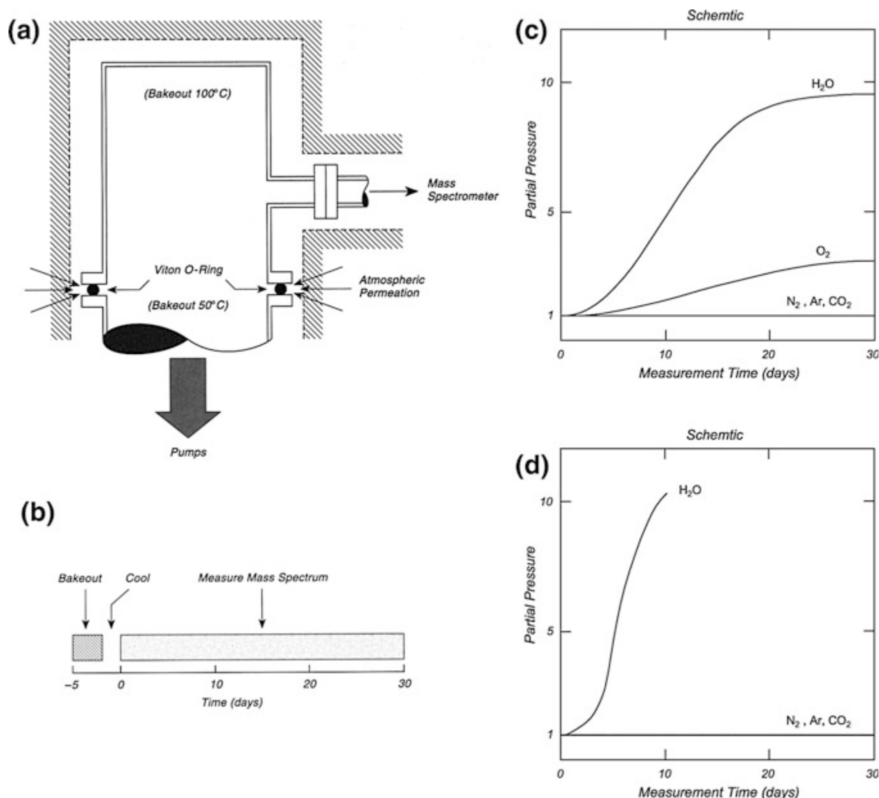

Fig. 9.3 Atmospheric permeation—Viton O-Ring. **a** Apparatus for O-Ring studies. **b** O-Ring test schedule. **c** Low humidity—permeation. **d** High humidity—permeation

These results suggest that the best application for Viton seals in ultrahigh vacuum systems is in cases where exposure of the seal to the atmosphere does not occur, i.e., where the seal is used internally for isolation of one part of the vacuum system from another. This is the case with Viton sealed gate valves mounted between sections of the vacuum system, where the seal is retained in vacuum during the time when the valve is opened.

A number of studies of outgassing and permeation of vacuum materials have been carried out [6–8].

References

1. G.L. Fowler, J. Vac. Sci. Technol. **A5**, 390 (1987)
2. W.F. Egelhoff Jr, J. Vac. Sci. Tech. **A6**, 2584 (1988)

3. Viton A is a copolymer between vinylidine fluoride and hexafluoropropylene with the formula [-FC(CF_3)-CF_2-CH_2-CF_2-]$_n$. Initial outgassing evolves water, oxygen, hydrogen, nitrogen, and some hydrocarbons (most prominent mass peak at 43 amu, probably from C_2F^+). After bakeout, the main gas observed was water [2]
4. R.S. Barton, R.R. Govier, J. Vac. Sci. Technol. **2**, 113 (1965)
5. N. Yoshimura, J. Vac. Sci. Technol. **A7**, 110 (1989)
6. W.G. Perkins, J. Vac. Sci. Technol. **10**, 543 (1973)
7. B.B. Dayton, *Transaction of the American Vacuum Society 6th Vacuum Symposium*, 101 (1959)
8. R.A. Redhead, J.R Hobson, E.V. Kornelson, *The Physical Basis of Ultrahigh Vacuum* (American Institute of Physics, New York, NY, 1993), chapter 10

Chapter 10
Specialized UHV Systems

10.1 Aluminum Ultrahigh Vacuum System

There are advantages in using aluminum UHV systems. For proton synchrotrons, the residual radioactivity produced in stainless systems may be reduced by one or two orders of magnitude, 100 h after machine shutdown, by employing Al instead of stainless steel. For electron synchrotron machines and electron storage rings, aluminum is preferred because of good thermal conductivity, ease of manufacture by extrusion, low residual radioactivity, nonmagnetic character, and low cost. The design here is an all aluminum system made of two types of aluminum alloy; aluminum flanges and gaskets are specially designed [1, 2][1].

A special aluminum alloy, 2219-T87, is found to have the necessary mechanical properties for making the sealing flanges and nut/bolt sets. As shown in Fig. 10.1, the sealing surface consists of a circular slot on each flange that houses a Helicoflex [3] O-ring containing an elastic spring core inside a pure aluminum sheath. The fixed depth of the O-ring groove was adjusted to correspond to the specified compression radius of the Helicoflex element—a 4.5-mm diameter Helicoflex required two 1.5-mm deep grooves.

The chamber body was made of a 6063-T alloy, which could be welded by an AC TIG welding process. Distortion after welding was negligible and remachining was not necessary. The entire chamber, except the O-ring sealing surfaces, was anodized to a 30-μm thickness. Bellows made of 6063-T6 alloy could be made by a rolling process yielding 0.5 mm thick walls. The bellows are employed for alignment purposes, not for dynamic motion. They also compensate for thermal expansion effects.

The O-rings were sealed by torquing the nut/bolt combinations, bringing the aluminum flange surfaces together. The torque (per unit area of the O-ring) used for tightening was between 140 and 215 kg/cm, with 200 kg/cm being normal.

[1]Which contains references to various papers on this subject.

© Springer International Publishing Switzerland 2015

J.T. Yates Jr., *Experimental Innovations in Surface Science*,
DOI 10.1007/978-3-319-17668-0_10

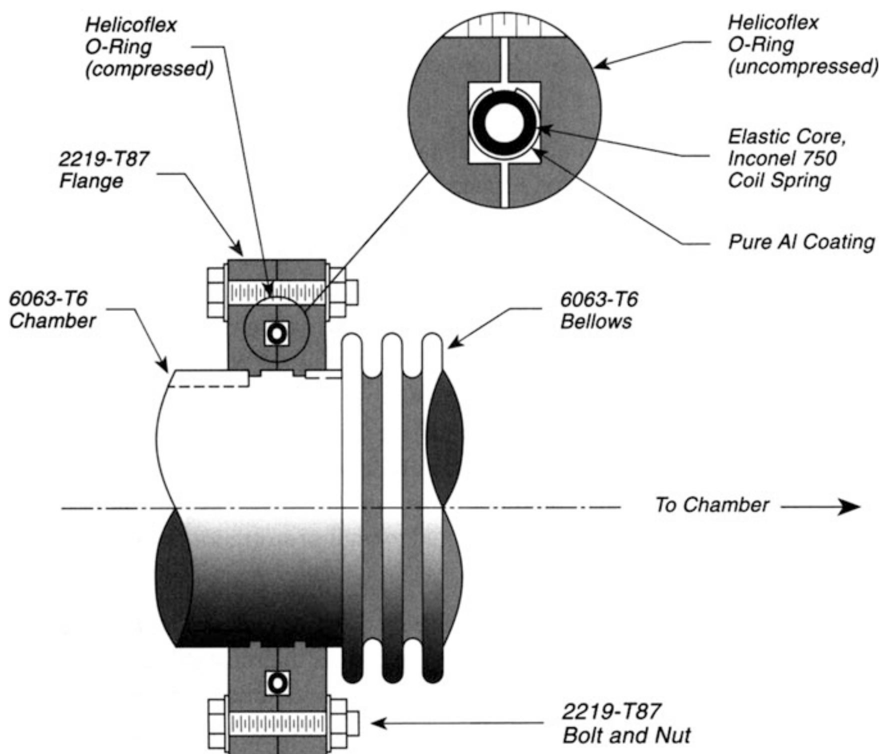

Fig. 10.1 Aluminum UHV chamber, flange, and bellows

Following bakeout at 200 °C, the leak rate at the Helicoflex seals was measured with a He leak detector. It is reported that the leak rate is less than 10^{-11} atm cm/s, where the units on this number suggest that a leak rate per cm^2 of sealing surface was calculated. The ultimate pressure in the system was 3 × 10^{-10} Torr after bakeout and the residual gases consisted mainly of H_2, CO, and CO_2. The 38-L system was pumped by a 220-L/s turbopump and a 160-L/s sputter ion pump. It is indicated that the practical upper bakeout temperature is limited to 170 °C by the 6063-T6 aluminum alloy.

A study of the outgassing rate of an aluminum vacuum system during bakeout is given in [4].

10.2 Surface Electrochemistry Apparatus

The development of the field of electrochemistry from the viewpoint of surface science has depended upon the experimental ability to prepare atomically clean single crystal surfaces and then to transfer these surfaces to an electrochemical

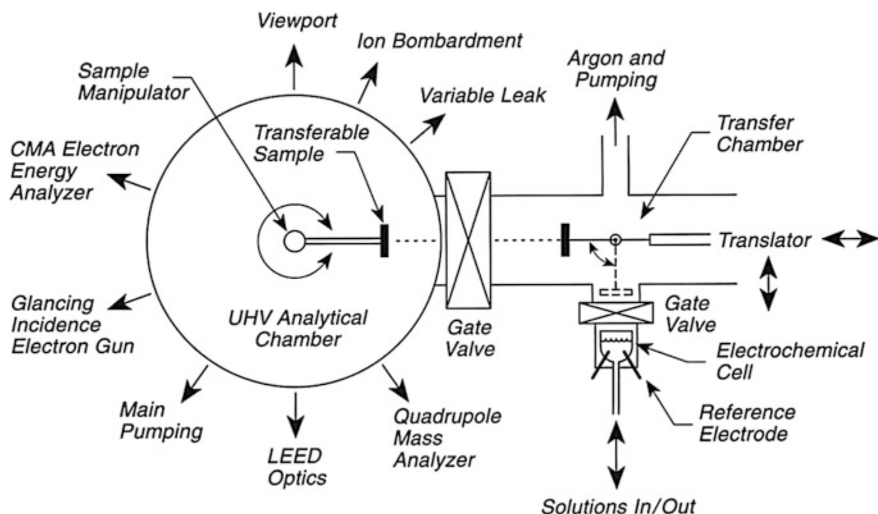

Fig. 10.2 Schematic of surface electrochemistry apparatus

environment for measurements of current versus voltage [5]. While a number of designs have been provided for this transfer operation, the design schematically shown in Fig. 10.2 is historically important and remains useful today.

A single crystal is mounted on a sample manipulator in the left-hand UHV system, which contains various facilities for surface cleaning and surface characterization. The sample, once cleaned and characterized, is unplugged in vacuum from the sample manipulator (see pp. 89 and 93) and is captured on a bellows type translator coming in from the right through an open gate valve. From here the sample may be immersed into the electrolyte of the electrochemical cell by means of moving the translator vertically and lowering the sample through the open gate valve. Four types of pumps are utilized on the right-hand side of the apparatus: two sorption pumps using zeolite pellets at 77 K; a cryogenic pump containing a charcoal-covered surface cooled to 14 K by a Joule-Thomson refrigerator, which lowers the pressure to about 10^{-7} Torr; ionization pumps to bring the pressure down to about 10^{-9} Torr; and a titanium sublimation pump for final pumping and for purification of Ar gas which is admitted to high pressure for the sample transfer to the electrochemical cell.

The solution-handling subsystem must exclude dissolved contaminants. Liquids are contained in deaerated (N_2 purged) Pyrex bottles. Air is the most difficult impurity to exclude, and Teflon tubing sheathed in Teflon bellows is used under inert gas purging conditions inside the annular space to exclude air diffusion through the Teflon to the electrolyte. Glass vacuum valves rather than stopcocks are used to avoid contact with the air. Teflon compression fittings are used to make tubing interconnections. All parts are soaked in chromic acid cleaning solution until needed, then rinsed with highly purified distilled water.

Potential-dependent interfacial properties of the electrode-sample are measured using a Pt electrode introduced through a 3-mm-diameter section of Teflon tubing. A silver wire, coated with silver chloride, and immersed in a chloride solution is a convenient reference electrode. By applying a potential between the Pt electrode and the sample, and monitoring this potential against the silver chloride/silver electrode, it is possible to plot out the current-voltage curves and to correlate with the nature of the electrode introduced.

A comprehensive listing of other types of electrochemical cells which are coupled to UHV systems is given in [6, 7], which also describe X-ray photoelectron spectroscopy (XPS) studies of the corrosive oxidation of a Ni surface.

References

1. H. Ishimaru, J. Vac. Sci. Technol. 15,1853 (1978)
2. H. Ishimaru, J. Vac. Sci. Technol. **A7**, 2439 (1989)
3. Helicoflex is a product of Helicoflex Co., P.O. Box 9889, Columbia, SC 29290
4. M. Suemitsu, T. Kaneko, N. Miyamoto, J. Vac. Sci. Technol. **A5**, 37 (1987)
5. A.T. Hubbard, in *Comprehensive Chemical Kinetics*, edited by C.H. Bamford, D.H.R Tipper, and R.G. Compton (Elsevier, Amsterdam, 1988), pp. 1–67
6. Y. Liang, D.K. Paul, Y. Xie, P.M.A. Sherwood, Anal. Chem. **65**, 2276 (1993)
7. P.M.A. Sherwood, Chem. Soc. Rev. **14**, 1 (1985)

Part II
Mechanical Fabrication Techniques

Chapter 11
Grids

11.1 Hemispherical Grids—Formation and Piercing

Formed grids are employed in ion and electron optical devices. Often these grids must be made of highly transparent woven stock, either of stainless steel or tungsten [1].

Woven grid material may be formed into a hemispherical shape using a mold or mandrel, as shown in Fig. 11.1a. Here the grid material is stretched over the mandrel and an annealed aluminum ring is slipped over the stretched grid, capturing it near the base of the mandrel. A steel pressure ring is then seated on the aluminum ring and pressure is applied causing the soft aluminum ring to distort into an L-shaped cross section as shown. This also encases the grid material, fixing it in the aluminum [2].

Another method for attaching a stretched grid to a support ring is shown in Fig. 11.1b. Here a mesh grid is stretched over a brass mandrel, and a stainless steel plate is clamped in place to hold the grid on the mandrel. The plate is tack-welded to the grid in about ten places and the clamps are released and the plate turned over. The grid wires are trimmed and individually spot-welded [3]. A more complex variation on this method is shown in Fig. 11.1c where the grid is captured between two shaped rings, R, which are bolted inside a jig. Spot-welding takes place through the holes, H, after the grid is stretched over the mandrel [4].

Grids must often be pierced in specific locations for the passage of hardware or source beams through the grid. Figure 11.1d shows a nice way to do this job accurately. The brass mandrel is punched with the location of the center of the hole. A scribe is then used to scratch a circular shape on the mandrel locating the cutting line on the grid. The grid is then stretched and spot welded, and the assembly is immersed into aqueous NaCl solution (50 g/L). An electrode to a spot welder (S_1) is attached to the assembly, and a second electrode, S_2, made of tungsten wire (0.5 mm) is sharpened to a radius about twice the diameter of the mesh wires to be cut. An electrical arc from the spot welder will cut the wires individually, usually between adjacent wires perpendicularly crossing the wire to be cut. The salt water prevents pitting on the brass mandrel by the electric arc [3].

© Springer International Publishing Switzerland 2015

J.T. Yates Jr., *Experimental Innovations in Surface Science*,
DOI 10.1007/978-3-319-17668-0_11

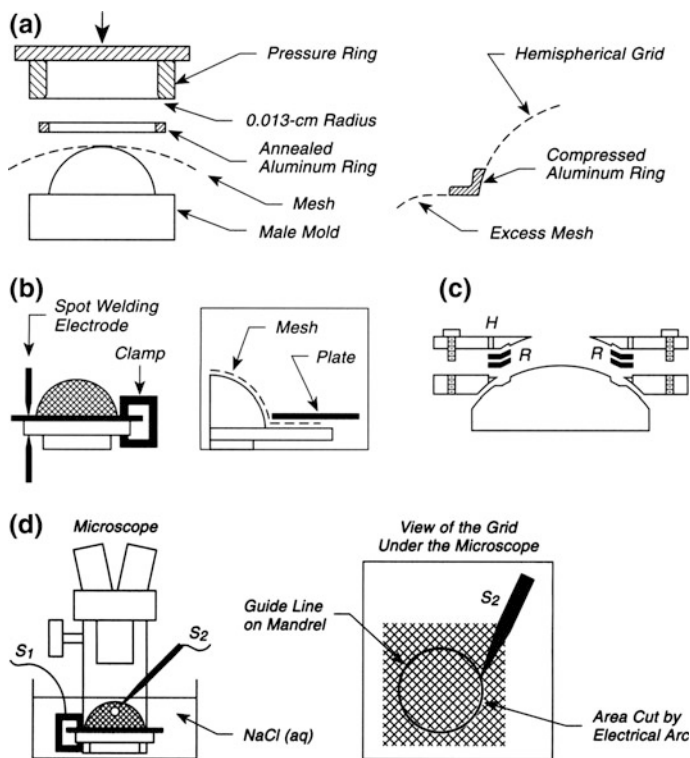

Fig. 11.1 Hemispherical grids—formation and Piercing. **a** Grid capture—Al Ring. **b** Grid capture—spot welding. **c** Grid capture—spot welding. **d** Piercing grid

This stretching method will not make perfect hemispherical grids, since some relaxation will occur upon removal from the mandrel. If more rigid grid material is needed, the stretched grid may be electroplated on the mandrel [5] or it may be fired in an oven. The electroplating stiffens the contact points between the meshes while firing will stiffen the wire itself. In the case of firing, a brass mandrel cannot be used, and release agents on the mandrel will be needed. Either Aquadag (colloidal graphite) or MoS_2 will work as release agents.

11.2 Making Flat Mesh Grids of Large Size

Electroformed mesh [6], having up to 85 % transparency, may be conveniently used as grid material in electron and ion optical applications. However, it is difficult to construct flat grids of many centimeter dimensions, and irregularities in flatness will influence the electrical field uniformity desired in front or between parallel grids.

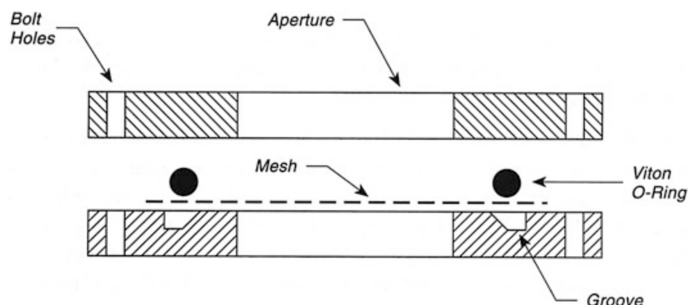

Fig. 11.2 Making large grids planar

Figure 11.2 shows a convenient method [7] for using a Viton O-ring to produce uniform stresses at the boundaries of electroformed grids, making them flat. The lower plate has a special groove cut in it with the inner wall beveled 30° with respect to the normal. When the sandwich involving the two plates, the grid, and the O-ring is compressed by adjusting bolts around the perimeter, the motion of the O-ring gradually pulls the mesh tight as the O-ring expands outward in the beveled groove under pressure. This produces the desired flat grid.

11.3 Grid Fabrication Techniques—Conical Grid

The fabrication of a grid having a precise geometry is accomplished by using a mandrel of the desired shape, and on p. 119, methods for making hemispherical grids are shown. Here we describe the fabrication of a conical grid that is used as an ion cage in a high-efficiency molecular beam ionization detector with a short ionization region [8].

The conical cage, which was designed with specific ion optical properties, is shown mounted on its lens plate in Fig. 11.3a. Four angled support wires are welded to the plate and provide rigidity for the grid.

Figure 11.3b shows the metal mandrel, which has been fabricated to the desired shape so that it can fit the lower electrode mount of a tabletop spot-welder. Ta wire (0.1 mm diameter) is wound on the mandrel on a lathe, operated at slow speed or by hand, and then the ends of the coil are fixed with tape or by a soluble glue dot. After the four support wires are spot-welded to the grid on the mandrel, the grid assembly may be removed by a short immersion in an ultrasonic bath. Following removal of the grid from the mandrel, the angled support wires are welded to the lens plate, using the mandrel for centering the grid assembly on the lens aperture [9].

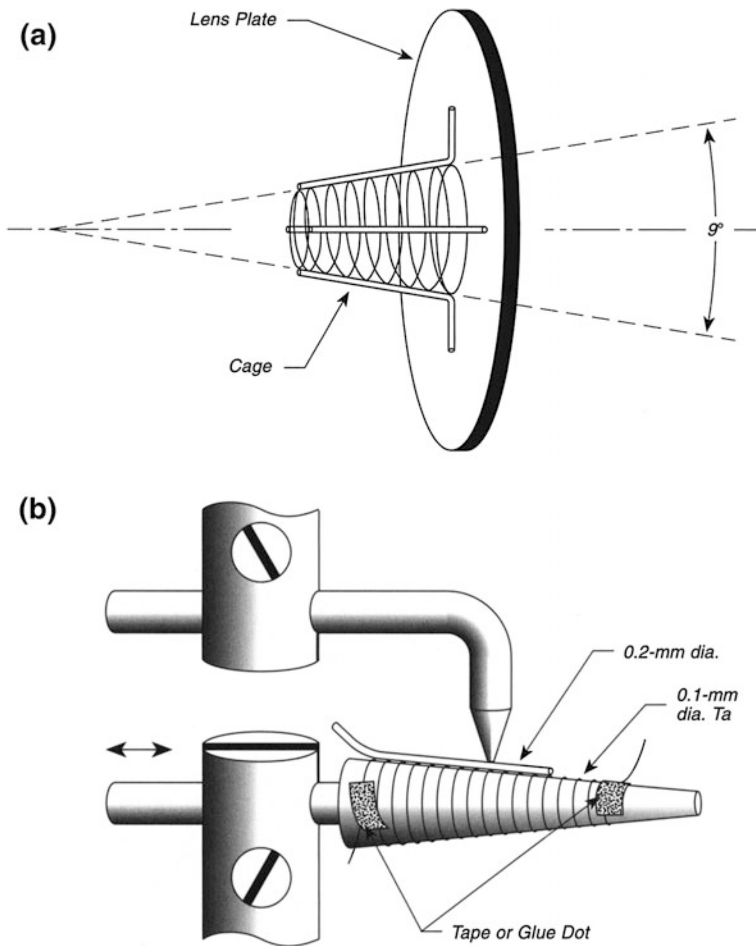

Fig. 11.3 Grid fabrication techniques—conical grid. **a** Conical grid. **b** Mandrel + spot-welding

References

1. Unique Wire Weaving Co., Inc., 762 Ramsey Avenue, Hillside, NI07205-1094; Electronic Space Products International, 1050 Bensen Way, Ashland, OR 97520
2. D.A. Shaw, D.A. Bennett, Rev. Sci. Instrum. **43**, 1706 (1972)
3. R.A. Taylor, J. Vac. Sci. Technol. **A6**, 2583 (1988)
4. J. Koch, Rev. Sci. Instrum. **45**, 1212 (1974)
5. P.W. Palmberg, D.C. Johnson, H.J. Boll, Rev. Sci. Instrum. **35**, 244 (1964)
6. Electroformed mesh is a product of Buckbee Mears, 245 E. Sixth Street, St. Paul, MN 55101, and it may be obtained in various materials, with various thicknesses and optical transmission
7. R.J. Noll, L.L. Ochalla, J.C. Weisshaar, Rev. Sci. Instrum. **62**, 246 (1991)
8. K. Kuhnke, K. Kern, R. David, G. Comsa, Rev. Sci. Instrum. **65**, 3458 (1994)
9. Dr. R. David, Institut fur Grenzflächenforschung und Vakuumphysik, Forschungszentrum Jülich GmbH, Postfach 1913, D-52425 Jülich, Germany (private communication)

Chapter 12
Conductive Coatings

12.1 Deposition of Electrically Conductive SnO_2 Films

Many devices used in surface science research require the deposition of electrically conductive films. These films are often used as the backing for phosphor screens in LEED apparatus and other electron beam display techniques.

Figure 12.1 shows the method used in many laboratories for the deposition of semiconducting SnO_2 films on Pyrex glass surfaces. A glass surface, appropriately shielded on the inside and outside with Aquadag (colloidal graphite) [1] to prevent unwanted deposition, is placed into a small furnace or glassblower's annealing oven. The oven is slowly brought to the annealing temperature of Pyrex, 550 °C. A saturated solution of SnCl2 in isopropanol is made up and loaded into the reservoir of an atomizer, as shown. Since we wish to deposit SnO_2, the atomizer is connected to a regulated oxygen tank, and oxygen gas is used to oxidize the tin from Sn(II) to Sn(IV) upon deposition of the $SnCl_2$ uniformly to the hot surface of the glass. The spraying is carried out in short bursts, and the oven door is then closed between bursts in order to rewarm the glass to the deposition temperature. An experienced operator can judge the conductivity of the film from its color. Blue and barely visible coatings possess approximately kΩ resistances between two points a few centimeters apart, while yellow or brown coatings give less than 1 kΩ resistance.

Caution should be taken not to breath in during the film deposition with the $SnCl_2$, since pungent HCl gas is a major product of the pyrolysis chemistry leading to SnO_2 deposition.

Following film deposition, the Aquadag can be removed using an abrasive kitchen cleanser and a cotton swab in water, or by heating in a glass annealing oven for long times, followed by washing.

The electrical contact to the conductive film can easily be made using a glass-metal feedthrough fabricated by the glassblower. To the inner end of the metal feedthrough, a small piece of platinum ribbon or wire is welded in such a manner

© Springer International Publishing Switzerland 2015

J.T. Yates Jr., *Experimental Innovations in Surface Science*,
DOI 10.1007/978-3-319-17668-0_12

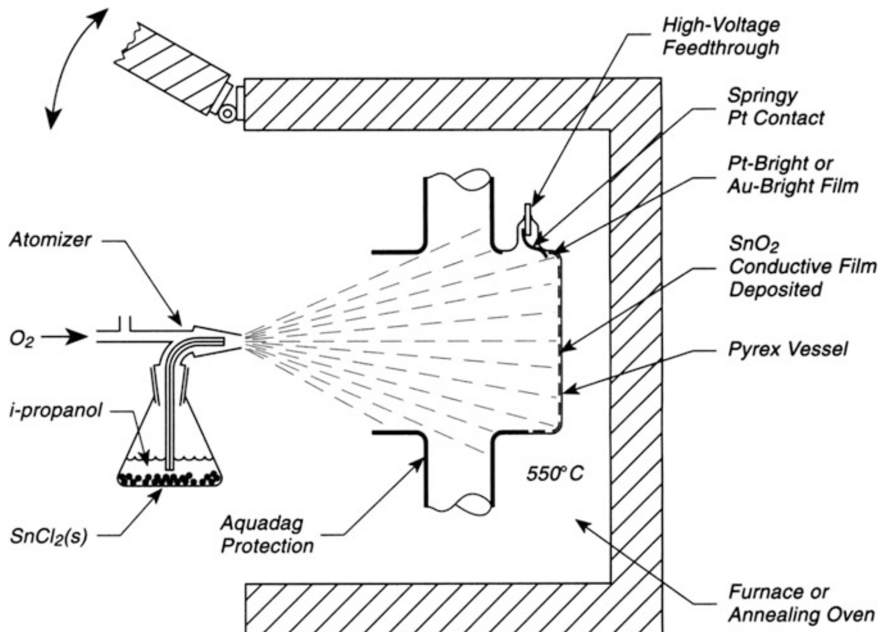

Fig. 12.1 Deposition of conductive SnO_2 films

that it makes good contact with the inner surface of the glass. The contact is made permanent by applying either platinum bright or gold bright paint [2] with a small camel's hair brush, followed by firing in the oven to produce a shiny film of metal which is both adherent and conductive. Alternate methods for making electrical contacts through glass to a conductive SnO_2 film are described in [3].

The work function of SnO_2 films prepared in this way has been measured using a retarding potential method for an incident electron beam. The coatings were found to have a work function of 4.79 ± 0.07 eV. Spatial variations in the work function averaged ±10 meV, and work function differences between samples were less than 100 meV [4].

The original scientific report of the use of SnO_2 films for producing conductive glass may be found in [5]. Here also is a study of the resistivity of a number of these films from 1.5 to 500 K.

Tin oxide films can be removed by "nascent hydrogen" produced near the film surface by dipping a cotton swab first in HCl(aq) and then in powdered zinc dust. This reactive mixture, when rubbed on the SnO_2 film, will efficiently remove it by a reduction process. Thorough washing in H_2O should then be carried out.

References

1. Aquadag colloidal suspensions may be obtained from Acheson Colloids Co., 1607 Washington Avenue, P.O. Drawer 611747, Port Huron, MI 48061-1747
2. Organometallic paints containing either Pt or Au may be obtained from the Hanovia Division of Engelhard Industries, 1 West Central Avenue, East Newark, NJ 07029. These paints contain the metal chemically bound with organic ligands which are thermally unstable
3. R. Gomer, *Field Emission and Field Ionization* (AIP, American Institute of Physics, New York, 1993), pp. 169–170
4. J. Burns, E. Yelke, Rev. Sci. Instrum. **40**, 1236 (1969)
5. R. Gomer, Rev. Sci. Instrum. **24**, 993 (1953)

Chapter 13
Phosphor Screens

13.1 Sedimentation Method for Depositing Phosphor Screens

A number of methods involving electron beam measurements require the use of phosphor screens that are uniform and adherent. The method described below is a variant of techniques originally described for coating cathode ray tube screens and field emission microscope screens [1–4]. The method may be used for either glass-based phosphor screens, which are viewed by transmission from the back side, or metal-based screens, which are viewed from the front side [5].

The essential requirements are to deposit a phosphor powder uniformly along with a binder substrate that will be adherent during bakeout and use. All such screens are sensitive to mechanical disturbance, including touching with the fingers.

For deposition of metal-based screens the underlying metal substrate must be pickled after chemical cleaning to prepare its surface. Two pickle agents are described for stainless steel substrates: (a) 30 volume % HNO_3 + 3 volume % HF in water—warming above room temperature will increase its rate of action and the substrate should be immersed for 30–60 s; (b) 10 volume % HNO_3 + 2 volume % HCl + 2 volume % HF in water-immerse screen for 5 min in an ultrasonic bath. One pickle agent is described for aluminum substrates: 12 volume % HF—then rinse with water and dip in 86 volume % HC1 for no longer than 60 s. If the aluminum turns black during the HC1 dip, repeat the HF step followed by the HC1 step [5].

The clean and pickled substrate is then transferred to the 3-L sedimentation chamber shown in Fig. 13.1, and is ready for application of the phosphor screen.

Two sedimentation solutions are prepared as described below:

Solution A This is an electrolyte solution that facilitates the gelation of the phosphor particles with the silicate. 300–500 ml water + 1.8 g $Ba(NO_3)_2$.

© Springer International Publishing Switzerland 2015
J.T. Yates Jr., *Experimental Innovations in Surface Science*,
DOI 10.1007/978-3-319-17668-0_13

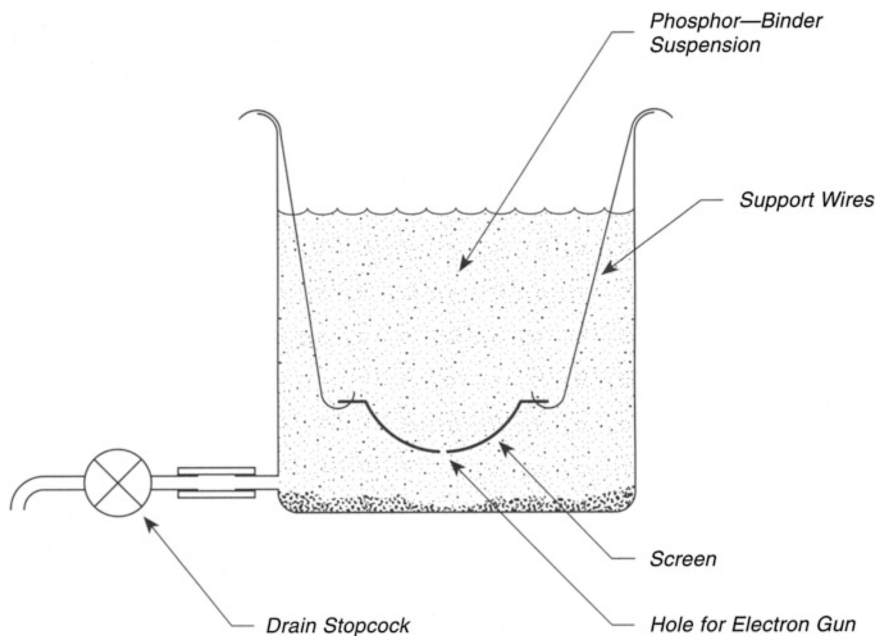

Fig. 13.1 Sedimentation deposition of phosphor screen

Suspension B 150–175 ml water + 0.18 g silica gel [6] + 3.2 g phosphor. This suspension should be agitated in an ultrasonic bath or an ultrasonicator (not the same thing).

After mixing thoroughly, transfer suspension B to a large Erlenmeyer flask and dilute to 500 ml with water, using a wash bottle to make a complete transfer. Add solution A and make a final volume of about 1 L. Shake vigorously and transfer to the ultrasonic bath for continued agitation for 10 min. Pour the suspension into a 3–4-L beaker and rinse all material into the beaker. Dilute to about 3 L, and stir rapidly for 5–10 min using a magnetic stirbar of 3-in. size. Turn off the stirrer and allow the suspension to partially settle, during which time the large particles will preferentially settle to the bottom. Decant the liquid into another 3-L beaker, being careful to leave the large particles on the bottom undisturbed. Allow this second suspension to settle for about 7 min and then carefully decant the solution into the sedimentation chamber containing the substrate. This should be done carefully, directing the suspension down the side of the sedimentation chamber using a large funnel and avoiding bubbles. Cover the sedimentation chamber and allow it to sit for 5–12 h without agitation or vibration. Following sedimentation, the most difficult task is to drain off the liquid without mechanically disturbing the screen. The drain stopcock should be opened very slightly so that a very slow drip is achieved, making the flow rate so small that about 6 or more hours are required to drain the liquid.

The drained screen should be air dried in the sedimentation chamber for several hours, keeping it covered to avoid dust. After drying, inspect for homogeneity. A "ring" on the screen indicates a discontinuity owing to a change in the drip rate, possibly due to a particle being trapped in the stopcock. Such discontinuities may not be serious unless photometry is to be employed, where phosphor thickness must be constant. Even without visible evidence of inhomogeneities, the phosphor thickness will vary over the screen surface owing to the variable angle of interception of the settling particles by the curved screen. Following drying, the screen should be baked in an oven at 80 °C for 30 min to remove additional water. Screens treated in this manner are satisfactory for use in ultrahigh vacuum and show little or no influence on the base pressure after a bakeout at 150 °C for 24 h [5].

For deposition of phosphor screens in glass vacuum envelopes, minor variations of the procedure described above may be used. The sedimentation chamber may be replaced by the envelope itself if the depth of the liquid suspension is sufficient. Alternatively, the glass vacuum envelope can be immersed in a large sedimentation vessel, and in either case the draining can be done by very, very slow tipping of the envelope using a slowly driven motor that turns once in 24 h.

Screens prepared in this manner are approximately 10 μm thick and well suited for electron beam imaging. Thicker screens may be subject to electrostatic charging.

An unusual electrostatic deposition and adhesion method has been described by Cetronio and Cross [7].

13.2 Dusting Method for Coating Phosphor Screens

Phosphor coating of screens for imaging electron beams may be achieved using a technique developed years ago at AT & T Bell Laboratories [8] and described briefly elsewhere [9]. This method has the advantage over the sedimentation method of producing more uniform phosphor coatings, since it does not sense a curved surface during the deposition procedure.

As shown in Fig. 13.2, a glass or metal substrate, cleaned with a strong hot alkaline detergent, has a stopper made of cork or plastic (but not rubber) that seals the hole for the electron gun or other source. A sticky uniform layer of phosphoric acid, H_3PO_4, is deposited by the following procedure:

Clean about 100 glass balls (3-mm diameter) and the screen with ethanol and acetone to degrease. Then from a solution consisting of 3 drops of H_3PO_4 in 25 ml of acetone, place 25 drops onto the screen substrate with the stopper in place. Place the glass balls onto the screen substrate and roll them around as the acetone evaporates. After 2–3 min, the acetone will have evaporated, and the phosphoric acid will uniformly wet the substrate. If streaks are observed, repeat the process. Then shake 1–2 cm^3 of phosphor powder onto the wet substrate and tap the screen until the phosphor coats the entire surface. Invert the screen and tap to remove the loose powder. Remove the stopper and using a gentle jet of nitrogen, blow off any

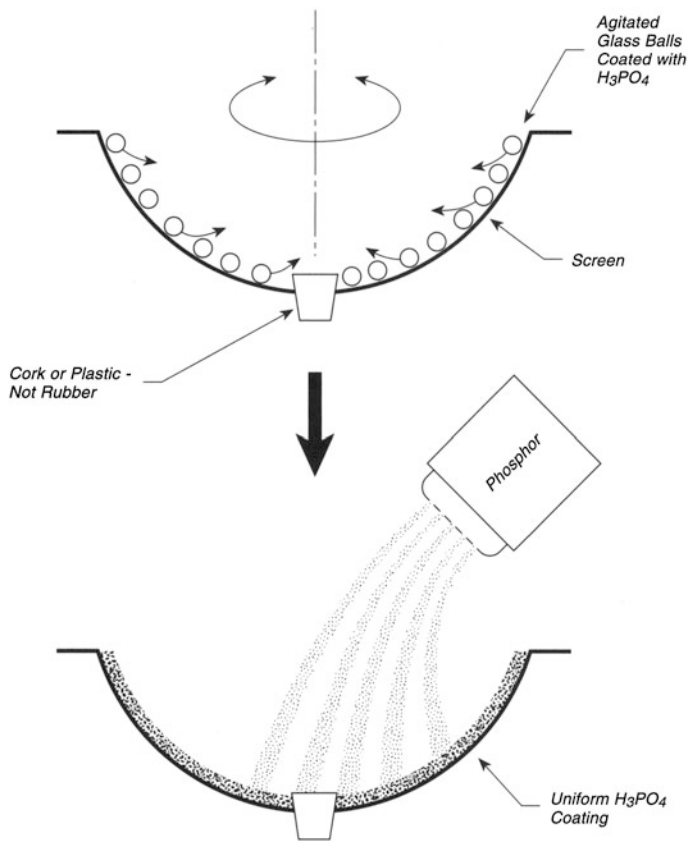

Fig. 13.2 Dusting method for deposition of phosphor screen

remaining loose phosphor. The screen should be baked in air at 200 °C for 2 h and it is then ready for use in ultrahigh vacuum.

Caution should be exercised to prevent breathing of phosphor or contact with the skin.

A unique method for electrostatically depositing and adhering a phosphor screen is described in [10].

Another unique method for depositing a phosphor powder on a flat, tin oxide-coated plate is described in [11]. Here, a glass plate which has been chilled in air below the dew point is coated with phosphor powder from an atomizer. The phosphor uniformly adheres to the moist plate. Drying the plate in a dessicator removes the water, and the phosphor adheres to the plate without any adhesive. The adhesion is sufficiently strong to permit the use of the phosphor screen in any position in a vacuum system, yet the coating can easily be removed by wiping under water.

References

1. F. Rosebury, *Handbook of Electron Tube and Vacuum Techniques* (American Institute of Physics, New York, 1993), pp. 251–254
2. J. Millman, *Vacuum-tube and Semiconductor Electronics* (McGraw-Hill, New York, 1958)
3. K.R. Spangenberg, *Vacuum Tubes* (McGraw-Hill, New York, 1948), pp. 429–432, 821
4. R. Gomer, *Field Emission and Field Ionization* (American Institute of Physics, New York, 1993), p. 167
5. D.K. Flynn-Sanders, S.-L. Chang, P.A. Thiel, and R. Imbihl, J. Vac. Sci. Technol. **A10**, 413 (1992). In addition to the phosphor deposition procedure described here, this paper has a description of several phosphors and their light emission properties. One should be especially careful with beryllium-containing phosphors because of their poisonous nature and their possible entry to the human body through cuts in the skin
6. Silica gel which works in this application a product of Davidson Chemical which is a division of W.R. Grace, 7221 W. Parkland Court, Milwaukee, WI 53223. The surface of the silica is hydroxylated and the total surface area is about 300 m2/g. In general silica gels have smaller particle sizes than silica powders
7. A. Cetronio, J.A. Cross, J. Vac. Sci. Technol. **15**, 1191 (1978)
8. R. Carr, E. Chaban, I. Vac, Sci. Technol. **A10**, 3595 (1992)
9. E.W. Muller, T.T. Tsong, *Field Ion Microscopy* (Elsevier, New York, 1969), p. 139
10. A. Cetronio, J.A. Cross, J. Vac. Sci. Technol. **15**, 1191 (1978)
11. R.C. Abbott, P.M. Brown, Rev. Sci. Instrum. **38**, 832 (1967)

Chapter 14
Thermionic Emitters

14.1 Thoriated Thermionic Emitters

Thermionic emitters are very widely used in surface science experiments as sources of electrons. The emission of electrons in the absence of applied electric fields follows the Richardson equation,

$$I/S = AT^2 e^{-e\phi/kT}$$

where *I/S* is the electron current density, ϕ = the work function of the emitter, *e* is the electronic charge, *T* is the temperature in K, and *k* is the Boltzmann constant. For metals, $A = 120\ \text{A/cm}^2\ \text{K}^2$.

Various coatings on thermionic emitters are used to reduce the work function, permitting the thermionic emitter to operate at lower temperatures while delivering the same current density as an unmodified emitter at higher temperatures. Some aspects of the various coatings and their advantages and disadvantages in ultrahigh vacuum systems are described by Redhead et al. [1]. For various reasons, ThO_2 coatings on W or Ir surfaces exhibit the most favorable properties for use in ultrahigh vacuum. While long-term operation in an oxygen ambient is not possible with either metal, Ir will withstand short accidental exposure to oxygen without burnout.

Figure 14.1a shows the simple experimental procedure that may be used for coating a thermionic emitter with a layer of ThO_2 by cataphoretic deposition [2]. A suspension of 200 mesh ThO_2 powder (5 g) in a solution containing 0.075 g of thorium nitrate in 100 ml of 95 % ethanol is used. This suspension is allowed to stand for a few minutes so that the large ThO_2 particles settle to the bottom and are removed from further considerations. The suspension is electrically deposited on the filament at a negative potential of a few volts relative to the Pt anode. The required current density depends on the shape of the surface being coated, and is found by trial and error. It is best to electropolish tungsten substrates in NaOH

© Springer International Publishing Switzerland 2015

J.T. Yates Jr., *Experimental Innovations in Surface Science*,
DOI 10.1007/978-3-319-17668-0_14

solution (tungsten positive) and to rinse in water before beginning the ThO_2 deposition. The white ThO_2 powder will form a very uniform deposit on the emitter surface, and when fired in vacuum, this coating will be rather strongly adherent. Coatings between 0.025 and 0.040 mm in thickness are satisfactory [2]. Firing in vacuum to about 1800 K brightness temperature activates the thoria fully [2]. Reference [2] contains many interesting measured properties of ThO_2.

The maximum current density that may be drawn from both clean W and ThO_2 surfaces is shown in Fig. 14.1b. Since the average work function of W (about 4.5 eV) is reduced to about 3.0 eV by thoriation, a tremendous enhancement of electron emission is achieved, as shown in Fig. 14.1b [1].

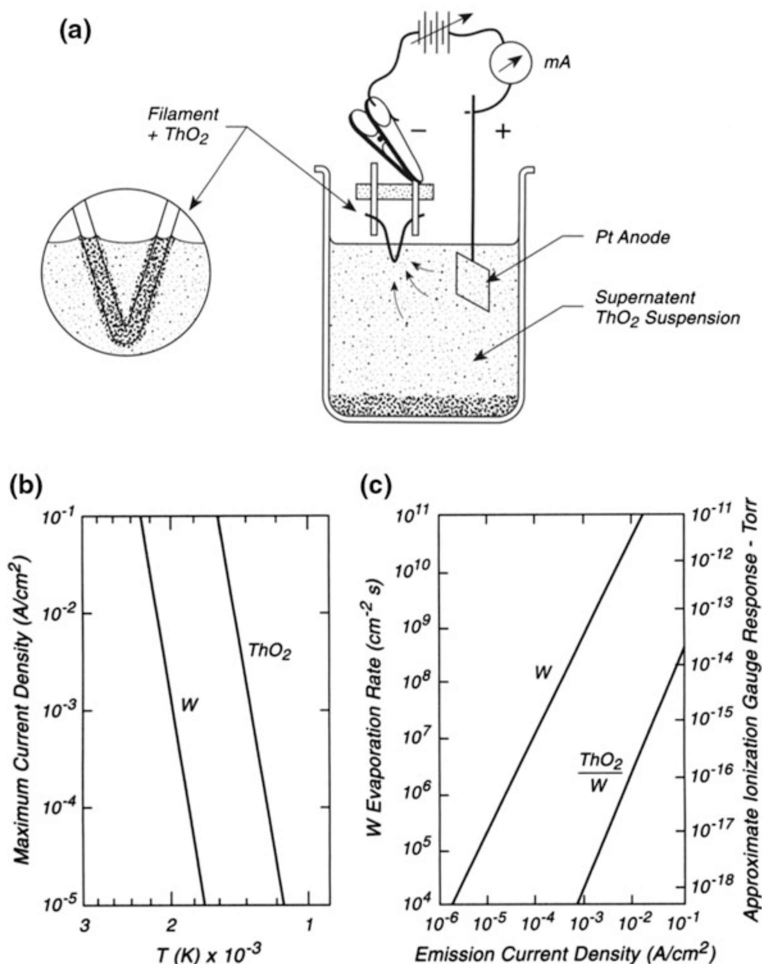

Fig. 14.1 Thoriated tungsten thermionic emitters. **a** Cataphoretic ThO_2 deposition on a thermionic emitter. **b** Maximum current density for thermionic emitters. **c** W Evaporation rate for thermionic emitters

One of the reasons for using thoriated thermionic emitters is to reduce the operating temperature for electron emission to levels that involve negligible evaporation of the metal. Figure 14.1c [1] shows the evaporation rate of W atoms versus electron emission current density for both W and ThO_2/W emitters. At the higher emission current densities for pure W, significant evaporation of W will occur over long experimental times, whereas ThO_2/W emitters involve negligible W evaporation rates.

It is important not to bombard the ThO_2 coating with electrons, which will cause damage. Even using AC accelerating voltages is detrimental in degassing ionization gauge grids, when the hot grid can be a thermionic emitter on the reverse half-cycle [1].

It has been reported that ThO_2-coated W filaments often emit unknown impurities that can be contaminants in surface science experiments [3]. This was studied for ThO_2/W filaments contaminated by F [4], and significant transfer of F or F-containing species to a clean single crystal of W was observed. Other halogen impurities such as Cl are also likely to be present in ThO_2 coatings exposed to new vacuum systems, since both HCl and HF are common pickling agents in cleaning stainless steel [5]. These effects can be eliminated eventually by outgassing new ThO_2-coated emitters for long periods of time [4]. Such halogen contamination of the grid surfaces of a Bayard-Alpert gauge renders the gauge useless for low pressure measurements, since electron impact desorption from the halogen-covered grid surface will supply spurious ion currents [6].

In addition to W wire thoriated by surface coatings of ThO_2, it is also possible to purchase W wire that contains alloyed Th at the 1–2 % level [7, 8]. This small amount of thoria was originally added to decrease crystallite slippage in the polycrystalline wire as it was formed by drawing through a die. These wires also exhibit greatly enhanced thermionic emission, compared to pure W. Despite high vacuum conditions, these emitters are readily poisoned [9]. This poisoning process may be diminished by carburizing the wire in a hydrocarbon gas, such as acetylene at temperatures near 1700 °C [8]. An outer layer of W_2C, about one-tenth the wire diameter in thickness is produced [8].

A thoriated Ir thermionic emitter has been reported to have high resistance to exposure to air and to exhibit low Th evaporation rates at operating temperatures [10].

Thorium carbide thermionic emitters exhibiting an effective work function of about 3.3 eV have been produced and will emit about 10 A/cm^2 at 2150 K [11].

14.2 Lanthanum Hexaboride Thermionic Emitters—Deposition on Metals

The use of cataphoretic deposition of thorium oxide, ThO_2, on thermionic emitter metal surfaces for the purpose of reducing the work function has been described on p. 133. A similar technique can be used to produce LaB_6-coated metal emitters.

Solid LaB6 thermionic emitters have been described on p. 137, but these are only useful for well-defined geometries and are costly. Thus for small, disposable LaB_6 emitters, cataphoretic deposition on metal ribbons or filaments provides an excellent route to useful thermionic emitters.

Five factors have been identified as being of importance in LaB_6 deposition. They are:

1. The particle size and the relationship between particle weight and surface area.
2. The concentration of cations in the suspension holding the LaB_6 particles.
3. The ability of cations to adsorb onto the LaB_6 surface, providing surface charge to permit particle migration under electrolytic conditions.
4. The electrostatic potential gradient causing the particles to migrate.
5. The adherence of the particles to the metal cathode surface.

The most efficient deposition occurs with particles having a high surface charge and migrating in a strong electrostatic field.

The present study [12] has been built on earlier methods [13, 14]. Re ribbons, $0.0025 \times 0.76 \times 12.7$ mm^3 were used. These filaments were heated white hot in vacuum to clean them before external cataphoretic deposition. A Ta anode was used, and the current (0.2–1.0 mA) was adjusted to achieve optimum deposition of LaB_6 in 30–300 s. For best results, 10 g of very finely divided LaB_6 was suspended in 100 ml of methanol and about 0.05 g of NH_4NO_3 was added as the electrolyte, dissolving this first in a small volume of methanol. These suspensions have a short lifetime of the order of several weeks owing to hydrolysis of the LaB_6, which produces a white coating on the powder that interferes with adhesion to the cathode. A Ta ribbon was used as an anode, and it was noted that the deposition occurs at the Re ribbon edges owing to higher electric field strength there. In order to avoid this, the geometry shown in Fig. 14.2 was used, with the Ta anode parallel to the meniscus of the suspension, and the ribbon pulled almost out of the suspension to reduce the tendency for deposition on the edges. A narrow gap between cathode and anode is preferred to increase the electrostatic field. In addition, deposition against the gravitational field leads to the selection of smaller LaB_6 particles which adhere better than large particles. The LaB_6 thickness could be adjusted up to 0.5 mm, but little difference in performance was noted for various thicknesses. Deposition on filaments can be done with a large anode and with the electrodes in a vertical position, since the electric field at the cylindrical filament surface is uniform [12, 14].

Failure in the adhesion of LaB_6 to Re supports has been observed following cataphoretic deposition. It was found that either boron or boric oxide impurity in the LaB_6 was responsible for the adhesion loss, and a purification procedure was described which produced LaB_6 with excellent adhesion properties on Re surfaces [13].

LaB_6 may also be deposited on Ta foil or filament surfaces if the surface is carburized first to produce a barrier layer of TaC that protects the underlying Ta from attack by the LaB_6 at high temperatures [15].

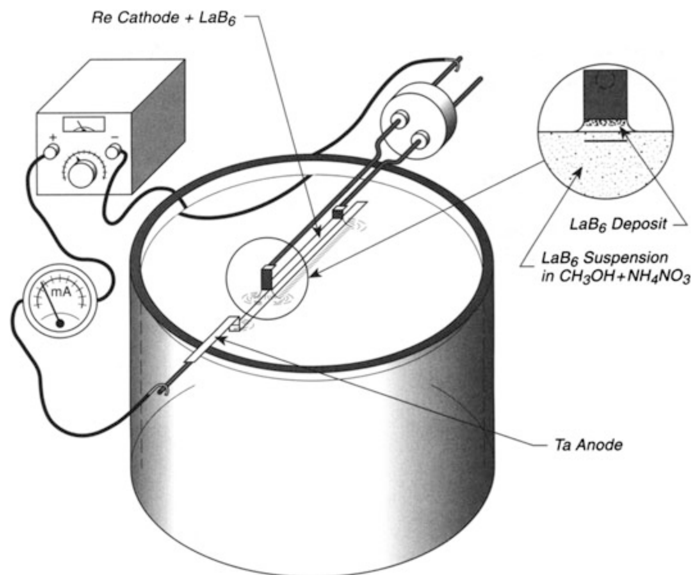

Fig. 14.2 LaB_6(s) Cataphoretic deposition

14.3 Directly Heated Lanthanum Hexaboride Thermionic Emitters

The work function of a tungsten thermionic emitter can be reduced significantly by using a thoria coating (see p. 133). In addition, it is well known that LaB_6 coatings on refractory metals such as W or Ta serve to produce a low work function thermionic emitter of limited lifetime [16] (see p. 135), and LaB_6-coated refractory metal emitters are widely used when high electron current densities are desired at low emitter temperatures [16]. The LaB_6 structure is also remarkably stable toward damage by positive ion bombardment that may occur in some high-voltage devices [16]. The degradation of LaB_6 occurs by means of B diffusion into the W or Ta substrate, accompanied by La vaporization. This effect can be minimized by carburizing the substrate before coating with LaB_6. With rhenium as the base metal, this degradation effect is minimized [17]. For bulk LaB_6, the surface La atoms vaporize slowly at high temperatures, and are replaced by La atoms from the bulk [16]. Other authors have also investigated the properties of LaB_6 as a thermionic emitter [18, 19].

Bulk LaB_6 may be used also as a thermionic emitter material. Questions about the best mounting procedure to avoid stresses (owing to thermal expansion) and to avoid degradation at the electrical contact points then come into play [17]. Figure 14.3a shows an unsuccessful mounting procedure for mounting a LaB_6 strip between two connecting electrodes made of graphite. While the emitter gave

Fig. 14.3 LaB_6(s) Thermionic emitters. **a** Rigid mount. **b** Flexible. **c** Flexible. **d** LaB_6(s)—T versus I. **e** LaB_6(s)—I_e/S versus T. **f** Wt. Loss versus I_e/S

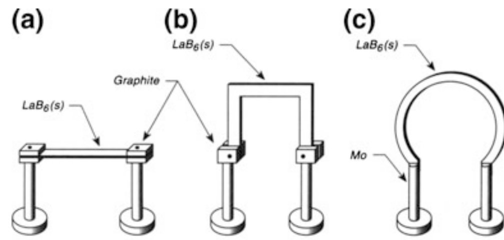

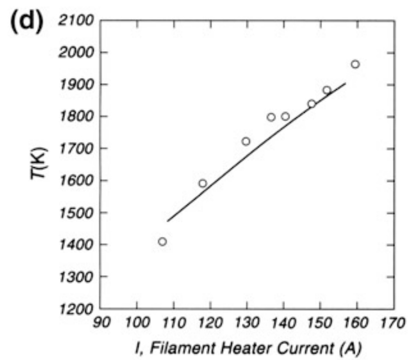

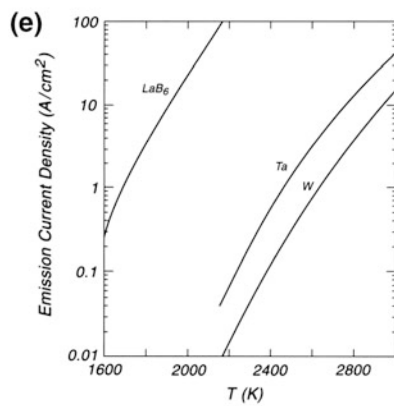

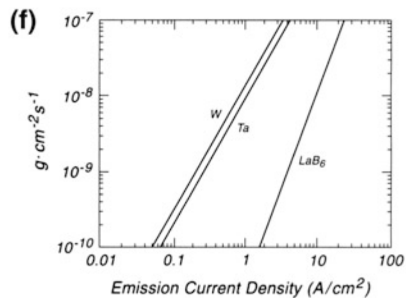

copious emission at 1400 °C, it cracked upon cooling as a result of its high coefficient of thermal expansion. To avoid this problem, rectangular and circular filaments were constructed as shown in Fig. 14.3b. These structures survived temperature cycling. The structure in Fig. 14.3b is mounted on graphite holders, while that in Fig. 14.3c is mounted on Mo holders.

Figure 14.3d gives the temperature versus current for a LaB_6 strip, 1.6 × 3 mm^2 in cross-sectional dimension. The points are experimental points, and the line is a theoretical line calculated on the basis of the ohmic heating and the radiative losses [17]. Figure 14.3e shows the thermionic electron emission of LaB_6 compared to Ta and W emitters. Approximately four to five orders of magnitude difference in current density is observed compared to the refractory metals.

As mentioned before, one is concerned with La evaporation from LaB_6 when it is heated to sufficient temperature. However, one is also concerned about metal evaporation effects when refractory metals are used as thermionic emitters, since they must work at very high temperatures (see p. 133). Figure 14.3f shows a comparison of the evaporation rate from LaB_6 compared to W and Ta, obtained from published data, where the ordinate is in g $cm^{-2}s^{-1}$. On this basis, a LaB_6 cathode can last for several thousands of hours at current densities of 10–20 A cm^{-2}. Above 50 A cm^{-2}, the useful life may still be greater than 200 h [18].

A method for welding small LaB_6 shapes to Re wire for making compact high-efficiency thermionic emitters has been described [20]. In addition, a method for protecting a W filament from LaB_6 attack by interposing a layer of ThO_2 has been described [21].

A method for mounting conical tipped LaB_6 cathodes for electron beam instruments has been commercially developed. The cathode is mounted between pyrolytic graphite blocks that are clamped between Mo/Re alloy support posts that have a high modulus of elastically at high temperatures. The method is also used for CeB_6 cathodes [22].

14.4 Thermionic Emitter Mounting

The provision of long-lived thermionic emitters for electron bombardment requires special mounting and connection procedures. Figure 14.4a shows the essentials of mounting a thermionic emitter for stability and also for ease of replacement [23]. A fixed alumina tube with two holes fits a spiral emitter, made from W/3%Re, about 0.2 mm in diameter. The coil is wound uniformly around a mandrel in such a fashion that its ends can be slipped into the holes in the alumina tube without producing any strain on the coil. If this is not done, the coil will distort severely upon first heating. The W/3%Re alloy is preferred over pure W because of its tendency to not become so brittle during heating.

Friction connections are made with heavier Mo conductor wires by slipping in 0.1–0.2-mm-diameter filler pieces from the back side until a tight fit is achieved

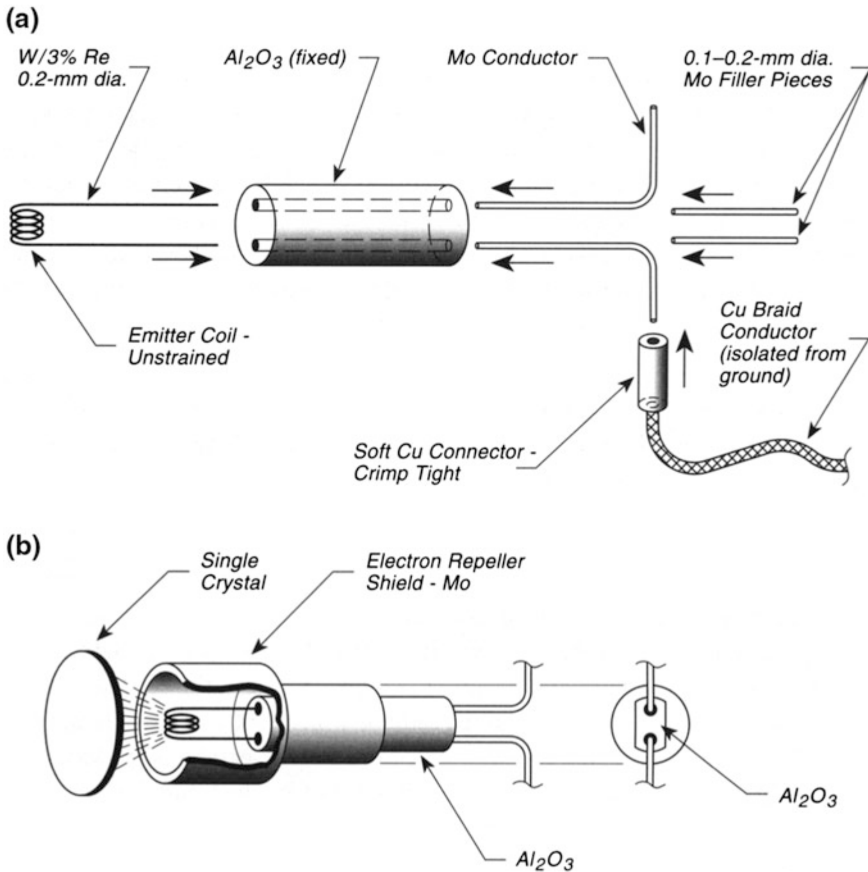

Fig. 14.4 Thermionic emitter mounting. **a** Open emitter. **b** Shielded emitter

between the emitter and the conductor wires. This method avoids welding and allows the emitter coil to be disassembled for replacement with ease.

Connection to the Mo conductor wires is conveniently made with Cu braid, and a soft Cu connector tube (annealed in a flame) that is crimped tight several times around the braid and the Mo wire using pliers. The assembly should be arranged such that the braid does not strain the Mo conductor wires by its weight or motion.

Figure 14.4b shows a similar device that utilizes a Mo electron repeller shield. The alumina tube is flattened on two sides and is placed into a fitted channel at the back of the Mo shield. The Mo shield will charge negatively during operation, but for heavy electron bombardment heating, the crystal must be biased positively.

Macor ceramic supports are inappropriate for these purposes for two reasons. The material degrades at high temperatures, and fluorine compounds are evolved at high working temperatures [24].

14.5 Indirectly Heated Cathodes for High-Temperature Operation

Cathodes for electron guns and other devices are often coated with low-work-function materials that permit higher current densities to be drawn than would be possible with pure refractory metal cathodes such as W or Mo (see p. 133). Coated cathodes are often heated to temperatures in excess of 2000 K for activation and operation. Directly heated cathodes may be employed, but the requirement for an emitter to be at equipotential over its surface rules out direct ohmic heating. Thus, indirectly heated cathodes are often used. The design shown in Fig. 14.5a uses an ohmically heated W filament to heat a Mo disk containing a work-function-lowering material on its surface [25].

A self-supporting W filament (0.38-mm diameter), wound in a double helix on a mandrel into a coil 9.5 mm in length, is used to heat a Mo disk cathode mounted on the helix axis. The Mo disk is at the end of a cathode cylinder, 3.8 mm in diameter and 10 mm long. Mounted on the outside of the Mo cathode cylinder are 3 (0.1-mm thick) polished Ta radiation shields. These shields reduce the radiation transmitted to the outer stainless steel support cylinder such that a measurable color temperature for the stainless steel sleeve is not reached.

Figure 14.5b shows the W heater life behavior versus the heater current for operation in ultrahigh vacuum. The temperatures associated with each point were measured pyrometrically on the Mo cathode surface.

In the example shown here, only radiation heating of the Mo cathode was used. However, this may be assisted by applying a positive potential to the cathode relative to the filament, and drawing electron bombardment current to the cathode. This method of heating is well suited for fast flashing of the cathode which is often necessary during activation of the cathode coating (about 2500 K for ThO_2). Electron bombardment also involves lower W heater temperatures, and will not shorten the heater lifetime.

14.6 Filament Power Supply Tester

Often it is necessary to be able to test a filament power supply without having a filament operating in vacuum use in the test. This circuit diagram shows a dummy filament which may be used in the test, without actually having to connect to a filament for the power supply test. The power supply filament and anode connectors are connected as shown. For DC operation, one has a choice of simulating a ~2A-filament or a ~3–4 A filament. Switch S2 controls the current range desired. For AC operation, switch S1a and S1b are open and the circuit utilizes the bridge rectifier, BR66. The part of the circuit to the right of the dashed line simulates the dummy filament thermionic emission using an NPN transistor, MJE 340. Filaments requiring about 2A involve tungsten wire of the order of 0.125 mm diameter; 3–4 A filaments involve tungsten wire of about 0.2 mm diameter [26] (Fig. 14.6).

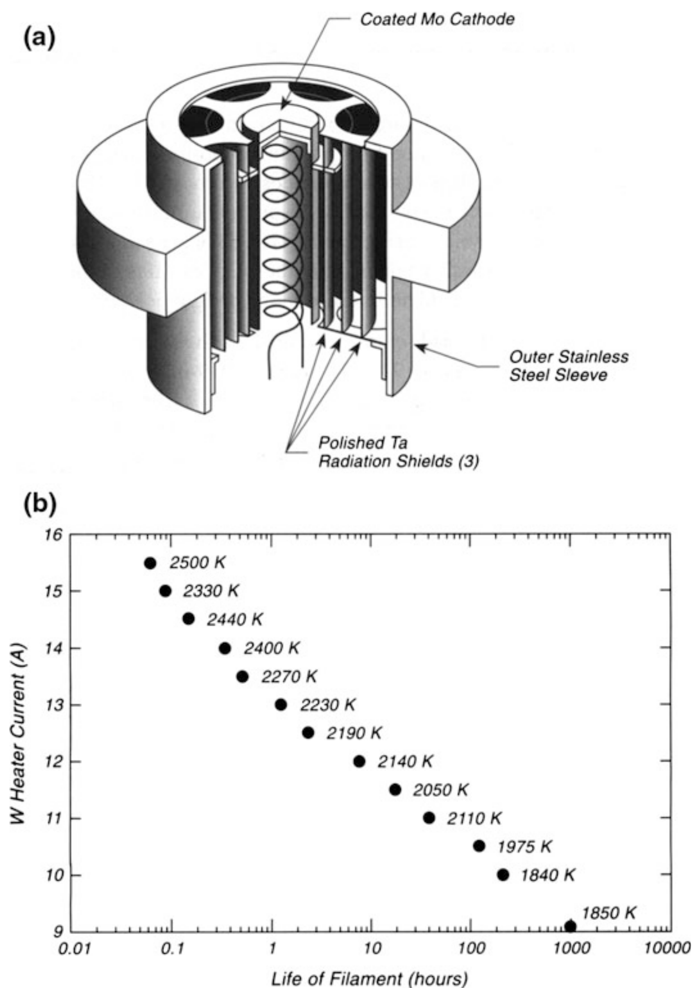

Fig. 14.5 Indirectly heated cathode for high temperature operation. **a** Cathode design, **b** Cathode lifetime versus heater current

14.7 Bayard-Alpert Ionization Gauge with Corrections for External Radiation and External Electron Flux Effects

Many workers have noted that external electron sources in UHV systems cause erratic readings in ionization gauges. In the case of ionization gauges in the vicinity of synchrotron or other radiation sources, there are also effects due to external radiation causing inaccurate gauge readings. In early work by Redhead [27], the effects of soft-X-ray production leading to photoelectron generation inside the

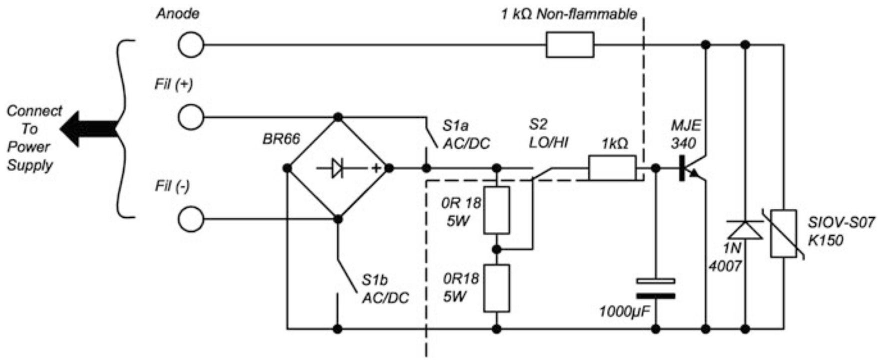

Fig. 14.6 Filament power supply tester

gauge itself were eliminated in various ways, resulting in new designs for gauges with for instance two collector electrodes (the modulated ionization gauge), or to gauges in which the ion collector was electrically and spatially isolated from the ionization region (suppressor and extractor gauges). These modifications also led to methods to compensate for positive errors caused by electron stimulated desorption from adsorbed gases on the ionization gauge grid.

A normal ion gauge operating in the vicinity of an external thermionic emitter or in a region containing high energy radiation will suffer major errors, caused by things like external electron collection by the grid or the collector. Also externally-produced photons interacting with the electrodes can cause X-ray production, leading to photo-emission within the gauge, and giving spurious ion current measurements. In the new gauge design shown in Fig. 14.7, measurements of the current due to externally-produced electrons are made at the correcting electrode in an auxilliary gauge which does not contain a thermionic emitter filament, and these measurements, applied to the current measurement from the normal gauge, can be used to make corrections to the measured ion current and calculated pressure. The details of this are dealt with in a recent paper [28], and background information will be found in earlier papers [29–35].

Figure 14.7 shows the side view of the gauge design and its logic. I_{CE} is the collector current from the ion collector in the correcting electrode (CE) attachment, and I_C is the current from the normal gauge. The measurement of I_{CEe}, the external electron current received by the grid (and hence available within the gauge structure for ionization of gases), is also employed to make corrections to the measured ion current in the normal gauge. Reference [28] gives a formula to measure a compensated pressure in this gauge. Figure 14.7 shows the measurements of the uncorrected gauge, BA-S4, compared to measurements of the corrected gauge, BA-S4. Both gauges are subjected to a flux of externally-produced electrons which enter the two gauges from the outside. The pressure measurements made with NIG-2F are made for a gauge which does not see externally produced electrons. The abscissa is a plot of the filament current causing thermionic emission in an

external electron source and large emitted electron currents are produced as one moves from 2 to 3 A. The indicated emission current in the ion gauge being tested remains essentially constant at 3.97 mA. It is seen that without compensation, the ion gauge suffers considerable negative errors when externally-generated electrons are present. The compensation circuit also includes a method for measuring the effect of external radiation on currents generated in coaxial cable, I_{CErr} and I_{Crr}.

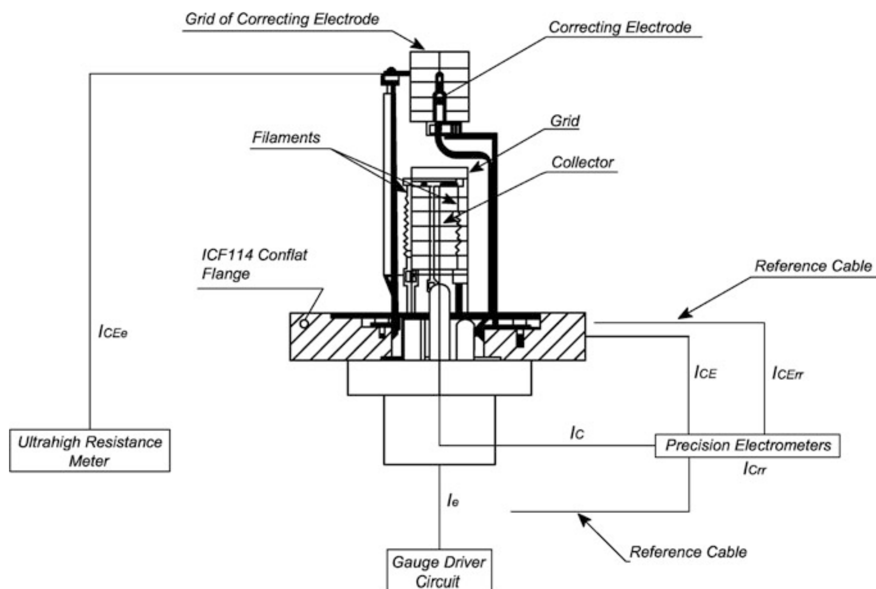

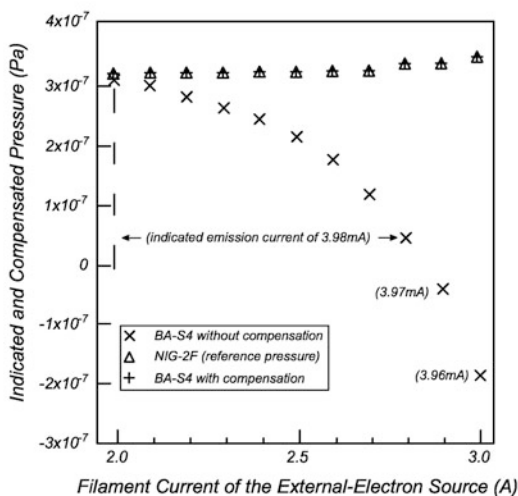

Fig. 14.7 Bayard alpert ionization gauge with corrections for external radiation and electron flux effects

14.8 Replacing Filaments in Glass Bayard-Alpert Gauges

Filament replacement in a glass Bayard-Alpert ionization gauge is quite simple if a glassblower will move the tubulation from the normal position to a position on the bottom of the gauge where the filament attachment posts are located [36]. Figure 14.8 shows the location of the new port, and the position of the original tubulation. The new tubulation is sealed to the outer envelope using Corning No. 3320 glass as a grade to Pyrex, and the seal is made with an oxidizing flame,

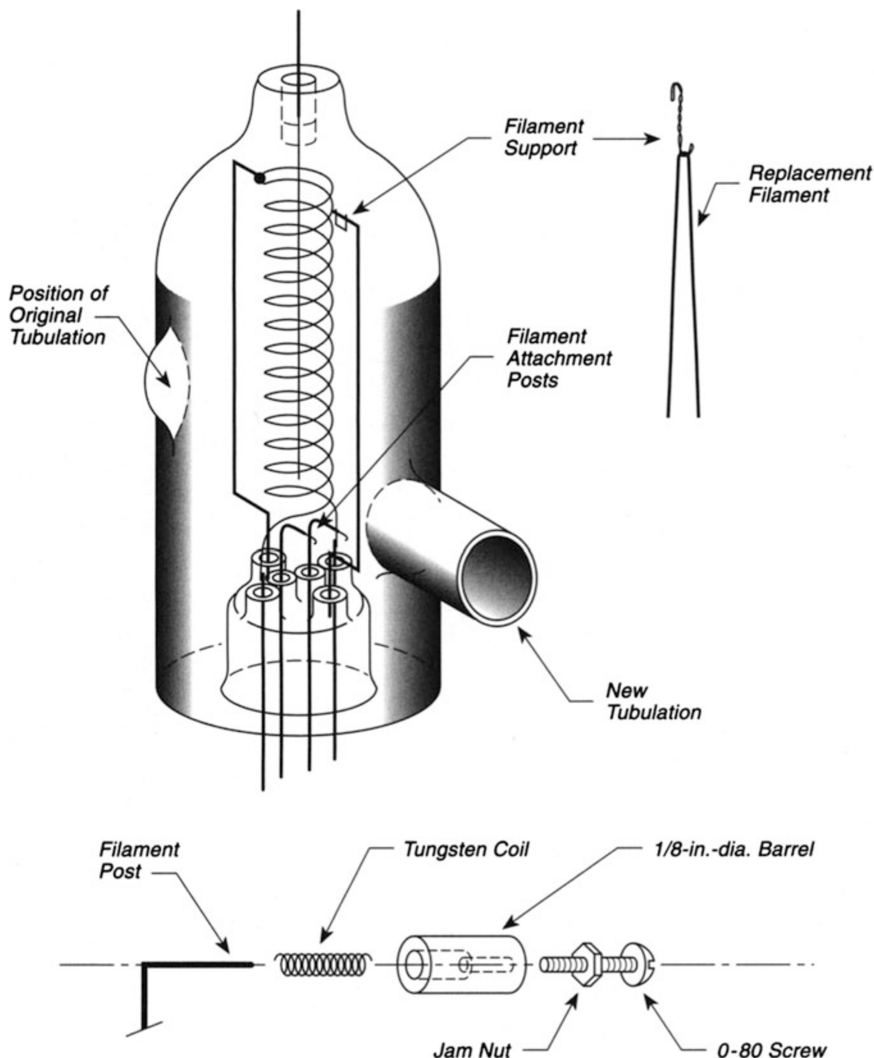

Fig. 14.8 Replacing filaments—Bayard-Alpert Gauges

after thorough cleaning of the gauge with Alconox detergent. The gauge should be annealed in the upright position before use.

Replacement filaments can be made of many materials, such as iridium, thoriated iridium, thoriated tungsten, etc. (see p. 133). The use of 0.010-in. diameter W is easiest. The bent filament is formed into a tight V-shape, and a hook is fabricated from the filament wire by first twisting the apex region of the wire and then making the hook as shown in Fig. 14.8. The hook is then inserted into a wire loop at the top of the filament support rod. When softer filament materials such as iridium are used, a tungsten hook made of 0.010-in. wire may be used for the upper support. Hemostats are reported to be useful in the filament insertion procedure.

The lower attachment of the two ends of the filament to the filament attachment posts can be made in three different ways:

1. Welding, using a tweezer spot welding assembly, and making small 0.002-in. thick Ta tabs that will weld nicely to W and Ir filaments.
2. The filament post is filed round, and a l/8-in.-diameter stainless steel barrel is fabricated as shown in Fig. 14.8. The small tungsten locking coil fits onto the filament post, and when the barrel is twisted in one direction, binding occurs. Twisting oppositely results in breaking the junction. A 0.020-in. clearance is needed when the tungsten locking coil is made of 0.010-in. W. The emitter filament is held under an 0–80 screw head placed in a tapped hole on the opposite end of the barrel, using a jam nut as shown.
3. The W filament may just be wrapped several times around the two support posts.

The gauge calibration seems to be well maintained after refabrication [36].

References

1. P.A. Redhead, J.P. Hobson, E.V. Kornelsen, *The Physical Basis of Ultrahigh Vacuum* (American Institute of Physics, New York, 1993), Chapter 7, section 7.6
2. T.E. Hanley, J. Appl. Phys. **19**, 583 (1948)
3. P.A. Redhead, J.P. Hobson, Br. J. Appl. Phys. **16**, 1555 (1965)
4. J.T. Yates Jr, D.A. King, J. Vac. Sci. Technol. **9**, 1256 (1972)
5. Stainless Steel Fabrication (Allegheny Ludlum Steel Corp., 1959), p. 309
6. H.E. Winters, J.W. Coburn, Surf. Sci. Rep. **14**, 161 (1992)
7. I. Langmuir, Phys. Rev. **22**, 357 (1923)
8. R.G. Murray, R.J. Collier, Rev. Sci. Instrum. **48**, 870 (1977)
9. R.O. Jenkins, W.G. Trodden, J. Electron. Control **12**, 1 (1963)
10. H.F. Gray, E.H. Harris, T. Pankey Jr, G.A. Haas, Rev. Sci. Instrum. **43**, 1113 (1972)
11. H.H. Glascock Jr, Rev. Sci. Instrum. **43**, 698 (1972)
12. J.E. Delmore, Rev. Sci. Instrum. **54**, 158 (1983)
13. L.J. Favreau, D.F. Koenig, Rev. Sci. Instrum. **38**, 841 (1967)
14. L.J. Favreau, Rev. Sci. Instrum. **36**, 856 (1965)
15. M. Nasini and G. Redaelli, Rev. Sci. Instrum. **42**
16. J.M. Lafferty, J. Appl. Phys. **22**, 299 (1951)
17. K.N. Leung, R.A. Pincosy, K.W. Ehlers, Rev. Sci. Instrum. **55**, 1064 (1984)

18. H. Ahmed, A.N. Broers, J. Appl. Phys. **43**, 2185 (1972)
19. S.P. Gordienko, E.A. Guseva, V.V. Fesenko, Teplofiz. Vys. Temp. **6**, 821 (1968)
20. K.N. Ramachandran, Rev. Sci. Instrum. **46**, 1662 (1975)
21. L. Bakker, ThJ van Velzen, Rev. Sci. Instrum. **37**, 1404 (1966)
22. Manufactured by FEI Company, P.O. Box 654, McMinnville, OR 97128
23. Dr. R. David, Institut fur Grenzflächenforschung und Vakuumphysik, Forschungszentrum Jülich GmbH, Postfach 1913, D-52425 Jülich, Germany (private communication)
24. Personal experience
25. J.T. Jensen Jr, J. Klebanoff, G.A. Haas, Rev. Sci. Instrum. **38**, 1178 (1967)
26. Michael Schmidt and Ulli Diebold, private communication
27. P.A. Redhead, J.P. Hobson, E.V. Kornelsen, "*The Physical Basis of Ultrahigh Vacuum*" (Chapman and Hall Ltd, Great Britain, 1968), pp. 304–349; reprinted as an American Vacuum Society Classic, AIP (1993)
28. H. Saeki, T. Magome, J. Vac. Sci. Technol. **A29**, 061601 (2011)
29. H. Saeki, T. Momose, J. Vac. Sci. Technol. **A18**, 244 (2000)
30. H. Saeki, T. Magome, T. Aoki, N. Gotoh, T. Momose, Rev. Sci. Instrum. **75**, 5152 (2004)
31. T. Magome, H. Saeki, J. Vac. Sci. Technol. **A23**, 725 (2005)
32. H. Saeki, T. Aoki, T. Momose, J. Vac. Sci. Technol. **A19**, 1022 (2001)
33. H. Saeki, T. Magome, Radiat. Meas. **41**, S271 (2007)
34. H. Saeki, T. Magome, Y. Shoji, J. Vac. Sci. Technol. **A24**, 1148 (2006)
35. H. Saeki, T. Magome, Rev. Sci. Instrum. **79**, 055102-1 (2008)
36. D. Bedding, T. Moran, A. Brown, Rev. Sci. Instrum. **56**, 2170 (1985)

Chapter 15
Shielding

15.1 Magnetic Shielding in Ultrahigh Vacuum

It is common to employ magnetic shields inside ultrahigh vacuum systems for the elimination in electron spectrometers of stray magnetic fields caused by the Earth or by magnets associated with ion pumps or other devices near the vacuum system. A number of formulas have been presented for the calculation of the efficiency of a magnetic shield [1–3]. These formulas do not consider deviations from pure cylindrical geometry caused by lips, caps, and pumpout ports. The calculation method studied here is able to approximate the nonideal conditions caused by deviations from perfect cylindrical geometry [4].

A computer code, JASON [5], has been used. This code solves the linear Poisson equation. The Earth's magnetic field is of the order of 500 mG. It is desired in this particular example to reduce the magnetic field to less than 1.0 mG inside the shield shown in Fig. 15.1. The following constraints exist in this design as well as in designs to be made in other ultrahigh vacuum systems: (1) A small number of shield layers should be employed to reduce the additional surface area and outgassing which occurs from these surfaces; (2) Holes must be cut into the shield for pumping by the ultrahigh vacuum system. The pumping speed through a hole for atmospheric gases is about 11 L/cm^2 s; (3) The sample must be moved into the magnetically shielded spectrometer along the Z axis of the cylindrical shield.

The optimum shield material thickness, t, is

$$t \leq 3a/2\mu \tag{15.1}$$

where a is the inner radius of the cylinder and μ is the permeability of the magnetic shielding material. If the value of t needed, based on (15.1), is larger than the thickness of available material, two concentric shells may be used in shielding, at the expense of introducing more surface area.

© Springer International Publishing Switzerland 2015

J.T. Yates Jr., *Experimental Innovations in Surface Science*,
DOI 10.1007/978-3-319-17668-0_15

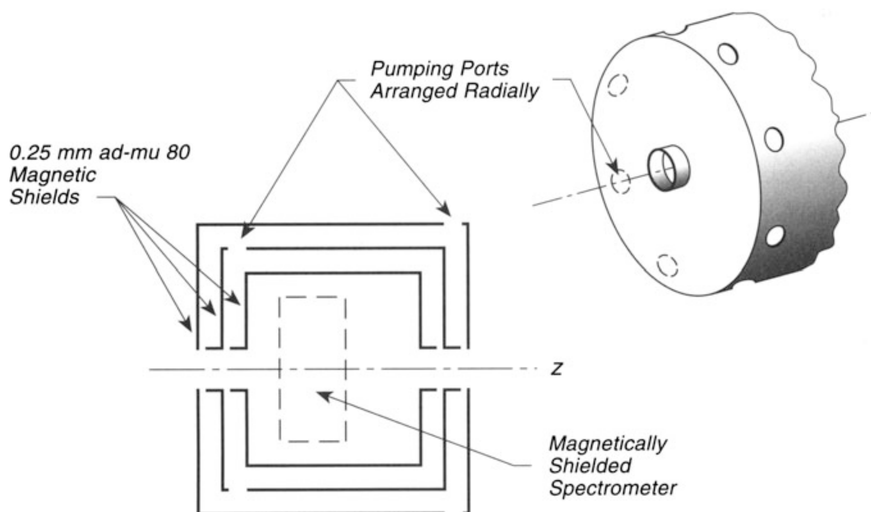

Fig. 15.1 Magnetic Shielding in UHV

Because the JASON program rotates a two-dimensional array about a cylinder axis, Z, it is geometrically impossible to specify three-dimensional holes along the shield perimeter. Instead, in a first-approximation method, a gap along the perimeter is used to model the desired hole size where the open area in the gap is equivalent to the hole area. This gap has the permeability of vacuum in the simulations. A second approximation method uses a gap with three times the pumping hole area, containing a magnetic shielding alloy that is two-thirds made of the shielding material, and one-third made of vacuum, i.e., specifying a "hole alloy." The actual hole configuration consists of radial holes of 3-cm-diameter, placed 6 cm apart around the ends of the two outer shields, as shown in Fig. 15.1.

The material chosen is a high permeability material, ad-mu 80 [6]. Its thickness, *t*, is 0.25 mm. The Figure shows a cross section through the optimized shield made of three concentric cylinders that contain pumpout ports as shown, as well as the axial sample insertion region. Approximation (1) gives approximately a 1000-fold attenuation of the Earth's field; approximation (2) gives approximately a 10,000-fold attenuation, both measured along the Z-direction at the center of the spectrometer. To make a rough comparison with actual measurements, the attenuation of an AC magnetic field, naturally present in the spectrometer room, was measured. Attenuation factors in the range 1900(X), 640(Y), and > 3600(Z) were measured in general agreement with the calculations.

It should be remembered that mechanically straining magnetic shielding made of mu metal will reduce its effectiveness. The effectiveness of annealing magnetic shielding is dealt with in [7].

15.2 Electrical Isolation of UHV Components

It is sometimes necessary to isolate electrically one ultrahigh vacuum component from another. This may be done using a conventional ceramic electrical isolator, connecting the two components with Conflat flanges on either side of the ceramic isolator. This arrangement requires linear space, and also, small lateral forces on the ceramic isolator may cause it to crack. A novel solution to this problem is presented in Fig. 15.2 [8].

Polyimide film (Type H), known as Kapton [9], is used. The film thickness is 0.127 mm. Two polyimide washers are cut with punches that have a clearance of 0.0127 mm. Sleeves, made by rolling up the polyimide film, with 2-mm overlap, are prepared and cemented with a fast-setting epoxy cement. This is best done using bolt-clearance holes drilled in a polyethylene block to hold the tubes during glue setting.

Two copper gaskets are sandwiched together around a polyimide spacer ring that is glued between the gaskets using a Dow Corning No. 997 silicone varnish [10]. The varnish is applied, the gaskets are placed on either side of the polyimide spacer, and the assembly is heated at 95 °C for 2 h in an oven for curing while being clamped under pressure. The polyimide spacer protrudes slightly beyond the inner and outer edges of the copper gaskets.

As shown in Fig. 15.2, the polyimide washers fit under stainless steel washers. The polyimide washers mechanically and electrically separate the stainless washers and bolt heads from the flange surface. The polyimide sleeves electrically separate the bolts from the bolt holes. The polyimide spacer ring between the copper gaskets separates the flanges from each other electrically.

Thermal shock tests between 260 and 10 °C resulted in no vacuum leak development. The devices do not add gas load to a vacuum system, and the UHV background mass spectrum did not change as a result of 10 of these devices being installed on the same system. The electrical resistance is greater than 10^{11} Ω, and electrical breakdown of the assembly did not occur below 17 kV. Breakdown does not result in failure of the vacuum integrity of the seals.

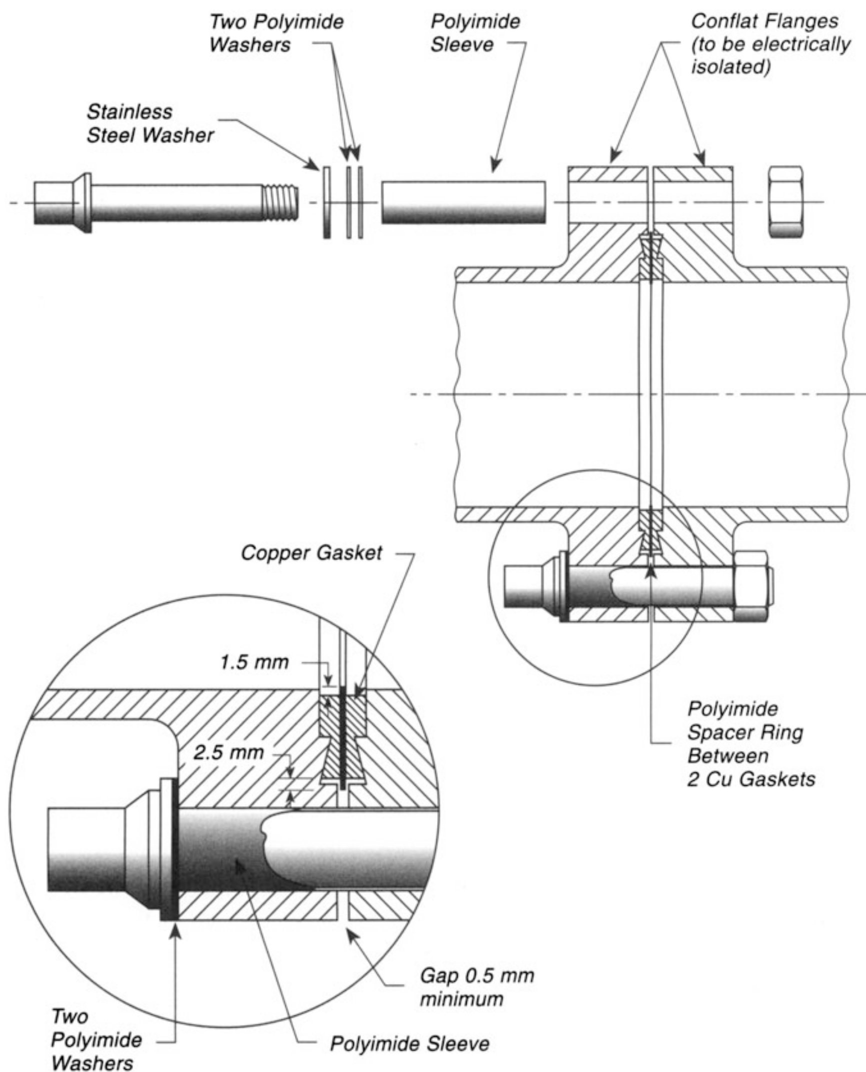

Fig. 15.2 Electrical isolation of UHV components

References

1. A.J. Mager, IEEE Trans. Mag. **MAG-6**, 67 (1970)
2. A. Mager, J. Appl. Phys. **39**, 1914 (1968)
3. D.U. Gubser, S.A. Wolf, J.E. Cox, Rev. Sci. Instrum. **50**, 751 (1979)
4. S. Dobscha, W. Siekhaus, Rev. Sci. Instrum. **57**, 3123 (1986)
5. S. Sackett, JASON, UCRL-18721, Lawrence livermore national laboratory, Livermore, CA 94550

6. Ad-Vance Magnetics, Inc., 625 Monroe Street, P.O. Box 69, Rochester, IN 46975
7. D.L. Martin, R.L. Snowdon, Rev. Sci. Instrum. **46**, 523 (1975)
8. J.C. Jones, Rev. Sci. Instrum. **46**, 489 (1975)
9. Obtained from: Dupont, 1007 Market Street, N-2426-A, Wilmington, DE 19898; see Dupont high performance films, Bulletin H-38492 (1983)
10. Obtained from: Dow Corning, P.O. Box 0994, Midland, MI 48640–0994

Chapter 16
Single Crystal Fabrication/Orientation

16.1 Making Small Au Single Crystals from Au Wire for STM and Other Studies

The production of small spherical single crystals from Au wire provides a convenient way of doing STM experiments on the various single crystal plane facets which are exposed on the surface [1]. A procedure outlined below has been employed in a number of STM studies on Au(111) and other crystal planes [2–10].

Low purity Au wire of 0.3 mm diameter was employed. The wire is first cleaned in piranha solution (3:1 mixture of concentrated H_2SO_4 with 30 % H_2O_2) to remove organic impurities and then in boiling concentrated HNO_3 to remove transition metals for about 20 min. The impurities from the bulk of the wire are removed by a "zone refining" procedure like that used in the semiconductor industry. The wire is clamped in a ceramic tweezer with the tweezer face horizontal and the wire hanging down. Use a 3 cm portion of the wire. Then bring a tiny hydrogen flame slowly from the lowest end of the wire and start melting it. Due to surface tension effects, the Au melts into a bead. Do this slowly, and as soon as the bead size is about the size of the wire diameter, remove the flame and allow the Au to crystallize. Then reheat, remelt and move the melting front (readily visible) upwards away from the bead. The impurities get stuck at the melting front and you then swipe them upwards from the bead to the junction between the bead and the wire. The impurities also segregate to the Au surface in this process.

After two or three cycles of this melting and sweeping procedure, repeat the cleaning procedure (boiling in HNO_3 and aqua regia—a mixture of concentrated HNO_3 and HCl which will dissolve Au) to dissolve a portion of the bead. The surface of the Au bead and the interface region between the bead and wire, containing zone-migrated impurities, will dissolve removing the impurities segregated there and the etched bead will appear non-specular. Then repeat the whole procedure several times and finally grow the bead to the desired size less than 1 mm in diameter. Facets will appear on the bead. If you inspect a facet and see a single

© Springer International Publishing Switzerland 2015

J.T. Yates Jr., *Experimental Innovations in Surface Science*,
DOI 10.1007/978-3-319-17668-0_16

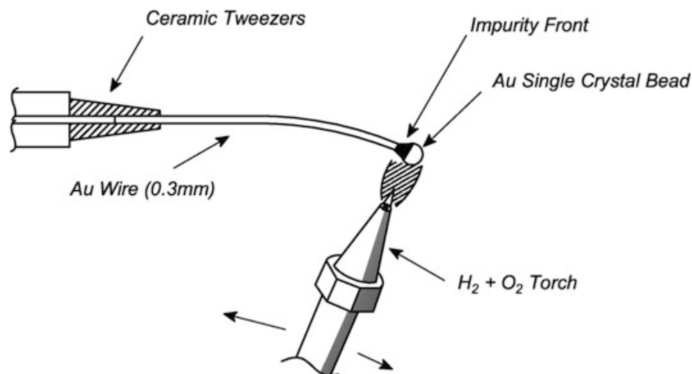

Fig. 16.1 Making small Au single crystal

visible particle, then the surface is not going to be STM clean. The single crystal bead is conveniently mounted by its Au wire tail, spot welding to a Ta foil support. The <111> facets will be several hundred μm in size. These facets feature zero miscut angles since they are natural facets. The (111) terrace width can be as large as several μm in the center of a facet. The edges of the facet approach the curved surface of the bead providing a variety of vicinal Au(111) surfaces, where single-atom steps form a superlattice.

This preparation should be done in a dust-free environment. Normally after installation in the STM the Au surface will need to be ion bombarded with Ar^+ and then annealed in vacuum to present a clean surface (Fig. 16.1).

16.2 Single Crystal Orientation, Grinding, and Polishing

The preparation of oriented single crystal surfaces by X-ray diffraction followed by grinding and polishing to a high degree of smoothness and flatness is of central importance in surface science experiments, and there is a long interconnected history of developments in this field [11–19]. At the present time, using the best methods, an orientational accuracy of ±0.05° [5, 8] and a flatness of one-twentieth the wavelength of sodium light [15] have been reported.

A brief history of the developments over almost 50 years follows. In 1949, Walker et al. [11] described a cylindrical crystal holder that contained a crystal holder platform that could be tilted so that the crystal could be crystallographically oriented in a mounting attached to an X-ray diffraction apparatus. The holder then could be transferred to cutting, grinding, and polishing apparatus without disturbing the crystal alignment. The cylindrical crystal holder is remarkably similar to a holder now marketed commercially as the Bond Barrell Holder [20]. In 1961, Bond [12] described a jig that held a cylindrical crystal holder for grinding an oriented crystal

on a flat grinding plate, called a lapping plate, containing an abrasive powder. Bond's holder was attached to a hardened steel ring that made contact with the lapping plate and provided a reference plane for the mechanical grinding and polishing processes. Bennett and Wilson [13], who used a grinding/polishing jig of different design, were not interested in accurate crystal orientation, but showed that lapping of hard crystals on soft metal plates containing embedded abrasive particles could result in surface flatness of the order of one-eighth the wavelength of sodium light. Butz et al. [15] described a goniometer-jig combination that was used for both orientation and lapping of crystals to an accuracy of 0.25° and to a flatness of one-twentieth the wavelength of sodium light. Berger et al. [17] described a goniometer-jig combination that possessed 2° of crystal tilt freedom, plus translational and azimuthal orientation freedom. They ground and polished a W crystal on a glass lap, with 15 μm $A1_2O_3$, 5 μm Al_2O_3, and 6-μm and 3-μm diamond abrasive paste. An interesting feature of this work was the production of a W crystal disk with five desired facet-planes, which were convenient for plane-to-plane comparisons. The accuracy of orienting and polishing single crystals has been brought to a very high level by Linke and Poelsema [18], who showed by He diffraction methods that Pt(lll) crystals oriented and polished as described previously [17] exhibited a mean terrace width of 3000 Å and an orientational error of ±0.05°. The reader is referred to the original papers for detailed designs of the goniometer-jig combinations.

Figure 16.2a shows a Bond Barrel Holder [20] mounted in a simple grinding-polishing jig made of hardened steel [21]. The Pt crystal on the holder platform has been crystallographically oriented using Laue X-ray diffraction, where the Bond Barrel Holder was held in a mount that fitted onto an optical rail that was part of the Laue apparatus. Typically, moving the Bond Barrel Holder from one mount to another can be done with an error of less than 0.1°. The single crystal was ground using a 600 grit abrasive paper mounted on a rotary wheel grinding and polishing machine. The weight of the Bond Barrel Holder forces the crystal onto the abrasive paper. The hardened steel jig is not appreciably affected by this process as should be determined periodically using a micrometer to measure its thickness around its circumference. When the crystal is flat, a series of polishing steps with smaller and smaller abrasive particles is performed as shown in Fig. 16.2b. It is extremely important to remove, by scrupulous washing and rinsing away from all parts of the apparatus, the abrasive from each step, or scratches owing to inadvertent abrasive particles will ruin the next steps in polishing with finer abrasive. The polishing cloth should of course be changed each time as the abrasive particle size is reduced.

Figure 16.2c shows a measurement made by the observation of interference fringes with an optical flat touching the finished crystal [21]. It was found, in duplicate experiments, that the surface was not flat, but instead had a curved profile with a typical radius from 4 to 2 m near the center, and a slope of from 0.05° to 0.08° at the edges. The limiting slope corresponds to one atomic step for about every 1000 Pt atoms measured horizontally, and for many experiments this is unimportant. Figure 16.2a shows a hypothesis about the origin of the slightly curved figure of the crystal, where slight buckling of the flexible abrasive paper is postulated to produce a wave that tends to round the crystal slightly. A small misfit

between the Bond Barrel Holder and the hardened steel jig can also result in a curved crystal [22].

Grinding and polishing to make highly flat surfaces can be carried out most effectively using rigid soft metal laps that are very flat and contain embedded abrasive particles [13, 15, 17]. Such an arrangement is shown in Fig. 16.2d. A set of laps, containing different particle size abrasive grains, is required, and cross-contamination with other abrasive grain sizes is to be avoided. Brass and tin are favorite lap materials. Grinding and polishing on laps has produced crystal surfaces flat to one-twentieth the wavelength of sodium light or about 250 Å/cm, which corresponds to only one atomic step for about 4×10^5 Pt atoms, measured horizontally [15]. At this level of step density resulting from departures from planarity, the step density owing to misalignment will be the dominant factor, being about 2 orders of magnitude greater for a misalignment of 0.05°. A polishing jig giving an accuracy of 0.02° in the orientation of a silicon single crystal has been reported [23]. A method, involving the observation of a single Bragg reflection with a diffractometer, and employing a crystal holder that can be rotated about its axis, has been described, and the reported accuracy is better than 0.003° [24].

Combined mechanical and electrochemical polishing techniques are often used and a description of one method for polishing copper single crystals and alloys is given in [25] and [26].

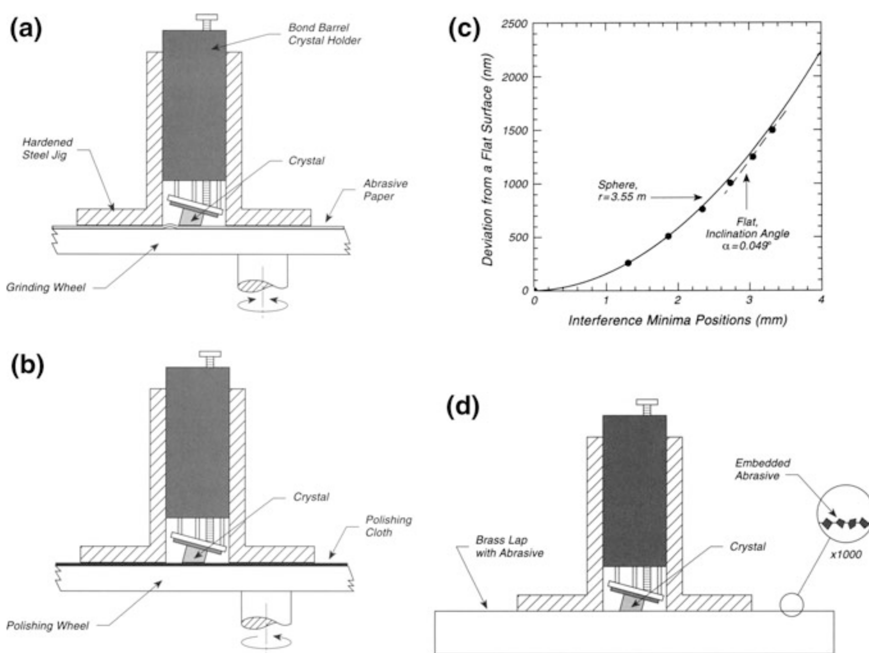

Fig. 16.2 Single crystal orientation, grinding and polishing. **a** Typical crystal grinding. **b** Typical crystal polishing. **c** Measured crystal curvature. **d** Crystal lapping for optimal flatness

A special holder for the grinding polishing jig, shown here, has been developed which allows the device to be used in an automatic grinding-polishing wheel device as is often employed to prepare metallurgical samples [27]. The holder uses ball bearings inside a ring which make contact with the outside of the hardened steel shell which makes contact with the polishing cloth and wheel. This ring-ball bearing apparatus allows the jig to rotate, while applying downward and lateral force which causes the polishing jig to translate and oscillate across the rotating wheel. Using this jig, a spherical surface with 3.4 m radius was generated near the center of the crystal, with surfaces fitting larger radii being produced near the crystal edge.

16.3 A Simple Goniometer for Cutting Single Crystals

A clever method for cutting single crystal boules along any plane involves a goniometer of very simple design, as shown in Fig. 16.3 [28]. Here, a single crystal boule is fastened into a holder with a crystal bond compound, using a plastic screw that will not deform the crystal when tightened against its outer surface. The holder is placed into a special wedge-shaped device with shoulders cut at angle α with respect to the upper surface. This wedge-shaped device can rotate inside a tilted cylinder with an upper surface inclined at angle a with respect to the base of the device. When the two wedges are rotated relative to each other, the tilt angle of the crystal, ω, will change.

The crystal is aligned by Laue back-reflection X-ray diffraction by manipulating the wedged device. A rotation of 180° will result in swinging the crystal axis by a, as shown in Fig. 16.3. Thus, if the saw cuts in a plane parallel to the baseplate of the goniometer, the crystal may be cut at any angle over the range α. An engraved angular scale is provided in two places as shown. The rotations are not simply

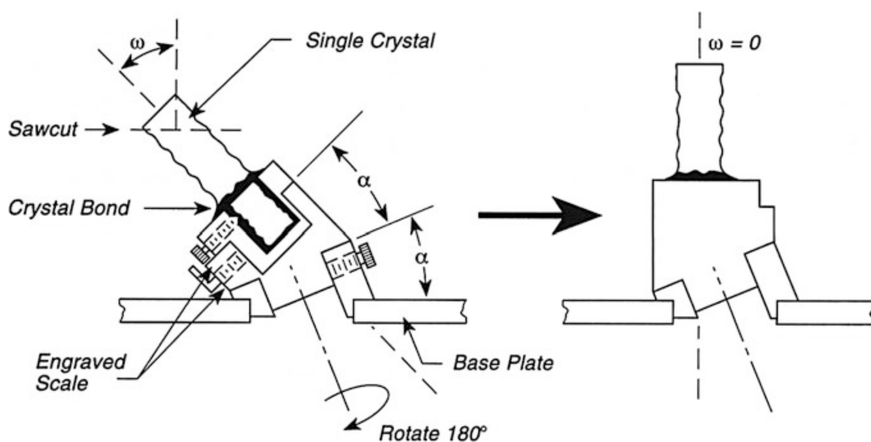

Fig. 16.3 Simple crystal cutting goniometer

related to the angles measured on the Greninger chart, used for X-ray diffraction measurements, but the original paper gives a method to achieve the conversion using a small programmable calculator [28].

16.4 Ion Beam Polishing of Crystals to Subnanometer Roughness

Crystalline substrates can be polished to near atomic perfection by sputtering under glancing incidence conditions [29–31] as shown in Fig. 16.4. If the glancing incidence angle is chosen such that the surface normal component of the incident beam kinetic energy is sufficiently low to ensure that the beam is reflected with unit probability from atomically flat, defect-free terraces, sputtering only occurs at ad-atom and step edge sites [30, 31]. Even at those defect sites, little damage to the subsurface regions appears to occur. The smoothing technique can be combined with annealing of the substrate, either simultaneously or after bombardment. By monitoring the width and peak position of the angular distribution of the scattered ion beam during sputtering, an indication of the surface quality and the change with time is conveniently obtained. A narrow, near specularly scattered beam indicates a low density of defects, on an atomic scale, over the length of the glancing incidence trajectory at least.

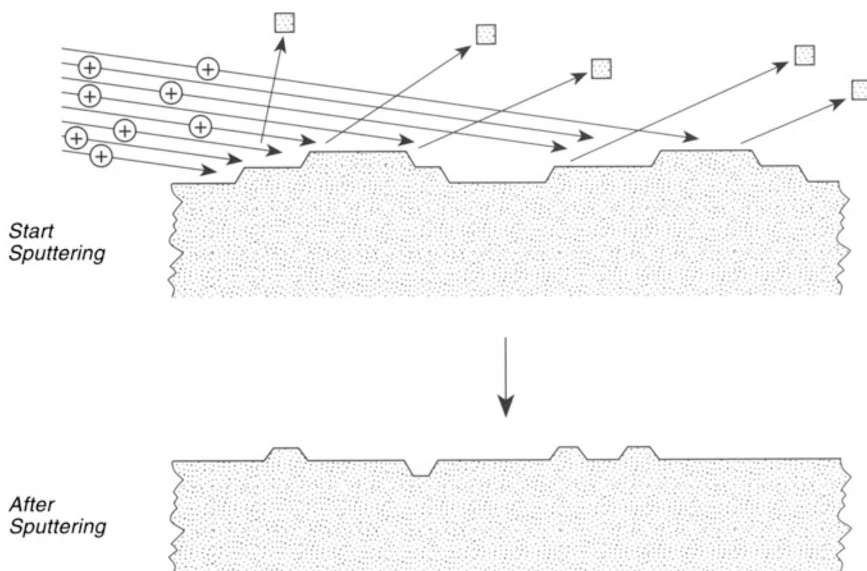

Fig. 16.4 Ion-beam polishing of crystals to subnanometer roughness

16.5 Crystal Optical Alignment

The alignment of highly reflective single crystals by using simple optical methods is commonly employed for the setting of vernier adjustments. In addition to the optical methods, electron beams can also be used for crystal alignment, as shown on pp. 253 and 255.

Figure 16.5a shows a very simple crystal alignment method [32], using only a flashlight in a darkened room. An image of the pupil of the eye is reflected off of the crystal and back into the eye. In addition, the image is also reflected from the window to the eye. When the crystal surface is parallel to the window surface, the two reflected images of the pupil will coincide.

Figure 16.5b shows the same method used outside the vacuum system to align a crystal in its tilt angle so that the normal of the crystal is parallel to the manipulator mounting flange face [32]. The manipulator is held in a carefully made holder that is square. The image of the eye, illuminated by a flashlight filament, is reflected from the crystal and passes back by a pointer. If the center of the image of the pupil is coincident to the pointer when the pointer is translated along the table, then the crystal normal is parallel to the tabletop and therefore to the manipulator reference flange face.

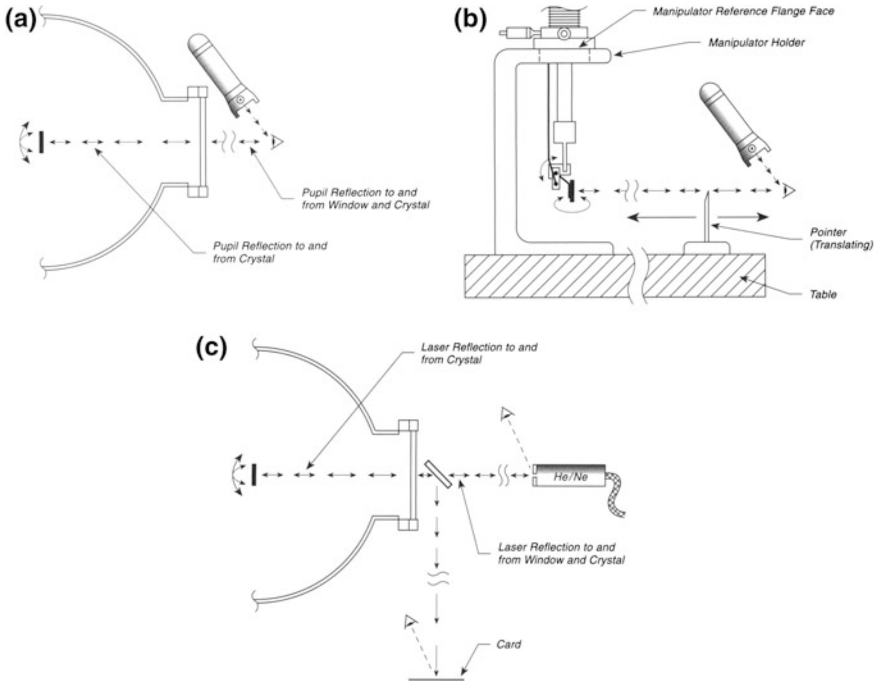

Fig. 16.5 Crystal optical alignment. **a** Crystal alignment by eye. **b** Crystal alignment by eye on table. **c** Crystal alignment by laser

Figure 16.5c shows the use of a He/Ne laser for crystal alignment. The laser is moved until its reflection from the window is aligned so that the laser beam returns to the laser as an aligned beam coincident with the incident beam. The crystal is then manipulated in the vacuum system until the reflection of the laser beam from the crystal is also coincident. In this case, then, the normal to the crystal and the normal to the window will be parallel. The accuracy of the laser alignment procedure will increase as the optical path is increased, and the accuracy of coalignment can easily be made to be 0.1°, or better. A partially reflecting glass slide may be used to deflect a fraction of the two reflected laser beams to a card located off the laser axis. The slight divergence of the laser ultimately limits the accuracy of the alignment procedures.

It should be pointed out that the establishment of laboratory coordinates inside an ultrahigh vacuum system, where reference is made to flange alignments, maybe in error because of machining errors and welding errors made in the fabrication of the chamber, as well as to distortion of the chamber which occurs both on welding and due to the atmospheric pressure.

16.6 Measurement of the Angles of Incidence in a LEED Experiment

It is often necessary to determine the angle of incidence of an electron beam in a low energy electron diffraction (LEED) apparatus relative to the crystal being studied. This can be done qualitatively using settings on the crystal manipulator goniometers or by simple measurements of the LEED beam pattern on the screen. However, for accurate work, it should be possible to use all or almost all of the LEED beam positions to do this with high accuracy, exceeding the accuracy of the average goniometer, which has an uncertain relationship to the crystal connected to it. The method to be described [33] outperforms earlier methods involving the use of an internal graduated circle and vernier [34], laser calibration of the manipulator outside of the vacuum system, or measurement of the 0, 0 beam position using a Faraday cup on a vernier circle.

Figure 16.6 shows a LEED screen with its axial electron gun, and the definition of the laboratory directions, x_l, y_l, and z_l. Similar angles relative to a crystallographic direction on the crystal are given by x_c, y_c, and z_c. The azimuthal angle is Ψ. The polar angle is given by Θ. The angle ε is the measured angle between the 0, 0 beam and an h, k beam.

By examination of a LEED photograph containing multiple LEED beams and making a series of angular measurements using a transparent angular scale made from circular graph paper, it is possible to map out many angles which permit the accurate determination of Θ and Ψ. The computer program for doing this is available from the authors [33], and accuracies of the order of 0.1° are achieved owing to the use of multiple angular measurements.

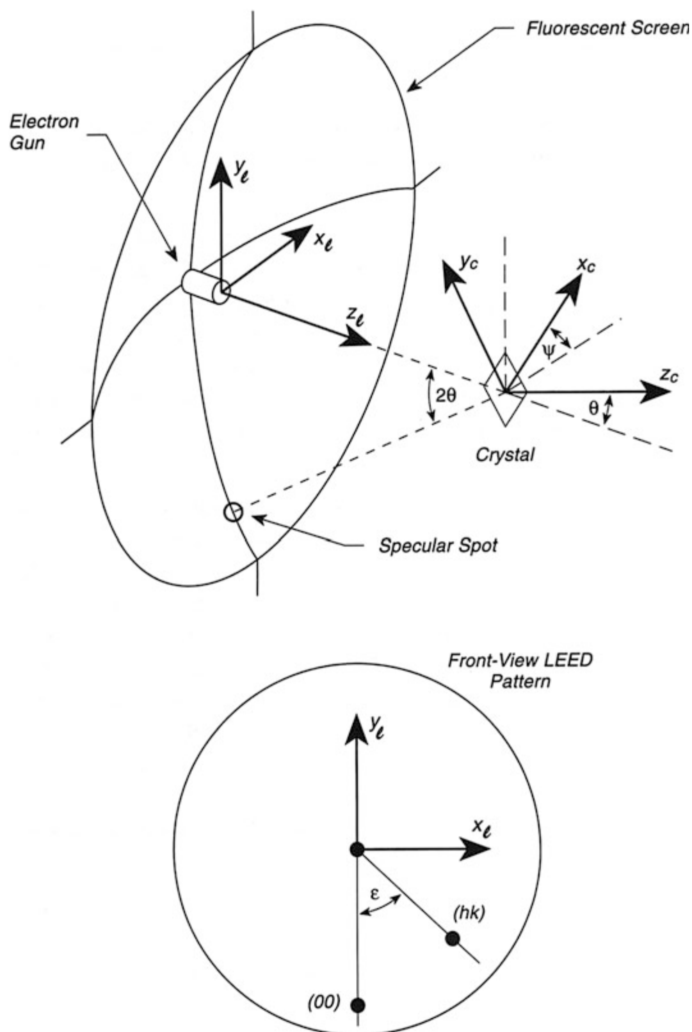

Fig. 16.6 Measuring angle of incidence in LEED

16.7 Measurement of Angle of Incidence of an Electron Beam on a Single Crystal

A simple method for measuring the angle of incidence of an electron beam on a single crystal that involves only the measurement of the collected current is described in Fig. 16.6.

When an electron beam of fixed kinetic energy is received by a single crystal, the reflectivity of the electrons will fall off as the angle of incidence is changed. By

differentiating the collected current with angle, plots that are symmetrical about the normal will be obtained, provided the plane of the angular scan is perpendicular to a mirror plane of the crystal. This behavior is a consequence of the band structure of the crystal, and the more free-electron-like a band is, the higher the electron coupling probability is to this band. Inside the band gap region the reflectivity of electrons with low energies can reach values close to unity.

The apparatus shown in Fig. 16.7a shows the electron gun and the electrical circuit used for differentiating the collected current at the crystal. The measurements

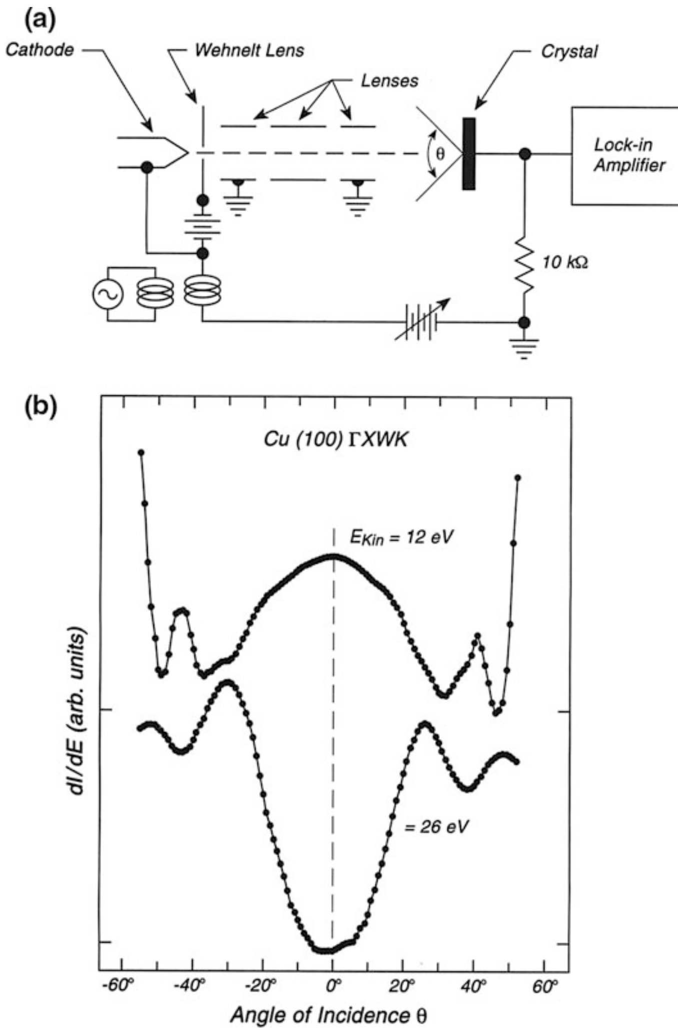

Fig. 16.7 Measuring angle of incidence of electrons. **a** Electron gun + circuit. **b** First derivative—collected current

were taken in the ΓXWK mirror plane of the Cu(100) crystal, perpendicular to another ΓXWK mirror plane. The angle of incidence was varied by rotating the electron gun around the crystal. The data shown in Fig. 16.7b clearly show the symmetry with respect to the normal incidence angle for two electron energies. The symmetry indicates the absence of external magnetic fields and the absence of stray electrical fields. It is estimated that the position of the normal can be estimated to ±0.5°, although the features in the wings differ in their maxima in the two directions by several degrees. The procedure can be used to determine the azimuthal orientation of the crystal by scanning the azimuthal angle. For off-normal angles of incidence, extrema should be observed when crossing a mirror plane of the crystal [35].

References

1. P. Maksymovych, private communication
2. P. Maksymovych, D.C. Sorescu, D. Dougherty, J.T. Yates Jr, J. Phys. Chem. B **109**, 22463 (2005)
3. P. Maksymovych, J.T. Yates Jr, Chem. Phys. Lett. **421**, 473 (2006)
4. P. Maksymovych, J.T. Yates Jr, J. Am. Chem. Soc. **128**, 10642 (2006)
5. P. Maksymovych, D.C. Sorescu, J.T. Yates Jr, Phys. Rev. Lett. **97**, 146103 (2006)
6. P. Maksymovych, D.C. Sorescu, J.T. Yates Jr, J. Phys. Chem. B **110**, 21161 (2006)
7. P. Maksymovych, D. Dougherty, X.-Y. Zhu, J.T. Yates Jr, Phys. Rev. Lett. **99**, 016101 (2007)
8. P. Maksymovych, J.T. Yates Jr, J. Am. Chem. Soc. **130**, 7518 (2008)
9. P. Maksymovych, D. Sorescu, K. Jordan, J.T. Yates Jr, Science **322**, 1664 (2008)
10. P. Masksymovych, O. Voznyy, D. Dougherty, D. Sorescu, J.T. Yates Jr, Prog. Surf. Sci. **85**, 2906 (2010)
11. J.G. Walker II, J. Williams, R.M. Bozorth, Rev. Sci. Instrum. **20**, 947 (1949)
12. W.L. Bond, J. Sci. Instrum. **38**, 63 (1961)
13. G.A. Bennett, R.B. Wilson, J. Sci. Instrum. **43**, 669 (1966)
14. D.E. Johnson, Rev. Sci. Instrum. **39**, 238 (1968)
15. R. Butz, B. Krahl-Urban, K. Mench, Rev. Sci. Instrum. **44**, 485 (1973)
16. J.F. Wendelken, S.P. Withrow, C.A. Foster, Rev. Sci. Instrum. **48**, 1215 (1977)
17. S. Berger, U. Linke, J. Phys. E: Sci. Instrum. **11**, 1097 (1978)
18. U. Linke, B. Poelsema, J. Phys. E: Sci. Instrum. **18**, 26 (1985)
19. Y.K. Chang, Rev. Sci. Instrum. **53**, 515 (1982)
20. Bond Barrel Holders may be purchased from Blake Industries, Inc., 660 Jerusalem Road, Scotch Plains, NJ 07076
21. C.E. Tripa, J.T. Yates Jr, J. Vac. Sci. Technol. **A14**, 2544 (1996)
22. Dr. W.F. Egelhoff, Jr., NIST, Gaithersburg, MD 20899 (private communication)
23. S.I. Mathiesen, L. Gerward, O. Pedersen, Rev. Sci. Instrum. **45**, 278 (1974)
24. M. Deutsch, I. Freund, Rev. Sci. Instrum. **46**, 765 (1975)
25. J.S. Aherarn Jr, J.P. Monaghan Jr, J.W. Mitchell, Rev. Sci. Instrum. **41**, 1853 (1970)
26. T.W. Snouse, Rev. Sci. Instrum. **36**, 866 (1965)
27. P. Maksymovych, T. Gasmire, S. Ohno, J.T. Yates Jr, J. Vac. Sci. Technol. **A23**, 362 (2005)
28. G.L. Price, Rev. Sci. Instrum. **51**, 1000 (1980)
29. Dr. K. J. Snowdon, Department of Physics, University of Newcastle, New Castle upon Tyne, NE 17RU, UK (private communication). The first report of this effect is in U. von Gemmingen and R. Sizmann, Surf. Sci. **114**, 445 (1982)

30. M. Holzwarth, M. Wissing, D.S. Simeonova, S. Tzanev, K.J. Snowdon, and O.I. Yordanov, Surf. Sci. **331-333**, 1093 (1995). Here polycrystalline Cr films were smoothed with a reduction in the rms roughness by a factor of 5 to 8 from 9.2 nm, as measured by the STM
31. M. Wissing, M. Batzill and K. Snowdon, Nanotechnology **8**, 40 (1997). Here, CaF_2 single crystal surfaces were smoothed from an rms roughness of 0.6 nm to better than 0.1 nm (the AFM noise level)
32. Dr. Oliver Schaff, Fritz Haber Institut der Max-Planck Gesellschaft, Faradayweg 4-6, D-14195 Berlin (private communication)
33. S.L. Cunningham, W.H. Weinberg, Rev. Sci. Instrum. **49**, 752 (1978)
34. J.M. Burkstrand, Rev. Sci. Instrum. **44**, 774 (1973)
35. R. Schneider, H. Durr, Th Fauster, V. Dose, J. Vac. Sci. Technol. **A8**, 3363 (1990)

Chapter 17
Tip Fabrication

17.1 Fabrication of Metal Tips Using Zone Electropolishing

Metal tips are required in field electron and field ion microscopy, as well as in scanning tunneling microscopy. One method for preparing such tips is to use zone electropolishing while viewing the process under an optical microscope [1–3].

Figure 17.1 shows the setup employed for both wire samples and for irregular specimens such as thin films stripped from their substrates or slivers of metal cut from a sheet. The electrolyte is held on a loop by surface tension, and its volume can be adjusted upward by transfer from a wet glass rod or downward by absorption by a piece of tissue paper. This loop can be moved laterally using an x, y, z micromanipulator as shown, and the specimen to be electropolished is attached mechanically and conductively to a specimen holder. For a wire specimen, selected regions of the tip may be electropolished by lateral motion of the loop to the desired region as shown in Fig. 17.1, inset A. Very sharp tips may be produced by first electropolishing a neck behind the tip apex and then reducing the necked-down region to a sharp point in an electrolyte film of about 0.2-mm thickness. Additional sharpening can be achieved by quick thrusts of the electrolyte film onto and away from the tip.

Irregular specimens can be shaped as shown in Fig. 17.1, inset B. Here, working on the sides of the sample, etching is achieved to bring the sample to a tip shape prior to sharpening the tip as shown in Fig. 17.1, inset A.

Either AC or DC electropolishing can be used. In addition, instead of using a micromanipulator, the lateral stage motion of the specimen holder or the stage of the microscope can be used with the sample being held rigidly in place.

The microscope magnification is either ×150 or ×600 with a long working distance objective. Note the protective coverglass for the objective to prevent etching of the glass lens by droplets of electrolyte produced during electropolishing.

© Springer International Publishing Switzerland 2015

J.T. Yates Jr., *Experimental Innovations in Surface Science*,
DOI 10.1007/978-3-319-17668-0_17

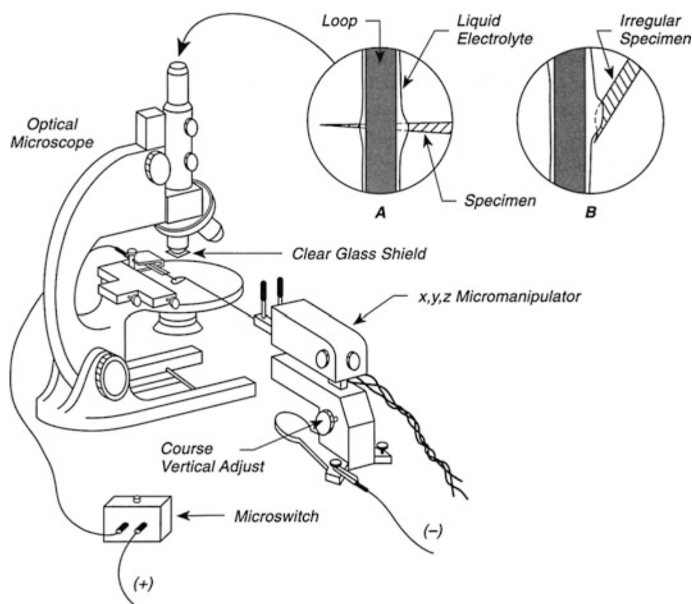

Fig. 17.1 Etching Field Ion Microscopy Tips

Special considerations in tip construction apply for tips to be used under electrolytes, where Faradaic currents may damage the tip. This damage problem may be eliminated by the use of Apiezon wax to shield the tip shank [4].

An excellent review on methods for sharpening STM tips is given in [5].

The use of AC waveform control in shaping tips for field ion microscopy has been described [6, 7]. Electrochemical etching of Ag tips has recently been described, using electronic control of the tip movement out of the electrolyte [8, 9].

A review comparing the instrumental characteristics of various STM [10].

17.2 Etching STM Tips Reproducibly

A simple apparatus [11] for making a number of STM tips while automatically replenishing the electrolyte is shown in Fig. 17.2. Section (a) shows a three-hole electrolyte support in which thin films of the electrolyte are held by surface tension effects. The central hole of 3-mm diameter is connected to smaller 2-mm diameter supply and withdrawal reservoirs in a 1-mm-thick Cu plate. Section (b) shows the beveled end of a (1-mm outside diameter, 0.45-mm inside diameter) supply tube for fresh electrolyte being fed into the supply reservoir. A similar tube is used to withdraw electrolyte from the other reservoir. The wire to be etched enters the

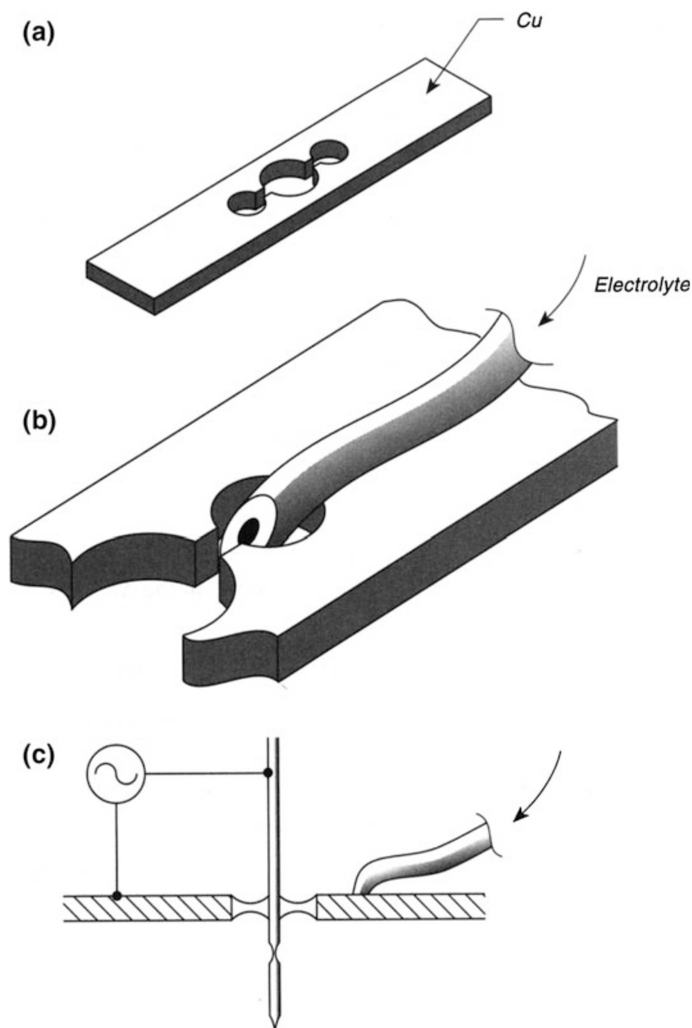

Fig. 17.2 Etching STM Tips Reproducibly

central hole, and projects below the bottom of the electrolyte film. This permits the etched tip to fall away under gravity when the etching is complete, and it is believed that as the lower tip falls away the local strain is likely to produce an atomic asperity [12] for STM imaging. Section (c) shows the application of AC current to the etching apparatus, and the profile of a tip just being started. The thin neck below the desired tip location is useful for making a detachable handle with which to hold the tip, and which can be broken off later.

The flow rate of electrolyte and the configuration of the meniscus can be adjusted by changing the level of electrolyte storage beakers on labjack platforms

that connect to the supply and withdrawal reservoirs. Tubing 30 cm in length is approximately correct. For an electrolyte solution of KOH(aq), 4 wt%, a flow rate of about 1 ml/h is correct for an etching current of 20 mA. A slightly concave upper and lower surface in the etching cell is preferable, achieved by fine height adjustments of the two beakers. Tips have had a wire diameter as small as 0.08 mm. Many tips can be produced in succession by this method. It is helpful to use a wax pencil to outline the three-hole device on both sides to prevent wetting and electrolyte creep across the horizontal surfaces. Another design for tip etching is shown on page 258 as well as others in [12, 13]. The use of Apiezon wax for protection of tip shanks used in electrolytes from Faradaic current effects is discussed in [13]. A general review of the performance of various STM instruments is given in [14], and a review of tip-making for field ion microscopy tips is given in [15]. An Auger spectroscopy study of the surface composition of etched tungsten tips is given in [16]. It was found that a 10-nm layer of tungsten oxide is mostly removed by heating to about 1800 K. The tungsten oxide film from an electrochemically etched W tip can also be removed by treatment in concentrated HF(aq) [17].

17.3 STM Tip Flasher

An Omicron STM tip carrier has been converted to a thermal tip flasher. In the design shown in Fig. 17.3, a Ta sheet, 0.125 mm thick, is fabricated with a key hole slot. This sheet, mounted by three holes which correspond in position to the holes in the tip carrier body, is electrically isolated from the supporting bolts by use of concentric ceramic tubes. The sheet is slightly bent as shown to be able to make contact with the tip at some point when the tip is magnetically attracted to a permanent magnet. Current is passed between the Ta sheet and the bottom of the carrier. Nominal flashing conditions are: 7 A × 3.5 V for 10 s, and outgassing causing $<5 \times 10^{-10}$ mbar pressure rise is reported [18]. A similar device was recently described [19].

17.4 Reverse Bias Method for Sharp Tip Etching

Many methods have been devised for making sharp tungsten tips for STM and other applications, and some of these are described in Sects. 17.1–17.3. It has been discovered that tip blunting can occur during the last stages of tip etching [20]. The method described here eliminates this blunting effect by control of the electrochemical potential during the moments just after tip separation in the etching solution.

Figure 17.4a shows a typical etching apparatus for making tungsten tips. Using 2 M KOH (aq) as electrolyte, suspended in a lens shaped droplet in an Ir loop, the

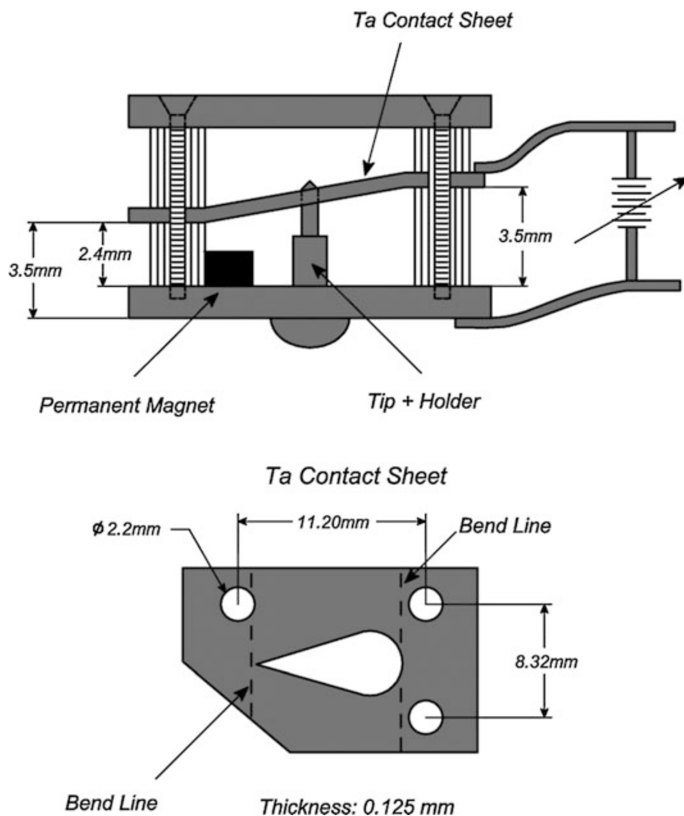

Fig. 17.3 STM Tip Flasher outgassing, tip flasher

tip is roughly etched to a point where the thinning of the neck is readily visible. The etching is then continued more slowly in a fine etching process with 0.1 M KOH (aq) solution until gravity separates the parts. At this point the etching potential is changed from V_1 to V_2 as shown in Fig. 17.4b. If the power supply is a normal dc supply, the applied potential can be dropped to zero at the moment of separation, but it has been observed that there is still a natural electrical potential which exists between the surface and the tip and the Ir ring, of order 0.5 V, and that charge will still flow at currents in the 10^{-7}–10^{-8} A range. This natural current causes blunting of the tip. Using a power supply designed to apply the reverse potential from that used for V_1, the blunting effect can be eliminated. The reverse bias is applied within 500 ns of the separation time by electronic detection of the moment of separation which triggers the application of the reverse bias. Figure 17.4c shows the measured tip radii versus post etching time at the natural potential compared to experiments where V_2 is applied as a reverse bias, eliminating etching. Figure 17.4d shows an electron micrograph of a tip etched with the reverse bias method, where a 4 nm radius is achieved. The blunting is thought to be due to the recession of the tip,

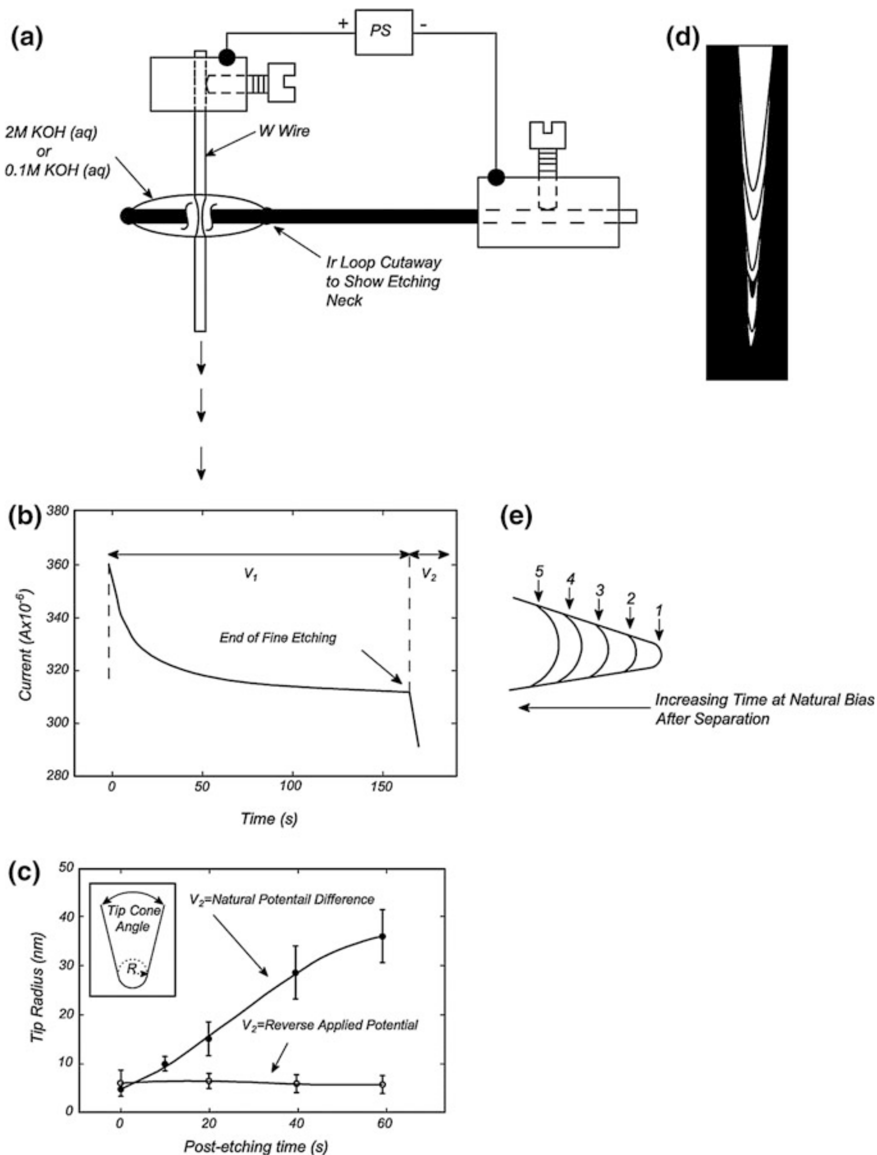

Fig. 17.4 Reverse bias method for sharp tip etching. **a** STM tip machine. **b** Current versus time during etching **c**. Tip radius versus post-etching time. **d** STM tip etching to r < 4 nm by Reverse Bias Technique. **e** Tip configuration if reverse bias is not used

during the post-separation etching, and the radius will be dependent on the cone angle achieved. A schematic of the blunting is shown for times increasing from 1 to 5 in Fig. 17.4e after the separation.

17.5 Sharpening Single Crystal Metal Tips by Ion Bombardment

Both tungsten and molybdenum single crystal wires can be sharpened into tips by using axial sputtering. The data shown here are for Mo(110) tips [21], but similar results are reported for W(111)-oriented wires [22], except in that work the ion beam direction was from behind the tip, producing very sharp pyramidal shapes.

The Mo(l10) crystal wire is mounted such that the axis of the wire is parallel to the ion beam, as shown in Fig. 17.5a. In addition, because of variation in ion current density across the ion beam, the tip should be centered in the beam to achieve symmetrical sputter etching. The ion beam in this case is 350 μm in diameter. It is found that Xe^+ ions are more effective in making less roughened tips; Ar^+ at low kinetic energies can produce very sharp asperities also. High-energy Ar^+ sputtering produces increased surface roughness compared to Xe^+.

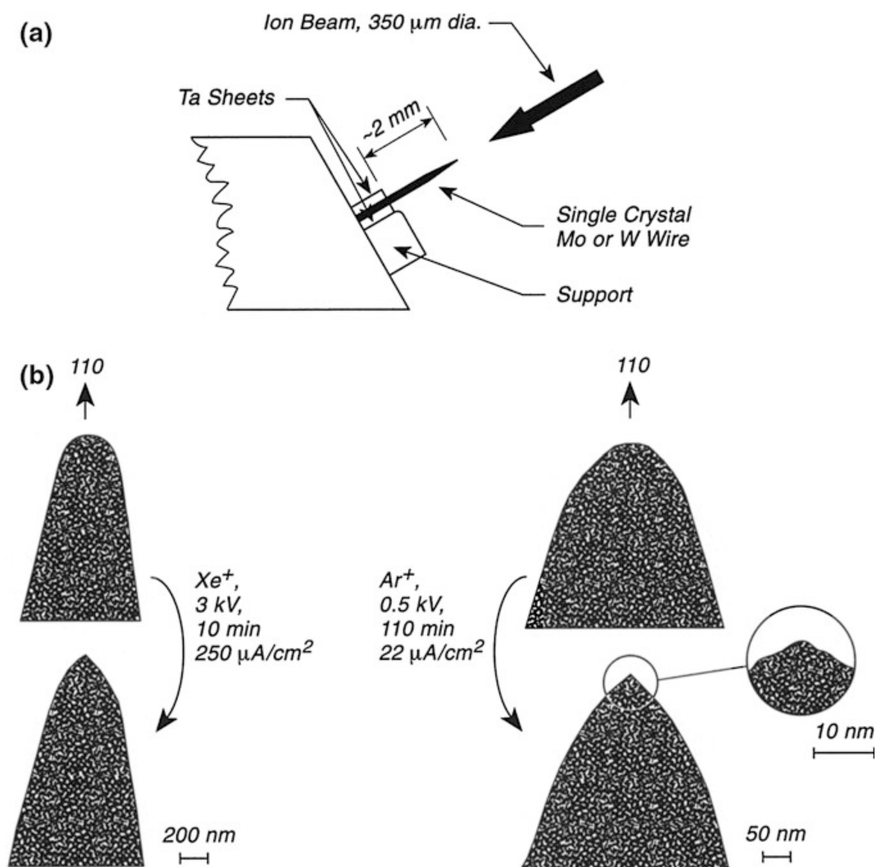

Fig. 17.5 Sharpening tips by ion bombardment. **a** Apparatus. **b** Tip profiles by TEM

The profiles of tips produced both by 3 kV Xe^+ and 0.5 kV Ar^+ sputtering are shown in Fig. 17.5b. It is estimated that the central asperity on the Ar^+ sputtered tip has a base diameter of about 10 Å.

Ion sputtering for sharpening field electron and field ion tips has been described [22, 23].

Polycrystalline wires cannot be shaped so well by this technique because of the presence of grain boundaries from which preferential sputter etching occurs [23]. However, single crystal tungsten tips have been ion milled to a point that is sharp on the atomic scale [24, 25].

A recent example of the use of a focused ion beam of Ga^+ ions for ion milling W and Pt/Ir tips is given in [26], which also summarizes much other work in this area.

Copper wires of 30–50 μm diameter have been ion etched into sharp tips, and the dynamics of the process have been studied [27].

References

1. A.J. Melmed and J.J. Carroll, J. Vac. Sci. Technol. **A2**, 1388 (1984)
2. A.J. Melmed, J. Vac. Sci. Technol. **B9**, 601 (1991)
3. H. Lemke, T. Goddenhenrich, H.P. Bochem, U. Hartmann, C. Heiden, Rev. Sci. Instrum. **61**, 2538 (1990)
4. L.A. Nagahara, T. Thundat, S.M. Lindsay, Rev. Sci. Instrum. **60**, 3128 (1989)
5. M. Fotino, Rev. Sci. Instrum. **65**, 159 (1993)
6. H. Morikawa, K. Goto, Rev. Sci. Instrum. **59**, 2195 (1988)
7. H. Bourque, R.M. Leblanc, Rev. Sci. Instrum. **66**, 2695 (1995)
8. K. Dickmann, F. Demming, J. Jersch, Rev. Sci. Instrum. **67**, 845 (1996)
9. A.A. Gorbunov, B. Wolf, Rev. Sci. Instrum. **64**, 2393 (1993)
10. Y. Kuk, P.J. Silverman, Rev. Sci. Instrum. **60**, 165 (1989)
11. J.O. Fiering, F.M. Ellis, Rev. Sci. Instrum. **61**, 3911 (1990)
12. P.J. Bryant, H.S. Kim, Y.C. Zheng, R. Yang, Rev. Sci. Instrum. **58**, 1115 (1987)
13. L.A. Nagahara, T. Thundat, S.M. Lindsay, Rev. Sci. Instrum. **60**, 3128 (1989)
14. Y. Kuk, P.J. Silverman, Rev. Sci. Instrum. **60**, 165 (1989)
15. E.W. Muller, T.T. Tsong, *Field Ion Microscopy* (Elsevier, New York, 1969)
16. A. Cricenti, E. Paparazzo, M.A. Scarselli, L. Moretto, G. Selci, Rev. Sci. Instrum. **65**, 1558 (1994)
17. L.A. Hockett, S.E. Creager, Rev. Sci. Instrum. **64**, 263 (1993)
18. B. Unal, A. Belianinov and P.A. Thiel, Private Communication
19. F. Bastiman, A.G. Cullis, M. Hopkinson, K.J. Briston, J. Vac. Sci. Technol. **B28**, 371 (2010)
20. O. Guise, J.W. Ahner, M.-C. Jung, P.C. Goughnour, J.T. Yates Jr, Nano Lett. **2**, 191 (2002)
21. S. Morishita, F. Okuyama, J. Vac. Sci. Technol. **A9**, 167 (1991)
22. J.M. Walls, H.N. Southworth, G.J. Rushton, Vacuum **24**, 475 (1974)
23. J.A. Kubby, B.M. Siegel, J. Vac. Sci. Technol. **B4**, 120 (1986)
24. D.K. Biegelsen, F.A. Ponce, and J.C. Tramontane Appl. Phys. Lett. **54**, 1223 (1989)
25. D.K. Biegelsen, F.A. Ponce, J.C. Tramontna, S.M. Koch, Appl. Phys. Lett. **50**, 696 (1987)
26. M.J. Vasile, D.A. Grigg, J.E. Griffith, EA. Fitzgerald, and RE. Russell, Rev. Sci. Instrum. **62**, 2167 (1992)
27. H. Hasuyama, Y. Kanda, T. Soeda, K. Niiya, M. Kimura, Matls. Sci. and Engr. **90**, 33 (1987)

Chapter 18
Spot-Welding

18.1 Spot-Welding Difficult Junctions

Many metal/metal junctions to be spot-welded are difficult to fabricate as a result of failure to understand the nature of the spot-welding process. A spot-weld is made when an electrical spark causes two surfaces in contact to fuse together as a result of the high local heating. Ideally, the surfaces to be welded should make only a point contact in order to focus the local heating at a single point. Thus, as shown in Fig. 18.1a, two cylindrical wires, placed orthogonally to each other, will theoretically contact each other only at one point, leading to efficient welding. In contrast, two wires oriented parallel to each other will contact along a line, making a broad contact and leading to a weak weld.

Figure 18.1b shows a way to weld a thermocouple or other wire to a metal single crystal. The crystal is placed on a rigid, clean, smooth surface that is a nonconductor. A single spot welding electrode presses the wire against the back of the crystal, and a second electrode also presses on the back of the crystal to make electrical continuity.

Often it is found that the welding leads stick to the weld when it is completed. This may be due to welding electrodes that have not been smoothed with emery paper before welding, or the application of too much power to make the weld. Sometimes sticking may be prevented by coating the welding electrode with carbon black from a match or candle flame, as shown in Fig. 18.1c.

Oxidation during the spot weld is often a problem owing to local heating. This may be prevented by welding under a droplet of methanol (Fig. 18.1d), which acts as a shield from the air and is also a reducing agent in the presence of the hot metal at the weld point.

In cases where a good weld is difficult to make, a sandwich weld is sometimes used as an intermediate material between two refractory metals. Tantalum and platinum foil are often good for this, as shown in Fig. 18.1e [1]. It is also reported

© Springer International Publishing Switzerland 2015

J.T. Yates Jr., *Experimental Innovations in Surface Science*,
DOI 10.1007/978-3-319-17668-0_18

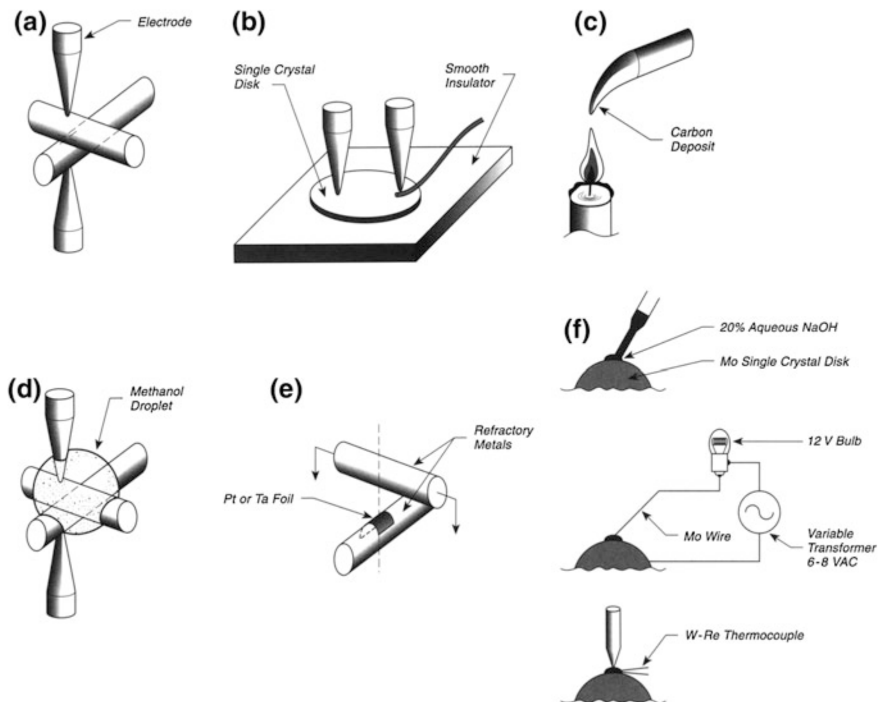

Fig. 18.1 Spot-welding difficult junctions. **a** Point contact weld. **b** Welding to single crystal. **c** Preventing electrode sticking. **d** Welding under methanol. **e** Sandwich weld between refractory metals. **f** In situ electropolishing+welding

that changing the welding tip polarity sometimes helps in making a difficult weld, although the reasons for this are not understood [2].

It is very important to only try to weld metals when the surfaces have been freshly cleaned. Thus, W and Mo are cleaned by electropolishing in NaOH(aq) solution, about 1 M in concentration. The surface to be welded is positive during electropolishing, or in some cases AC electropolishing may be used.

Figure 18.1f shows a clever way to electropolish the metal and then to use the elec-tropolish solution as a protective boundary from air oxidation. Here, a Mo single crystal is to be welded to a Mo wire at the crystal edge. The NaOH(aq) solution in a droplet is placed on the crystal, and electropolishing of the edge is carried out using a Mo wire electrode in series with a light bulb and a transformer. The light bulb supplies a protective load if a short circuit to the crystal occurs. Once the electropolishing is complete, the droplet of solution is left in place, and the spot-weld of a We/Re thermocouple in this case is made under the electrolyte [3]. After spot-welding, the droplet of electrolyte is pipetted away, and the assembly is washed well with distilled water. It was noted that lower power was needed to make effective spot-welds in this manner [3].

It is important to make many practice spot-welds before assembling the desired object. With practice, a careful welder can make ten successful practice welds in series, therefore almost guaranteeing that the eleventh will be good. Adjustments of the power per weld, the pressure used at the weld, and the composition of the welding tips must be made to achieve a good weld. Once the proper conditions are found, a single weld is all that is needed, and in fact multiple welds at the same point can result in metal work hardening and weakening and should be avoided. Metals with very high thermal conductivity (Al, Ag, Cu) are difficult to weld, and slotted crystals of those metals are often used where the slot accommodates a refractory heating/support wire [4]. It is reported that a Pt sandwich will facilitate refractory metal spot-welds to Cu [2].

References

1. D.C. Carlyle, Rev. Sci. Instrum. **41**, 599 (1970)
2. W.R Egelhoff, Jr., National Institute of Standards and Technology, Gaithersburg, MD 20899-0001 (private communication)
3. M.E. Jones, B.E. Koel, R.T. Weppner, Rev. Sci. Instrum. **60**, 3067 (1989)
4. J.E. Crowell, J.G. Chen, J.T. Yates Jr, Surf. Sci. **165**, 37 (1986)

Chapter 19
Mechanical Procedures

19.1 Stretching Thin Metal Foils to a Wrinkle-Free Condition

In some cases, the provision of wrinkle-free metal foil for windows may be needed. A very simple method, related to the differential thermal expansion of metal and Pyrex glass, may be employed to achieve this objective [1].

Figure 19.1a shows a short cylinder of fused quartz or Pyrex glass ground flat on its end, mounted on top of the wavy foil. The thin foil is supported on its bottom by a horizontal substrate such as a lapped flat plate of aluminum, coated with a fluorocarbon dry lubricant [2]. The foil is attached to the plate at the edges with an adhesive tape to prevent curling. An epoxy adhesive (Torr seal [3]) is applied to the lower edge of the glass tube and the tube is placed on the wrinkled foil. The assembly is heated in an oven for several hours at about 60 °C, and then allowed to slowly cool in the oven overnight. When the assembly is heated, the areal expansion of the metal foil exceeds that of the glass cylinder due to the thermal expansion coefficient differences. The light weight glass cylinder does not impede the foil expansion, and wrinkling does not occur in the center of the glass form. Upon cooling, the foil contracts more than the glass, resulting in a uniformly stretched foil as shown in Fig. 19.1b. This technique can be used for stretching foil over an aperture that cannot be heated; the glass form is larger than the aperture, and the aperture is attached by cement to the foil, previously stretched as shown. A simple consideration of the strain effects in the circumferential and the radial directions indicates that for the circular geometry of the glass cylinder, the strain in both directions is equal, meaning that no shear stress takes place on cooling. This leads to a uniform tension and a flattening of the foil [1]. HAVAR foil (0.005 mm thick) [4], aluminum foil (0.025 mm thick) and Mylar foil (0.025 mm thick) have all been stretched flat in this manner.

© Springer International Publishing Switzerland 2015

J.T. Yates Jr., *Experimental Innovations in Surface Science*,
DOI 10.1007/978-3-319-17668-0_19

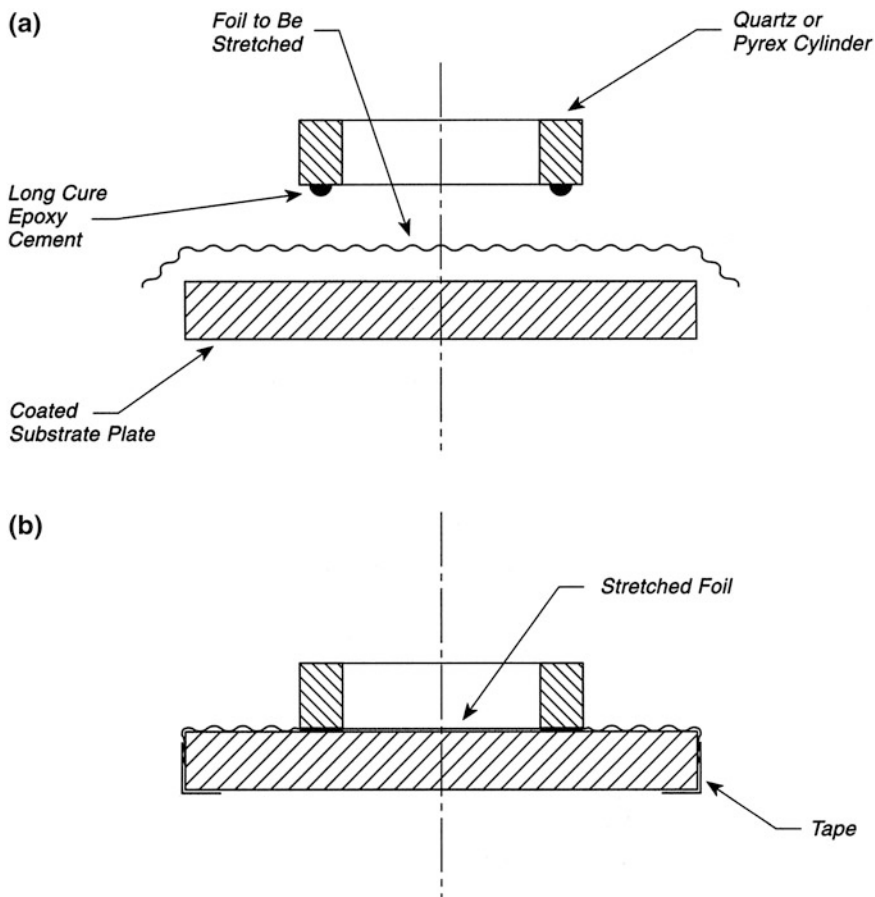

Fig. 19.1 Stretching metal foils. **a** Before assembly. **b** After cure and cooling

19.2 Making Micron-Size Holes for Supersonic Nozzles

Two methods are outlined for producing micron-sized holes in the ends of tubes to be used as supersonic jet sources in vacuum [5].

19.2.1 Method I—Fig. 19.2a

A tube of the appropriate length and inner and outer diameter is made with only one end open. An inner rod, which fits into the tube, is made with its length just slightly longer than the inside dimension of the tube. This rod is sharpened on one end, and

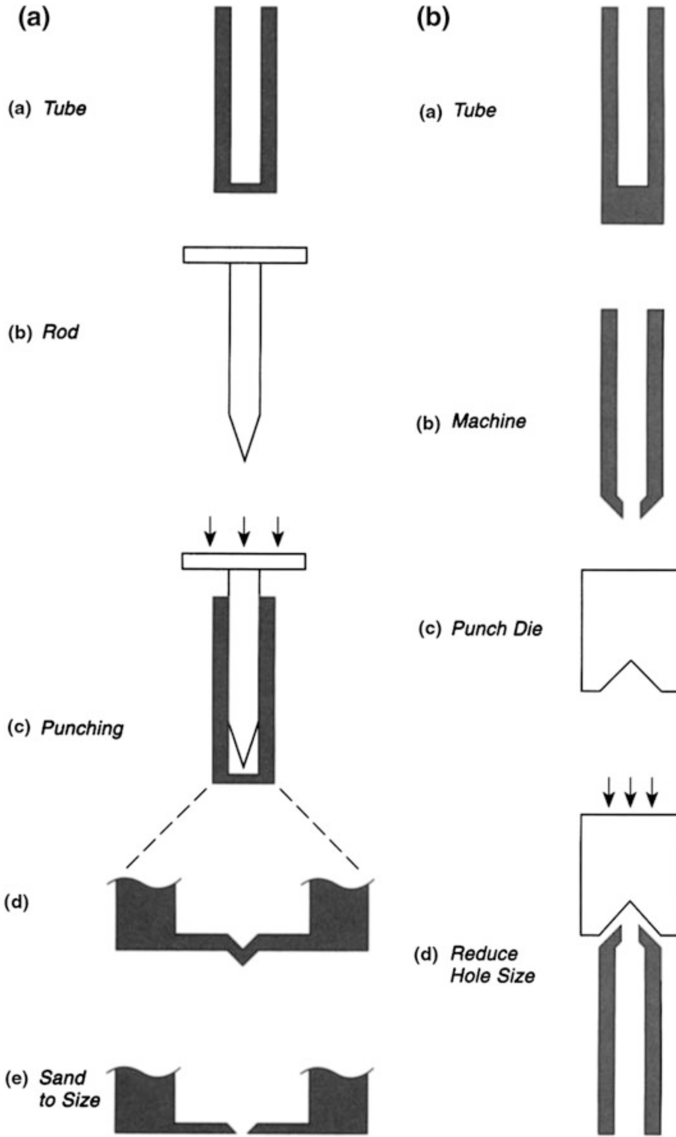

Fig. 19.2 Making micron-size holes for supersonic nozzles. **a** Method I. **b** Method II

a cap is machined on its upper end. By varying the cone angle of the sharpened tip, the hole size can be controlled. The sharpened rod is then punched with a hammer until the cap is tightly in contact with the upper tube edge. This should produce a cone-shaped indentation in the end of the tube as shown. The outer surface of the tube is then sanded down carefully until a hole just begins to appear. A microscope is used to judge the hole size using both reflected and transmitted light [6].

19.2.2 Method II—Fig. 19.2b

A tube of the appropriate length and inner and outer diameter is made with only one end open. The closed end is cut down with a conical surface on a lathe until a tiny hole appears on the end. A punch die with the same cone angle as the tube end is made. The punch die is then hammered on top of the tube end to close down the hole until the desired size is obtained. A microscope is used to monitor the changes in the hole size using both reflected and transmitted light [7].

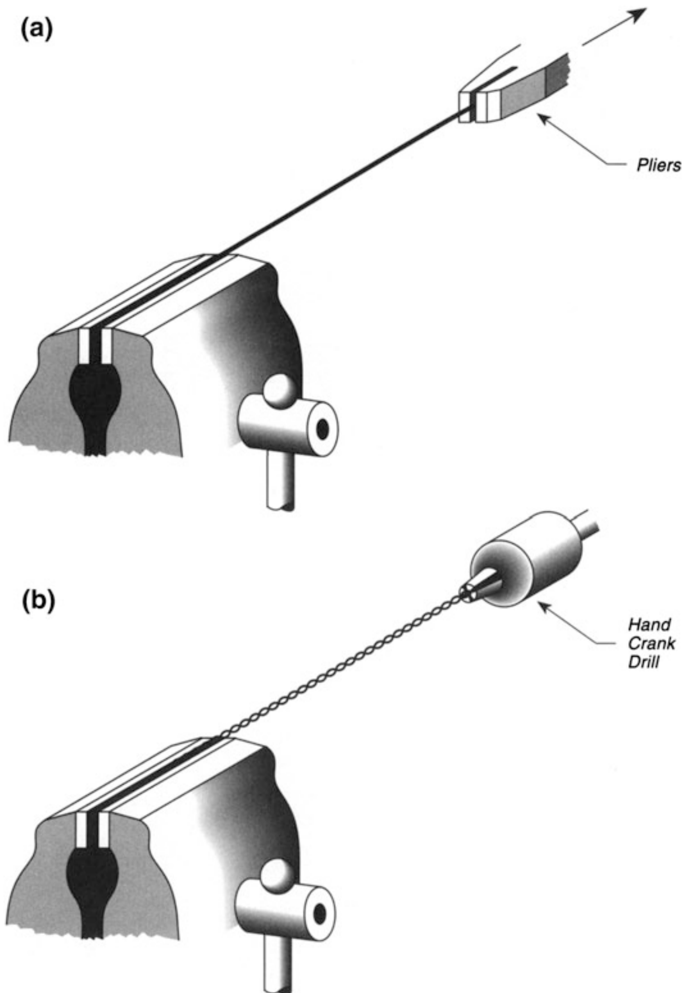

Fig. 19.3 Straightening and braiding wires. **a** Stretching a wire to straighten. **b** Making uniform braided wire

19.3 Straightening and Braiding Wires

It is often advisable to work with very straight segments of wire, for example, in placing wires along the outside of a manipulator shaft (see p. 67), where bends might interfere with the linear construction or where a tight fit through tubulations is needed. Figure 19.3a shows a method which works for nonrefractory metal wires such as-Cu, Ni, Ag, and stainless steel [8]. The end of the wire is rigidly clamped in a vise, and with a pair of pliers, the wire is stretched only a fraction of a percent. The elastic limit should not be exceeded, and one can feel the give in the wire as stretching occurs below the elastic limit. It is wise to have prepared a place to store the straightened wire and a storage tube is recommended for this. After straightening, many wires become work hardened so that further straightening by this method will not work unless the wire is annealed.

Thin refractory wire will not straighten by this method, and another method must be used [8]. Lay the wire on a paper tablet and stroke the wire with a round tool at right angles to the wire axis, keeping the arch upward by rotating the wire during straightening. A pair of smooth jaw pliers will hold the wire in the desired position. Work on only a few inches at a time.

Braided wire may be conveniently produced in a uniform bundle by placing the wires together and holding one end in a vise. A hand-cranked drill is chucked to the other end of the wire bundle and turned slowly to make a uniform braid, as shown in Fig. 19.3b.

References

1. W.H. Holt, C.M. Blackmon, Rev. Sci. Instrum. **51**, 671 (1980)
2. Obtained from Miller-Stephenson Chemical Co., Inc., George Washington Highway, Danbury, CT 06810
3. Obtained from Varian Vacuum Products, 121 Hartwell Avenue, Lexington, MA 02173
4. Obtained from Hamilton Technology, Inc., 101 N. Queen Street, P.O. Box 4787, Lancaster, PA 17604
5. Professor Thomas Engel, Department of Chemistry, Box 351700, University of Washington, Seattle, WA 98195-1700 (private communication). The ideas are not original from the Engel group and are believed to originate from Dr. Adi Scheidemann, from Peter Toennies' group, Göttingen University, Göttingen, Germany
6. From Steve Moskovits, T. Engel group, University of Washington
7. From B. Holm, machinist, University of Washington
8. G.L. Fowler, 6816 Kelly Ave., N.E., Albuquerque, NM 87109 (private communication)

Part III
Measurement Methods

Chapter 20
Electrons

20.1 Electron Gun Design and Behavior

Many descriptions of the design and properties of electron guns are presented in the literature [1–5] and it is not the purpose of this treatment to summarize this practically important field. Instead, an ordinary electron gun [6] is described to give the reader a beginning picture of this technology [7].

Figure 20.1a shows a drawing of the arrangement of elements in an electron gun like those used in LEED and other surface science probes. It consists of a thermionic emitter filament or ribbon, usually coated with a material that lowers the work function, yielding higher operating currents at lower filament temperatures. For this directly heated tungsten cathode, either thoriated tungsten, or ThO_2, or LaB_6 coatings can be used, as discussed on pp. 206 and 210. Some electron guns, such as the widely used Varian Model 981-2125, have the thermionic emitter mounted off axis to avoid line-of-sight exposure to the crystal reducing the possibility of contamination as well as reducing light output. The thermionic cathode is housed in a Wehnelt cylinder that surrounds it except for the beam extraction aperture. The Wehnelt cylinder can be biased either positively or negatively, and is usually kept near the potential of the cathode. This may be done by placing a resistor between the cathode and the Wehnelt, which results in self-biasing of the Wehnelt; a typical value of 570 kΩ will produce a small negative bias of the cylinder relative to the cathode and will maintain beam focus over a several hundred volt range. The electron beam is extracted by the first lens, G_1, which then focuses the initially divergent beam. This lens forms an image of either the emitter or the aperture of the Wehnelt cylinder, depending on geometrical factors and the potentials applied. The focal length is of the order of 10–30 cm. The drift tube, the lens G_3, and the exit aperture form an Einzel lens that focuses the beam. The beam diameter is typically about 1 mm, and this can be reduced by decreasing the first two aperture sizes (0.4-mm apertures in guns working at 100 eV energy typically deliver 1 μA current). For 0.1-μA beam currents, a minimum beam size of 0.2 mm and a divergence

© Springer International Publishing Switzerland 2015

J.T. Yates Jr., *Experimental Innovations in Surface Science*,
DOI 10.1007/978-3-319-17668-0_20

of 0.2° are possible. Changing the bias on the Wehnelt cylinder with respect to the cathode drastically affects the beam current and its stability.

Figure 20.1b shows an experimental plot of the electron beam width for the electron gun in Fig. 20.1a, c shows the beam divergence versus electron energy. These properties were measured with the multiple Faraday cup assembly and procedure shown on p. 198.

Modeling of the behavior of an electron gun with cylindrical symmetry such as this one can be carried out using an electrostatic computer program that is readily available [8].

High-quality electron guns for high-resolution LEED measurements have been described and often involve field emission electron sources [9, 10].

A high-resolution low-energy electron source involving a pair of 127° cylindrical selectors and delivering 3×10^{-8} A with 30-meV resolution has been described [11].

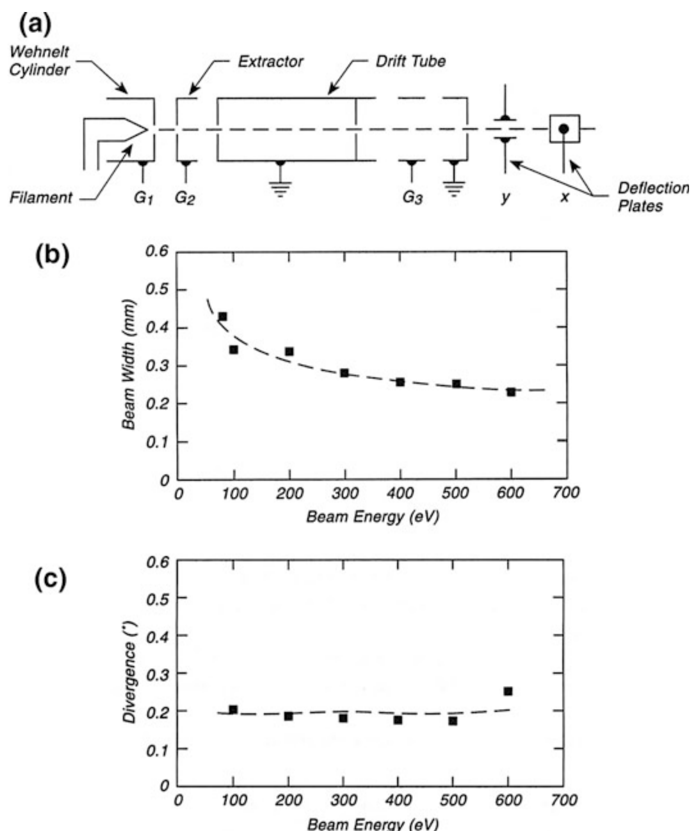

Fig. 20.1 Electron gun properties. **a** Ordinary electron gun. **b** Beam width. **c** Beam divergence

A simple technique for precise regulation of the emission current from an electron gun has been published. It uses the returning ground current which is matched to a reference current. The difference is optically coupled to control the filament to Wehnelt cylinder potential allowing beam currents of 0.1 μA to be regulated to 1 % [12].

A pulsed electron gun with picosecond pulses has recently been described. The pulse is generated by a pulsed laser that produces photoemitted electrons [13].

20.2 Low-Energy Electron Gun for Broad-Beam Irradiation

Electron sources for irradiation of cm^2 area surfaces often employ stray electrons that originate from thermionic emitters in mass spectrometers and ionization gauges, or from bare filaments some distance from the target. While this is often satisfactory, without adequate modeling of the distribution of electrons originating from these sources, one may be dealing with non-uniform current densities on the surface being irradiated. Extended electron beams are employed in cases where surface analysis over a broad target area is to be done following damage to the surface by electron bombardment.

A simple electron gun [14] designed to give a uniform current density across an extended surface is shown in Fig. 20.2a. The gun contains a thoriated tungsten filament (0.019-cm diameter) (see p. 206) which is hidden from line-of-sight to the target by an L-shaped shield. Electrons are accelerated through a mesh grid (80 % transparency) and then decelerated on the way to the target. The SIMION electrostatic lens and analysis program [15] was used to model the behavior of the electron gun as a function of various potentials, and Fig. 20.2b shows some electron trajectories calculated for various electron energies. A fairly uniform flux in the vertical plane is observed for electron energies above 2 eV.

Because of end effects on the thoriated emitter [16], to achieve a uniform current density laterally, it would be wise to employ a gun width that is perhaps two times larger than the target width, as was done here.

The current collected by the mesh grid and the target is shown in Fig. 20.2c. Currents at the crystal in the 2–20 μA range are measured for electron energies in the 2–31 eV range. Even at the lowest electron energies, about 1 in 5 electrons emitted are collected by the target for mesh potentials above 10 V.

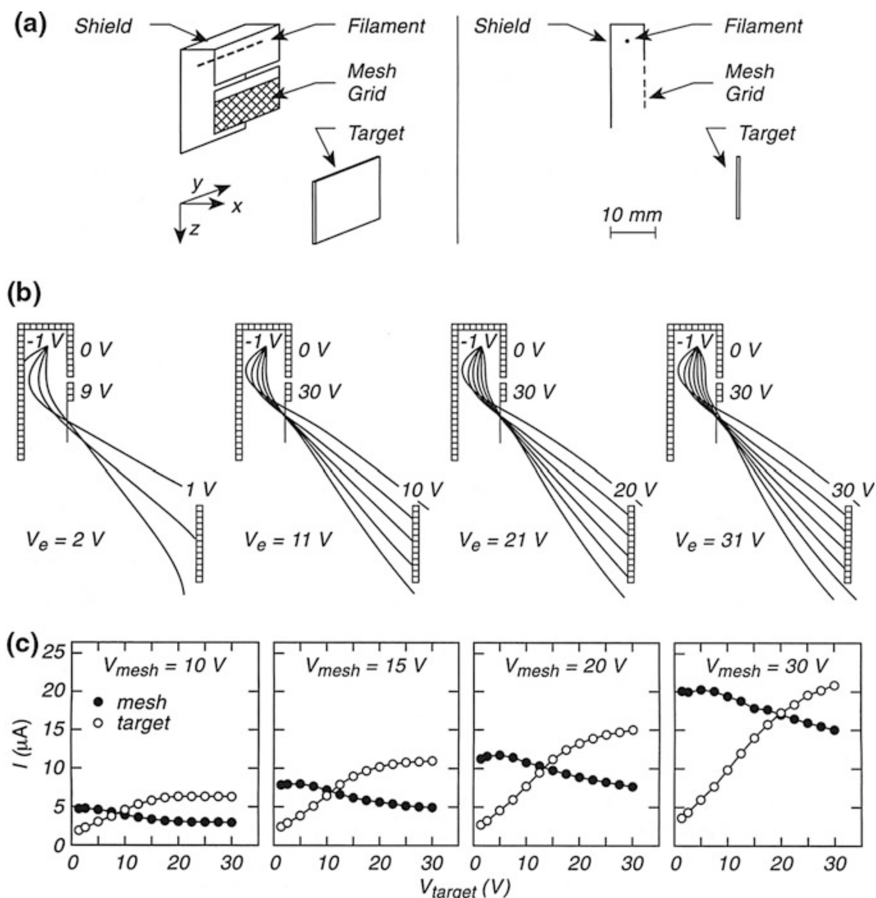

Fig. 20.2 Low-energy/broad-beam electron gun. **a** Electron gun design. **b** Electron trajectory analysis. **c** Current/voltage performance

20.3 Low-Energy Electron Gun for Broad-Beam Irradiation—Cylindrical Symmetry

The electron gun described here provides a broad, cylindrically symmetric electron beam, as opposed to a simpler gun described on p. 290, which has only planar symmetry. Low-energy electron beams produced by guns of these designs are used to cause surface chemical reactions by controlled electron beam damage, where the entire surface of a macroscopic sample is to be irradiated with uniform current density. Since electron-induced surface reaction is expected to happen at low electron energies, special design provisions must be made for delivery of high current densities at low energies.

Figure 20.3a shows a cylindrical gun design [17]. A BaO-coated disk cathode [18] is mounted inside a cylindrical repeller electrode. An anode plate with a 2-mm-diameter, 4-mm-long cylindrical hole is located close to the emitter disk. Four cylindrical lenses are used to focus the electron beam, and these are stacked between ceramic spacers [19]. A single positioning ring at the end of the stack holds the assembly together, and the assembly is housed inside a metal tube housing. To minimize work function differences along the gun, the inside of the lens is gold plated.

Figure 20.3b shows calculated electron trajectories for different electrode potentials. At the top, an anode at high positive potential withdraws electrons from the cathode, and the trajectories are shaped by the four lenses set for potentials from +30 V to 0 V as shown. This focuses the beam on the crystal at ground potential.

Figure 20.3c shows the electrostatic potential in the cathode region in a three-dimensional plot for electrons. The geometry and potential of the repeller and anode create a steep potential drop for electrons. The shape of the potential is designed to increase the lateral momentum of the electrons in order to achieve a broad electron beam. The broad beam exhibits very uniform current density as may been seen from the trajectory spacings in Fig. 20.3b.

In the simulations, it was found that the emission is very sensitive to the exact position of the cathode disk relative to the repeller cap and the anode opening.

Figure 20.3d shows the performance of the gun for various electron beam energies. At an electron energy of 10 eV, a current of 7 μA is obtained at the crystal, comparable to the performance of the gun shown on p. 293. The optimized anode and repeller potential are shown for various electron energies in Fig. 20.3e.

20.4 Electron Energy Analyzers

It is not the purpose of this book to discuss the details of the various forms of electron energy analyzers that are used for the analysis of surface phenomena. Instead, a practical guide to the selection, construction, and use of electron energy analyzers is available [20]. In addition, an extensive bibliography dealing with the various design analyzers is also presented in [20].

Six types of electron energy analyzers are described in [20], and these constitute the most widely used instruments. The analyzers are briefly categorized below.

Figure 20.4a—Time-of-Flight Analyzers

These analyzers are used primarily for ion detection owing to the extremely high velocity of electrons. However, time-of-flight methods have also been used for rapid pulsed sources of slow electrons. Electrons are allowed to drift in a field-free region, and their arrival at a microchannel plate detector is recorded by a suitable waveform digitizer. MicroChannel plate systems can provide gains of 10^6–10^7 and

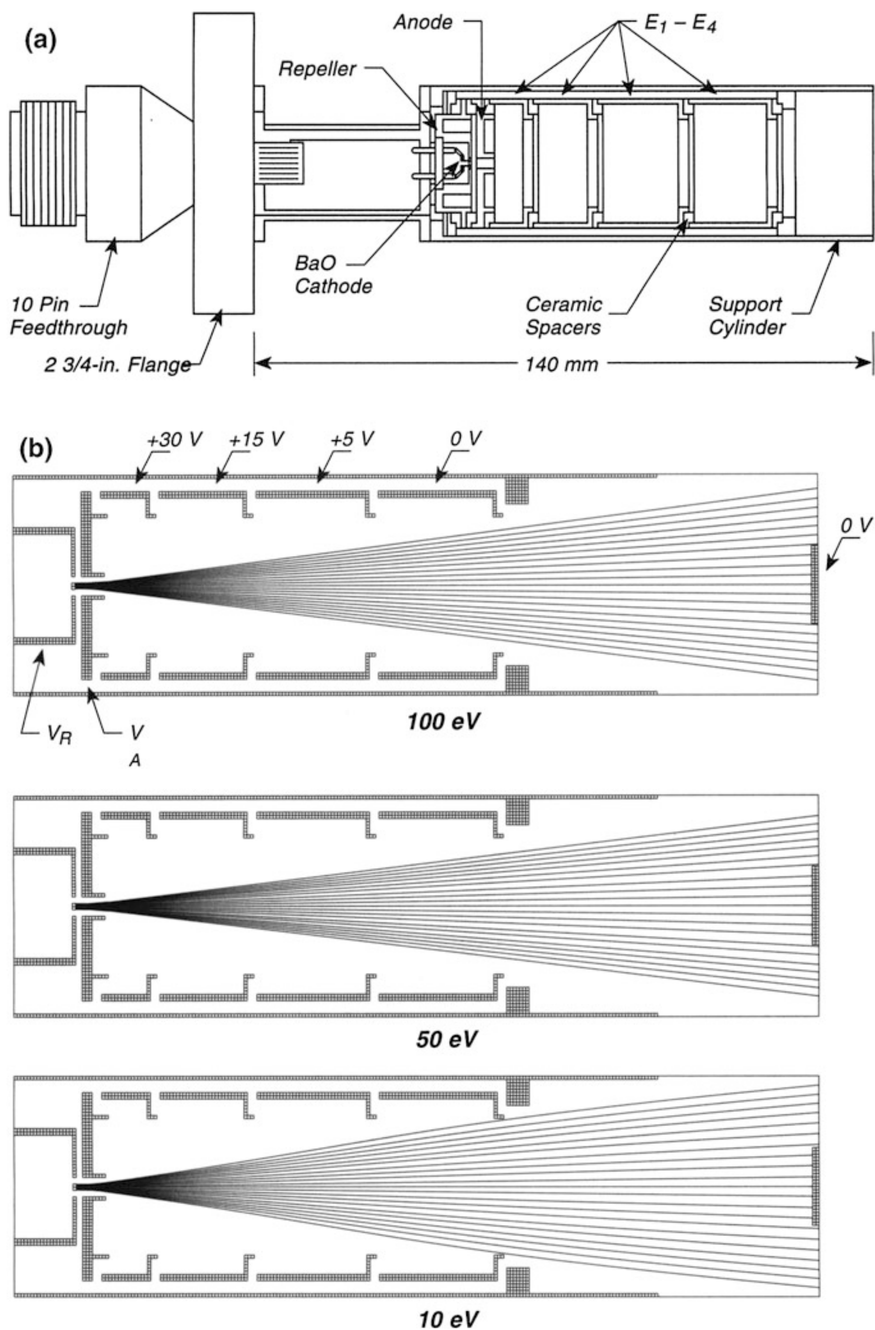

Fig. 20.3 Low-energy electron gun—broad beam **a** Design of the low-energy electron gun. **b** Beam profile for different electron energies. **c** Shape of the potential near the cathode. **d** Emission current from low-energy electron gun. **e** Potential settings for broad beam operation and constant electrode potentials

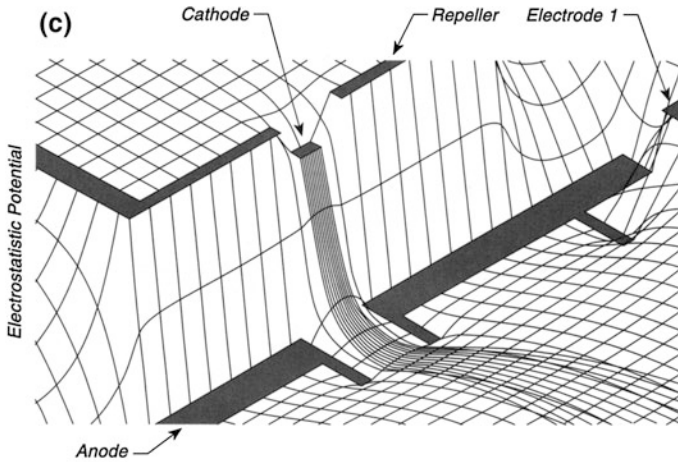

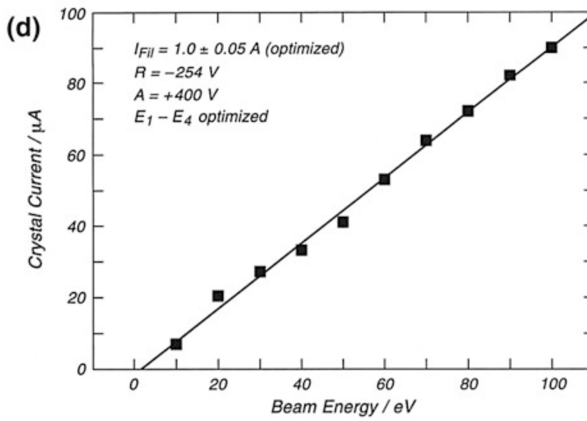

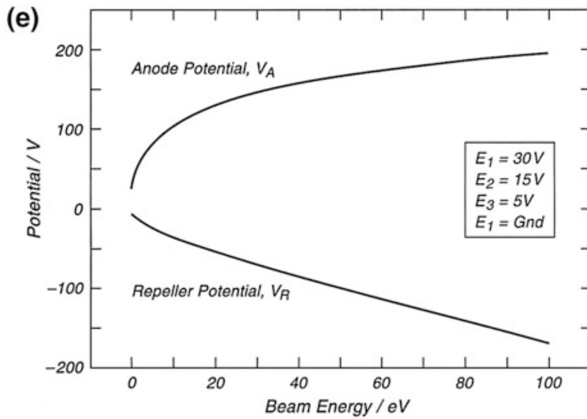

Fig. 20.3 (continued)

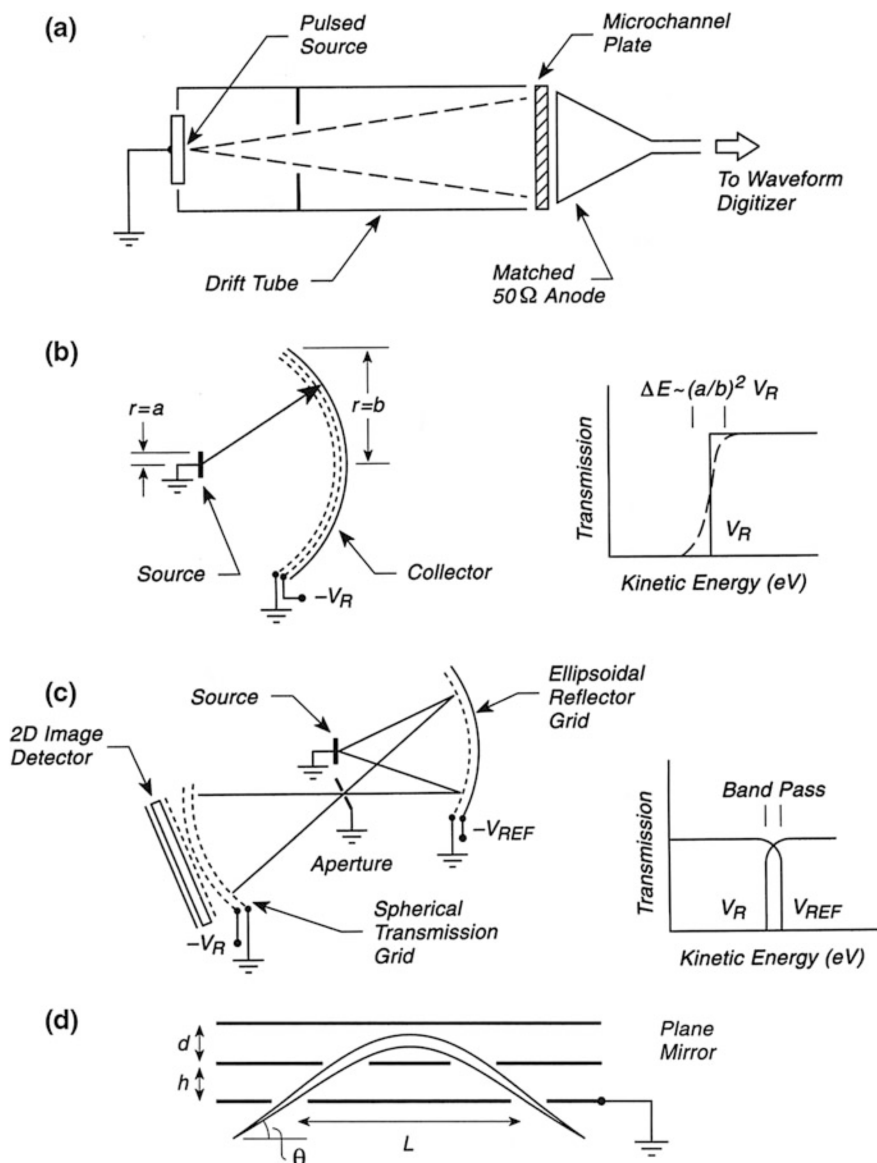

Fig. 20.4 Electron energy analyzers. **a** Time-of-flight analyzer. **b** Retarding grid analyzer. **c** Tandem reflection—transmission analyzer. **d** Plane mirror deflection analyzer. **e** Cylindrical mirror deflection analyzer. **f** Cylindrical deflection analyzer. **g** Spherical deflection analyzer

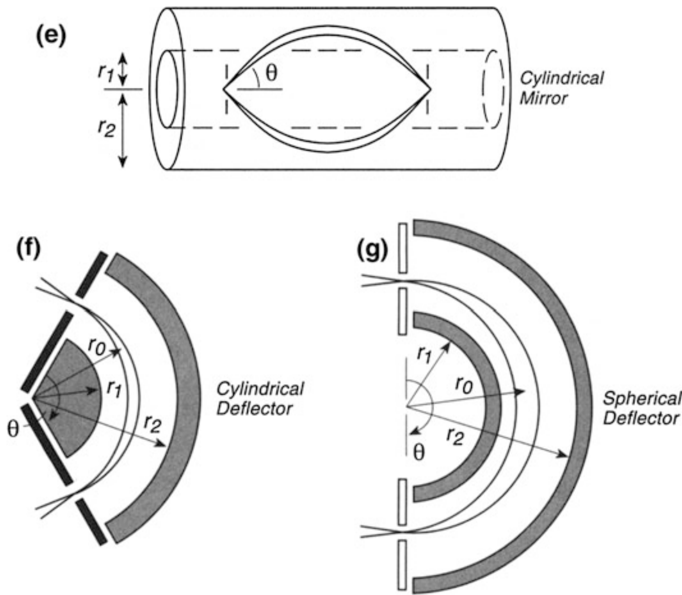

Fig. 20.4 (continued)

pulse widths of 1 ns. Drift-tube lengths of a few meters are employed, and in such long tubes magnetic field effects may be significant.

Figure 20.4b—Retarding Grid Analyzers

Here, the source is located at the center of two hemispherical grids and a spherical collector. The source and the inner grid are grounded to make a field-free intervening region. The outer grid, biased at—V_R, retards the electrons, and the collector is biased positive relative to ground to collect all electrons that pass the retarding grid. The energy resolution is estimated from the assumption that the source is spherical, of radius $r = a$, and that the radius of the collector is $r = b$. A schematic of the transmission of the device versus kinetic energy is shown when the retarding grid is set at V_R. The energy resolution, ΔE, at V_R is given by the equation in Fig. 20.4b.

Figure 20.4c—Tandem Reflection-Transmission Analyzer

This type of analyzer allows bandpass filtering of the energy distribution of electrons emitted from the source. The first grid system is a low-pass filter. Electrons having energies greater than eV_{REF} can overcome the retarding field and are collected on the ellipsoidal collector. Lower-energy electrons are reflected and focused through a grounded aperture, and thence to a retarding grid analyzer something like that shown in Fig. 20.4b. The two-dimensional image detector makes possible the simultaneous detection of the energy and the emission angle of the electrons received in the band pass of the two analyzers, as shown in the transmission

diagram for the tandem analyzers. Analyzers of 100-meV resolution and large angular acceptance have been constructed.

Figure 20.4d—Plane Mirror Deflection Analyzer

This represents the most elementary type of the deflection analyzers. Electrons, constrained to a certain angular range by the apertures, enter from the left into a region of width = h in which field-free conditions exist. From there, they enter a second region of width = d, where a constant electric field exists, which field is produced by making the upper plate negative. Here, the electrons travel in parabolic paths in the uniform field. Electrons having a specific energy arrive at the exit slits on the right and are measured below the lower grounded plate.

Figure 20.4e—Cylindrical Mirror Deflection Analyzer

Here principles similar to those used in the plane mirror analyzer apply. However, because of the cylindrical symmetry, a wide solid angle of acceptance exists, leading to high throughput and sensitivity. The cylindrical geometry is also convenient for the placement of the electron gun on axis, and has made this geometry popular for Auger electron spectroscopy (AES).

Figure 20.4f—Cylindrical Deflector Analyzer

This type of analyzer is widely used in high-resolution electron energy loss spectroscopy (HREELS). The optimum angle between the entrance and exit slits is $\theta = 127°$. Analyzers of this type are particularly useful for measuring the angular distribution of electrons emitted from a surface.

Figure 20.4g—Spherical Deflection Analyzer

This type of analyzer is widely used in photoelectron spectroscopy. The optimum angle between the entrance and exit slits of the analyzer is $\theta = 180°$.

Improvements in the resolution and throughput of these analyzers can be achieved by preretarding the incident electrons prior to entry into the analyzer [20].

20.5 Electron Spectrometer Calibration Using Graphite

The accurate location of the Fermi level (E_F, sample) is often an important requirement for the calibration of electron spectrometers. Often in ultraviolet photoelec-tron spectroscopy (UPS) the Fermi level can be determined by measuring the Fermi edge feature of a clean metal surface. However, if UPS is not available, the precise calibration of the Fermi edge position often cannot be carried out. A method to do this, using the secondary electron emission from electron impact excitation, X-ray photons, or UV photons on a graphite reference sample is described below [21].

Figure 20.5 shows the secondary electron emission region of a sample of graphite (highly oriented pyrolytic graphite, or HOPG) and a sample of Aquadag

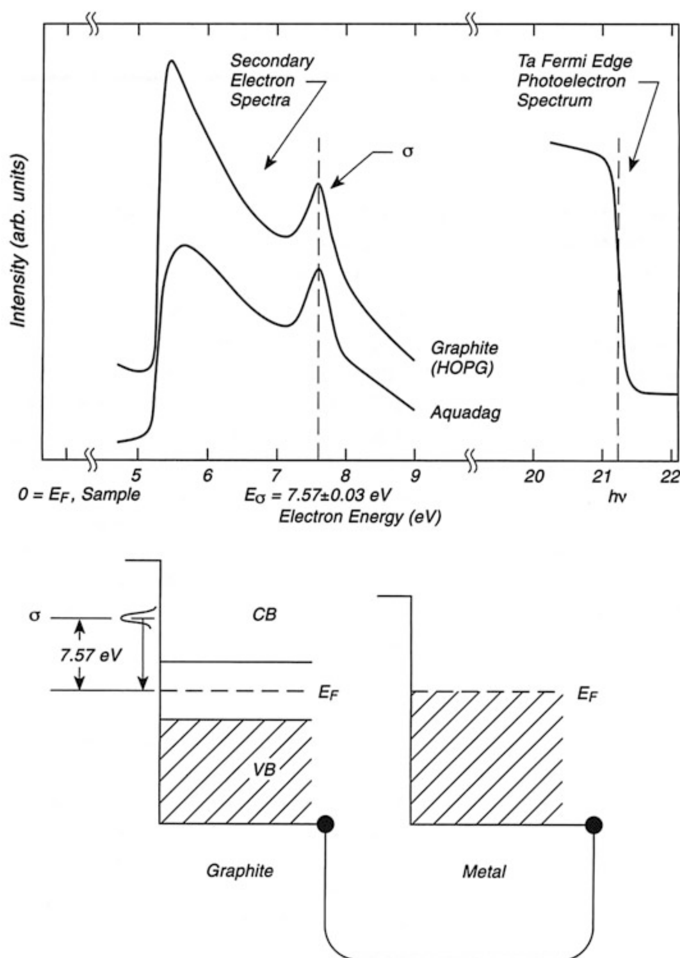

Fig. 20.5 Electron spectrometer calibration

(colloidal graphite) [22] that have been excited by He I (21.22 eV) radiation. In addition, the upper energy photoelectrons in the vicinity of the Fermi edge are also shown from a cleaned Ta sample in electrical contact with the graphite samples. The fact that the upper energy measured is at 21.22 eV indicates that the spectrometer energy scale is properly calibrated in this measurement. It can be seen in the secondary electron emission region that there is a distinct emission feature centered above the Fermi level at 7.57 ± 0.03 eV and superimposed on the broad secondary emission tail. This feature is related to electronic excitation of the a state present in the conduction band of the graphite. This state arises from the a electrons

in the C–C bonds in the graphite lattice and has been well studied previously [23, 24]. The energy of the σ peak from graphite is independent of the energy of the exciting radiation or electrons and hence can be used to locate the Fermi level accurately when it is otherwise not accessible.

The behavior of the a state is independent of the annealing temperature of the Aquadag over the range 230–750 °C and is independent of air exposure. Also, the energy is invariant with the angle of emission. From the low-energy cutoff in the secondary electron spectrum, the sample or electron analyzer work function can be determined [21].

20.6 Measurement of Electron Beam Angular Divergence

The response of an instrument measuring an electron diffraction beam is determined by many factors. Included are the source extension (or the angular divergence of the electron beam), the beam width, and the electron energy distribution. The most difficult factor to measure is the angular divergence of the beam, and this factor has generally been measured by the elimination of other parameters.

The method to be described can measure both the beam width and the angular divergence of the beam. Figure 20.6 shows a schematic view of the apparatus [25]. A stationary electron gun is directed toward a set of three Faraday cups that are translated by an electrically driven bellows. The Faraday cup detectors are located at different distances along the electron beam, and each 2-mm-diameter hole is half-covered with a razor blade acting as a knife edge. The current to each Faraday cup is measured as the assembly is translated across the beam. Thus, the shape of the electron beam is measured at three z-positions, and this permits the divergence to be obtained by comparing the full width at half maximum (FWHM) at each of the three cup positions. Placing one of the Faraday cups at the distance of the sample in normal use allows the beam character to be measured at the sample position. The loss of current through secondary electron emission is minimized by using Faraday cups that are at least three times as deep as their 2 mm apertures, and losses of a few percent are found in the 50–600-eV region [26]. The cups are not biased, and coaxial cables are used inside and outside the vacuum system to minimize noise.

An AC method may be used to make measurements of the first derivative of the collected current versus translation position. A small sinusoidal modulation is applied to one pair of deflection plates to provide a slight motion of the beam perpendicular to the knife edge on the collector. A lock-in amplifier measures the derivative signal as a function of translation position (measured electrically) and an accurate beam profile is plotted out with improved stability and noise compared to using the DC method. No mechanical instability was observed in measuring

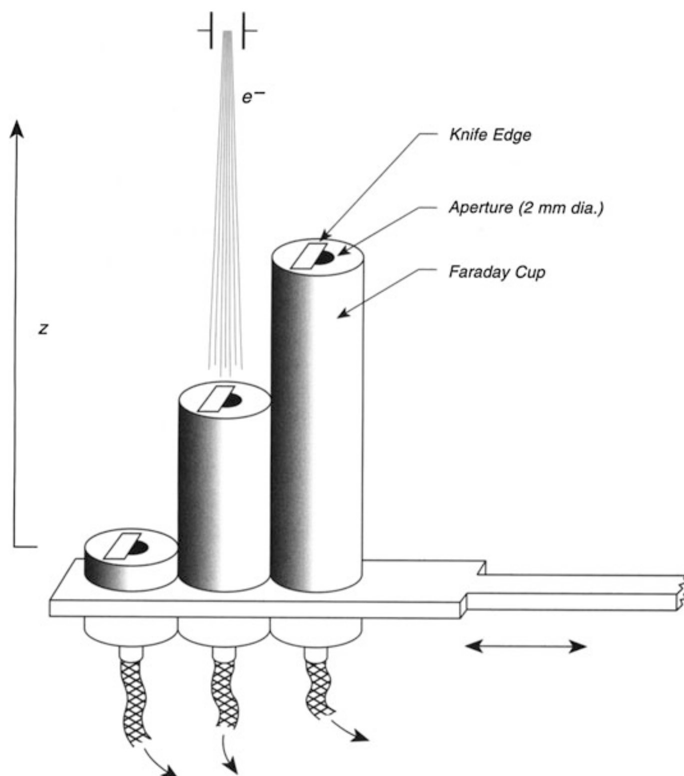

Fig. 20.6 Measurement of electron beam divergence

50–600-eV beams having a typical FWHM of 0.1 mm. A beam divergence of less than 0.1° may be measured, and typical electron guns exhibit divergences of about 0.2°.

The application of information obtained by the above method to actual LEED instruments is described in an excellent review article [27].

For the approximate measurement of electron and ion beam (>400 eV) dimensions, a phosphor screen may be used. A nice method to measure the beam dimensions involves the use of a small stainless steel plate with a precise grid overlay attached by welding. A grid that has 0.2 × 0.2 mm^2 openings, photolithographically etched, is ideal. A grid thickness of 0.025 mm is appropriate [28]. The phosphor, mixed with ethanol, is applied to the screen, and excess phosphor is removed from the outer surface of the grid overlay. When dry, the phosphor will adhere only inside the grid spacings, and the known dimensions of the grid provide a direct calibration scale for the electron beam [29].

20.7 Measuring Anisotropy of Electrical Conductivity of a Single Crystal—Four Point Probe

The bulk electrical conductivity of single crystal semiconductor materials is of importance in understanding their behavior in devices such as photocells. A four-point probe can be employed for the measurement at 300 K in air as schematically indicated in Fig. 20.7a [30]. Here four spring-loaded SiC tips are pressed into the crystal to make good contact with the bulk. The contact breaks the surface of the

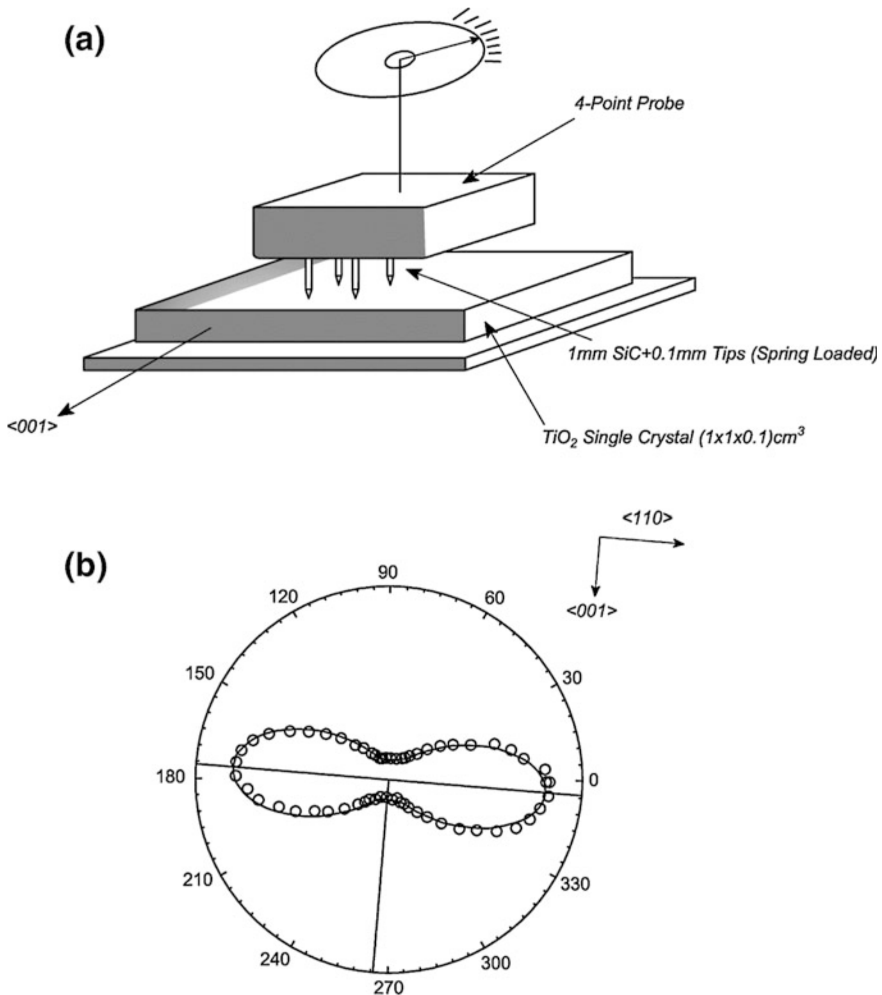

Fig. 20.7 Measuring anisotropy of electrical conductivity of a single crystal—four point probe. **a** Four point probe. **b** Anisotropy in conductivity of $TiO_2(110)$. The radius observed is proportional to the electrical conductivity of the single crystal in the measured direction

TiO_2. The force on each tip was equivalent to 100 g. The SiC contact points are located at the corners of a 1 mm square and are 0.1 mm in diameter. Current is passed through two non-diagonal tips and the potential drop is measured through the other two tips. From this information, the electrical conductivity is measured at the angle of the probe with respect to the <001> crystal axis. The calculation method of Yamashita [31] was employed. This method takes into account the finite width and thickness of the crystal. The four-point probe is rotated in a systematic manner and a new conductivity is measured at each azimuth. Figure 20.7b shows a directional conductivity measurement for TiO_2 measured on the well studied <110> face [30].

20.8 Spot Photometer for LEED Intensity Measurements

The measurement of LEED beam intensities using a spot photometer may be carried out in the absence of a Faraday cup or electronic image-enhancing display method. The use of a uniform phosphor screen makes these measurements satisfactory for many purposes.

The construction of a spot photometer is shown in Fig. 20.8. The detector is equipped for synchronous detection, eliminating interference from background

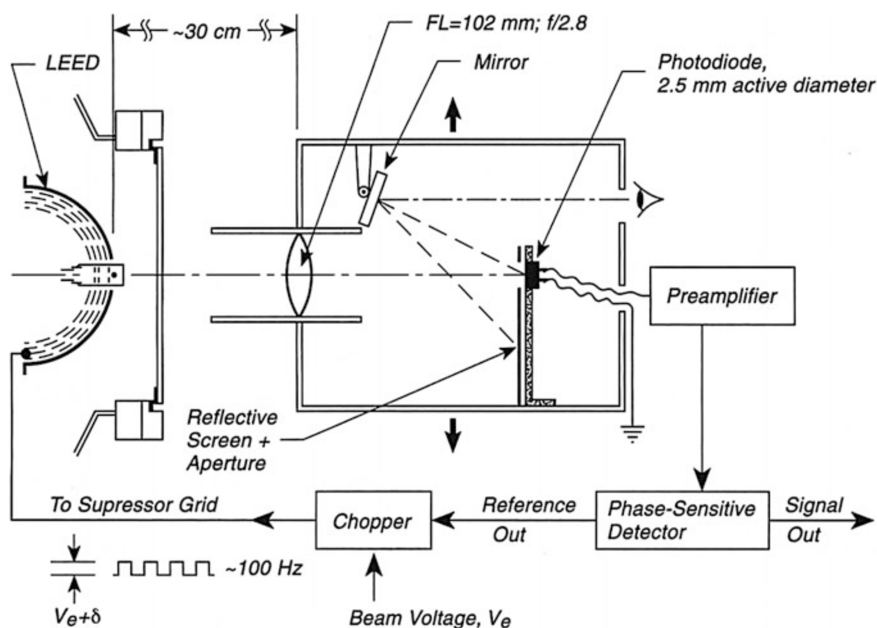

Fig. 20.8 Spot photometer for LEED intensity measurements

light. A lens focuses the light from a LEED beam on a photodiode that is mounted behind an aperture placed in a thin reflective metal screen. The LEED pattern can be observed visually through a port using the reflective screen and the spot photometer is moved laterally for measurement of individual beams. A photodiode mounted behind the aperture integrates the light received from a selected beam plus the surrounding background. The diffraction pattern is modulated at 100 Hz by applying a chopping voltage to the suppressor grid of the order of $V_e + \delta$, which is sufficient to suppress the LEED pattern [32].

At a spacing of 30 cm from the LEED screen, the photodiode sees a circular area of about 5.4-mm diameter, about five times the average diameter of a diffraction spot in the apparatus. The photodiode is a low-noise planar-diffused silicon sensor photodiode [33]. The reader may see examples of the use of this apparatus in [34, 35].

Newer methods involving vidicon detectors are widely employed for the study of LEED patterns and intensities on phosphor screens. It is possible to employ a bandpass optical filter to remove stray light from high temperature filaments and emission from a hot sample. For a P11 phosphor, with a narrow band of emission at 459 nm, an interference filter with a central wavelength of 460 nm and a bandwidth of 50 nm is excellent for removal of the stray light, permitting more accurate measurement of LEED intensities on a background that is closely similar to the dark current of the vidicon [36].

20.9 Modified Faraday Cup for Electron Current Measurement

Faraday cups are employed for the collection of electrons in collimated beams. One problem is that specularly reflected electrons from the bottom of the Faraday cup may be reemitted, causing the measured collected current to be diminished. Various methods for the suppression of specularly reflected and secondary electron emission are employed, and one principle employed is to make the Faraday cup depth a number of times the aperture width. But even this design criterion does not prevent the reflection of specular electrons from the bottom of the cup. Surfaces are known to have high reflectivities for low-energy electrons of a few eV energy.

To avoid this problem, a stainless steel cone was inserted in the cup [37], as shown in Fig. 20.9a. The specularly reflected electrons from this conical surface maintain their forward component of velocity along the optical axis of the cup. These electrons have no velocity component along the optical axis toward the aperture. Thus this design is the electron optical equivalent of a light trap. The design invalidates the principle that the depth of the cup should be large compared to the aperture.

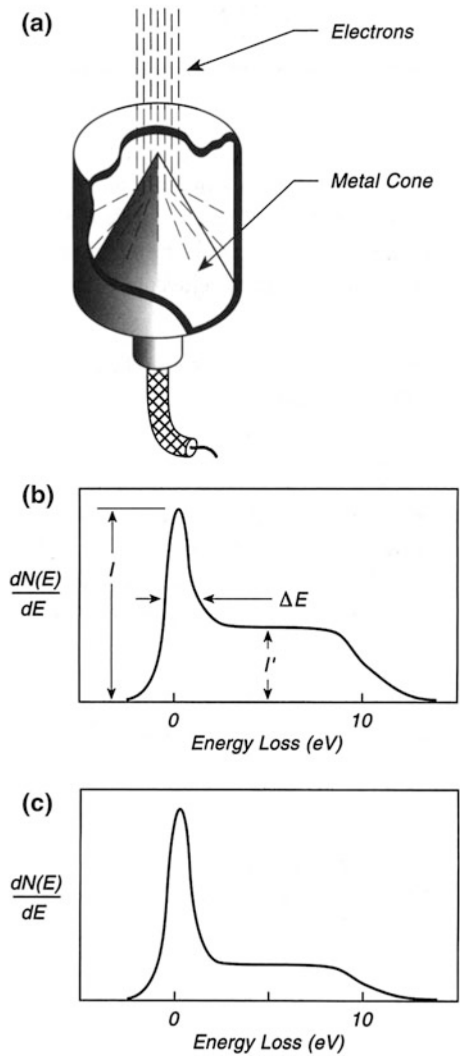

Fig. 20.9 Modified faraday cup. **a** Faraday cup with internal cone. **b** Electron energy distribution—no cone. **c** Electron energy distribution—with cone

The energy distribution of the collected electrons (10^{-11} A) versus retarding potential is shown in Figs. 20.9b, c for the unmodified Faraday cup and the Faraday cup containing the inner conical surface. It is seen that the ratio I/V can be increased by a factor of 2 from 2.5 to 5 when the cup contains the conical insert. At the same time, AE increased from 1.2 to 1.6 eV. No explanation for the existence of the plateau extending into the loss region by about 8 eV was presented in the paper [37].

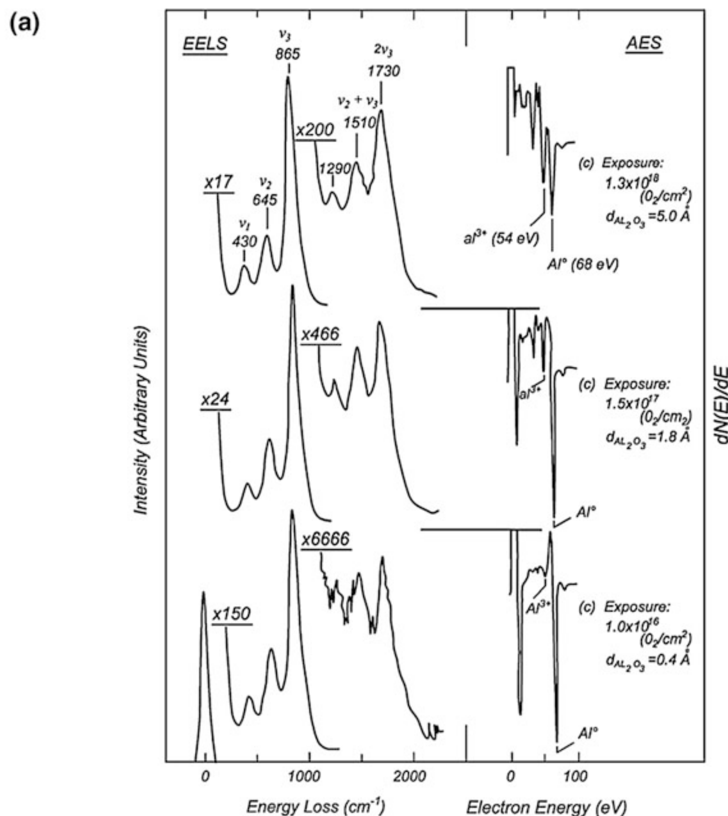

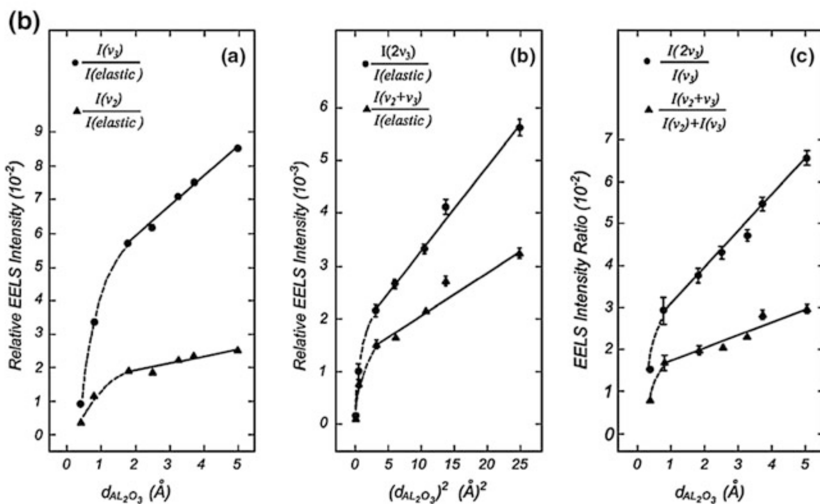

Fig. 20.10 HREELS-discrimination between single and multiple electron scattering events. **a** EELS and AES measurements of Al_2O_3/Al(111) at three different levels of oxidation. **b** Correlation between the EELS intensities and the Al_2O_3 thickness

20.10 HREELS-Discrimination Between Single and Multiple Electron Scattering Events

High resolution electron energy loss spectroscopy (HREELS) is widely used to study the vibrational spectrum of adsorbed molecules and the phonon spectrum of thin films. In addition to the excitation of fundamental vibrational modes ($\nu = 0 \rightarrow \nu = 1$), it is possible to excite more complex modes such as overtones and combination losses. These processes differ in the number of vibrational quanta excited or the number of scattering events the electron undergoes. In fundamental and overtone loss processes, a single electron excites a single mode; in the case of multiple electron energy loss processes, an electron undergoes two or more scattering events. Combination loss processes often fall into the category where the electron undergoes multiple scattering.

The multiple scattering events (here double scattering) should scale as the square of the thickness of the film being investigated, whereas fundamental modes should be linearly dependent on the thickness. This is demonstrated in the case of an Al_2O_3 film on an Al(111) substrate, as shown in Fig. 20.10a. Here the three low frequency modes, ν_1, ν_2, and ν_3 are fundamental phonon modes of the oxide which involve single electron scattering. The higher frequency modes involve multiple scattering. As the thickness of the Al_2O_3 film grows, as evidenced by the Auger spectra, the relative intensity of the multiple loss modes increases non-linearly with respect to the single scattering modes, as may be seen by the changing magnification scale (from 6666x to 200x) needed to maintain the appearance of similar spectra for the three film thicknesses. In Fig. 20.10b, plots of intensity versus the thickness, d, or the thickness squared, d^2, are shown. In Fig. 20.10b(b), the multiple scattering modes scale in their later stage of development with d^2, whereas in Fig. 20.10b(a), the single scattering modes scale with d. This may also be seen in Fig. 20.10b(c) where the ratio of intensities of the multiple to single scattering modes increases as film thickness increases. The drop off of intensity seen in all three figures for thin films is due to imperfections of the film thickness measurement using Auger spectroscopy [38].

20.11 Rejuvenation of Cu/Be Electron Multipliers

The deposition of thin films onto electron multipler surfaces occurs after long use, particularly in vacuum systems having a background of oil vapors or in systems that have been used for reactive gases, such as fluorine [39]. A simple rejuvention method has been reported for Cu/Be dynodes exposed to fluorine to the extent that the multiplier gain had dropped to 1/300 of its original gain. Complete rejuvenation back to the original gain was observed [39].

For the particular case here, it was decided to expose the dynodes to a plasma discharge in hydrogen to remove the fluorine, and then to expose them to a plasma

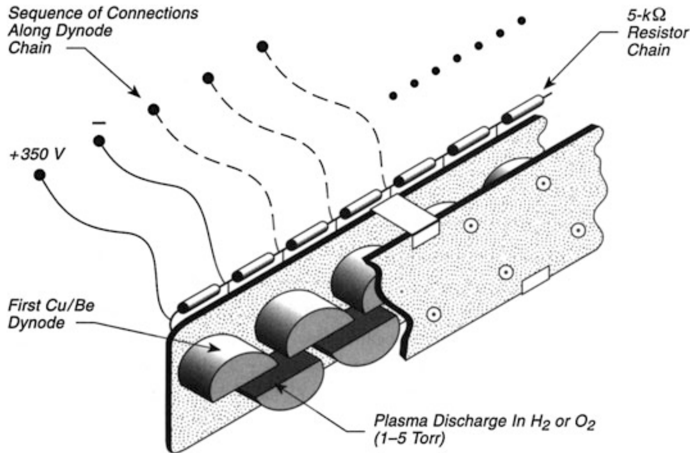

Fig. 20.11 Rejuvenation of Cu/Be electron multipliers

discharge in oxygen to reoxidize the dynode surfaces. This was done, of course, by removing the multiplier and treating it in a separate metal vacuum system. In Fig. 20.11, a sequence of rejuvenation steps is carried out, in which neighboring dynodes are used as anode/cathode combinations, working up the multiplier chain. For hydrogen plasma generation, a pressure of about 1 Torr of H_2 was used, under flow conditions, with a 350 V DC power supply connected through 5000 Ω between adjacent dynodes. A Tesla coil was used to initiate the plasma, and the pressure was increased in the range 1–5 Torr until about 30 mA of current passed. Hydrogen plasma treatment was carried out for 2 min. After this, for O_2 plasma generation, about 10 mA of current was used for 1 min. The multiplier anode was not treated.

A cleaning and oxidation treatment, designed to avoid copper oxide formation on the dynode structures and to place beryllium oxide films on the dynodes, has been described [40]. Here, oxidation in water vapor at pressures up to 5×10^{-2} Torr was carried out in cycles in an RF-heated furnace at 625 °C. Beryllium oxide exhibits a higher secondary electron yield than copper oxide [40].

20.12 Geiger-Müller Counter for Inverse Photoemission

Inverse photoemission involves the emission of ultraviolet photons from a surface when the surface is excited by electron impact. This method samples the empty density of states of the surface and near surface regions of a solid. The intensity of photon emission is measured as a function of incident electron energy. A Geiger-Müller counter, with windows passing ultraviolet light, is used for the measurements [41, 42].

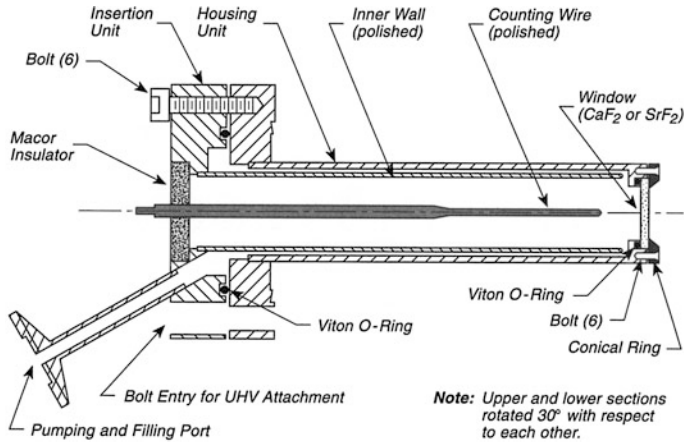

Fig. 20.12 Geiger-müller counter for inverse Photoemission

Figure 20.12 shows the counter, which consists of two parts, the housing unit and the insertion unit. The housing unit is mounted on a 2 3/4-in. Conflat flange. A conical ring presses either CaF_2 or SrF_2 windows [43] onto the housing containing a Viton O-ring. The inner surface of the ring is beveled at 45° to minimize photon emission from this surface by stray electrons. The window has a diameter of 20 mm and a thickness of 2 mm.

The insertion unit is mounted inside the housing unit, and can be removed for bakeout. It too is sealed with a Viton O-ring at the 2 3/4-in. flange. Both the inner wall of the insertion unit and the counting wire (1.5-mm diameter) are polished. The counting wire is electrically isolated from the apparatus by a Macor insulator, which is glued to the outer flange and to the counting wire with vacuum cement [44]. The active length of the counting wire is 40 mm and its end is located 10 mm from the window. The glue joint is made with the counter wire accurately centered in the insertion unit. The port serves to evacuate the counter as well as being an inlet for Ar background gas.

The counter is assembled with the help of a He leak detector to assure tight sealing between the housing unit and the entrance window with minimum force on the front-end bolts. After installation, the assembled unit is pumped overnight, then opened and a few crystals of iodine are dropped in. After pumping again for 30 min, Ar is introduced to a pressure of 100–200 mbar, and the counter is valved off.

Typical operating voltages are 400–500 volts. All pulses should be of identical height (about 0.2 V). Occasionally the counter is pumped again and refilled with Ar. Repeated fillings with Ar may also help if the counter does not work initially. Deterioration of the counter performance (requiring a steady increase in voltage) usually indicates insufficient vacuum conditions.

References

1. K.R. Spangenberg, *Vacuum Tubes* (McGraw-Hill, New York, 1948)
2. J.A. Simpson, C.E. Kuyatt, J. Res. Nat. Bur. Stand. **67C**, 279 (1963)
3. J.R. Pierce, *Theory and Design of Electron Beams* (D. Van Nostrand Co., Inc, New York, 1949)
4. F. Rosebury, *Handbook of Electron Tubes and Vacuum Techniques* (American Institute of Physics, New York, 1993)
5. A particularly excellent account of practical aspects of electron optics is given in J.H. Moore, C.C. Davis, M.A. Coplan, *Building Scientific Apparatus* (Addison-Wesley, Reading, MA, 1983), chapter 5
6. Cliftronics, Inc., 15 South Street, Clifton Springs, NY 14432. Model 406-S; Another sup-plier of electron guns is Kimball Physics, Inc., 311 Kimball Hill Road, Wilton, NH 03086-9742
7. M.G. Lagally, J.A. Martin, Rev. Sci. Instrum. **54**, 1273 (1983)
8. This program, which is periodically updated, is available from Idaho National Engineering Laboratory, EG8cG Idaho, P.O. Box 1625, Idaho Falls, ID 83415
9. R.Q. Hwang, E.D. Williams, R.L. Park, Rev. Sci. Instrum. **60**, 2945 (1989)
10. R.N. Lee, Rev. Sci. Instrum. **39**, 1306 (1968)
11. M. Proulx, P. Marmet, R. Dutil, Rev. Sci. Instrum. **53**, 778 (1982)
12. M.K. Debe, D.C. Johnson, Rev. Sci. Instrum. **47**, 37 (1976)
13. M. Aeschlimann, E. Hull, J. Cao, C.A. Schmuttenmaer, L.G. Jahn, Y. Gao, H.E. Elsayed-Ali, D.A. Mantell, M.R. Scheinfein, Rev. Sci. Instrum. **66**, 1000 (1995)
14. J.-L. Liang, J.T. Yates Jr, J. Vac. Sci. Technol. **A12**, 2795 (1994)
15. This program, which is periodically updated, is available from Idaho National Engineering Laboratory, EG&G Idaho, P.O. Box 1625, Idaho Falls, ID 83415
16. J.C. Lin, R. Gomer, Surf. Sci. **172**, 183 (1986)
17. T.R. Barefoot, H.D. Ebinger, J.T. Yates Jr, J. Vac. Sci. Technol. **A15**, 2740 (1997)
18. BaO disk cathode, ES-015 on AEI base, Kimball Physics, Inc., 311 Kimball Hill Road, Wilton, NH 03086-9642
19. $A1_2O_3$ ceramic insulator—Finnigan # 40005-20070, Scientific Instrumentation Services, Inc., 1027 Old York Road, Ringoes, NJ
20. J.L. Erskine, *Experimental Methods in the Physical Sciences*, vol. 29A (Academic Press, Inc., 1995), p. 209
21. P. Oelhafen, I.L. Freeouf, J. Vac. Sci. Technol. **A1**, 96 (1983)
22. Aquadag may be obtained from Acheson Colloids, 1607 Washington Avenue, P.O. Drawer 611747, Port Huron, MI 48061-1747. In applications of this type, it may be painted onto the sample to yield the desired reference energy above the Fermi level
23. J. Krieg, P. Oelhafen, H.-J. Guntherodt, Solid State Comm. **42**, 831 (1982)
24. R.F. Willis, B. Feuerbacher, B. Fitton, Phys. Rev. B. **4**, 2441 (1971)
25. J.A. Martin, M.G. Lagally, J. Vac. Sci. Technol. **18**, 58 (1981)
26. M.G. Lagally, Ph.D. Dissertation, University of Wisconsin, 1968
27. M.G. Lagally, J.A. Martin, Rev. Sci. Instrum. **54**, 1273 (1983)
28. Photolithograph W grid is available from Buckbee Mears Corp., 245 East 6th Street, St. Paul, MN 55101-1959
29. Dr. R. David, Institut fur Grenzflächenforschung und Vakuum-physik, Forschungszentrum Jülich GmbH, Postfach 1913, D-5170 Jülich, Germany (private communication)
30. O. Byl, J.T. Yates Jr, J. Phys. Chem. B. **110**, 22966 (2006)
31. M. Yamashita, M. Agu, Jap. J. Appl. Phys. **23**, 1499 (1984)
32. A.G. Schrott, M.D. Chinn, C.G. Shaw, S.C. Fain Jr, J. Vac. Sci. Technol. **21**, 101 (1982)
33. PIN-5DP, United Detector, 12525 Chadron Avenue, Hawthorne, CA 90250
34. C.G. Shaw, S.C. Fain Jr, M.D. Chinn, M.F. Toney, Surf. Sci. **97**, 128 (1980)
35. R.D. Diehl, M.F. Toney, S.C. Fain Jr, Phys. Rev. Lett. **48**, 177 (1982)
36. R.J. Phaneuf, H.-C. Kan, Rev. Sci. Instrum. **65**, 3871 (1994)

37. W.R. Miller Jr, N.N. Axelrod, Rev. Sci. Instrum. **37**, 1096 (1966)
38. J.G. Chen, J.E. Crowell, J.T. Yates Jr, Rapid communications. Phys. Rev. B. **35**, 5299 (1987)
39. G.E. Salser, Rev. Sci. Instrum. **37**, 674 (1966)
40. M.B. Pongratz, Rev. Sci. Instrum. **43**, 1714 (1972)
41. V. Dose, Rev. Sci. Instrum. **39**, 1055 (1968)
42. V. Dose, Th Fauster, R. Schneider, Appl. Phys. A. **40**, 203 (1986)
43. CaF_2 and SrF_2 windows are available from Harshaw Optical/Bicron, 6801 Cochran Road, Solon, OH 44139
44. The vacuum cement used is Araldit ATI, Ciba-Geigy GmbH, Oeflinger Str. D-79664 Wehr (Baden), Germany

Chapter 21
Ions

21.1 Ion Sputter Gun with Low Gas Emission

Normal ion guns operate in an ambient pressure of the gas to be used for sputtering. This pressure needed to generate a satisfactory ion bombardment current is normally in the 10^{-6}–10^{-5} Torr range [1]. Improved ion gun designs involve a direct feed of the inert gas into the ionization region, and these designs normally involve an ambient pressure in the 10^{-8} Torr range. However, any rise in the pressure in the main chamber during the cleaning process is detrimental, since it is known that gas release from the chamber walls, from the ionization pump (if left on) and from the sublimation pump is caused by an increase in the pressure of even an inert gas. This undesirable gas evolution depends upon the previous history of the vacuum system and influences the time required to pump down to the base pressure after ion sputtering.

The design shown in Fig. 21.1a involves direct injection of the sputtering gas into the ion gun and direct pumping from the ion gun into a turbopump. The gas beam inside the ion gun is created by a multicapillary array collimator (see p. 421 for gas doser designs employing this collimation principle). The angular distribution of sputter gas molecules exiting from the array may be calculated [2, 3]. The sputtering gas is injected into the ion gun through transparent Ta grids that are welded over windows cut into the walls of the outer shield of the ionization gun. A multicapillary array of 13-mm diameter and 3-mm thickness is used, with 10-μm diameter capillaries. Control of the gas pressure is achieved with a leak valve, as shown in Fig. 21.1b. Two gate valves are used to isolate the main chamber from the turbopump after sputtering when an ion pump is used for maintenance of UHV. Normally the 360-L/s turbopump is used to pump the main chamber in parallel to an ion pump and a Ti sublimation pump (not shown) [4].

While an IQ 10/35 ion gun is shown in the example here, many ion gun designs will work with this modification.

© Springer International Publishing Switzerland 2015
J.T. Yates Jr., *Experimental Innovations in Surface Science*,
DOI 10.1007/978-3-319-17668-0_21

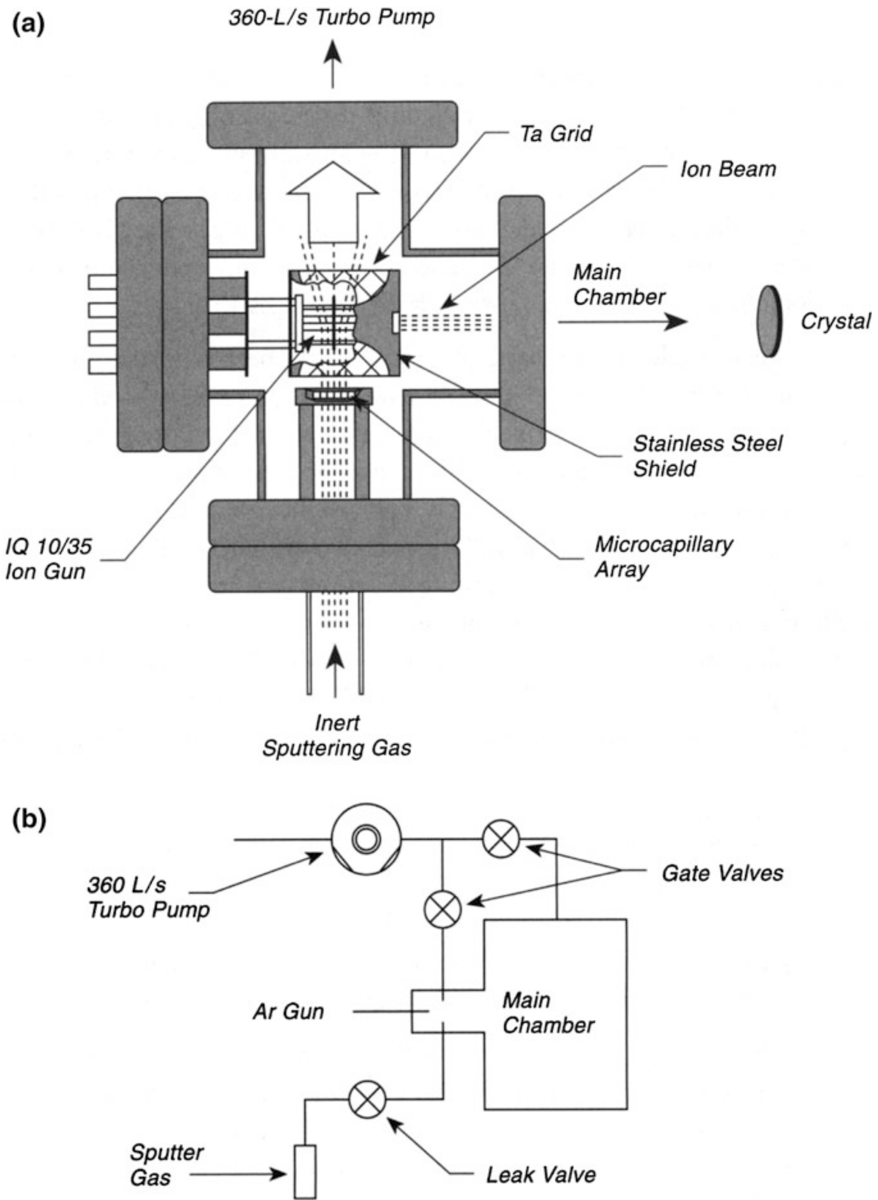

Fig. 21.1 Ion sputter gun with low gas emission. **a** Modified ion gun. **b** Schematic of vacuum system

21.2 Alternate Ion Bombardment Sources

Ion bombardment of elemental crystal surfaces is widely used for removing both surface and bulk impurities. In the case of bulk impurities, cleaning by sputtering is often accomplished at elevated temperatures, permitting bulk impurities to diffuse to the surface for removal. Normally an ion gun is employed for this and guns giving both focused beams and more diffuse beams are available. Admission of Ar gas directly to the ionization region of the ion gun will reduce the gas load in the vacuum system and hence reduce contamination effects during and after sputtering (see pp. 87–91).

Alternately, very simple ion bombardment sources have been reported, and two examples of these are illustrated here. In Fig. 21.2a, an open ion gauge is used as a source of Ar^+ ions [5]. The vacuum system is filled with Ar gas to about 10^{-3} Torr, permitting ample gas density within the ionization region of the gauge for

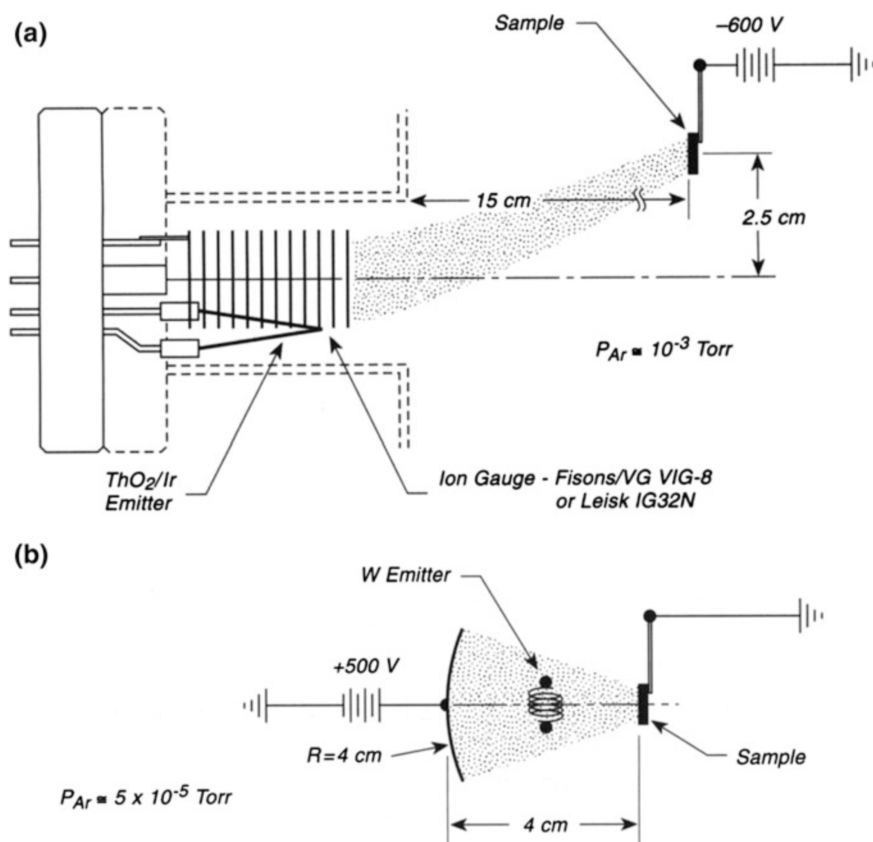

Fig. 21.2 Two alternate ion bombardment sources. **a** Ion gauge sputter source. **b** Reflector sputter source

producing an ion current which is collected at the sample biased at −600 V. It is reported that for an electron emission current of 10 mA, ion currents of 10–15 μA are collected at the crystal, depending on the negative bias. The gauge becomes inaccurate for pressure readings under these conditions. In addition, sputtered metal from the elements of the gauge will soon coat the insulator, which isolates the central collector electrode, causing leakage currents that disable the gauge as a pressure-measuring device. A shield below the grid structure preventing metal deposition on the collector insulator has been used to prevent these effects. The gauge is normally cleaned extensively by electron bombardment of the grid before use as an ion source, keeping the sample positioned elsewhere without its electrical bias.

Ion bombardment sources made without the use of carefully designed ion extraction optics have the capability of delivering impurity metal to the sample from sputtering processes inside and around the gauge components. Therefore, one should be very certain in controlled, and high-sensitivity Auger studies, that these contamination effects do not occur. For the design shown here, with the dimensions and mounting geometry indicated in Fig. 21.2a, Pt and Cu crystals were successfully cleaned and comparisons with a conventional ion gun showed that no differences in the surface preparation could be detected by Auger spectroscopy and other surface characterization methods [5].

Figure 21.2b shows an even simpler ion bombardment source. A tungsten filament is mounted on two tungsten feedthrough wires between a curved anode and the sample. Electron emission current of the order of 18 μA is collected by the curved anode at a bias potential of +500 V, and at an Ar pressure of about 5×10^{-5} Torr, an Ar^+ current density of about 20 $\mu A/cm^2$ is collected by the sample at ground potential. At 3×10^{-4} Torr Ar pressure, ion current densities of 50–60 $\mu A/cm^2$ are reported. The ion source should be scrupulously cleaned by heating the emitter for a long time to remove desorbing gases, and also by electron bombarding the curved anode extensively to remove adsorbed gases that might undergo electron stimulated desorption during use of the source for sputtering. Again, with this device, special care should be taken to eliminate the possibility of metal deposition from extraneous sources, although the report [6] indicates that this effect is not observed on a GaAs wafer sample.

A more complex ion gun source made from a Bayard-Alpert gauge is described on p. 214.

21.3 Ion Gun Based on Bayard-Alpert Gauge

A more complex ion gun than that described on p. 211 and 213 is presented here [7]. A Bayard-Alpert gauge is modified in two ways: first, by removal of the top part of the cylindrical grid cage for addition of the ion extraction electrodes; and second, by the addition of a metal shield around the gauge body and the thermionic emitter.

Figure 21.3a shows a schematic of the gun design and the electrical components. A tantalum cylindrical shield to repel electrons is mounted around the gauge body and its electrical potential is maintained at the same potential as the positive end of the thermionic emitter filament. An extractor lens shaped with a waist withdraws ions from the region enclosed by the grid and these pass into an accelerator region, and thence into a cylindrical lens and a quadrupole lens, where the ions are ejected into vacuum and to the target. The flange holding the ion gun is equipped with radial feedthroughs about its outer edge for supplying potentials to the ion gun elements.

The extractor lens accelerates mainly off-axis ions to an on-axis focal point, and its potential can be as high as −200 V. The divergence of the ion beam is controlled by the bore of the accelerator electrode, and the final focusing is done by the lens. Since all potentials in the gun, except for the lenses, are referenced to the primary energy, the extraction of ions is independent of the final beam energy. At low energies, the ions are of high energy when they arrive at the lens, and are decelerated there, while being focused. This leads to high currents at low ion energies. The quadrupole lens consists of four plates at 90° to each other symmetrically placed around the gun axis, but its use is not described in the original article [7].

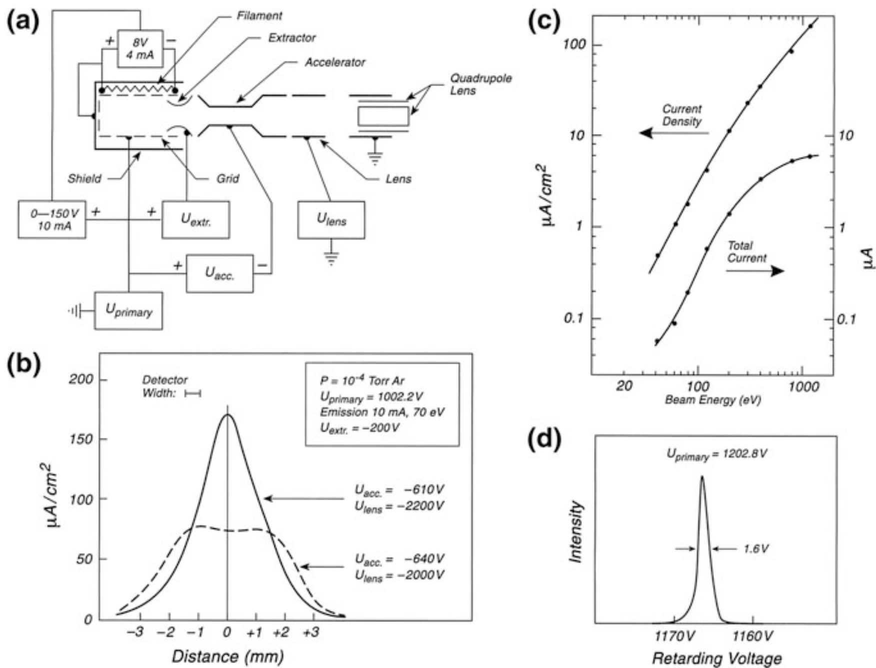

Fig. 21.3 Ion gun based on Bayard-Alpert gauge. **a** Ion gun and circuit. **b** Ion spatial distribution. **c** Current and current density. **d** Ion beam energy distribution

The spatial distribution of the ions may be adjusted as shown in Fig. 21.3b. Either a sharply peaked ion beam with high current density at the center may be produced, or alternatively, a flat-topped beam profile may be produced by adjusting the acceleration and lens voltages.

In Fig. 21.3c, the current and current density are plotted for a pressure of 1×10^{-4} Torr Ar pressure. Current densities between 0.1 and 120 $\mu A/cm^2$ are obtained at various ion energies. The current collected near 1 keV energy is limited by space charge effects in the extractor region. The collector in these cases was located 4 cm from the end of the gun.

Figure 21.3d shows the energy distribution measured with a retarding field analyzer and showing that at 1.2 keV, an ion beam halfwidth of 1.6 eV may be obtained using an extractor voltage of about −30 V. The ion beam was also mass analyzed, and at an electron energy of 70 eV, a 1:10 ratio of Ar^{++} to Ar^{+} was measured.

An earlier version of this design for an ion gun has been published [8].

21.4 Sputter Ion Gun—Cold Cathode

A cold cathode ion gun, useful for sputter deposition, can be made, as shown in Fig. 21.4 [9]. The gun is useful for sputter deposition from any conducting target material. The ion gun was first described in [10], and this is a modification of that design. The gun is capable of producing an ion beam of 1-mA current at a kinetic energy of 2–6 keV, impinging on an area 5–10 mm in diameter. There is no filament, and the gun can be operated for hundreds of hours without maintenance. Currents in excess of 1 mA cause tip heating which shortens the tip life. Sputter deposition rates of 1–4 Å/s can be obtained.

The beam gas is admitted from a pumped gas handling system through two ceramic insulator nipples and through a metal frit particle filter into a Conflat flange-mounted electrical feedthrough passing a 1/4-in. tube that is connected via Swagelok connectors to a hollow tube made of l/16-in.-diameter tungsten or tungsten carbide alloy. This needle is 0.625-in. long and has an orifice of 0.05–0.075-mm diameter. It is called a wire bonding tool [11]. The high electrical field at the tip ionizes the gas as it passes through the tip, resulting in a plasma cone that extends to the target. The diameter of the cone depends on the orifice diameter, supply gas pressure, and target distance. A 2.5 Torr beam of gas in the gun, combined with a tip-target distance of 6 mm and a 0.050-mm-diameter orifice produces a beam crater diameter of 7–10 mm.

A principal difficulty is keeping particles out of the tip. The tip may be unplugged by passing a 0.003-in.-diameter W wire from the back end. This wire may be made from larger stock by electrolytic etching in NaOH (aq) solution. Final cleaning of the tip is done in an ultrasonic bath with acetone.

The beam current and stability depend on the pressure of gas entering the gun. Stable operation is obtained when the chamber pressure is in the 5×10^{-4} to

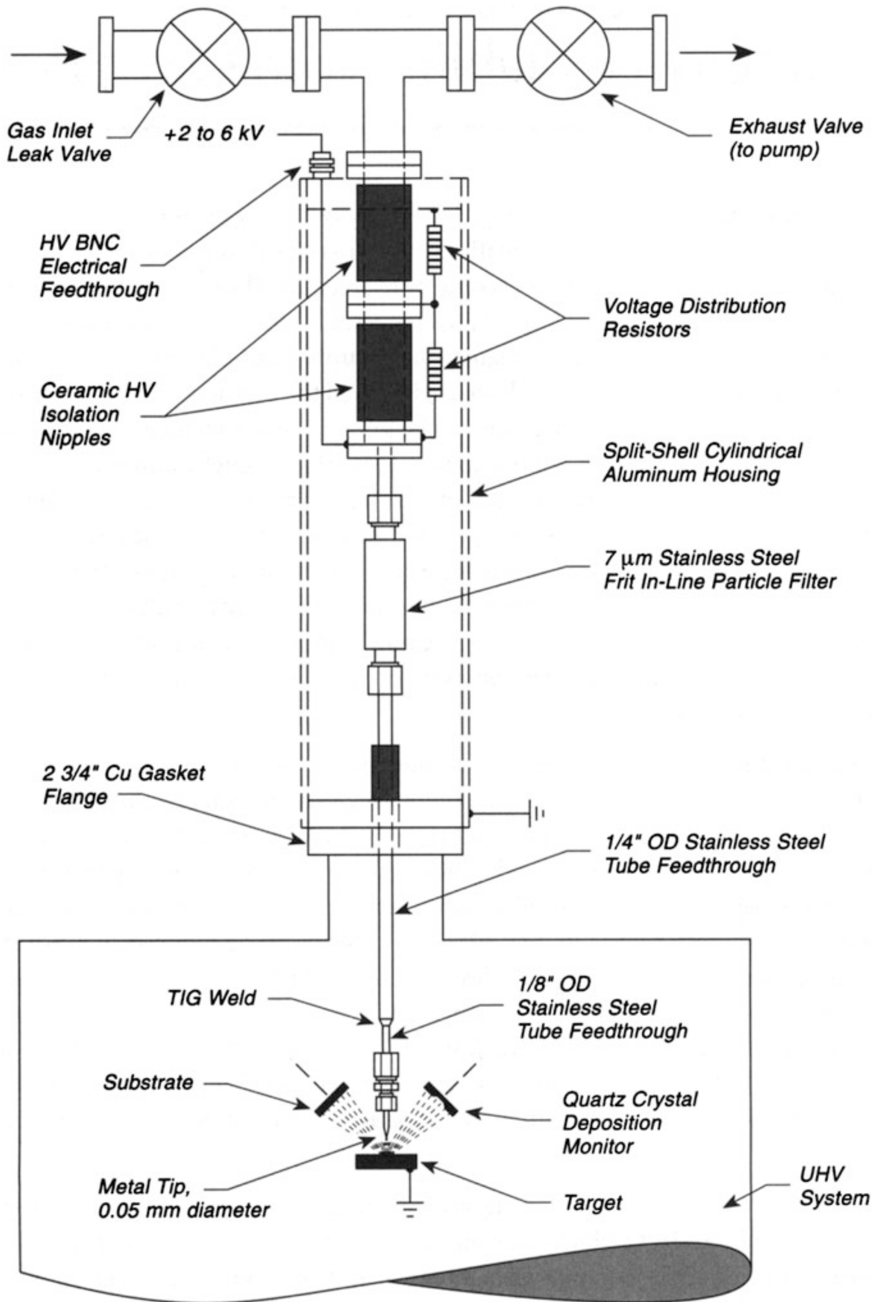

Fig. 21.4 Sputter ion gun—cold cathode

3×10^{-3} Torr range. If the supply pressure is too low, arcing will occur in the high-voltage nipples on the gas supply line. If the pressure is too high, or the orifice diameter is too large, a glow discharge will occur in the chamber with little apparent localization. The beam current increases with supply gas pressure up to the point of glow discharge initiation. The high-voltage power supply should be current limited to prevent more than 5–10 mA of current from flowing during such an event.

Another design of a cold cathode sputtering source for metal deposition maybe found in [12].

21.5 Broad Ion Sources—Improved Stability with Oxygen

Broad-beam ion sources are employed for many purposes including sputter deposition, etching, etc. Figure 21.5 schematically shows a typical conventional source, which illustrates the basic principles of more complex sources [13, 14]. The cylindrical chamber contains a cylindrical anode and an axially positioned cathode. Gas for ionization is admitted from the rear of the source. A magnetic field, supplied by either an electromagnetic winding or a permanent magnet, is aligned axially, and the magnetic field diverges slightly as one approaches the front of the source. The purpose of the magnetic field is to cause the electrons emitted from the cathode to have a spiral path length sufficiently long such that each will cause a gas phase ionization event before reaching the anode. The source has two grids on its

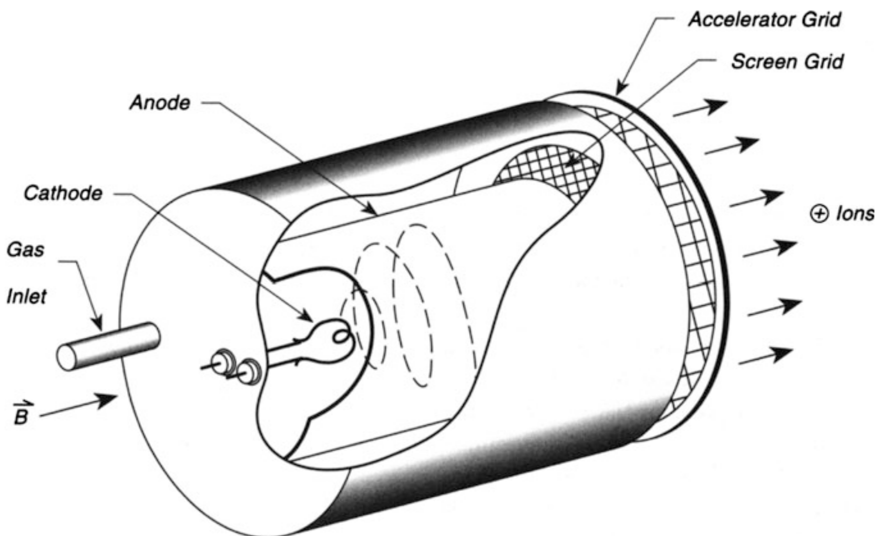

Fig. 21.5 Ion source—axial magnetic field

front side—a screen grid and an accelerator grid. The discharge chamber is normally operated under low-pressure conditions where the mean free path of an electron for ionization is much longer than the apparatus dimensions. The plasma potential is usually within a few volts of the anode potential, and the primary electrons emitted from the cathode therefore have energies close to the potential difference between cathode and anode [13, 14].

When Kaufman sources [13, 14] are used with inert gases or reactive gases at low power levels, they operate for long times without failure. However, at high pressures with reactive gases like O_2, the ion source lifetime is shortened. This is due to failure of the refractory cathode (such as W or Ta), or to buildup of an insulating oxide layer on the anode. Such an insulating layer on the anode reduces the discharge current until it is no longer possible to support a discharge [15]. This lifetime problem can be reduced significantly by using thorium oxide coated Ir cathodes (see p. 133) instead of the more standard bare refractory filaments. For electron emission current densities of 0.2 A/cm^2, the thoriated filament lifetime is 1000 h or longer [16]. As the emission current density is increased, the lifetime decreases as the square of the current density. Multiple filaments, used in series, can extend the lifetime by reducing the current density at each filament [15].

To avoid the buildup of an insulating layer on the anode, it may be sputter-coated with a 1-μm-thick film of IrO_2, which is a conductive metallic oxide. Because this oxide cannot be oxidized further, operation in an intense plasma will not form an insulating layer, as with many anode metal materials. The source, containing both a thoria-coated Ir filament and an IrO_2-coated anode has been operated at 100-W discharge power for about 50 h without degradation of source performance. With an uncoated stainless steel anode, failure occurred in 30 min [15].

Other possibilities exist for using this idea. The anode may be coated with other con-ductive metal oxides such as those from Ru or Re [17, 18]. Alternatively, the anode could be made from the oxide by chemical vapor deposition. Finally, the anode could be made from solid Ir, since an insulating oxide layer will result from its oxidation by the atomic O and other active oxygen species produced in the source [15].

Steinbruchel [19, 20] has studied the emission of both neutral and ionized species produced from a Kaufman-type ion source operating with fluoro- and chlorocarbon species, as well as Ar, Ne, O_2, N_2, and BCl_3. This work involved a line-of-sight quadrupole mass spectrometer as the detector.

Ensinger [21] has written an excellent review of a broad range of ion source designs for many purposes.

21.6 Focusing of Low-Energy Ions by Magnetic Field

There is some interest in producing surface chemical reactions with low-energy ions impinging on the surface. In order to do this effectively, ion current densities at very low energies must be maintained at sufficient levels to carry out surface reactions in a reasonable time. A method is described in which the efficiency of collection of a beam of ions with a diameter of about 7 mm is markedly enhanced with an axial magnetic field [22].

The ions are generated by a Colutron GD-2 ion beam source, and ions are produced with an energy spread of as low as ±0.1 eV. The ions are extracted, focused by an Einzel lens, and mass-filtered with a Wien filter. These ions are directed at an aperture plate of 12-mm thickness containing a 7-mm-diameter hole, as shown in Fig. 21.6a. A tungsten grid (90 % transparency) is placed across the aperture plate. The gap between the grid and the sample to be bombarded is kept between 2 and 5 cm and the ions are decelerated here. The difference between the beam potential and the positively biased sample defines the ion energy at the sample surface. A 2000 G Co-Sm permanent magnet (4-cm diameter) is placed behind the sample at a distance of about 0.5 cm. This magnet can be electrically biased, and sometimes a magnet potential of +200 V above that of the sample has been found to increase the measured ion current collected by the sample. This effect may be due to the collection of secondary electrons from the grid. The 0.5-cm gap is varied during ion collection to maximize the collected ion current at the sample. The magnet can also be removed when surface analytical methods influenced by external magnetic fields are employed. Obviously the sample must be nonmagnetic.

Figure 21.6b shows the effect of magnetic focusing on an Ar^+ ion beam incident on a Pt sample. A dramatic increase in the collected current below an ion energy of 10 eV is noted, where the initial ion current at 1000 eV is 400 nA. The ion beam energy spread at the sample is about ±0.5 eV. The paper [22] describing this work contains an analysis of the effect of the cyclotron motion of the ions in the magnetic field on their divergence. This method is simple and cost effective compared to electrostatic focusing methods when a small ion beam spot diameter is not a critical concern.

21.7 Low Energy Ion Gun—Construction and Performance

The conversion of a conventional high energy ion gun into a low energy gun can be carried out, preserving the ion current capability as well as the spatial and the energy resolution capability [23]. Several low energy ion guns have been described in Sects. 21.1–21.6 of this book, but all requizre the construction of new ion optics. This design uses existing ion optics and electronic control capabilities of a commercial ion gun. It can be used where it is desired to use low energy ions as reactive

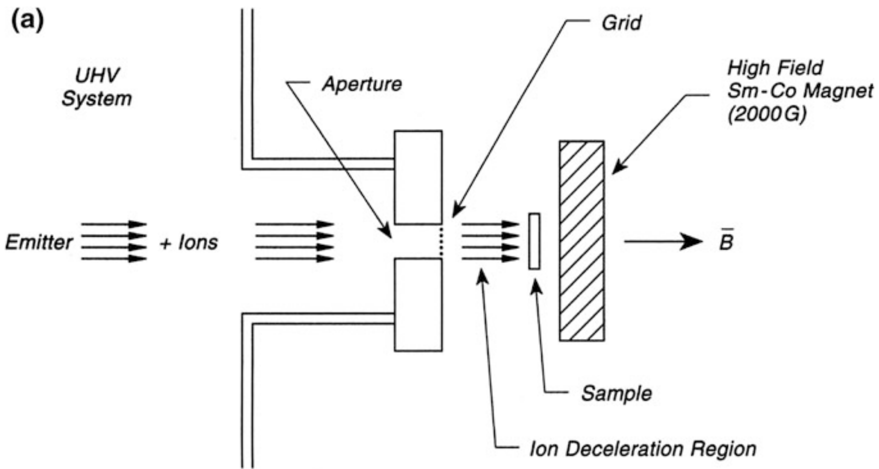

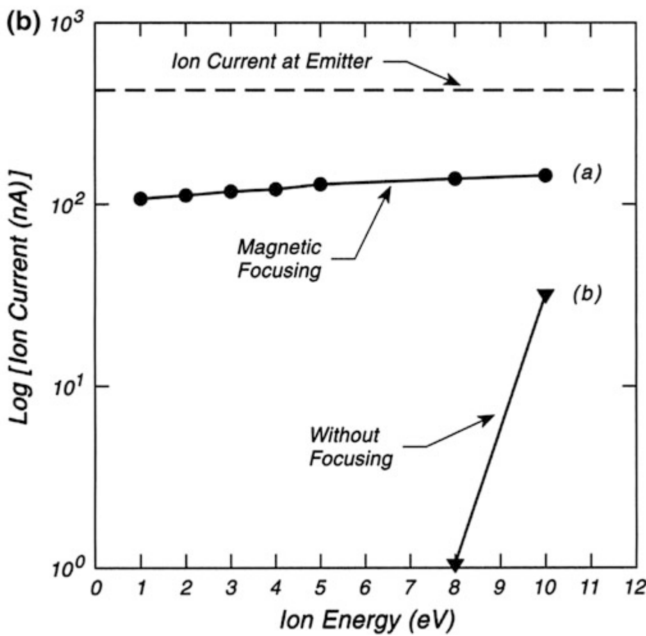

Fig. 21.6 Focusing of low-energy ions by magnetic field. **a** Ion deceleration in magnetic field. **b** Ion collection efficiency

species without significant sputter damage at the target. The chemistry measured will be that of the neutral, ion because of efficient ion neutralization at surfaces.

Figure 21.7a shows a schematic of the original and modified ion guns. Essentially, the conversion to the low ion energy regime is achieved by biasing the entire ion gun to about −5 kV. This is achieved by the use of ceramic standoffs to

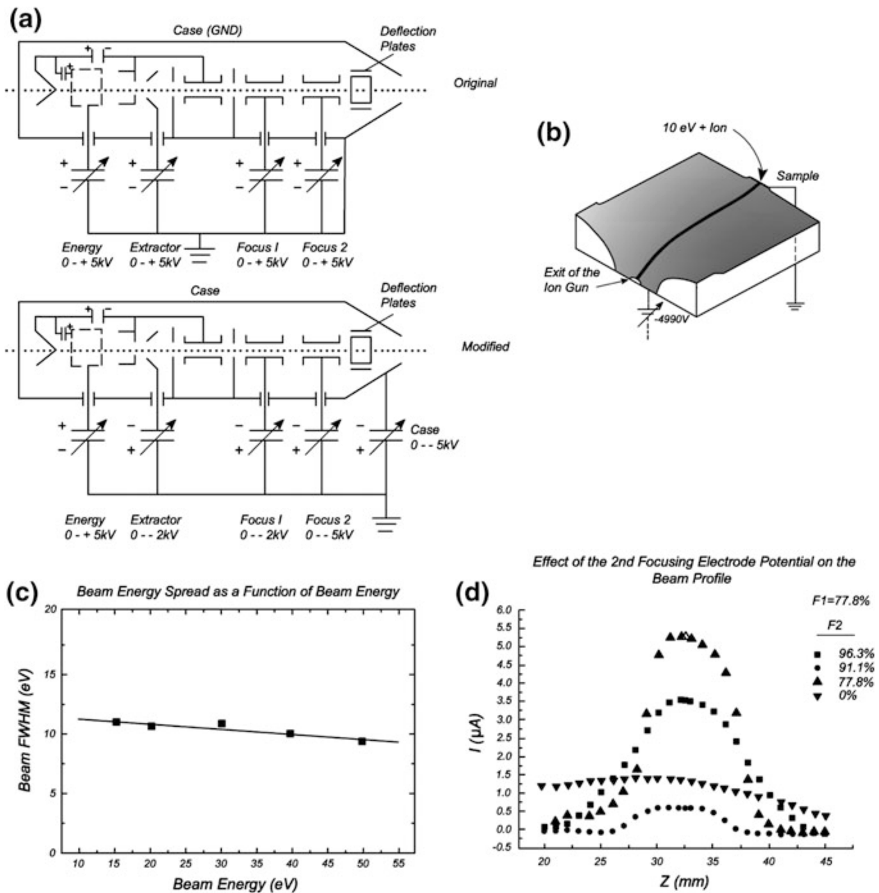

Fig. 21.7 Low energy ion gun. **a** Modification to the ion gun for low energy application. **b** Ion potential energy. **c** Energy spread. **d** Ion beam profile

isolate the outer case of the ion gun at its 2¾ in. Conflat flange, and then to float the gun at high negative potential. Great care should be used to prevent laboratory workers from making accidental contact with the lethal retarding voltages on the electrically isolated ion gun. This can be done by covering everything at high potential with a plexiglass shield.

Figure 21.7b shows the potential energy surface experienced by a positive ion under conditions when it is desired to deliver the ion to a surface with 10 eV of kinetic energy. Most of the loss of ion energy occurs near the exit of the ion gun, but small additional retardation occurs near the front of the sample as shown. In this particular simulation [24], the sample and the walls of the vacuum are at ground.

The measured beam energy spread as a function of ion energy is shown in Fig. 21.7c. About 2 eV change in halfwidth of the ion beam is seen over the energy range 10–50 eV.

By moving the sample across the ion beam, an approximate estimate of the beam profile could be made. Using the % FI potential shown, the F2 % potential is varied. For F2 from 77.8 to 91.1 %, total beam widths from 3–4 mm are observed. As F2 is raised to 96.3 % the beam width degrades to 8–9 mm. In addition the maximum ion current received by the sample decreases at high values of F2. Ion beam profiles are shown in Fig. 21.7d.

21.8 Measuring Ion Beam Dimensions

The size of ion beams used in research can be measured easily [25] by using the fact that ion-irradiated $Gd_2(MoO_4)_3$, called GMO, becomes passivated toward attack by dilute hydrofluoric acid, HF(aq). This passivation occurs for the *c*-surfaces (001 plane) of GMO crystals, when irradiated with 1–2 keV He^+, Ne^+, and Ar^+.

The GMO crystal is polished down to a surface finish achieved with 1-μm alumina abrasive and then may be irradiated with the ion beam as shown in Fig. 21.8. Following irradiation, the crystal is removed and etched with 1 % HF(aq). The area exposed to the ion beam is almost unaffected by the HF, whereas the surrounding areas are etched away. The imaging of the ion beam is reported to have l-μm lateral resolution, and to be much more sensitive than the competitive technique in which a Ta_2O_5 anodic film on Ta is bombarded until metallic Ta is exposed. The authors warn that the technique is an integrating technique, and the pattern will therefore reflect any wandering of the ion beam during the irradiation period. The technique is quite useful for grazing incidence ion beams.

Three more accurate methods for measuring ion beam sizes and the divergence of an ion beam are given in [26]. Here, a HgCdTe substrate covered with a photoresist is used in one method, or movable collectors are used in the latter two methods.

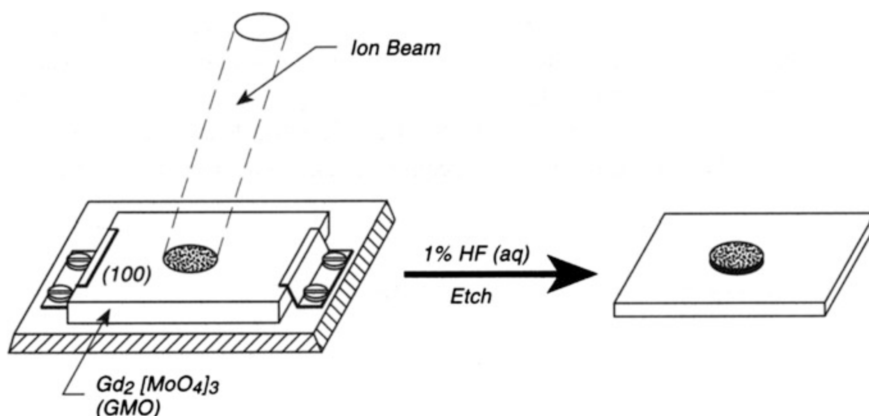

Fig. 21.8 Measuring ion beam dimensions

21.9 Beam Position Monitor—Charged Particles

The alignment of a beam of ions or electrons may be facilitated by the use of a segmented aperture device [27] shown in Fig. 21.9. A simple bridge circuit is used, with a current measuring device to monitor the imbalance in collected current between opposing segments of the aperture. Only one of the two bridges is shown in the Figure. Several of these monitors may be placed along the beam axis, and any ions or electrons scattered by the edges of the apertures are removed by other apertures further down the beam axis. The variable shunt around the monitor allows the fraction of the collected current going to the current monitor to be adjusted.

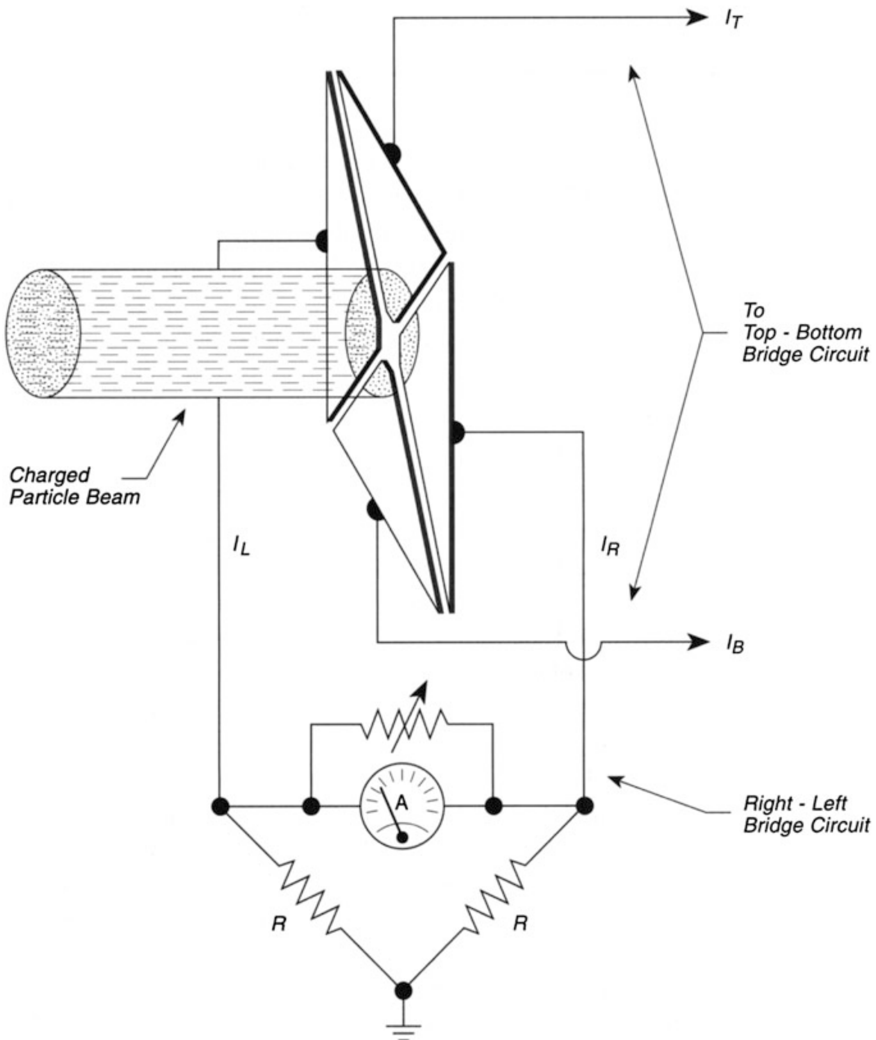

Fig. 21.9 Beam position monitor—charged particles

Varying the value of the resistance, R, over a wide range has little effect on the meter deflection, but R should be kept as small as possible to avoid charge buildup on the segments that could cause beam aberrations.

21.10 Pulse-Counting LEED/ESDIAD Analyzer—Using MicroChannel Plate Detection

There are many advantages in pulse counting during the measurement of either electron diffraction or ion angular distribution patterns produced by electron beam excitation of surfaces (ESDIAD). Pulse counting affords the maximum sensitivity to particle measurement, assuming)each pulse is counted. The digitized information arising from pulse counting allows easy handling in computer analysis and error analysis. But most importantly, the high sensitivity of pulse counting techniques allows one to work with electron beams having low intensities, thereby minimizing damage to the surface layer during measurement [28, 29].

Figure 21.10a shows a LEED/ESDIAD apparatus [30] that uses four grids in front of a pair of microchannel plate (MCP) amplifiers [31]. Charged particles (and, in some cases, excited neutral particles) are transmitted through the grid system to the microchannel plate amplifiers, where each particle exciting the microchannel plate produces a cascade of electrons that exit the back of the second microchannel plate and are accelerated into a two-dimensional resistive anode detector [32]. This pulse of about 10^5 or 10^6 electrons expands radially from the point of impact and is collected at the four corners of the resistive anode. Since the local intensity of expanding charge decreases as $1/r$, the pulse height arriving at the four corners can be used to calculate the coordinates of the point of impact (the centroid). The pulses at the four corners are capacitively coupled into four preamplifiers, A-D. These amplified pulses then travel into the position computer [33]. The position computer then generates a pair of pulses which are proportional to the x- and y-coordinates of the impact point on the resistive anode. The x- and y-pulses are then sent to a pair of analog-to-digital converters that form the input to either a multichannel analyzer [34] or to a computer. A three-dimensional display of the collected angular distribution of the electron or ion or excited neutral pattern is then displayed. It is important to point out that the excitation of the crystal surface by the electron beam will produce a background due to soft X-rays, and this must be subtracted from the measured patterns [35, 36]. The ultimate spatial resolution of the apparatus is about 0.3°. Typical electron beam currents of the order of 1×10^{-9} A are employed over time periods of the order of 100 s. Damage to even the most electron-beam-sensitive surface species is generally less than 1 %. The positive ion patterns viewed in this apparatus may be compressed by applying a positive potential, V_c, to the crystal.

Examples of both typical LEED patterns and ESDIAD patterns are shown in Fig. 21.10b, c for the case Cu(110) and CO chemisorbed on Cu(110) [37]. An earlier example of this technology applied to LEED measurements alone can be found in [38].

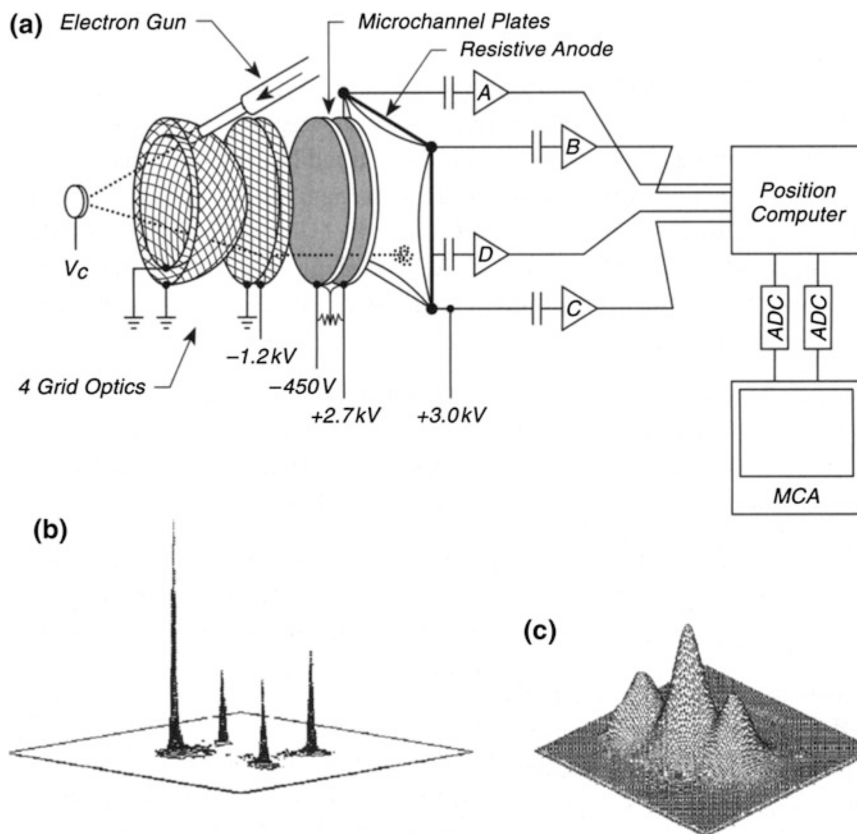

Fig. 21.10 Pulse counting LEED/ESDIAD. **a** Pulse counting LEED/ESDIAD analyzer. **b** Typical LEED pattern—Cu(110). **c** Typical ESDIAD pattern—CO/Cu(110)

Earlier examples of the use of microchannel plate amplification for ESDIAD or LEED measurements involved the production of images on phosphor screens and either photographic [39–42] or video camera [43–47] data acquisition. The video camera method is efficient in the sense that a single video camera can be used on multiple systems.

An alternate high-resolution position detector is the wedge-and-strip anode [40, 41] that captures the electron pulses on a conductive sheet containing accurately shaped wedge and strip conductive regions. The spatial resolution of these devices exceeds the inherent resolution limitations of the microchannel plate amplifiers [40, 41].

A LEED analyzer built along the principle of the MCP/resistive anode combination has been reported by others [46, 48, 49]. In addition, a gated movable channeltron detector, coupled with a chopped electron beam, has been used to reduce background effects [50].

The counting efficiency for ions on a MCP detector has been carefully measured using a field evaporation apparatus [51]. It was found that the application of a positive bias on the front surface of the channel plate did not increase the capture/counting efficiency much above that expected from the fractional area of open channels present on the plate. It was, however, argued by others that a small positive potential (20 V) facilitated capture of secondary electrons and hence enhanced the counting efficiency [52], and this effect was verified in a careful paper in which the absolute detection efficiencies for He^+, H^+, and O^+ ions was directly measured using a Faraday cup to compare with the count rate. Ion detection efficiencies ranged from 18 to 63 % in the energy range 250–5000 eV [53]. These workers also measured the detection efficiency as a function of incident angle, finding that an incident angle of about 10° yielded maximum efficiency, with the efficiency falling 24 % in the range 20–40° off the channel axis direction [53].

The basic physical properties of straight through MCP arrays, chevron MCP arrays, and curved channel MCP arrays are discussed in some detail in [54].

Field penetration effects from one region of the LEED apparatus to another can be prevented in most cases by using neighboring grids at the same bias potential to screen elements at high potential (such as the front of the MCP) from the interior of the grid system [55].

The hemispherical grid analyzer may be used as a retarding field energy analyzer for either electrons or ions. For these measurements, the retarding potential ramp is applied to a central grid along with a small sinusoidal modulating voltage, and lock-in detection is applied to the transmitted current. This has been discussed in detail in [56].

A planar grid ESDIAD apparatus has been used to monitor the angular distribution of ions emitted from an insulator surface as a result of excimer laser pulses [57].

21.11 Time-of-Flight Measurements for Ions Generated in ESDIAD

Section 21.10 describes the design and use of an ESDIAD apparatus in which positive ions, produced in electron stimulated desorption (ESD), are imaged spatially as they are ejected from surface species. These measurements are used to determine the chemical bond directions in adsorbed species on single crystal surfaces [29] and the dynamical behavior of the molecules as they undergo low frequency motions on their binding sites [58].

Detailed information about desorbing ions can be obtained if their momentum is also measured, using a pulsed electron beam, and measuring the flight time between the crystal and the detector. The flight time will directly yield the ion velocity, except that it is safest to measure changes in flight times with various accelerating potentials to derive the ion energy and mass (i.e. the momentum). An apparatus [59] to measure the time-of-flight (TOF) of desorbing ions is shown in Fig. 21.11a. The apparatus is capable of measuring the desorbing direction and the flight time for

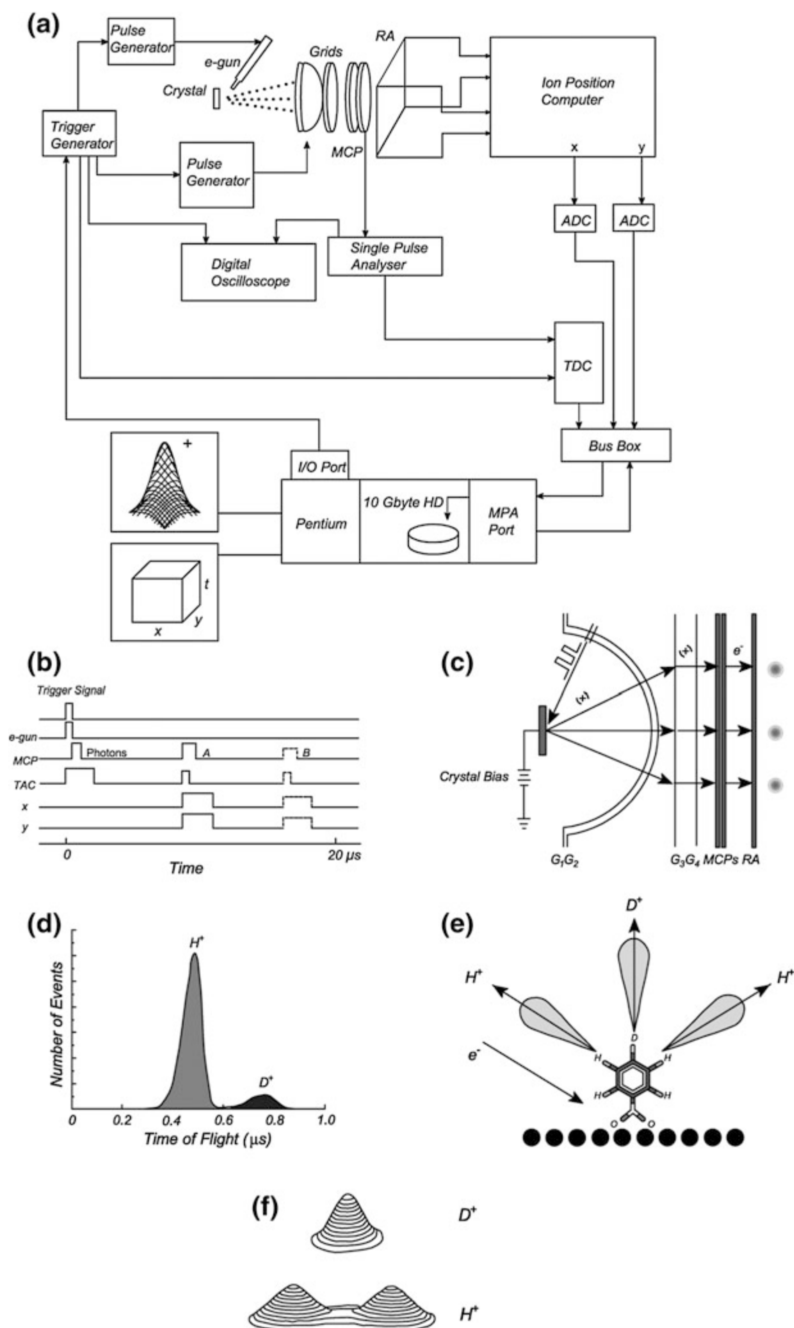

Fig. 21.11 Time of flight measurements in ESDIAD. **a** Schematic circuit for TOF measurement of positive ions in ESDIAD. **b** Time sequence of pulses and signals. **c** ESDIAD analyzer and pulsed electron beam. **d** Time-of-flight separation of H^+ and D^+. **e** Benzoate on Cu(110). **f** ESDIAD patterns of H^+ and D^+ from isotopic benzoate molecules

each ion comprising the ESDIAD pattern. Time resolution is in the picosecond range and data acquisition up to 100 kHz is achievable. This enables the deconvolution of the spatial distribution and the momentum of each ion. The reader is referred to [59] for details of the electronics shown in Fig. 21.11a.

Figure 21.11b shows the time sequences for various pulses. Initiated by a trigger signal, an electron gun ejects an electron pulse of variable time width down to 5 ns. Positive ions A and B arrive at the MCPs at different times. The flight time of an ion is recorded along with the x and y coordinates of its arrival at the MCP. A drawing of the hemispherical analyzer and the pulsed electron and ion beams is shown in Fig. 21.11c. The ions, after being amplified and converted to electrons in the MCPs, are counted by the resistive anode (RA) which yields the coordinates of ion arrival there. For the adsorption of the benzoate ion, oriented normally on Cu(110) by adsorption through the COO group, three hydrogenic ion beams are shown in Fig. 21.11e corresponding to the 3-, 4-, and 5- positions on the phenyl ring. By using the TOF method, the two H^+ ions corresponding to the 3- and 5- C–H bonds are measured at 60° to the normal. Using a deuterium label at the 4-position, a D^+ beam is observed at the 4-position which produces a normally-oriented beam [60, 61]. The D^+ ion has a longer TOF due to its heavier mass as shown in Fig. 21.11d. The separate ion angles are plotted in Fig. 21.11f as contour diagrams. The difference in yield of H^+ and D^+ is due to several factors related to the departing speed of the ion which strongly controls its neutralization and to smaller differences in the rate of the neutralization of the departing ions originating from different positions on the phenyl ring [61].

21.12 Ion Detection with Kinetic Energy and Mass Resolution Using a Hemispherical Energy Analyzer

In photon or electron stimulated desorption one may require both mass analysis of the ions as well as energy resolution. This problem was first addressed by Feulner [62, 63], using a simple retarding field analyzer coupled to a microchannel plate (MCP) assembly and readout by a multichannel analyzer (MCA), as shown in Fig. 21.12a. The macrostructure of the ion peaks yields the masses of the ions in each peak; the microstructure (peak shape) yields the energy distribution as schematically indicated in the spectrum shown.

A more elaborate analyzer can be made from a hemispherical electron energy analyzer as shown in Fig. 21.12b. If "single punch (pulsed) light" is not available, an electrostatic gate is placed in front of the entrance aperture to the hemispherical analyzer. It is a pair of deflection plates placed inside a screening box. A symmetric square wave is applied to these deflection plates in order to modulate the transmitted ion beam. The signals from the 5 channeltron multipliers—used for

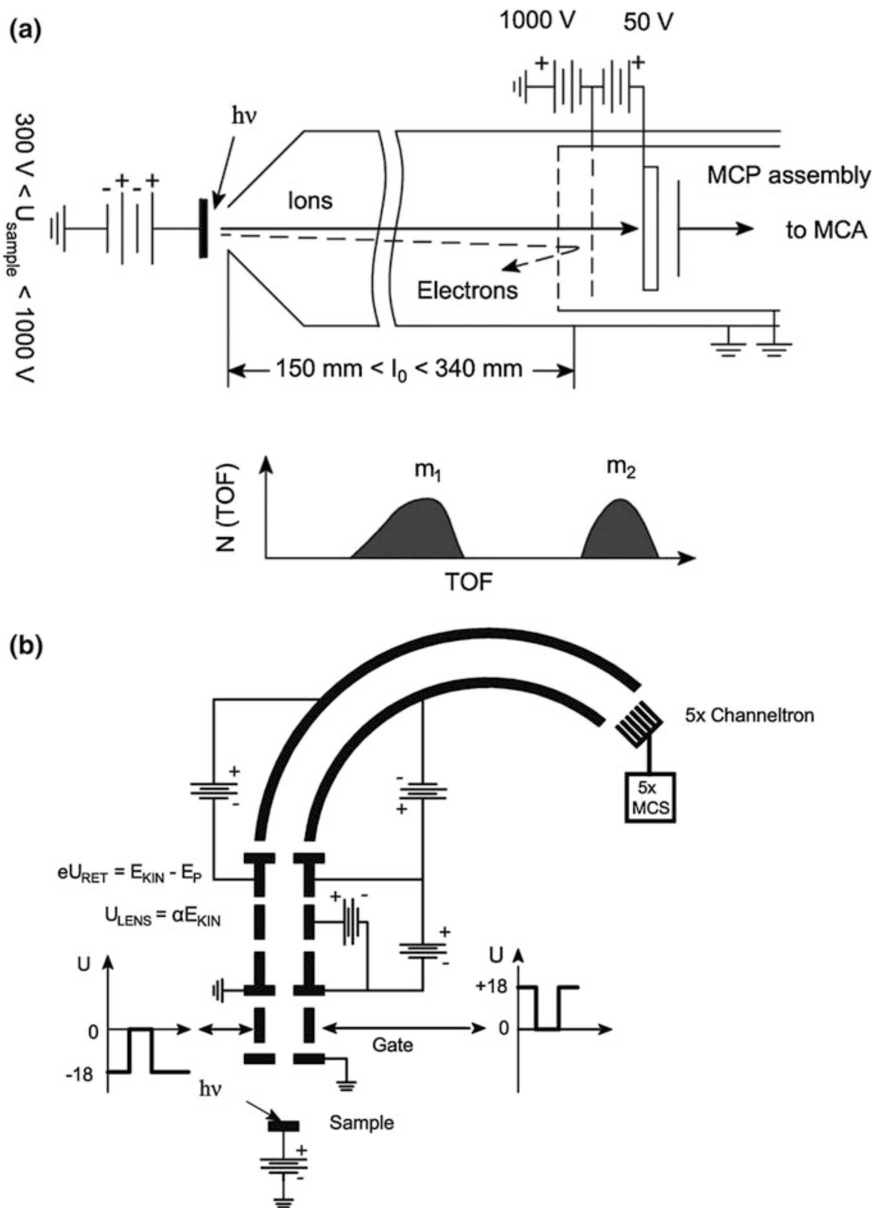

Fig. 21.12 Ion detector—kinetic energy and mass resolution. **a** Retarding field TOF [58]. **b** Hemispherical-TOF analyzer

increased sensitivity—are fed into multi-page, multi-channel scalars that are synchronized with the modulation of the ions. In this manner, 2D fields are obtained with the axes "kinetic energy" and "flight time". From this information the kinetic energy distributions of the individual ions can be extracted [62].

21.13 Time-of-Flight Detection for Laser-Ionized Neutrals

The detection of neutral atoms and molecules that have been generated from surfaces using scattering, electron- and photon-stimulated desorption, and ion-induced desorption is facilitated by tunable nanosecond pulsed lasers. Laser excitation permits particle detection with quantum state specificity using laser-induced fluorescence (LIF) or resonance-enhanced multiphoton ionization (REMPI) methods. The REMPI technique has proven to be more popular because of the high sensitivity of the ion detection technique and the ability to image ion angular distributions analogous to the ESDIAD technique (see p. 225).

The apparatus shown in Fig. 21.13 was designed to detect laser-ionized neutral atoms and molecules that have undergone electron stimulated desorption from a single crystal surface [64, 65]. It is based on the design developed by N. Winograd et al. [66] for the detection of neutral atoms desorbed by ion bombardment. The

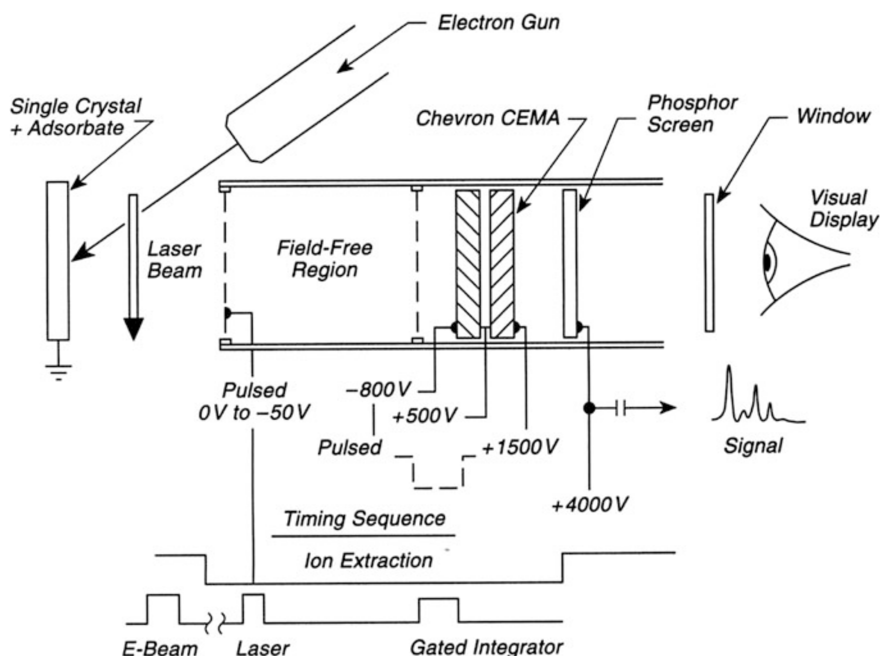

Fig. 21.13 Time-of-flight detection for laser-ionized neutrals

pulsed electron gun shown in the Figure therefore can be replaced by a pulsed ion gun or a pulsed laser, and the detection scheme is the same. The principle is as follows. Neutral products that leave the surface as a result of excitation by the pulsed source must travel a specified distance before they enter the ionizing laser beam, which is directed parallel to the crystal surface. The laser generated ions are then accelerated into the chevron electron multichannel plate array (CEMA) detector [67]. The output of the detector is coupled to a phosphor screen. Provided that the laser is focused in a sheet-like fashion, the visual display on the phosphor screen provides angular resolved patterns of the desorbed neutrals, as in the ESDIAD method, but now with full internal quantum state resolution [65, 66]. The integrated signal can be detected with a gated integrator or the two-dimensional image can be digitized using a charge-coupled device (CCD) camera.

By pulsing the electron beam rapidly (1 μs), the velocities of the neutrals can be measured by the time delay between the pulses of the electron gun and the laser. Desorbed ions can be a problem, but they can be swept away prior to the laser pulse by an applied potential to the first grid and/or the crystal. It is also possible to discriminate against unwanted signals by pulsing the applied voltage on one of the multichannel plates. Recently several groups have oriented the detection assembly 90° to the surface normal, so that the spread in velocities is obtained simultaneously with the angular distribution [68].

References

1. Data sheet for Ion source IQ 10/35, SPECS, GmbH (1996)
2. C.T. Campbell, S.M. Valone, J. Vac. Sci. Technol. **A3**, 408 (1985)
3. A. Winkler, J.T. Yates Jr, J. Vac. Sci. Technol. **A6**, 2929 (1989)
4. Design provided by Dr. J. Ahner and D. Mocuta, Surface Science Center, University of Pittsburgh
5. T. McCabe, J. Somers, M.E. Bridge, D.R. Lloyd, J. Vac. Sci. Technol. **A5**, 119 (1987)
6. V.M. Bermudez, R.E. Thomas, J. Vac. Sci. Technol. **A1**, 1557 (1983)
7. J. Kirschner, Rev. Sci. Instrum. **57**, 2640 (1986)
8. M. Khan, J.M. Schroeer, Rev. Sci. Instrum. **42**, 1348 (1971)
9. A.R. Krauss, Argonne National Laboratory, 9700 South Cass Avenue, Argonne, IL 60439 (private communication)
10. J.F. Mahoney, J. Perel, A.T. Forrester, Appl. Phys. Lett. **38**, 320 (1981)
11. The wire bonding tool is available from Technical Devices, Inc., 5721 Prescott Road, Prescott, AZ 86301
12. C. Kim, D.F. Ogeltree, M.B. Salmeron, X. Godechot, G.A. Somorjai, I.G. Brown, Appl. Surf. Sci. **59**, 261 (1992)
13. H.R. Kaufman, J.J. Cuomo, J.M.E. Harper, J. Vac. Sci. Technol. **21**, 725 (1982)
14. J.M.E. Harper, J.J. Cuomo, H.R. Kaufman, J. Vac. Sci. Technol. **21**, 737 (1982)
15. C.R. Guarnieri, K.V. Ramanathan, D.S. Yee, J.J. Cuomo, J. Vac. Sci. Technol. **A6**, 2582 (1988)
16. G.A. Haas, Thermionic emission sources (AD266039 Electron Tubes Branch, Electronic Division, U.S. Naval Research Laboratory, Washington D.C., 1961), p. 13. (For sale by Superintendent of Documents, U.S. Government)
17. D.B. Rogers, R.D. Shannon, A.W. Sleight, J.L. Gillson, Inorg. Chem. **8**, 841 (1969)

18. L.F. Mattheiss, Phys. Rev. **181**, 987 (1969)
19. Ch. Steinbruchel, J. Vac. Sci. Technol. **B2**, 38 (1984)
20. Ch. Steinbruchel, J. Appl. Phys. **59**, 4151 (1986)
21. W. Ensinger, Rev. Sci. Instrum. **63**, 5217 (1992)
22. D.R. Strongin, J.K. Mowlem, K.G. Lynn, Y. Kong, Rev. Sci. Instrum. **63**, 175 (1992)
23. I. Popova, R. Muha, Z. Chen, J.T. Yates Jr, J. Vac. Sci. Technol. **A21**, 401 (2003)
24. SimIon program 7.0
25. A.S. Bhalla, L.L. Tongson, J. Vac. Sci. Technol. **21**, 1039 (1982)
26. S. Maniv, Rev. Sci. Instrum. **62**, 1179 (1991)
27. K.J. Snowdon, C.H. Barber, J. Phys. **E12**, 923 (1979)
28. C.G. Pantano, T.E. Madey, Appl. Surf. Sci. **7**, 115 (1981)
29. R.D. Ramsier, J.T. Yates Jr, Surf. Sci. Rep. **12**, 243 (1991)
30. J.T. Yates, Jr., M.D. Alvey, K.W. Kolasinski, and M.J. Dresser, Nucl. Inst, and Methods in Phys. Res. **B27**, 147 (1987). The first apparatus of this sort for low incident current LEED studies was reported in P.C. Stair, Rev. Sci. Inst. **51**, 132 (1980)
31. Galileo Electro-Optics Corp., Galileo Park, P.O. Box 550, Sturbridge, MA 01566
32. No. 3394D Quantar Technology, Inc., 3004 Mission Street, Santa Cruz, CA 95060–95700
33. No. 2401 Quantar Technology, Inc., 3004 Mission Street, Santa Cruz, CA 95060–95700
34. No 76B Canberra Industries, Inc., Nuclear Products Group, 800 Research Parkway, Meriden, CT 06450
35. M.J. Dresser, M.D. Alvey, J.T. Yates Jr, Surf. Sci. **169**, 91 (1986)
36. M.J. Dresser, M.D. Alvey, J.T. Yates Jr, J. Vac. Sci. Technol. **A4**, 1446 (1986)
37. J. Ahner, D. Mocuta, R.D. Ramsier, J.T. Yates Jr, J. Vac. Sci. Technol. **A14**, 1583 (1996)
38. P.C. Stair, Rev. Sci. Instrum. **51**, 132 (1980)
39. J.J. Czyzewski, T.E. Madey, J.T. Yates Jr, Phys. Rev. Lett. **32**, 777 (1974)
40. M.G. Lagally, J.A. Martin, Rev. Sci. Instrum. **54**, 1273 (1983)
41. D.F. Ogletree, G.S. Black-man, R.Q. Hwang, U. Starke, G.A. Somorjai, J.E. Katz, Rev. Sci. Instrum. **63**, 104 (1992)
42. V.M. Bermudez, J. Vac. Sci. Technol. **A5**, 2975 (1987)
43. T.E. Madey, J. Vac. Sci. Technol. **A4**, 257 (1986)
44. T.E. Madey, Science **234**, 316 (1986)
45. D.F. Ogletree, G.A. Somorjai, J.E. Katz, Rev. Sci. Instrum. **57**, 3012 (1986)
46. R.A. Malic, Rev. Sci. Instrum. **59**, 1951 (1988)
47. G. Held, S. Uremovic, C. Stellwag, D. Menzel, Rev. Sci. Instrum. **67**, 378 (1996)
48. E.G. McRae, R.A. Malic, D.A. Kapilow, Rev. Sci. Instrum. **56**, 2077 (1985)
49. F.-K. Men, B.L. Clothier, J.L. Erskine, Rev. Sci. Instrum. **64**, 1883 (1993)
50. H. Niehus, B. Krahl-Urban, Rev. Sci. Instrum. **52**, 56 (1981)
51. T. Sakurai, T. Hashizume, Rev. Sci. Instrum. **57**, 236 (1986)
52. J.A. Panitz, J.A. Foesch, Rev. Sci. Instrum. **47**, 44 (1976)
53. R.S. Gao, P.S. Gibner, J.H. Newman, K.A. Smith, R.F. Stebbings, Rev. Sci. Instrum. **55**, 1756 (1984)
54. J.G. Timothy, Rev. Sci. Instrum. **52**, 1131 (1981)
55. C.W. Caldwell Jr, Rev. Sci. Instrum. **36**, 1500 (1965)
56. N.J. Taylor, Rev. Sci. Instrum. **40**, 792 (1969)
57. J.T. Dickinson, S.C. Langford, J.J. Shin, D.L. Doering, Phys. Rev. Lett. **73**, 2630 (1994)
58. J.T. Yates Jr, J. Ahner, D. Mocuta, Proc. Nat. Acad. Sci. **95**, 443 (1998)
59. J. Ahner, D. Mocuta, J.T. Yates Jr, J. Vac. Sci. Technol., A **17**, 2333 (1999)
60. J. Lee, O. Kuzmych, J.T. Yates Jr, Surf. Sci. **582**, 117 (2005)
61. J. Lee, I.A. Balabin, D.N. Baratan, J.-G. Lee, J.T. Yates Jr, Chem. Phys. Lett. **412**, 171 (2005)
62. R. Weimar, R. Romberg, S.P. Frigo, B. Kassühlke, P. Feulner, Surf. Sci. **451**, 124 (2000)
63. P. Feulner, private communication
64. A.R. Burns, E.B. Stechel, D.R. Jennison, in *Desorption Induced by Electronic Transitions, DIET III*, ed. by R.H. Stuhlen, M.L. Knotek (Springer, Heidelberg, 1988), p. 67
65. A.R. Burns, Surf. Sci. **280**, 349 (1993)

66. R.H. Kobrin, G.A. Schick, J.P. Baxter, N. Winograd, Rev. Sci. Instrum. **57**, 1354 (1986)
67. CEMA assemblies are available from Galileo Electro-Optics Corp., Galileo Park, P.O. Box 550, Sturbridge, MA 01566
68. M. Menges, B. Baumeister, K. Al-Shamery, B. Adam, T. Mull, H.-J. Freund et al., in Desorption Induced by Electronic Transitions, DIET V, ed. by A.R. Burns, E.B. Stechel, D.R. Jennison (Springer, New York, 1993), p. 275

Chapter 22
Photons (UV)

22.1 Hollow Cathode Resonance Lamp for He(II) (40.8 eV) Photoemission

The use of vacuum ultraviolet sources for valence band photoemission studies of the surfaces of solids is widespread, and many such studies are made on synchrotron sources. Small laboratory vacuum UV sources predated synchrotron sources, and are still widely used. A high-intensity source delivering both He(I) and He(II) radiation, depending upon the discharge conditions, is shown schematically in Fig. 22.1a [1]. He gas is admitted to a differentially pumped region containing a hollow cathode, and is pumped away continuously by a trapped forepump. A second stage of differential pumping occurs closer to the ultrahigh vacuum chamber using a diffusion pump that is backed by the same forepump. The forepump (rated at 500 L/min) speed was measured to be 100–200 L/min at the lamp and 30–70 L/min at the back of the diffusion pump for typical operation [2]. The forepump was trapped with a water-cooled Cu trap and a zeolite trap. An 8-cm-diameter port at the lamp leading to the liquid nitrogen trap before the diffusion pump was used [1], as an aid to improve pumping speed over that originally used [2]. This large port was made from a straight-through valve. This permits the lamp to be isolated from the UHV system.

Figure 22.1b shows the details of the He lamp. A high-voltage UHV feed through holds a hollow cathode cylinder made of 0.5 mm Ta sheet. This cathode, 2 cm in diameter and 4–6 cm in length, is held inside a glass tube in a location in which a stainless steel capillary (2.3-mm internal diameter) picks up radiation at a distance of 1–1.5 cm from the end of the cathode. The glass discharge region can be removed for cleaning. A needle valve admits He into the side of a Conflat flange that mates to the flange holding the first stainless capillary tube. Below the first capillary is the region pumped by the forepump, region A-B. A second capillary, mounted between B and C, directs the radiation to a third capillary which enters the UHV chamber. The He pressure in the system with the lamp operating is approximately 1×10^{-8} Torr. Contaminant gases are measured to be below 10^{-10} Torr, although such gases will be

© Springer International Publishing Switzerland 2015

J.T. Yates Jr., *Experimental Innovations in Surface Science*,
DOI 10.1007/978-3-319-17668-0_22

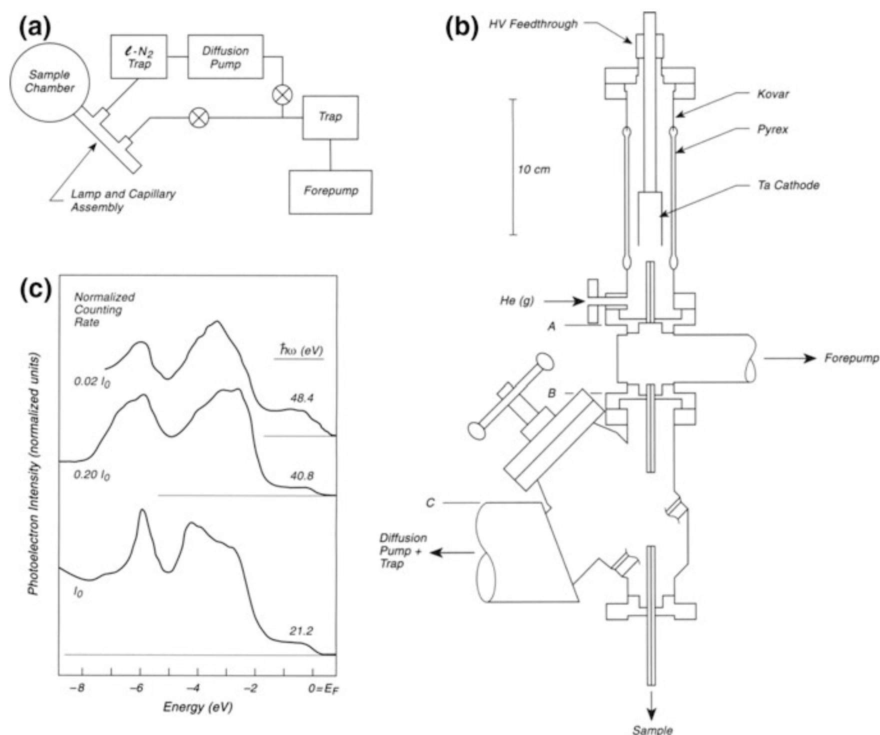

Fig. 22.1 Hollow Cathode resonance lamp—He(II) source. **a** Pumping system. **b** VUV lamp. **c** Au UPS spectrum

highly directed as a beam to the sample by the capillaries, and one should be alert to the possible build up of surface contamination.

The performance of the lamp for both He(I) (21.2 eV) and He(II) (40.8 eV), and for 48.4 eV radiation, is shown in Fig. 22.1c, where an evaporated Au film was studied, using a double-pass CMA electron spectrometer for measurement of the photoelectron spectrum at a constant resolution of 0.2 eV. The pressure of He in the discharge was about 1 Torr for optimum He(I) intensity and 0.1–0.2 Torr for 40.8 eV and 48.4 eV photons. This lamp has improved He(II) intensity compared to earlier lamps utilizing a microwave discharge [3].

22.2 He(I) and He(II) Ultraviolet Resonance Source

A laboratory source of vacuum ultraviolet radiation useful for photoelectron spectroscopy in an ultrahigh vacuum chamber is described [4]. The source is based on the principle of the charged particle oscillator [5–8]. The production of maximum He(I) (21.22 eV) and He(II) (40.81 eV) radiation occurs at a discharge

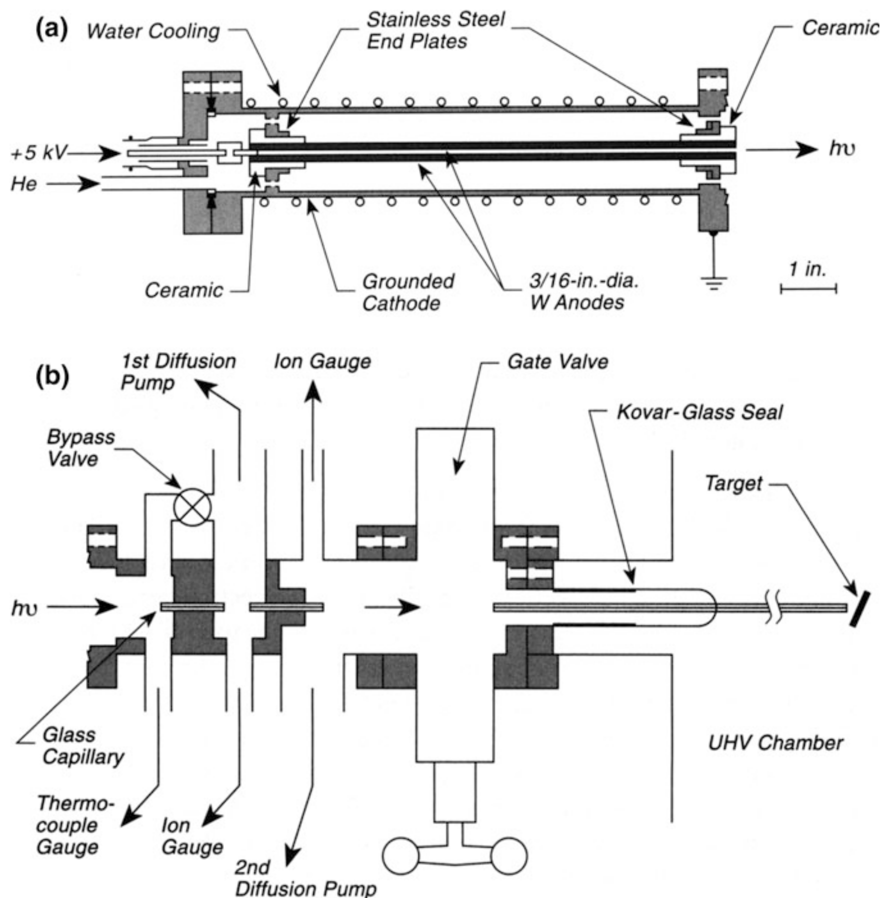

Fig. 22.2 He(I) and He(II) UV source. **a** Cold cathode discharge UV source. **b** Differential pumping system

pressure of He of about 8×10^{-2} Torr. By means of two stages of differential pumping in the source, the pressure in the main UHV chamber can be maintained at 2×10^{-10} Torr during operation.

Figure 22.2a shows the UV source. It consists of a grounded outer cathode cylinder made of 304 stainless steel. Two 3/16-in.-diameter tungsten rods serve as the anode, and they are supported and separated from the outer cathode by machinable ceramic fittings. The W rods can expand and slide in loosely fitting holes in the ceramic as the lamp heats during operation. The ceramic also contains larger holes for conductance of He. The anode potential of 0 to +5 kV is supplied through a high-voltage feedthrough at the rear of the source. Grounded stainless steel end plates cover the inner side of the ceramic fittings to reflect electrons traveling in the axial direction back into the source volume. Photons emerge

through a 0.1-in.-diameter exit aperture between the anodes at the front of the lamp. An aperture with a diameter less than one-third the inner diameter of the cathode allows sampling of the radiation without allowing electrons to escape [9]. The gas used here was 99.9995 % He, which flows through an activated charcoal trap at 77 K and a variable leak valve. A 0 to +5 kV DC power supply (0.500 mA) is connected through a variable resistance ballast set at 16 kΩ. This prevents current surges during initiation of the discharge whose resistance varies from infinity (before activation) to several kΩ during operation.

The pumping system in the lamp consists of two stages of differential pumping, followed by a third stage in the UHV chamber. The first stage, across a 1.5-mm-i.d. Pyrex capillary, 3 cm long, is pumped by a chilled water-trapped 325-L/s oil diffusion pump. This stage can be eliminated by opening a bypass valve between entrance region and the first stage of diffusion pumping. The second stage is also across a similar capillary and is pumped by a liquid-nitrogen-trapped 325-L/s oil diffusion pump. The third stage of pumping across the exit capillary (2.5 mm i.d, 22.86 cm long) is pumped by the UHV system pumps, which consist of a 450-L/s turbopump and a 500-L/s ion pump. A gate valve is used to isolate the source from the UHV system. The original paper shows plots of photoelectron intensity from a Au surface versus pressure [4].

Under optimal operating conditions, the He(I)/He(II) intensity ratio produces a 10/1 ratio of photoelectrons from the two spectral lines from the Au surface.

22.3 Photochemistry on Surfaces Using an Ultraviolet Lamp

Although ultraviolet induced photochemistry research has been carried out for more than 60 years in homogeneous phase, detailed studies of photochemical processes on well-defined single crystal surfaces are much more recent. Because ultraviolet lamps emit more photons over an extended exposure time than most laboratory lasers, these lamps are often used for inducing photochemical processes on surfaces. Both intensity measurements and photon energy range selection using filters are conveniently carried out, permitting good measurements of cross sections versus photon energy for surface process induced photolytically.

Figure 22.3a shows an ultrahigh vacuum chamber [10] set up so that a single crystal may be irradiated with ultraviolet light from a high-pressure Hg arc source [11]. The single crystal is located in front of an aperture that leads to a quadrupole mass spectrometer in a differentially pumped section, permitting the direct measurement of photodesorbed species. In addition, the mass spectrometer maybe used also for thermal desorption studies after ultraviolet irradiation to access the changes that have occurred due to irradiation of an adsorbed layer. The ultraviolet light passes through a 10-cm distilled water filter that filters out infrared radiation. A 200-mm f/1 quartz condensing lens focuses the light onto the crystal through a UV-grade sapphire window. Interference filters (Oriel Corporation) centered on the

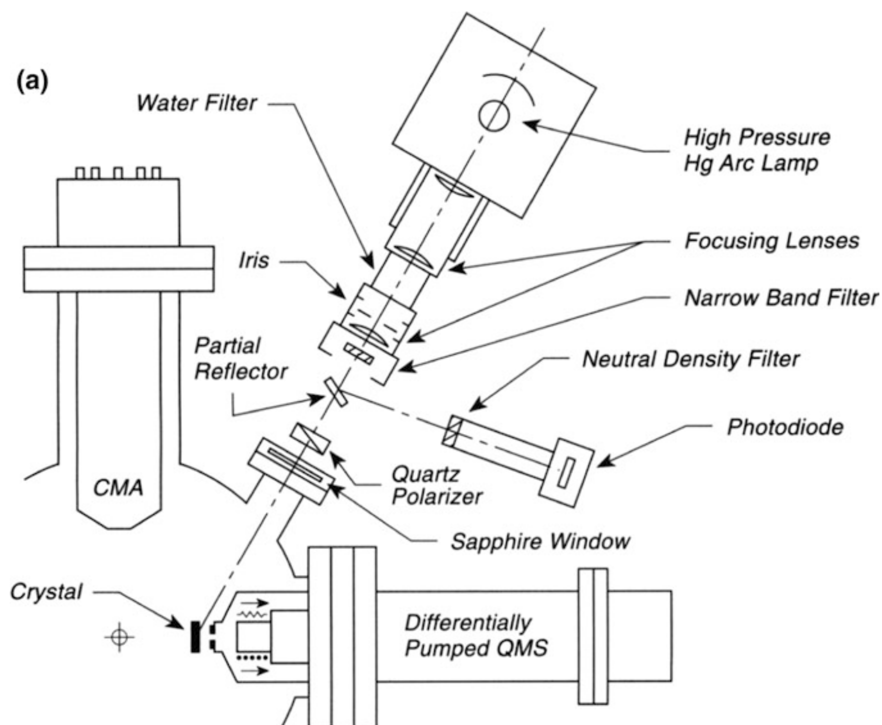

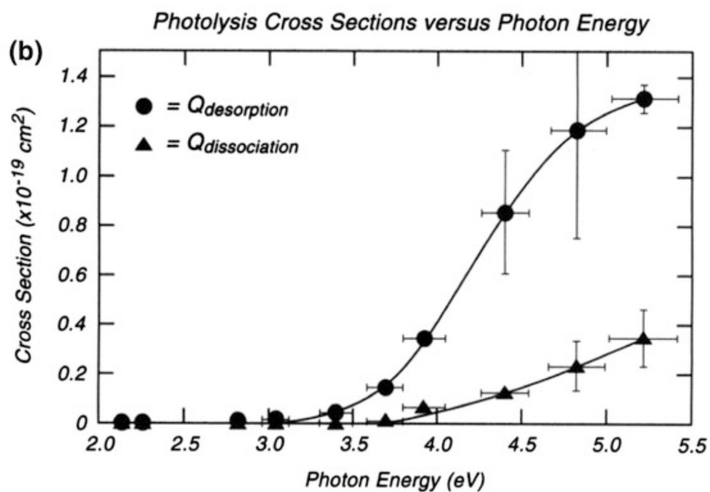

Fig. 22.3 Photochemistry using ultraviolet lamp. **a** Ultraviolet lamp for photochemistry using filters and polarizer. **b** Typical cross section measurements from TPD analysis

intense lines of the mercury arc are often used to produce narrowband radiation and have a transmission of from 15 to 50 % at the center of the band with a full width at half maximum (FWHM) of 10 nm, except for the 237-nm filter, which has a FWHM of 20 nm. One must be careful in using these filters for long irradiation times, since the transmission band center can shift up to 2 nm when extensive irradiation occurs.

The apparatus contains a quartz flat partial reflector used to measure continuously the light intensity. The quartz flat reflects roughly 10 % of the light, and this is directed to a neutral density filter (1 % transmission) and then into a blackened housing which holds a calibrated photodiode [12]. The calibration of the photodiode relative to an absolute thermopile detector can be done externally on an optical bench, with the thermopile being placed in the same position as would be occupied by the crystal. Such measurements have found that the intensity of UV radiation from the arc source is not uniform, and it is interesting to map out the intensity pattern which gives a view of the arc location in the source in the most intense region of emission.

A commercially available UV quartz prism polarizer may be placed into the beam if either *s*- or *p*-polarized radiation is desired (see p. 240).

By combining the photoirradiation experiments at various photon energies with analysis of the surface before and after irradiation (using thermal desorption in this case) it was possible to observe two major separate photochemical processes for molecular oxygen chemisorbed on Pd(111)-desorption of O_2 and dissociation to produce chemisorbed O. The cross sections for these two processes are plotted versus photon energy in Fig. 22.3b, giving an idea of the random errors inherent in this type of measurement [10]. These cross sections were also measured in another laboratory using laser-induced photochemistry and the results were in agreement to within a factor of 2–3 [13].

A photoreactor for studies of powders and single crystals has been described in [14]. This device can operate at high or low gas pressures.

22.4 Use of Polarized Ultraviolet Light for Photochemistry

The use of polarized UV radiation to induce photochemical processes on surface is of importance because of the ability to use this information to obtain information about the mechanism of the electronic processes responsible for photoactivation of the surface [15, 16]. The photochemical activation of chemisorbed molecular O_2 is a model system, discussed briefly on p. 238, and here we show how polarized radiation may be used for studies of the same system.

Figure 22.4a shows the configuration of the photochemical system [17]. Ultraviolet light, originating from a lamp source, may be polarized by using a UV-grade quartz prism polarizer, directing either *p*- or *s*-polarized radiation to the single crystal surface. The single crystal may be used as a "calorimeter" to measure the thermal energy deposited from the radiation incident on its surface. This

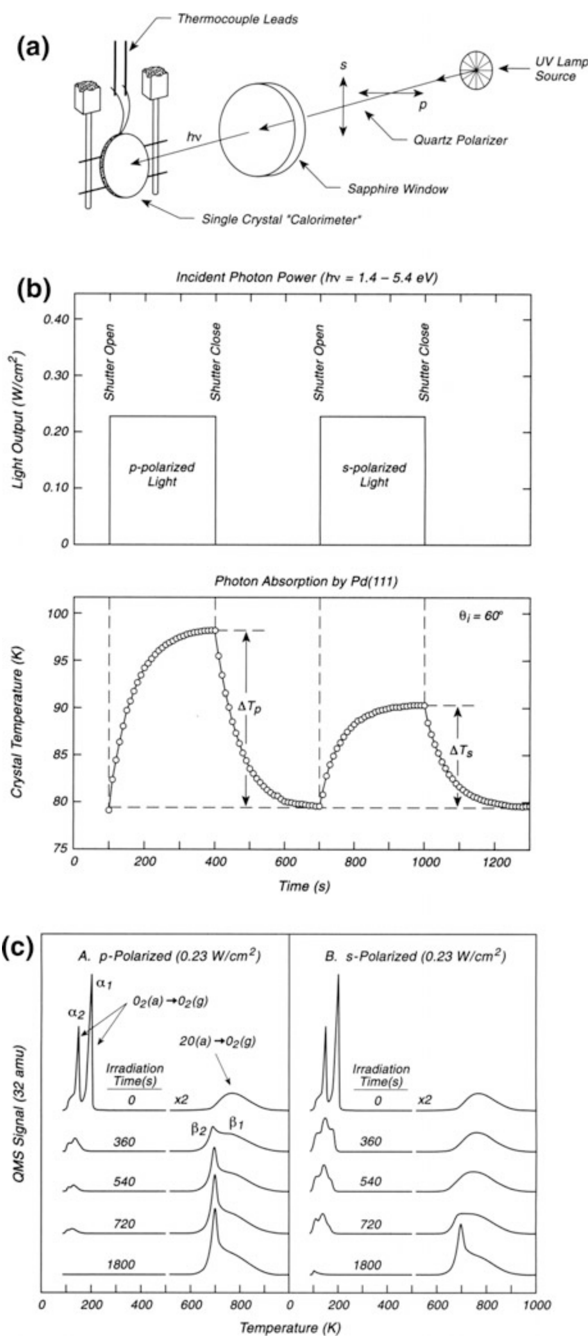

Fig. 22.4 Measurements with polarized UV light. **a** Configuration for irradiation with polarized UV light. **b** "Calorimetric" measurement for p- and s-polarization. **c** Effect of polarization on oxygen desorption state distribution

absorbed energy will vary in accordance with Fresnel's laws and the optical constants of the crystal absorber. Figure 22.4b shows a calorimetric experiment in which polarized broad band radiation having 0.23 W/cm^2 power density is allowed to warm the crystal from 79 K. For an incidence angle of 60°, one can see that the p-polarized radiation is more efficiently absorbed than the s-polarized radiation, as indicated by the relative increases in temperature. The measured difference in absorptivity is in fair agreement with the optical constants considering the errors inherent in this type of experiment [17].

Figure 22.4c shows the comparative effect of *s*- and *p*-polarized radiation on a molecular O_2 layer on Pd(111) as studied by thermal desorption following various periods of irradiation. The α_1- and α_2-molecular oxygen states desorb by photostimulation, and also photochemically dissociate to produce a thermal desorption feature labeled β_2. It may be seen that *p*-polarized radiation is more efficient in causing these desorption and dissociation processes than is *s*-polarized radiation [17]. This is consistent with a process in which electronic excitation of the metal by ultraviolet light is responsible for the surface photochemical processes, but more detailed studies would be needed to prove this.

22.5 Photoreduction of Ag on Doped TiO_2—Making Enhanced Photoactivity Visible

While many chemical methods may be used to witness photoactivity and its enhancement on semiconductors, the production of clusters of Ag by photoreduction of Ag^+ ions in solution to produce Ag^0 clusters is novel in its ability to statistically witness the reaction, using AFM to measure the cluster density and size [18–21].

As shown in Fig. 22.5a, slices of a TiO_2(110) crystal, glued to a microscope slide, are immersed in a 0.1 M $AgNO_3$(aq) solution. Exposure to about 10^{17} $photons/cm^2$ causes photo-produced electrons in the TiO_2 to reduce Ag^+ ions to Ag^0 atoms which cluster together to produce AFM-visible deposits. Figure 22.5b shows an AFM image of the undoped TiO_2 compared to the doped TiO_2 and the enhanced density of silver clusters clearly indicates that doping was effective in enhancing the frequency of Ag^+ reduction events. The volume of the Ag clusters produced allows an estimate of the quantum yield for the process, and Fig. 22.5c shows a plot, versus photon energy, of the quantum yield which falls in the 1 % range. In the case shown, doping was done by treating the TiO_2(110) crystal in NH_3(g) at 1 atm and 870 K for 5 min. Initial heating and cooling of the crystal to 870 K was achieved in Ar(g) at 1 atm.

Figure 22.5d shows the N(1s) XPS spectrum achieved after doping. Spectrum a corresponds to the removal of about 5 Å of the surface by sputtering in order to achieve a clean surface after handling in air and NH_3. After the removal of 60 Å of material, two N(1s) features are observed. It was shown that the 399.6 eV feature, due probably to N-H type species, is active for doping, giving a photon threshold energy at about 2.4 eV which is 0.6 eV below the bandgap of rutile TiO_2 [21].

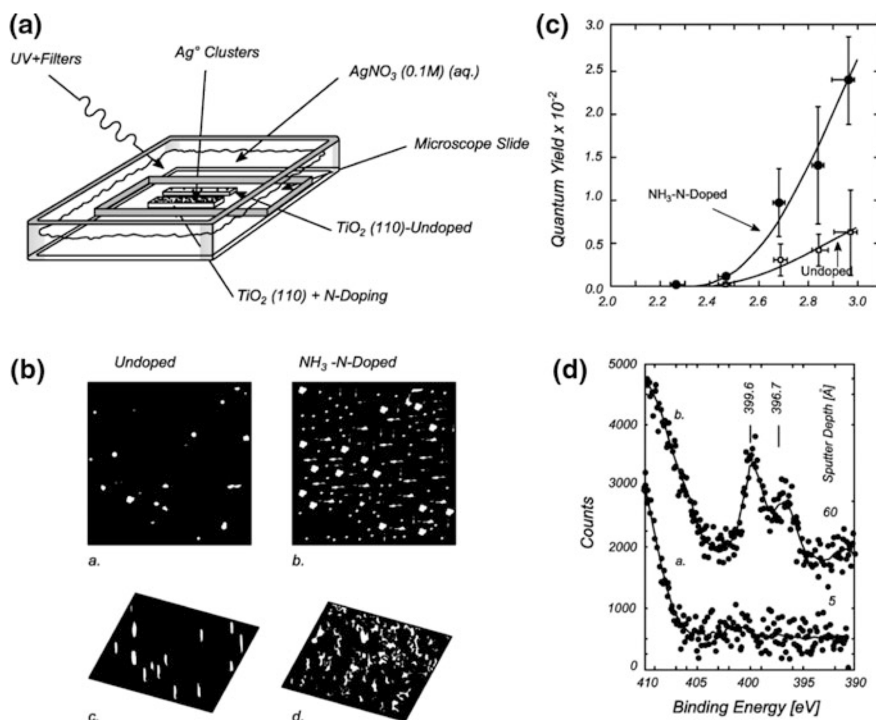

Fig. 22.5 Photoreduction of Ag on Doped TiO_2—making enhanced photoactivity visible. **a** Photoreduction of Ag on doped TiO_2. **b** Ag photoreduction on TiO_2; hν = 2.47 eV. **c** Action curve for photoreduced Ag-deposition on TiO_2(110). **d** N(1s) XPS spectra for NH_3-treated TiO_2(110)

22.6 Reducing Radiation Damage in Raman Spectroscopy of Solids

A serious problem often encountered in measuring the Raman spectrum of a solid is the effect of the high power laser on damaging the sample [22]. A standard approach to eliminating or minimizing the effect is to rotate the sample while it is under study, thereby distributing the excitation over the sample and reducing the local heating effect [23]. The method reported here is able to do this with a static sample. Such sample holders are often more convenient when studying high area solids which cannot be rotated because of other types of measurements which must be made under static conditions [24].

The unique feature of the mounting procedure is the use of a tungsten mesh grid to hold the powdered sample. This mesh is photoetched in 0.025 mm thick tungsten foil and contains regular square openings of $0.22 \times 0.22\ mm^2$ area. The squares are bonded by tungsten borders of 0.038 mm width. The powder is mechanically pressed as described by Ballinger [25]. This method of holding powdered samples

has been widely used in IR spectroscopy as discussed elsewhere in this book. The grid is held in a square frame with a 1.4 × 1.4 cm^2 opening and consists (for strength) of a front frame made of stainless steel (1.5 mm thick) and a rear Cu (OFHC) frame for maximum thermal conductivity, which is brazed to Ni leads. Six bolts and nuts clamp the frame to the grid. The sample is mounted in a Pyrex Raman cell with provisions for cooling with liquid nitrogen.

The arrangement was compared to a conventional rotating Raman sample holder, using an OMARS 89 triple-monochromator spectrometer (Dilor, Lille, France) equipped with a thermoelectrically cooled CCD camera (Princeton Instruments). A test was carried out with a WO_x/ZrO_2 catalyst. The Raman spectrum was recorded with a rotating holder as shown in Fig. 22.6b, using three laser power levels from a 488-nm Ar^+ ion laser (Spectra Physics, Type 2020). Since the spectrum does not change during irradiation at any level, the rotating sample holder is able to prevent radiation damage. In Fig. 22.6c, radiation damage is not seen for the mesh-supported sample until the power is increased above 90 mW, where a new band at 1015 nm appears. An $Os_3(CO)_{12}/SiO_2$ was studied also, and the cryogenically-cooled sample was stable to 24 mW power. These studies show that non-rotating cryogenically cooled powdered samples held in a grid may be stabilized against laser damage, but that the rotating sample method is superior for reducing damage [24].

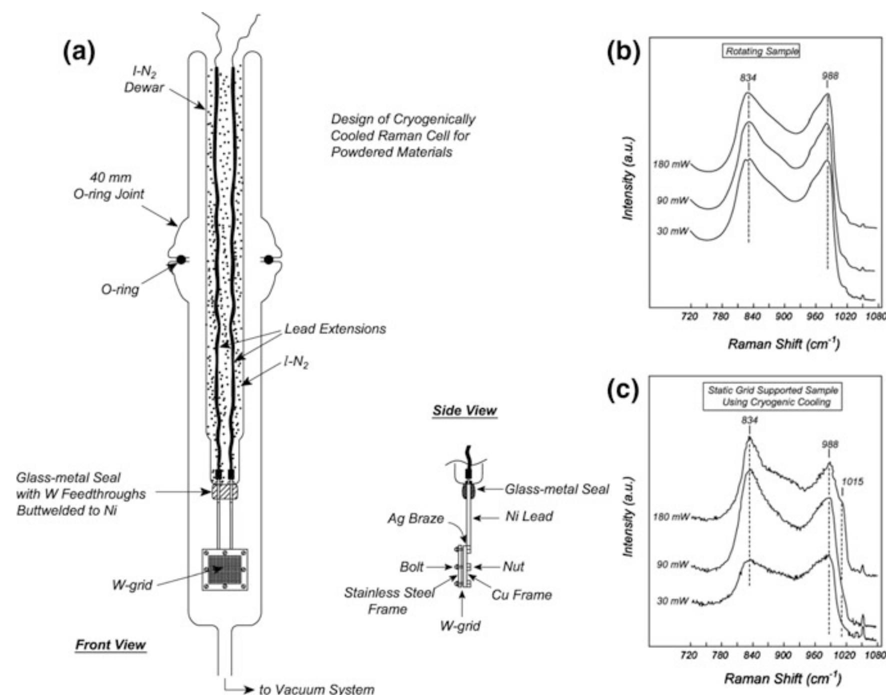

Fig. 22.6 Reducing radiation damage in Raman spectroscopy of solids. **a** Cryogenically cooled non-rotating Raman cell. **b**, **c** Raman spectrum—WO_x/ZrO_2

22.7 Lyman-α Lamp Calibration Using a Chemical Actinometer

The measurement of the light flux from vacuum UV lamps is important in a number of areas of photochemistry such as astrochemistry and atmospheric chemistry. Different methods are used to calibrate such lamps including photoelectron generation, photoionization of gases, and photodecomposition of gases [26–31]. There are only a few reports of the use of chemical actinometry for the calibration of Lyman-α lamps [29–36] (which operate at 10.2 eV). The results of a variety of calibrations of these lamps are tabulated in [37] and show typical light fluxes measured over a 47 year history. It can be seen that the various Lyman-α lamps used in the past have been shown by various methods to deliver approximately 10^{15} photons s^{-1} cm^{-2} over a range of approximately 10-fold.

A chemical actinometer successfully used recently for the calibration involves the photodecomposition of N_2O and the use of transmission IR spectroscopy to measure the N_2O destruction as well as the production NO and NO_2 [37]. N_2O decomposes when illuminated by Lyman-α radiation according to the reactions (22.1)–(22.4):

$$N_2O + h\nu \rightarrow N_2 + O \tag{22.1}$$

$$N_2O + h\nu \rightarrow NO + N \tag{22.2}$$

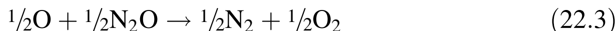

$$\tfrac{1}{2}O + \tfrac{1}{2}N_2O \rightarrow \tfrac{1}{2}N_2 + \tfrac{1}{2}O_2 \tag{22.3}$$

$$\tfrac{1}{2}O + \tfrac{1}{2}N_2O \rightarrow NO \tag{22.4}$$

The quartz Lyman-α lamp was mounted with a Viton O-ring onto a stainless steel Conflat flange containing a MgF_2 window. The lamp was supplied with a continuous flow of a 10 % H_2/90 % Ar mixture at 1 Torr pressure and was excited by a 60 W microwave supply. The MgF_2 effectively cuts off radiation at wavelengths above 1100 Å, thereby removing Ar emission [38]. The vacuum UV radiation passes into a bakeable high vacuum stainless steel transmission IR cell (Volume = 1.9 L) equipped with turbopumping, Baratron capacitance manometer pressure gauges, and a mass spectrometer, and having a base pressure of about 1×10^{-8} Torr as shown in Fig. 22.7a. For the lamp calibration, between 1 and 10 Torr of N_2O was admitted to the cell and the lamp was turned on and stabilized. The IR spectrum for N_2O and the products during photolysis is shown in Fig. 22.7b. The rate of consumption of N_2O was measured by following the integrated absorbance (at 2 cm^{-1} resolution) at two strong fundamental frequencies, ν_1 and ν_3, where the IR beam travelled transversely through the cell. Separate pressure versus integrated absorbance curves were measured for N_2O at these frequencies, and the consumption of N_2O, calculated in Torr s^{-1}, was determined. Figure 22.7c shows a sample of the N_2O depletion curves where about 10 % consumption of N_2O was measured, yielding linear plots. It may be seen that the values of dP/dt, measured

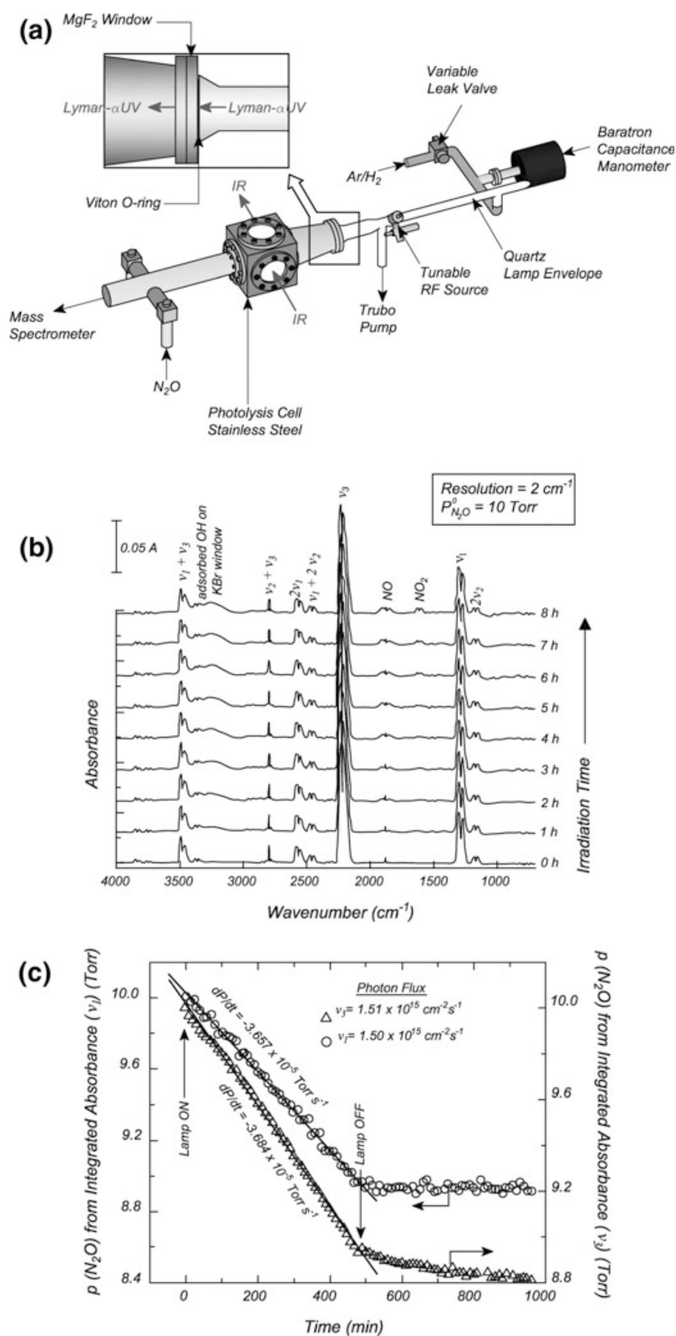

Fig. 22.7 Calibration apparatus for N_2O photodecomposition by Lyman-α radiation. **a** FTIR cell and Lyman-α source. **b** Spectral evolution of N_2O, NO and NO_2 features during the photodecomposition of N_2O. **c** Determination of photon flux

from ν_1 and ν_3, are in excellent agreement, with less than 1 % difference. The flux of the Lyman-α light was estimated using a measured efficiency from the literature [39] of 0.69 ± 0.02 photons/N_2O. One should not employ pressure changes in estimating the light flux as heating effects were found to confuse such measurements. It is interesting to recognize that in the pressure region from 1 to 10 Torr, all Lyman-α radiation is absorbed in the first few cm from the MgF_2 window and the assumption of fast mixing of the gas was found to hold. In addition, a slight pressure dependence of the photodecomposition kinetics was found and attributed to wall effects which become more significant at low pressure [37].

22.8 Pulsed Vacuum UV Light Source

Photochemistry studies are being extended to higher and higher photon energies because of scientific interest in processes involving deep ionization in molecules, in solids and on surfaces. A source of radiation of this energy range can be UV lamps, such as the Lyman-α lamp (10.2 eV), and various other gas lamps excited by radiofrequency radiation (see Sect. 22.7). Another source of such radiation is synchrotron radiation which extends far into the X-ray region, and which is commonly monochromatized for use in photoelectron spectroscopy. A laser plasma light source is another source of Vacuum UV (VUV) or Extreme UV (EUV) light. In the example shown here, a Ta plasma is generated by a 1064 nm pulsed laser and light is monochromatized by toroidal gratings in the vacuum spectrometer for the range 4–108 nm (310–11.5 eV). The apparatus is more than 3 m in length and is pumped by turbomolecular pumps (TMP) as well as Ti sublimation pumps (TSP) as shown.

As shown in the data below the spectra in Fig. 22.8c, 10^6 to 10^8 photons per pulse are generated which over the duty cycle yields 5×10^7 to 5×10^9 photons/s averaged over a long time period [40]. This is a far smaller number of photons than can be generated by a gas discharge lamp such as a Lyman-α lamp, where over the whole spectrum in the region of 10.2 eV, about 10^{15} photons/s are generated [37].

22.9 Grazing Incidence X-Ray Photoemission Spectroscopy (GIXPS): Enhanced Surface Sensitivity

GIXPS was first described by Henke [41] and has seen limited use. The technique is based upon the angle-dependent X-ray penetration depth at small incidence angles (measured from grazing angle). X-rays that impinge on a flat surface at $\sim$1 keV at sufficiently small angles undergo total external reflections and their penetration depth is strongly attenuated. This means that the photoelectron yield contains an increased contribution from the surface of the solid. As the angle of the X-rays increases, increased contributions from deeper layers are observed. Therefore, depth dependent XPS analysis is possible. The theory behind GIXPS is given in [42].

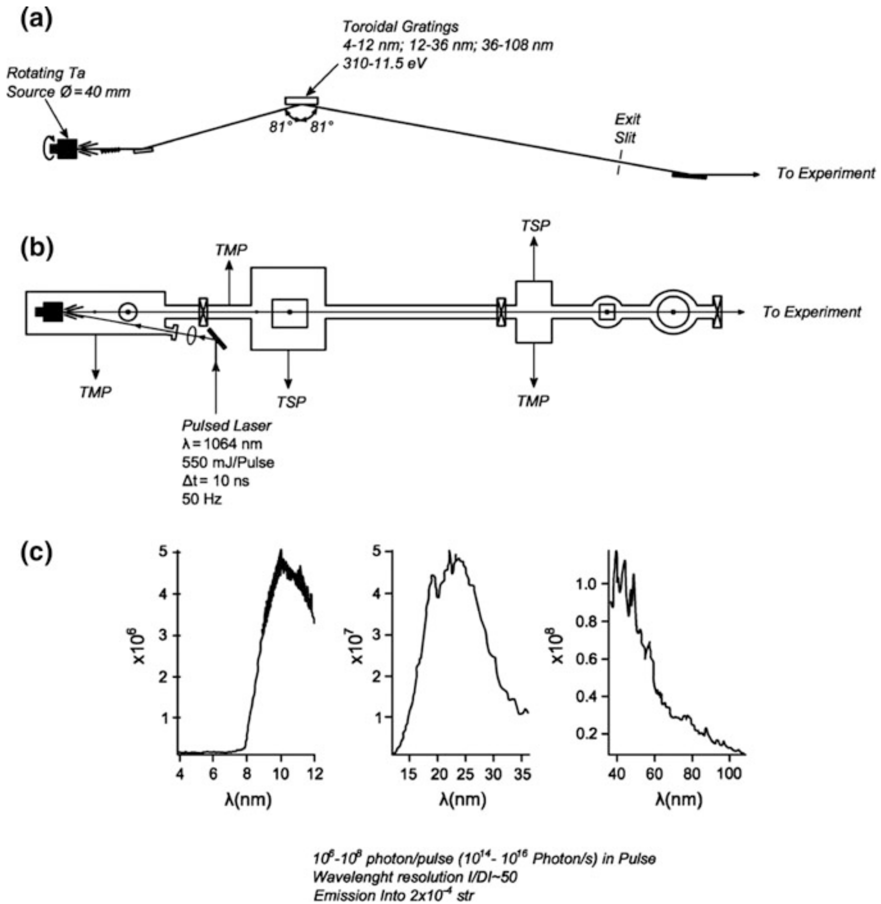

Fig. 22.8 Pulsed vacuum UV light source. **a** Top view. **b** Side view. **c** Intensity (photon/pulse)

Figure 22.9a shows a laboratory design for making GIXPS measurements, using a small X-ray source. The X-ray source may be rotated in angle of incidence and the center of rotation is the analysis position on the sample. The microchannel plate amplifier is used to measure the reflected X-ray radiation. A double pass cylindrical mirror electron analyzer is used. Normalized sample spectra for oxidized and unoxidized GaAs(100) are shown in Fig. 22.9b, and it may be seen that at higher angles (66 mR) the relative contribution from the bulk—derived As^{0}(3d) feature (binding energy = 41 eV) is enhanced compared to As^{5+} and As^{3+} which come from the surface oxide film and overlap near a binding energy = 45 eV [42]. A patent has been issued [43].

Figure 22.9c shows a schematic for the performance of GIXPS using synchrotron excitation. Here, the sample is rotated in the X-ray beam, maintaining the

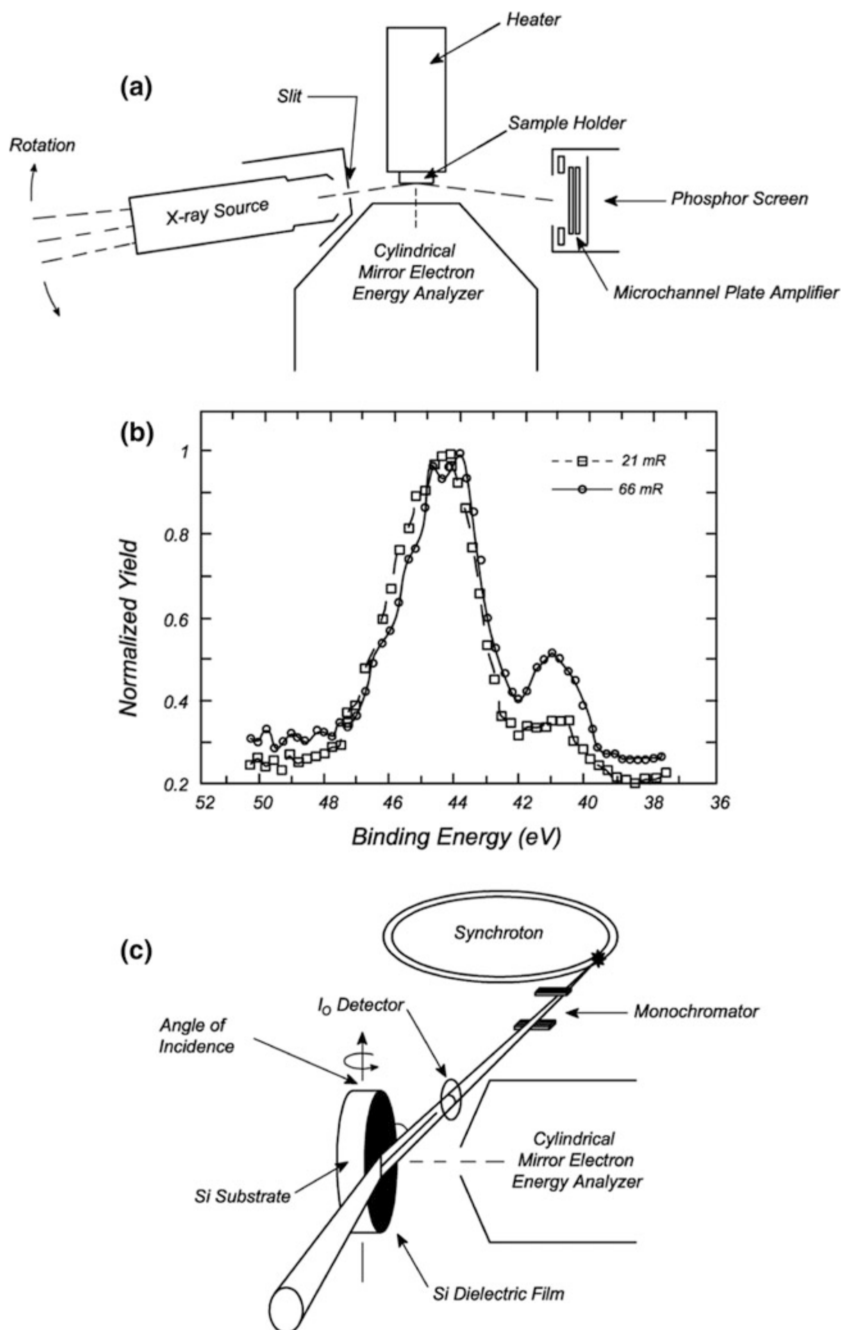

Fig. 22.9 Grazing X-ray photoemission spectroscopy—enhanced surface sensitivity. **a** Laboratory-based GIXPS. **b** As (3d) GIXPS spectra for oxidized GaAs(100). **c** Synchrotron-based GIXPS

origin of photoelectrons at a constant position with respect to the cylindrical mirror electron analyzer. This work has been focused on measuring the thickness and chemistry of ultrathin gate oxide films on Si [44].

References

1. J.E. Rowe, S.B. Christman, E.E. Chaban, Rev. Sci. Instrum. **56**, 759 (1985)
2. J.E. Rowe, S.B. Christman, E.E. Chaban, Rev. Sci. Instrum. **44**, 1675 (1973)
3. T.V. Vorburger, B.J. Waclawski, D.R. Sandstrom, Rev. Sci. Instrum. **47**, 501 (1976)
4. G.M. Lancaster, J.A. Taylor, A. Ignatiev, J.W. Rabalais, J. Electron Spectrosc. Relat. Phenom. **14**, 143 (1978)
5. A.H. Mcllraith, Nature **212**, 1422 (1966)
6. A.H. Mcllraith, J. Vac. Sci. Technol. **9**, 209 (1972)
7. R.K. Fitch, T. Mulvey, W.J. Thatcher, A.H. Mcllraith, J. Phys. **D3**, 1399 (1970)
8. R.K. Fitch, T. Mulvey, W.J. Thatcher, A.H. Mcllraith, J. Phys. **E4**, 533 (1971)
9. A.H. Mcllraith, private communication to J.W. Rabalais
10. L. Hanley, X.-C. Guo, J.T. Yates Jr., J. Chem. Phys. **91**, 7220 (1989)
11. Oriel, 250 Long Beach Boulevard, P.O. Box 872, Stratford, CT 06497-0872 (Model 66014, 350 watt)
12. The l-cm^2-area circular photodiode-preamplifier package is sensitive from 185 to 1150 nm, and is calibrated by the manufacturer with standards traceable back to the National Institute of Science and Technology (EG and G HUV-4000B)
13. F. Weik, A. de Meijere, E. Hasselbrink, J. Chem. Phys. **99**, 682 (1993)
14. A.Z. Moshfegh, A. Ignatiev, Rev. Sci. Instrum. **59**, 2202 (1988)
15. S.A. Buntin, L.J. Richter, D.S. King, R.R. Cavanagh, J. Chem. Phys. **91**, 6429 (1989)
16. E. Hasselbrink, S. Nettesheim, M. Wolf, A. Cassuto, G. Ertl, in *Springer Series in Surface Science*, vol. 19, DIET IV (1990), p. 75
17. J. Yoshinobu, X.-C. Guo, J.T. Yates Jr., Chem. Phys. Lett. **169**, 209 (1990)
18. P.D. Fleischauer, H.K.A. Kahn, J.R. Shepherd, J. Am. Chem. Soc. **94**, 283 (1972)
19. P.A.M. Hotsenpiller, J.D. Bolt, W.E. Farneth, J.B. Lowekamp, G.S. Rohrer, J. Phys. Chem. B **102**, 3216 (1998)
20. J.B. Lowekamp, G.S. Rohrer, P.A.M. Hotsenpiller, J.D. Bolt, W.E. Farneth, J. Phys. Chem. B **102**, 7323 (1998)
21. O. Diwald, T.L. Thompson, T. Zubkov, E.G. Goralski, S.D. Walck, J.T. Yates, Jr., J. Phys. Chem. B **108**, 6004 (2004)
22. J.M. Stencel, *Raman Spectroscopy for Catalysis* (Van Nostrand Reinhold, New York, 1990), p. 32
23. S. Chan, A.T. Bell, J. Catal. **89**, 433 (1984)
24. E.A. Wovchko, J.T. Yates Jr., M. Scheithauer, H. Knozinger, Langmuir **14**, 552 (1998)
25. T.H. Ballinger, J.C.S. Wong, J.T. Yates Jr., Langmuir **8**, 1676 (1992)
26. T.A. Chubb, H. Friedman, Rev. Sci. Instrum. **26**, 493 (1955)
27. J.J. Bollinger, F.M. Pipkin, Rev. Sci. Instrum. **52**, 938 (1981)
28. K. Watanabe, F.F. Marmo, E.C.Y. Inn, Phys. Rev. **91**, 1155 (1953)
29. H. Cottin, M.H. Moore, Y.B. Nilan, J. Astrophys. **590**, 874 (2003)
30. M.S. Westley, R.A. Baragiola, R.E. Johnson, G.A. Baratta, Nature **373**, 405 (1995)
31. P. Warneck, Appl. Opt. **1**, 721 (1962)
32. H. Okabe, J. Opt. Soc. Am. **54**, 478 (1964)
33. D. Davis, W. Braun, Appl. Opt. **7**, 2071 (1968)
34. I. Yamashita, Jpn. J. Appl. Phys. **14**, 70 (1975)
35. P. Weber, J.M. Greenburg, Nature **316**, 403 (1985)
36. G.A. Baratta, G. Leto, M.E. Palumbo, Astron. Astrophys. **384**, 343 (2002)

37. M. Rajappan, M. Buttner, C. Cox, J.T. Yates Jr., J. Phys. Chem. A **114**, 3443 (2010)
38. A. Duncanson, R.W.H. Stevenson, Proc. Phys. Soc., London **72**, 1001 (1958)
39. W.E. Groth, W.E. Schierholz, Planet. Space Sci. **1**, 333 (1959)
40. I. Arakawa, private communication
41. B.L. Henke, Phys. Rev. A **6**, 94 (1972)
42. M.A. Chester, T. Jach, J. Vac. Sci. Technol., B **11**, 1609 (1993)
43. Jach et al., United States Patent 5,280,176 (1994)
44. T. Jach, E. Landree, J. Surf. Anal. **9**, 339 (2002)

Chapter 23
Kinetics of Adsorption/Adsorbate Coverages

23.1 Absolute Adsorption Uptake Measurements from a Calibrated Effusive Molecular Beam

The measurement of the kinetics of adsorption and the absolute saturation coverage of an adsorbate on a single crystal is basic to our understanding of surface chemistry. While relative surface coverages, compared to the saturation coverage, are fairly easy to measure using various surface spectroscopies, the measurement of the absolute coverage and the absolute sticking coefficient are more difficult. One of the absolute methods employed in some cases involves the use of nuclear activation of the adsorbed layer, where absolute counting of nuclear disintegration events after activation may be used with high accuracy [1]. Unfortunately, not all adsorbates are amenable to this method.

Figure 23.1a shows an apparatus that is capable of measuring both the absolute sticking coefficient and the absolute surface coverage during an adsorption experiment. The method is a version of the King and Wells method, developed in 1972 [2]. A multicapillary doser, with an absolutely known flux of effusing molecules in a known angular distribution (see p. 421) is incident on a single crystal of known size, located at a known distance from the doser. A quadrupole mass spectrometer, shielded from direct line of sight from the crystal and doser, measures the random flux of gas in the vacuum system as a function of the exposure of the crystal to the incident beam. A shutter can be rotated to intercept the beam, shielding the crystal from the direct flux, and converting all of the incident beam into a random flux by reflection from its surface. In order to make an uptake measurement, the crystal is cleaned, brought to adsorption temperature, and positioned behind the shutter. Gas is admitted, as shown in Fig. 23.1b, and the system pressure rises quickly to a sharp point where the rate of rise decreases significantly. At time t_1, the shutter is opened, and gas begins to be adsorbed on the crystal, causing the random flux of gas to decrease. Region A of the uptake curve represents the first phase of adsorption, and the horizontal trace indicates that the sticking coefficient is constant (and probably

© Springer International Publishing Switzerland 2015

J.T. Yates Jr., *Experimental Innovations in Surface Science*,
DOI 10.1007/978-3-319-17668-0_23

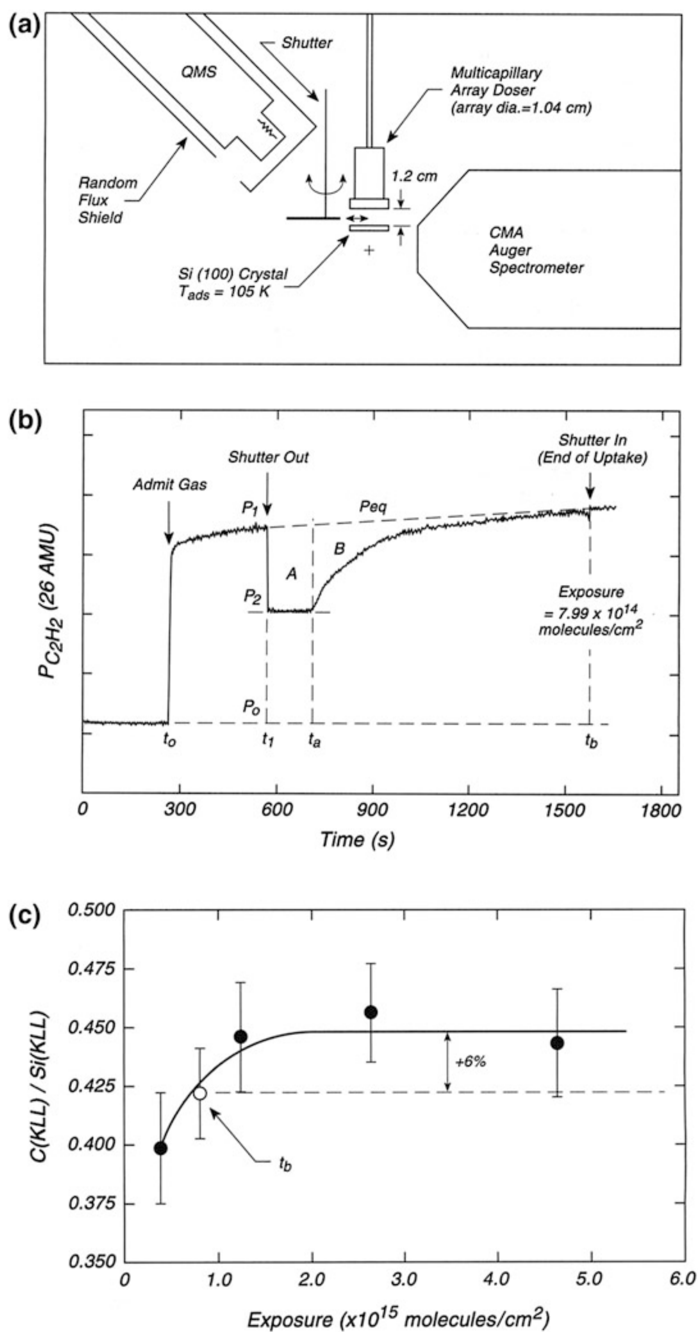

Fig. 23.1 Absolute adsorption uptake measurement from calibrated beam. **a** Apparatus for absolute adsorption uptake measurement. **b** Typical uptake curve C_2H_2/Si(100). **c** Increase in C_2H_2 coverage beyond t_b owing to continued slow adsorption

unity) in this region. Following adsorption to point t_a, it is observed that the random flux begins to rise in region B as the sticking coefficient decreases below its value in region A. At the end of the experiment, the random flux has asymptotically risen to the dashed line, which indicates that, at the sensitivity level of this experiment, the uptake is complete. Placing the shutter into the beam causes little effect at point t_b, since the complete reflection of incident molecules by the inert shutter is identical in magnitude to the reflection of incident molecules by the saturated crystal. The area of region A and region B may be used to compute the final absolute coverage at t_b [3].

There are three issues that contribute to the uncertainty of this measurement:

1. The nonhorizontal character of the dashed line against which the integrals are measured. This error is probably due to slow pumping by the vacuum system walls, which decreases as the exposure is increased. The empirical solution to this problem is to treat the dashed limiting line as a baseline; it is designated P_{eq}.
2. The adsorption of gas from the random flux. A small correction can be made for this effect, which typically amounts to 1 % in the region from t_0 to t_1. This initial coverage is designated $N(t)_{\mathrm{initial}}$.
3. The low accuracy of determining the saturation point, t_b. Here, Auger spectroscopy was employed to show that for long exposures beyond t_b, the rise in adsorbate coverage was 6 % as shown in Fig. 23.1c for the example chosen here.

The equation that governs the adsorption is

$$N(t)_{total} = N(t)_{initial} + (F + F_r) \cdot \int S(t)dt, \tag{23.1}$$

where $N(t)_{\mathrm{total}}$ = the total coverage at saturation; F = the beam flux; F_r = the random flux; and $S(t)$ = the sticking coefficient. $S(t) = [P_{\mathrm{eq}} - P(t)]/fP_{eq}$ and f = the fraction of the beam intercepted by the crystal. The value $N(t)_{\mathrm{total}}$ is then increased to account for the small correction mentioned above in issue 3.

A variation on this technique uses a diffuse source of adsorbate from an uncalibrated leak valve and a collimated detector used to measure the rate of adsorbate reflection from the surface during adsorption [4].

23.2 Measurement of Absolute Sticking Coefficient at Desorption Temperature

Conventional measurement techniques measure the net sticking probability, which is related to the difference between the absolute rate of adsorption, r_a, and the absolute rate of desorption, r_d, according to (23.2).

$$s_{net} = (r_a - r_d)/z \tag{23.2}$$

Here z = the impingement rate for the incident gas.

It is often desired to measure the absolute sticking coefficient, s_{abs}, which is given by (23.3).

$$s_{abs} = r_a/z \tag{23.3}$$

The absolute sticking coefficient is equal to the net sticking coefficient only when the rate of desorption is zero, so in order to achieve this condition, conventional sticking coefficient measurements are made at temperatures below the desorption temperature.

Substituting (23.2) into (23.3) gives (23.4).

$$s_{abs} = s_{net} + r_d/z \tag{23.4}$$

Equation (23.4) yields

$$s_{abs} = \lim_{1/z \to 0} s_{net}(z) \tag{23.5}$$

Normally, a plot of s_{net} versus $1/z$ at constant temperature will give an intercept of s_{abs} and slope r_d. Figure 23.2 shows a three-dimensional plot with the linear extrapolation of the family of curves (black points) to the limit of $1/z = 0$, yielding the white points which form a trace of the absolute sticking probability in the limit of very high impingement rate, z. Here the symbol ML = monolayer.

The data shown in the Figure are taken at 400 K, whereas the desorption temperature for CO in this case is in the range 350–550 K [5]. The method works well when $r_d < z$, or correspondingly, when $1/r_d > 1/z$.

An alternate method, particularly useful for irreversible dissociative chemisorption, has been described by Xia et al. [6].

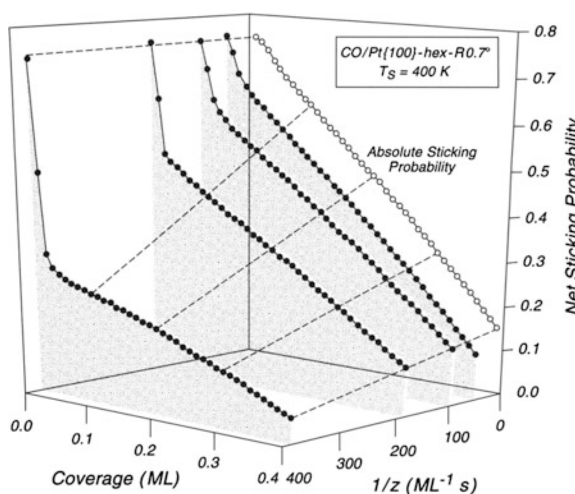

Fig. 23.2 Absolute sticking coefficient method at desorption temperature at desorption temperature

References

1. Z.H. Lu, K. Griffiths, P.R. Norton, T.K. Sham, Phys. Rev. Lett. **68**, 1343 (1992)
2. D.A. King, M.G. Wells, Surf. Sci. **29**, 454 (1972)
3. C.C. Cheng, R.M. Wallace, P.A. Taylor, W.J. Choyke, J.T. Yates Jr, J. Appl. Phys. **67**, 3693 (1990)
4. A.M. Glines, M.A. DeAngelis, A.B. Anton, J. Vac. Sci. Technol. **A10**, 3179 (1992)
5. X.-C. Guo, D.A. King, Surf. Sci. **302**, L251 (1994)
6. L.-Q. Xia, M.E. Jones, N. Maity, J.R. Engstrom, J. Vac. Sci. Technol. **A13**, 2651 (1995)

Chapter 24
Mass Spectrometry

24.1 Shielded Quadrupole Mass Spectrometers—Temperature-Programmed Desorption

One of the most widely used and versatile techniques for the study of adsorbed species on single crystal surfaces is temperature-programmed desorption (TPD), often called thermal desorption spectroscopy (TDS). The method extends back to the early work of Taylor and Langmuir, 60 years ago, who studied the desorption of Cs from polycrystalline tungsten filaments [1]. The method was extended to other adsorbates on polycrystalline surfaces by Becker and Hartman [2], Ehrlich [3], and by Redhead [4]. A review of the early work can be found in [5]. Temperature-programmed desorption is now used extensively for studies on single crystal surfaces of metals, semiconductors, and insulators. A comprehensive review of ten methods for analyzing TPD data, and an evaluation of each was recently written by de Jong and Niemantsverdriet [6].

The collection of TPD data has progressed from the early use of ionization gauges to the almost universal employment of quadrupole mass spectrometers (QMS) for the detection of desorbing gases. Using the mass spectrometer in the multiplex mode, one can simultaneously measure the evolution of various gas products as the temperature of the crystal is raised. This can also be extended to the study of isotopic mixing between labeled adsorbates, as was first demonstrated for adsorbed CO desorbing from polycrystalline W [7]. Large differences in the desorption kinetics from different single crystal faces was first demonstrated for H_2 desorbing from W(100), W(111), and W(110) by the combined works of various authors [8–12].

The early work with single crystals employed unshielded mass spectrometers that sampled the random flux of desorbing gases originating from the front of the crystal, from the electrical support leads to the crystal, and from the back of the crystal disk. These effects could be eliminated to various degrees by using a differentially pumped and shielded mass spectrometer that preferentially collected

© Springer International Publishing Switzerland 2015

J.T. Yates Jr., *Experimental Innovations in Surface Science*,
DOI 10.1007/978-3-319-17668-0_24

desorbing gas only from the front of the crystal. The enhanced sensitivity to desorbing gas as a result of the shield is related to the fact that the shield retains gas molecules for an average time period of τ = V/S, where V = volume and S = pumping speed, both relating to the shield region itself. Values of τ = 50 −100 ms are common, permitting each trapped molecule to pass through the ion source many times before being pumped away. The apertured shield is selective for desorption from the front of the crystal, but it is not measuring significant desorption for molecules making a single pass, compared to the contribution from trapped molecules within the shield which make multiple passes through the ionization source. The value of τ must be kept below the characteristic time for the desorption process measured, which is usually of the order of seconds for temperature scan rates of a few K/s.

Figure 24.1a shows a glass shield that was just slipped over the ionization source of a mass spectrometer. Pumping occurs from the annular space at the rear of the shield [13]. Variations on this design (Fig. 24.1b) involve a metal shield with pumping holes present on the side of the shield behind the ionization source. For N_2(g) at 300 K, a 1-cm^2 aperture will provide a pumping speed, S = 11 L/s, where the total pumping aperture area considered should also include the area of the entrance aperture. Figure 24.1c shows a quadrupole mass spectrometer mounted in an apertured shield and differentially pumped by a dedicated pump [14], which may be either an ion pump, a titanium sublimation pump (TSP) [15], or a turbopump. The reader is referred to p. 72 for a discussion of the relative merits of an ion pump and a TSP in this application.

The ionization source of the quadrupole mass spectrometer contains a thermionic emitter producing electron emission at mA currents. A fraction of these electrons escape from the axial aperture and may be collected by the crystal, causing electron beam damage of the adsorbate. Stray currents of the order of 10 μA are often observed. These effects may be eliminated by either biasing the crystal at a negative potential to retard the collection of electrons, or by using a separately negatively biased aperture, as shown in Fig. 24.1d [16]. The effect of electron beam damage from stray electrons in the absence of these precautions can be profound in altering the chemistry on the crystal surface.

Figure 24.1d also shows a helpful device useful for reproducibly locating the crystal at a fixed distance from the aperture [16]. A Ta contact with a gently rounded end is connected to the electrically isolated aperture, and the connection to the bias potential is opened. An ohmmeter, working on the MΩ scale, is connected between the Ta contact and ground. The crystal is slowly advanced to the Ta contact until MQ resistance is measured as a result of very light contact. This allows one to calibrate the horizontal micrometer drive for the crystal at a fixed point in the apparatus. The micrometer drive is then retracted by a measured amount, and knowing the position of the Ta contact allows one to calculate the position of the crystal relative to the aperture.

The fractional interception of desorbing gas from the crystal will depend on the distance between the crystal and the aperture and also on the angular distribution of the desorbing gas, expressed as $\cos^n\theta$. For a crystal of 3.5 mm radius, and an

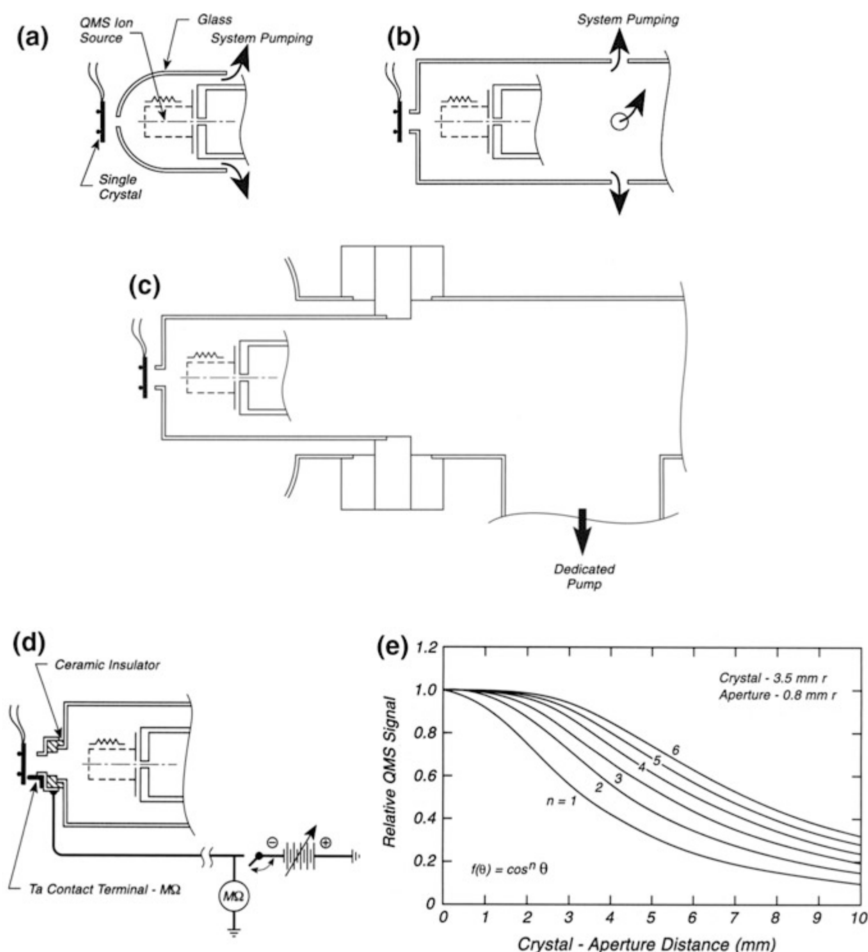

Fig. 24.1 Shielded quadrupole mass spectrometers—temperature-programmed desorption. **a** Glass shield. **b** Metal shield. **c** Differentially pumped shield. **d** Stray electron Suppression + Crystal positioning contact. **e** Relative signal for desorption into aperture

aperture of 0.8 mm radius, the relative collected signal for various values of n is shown in Fig. 24.1e. It is noted that only small losses are observed in the first 1-mm crystal-aperture distance, and also that an error in distance will make a smaller effect in the first 1-mm range compared to errors at larger ranges [17].

A critical review of the advantages and disadvantages of using a shielded mass spectrometer for temperature programmed desorption studies has been given by Schlichting and Menzel [18]. A shielded mass spectrometer such as that shown in Fig. 24.1a will have a constant pumping speed determined by the geometry of the aperture and the opening at the rear, whereas the pumping speed of a vacuum system used with an unshielded mass spectrometer will be variable. Also effects due

to non-Boltzmann energy distributions and noncosine angular distributions in the desorbing flux will be reduced by the shield, which is primarily sensing molecules scattered from its inner walls. These effects can be totally eliminated by internally blocking the ionization source from the sample by means of a shutter [18]. The disadvantages are the dependence of the detected signal on the distance from the crystal to the aperture (Fig. 24.1e), and the contribution of readsorption on the crystal during the TPD measurement because of gas readmission from the shielded mass spectrometer through the sampling aperture. By considering these factors, the dynamic range of the TPD coverage and kinetic measurement technique has been extended from monolayer detection down four or five orders of magnitude [18].

For the desorption of complex molecules, or mixtures of species, it is important to employ multiplex methods in which various mass peaks are rapidly monitored in sequence many times during the desorption process. A recent development involves monitoring the complete mass spectrum consecutively for many cycles during the evolution of thermal desorption products [19, 20].

A comparison between the sensitivity of a mass spectrometer in measuring gas pulses and also in measuring steady-state pressures, compared with a nude ionization gauge, has been published [21]. This paper shows that for eight different gases, the ionization gauge signal and the mass spectrometer signal are linear with the gas pulse size over six orders of magnitude for pulses ranging from 10^{-11} to 10^{-5} atm cm^3. The authors were surprised at the high sensitivity of the Bayard-Alpert gauge in these measurements [21].

24.2 Enhanced Signal-to-Noise in Quadrupole Mass Spectrometers

The quadrupole mass spectrometer is widely used in surface science for residual gas analysis as well as for the study of desorbing species from surfaces. Thermal desorption, and electron- and photon-induced desorption (including laser-induced desorption) have been widely studied. For most quadrupole mass spectrometers, a channeltron multiplier is employed for detection of the mass-separated ions. A method is described here for improvement of the signal-to-noise ratio of a channeltron detector; and in addition, the behavior of a channeltron detector is also described [22].

An electron multiplier has a low inherent noise, leading to a dark current. In the case of a channeltron multiplier mounted behind quadrupole rods with line of sight to the ionization source, there are additional background effects that increase as the electron emission current increases and also as the pressure in the mass spectrometer is increased. While these effects are not fully understood [22], they are thought to be due to soft X-rays and UV photons produced in the ion source, and also to excited neutral species, both of which pass down through the quadrupole rods without deflection. The use of an off-axis ion multiplier enables one to

eliminate these effects to a large degree, and the modification described here accomplishes this while not causing unacceptable reduction of the ion collection efficiency.

Figure 24.2a shows the off-axis channeltron detector located beneath the quadrupole rods. Between the exit region of the quadrupole rods and the channeltron entrance are two ion deflection plates, designed to steer ions into the channeltron. The channeltron is located 10 mm off axis. A multiplier shield plate, 8 mm in diameter, is mounted 2 mm in front of the channeltron entrance cone. A deflector plate, with a 45° angle to the shield plate, is mounted on the axis of the quadrupole, and a second deflector plate is mounted in a direction perpendicular to the shield plate, and 15 mm from the quadrupole axis. The distance between these deflector plates and the exit aperture of the quadrupole lens is 2 mm. The 45° deflector plate may be biased by an isolated lead, which is separately shielded. The entire structure is housed in a shield can to prevent both photons and charged particles from entering the channeltron.

Figure 24.2b shows the performance of the channeltron for various applied multiplier voltages, and also for various positive deflector plate voltages. The large enhancement of output current for a slight increase of multiplier voltage is evident from the three curves; in addition, a large effect of the positive deflector plate is also seen, with maximum transmission of ions being observed at +10 V plate bias.

Figure 24.2c shows the behavior of the dark current versus electron emission current in the ionization source of the mass spectrometer. A slope of 1.3 in this log–log plot indicates that slight nonlinearities exist as the filament temperature is raised in the ionization source to produce a larger electron emission current. A 100-fold improvement in the dark current is observed for the off-axis detector.

Figure 24.2d shows the behavior of the dark current as a function of Ar pressure in the mass spectrometer, with data taken at 1 mA emission current. The dark current rises as the 1.1 power of the pressure in both of these measurements. The off axis detector reduced the dark current here by a factor of 140.

The performance of the mass spectrometer with the two configurations of the chan-neltron detector can be summarized in (24.1) and (24.2) below:

$$\text{For on} - \text{axis detector} : I_i = 3.5 \cdot P^{1.1} \cdot I_e^{1.3} \tag{24.1}$$

$$\text{For off} - \text{axis detector} : I_i = 0.0025 \cdot P^{1.1} \cdot I_e^{1.3} \tag{24.2}$$

where I_i = measured ion current; P = Ar pressure; and I_e = electron emission current.

An ion current of the order of 10^{-18} A can be detected with the off-axis channeltron.

Earlier improvements in the detection efficiency of quadrupole mass spectrometers are described in [23]. The regeneration of Ag-Mg and Cu-Be dynode multipliers by heating to 300 °C in oxygen gas at 1 atm has been described [24].

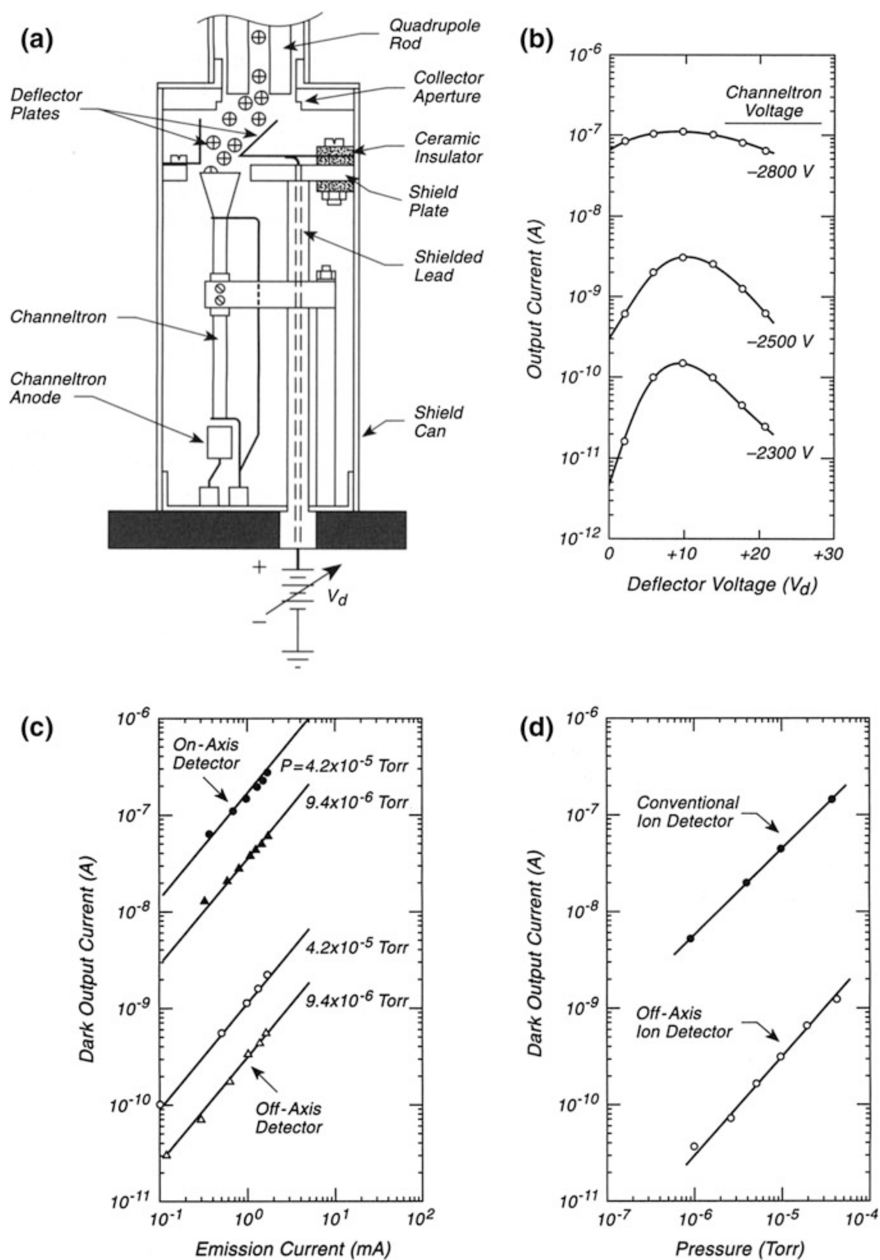

Fig. 24.2 Enhanced signal-to-noise—QMS. **a** Off axis channeltron detector, **b** detector performance, **c** Dark current behavior, **d** Dark current behavior

24.3 Elimination of Spurious Electron Emission from a Quadrupole Mass Spectrometer

Electrons emitted from the ion source of a mass spectrometer can be a source of error in measurements when the electrons strike and damage a sample in front of the mass spectrometer. For an enclosed mass spectrometer, with an aperture, placing a negative bias on the aperture will repel electrons and prevent this effect (see p. 259). The effect of spurious electron emission may also be eliminated by biasing the sample negative to repel electrons. A third method involves the use of a floating grid surrounding the mass spectrometer ion source, which is automatically brought to the potential of the thermionic emitter (usually −70 V in a mass spectrometer). This occurs as a result of the charging of the isolated grid by the emitted electrons [25].

Figures 24.3a–c show the steps in rebuilding a mass spectrometer ionizer to provide the floating grid. In Fig. 24.3a, an inner grid cap is placed over the existing inner grid cage. In Fig. 24.3b, the existing electron repeller grid cage is placed on the ion source. Inside the repeller grid is the thermionic emitter assembly, not shown in the drawing. Finally, in Fig. 24.3c, the floating grid, consisting of a cylindrical grid cage capped with a planar grid, is installed. The floating grid is electrically isolated by means of a ceramic ring that can be bolted to the mass spectrometer housing by means of three standoff bolts as shown.

The floating grid at negative potential is capable of extracting positive ions from the ionizing region inside the inner grid. This is the reason for the addition of the inner grid cap on the ionizing region, which acts as a shield to prevent positive ion extraction.

The floating grid collects electron current so that the electron emission current to the inner grid cage is somewhat reduced. Thus, in the UTI mass spectrometer, the filament protect circuit must be deactivated, since it will trip when it senses too little current at the inner grid. With the floating grid design, spurious emitted electron currents are reduced from about 10 μA to less than 1 nA [25].

A large O^+ signal and a large F^+ signal may be observed in the mass spectrometer operating with the floating grid (the latter especially if fluorinated molecules are introduced to the chamber deliberately). These signals probably originate from electron stimulated desorption effects from the ceramic ring and from the grid material itself [25]. Fluorine, a well-known surface contaminant in UHV systems, with a very high cross section for electron-stimulated desorption as a positive ion, is often seen when contaminated surfaces are electron bombarded [26].

24.4 Ta Mass Spectrometer Filament

Many mass spectrometers use either W, thoriated W, or thoriated Ir thermionic emitters as described on p. 133. The use of Ta as an emitter offers some advantages [27] as described below.

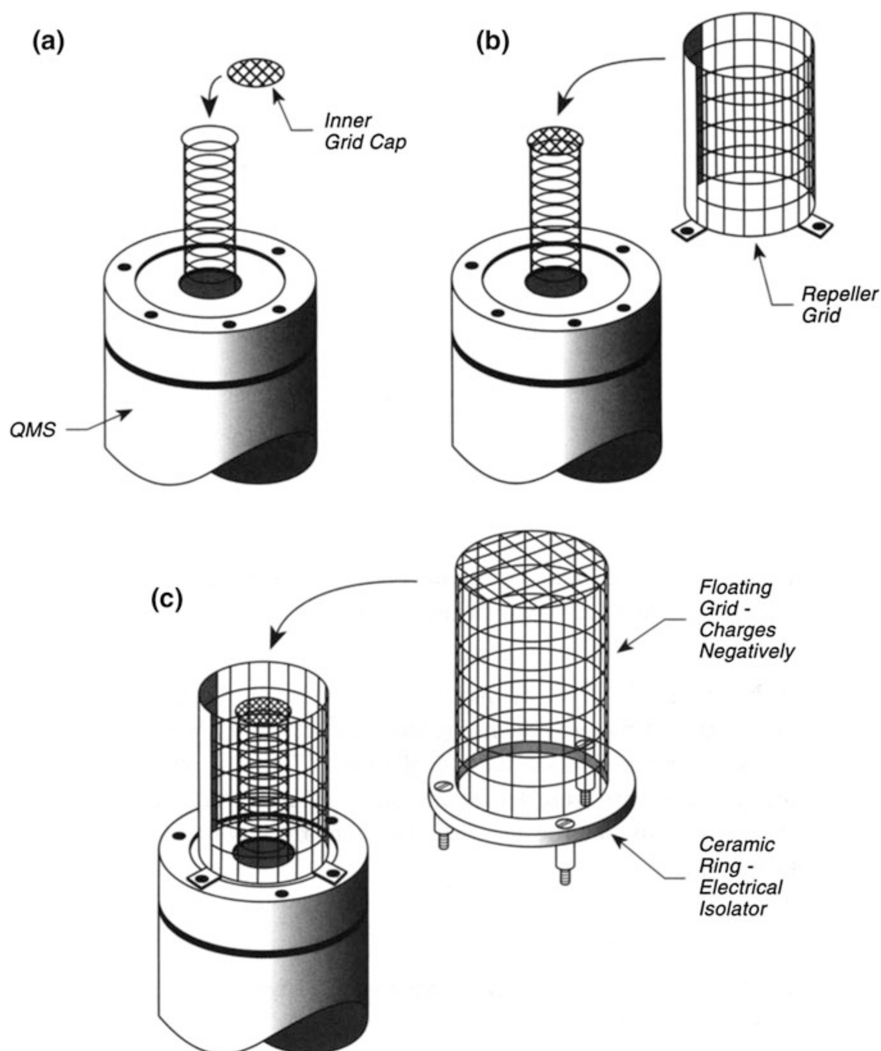

Fig. 24.3 Elimination of spurious electron emission from a Quadrupole Mass Spectrometer. **a** Placing inner grid cap, **b** Placing repeller grid + emitter (not shown), **c** Placing floating grid

Ta is much more ductile than W at room temperature and can be wound and welded easily compared to W. Ta wire (0.006-in. diameter) is wound around a rod (typically 0.040-in. diameter) to form a coil before being installed into the mass spectrometer as shown in Fig. 24.4.

A Ta emitter has a built-in property that is sometimes useful. Ta has a sufficiently high vapor pressure that at filament operating temperature there is a detectable signal from ^{181}Ta, the most abundant isotope. This signal for the $^{181}Ta^{+2}$

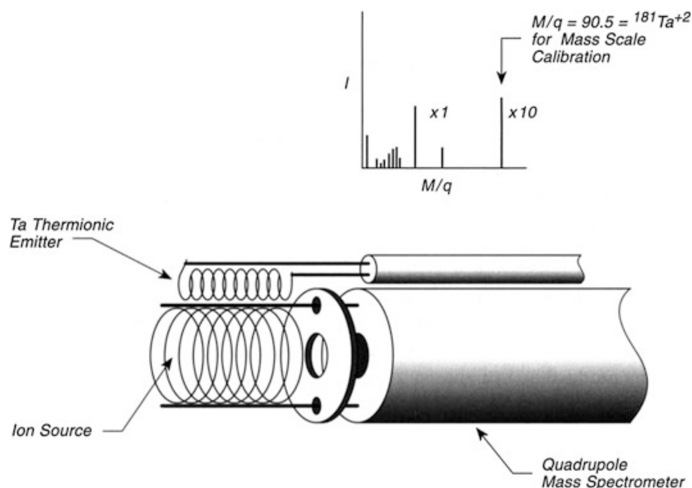

Fig. 24.4 Ta mass spectrometer filament

ion, observed at M/q = 90.5, may be used as a mass spectrometer calibration point, and interference from other ions in this region will be absent. The lifetime of the Ta filament will be years despite its slow evaporation during use.

24.5 Modulated QMS Ion Source for Enhanced Sensitivity

The enhancement of the sensitivity of a QMS for TPD measurements is important if the TPD signal is low. For example, when a differentially-pumped shield is used where incident molecules which strike the shield walls are adsorbed, the mass spectrometer signal can be dramatically reduced. The circuit to be described here modulates the ion signal in the ion source region and then uses lock-in detection of the multiplier signal for enhancement of signal/noise. The mass spectrometer is operated at a single mass. Normally the signal from the multiplier is converted through a current-to-voltage converter and is then amplified and digitized. The software periodically corrects for baseline offsets in the electronics by switching the ion source off and then measuring the signal in the absence of ions. The circuit shown in Fig. 24.5a is able to take advantage of this capability. In one application the ions are extracted from the source by running it at about +3 V, and is then switched off by decreasing the source voltage to about −4 V. The frequency is selectable from 7.5 Hz to 1 kHz. The ICM 7555 timing chip generates a TTL-compatible square wave. The square wave from the timing chip does not have a 50 % duty cycle, and is therefore sent to a D-type flipflop circuit, with a square

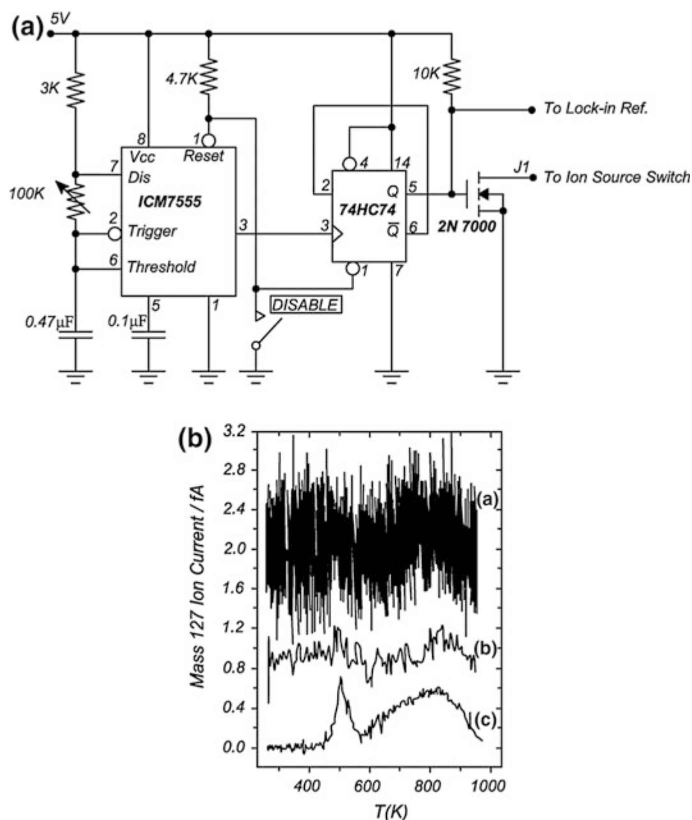

Fig. 24.5 Modulated QMS ion source for enhanced sensitivity. **a** Modulation for circuit, **b** Enhanced TPD spectrum

wave output at 50 % of the timing chip frequency. The 100 kΩ variable resistor is used to vary the frequency. When the disable switch is manually closed the ion source is not modulated and the QMS operates normally.

The advantage of measuring the modulated QMS signal is illustrated in Fig. 24.5b. Here a fraction of a ML of iodine from Pt(111) is being monitored by thermal desorption at a temperature sweep rate of 0.1 K/s. In (a), the unmodulated signal is shown and is very noisy. A smoothing routine is applied to this signal as shown in (b), and two desorption peaks are barely resolved. In (c), the modulated signal is shown with good resolution of two desorption processes. By enhancing the speed of the temperature ramp, further improvements in signal intensity will be found, but the resolution of overlapping peaks will begin to degrade [28]. Of course, the method may also be used to enhance the mass spectrometer sensitivity in other types of measurements.

24.6 Line-of-Sight Mass Spectrometry for Thermal Desorption

A mass spectrometer may be used for line-of-sight detection if all arriving molecules from the background are removed. By placing the mass spectrometer behind apertures which connect to baffle surfaces at 77 K, many gases may be sampled in this manner. Any molecule with an approximate desorption enthalpy of ≥ 18 kJ mol^{-1} will be pumped at 77 K, and this includes molecules such as water, ethene and almost all higher molecular weight organic and inorganic compounds. Molecules such as H_2, O_2, N_2, CO, Ar and CO_2 will not be pumped at 77 K.

Figure 24.6 shows a schematic of the cryo-shield [29–31]. The mass spectrometer should have its shield removed to prevent internal reflection from warm walls. Liquid N_2 fills the tank from a reentrant tube which leads to the outside. Two cylindrical shields, heat stationed on the cryo-reservoir are cooled by conduction. An entrance aperture, N, admits a beam of molecules originating from the crystal surface during a desorption experiment. All molecules originating from outside the focal area will hit a cold surface and be retained. For a gas being admitted from the focal area at a pressure of 10^{-8} mbar, the pressure in the mass spectrometer ionization volume will be about 10^{-12} mbar at a sample-to-ionization volume distance of ~ 30 cm. A mass spectrometer with a multiplier operating at 10^6 amplification factor typically has a sensitivity of better than 10^{-14} mbar. The exit aperture, M, does not have to be maintained at 77 K, since molecules reflected from its surface will reach the cooled inner cylindrical shield surrounding the mass spectrometer and be captured. To eliminate the influence of background gas produced in the mass spectrometer, chopping of the desorbing gas may be carried out.

This method of beam measurement eliminates desorption from the crystal support assembly and may be used to measure accurate thermal desorption spectra [31–34]. It may also be used to measure the sticking probability [29–32, 34];

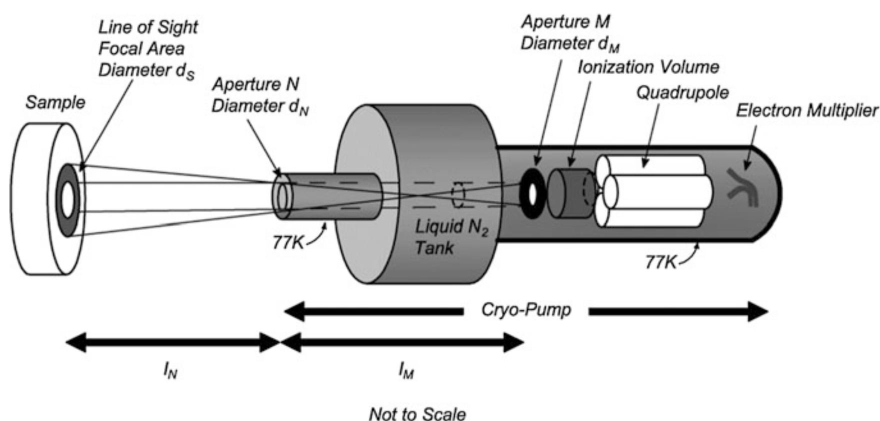

Fig. 24.6 Line-of-sight mass spectrometry for thermal desorption

surface reactions can be measured either isothermally or during heating [30, 31, 34, 35]; and radical desorption may be directly measured [30].

The upper pressure limit for the apparatus is about 10^{-4} mbar, where mean free path considerations will disrupt the trajectories of molecules coming from the crystal.

24.7 Mass Spectrometer Calibration by Molecular Decomposition

Many factors make it difficult to control the partial pressures of two or more gases in a pumped vacuum system and to know the absolute ratios of partial pressures, much less the absolute partial pressures themselves. The factors that prevent such calibrations have to do with fundamental issues such as the pumping speed, for individual gases, the relative differences in sticking coefficients on the chamber walls for different molecules, and the absence of absolute knowledge of gas fluxes from calibrated dosers, etc. One way to overcome some of these difficulties is to utilize the thermal decomposition of molecules, containing known stoichiometric ratios of the elements, and to measure the relative signals from the gaseous decomposition products under dynamic pumping conditions [36].

Figure 24.7 shows a general arrangement that maybe utilized for these measurements. A molecular beam consisting of the pure compound is directed at a heated surface that is known to decompose the compound, producing only gaseous products. A mass spectrometer samples the desorbing gas products and yields signals of the mass spectrometer cracking products and parent ions of the product molecules from the decomposition.

The absolute mass spectrometer sensitivity, β_x, is defined as

$$\beta_x = kT_g / S_x \eta_x \tag{24.3}$$

Here we define η_x as a proportionality constant such that $P_x = \eta_x I_x$ and is often called the mass spectrometer sensitivity, converting an ion signal into a partial pressure. The quantity η_x contains factors such as the ionization probability of the molecule, the transmission probability of the ions through the mass spectrometer, and the electron multiplier gain, which is generally considered to have a $M^{-1/2}$ dependence, where M = molecular mass.

On this basis, the ratio β_x/β_y will be the relative mass spectrometer sensitivity for the two species, x and y.

If we can generate the two species in a known stoichiometric ratio by decomposition of a molecule on a hot surface, and if we know the pumping speeds for the two molecules from their molecular weights (scaling as $M^{-1/2}$), then the relative sensitivities β_x/β_y can be determined. It is of course important to measure changes in I_x above the background and to consider that a particular mass spectrometric ion

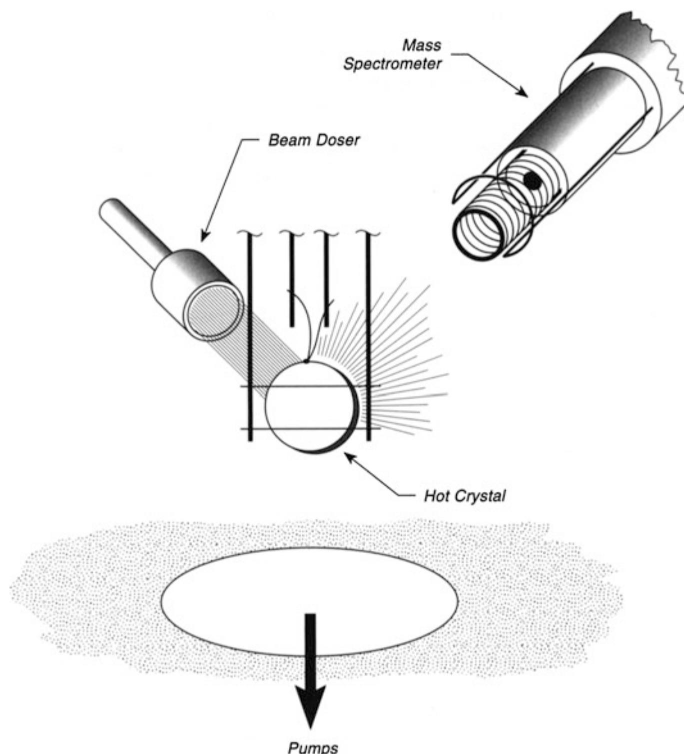

Fig. 24.7 Mass spectrometer calibration by molecular decomposition

may contain contributions from the cracking of more than one type of molecule. It is also important to remember that this method assumes that the angular distribution of all of the product molecules from the molecular decomposition is the same, and probably of cosine form if surface equi-librium is achieved before release of the product molecules.

The method has been used for two molecules to determine the relative sensitivies for four gases as diagrammed below:

$$H_2CO \rightarrow H_2 + CO \tag{24.4}$$

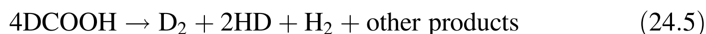

$$4DCOOH \rightarrow D_2 + 2HD + H_2 + \text{other products} \tag{24.5}$$

In the case of the isotopicallylabeled formic acid, an equilibrium mixture of the three hydrogen isotopes will be produced, since possible kinetic isotope effects changing this ratio are likely to be small at the high surface temperature of the decomposition.

For the vacuum system used in [36], in which a UTI-100C mass spectrometer was employed, the following relative sensitivities were determined:

$$\beta_{H2} : \beta_{HD} : \beta_{D2} : \beta_{CO} = 1.00 : 0.80 : 0.63 : 0.98 \tag{24.6}$$

References

1. J.B. Taylor, I. Langmuir, Phys. Rev. **44**, 423 (1933)
2. J.A. Becker, C.D. Hartman, J. Phys. Chem. **57**, 153 (1953)
3. An excellent review may be found in: G. Ehrlich, Adv. Catal. 14, 255 (1963)
4. P.A. Redhead, Trans. Faraday Soc. **57**, 641 (1961)
5. J.T. Yates Jr, *Methods of Experimental Physics*, vol. 22 (Academic Press, Orlando, FL, 1985), p. 425
6. A.M. de Jong, J.W. Niemantsverdriet, Surf. Sci. **233**, 355 (1990)
7. T.E. Madey, J.T. Yates Jr, R.C. Stern, J. Chem. Phys. **42**, 1372 (1965)
8. P.W. Tamm, L.D. Schmidt, J. Chem. Phys. **51**, 5352 (1969)
9. T.E. Madey and J.T. Yates, Jr., in *Structure et Properties des Surfaces des Solides* No. 187 (CNRS, Paris, 1970), p. 155
10. P.W. Tamm, L.D. Schmidt, J. Chem. Phys. **54**, 4775 (1971)
11. T.E. Madey, Surf. Sci. **29**, 571 (1972)
12. T.E. Madey, J.T. Yates Jr, Surf. Sci. **63**, 203 (1977)
13. P. Feulner, D. Menzel, J. Vac. Sci. Technol. **17**, 662 (1980)
14. S.M. Gates, J.N. Russell Jr, J.T. Yates Jr, Surf. Sci. **146**, 199 (1984)
15. G. Lu, A.L. Linsebigler, J.T. Yates Jr, J. Vac. Sci. Technol. **A12**, 384 (1994)
16. V.S. Smentkowski, J.T. Yates Jr, J. Vac. Sci. Technol. **A7**, 3325 (1989)
17. A. Winkler, J.T. Yates Jr, J. Vac. Sci. Technol. **A6**, 2929 (1988)
18. H. Schlichting, D. Menzel, Surf. Sci. **285**, 209 (1993)
19. L.H. Dubois, Rev. Sci. Instrum. **60**, 410 (1989)
20. A.C. Liu, C.M. Friend, Rev. Sci. Instrum. **57**, 1519 (1986)
21. W.M. Graven, D.E. Gilmartin, Rev. Sci. Instrum. **55**, 1827 (1984)
22. F. Nakao, Rev. Sci. Instrum. **46**, 1489 (1975)
23. P. Marchand, C. Paquet, P. Marmet, Rev. Sci. Instrum. **37**, 1702 (1966)
24. J.R. Young, Rev. Sci. Instrum. **37**, 1414 (1966)
25. Professor Patricia Thiel, Department of Chemistry, Iowa State University, Ames, Iowa 50011 (private communication); taken from the Ph. D. Thesis of M.M. Walczak, Iowa State University (1989); the original idea comes from A.L. Johnson, Ph.D. Thesis, University of California, Berkeley (1986)
26. J.T. Yates Jr, D.A. King, J. Vac. Sci. Technol. **9**, 1256 (1972)
27. Professor J.B. Hudson, Materials Engineering Department, Rensselaer Polytechnic Institute, Troy, NY 12180 (private communication)
28. S.A. Furman, M. Labayen, R.G. Dean, D.A. Harrington, J. Vac. Sci. Technol., A **19**, 1032 (2001)
29. R.G. Jones, C.J. Fisher, Surf. Sci. **424**, 127 (1999)
30. A.S.Y. Chan, M.P. Skegg, R.G. Jones, J. Vac. Sci. Technol., A **19**, 2007 (2001)
31. R.G. Jones, C.A. Clifford, Phys. Chem. Chem. Phys. **1**, 5223 (1999)
32. M.G. Roper, R.G. Jones, Phys. Chem. Chem. Phys. **10**, 1336 (2008)
33. A. Deyko et al., Phys. Chem. Chem. Phys. **11**, 8544 (2009)
34. M.G. Roper, R.G. Jones, Langmuir **21**, 11684 (2005)
35. A.S.Y. Chan, R.G. Jones, Surf. Sci. **451**, 232 (2000)
36. Y.-K. Sun, W.H. Weinberg, J. Vac. Sci. Technol. **A7**, 3121 (1989)

Chapter 25
Temperature-Programmed Desorption/Reaction

25.1 Thermal Desorption—Angular Resolved

The measurement of the angular distribution of molecules desorbing from single crystal surfaces provides information on the dynamics of the desorption process. For desorption from completely equilibrated surface species, a cosine distribution is expected. However, often a noncosine distribution is observed, and this may be related to processes such as atom recombination at a point on a repulsive adsorbate-surface potential energy curve in the region of the transition state. A simple apparatus to measure the angular distribution is shown in Fig. 25.1a [1].

A collimator is used to select particles desorbing at a certain angle, Θ, with respect to the surface normal. The crystal is of rectangular geometry (10 mm × 10 mm × 1 mm), and the apertures have dimensions a_1 = 1.5 mm × 6 mm; a_2 = a_3 = 30-mm diameter; a_4 = 6 mm × 10 mm). The length of the collimator is 100 mm and the distance to the crystal is 23 mm in these measurements. The acceptance angle outside and inside the collimator is 2.1°, and a region on the crystal measuring 3 × 9 mm^2 will be sampled in the normal direction; at 70°, a 9 × 9 mm^2 region will be sampled. An angular distribution of form $\cos^n\Theta$ will give a signal proportional to $\cos^{(n-1)}\Theta$.

The collimator is internally pumped by means of a Ti getter film which is deposited by evaporation from a Ti wire source, and this will act as a very fast internal pump for the collimator (see p. 72).

The ionization gauge is located off-axis so that only a random flux of gas, thermally equilibrated with the walls of the chamber containing the gauge and ion pump, will be measured. The ionization gauge was thermostatted by means of a water bath, and the ion pump was operated with a stabilized DC power supply to reduce fluctuations in pumping speed. It was found that a pulse of H_2 into the ionization gauge chamber resulted in a short period decrease in the background signal, so for measurements of H_2, a continuous minute constant flux of H_2 was added. No difficulties of this kind were observed with CO.

© Springer International Publishing Switzerland 2015
J.T. Yates Jr., *Experimental Innovations in Surface Science*,
DOI 10.1007/978-3-319-17668-0_25

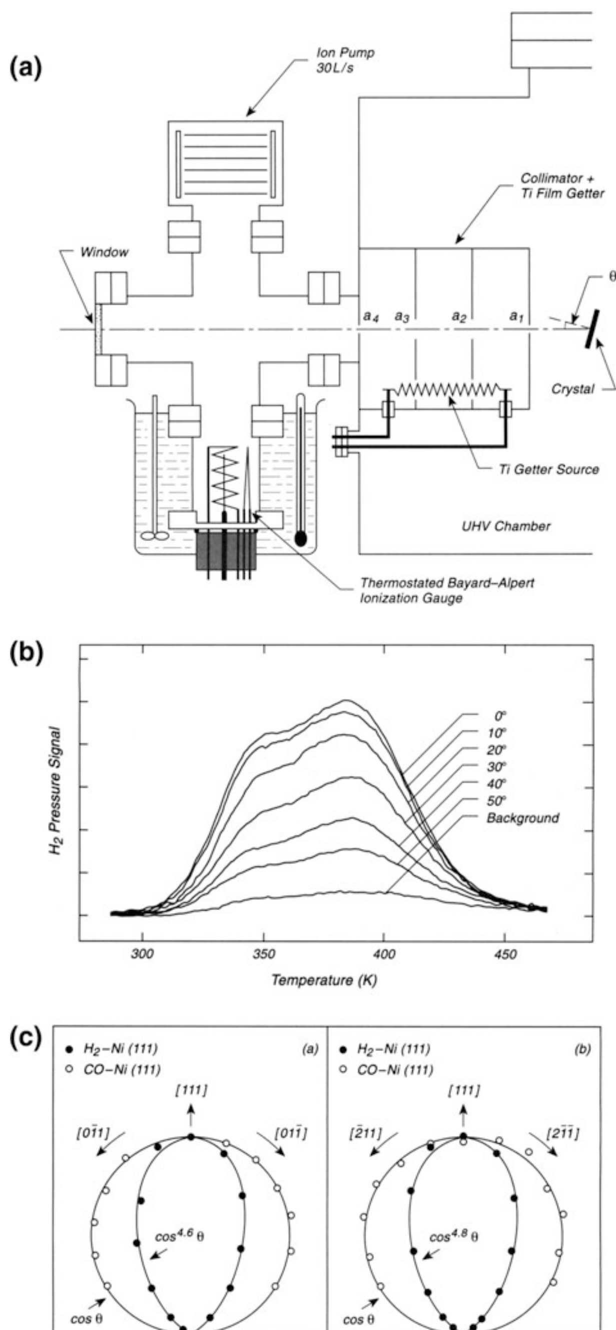

Fig. 25.1 Thermal desorption—angular resolved . **a** Desorption apparatus. **b** Desorption spectra —H_2/Ni(111). **c** Measured angular distribution for H_2 and CO

Figure 25.1b shows typical desorption spectra for H_2 from Ni(111) that has been saturated with H_2. The angular distributions of both H_2 and CO from Ni(111) are shown in Fig. 25.1c. It can be seen that CO desorbs in the two azimuths measured with a $\cos\Theta$ distribution, whereas H_2 has a sharper distribution, described as $\cos^n\Theta$, where n = 4.6 or 4.8.

25.2 Magic-Angle Thermal Desorption Mass Spectroscopy

The thermal desorption of species from surfaces is widely used throughout the field of surface science for studies of adsorbates on metal foils and single crystal surfaces (see p. 273). Often an unshielded mass spectrometer is used for detection of the desorbing particles and it will generally measure the density of gas produced in a random flux within the vacuum chamber. More modern methods involve the use of apertured mass spectrometers that are differentially pumped within the surrounding shield (see p. 72). The aperture is often close-coupled to the crystal surface along the surface normal in order to collect the majority of the desorbing gas evolved from the region of the crystal viewed by the aperture. Under these conditions of efficient collection, considerations of the angular distribution of the desorbing gas are of second-order importance.

However, when the apertured mass spectrometer is located far from the crystal surface, considerations of the angular distribution of the desorbing gases become very important, especially if measurements are made of the relative signal from different gases desorbing simultaneously (and sampled by multiplex methods). Thus, gases are known to desorb with angular distributions approximated by $\cos^n\Phi$ where Φ is the angle from the normal. Here n can have a value of unity, or values running to about 20 in extreme cases. If the value of n differs significantly for two species desorbing simultaneously, then errors in estimating the relative signal intensities will occur, and these errors can approach 400 % for collection along the normal direction when the mass spectrometer is distant from the crystal. Pauls and Campbell [2] have considered this problem and have found that there is a magic angle for the mass spectrometer location that will minimize the error in comparing desorption signals with n varying over the range 1–9. Figure 25.2a shows the geometry of the mass spectrometer collection optics, where r is the crystal radius, and d is the distance to the aperture. The polar angle Φ is shown. Figure 25.2b shows the magic angle, which minimizes the error in the relative magnitude of the desorption signals having varying angular distribution, where an integration over the emitting surface of the crystal has been carried out. The function shown varies as the value of the ratio d/r varies. For typical values of d/r from 2 to 5, the magic angle varies from 42° to 34°, and at large values of d/r, the optimal angle of $\Phi_m = 34°$ is found. The variations in the signal for the range of n considered is only about 26 % at $\Phi_m = 42°$.

It should be mentioned that the mass spectrometer detection behavior may vary between two limits. For very fast pumping within the shield, only a single pass of

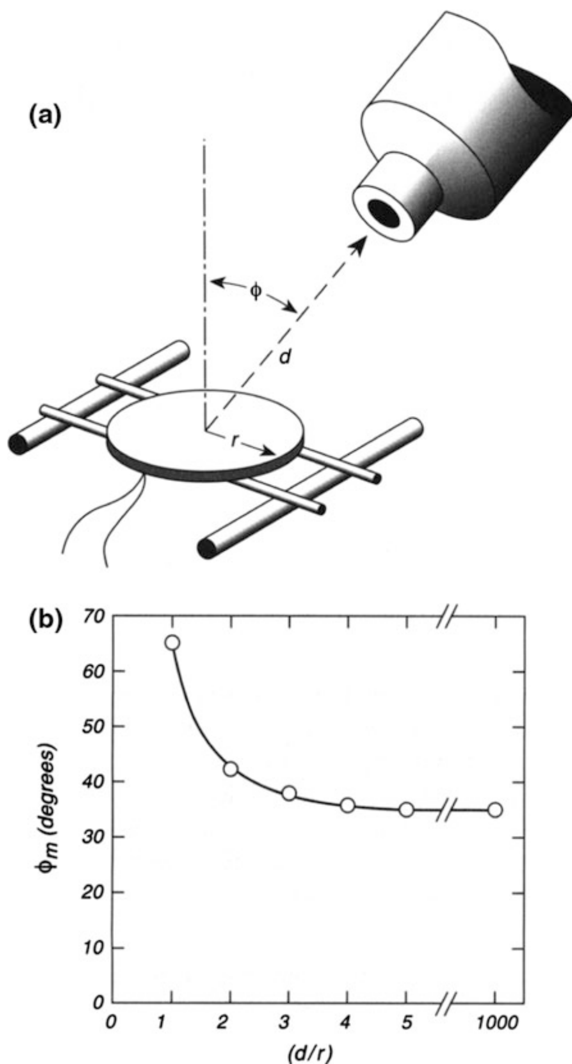

Fig. 25.2 Magic-angle thermal desorption spectroscopy. **a** Mass spectrometer aperture—collection angle. **b** Magic-angle, Φ_{m}, for aperture collection

the desorbing species occurs through the ionizing optics, and considerations of the molecular velocities of the gas molecules would be necessary in measuring relative fluxes [3]. For very slow pumping in the shield, which is the normal method of operating the shielded mass spectrometer at high sensitivity (see p. 259), the desorbing particles will probably acquire the temperature of the ionizing source and then these considerations of molecular velocity will be unneeded. The detector signal is then truly proportional to the flux entering the aperture [2].

These considerations also apply to the measurement of any particle desorption technique, for example sputtering of neutral species from surfaces [4].

25.3 High-Temperature Thermal Desorption Spectroscopy

The extension of thermal desorption spectroscopy into temperature regions well over 2000 K involves the use of electron bombardment heating rather than ohmic heating. Electron bombardment heating introduces experimental complications into the method, which have been overcome as shown below [5].

The experimental difficulties introduced by electron bombardment heating are listed below:

1. The accelerating potential for electrons must be in the kV region. If the crystal is grounded, and the emitter is biased negatively, then spurious desorption may occur from regions other than the crystal that are also at ground potential. Therefore, biasing the crystal positive is the preferred mode. This requires that the thermocouple be measured using a high-voltage isolation amplifier, and the amplifier must be able to handle short high-voltage common mode signals if shorting occurs between the sample/thermocouple assembly and grounded regions of the support assembly. A suitable high-voltage precision isolation amplifier is commercially available [6].
2. Because of radiative heating of the emitter filament by the incandescent crystal, causing enhanced thermionic emission, the heating current to the emitter must be controlled by a computer working in feedback style. The LabVIEW computer (see p. 351) and program are ideal for this, but another program was used in the work described here.
3. The mechanical mounting of the spiral emitter filament is critical. It must be rather close to the back of the crystal, and it should be mounted in a strain-free condition prior to first heating. Even then, distortion of the filament may occur, and because of its brittle character after heating, readjustment of its position by bending the W is impossible. However, if the filament is mounted on ductile Ta posts, they may be slightly adjusted by bending after the filament is embrittled, moving the filament to the correct position. Spiral W emitters, wound to specified dimensions, are commercially available [7].
4. The thermocouple wires, because of their small radius of curvature, will concentrate the electric field lines to themselves, and will undergo electron bombardment with a higher current density than the flat crystal, causing excess local heating. This may be avoided by mounting the thermocouple close to the top of the crystal, and placing the emitter closer to the bottom as shown in Fig. 25.3a.

The desorption of Pt from a W(211) crystal is shown in Fig. 25.3b, where a quadrupole mass spectrometer, working in the line-of-sight mode was employed for detection [5].

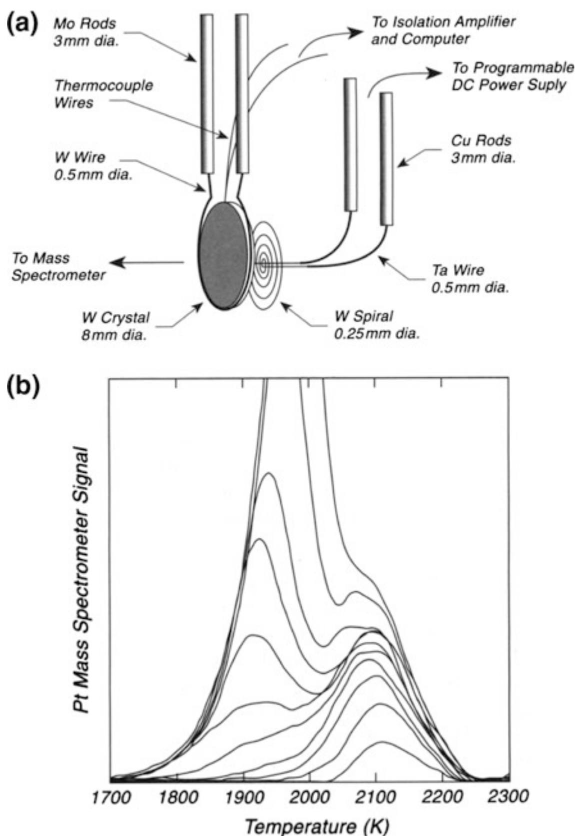

Fig. 25.3 High-temperature thermal desorption spectroscopy. **a** Electron bombardment design. **b** Pt thermal desorption from W (211)

25.4 Automated Temperature Programmed Desorption (TPD) Apparatus

A computer-controlled system allowing acquisition of large data sets automatically is shown [8]. The system has a single crystal, mounted off-center, a molecular beam doser at position 1 and a shielded quadrupole mass spectrometer at position 2. The crystal is moved, after automated cleaning by heating, to the doser, where for a specified time it is dosed with gas. It is then moved to the mass spectrometer (QMS) position for the measurement of the TPD spectrum as the sample temperature is automatically programmed upwards. In between each separate adsorption experiment, the mass spectrometer is recalibrated against the steady small background pressure of the gas being continuously dosed to compensate for drifts in the multiplier gain.

Figure 25.4a shows a schematic of the apparatus. Two stepper motors (type Nema 23, 1 A current rating) are used to rotate the sample and to translate the sample as shown by the arrows on the drawing. The motors operate on an open loop

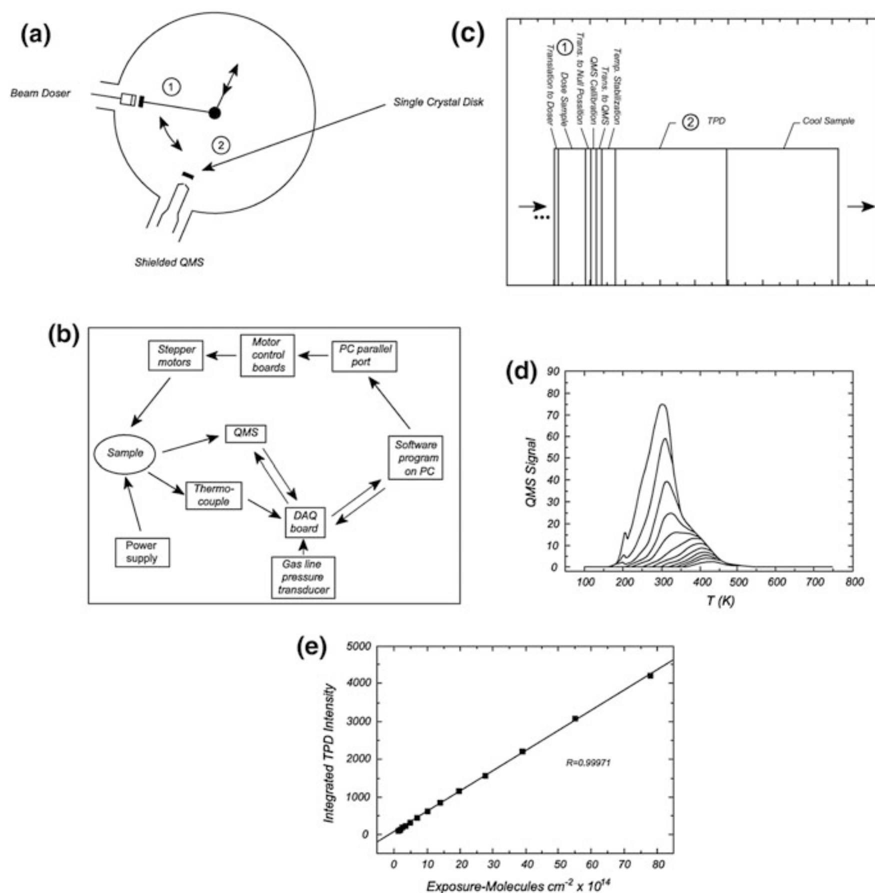

Fig. 25.4 Automated temperature programmed desorption. **a** Two position-automated TPD apparatus. **b** Schematic of control system. **c** Automated TPD program. **d** Typical TPD. **e** Integrated desorption yield

control system without position feedback to the computer. Figure 25.4b shows the main function blocks for control. Through the DAQ board, the computer controls the power supply that feeds the heating current to the crystal. It also reads the amplified output of the thermocouple attached to the crystal. The stepper motors are driven by two motor control boards (Motion Group, model MS2.0). The motors provide an angular resolution of 1.8º translating into an angular resolution of 0.045º inside the vacuum system. The resolution of the micrometer giving linear motion to the crystal is in the μm range.

The timing of separate steps is shown in Fig. 25.4c. Dosing of the sample to different doses of gas is accomplished in the constant-gas flow by adjusting the time of exposure. QMS calibration is then performed with the crystal in a null position.

TPD is next carried out with the crystal at position 2 in front of the shielded QMS. After the upward temperature ramp, the crystal is cooled before continuing the cycle. Figure 25.4d shows a stack of typical TPD measurements made, where the exposure is automatically increased by a factor of $2^{1/2}$ in each step. Figure 25.4e shows that the coverage increases linearly with exposure, to great accuracy. This means that the adsorption process is governed by the production of a mobile precursor species.

The automatic method is highly accurate since it does not involve human intervention.

25.5 Scanning Kinetic Spectroscopy—A Survey Method for Investigation of Surface Reaction Processes

Multiple reaction pathways are available to a polyatomic molecule interacting with a solid surface. It is often useful, in a survey experiment, to delineate the temperature regions where various reaction steps are either active or inactive. The scanning kinetic spectroscopy (SKS) method [9] permits this to be done efficiently in many cases [10, 11].

Figure 25.5a shows an SKS apparatus for the study of a molecule's decomposition routes on a single crystal surface. The cleaned single crystal is first covered with a monolayer of the adsorbate to be studied at a temperature below the dissociation temperature of any of the bonds in the molecule. At this point, the crystal is rotated into a beam of the molecules originating from a collimated beam doser, as described on p. 421. Initially, the incident beam is reflected off of the saturated monolayer on the crystal, providing a reference signal in the mass spectrometer which is located behind an apertured shield (see p. 259) and is differentially pumped (see p. 72). The crystal is then programmed upward in temperature, and the mass spectrometer records, in the multiplex mode, all of the relevant mass peaks related to consumption of the parent reactant molecule and to liberation of product molecules, as shown schematically in the bottom section of Fig. 25.5a.

Figure 25.5b shows a typical set of SKS measurements, made in multiplex mode, which characterizes the temperatures where the various elementary steps occur. The steps themselves are shown in Fig. 25.5c. Here, the reaction of the methanol molecule on Ni(111) is investigated.

Let us follow the processes observed in Fig. 25.5b and outlined in Fig. 25.5c. In this example, the isotopically labeled molecule, CD_3OH, is being employed as the reactant at a known flux onto the crystal. The covered crystal is rotated into the CD_3OH beam at the double-headed arrow on the left. In the top panel of Fig. 25.5b, at temperatures below 187 K, CD_3OH merely reflects off of the monolayer of CD_3OH previously adsorbed, and a flat line for mass 33 is observed in this region. Upon beginning the temperature program, α-CD_3OH is first observed to desorb, originating from undissociated methanol molecules. At the dashed line, 290 K, a

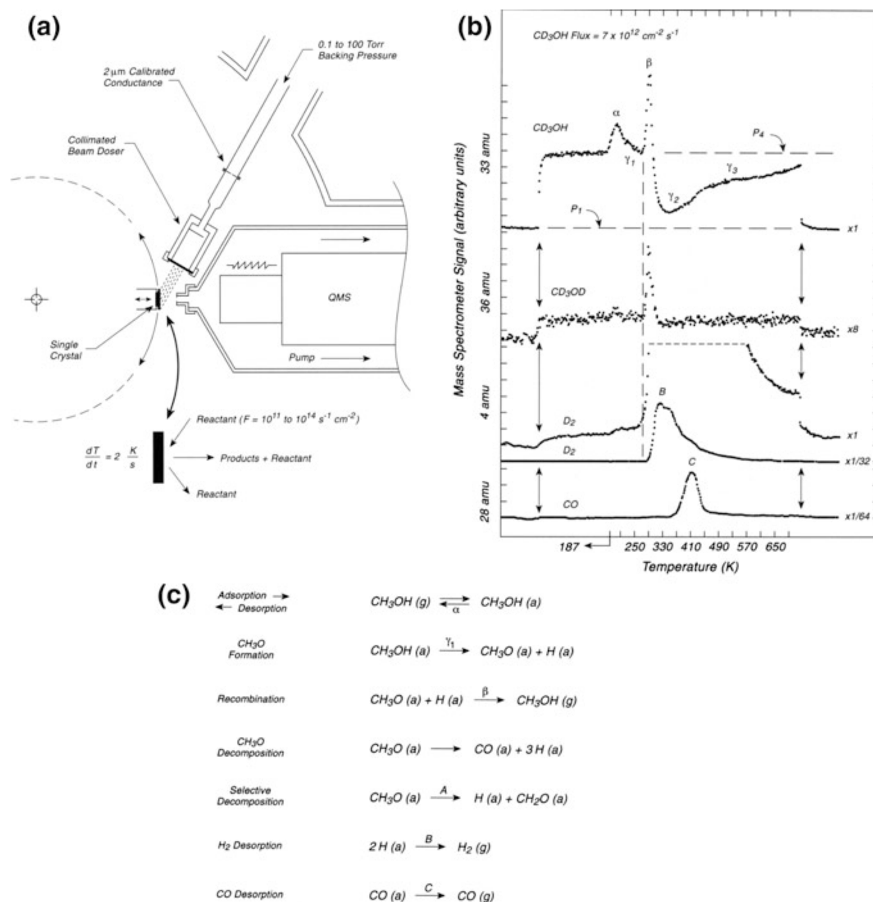

Fig. 25.5 Scanning kinetic spectroscopy (SKS). **a** SKS apparatus. **b** Typical SKS data. **c** Elementary reaction steps as inferred from B

β-CD_3OH feature is sharply evolved. The β-process is due to an elementary step involving the recombination of adsorbed H (from CD_3O–H bond scission) with adsorbed methoxy, CD_3O. It is informative to note that when the isotopic molecule, CD_3OD, is monitored at mass 36, the β-process is also observed, and the D atom involved here can only come from the breaking of a C–D bond in adsorbed CD_3O. This probably occurs by the production of adsorbed formaldehyde, CH_2O (a), shown (Fig. 25.5c) in process A, where the isotopic composition is not written for any of the molecules in Fig. 25.5c. When mass 4 is monitored in Fig. 25.5b, D_2 is observed to desorb at 330 K, opening up sites on the surface. When mass 28 is monitored in Fig. 25.5b, CO is observed to desorb at 420 K, also opening up sites.

Three processes labeled γ are also indicated on the top SKS spectrum. The process γ_1 for adsorbed CH_3O formation by O–H bond scission is not defined, since

a volatile product is not liberated from this process, but O–H bond scission must begin below 290 K since the β-recombination process begins at 290 K. The process γ_2 and γ_3 involve the consumption of the reactant molecule since the reflected flux of reactant falls below the reference line in this temperature region. These consumption processes are closely correlated with the D_2 and CO desorption processes, shown near the bottom of Fig. 25.5b, which open Ni sites for adsorption and reaction processes.

The SKS method is a fast survey method, giving one a partial view of the characteristic temperatures for various adsorption, desorption, and surface dissociation processes. It has been effectively used with intentional poisoning of the surface by added species, and with intentional addition of known reactants to the surface [9]. It has been successfully used to observe deuterium kinetic isotope effects that give insight into the rate-controlling steps in surface reactions involving the hydrogen moiety [9, 11]. The original concept of temperature scanning while making reaction kinetic measurements on single crystal surfaces was first presented in 1981 by Goschnick and Grunze [12]. The SKS method also resembles the familiar temperature-programmed reaction spectroscopy (TPRS) [13, 14] (see p. 282), but SKS has added advantages of working like a flow reactor where fresh reactant is continuously supplied during the measurements.

The ability to rapidly scan many mass peaks and to record the time behavior of selected mass peaks has been a familiar subject for a number of years. Recently, a fast multimass measurement method has been introduced that permits up to 15 mass spectra of 50 amu width to be recorded per second, using a quadrupole mass spectrometer [15]. Another variation on this method scans up to 100 complete mass spectra per thermal desorption experiment. Enhanced signal-to-noise is achieved by integrating each of the mass peaks rather than by measurement of the peak height only [16].

There are many other mass-spectrometer based methods used for the study of surface reactions in which transient surface species may be detected. Among these is laser induced desorption, in which a Fourier transform mass spectrometer is often used [17]. Here, the laser may be used to desorb surface species without extensive thermally induced fragmentation.

25.6 Temperature-Programmed Reaction Spectroscopy (TPRS)

This method extends the basic concepts of temperature-programmed desorption (TPD) (see p. 259) to examine complex surface reactions. Multiple mass channels are monitored simultaneously during programmed heating. The method has been widely used to unravel the kinetic steps in both decomposition and synthesis reactions on single crystal surfaces. The method also resembles scanning kinetic spectroscopy (SKS) described on p. 280.

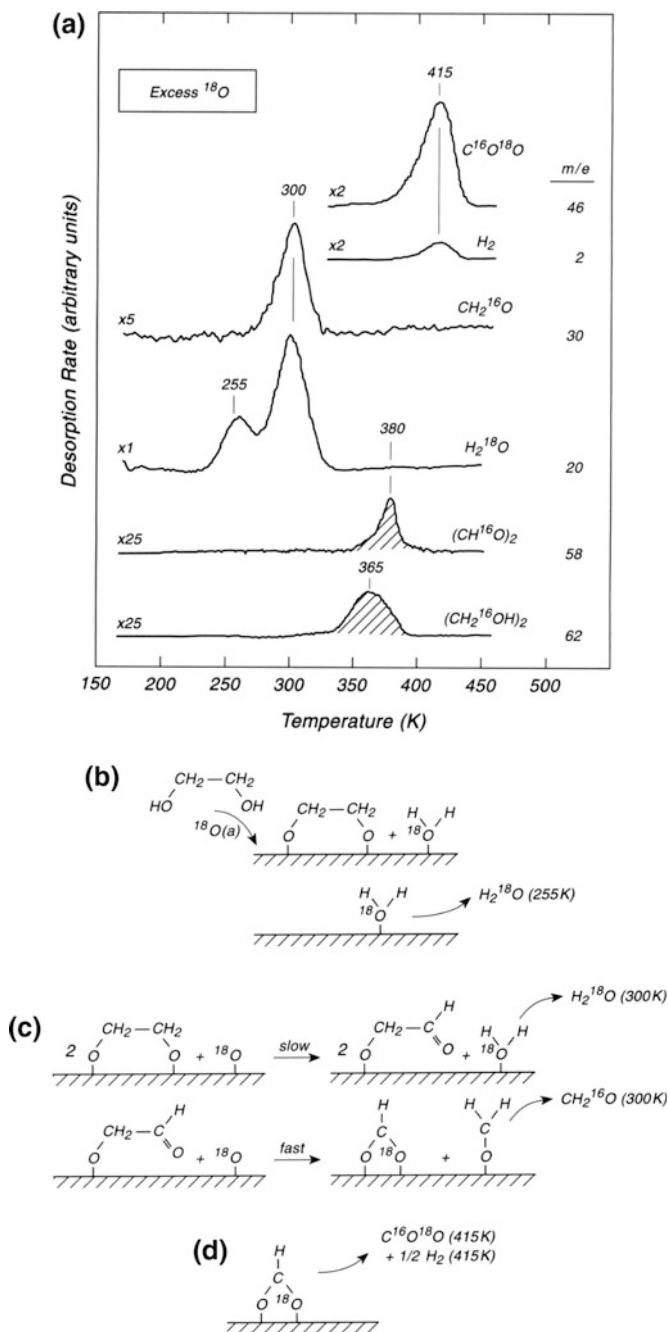

Fig. 25.6 Temperature-programmed reaction spectroscopy (TPRS) **a** TPRS data—$(CH_2^{16}OH)_2$ + $^{18}O/Ag(110)$. **b** Dissociative adsorption followed by $H_2^{18}O$ evolution. **c** $H_2^{18}O$ and $CH_2^{16}O$ evolution. **d** $HCO^{18}O$ decomposition

An example of the use of TPRS is given here [18]. The interaction of ethylene glycol, $(CH_2^{16}OH)_2$, with fractional monolayers of chemisorbed ^{18}O on Ag(110) has been studied. First, up to 200 mass peaks are scanned to survey the products. Then, using methods which scan 10 mass peaks in a multiplex mode in 20 ms, the temperature dependence of evolution of a variety of products was measured as shown in Fig. 25.6a. The two cross-hatched desorption processes occur in surface reaction limited processes and contain no ^{18}O, and are the end result of the oxidative dehydrogenation of the ethylene glycol. The five remaining product peaks are indicative of reactions involving the chemisorbed ^{18}O.

The desorption of $H_2^{18}O$ at 255 K occurs as a result of the direct reaction of O–H bonds of the two O–H groups of the ethylene glycol with adsorbed ^{18}O, as illustrated in Fig. 25.6b. The desorption together of $H_2^{18}O$ and $CH_2^{16}O$ with a peak temperature of 300 K is indicative of a surface reaction controlled by C–H bond scission in the CH_2 groups of the 1,2 ethanedioxy species as shown in Fig. 25.6c. The simultaneous evolution of H_2 and $C^{16}O^{18}O$ at 415 K is indicative of the decomposition of adsorbed formate, $HC^{18}OO$, on the surface. Similar reactions were observed in separate experiments with adsorbed formate, and are illustrated in Fig. 25.6d.

There are other possible mechanisms that might participate in the surface reactions, and these were eliminated by using D substitution for H in the CH_2 groups of the ethylene diol and looking to see whether a primary kinetic isotope effect was seen, in which the scission of the C–D bond occurs at a significantly higher temperature than the C–H bond in the unlabeled molecule. This isotope effect was observed, pointing to C–H bond scission as being a key elementary step in the surface chemistry.

Two reviews on TPRS have been written [14, 19].

References

1. H.R Steinruck, A. Winkler, K.D. Rendulic, Surf. Sci. **152/153**, 323 (1985)
2. S.W. Pauls, C.T. Campbell, Surf. Sci. **226**, 250 (1990)
3. G. Comsa, R. David, Surf. Sci. Rep. **5**, 145 (1985)
4. A. Wucher, F. Novak, W. Reuter, J. Vac. Sci. Technol. **A6**, 2265 (1988)
5. K. Pelhos, T.E. Madey, Department of Physics and Astronomy, Laboratory for Surface Modification, Rutgers, The State University, Piscataway, NJ 08855 (private communication)
6. Model AD210AN. Analog Devices, One Technology Way, Norwood, MA 02062-9106
7. C.M. Furnaces, Inc., 103 Dewey Street, Bloomfield, NJ 07003
8. P. Kondratyuk, J.T. Yates Jr, J. Vac. Sci. Technol. **A23**, 215 (2005)
9. S.M. Gates, J.N. Russell Jr, J.T. Yates Jr, Surf. Sci. **159**, 233 (1985)
10. I. Chorkendorff, J.N. Russell Jr, J.T. Yates Jr, J. Chem. Phys. **86**, 4692 (1987)
11. P.L. Hagans, I. Chorkendorff, J.T. Yates Jr, J. Phys. Chem. **92**, 471 (1988)
12. J. Goschnick, M. Grunze, J. Vac. Sci. Technol. **18**, 561 (1981)
13. R.J. Madix, J. Benziger, Ann. Rev. Phys. Chem. **29**, 285 (1978)
14. R.J. Madix, in *Chemistry and Physics of Solid Surfaces*, vol. II, ed by R. Vanselow (CRC Press, Boca Raton, FL, 1979)

15. G. Zagatta, H. Muller, N. Bowering, U. Heinzmann, Rev. Sci. Instrum. **65**, 359 (1994)
16. L.H. Dubois, Rev. Sci. Instrum. **60**, 410 (1989)
17. D.P. Land, C.L. Pettiette-Hall, D. Sander, R.T. Mclver Jr, J.C. Hemminger, Rev. Sci. Instrum. **61**, 1674 (1990)
18. A.J. Capote, R.J. Madix, Surf. Sci. **214**, 276 (1989)
19. R.J. Madix, J. Benziger, Annu. Rev. Phys. Chem. **29**, 285 (1978)

Chapter 26
Gas Chromatography—Enhanced Sensitivity

26.1 Gas Chromatography—Sensitivity Enhancement

The sampling of gases for gas chromatography analysis suffers from the fact that gas expansion in the sampling lines invariably causes loss of analytical sensitivity. This behavior may be reversed by using a high-pressure pulse of the carrier gas to compress the low-pressure gas sample into the sample loop, where it is then swept into the gas chromatograph. A factor of 20 or more sensitivity enhancement may be achieved. The application shown here involves sampling a high-pressure reactor being used to study the kinetics of a catalytic reaction over a single crystal.[1]

As shown in Fig. 26.1a, the reactor volume to be sampled is connected by valve V_1 to a length of capillary tubing containing an aliquot volume. The tube is then connected via a tee to a gas chromatography sampling valve. Gas from the reactor is expanded into the aliquot volume and the thin tubing (V_5 open) and its pressure is read with a low-volume pressure gauge. The valve V_2 to the pump is closed and valve V_3 is opened to the high pressure of the carrier gas regulator (about 800 Torr). Valve V_4 is then opened, and the carrier gas acts as a piston, compressing the sample gas into the sample loop located on the sampling valve. The contents of the sample loop are then injected into the gas chromatograph, as shown in Fig. 26.1b. In the case shown here, the sampling volume is the aliquot volume plus the volume of the thin tubing, valve, and sampling loop. By keeping valve V_5 closed during sampling, the sampling volume is just the aliquot volume. It was shown that two consecutive analyses using this method differed by less than 4 %.

[1]Personally contributed by Professor C.T. Campbell, Department of Chemistry, University of Washington, Seattle, WA 98195. See also [1].

© Springer International Publishing Switzerland 2015

J.T. Yates Jr., *Experimental Innovations in Surface Science*,
DOI 10.1007/978-3-319-17668-0_26

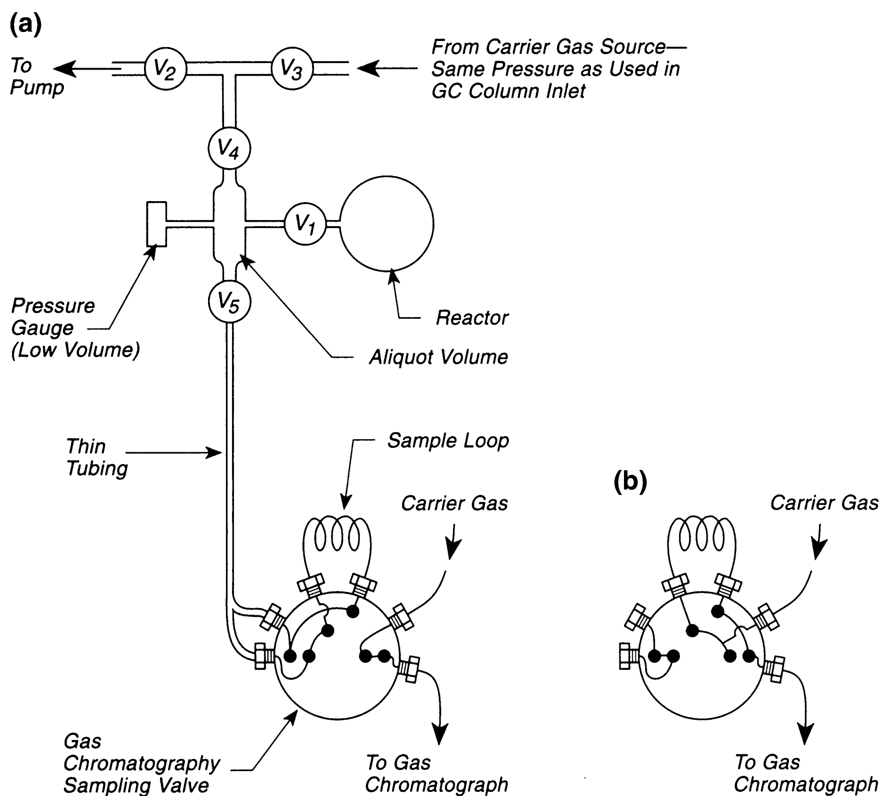

Fig. 26.1 Gas chromatography—sensitivity enhancement. **a** “Fill loop”. **b** “Inject”

Reference

1. C.T. Campbell, K.A. Daube, J. Catalysis **104**, 109 (1987)

Chapter 27
Work Function, Tunneling Spectroscopy and Ellipsometry

27.1 Work Function Changes Using Retarding Diode Method

The use of a retarding diode method for measuring work function changes upon adsorption is one of the oldest and simplest methods for measurement in surface science. The literature related to this method is mostly from the 1960s or 1970s [1–6]. Other methods for measuring work function changes are described elsewhere in Sects. 27.2–27.6.

In Fig. 27.1a is shown a thermionic emitter housed in an ultrahigh vacuum system and facing a sample whose work function change, $\Delta\phi$, is to be measured as a result of adsorption or desorption. The emission current collected by the sample as a function of the applied voltage, U, is given by

$$I(U) = AT^2 \exp[-e(U + \phi)/kT] \qquad (27.1)$$

where A is a constant (proportional to the cathode area), T is the absolute emitter temperature, k is the Boltzmann constant, and ϕ is the sample work function, and e is the electronic charge. Equation (27.1) applies only for the initial section of the retarding potential curve where space charge effects are absent [4].

In Fig. 27.1b, a plot of the collected current versus the retarding potential, U, is shown for a sample which has undergone a work function change, $\Delta\phi$. The difference in the retarding potential measured at constant current on the linear sections of the curves is equivalent to the work function change, assuming that the emitter work function has not changed and that the emitter temperature remains constant. This difference measurement is made where the two "linear" portions of the curve are exactly parallel.

In practice, the resistance, R_e, of the emitter is kept constant using a Wheatstone bridge, and if the dimensions of the emitter filament have not changed due to oxidation of the material of which it is made or to sublimation of the emitter, the

© Springer International Publishing Switzerland 2015

J.T. Yates Jr., *Experimental Innovations in Surface Science*,
DOI 10.1007/978-3-319-17668-0_27

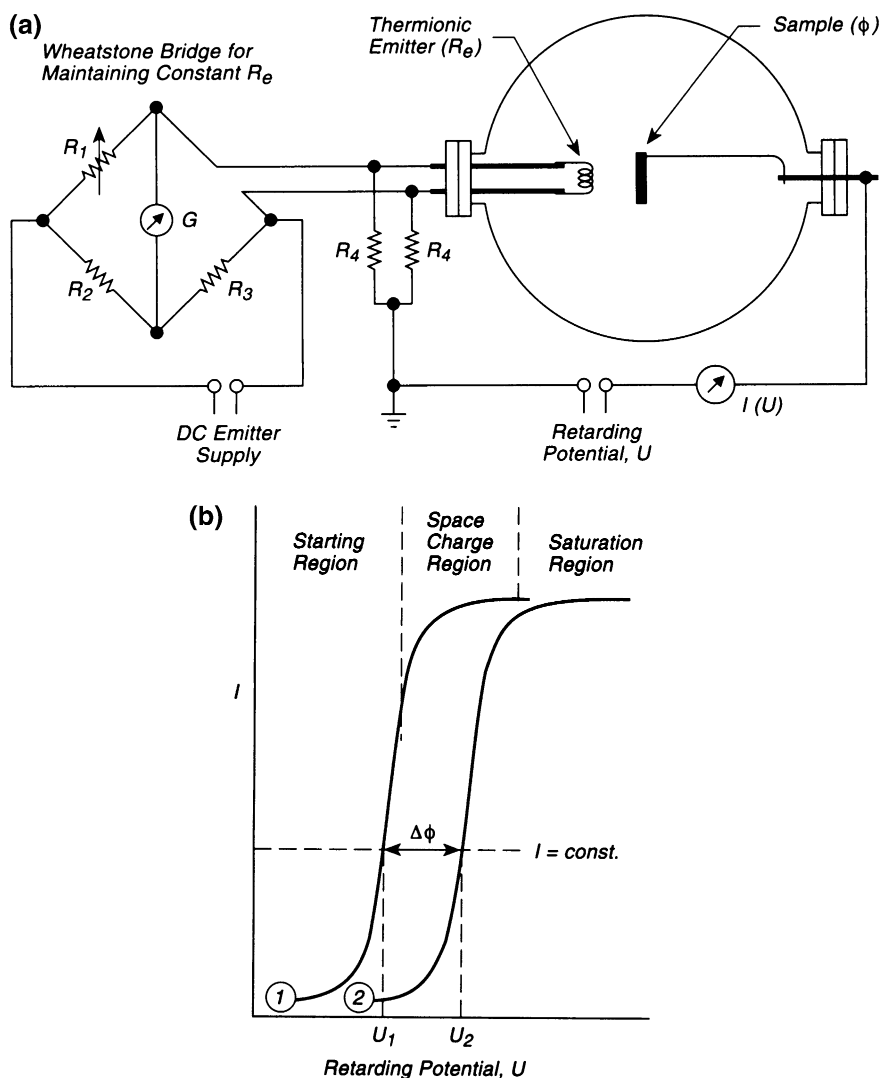

Fig. 27.1 Retarding diode for measuring work-function changes. **a** Schematic of circuit, **b** Collected current versus retarding potential

temperature will also be constant. The temperature of the cathode emitter will be sensitive to the heat loss through the leads to the emitter, and thermostating these at constant temperature with a water cooling jacket will remove this variable.

There are several factors that can affect the measurements using this simple device. One possible problem is the emission of impurity gases from the hot emitter

filament, which will influence the work function of the sample. Second is the effect of the hot filament on the residual gases in the vacuum system (for example, H_2 dissociation) making them reactive with the sample. This effect can be eliminated by turning off the emitter during gas admission. The method will not work well at pressures above about 10^{-4} Torr, since otherwise the cathode might be cooled by heat conduction through the gas. Finally, the effect of electron bombardment and radiation on the surface layer on the sample must be understood when using this method.

The retarding diode method has been employed in a conventional LEED apparatus with continuous derivative measurement of the work function change during adsorption. A sensitivity of about 5 meV was obtained, using the lock-in amplifier method for making continuous measurements of the changing work function [7]. Reference [7] also summarizes background papers in this area.

27.2 Work Function Measurements Using an Electron Gun

One of the simplest methods to measure the work function change during adsorption on a metal single crystal is to employ a retarding potential method, using an ordinary electron gun and an interposed grid or aperture. Figure 27.2a shows a simple device first used for the study of hydrogen, nitrogen and xenon adsorption on tungsten surfaces [8–10]. An electron gun of ordinary design supplies current to the crystal through an aperture made of coiled tungsten in this case. The coiled tungsten is also used as an electron emitter for thermally cleaning the tungsten crystal at 2500 K. The crystal is welded to a thin wire support which may be cooled with liquid nitrogen. By using 25 eV electrons, and retarding between the aperture and the crystal surface, I–V plots are obtained, and from the shift in electrical potential of the knee region, the work function change may be deduced as gases are adsorbed on the crystal. The reproducibility of duplicate measurements is about ±20 meV.

Figure 27.2b shows the linear work function change versus coverage for H_2 adsorption on W(100). The linearity versus measured coverage (using thermal desorption spectroscopy) suggests that depolarization effects between neighbor H atoms are small in this case [8]. Figure 27.2c shows measurements of the adsorption of N_2 on W(110) at 123 K. Here, the work function change is nonlinear with coverage, and this indicates that depolarization effects exist between the adsorbed molecular N_2 molecules [9]. The plot shown in Fig. 27.2c is a fit to the immobile Topping model, and the N_2 polarizability may be obtained from this fit [9, 11].

The use of an electron gun in a display LEED apparatus for retarding potential measurements of work function changes has been described [12].

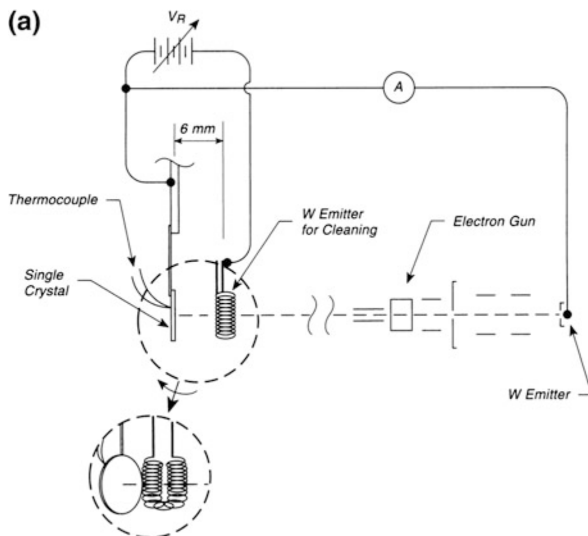

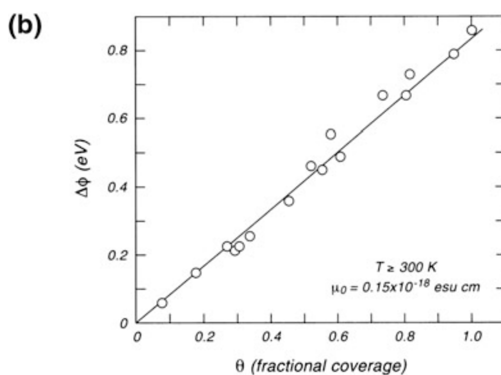

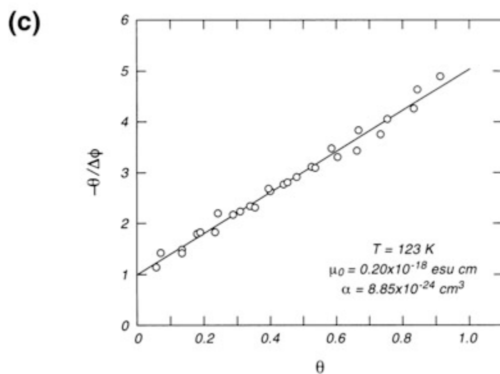

Fig. 27.2 Work-function changes using electron gun. **a** Retarding potential measurement system using an electron gun, **b** Work function change—H_2/W(100), **c** Topping model plot—N_2/W (100) work function measurement

27.3 Work Function and Electron Reflection Coefficient Measurements with the Shelton Diode

The use of the Shelton diode [13, 14] to measure the work-function difference between two surfaces, an emitter and a collector, has been employed to determine the difference in work function between two crystal planes of tungsten. In addition, the work-function change during adsorption of a gas on the collector, and the energy-dependent reflection coefficient for electrons incident normally on the collector surface, can be measured with this device [15].

Figure 27.3a shows the schematic arrangement used [15]. Two single crystals of different crystallographic orientation are mounted by wires and a tungsten spring in support rings. These crystals face a movable septum containing a small aperture. Either crystal may be heated by electron bombardment to a temperature where thermionic emission occurs, and a feedback stabilized controller is used to maintain emitter and crystal temperature constant, using the current collected from the crystal emitter by the septum for regulation of the temperature of the spiral tungsten emitter located behind the emitter crystal. The entire assembly is placed in an axial magnetic field of 3600 G, causing the emitted electrons to travel in tight spiral paths from the emitter to the collector crystal. The movable septum permits sampling of different regions of the emitter and collector. The collector crystal current is plotted against the retarding potential applied between emitter and collector, and a typical retarding potential plot, as shown in Fig. 27.3b, may be measured. The collected current follows the equation

$$I = I_0 \exp[-e(V_R + \Delta\phi)/kT] \tag{27.2}$$

where I_0 is the emitted current from the emitter, V_R is the retarding potential applied, and $\Delta\phi$ is the difference in work function between the collector and the emitter, and e is the electronic charge. Thus as the work function of the collector changes, the retarding potential plot (Fig. 27.3b) will shift. The shift of the “knee” in the plot is a measure of the work-function change of the collector, and may be used as a measure of the adsorption of a gas on the collector, the emitter remaining clean at its high operating temperature. The device shown in Fig. 27.3a measures collected currents of the order of 0.01 μA and to avoid problems with leakage currents, the terminals to each crystal are shielded from evaporating metal films by the hat-shaped shields shown on each feedthrough. The device is symmetric, so that it may be operated with either crystal acting as the emitter, but such a symmetrical arrangement is of course unnecessary if one is interested in only one crystal. In contrast to similar devices [13, 14] that used ohmic heating of the emitter, this device does not have a potential drop across the emitter region sampled by the aperture and should therefore perform better by having less uncertainty of the electrical potential distribution in the sampled emitter region.

By varying the electron energy and measuring the collected current, curves like those shown in Fig. 27.3c may be generated. These curves are related to the

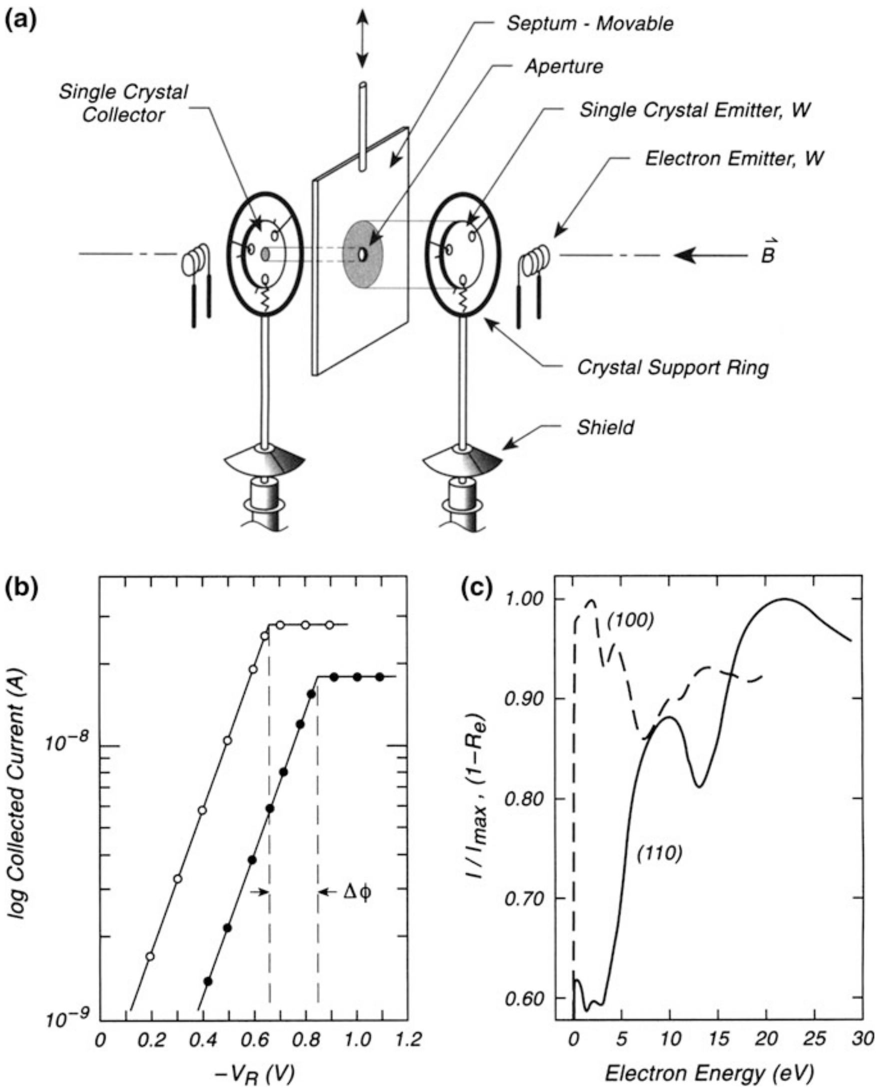

Fig. 27.3 Work function measurements—shelton thermionic diode. **a** Shelton diode, **b** Retarding potential plot, **c** Reflection coefficient plot

effective electron reflection coefficient in the plateau region and have to do with band structure and other possible effects at the collector.

The accuracy of work-function measurements made with this device is of the order of ±20 meV over many months of operation with tungsten crystals.

27.4 Improved Piezoelectric Drive Kelvin Probe

The Kelvin-Zisman vibrating capacitor method for measuring changes in the work function of a surface is widely used in surface science studies. The principles of this method are well described in the literature [16, 17] and will not be discussed in detail here. Basically, a reference electrode is caused to oscillate at audio frequency and the electrical potential of the reference electrode is adjusted to yield a null signal in the capacitance circuit. As the work function of the sample changes due to adsorption or to changes in temperature, the potential applied to the reference electrode is adjusted to maintain a null signal in the AC circuit. The change in the applied potential is equal to the change in the work function or surface potential of the sample. It is of course important to know that the reference electrode is not changing its work function during the measurements, and inert electrodes such as Au or SnO_2 films are often used. The vibrational motion of the reference electrode is commonly produced by mechanical excitation of the resonant frequency of the device, by an electromagnetic driving mechanism, or by the use of a piezocrystal oscillator.

The design shown in Fig. 27.4a involves the use of a piezoceramic foil actuator [18]. This avoids the interaction of stray magnetic fields from an electromagnet driver with the sample, which could cause problems if the sample is magnetic. In addition, the measured signal is taken from the reference electrode, not the sample, avoiding complications owing to the connection of the sample to both the heating circuit and the thermocouple circuit. The device described in Fig. 27.4a is a modification of the piezoelectric Kelvin probe built by Besocke and Berger [19, 20]. The device was used to study magnetic materials and yielded an accuracy of ±1 meV [21]. This compares to a reported sensitivity of better than 0.1 meV in the original device built by Besocke and Berger [19]. The reader is referred to the original paper [18] for dimensional details of the Kelvin probe shown in Fig. 27.4a. The reference electrode is an L-shaped piece of gold, connected by a tungsten wire to a quartz rod and thence to a shield plate. This assembly is actuated by a piezoceramic foil [22], containing vapor deposited Ag contacts on both surfaces, and glued using UHV leak sealer to a tungsten reed, 20 mm × 4 mm × 0.1 mm thick. The signal from the Au reference electrode is measured through a very thin wire connected to a support ceramic before exiting the apparatus. The stable resonance frequency of the reed is about 130 Hz, the amplitude of vibration is about 0.1 mm, and the AC driving voltage is about 1.0 V_{rms}. The spacing between the reference electrode and the sample is about 0.5 mm.

Before operating, the piezoceramic foil is polarized by a DC voltage pulse above 300 V. The polarization remains as long as the piezoceramic is not heated significantly.

Figure 27.4b shows a block diagram of the self-compensating feedback circuit which allows a continuous measurement of the work function change. It is estimated that the drift is about 1 meV/h and the noise is about ±0.5 meV. The response time constant of the system is less than 10 s. The variable DC power supply

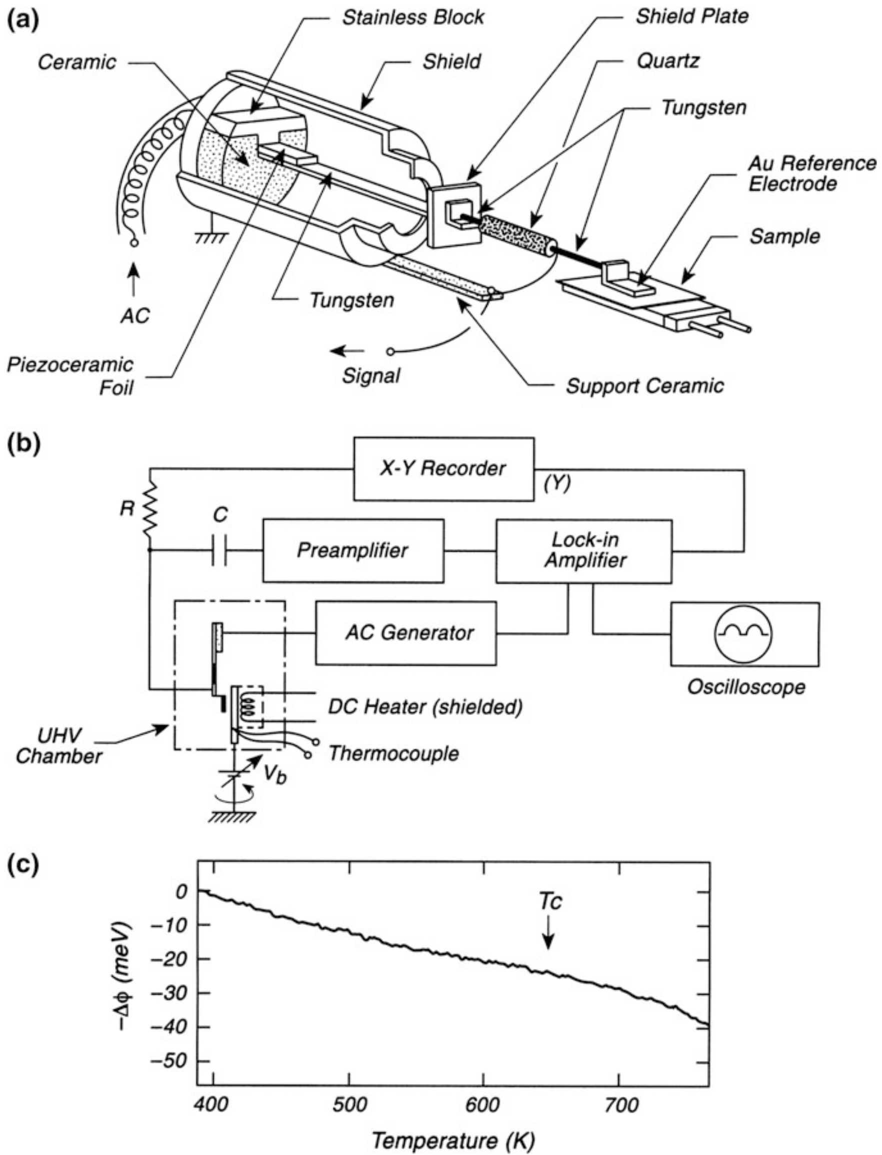

Fig. 27.4 Improved kelvin probe—piezodrive. **a** Piezodriven kelvin probe, **b** Circuit for Δφ measurements, **c** Work function change on cooling Ni (poly.)

supplies a variable compensating voltage, V_b. The authors note that electron emission from thermionic sources can disturb the electrical isolation of the sample and the reference electrode [18].

Figure 27.4c shows a record of the increase in the work function of a polycrystalline Ni sample as it cools through the Curie temperature, T_C.

Excellent reviews and analysis of the effects of stray capacitance [23, 24] and noise [25] on the performance of the Kelvin probe have been published. Kelvin probes, driven by an electromagnetic voice coil and possessing superior noise levels, have been described [26, 27].

The Kelvin probe has been used in dynamic measurements of the desorption of one desorbing surface species from a single crystal surface [28]. The method was shown to give superior resolution of overlapping desorption processes compared to temperature programmed desorption into a large chamber with gas monitoring by a quadrupole mass spectrometer [28]. Also, the dynamic work function change method can be used over a wider range of dT/dt than the mass spectrometer method [28].

For more complicated surface phenomena in which surface decomposition of a molecule may occur without product desorption, the use of the Kelvin probe for observing work-function changes associated with decomposition has proven helpful [29]. The Kelvin probe may also be used to measure work-function changes on semiconductor surfaces when adsorption occurs [30].

27.5 Improved Electromagnetic Drive Kelvin Probe

In comparison to the piezodriven Kelvin probe shown on p. 295, an electromagnet-driven device is described here with somewhat different features.

In the design shown in Fig. 27.5a, great attention has been paid to the elimination of stray capacitances [31]. This is accomplished by electrical adjustments of a potential applied to the electrical shielding as described in the original paper [31]. The reference electrode is a grid of 80 % transparent stainless steel mesh, stretched across a 3–4-mm-diameter Mo ring, and coated with SnO_2 (see p. 123) to produce an inert surface of constant work function during gas adsorption. The spacing between the reference electrode and the sample is 0.3–0.5 mm. The transparent grid electrode is used in order to allow the sample to have almost full access to gas during adsorption rather than having partial blocking by a solid electrode. The frequency of the device is about 160 Hz, but it is advantageous to operate at higher frequencies, so that an overtone frequency of 1150 Hz was used. Working at such high frequencies has the effect of removing disturbances owing to low frequency noise, caused by effects such as bumping the apparatus. Because the resonant overtone frequency is sharp (<0.5 Hz) a quartz oscillator was used for stability. The amplitude of the vibration is about 0.1 mm. The response time constant was measured by applying a sudden potential to the sample, and was 20 ms.

The Kelvin probe is constructed using a light stainless steel tube to connect the reference electrode to the holder. A lightweight mu metal platelet was welded onto the tube in the position of the electromagnet, and the assembly was clamped in a stainless steel holder, electrically isolated by ceramic insulators from the

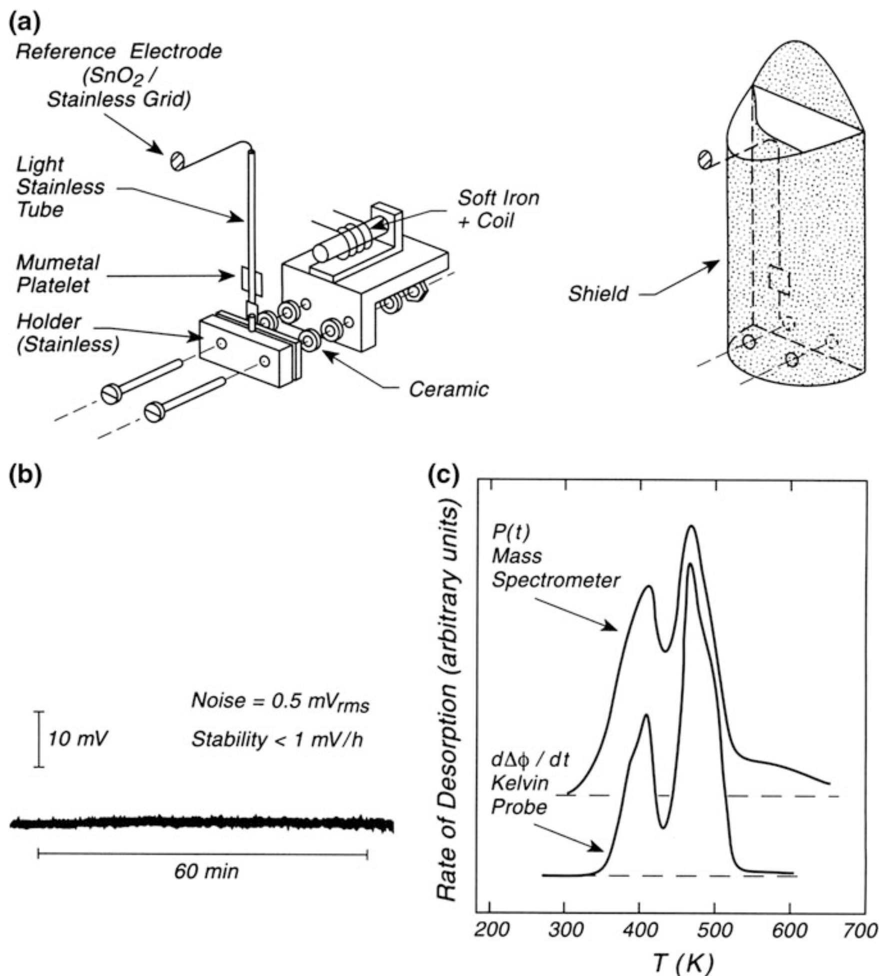

Fig. 27.5 Improved kelvin probe—electromagnet drive. **a** Electromagnet-driven kelvin probe, **b** Stability and noise, **c** Thermal desorption of CO/Ru(001) measured two ways

electromagnet mounting. The electromagnet is made of soft iron and is wrapped with a few turns of aluminum winding wire, which has an anodized oxide insulating surface film for isolation. All electrical measurements are made from the isolated reference electrode assembly, using rigid partially screened conductor wires that are free of microphonics, and that are connected to vacuum feed throughs. Figure 27.5b shows a measure of the noise and long term stability of the device.

The quality of the measurements made with this apparatus permit one to study the time derivative of the work-function change on the sample as adsorbate surface coverage changes. Assuming that the work function is linearly proportional to coverage, the thermal desorption spectrum obtained with the mass spectrometer

should agree with that obtained from the derivative of the work function. It was found that an improvement in the resolution of the thermal desorption spectroscopy could be achieved by using the Kelvin probe, compared to the mass spectrometer detector of desorbing gas. However, the two kinetic curves do not agree because of the nonlinear behavior of work function with coverage. Figure 27.5c shows data for the thermal desorption of CO from Ru(001) measured both ways [31].

Reference [31] gives an excellent review of the development of the vibrating capacitor method for work-function measurements.

An excellent analysis of the effect of stray capacitance on Kelvin probe measurement is given in [32], and the effect of noise on Kelvin probe measurements is given in [33]. Reference [34] gives a new design for a Kelvin probe involving a voice coil driver. Reference [35] gives design and performance features for a Kelvin probe with a reproducibility of 1 meV over long periods of time. In addition, methods for measuring the work-function change during ohmic heating of a metal crystal are described [35].

27.6 Kelvin Probe—High Temperature Flow Reactor

The vibrating Kelvin probe has been described on pp. 295–299. Both mechanical and electromechanical activation of the motion of the reference electrode have been employed. For electromechanical activation, a piezoceramic actuator is often used, but because the upper temperature limitation is near 415 K for these actuators, they are not generally useful for high-temperature studies.

Figure 27.6 shows a method for using a piezoceramic actuator [36] to drive a Kelvin probe at some distance from a high-temperature sample [37]. The device, with a balanced quartz tube lever of 180-mm length, has the actuator on one end and the Au Kelvin probe electrode on the other. The quartz tube (2-mm diameter) lever arm is balanced on sapphire rods, as shown in the drawing. The actuator is coupled to the quartz tube lever with a light weight stainless steel spring. This refinement avoids the addition of a large mass to the actuator, and the resonant frequency of the device is close to that of the free actuator (in this case, 325 Hz).

The apparatus is used to study chemical reactions on a single crystal sample placed under the Kelvin probe. This sample may be heated in flowing gas while the work function is being measured. The large distance between the hot sample and the actuator avoids heating of the actuator. In addition, the large separation distance prevents electromagnetic pickup in the work function measurement from the piezodrive unit. A sampling tube permits the gas composition to be measured in the vicinity of the sample, and this provides a measurement of the local rather than the incident gas composition.

The resolution of the probe was estimated to be better than 5 meV, using known applied potentials on the sample for calibration. It is believed that improvements in the electrical measurement methods will lead to substantially lower noise and higher resolution [37].

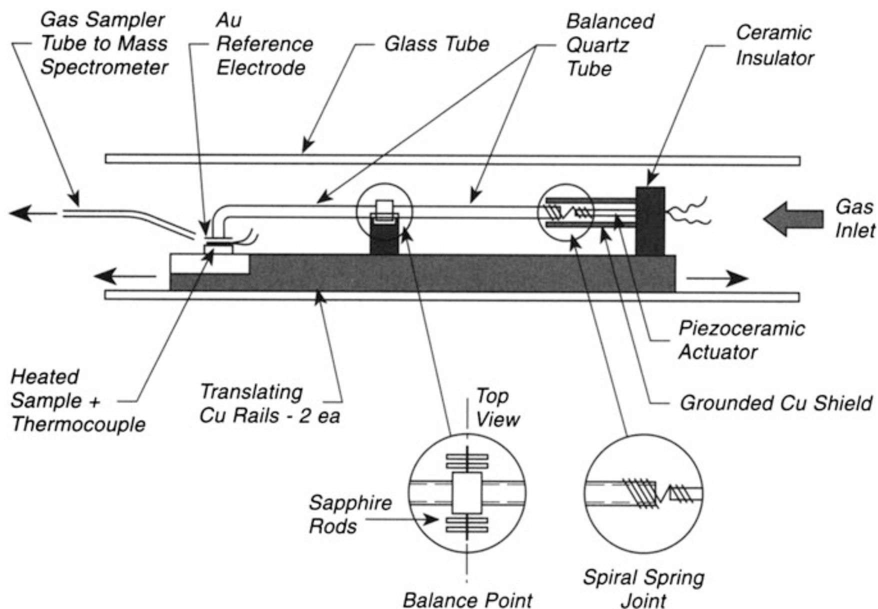

Fig. 27.6 Kelvin probe—high-temperature flow reactorhigh-temperature flow reactor

27.7 Scanning Tunneling Spectroscopy (STS)—Compensation for Density of States of the Tip

Many examples if the use of I/V measurements for probing the local density of electronic states (LDOS) of adsorbed atoms and molecules are now present in the literature. Similarly, for alloy metal surfaces, STM-STS measurements are often used for studying the individual metal atoms, either in the surface or the subsurface layers of the metal. A common difficulty with these measurements is that the I–V and dI/dV measurements versus V contain a contribution from the LDOS of the tip atoms which is mixed in. In the method to be described here, a subtraction of STS spectra is made in order to cancel out the LDOS contribution from the tip.

Figure 27.7a shows a schematic alloy of composition A_xB_y. The STM, through a number of averaged scans across an identical region, provides first a dI/dV scan of atom A, which contains, also the tip contribution. A similar number of scans across atom B provides a second dI/dV scan, also containing the tip contribution. By subtracting A−B, the tip contribution is cancelled out, and the difference spectrum represents the change in dI/dV when one moves from atom A to atom B. These differences are able to be handled more easily by theory than the convoluted spectra from which the difference spectrum is derived [38].

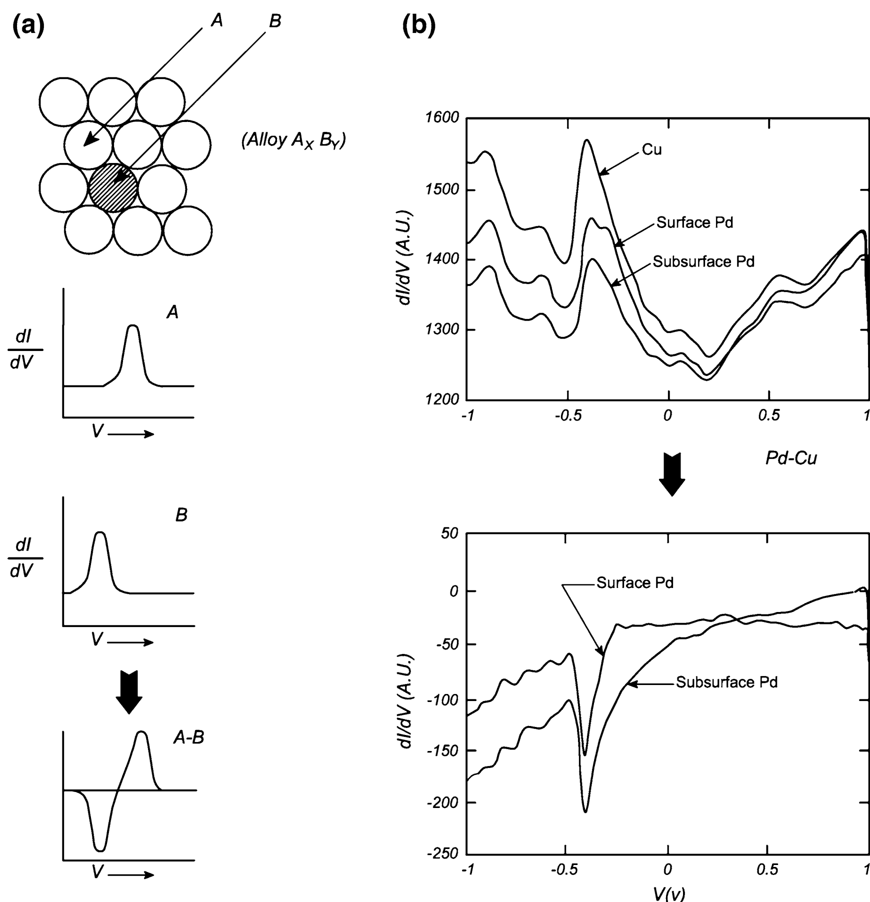

Fig. 27.7 Difference I/V spectra—STM. **a** Schematic differences in A and B spectra—STM, **b** Pd-Cu alloy differences—STM

One example shown in Fig. 27.7b concerns the Cu-Pd alloy, where STM can distinguish surface Cu atoms, surface Pd atoms, and subsurface Pd atoms. The data, when subtracted give a difference spectrum for the two types of Pd. Here the Cu spectrum has been used as a subtraction spectrum, removing the tip contribution. The difference spectrum therefore represents the difference between Pd and Cu. It is seen that at about −0.4 V, both types of Pd atoms exhibit a slightly lower LDOS than Cu atoms. Consequently, charge transfer takes place from Pd to Cu atoms, just the opposite from a prediction based on the higher work function of Pd (5.12 eV) versus Cu (4.65 eV) [39].

27.8 Ellipsometry as a Tool for Studying Adsorption

Ellipsometry has been used for years to study adsorption on surfaces, especially in the study of oxide films grown on metals. There are few comparisons of adsorption measurements with other surface measurements, especially under ultrahigh vacuum conditions for model systems with well-understood behavior.

The ellipsometer is an automatic null system with a polarizer-compensator-sample-analyzer (PCSA) configuration as shown in Fig. 27.8a. Here, two ellipsometry parameters are measured: "phase shift" Δ, and "amplitude reflectance ratio" ψ, which are components of the optical constant of the surface. The relative change in Δ, $\delta\Delta$, measured versus the clean substrate is used as a measure of the amount of adsorption. This is due to the fact that $\delta\Delta$ is much more sensitive than $\delta\psi$ for a physisorbed film thinner than a few 10s of nm [40]. The apparatus shown also contains XLEED, which is a sensitive low energy electron diffraction method using a low current electron beam with microchannel plate amplification of the diffraction pattern. XLEED eliminates the problem of electron stimulated desorption (ESD). Measurement of the coverage behavior of Xe is achieved by measuring the intensity of the diffracted Ag(10) beam [41, 43].

Figure 27.8b shows a comparison of Ellipsometry and XLEED for the measurement to the adsorption of Xe on both Ag(111) and Ag(100). At a constant pressure of Xe of 1.1×10^{-5} Pa, the temperature of the crystal was slowly lowered from 82 to 56 K. The broken line shows the behavior of the ellipsometry measurement of $\delta\Delta$, versus T, where equilibrium is maintained at all temperatures. The initial increase is due to the adsorption of 1 ML of Xe, followed by a second increase due to the formation of a second layer. The solid line shows the XLEED behavior of the [10] beam. The two experimental methods compare two crystals, but even in this case, it may be seen that the condensation temperature for the second layer is identical to 0.1 K. The slight difference in condensation temperature for the monolayer, measured by the two techniques, is not due to differences between the techniques, but is due to slight differences in the polarization of Xe on the two Ag surfaces, leading to a difference of 0.2−0.4 K in the position of the step corresponding to monolayer completion.

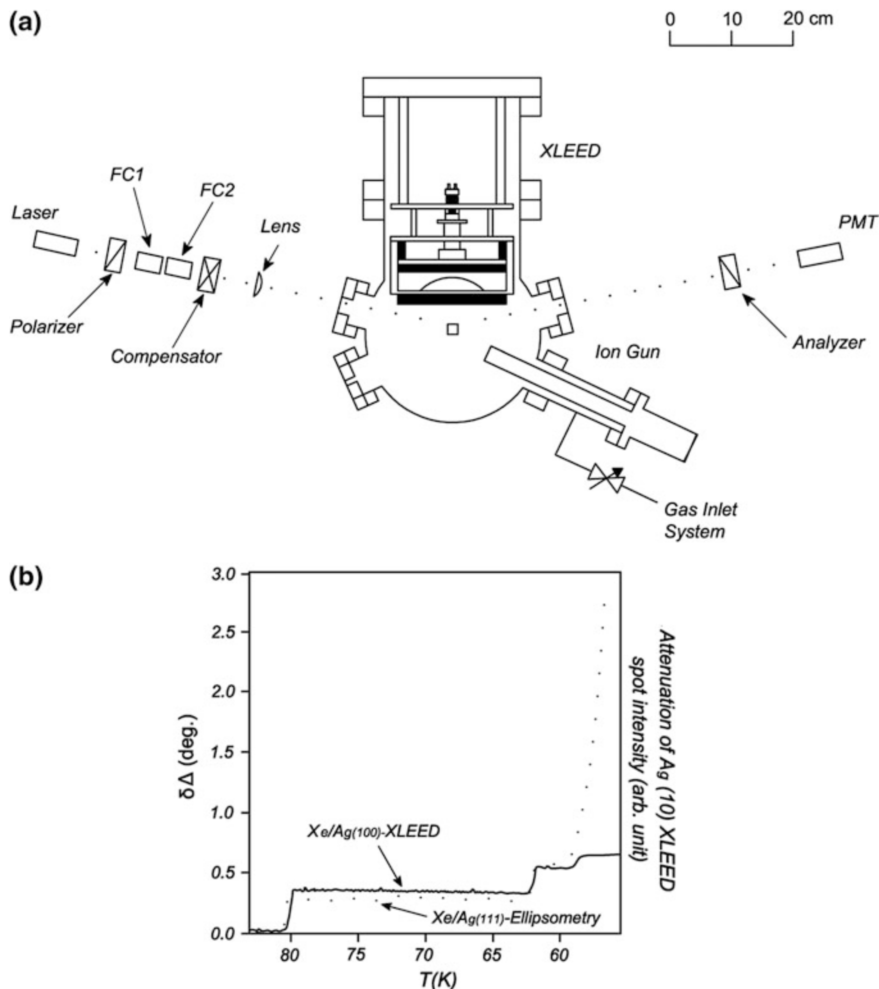

Fig. 27.8 Ellipsometry for monolayer measurement. **a** Ellipsometry-XLEED apparatus, **b** Adsorption of Xe on Ag(100) and Ag(111)

References

1. Z. Knor, V. Ponec, Coll. Czech. Chem. Commun. **31**, 1172 (1966)
2. T. Jirsak, V. Nikolajenko, Z. Knor, Czech. Chem. Commun. **59**, 1709 (1994)
3. See literature quoted in V. Ponec, Z. Knor, and S. Cerny, *Adsorption on Solids* (Butterworth, London, 1974)
4. A. Eberhagen, Fortschritte d. Physik **8**, 245 (1960)
5. E.C. Tompkins, *Chemisorption of Gases on Metals* (Academic Press, London, 1978)
6. G. Ertl, J. Küppers, Low Energy Electrons and Surface Chemistry (Verlag Chemie, Weinheim, 1974), Chap. 8

7. J.L. Taylor, W.H. Weinberg, J. Vac. Sci. Technol. **15**, 1811 (1978)
8. T.E. Madey, J.T. Yates, Jr., Colloques Internationaux du Centre National de la Recherche Scientifique, No. 187, 155 (1970)
9. J.T. Yates Jr, R. Klein, T.E. Madey, Surf. Sci. **58**, 469 (1976)
10. M.J. Dresser, T.E. Madey, J.T. Yates Jr, Surf. Sci. **42**, 533 (1974)
11. J.R. MacDonald, C.A. Barlow Jr, J. Chem. Phys. **39**, 412 (1963)
12. J.H. Fritz, C.A. Haque, Rev. Sci. Instrum. **44**, 394 (1973)
13. H. Shelton, Phys. Rev. **107**, 1553 (1957)
14. P. Kisliuk, Phys. Rev. **122**, 405 (1961)
15. T.E. Madey and J.T. Yates, Jr., Supplemento al Nuovo Cimento, No. 2, Series I, 5, 483, (1967)
16. G. Ertl and J. Küppers, *Low Energy Electrons and Surface Chemistry* (Verlag Chemie, GmbH, D-694 Weinheim, 1974), p. 120
17. J. Holzl, F.K. Schulte, in Solid Surface Physics, ed. by G. Hohler, vol 85 (Springer, Berlin, 1979), p. 1
18. S. Saito, T. Soumura, T. Maeda, J. Vac. Sci. Technol. **A2**, 1389 (1984)
19. K. Besocke, S. Berger, Rev. Sci. Instrum. **47**, 840 (1976)
20. G. Wedler, R. Ruhmann, Appl. Surf. Sci. 14, 137 (1982–1983)
21. S. Saito, T. Maeda, J. Vac. Soc. Jpn. **25**, 190 (1981)
22. Piezofoil can be obtained from Kyoto Ceramic Ltd., Kyoto, Japan
23. I.D. Baikie, E. Venderbosch, J.A. Meyer, P.J.Z. Estrup, Rev. Sci. Instrum. **62**, 725 (1991)
24. see also J.S.W. de Boer, H.J. Krusemeyer, N.C. Burhoven Jaspers, Rev. Sci. Instrum. 44, 1003 (1973)
25. I.D. Baikie, S. Mackenzie, P.J.Z. Estrup, J.A. Meyer, Rev. Sci. Instrum. **62**, 1326 (1991)
26. I.D. Baikie, K.O. van der Werf, H. Oerbekke, J. Broeze, A. van Silfhout, Rev. Sci. Instrum. **60**, 930 (1989)
27. C.S. Kumar, A. Subrahmanyam, J. Majhi, Rev. Sci. Instrum. **67**, 805 (1996)
28. P. Feulner, D. Menzel, J. Vac. Sci. Technol. **17**, 662 (1980)
29. L. Hanley, X. Guo, J.T. Yates Jr, J. Phys. Chem. **93**, 6754 (1989)
30. J. Abelson, G. de Rosny, J. Physique **44**, 993 (1983)
31. H.A. Engelhardt, P. Feulner, H. Pfnur, D. Menzel, J. Phys. **E10**, 1133 (1977)
32. I.D. Baikie, E. Venderbosch, J.A. Meyer, P.J.Z. Estrup, Rev. Sci. Instrum. **62**, 725 (1991)
33. I.D. Baikie, S. Mackenzie, P.J.Z. Estrup, J.A. Meyer, Rev. Sci. Instrum. **62**, 1326 (1991)
34. I.D. Baikie, K.O. van der Werf, H. Oerbekke, J. Broeze, A. van Silfhout, Rev. Sci. Instrum. **60**, 930 (1989)
35. M. Chelvayohan, R. Gomer, Surf. Sci. **172**, 337 (1986)
36. A Phillips PXE 5 piezoactuator with length of 27 mm was used
37. S. Lundgren, B. Kasemo, Rev. Sci. Instrum. **66**, 3976 (1995)
38. H.L. Tierney, A.E. Baber, E.C.H. Sykes, J. Phys. Chem. C **113**, 7246 (2009)
39. A.E. Baber, H.L. Tierney, E.C.H. Sykes, ACS Nano **4**, 1637 (2010)
40. A. Itakura, I. Arakawa, J. Vac. Sci. Technol., A **9**, 1779 (1991)
41. S. Igarsshi, Y. Abe, Y. Irie, T. Hirayama, I. Arakawa, J. Vac. Sci. Technol., A **16**, 974 (1998)
42. S. Igarashi, A. Tosaka, T. Hirayama, I. Arakawa, Langmuir **19**, 4627 (2003)
43. A. Tosaka, I. Arakawa, Surf. Sci. **600**, 1071 (2006)

Chapter 28
Radioactive Adsorbates

28.1 Radiotracer Techniques for Surface Studies

The high sensitivity of radiochemical methods suggests that these methods would have utility in studies of chemisorption and reaction on single crystal surfaces. This description of the use of a silicon surface barrier detector for the measurement of ^{14}C in chemisorbed layers on Pt(111) represents one of the few attempts to make measurements of this type [1]. Earlier studies using a Geiger-Müller counter were also successful [2, 3].

The surface barrier detector [4] is a large area diode consisting of a depleted slice of *n*-type Si mounted in an insulator ring as shown in Fig. 28.1a. The front and back surfaces are metallized. The thickness of the Au front surface coating is optimized for low energy β counting (158 keV) from ^{14}C. Also, the depth of the depletion region (300 μm) is chosen to optimize the detection of the β-electrons from ^{14}C, which have a range of about 150 μm in Si. Free charge carriers produced by the β-emission are separated by an applied electric bias (50 V). Integration of the current induced between the front and back electrodes yields an output pulse that is proportional to the ionizing energy. Either β-spectra may be collected or a ratemeter may be used to count the level of radioactive material, using the appropriate discriminator settings to eliminate noise.

The detector, ~20-mm in diameter, is mounted on a rotary feedthrough that allows it to be positioned in front of the Pt crystal at a distance of 5–10 mm, as shown in Fig. 28.1b. In the opposite orientation, background counting may be done. When a bias is applied to the detector, the temperature must be maintained between −30 °C and +30 °C. This is done by using a flexible Cu braid (see p. 392) that is anchored on a copper block maintained at the desired temperature. To avoid contributions from detector noise, the lower discriminator was set at 35 keV, and this resulted in rejection of about 40 % of the ^{14}C β-signal as determined in separate calibrations. The counting efficiency was determined as 2.9 ± 0.3 % for the geometry and discriminator settings used here.

© Springer International Publishing Switzerland 2015
J.T. Yates Jr., *Experimental Innovations in Surface Science*,
DOI 10.1007/978-3-319-17668-0_28

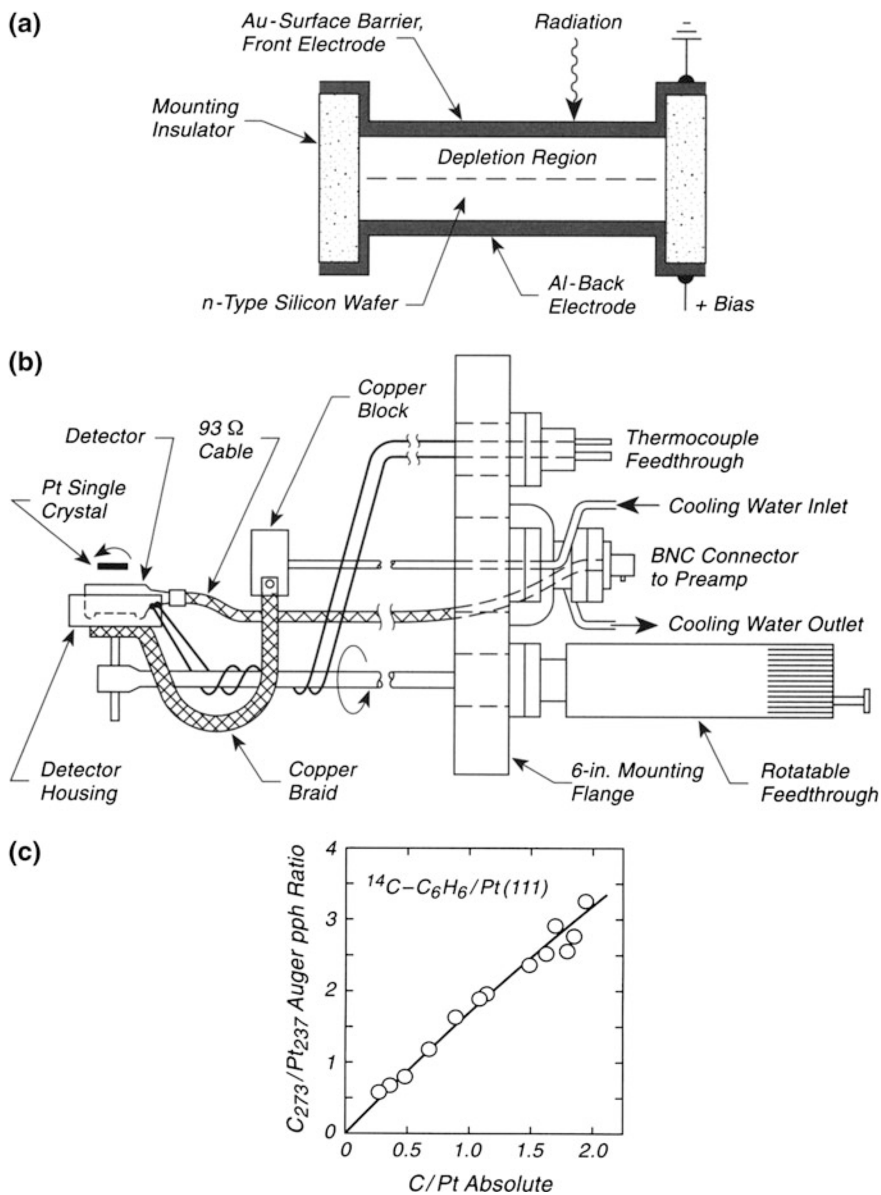

Fig. 28.1 Radiotracer techniques for surface science. **a** Si surface barrier detector. **b**. Detector geometry. **c** C Auger signal versus radioactive ^{14}C coverage absolute surface coverages

Table 28.1 Partial listing of radioisotopes useful for surface studies using a barrier detector [1]

Isotope	E_{max} (keV)	Half-life (years)
^{14}C	158	5720
^{11}Na	544	2.6
^{26}Al	1160	740,000
^{32}Si	210	710
^{35}S	167	0.24
^{36}Cl	714	300,000
^{137}Cs	510	30

Figure 28.1c shows the correlation between the measured count rate and the Auger intensity from carbon deposited as $^{14}C–C_6H_6$ on the Pt (111) crystal. The linear correlation between the two measurements indicates that both are measuring the carbon coverage as expected.

The sensitivity of the ^{14}C counting method depends upon many factors such as geometry, detector parameters, and the specific activity of the carbon-containing compounds used. While many hydrocarbons and other molecules may be obtained with activities up to 64 mCi/mmol, a nominal value of 10 mCi/mmol is more common. Assuming a detection efficiency of 3 %, and a background signal of 3 counts/min, the detection sensitivities for 20-min counting, at nominal labeling levels, are 1×10^{13} (23 % standard deviation), 5×10^{13} (10 % standard deviation), and 1×10^{14} (4 % standard deviation) molecules/cm^2. Thus, coverages of 1 % of a monolayer may be determined accurately. It is found that repeated adsorption experiments lead to increasing background radioactivity during measurements over a day; pumping overnight restores the background to a low level.

A second example of the use of this method for the study of hydrocarbon chemistry on Pt(111) can be found in [5].

The use of radioactive adsorbates is not limited to those labeled with ^{14}C as may be seen in Table 28.1.

References

1. S.M. Davis, B.E. Gordon, M. Press, G.A. Somorjai, J. Vac. Sci. Technol. **A19**, 231 (1981)
2. K. Klier, Rev. Sci. Instrum. **40**, 372 (1969)
3. K. Klier, A.C. Zettlemoyer, H. Leidheiser Jr, J. Chem. Phys. **52**, 589 (1970)
4. Ortec TA-23-25-300. Obtained from Ortec, P.O. Box 1397, Easley, SC 29640
5. S.M. Davis, F. Zaera, B.E. Gordon, G.A. Somorjai, J. Catal. **92**, 240 (1985)

Chapter 29
Thin Film Deposition

29.1 Thin Film Deposition to Absolute Surface Coverages

The ability to evaporate clean thin films and to achieve desired surface coverages that are absolutely known is of fundamental importance in many areas of surface science research. Fortunately, quartz thickness monitors (QTM) are commercially available that have sensitivities of the order of a nominal thickness of 1 Å of deposited material. With appropriate use, these monitors can be used to monitor, absolutely, the deposition of thin films on substrates of interest.

Figure 29.1a shows a successful arrangement for producing absolute coverages of metal on a single crystal [1]. In the case of this work, the metal deposited was Pt and the substrate was atomically clean Mo(110). The metal deposition source consists of a tungsten hairpin filament, mounted on degassing loops (see pp. 407 and 437), which is shielded by a metal shield containing a 15-mm-diameter hole near the source. A thermostated QTM is able to be moved quickly between three positions—1, 2, and 3. When the QTM is in position 1, the Pt source is completely shielded, so that metal does not escape into the vacuum chamber. Position 1 is used for through outgassing of the source. When the QTM is moved to position 2, the QTM collects evaporated metal and radiation from the hot source. Thermostatting with circulating water from a temperature-regulated source maintains the QTM temperature constant to ±0.5 K, and this condition is necessary for absolute accuracy of the QTM. When the QTM is rotated to position 3, the crystal receives the metal vapor and the QTM is out of line-of-sight with the metal source. Stable operation of the metal source can be achieved by monitoring the current and voltage drop across the source and making the product of these constant. In practice, the source is stable over hours of operation without sophisticated wattage regulation. The relative flux at the crystal and the QTM is determined from the distances by the ratio, $d^2_{QTM}/d^2_{crystal}$.

Figure 29.1b shows the duty cycle described above as monitored by the QTM. In position 1, no Pt is received either by the QTM or the crystal. In position 2, the mass of the deposited platinum on the QTM rises linearly with time. In position 3,

© Springer International Publishing Switzerland 2015

J.T. Yates Jr., *Experimental Innovations in Surface Science*,
DOI 10.1007/978-3-319-17668-0_29

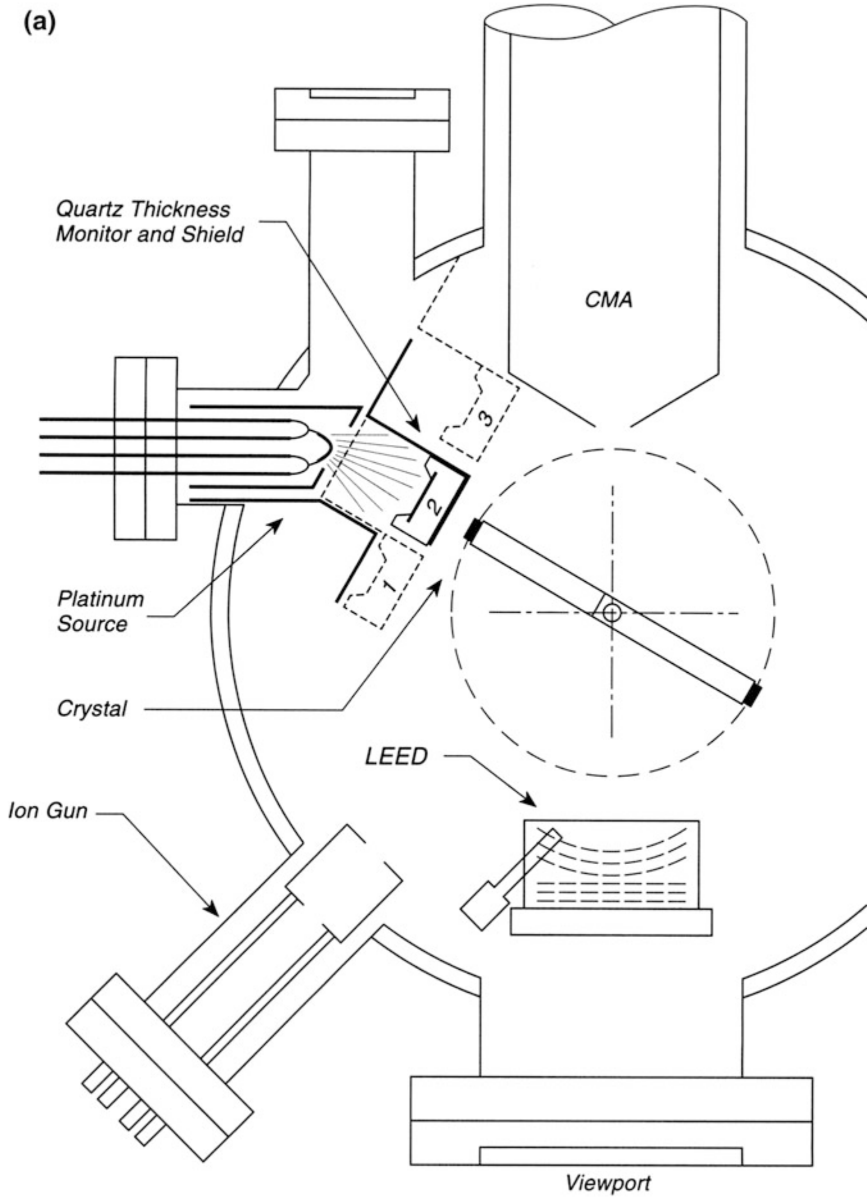

Fig. 29.1 Thin Film Deposition to Absolute Surface Coverage. **a** Metal evaporation/quartz thickness monitor. **b** Duty cycle for evaporation/measurement. **c** Layer-by-layer growth kinetics Pt deposition measurement

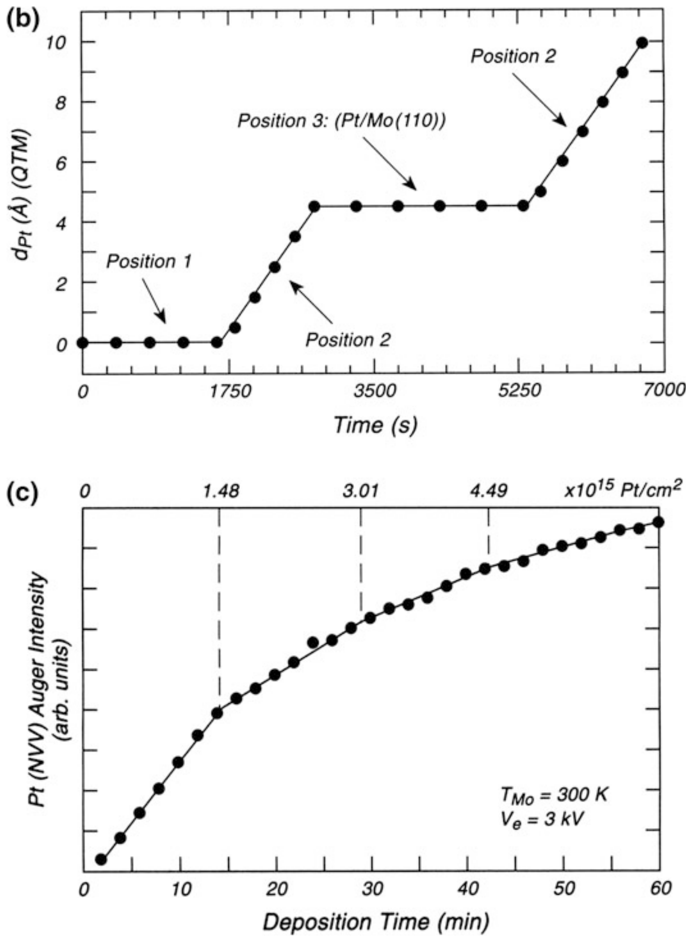

Fig. 29.1 (continued)

Pt is deposited on the Mo(110) substrate and the QTM again does not show any change in mass. Finally, in position 2 for the second time, the QTM again receives Pt, to check that the rate of evaporation has not changed significantly during deposition. The two slopes in position 2 agree to within 0.4 %.

Following each deposition cycle, the Mo(110) crystal was rotated to the CMA Auger spectrometer position for measurement of the Pt(NW) intensity, which is a secondary measure of the extent of Pt deposition. It can be seen in Fig. 29.1c that the Pt Auger signal grows linearly in at least three branches of different slope. The break points, located analytically, correspond to the completion of a monolayer of Pt and the start of the formation of a second layer of Pt as growth proceeds by a layer-by-layer mechanism. It is interesting to note that the three labeled break points correspond well, in absolute Pt coverage as measured with the QTM, with the

number of Pt atoms in a close-packed Pt(111) layer which has a coverage of 1.504×10^{15} Pt/cm^2. The location of the break points were used to calculate the average attenuation length for 64 eV Pt(NVV) electrons, using the bulk (111) interplane spacing for Pt of 2.47 Å. These experiments gave an average attenuation length of 4.1 ± 0.3 Å, in close agreement with calculated values for this quantity [1, 2].

Even with the care taken in this experiment, a propagation of systematic and random errors results in a ±16 % error estimate in the absolute coverages measured.

The use of quartz microbalance measurements stretch back to the pioneering work of Sauerbrey [3], Slutsky and Wade [4], and to Kasemo and Tornqvist [5], who showed the usefulness and sensitivity of these devices for adsorption and thin film studies. A good review of the history of the development of the quartz microbalance may be found in [6]. A paper concerned with improvement in the accuracy of the quartz microbalance to allow the measurement of the acoustic impedence ratio of the film to the crystal, using two non-harmonically related resonant modes is given in [7].

A method to compensate for the effects of temperature changes owing to radiation heating is described in [8, 9]. Here, a thermocouple pair measures the difference between the temperature of the quartz crystal detector and a matched reference detector in the vacuum system. A heater, driven by a feedback circuit working off the thermocouple pair adjusts the reference crystal temperature to within 0.1 K. An accuracy of thickness measurement of at least 0.01 nm is estimated [8, 9].

A description of the calibration of a quartz microbalance against an electrostatic balance is given in [10]. The probable error of the microbalance was found to be 0.6 %, compared to the theoretical expectation.

A description of the use of a quartz microbalance at cryogenic temperatures is given in [11–13].

A description of the use of a quartz microbalance for the calibration of an Auger spectrometer used to measure oxygen chemisorption on Ni is found in [14, 15].

Recent advances in improving the sensitivity and accuracy of the QTM technology depend upon improved temperature stability (±0.03 K) over several hours. In addition temperature stabilization of the electronics were investigated, as well as grounding effects. A frequency stability of $1{:}10^8$ (0.06 Hz) over 0.5 h. was achieved, equivalent to a mass resolution of 2 % of an atomic monolayer of O over 0.5 h. It was reported that irreversible uptake of oxygen into the bulk of the quartz crystal on its rear face may be a factor causing error [16].

29.2 Gold Evaporation Source

The evaporation of Au is sometime difficult because Au droplets on a W wire have a tendency to detach. A neat trick to prevent this is to produce a notched W wire support [17] which is more readily wet by the Au than a wire without the Vee shape. Apparently gravity and surface tension effects combine to hold the Au

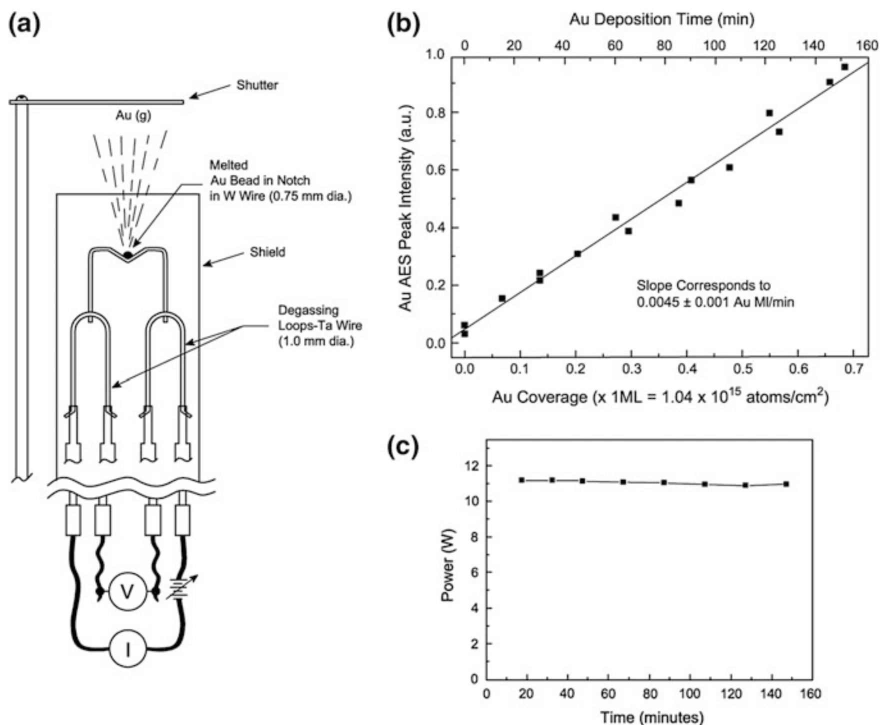

Fig. 29.2 Au Evaporation Source. **a** Au evaporation source. **b** Evaporation versus time. **c** Power consumption (I × V) versus time

droplet in the notch region. In Fig. 29.2a, the evaporation source is shown. It consists of a W wire [18] with the notch, welded between two Ta degassing loops. These loops can be independently degassed at higher temperatures than employed for the Au evaporation and eliminate outgassing effects, as described in Sect. 38.1. Current and voltage measurements (Fig. 29.2b) are made as shown, allowing one to measure the watts expended and to keep this quantity constant throughout the evaporation. Measuring the voltage drop across the active W evaporation filament is superior to measurements made across the entire device, since one wishes to control the resistance and temperature of the active evaporation element. Figure 29.2c shows a series of Au deposition rate measurements made over several months. The reproducibly is better than ±20 %, and allows Au to be deposited far down into the submonolayer range at a slow rate. The thickness measurements for the Au film are made by measuring the Auger attenuation of the substrate, which in this case is a TiO_2(110) single crystal [19].

29.3 Ionization Gauge Measurement of Film Evaporation Rate

A convenient and inexpensive secondary standard for the measurement of the rate of metal evaporation may be established using a pair of ionization gauges with matched geometry. The flux of metal atoms through one gauge is measured by an increase in ion current owing to the metal atom steady state gas density during evaporation. A second gauge is used to make a small correction for the presence of residual gases produced during evaporation. The calibration of the ion gauge is made against a quartz thickness monitor (QTM) [20] (see p. 309).

Figure 29.3a shows the design of the apparatus, where a translatable QTM is located line-of-sight to a metal evaporation source that contains two separate sources housed in a shield. It is desired to evaporate known coverages of metal onto the crystal, and the QTM is located very near the crystal location. After outgassing of the source, the crystal is moved to a line-of-sight position and measurements of the mass received by the QTM are made. Simultaneously, measurements of the difference between the two ionization gauge readings are integrated versus time, and this difference is related to the metal vapor steady state gas density inside the ionization gauge assembly, which is located line-of-sight between the source and the crystal and the QTM.

Figure 29.3b shows a cross calibration obtained for Sn evaporation. The linear correlation over a wide Sn thickness range indicates that both measurement methods are behaving as expected. However, the sensitivity of the ion gauge is high compared to the commercial QTM, so that small film thicknesses can be measured with the ionization gauge conveniently.

The dual-ionization gauge arrangement could also be calibrated against other thickness standards such as RHEED intensity measurements made during layer-by-layer growth [21].

29.4 Reusable Quartz Crystals for Film Thickness Measurement

Quartz crystals used in thin film measurement are able to hold only so much deposited material before becoming unusable. Typical thickness limitations are approximately 105 Å of metal deposit. The thin films can sometimes be etched away to recover the clean quartz oscillator, but strong chemical etchants will often destroy the metallic electrodes that activate the crystal, requiring redeposition of the electrodes [22].

A simple solution has been found to allow thin film overlayers on quartz crystals to be removed without harming the electrodes [23]. A photoresist coating is

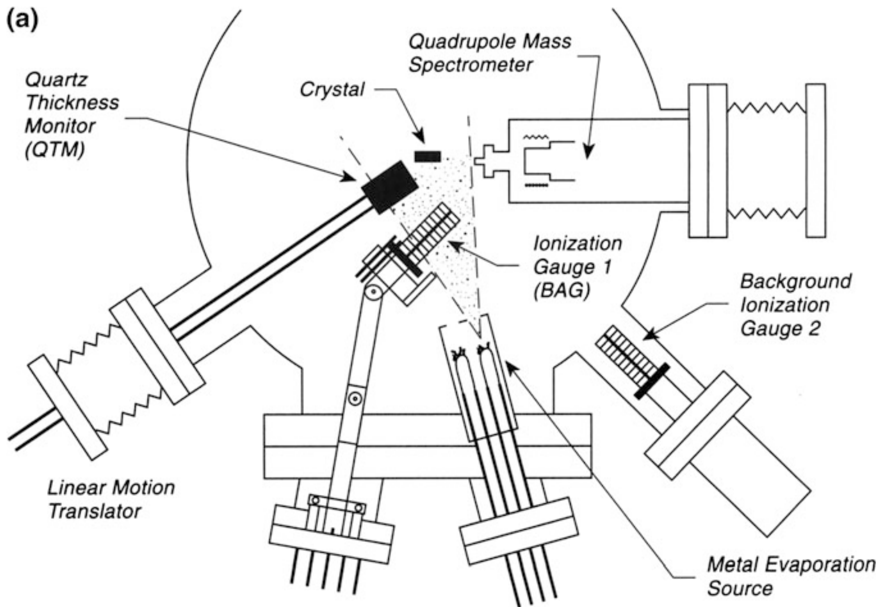

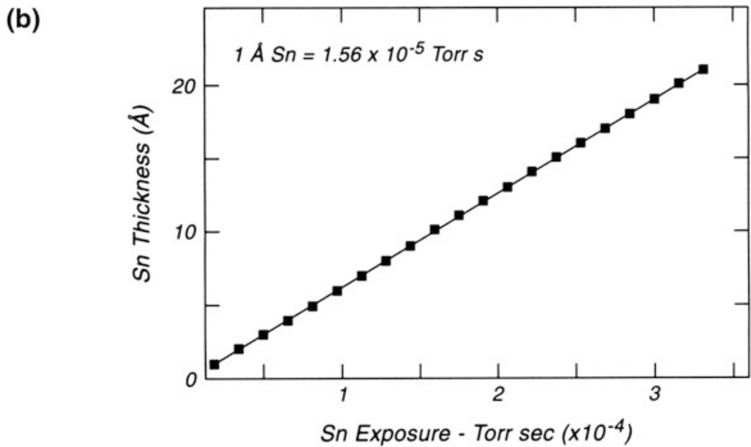

Fig. 29.3 Ionization Gauge Measurements of film Evaporation Rate. **a** Ionization gauge geometry. **b** Correlation of QTM and BAG

deposited on the clean quartz crystal before use. Later, using acetone as a solvent for the photoresist, the thin film to be removed is stripped away by dissolving the underlying photoresist layer as shown in Fig. 29.4. It was found that a photoresist layer of at least 3000 Å thickness is needed to permit stripping of all overlayer

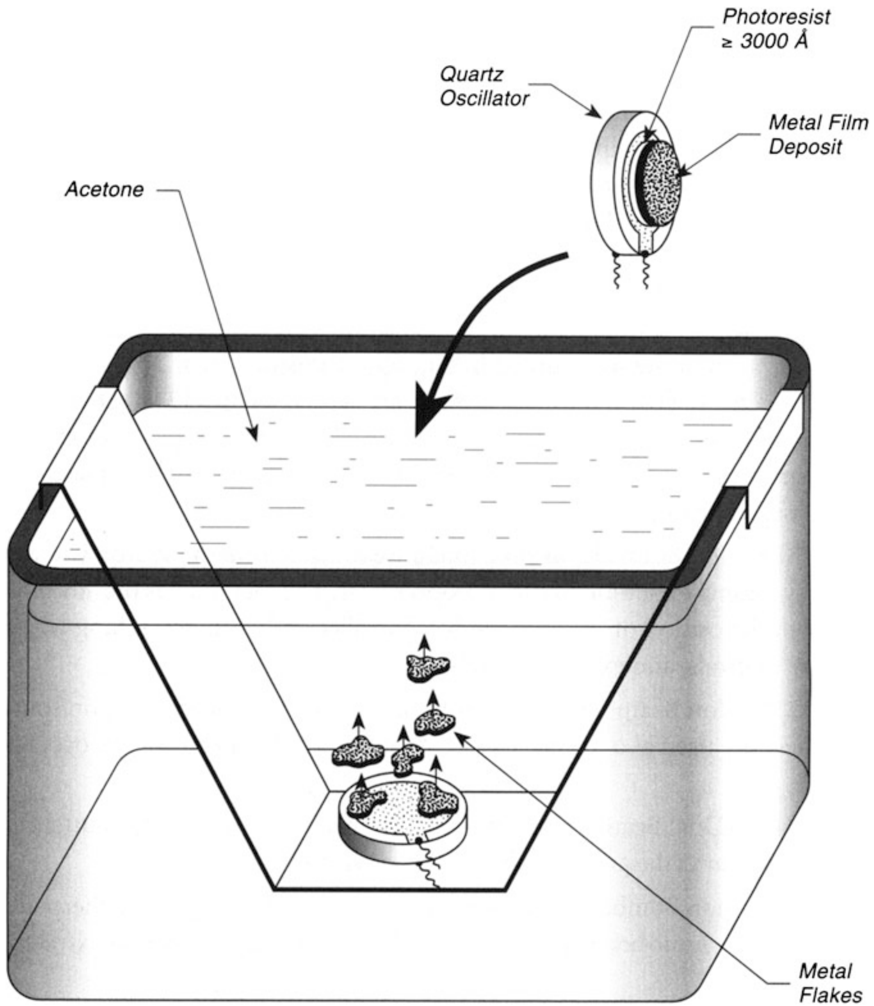

Fig. 29.4 Reusable quartz crystal oscillatorcoating tube inner walls

deposits cleanly. This loads the quartz crystal only to about 1 % of its mass capacity. The photoresist [24] is deposited using a spin-coating method, baked at 120 °C for 20 min, and then patterned to cover the area on the crystal used for deposition. The photoresist coatings made in this manner can be stored in air but should not be baked at temperatures approaching 200 °C because this makes the photoresist insoluble in acetone.

29.5 Hybrid Thin Film Deposition Processes—Stable and Metastable Films

The deposition of thin films with desirable chemical and physical properties is widely used for the production of electronic materials, tribological coatings, and optical coatings. The processes used may be divided into those that produce thermodynamically stable compound films and those that produce metastable materials. It is beyond the scope of this book to describe the wide range of film deposition methods and materials that have been deposited in thin film form. Books and reviews are widely available. Below, a short description of the some of the hybrid film deposition methods is given [25], and figures schematically describing each method are shown. Figure 29.5a–d illustrate ion bombardment from an external plasma. Figure 29.5e illustrates the use of ions extracted from a plasma near the substrate, and this method is now used widely in plasma assisted vapor deposition processes.

Figure 29.5a—Ion Beam Deposition: Ions are extracted from the source where they are produced by plasma excitation of the appropriate gas. The method has the advantage that the energy of deposition of the ions can be controlled rather than working with a mixture of ions, neutrals, and excited neutrals.

Figure 29.5b—Ion Beam Sputter Deposition: Ions are produced in an ion source by a plasma. These are used as a means for sputttering a target, and collection occurs on the substrate.

Figure 29.5c—Dual Beam Sputtering: Two ion beams are used. One sputters a target; the second bombards the growing film on the substrate.

Figure 29.5d—Ion Bombardment Evaporation: Material is evaporated thermally using electron beam or ohmic heating. The growing film is bombarded by ions extracted from an ion source.

Figure 29.5e—Reactive Sputtering with Dissociable Reactive Gas: Metals are sputter-deposited in a reactive gas such as silane to produce metal silicide films.

Many variations on the schematic methods shown in Fig. 29.5a–e are employed and a wide variety of preparation methods are described in the literature [26, 27].

29.6 Sputter-Coating Inner Walls of Tubes

The need to coat the inside of a metal or insulator tube with a metal film can be met by both electrochemical and chemical vapor deposition methods. It is also possible to deposit pure metal films inside a tube using a special sputtering procedure described here [28].

As shown in Fig. 29.6, a conical metal target, placed on the axis of a polished steel tube to be coated, is exposed to a beam of ions that are directed down the tube. The conical metal target is moved along the tube toward the ion source by an electrical drive mechanism. In the particular case studied here, the inner diameter of

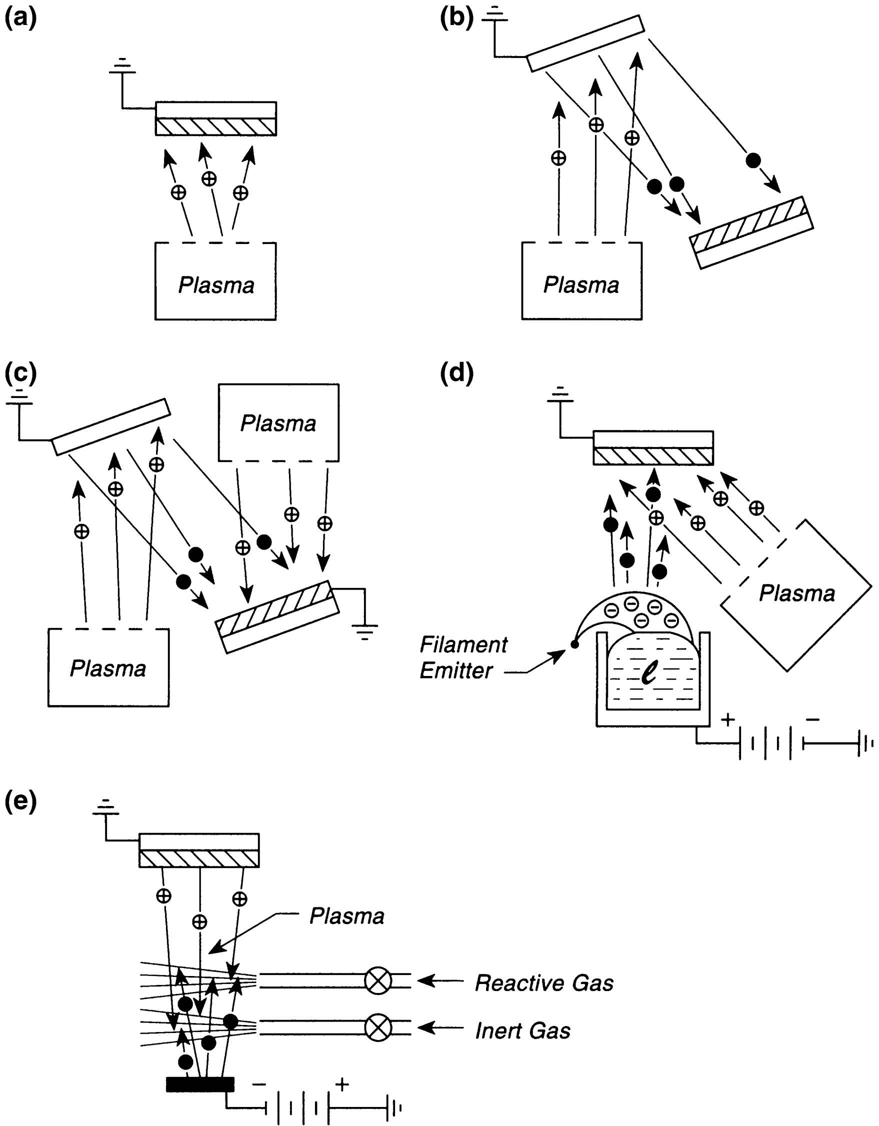

Fig. 29.5 Hybrid thin film deposition processes. **a** Ion beam deposition. **b** Ion beam sputtering. **c** Dual beam sputtering. **d** Ion bombardment—evaporative deposition. **e** Reactive sputtering—dissociable reactive gases

the tube was 6 mm, and a conical Ag target of 5 mm diameter was employed. The target was pushed through the tube at a rate of 0.05 mm/s, while a 2 keV Ar^+ beam was incident. A sputter yield of about 7 Ag/Ar^+ was measured for a 60° incidence angle.

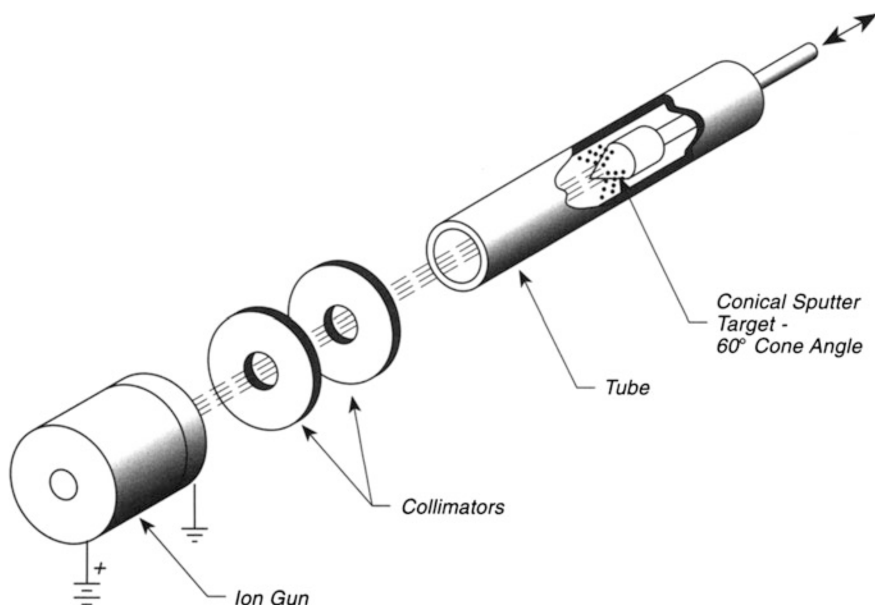

Fig. 29.6 Sputter-coating inner walls of tubes

The conical target was chosen so that the maximum sputter yield could be achieved using a 60° angle of incidence for the ions on the target surface. This optimum Ar^+ incidence angle for Ag sputter deposition was determined experimentally using a separate apparatus that permitted the collection of the Ag metal sputter deposit and its measurement by chemical analysis.

To determine that the Ag film deposited was uniform in thickness, the tube was cut along its axis in four sections. Visual inspection showed that a complete Ag film was deposited along the tube length, and sputter-depth profile measurements showed that depth of the film was uniform to within about 10 %.

Experiments with Pt deposition on Ta tubes were also carried out and subsequent mechanical embrittlement tests showed that the Pt deposit was very effective in preventing hydrogen-induced embrittlement of the Ta tubes.

References

1. A. Linsebigler, G. Lu, J.T. Yates Jr, Surf. Sci. **294**, 284 (1993)
2. S. Tanuma, C.J. Powell, D.R. Penn, W.F. Egelhoff Jr, J. Vac. Sci. Technol **A8**, 2213 (1990)
3. G. Sauerbrey, Zeit. Phys. **155**, 206 (1959)
4. L.J. Slutsky, W.H. Wade, J. Chem. Phys. **36**, 2688 (1962)
5. B. Kasemo, E. Tornqvist, Surf. Sci. **77**, 209 (1978)
6. C. Lu and A. W. Czanderna, in *Applications of Piezoelectric Quartz Crystal Microbalances* (Elsevier, New York, 1983), Chapter 2

7. A. Wajid, Rev. Sci. Instrum. **62**, 2026 (1991)
8. G. Kremer, L.A. Moraga, Rev. Sci. Instrum. **56**, 1467 (1985)
9. B. Ramadan, K. Piyakis, J.R. Kos, Rev. Sci. Instrum. **50**, 867 (1979)
10. R.M. Mueller, W. White, Rev. Sci. Instrum. **39**, 291 (1968)
11. L.L. Levenson, Supple. al Nuovo Cimento, Serie I, **5**(2), 321 (1967)
12. L.L. Levenson, J. Vac. Sci. Technol. **8**, 629 (1971)
13. C. Wang, R. Gomer, Surf. Sci. **74**, 389 (1978)
14. A. Winkler, K.D. Rendulic, K. Wendl, Appl. Surf. Sci. **14**, 209 (1982–83)
15. A. Winkler, Fresenius. Z. Anal. Chem. **319**, 635 (1984)
16. A.J. Slavin, Rev. Sci. Instrum. **81**, 1 (2010)
17. D.W. Goodman, private communication
18. H. Luth, *Surfaces and Interfaces of Solid Materials*, 3rd edn. (Springer, Berlin, 1995), p. 39
19. Z. Zhang, W. Tang, M. Neurock, J.T. Yates Jr, J. Phys. Chem. C **115**, 23848–23853 (2011)
20. D.S. Campbell, in *Physics of Nonmetallic Thin Films*, ed. by C.H. Dupuy, A. Cachard (Plenum, NY, 1976), p. 179. I first learned of this technique from Dr. W.F. Egelhoff, Jr. of the National Institute of Standards and Technology (NIST). The work shown here is from P. J. Chen, M.L. Colaianni, J.T. Yates, Jr., and M. Arbab, J. of Non-Crystalline Solids **155**, 131 (1993)
21. D.A. Steigerwald, I. Jacob, W.F. Egelhoff Jr, Surf. Sci. **202**, 472 (1988)
22. Recoating services are provided by Lebow Company, 5960 Mandarin Avenue, Goleta, CA 93117
23. W.K. Chao, H.K. Wong, J. Vac. Sci. Technol. **A8**, 150 (1990)
24. Photoresist AZ-1300-31 purchased from Shipley Company, Inc., 2300 Washington Street, Newton, MA 02162
25. R.F. Bunshah, Miner. Process. Extr. Metall. Rev. **9**, 147 (1992)
26. R.F. Bunshah, in *Evaporation in Deposition Technologies for Films and Coatings,* ed by R.F. Bunshah, Second edn. (Noyes Publications, Park Ridge, 1994) p. 131
27. C.V. Deshpandey, R.F. Bunshah, Thin Solid Films **163**, 131 (1988)
28. W. Ensinger, Rev. Sci. Instrum. **67**, 318 (1996)

Chapter 30
Infrared Spectroscopy

30.1 Infrared Reflection Absorption Spectrometer

The use of infrared reflection-absorption spectroscopy (IRAS) has grown in popularity since the publication of the classic papers by Greenler on this subject. While the first IRAS measurements in ultrahigh vacuum were made with grating spectrometers [1–3] the measurement technique has been revolutionized by Fourier transform (FTIR) spectrometers, which possess greatly enhanced signal-to-noise capabilities at high spectral resolution [4]. Various technical methods have been used to improve the performance of FTIR spectrometers operating as IRAS instruments [5–11]. The field has been well reviewed [12, 13].

The instrument shown in Fig. 30.1a, b has special characteristics which are designed to improve the performance beyond that of conventional single beam IRAS instruments. A collimated IR beam from the FTIR spectrometer is reflected into an external optical bench by a flat mirror. The beam is split into two parts by a right-angled aluminized beam splitter (made from a 90° glass prism) in the external optical bench. One beam enters the IRAS cell containing the crystal, and the second beam enters the reference cell, which is at ultrahigh vacuum. The beam splitter is able to be moved laterally by a micrometer drive, a novel feature which allows the ratio of the two beam intensities to be accurately and reproducibly adjusted. Both beams are focused with KBr lenses. A beam collector, which is identical to the beam splitter, collects both infrared beams from the IRAS cell and the reference cell and reflects them onto the focussing mirror to the mercury cadmium telluride (MCT) detector. Two electrically driven shutters in the infrared beams enable the detection of these beams independently. For study of adsorbates on metal single crystals, the use of a *p*-polarizer in the incident beam, as shown, will improve the spectroscopic signal-to-noise ratio, since the polarization selection rule is strongly obeyed in this case, and *s*-polarized light is ineffective in detecting the adsorbate.

The collection of infrared spectra is interfered with by the presence of H_2O and CO_2 in the atmosphere within the optical path outside the ultrahigh vacuum system.

© Springer International Publishing Switzerland 2015

J.T. Yates Jr., *Experimental Innovations in Surface Science*,
DOI 10.1007/978-3-319-17668-0_30

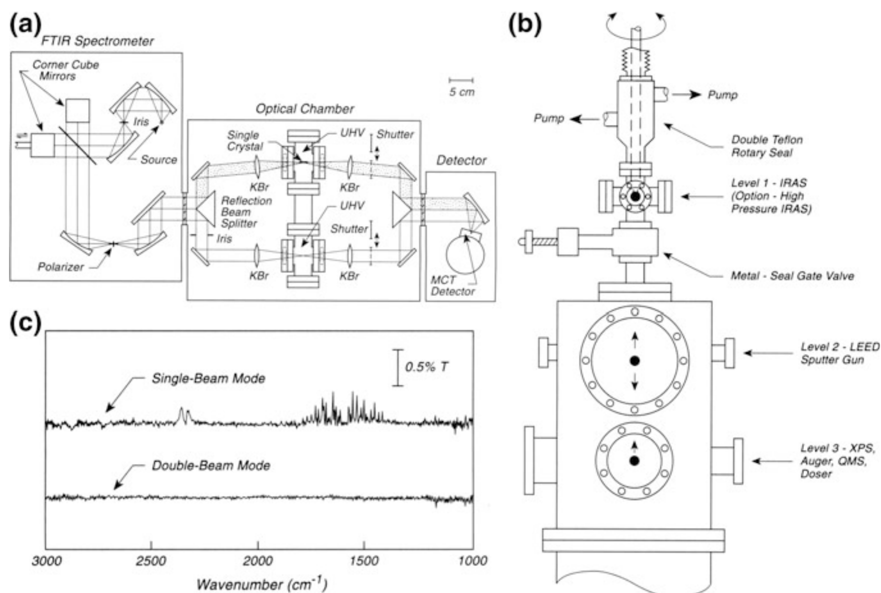

Fig. 30.1 Infrared reflection-absorption spectroscopy—IRAS. **a** IRAS-FTIR spectrometer for surface studies (N_2-Purged)—*top view*. **b** Vacuum system—*side view*. **c** Comparison of two data acquisition methods in IRAS (6 h after baseline)

The "double-beam" arrangement shown here reduces this contribution significantly. As an example, if a H_2O band is 5 % of the total transmission, a 1 % drift of the H_2O partial pressure will yield, in a direct ratio measurement, a 0.05 % H_2O absorption band which would be greater in intensity than many weak surface species' absorption bands. Therefore, the optical path is purged extensively with very dry nitrogen gas from boil off of a liquid nitrogen dewar. With the double-beam method, small variations in the purged gas background spectrum can be reduced as shown next.

In single-beam measurements, if the background spectrum signal is S_0 and the adsorbate spectrum signal is S_1, then the desired adsorbate spectrum is $\log(S_1/S_0)$, which includes any possible changes during the time period between the measurements of S_0 and S_1. By the double beam method, we record the background absorbance spectrum as $\log(S_0/R_0)$ and the adsorbate absorbance spectrum as $\log(S_1/R_1)$. Then the difference absorbance spectrum is obtained by subtracting the background absorbance spectrum from the adsorbate absorbance spectrum,

$$\log(\mathrm{S}_1/\mathrm{R}_1) - \log(\mathrm{S}_0/\mathrm{R}_0) = \log(\mathrm{S}_1/\mathrm{S}_0)(\mathrm{R}_0/\mathrm{R}_1) \qquad (30.1)$$

In (30.1), the term R_0/R_1 produces a cancellation of all changes in environment during the period of taking the two spectra. This could include drifts of composition of the purging gas, drifts in the source and detector, etc. In doing measurements on

the crystal in the optical cell with a high pressure of gas also present, the spectral contribution from the gas phase can be canceled almost completely.

As shown in Fig. 30.1b, the single crystal is moved by a long throw manipulator from the surface analytical positions in the ultrahigh vacuum chamber (Level 2 and Level 3) up into the IRAS cell (Level 1). The crystal can be rotated through 360° by means of a doubly differentially pumped Teflon rotary seal (see p. 6) for precise and reproducible angular orientation to the IR beam, which typically has an angle of incidence of about 86°. The windows of the IR cell can be made of single crystal CaF_2 mounted in Conflat flanges [4] or can be made of KBr single crystals mounted by means of a differentially pumped double Viton seal assembly (see p. 521). The small optical chamber is sealed by a metal-seal gate valve that does not have the problem of Viton O-ring outgassing under compression nor the problem of permeation. For a sealed-off static cell, this is important. For high pressure experiments, the composition and pressure of the gas phase may be determined by spectroscopic measurements through the reference cell for infrared active gases.

Figure 30.1c shows a comparison of operation of the IRAS apparatus in single beam mode and in double-beam mode. The optical path is purged with dry nitrogen. After 6 h, a severe intensity drift in atmospheric H_2O (about 0.4 % T) and atmospheric CO_2 (about 0.2 % T) can be seen in the spectrum obtained by the single beam method. In the spectrum obtained by the double-beam method, this effect is eliminated. The comparison on Fig. 30.1c shows the ability of the double-beam method to eliminate background effects owing to slow drifts during long periods. For 900 scans for both S and R infrared measurements, a noise level of about 1×10^{-4} absorbance unit may be routinely obtained. The amount of light delivered to the detector is significant in determining the noise level. Therefore, large single crystals of the order of 15 mm diameter are favored in this work.

A FTIR spectrometer mounted on a precision optical mount has been employed for IRAS measurements in which the path length between the spectrometer and the external detector has been minimized by using only KBr lenses for focusing the radiation [14]. Both the spectrometer and the detector are coupled to the UHV chamber by small bellows, permitting each unit to be independently adjusted with precision XYZ optical mountings.

Recently, an instrument designed to measure the mass of adsorbate on a thin film in addition to the infrared spectrum has been described [15]. The working temperature range of the quartz crystal oscillator (see p. 309) used for adsorbate mass measurements is 80–350 K [15].

The instrument shown in Fig. 30.1 is described in detail in [16].

30.2 IRAS Measurements at High Pressure

The IRAS apparatus described on p. 321 has the special capability if working at elevated pressures. At these pressures, electron spectroscopies fail because of the reduction of the mean free path of electrons to lengths comparable to or less than

the electron traveling distances inside the apparatus. Fortunately, no such limitations exist for optical techniques, assuming the gas phase at high density is optically transparent in the required spectral regions.

An example is shown of the study of N_2 adsorption on the Ni(111) surface. Figure 30.2a shows that as the N_2 pressure is raised over 4 orders of magnitude from 1×10^{-8} to 2.9×10^{-4} mbar, the equilibrium coverage of chemisorbed N_2 at a crystal temperature of 89 K increases as indicated by the increase in the absorbance of the chemisorbed N_2. Data of this sort were collected as a function of crystal temperature in the range 89–115 K, and the results are shown in Fig. 30.2b, where the vertical scale is the integrated IRAS absorbance. It is clear that as the temperature is increased, higher pressures of N_2 must be employed to produce a given integrated absorbance for the chemisorbed N_2. If one assumes that the integrated absorbance is proportional to surface coverage (an approximation of unknown accuracy) then the "isoabsorbance" plots versus reciprocal absolute temperature can be made, as shown in Fig. 30.2c, and from the slope of these plots the enthalpy of adsorption may be deduced at particular integrated absorbances. The inset to Fig. 30.2c shows this plot, indicating that the enthalpy of adsorption is almost constant, or rises very slightly with increasing absorbance (or coverage within the approximation used above).

Work of this type, in which an initially clean single crystal is exposed to high pressures of a gas, must be carefully done with highly purified gas in order to avoid contamination. For the example of about 10^{-4} mbar of gas, impurity levels of only 10 ppm will give sufficient impurity partial pressure that in about 1000 s of exposure, one monolayer of impurity could be adsorbed if the impurity has a sticking coefficient of unity over its coverage range in the presence of the dominant gas. Effects of this type can often be discovered by examining the reversibility of the spectral changes, or by desorption of the dominant adsorbate, followed by readsorption. The purification of gases is discussed on pp. 505–514.

The slight changes in the vibrational spectrum of the chemisorbed N_2 are thought to be due to various island structures that develop at various equilibrium coverages. The fact that so little shift occurs in the N–N stretching mode (a 24 cm^{-1} range) suggests that the electronic character of the chemisorbed N_2 is not strongly affected by changes in coverage, and suggests that the approximation that integrated absorbance is proportional to coverage may be valid [17].

30.3 Internal Reflection IR Spectroscopy—Silicon

The use of infrared spectroscopy to probe the vibrational spectrum of adsorbates on semiconductor surfaces has opened up a wide range of new physical understanding of surface species structure and dynamics. In contrast to the reflection IR method used on metallic surfaces (see p. 321), it is most appropriate to use internal reflection IR spectroscopy for semiconductor surfaces. This permits the IR beam to make many reflections at the interface, increasing the signal-to-noise ratio significantly.

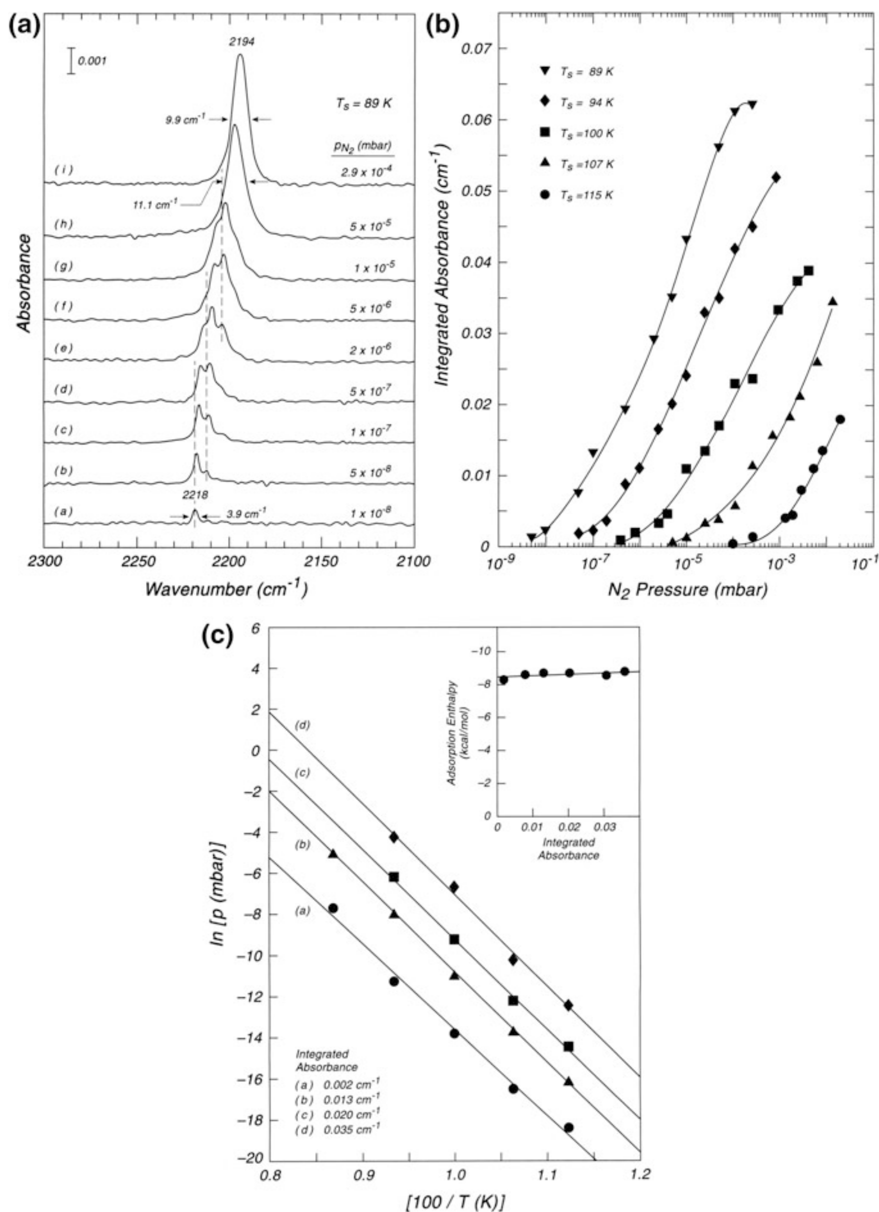

Fig. 30.2 IRAS measurements at high pressure. **a** Development of IRAS Spectra of N_2/Ni(111). **b** N_2 Adsorption Isotherms on Ni(111) by IRAS. **c** Isosteric heat of adsorption N_2/Ni(111) Infrared reflection-absorption spectroscopy (IRAS)

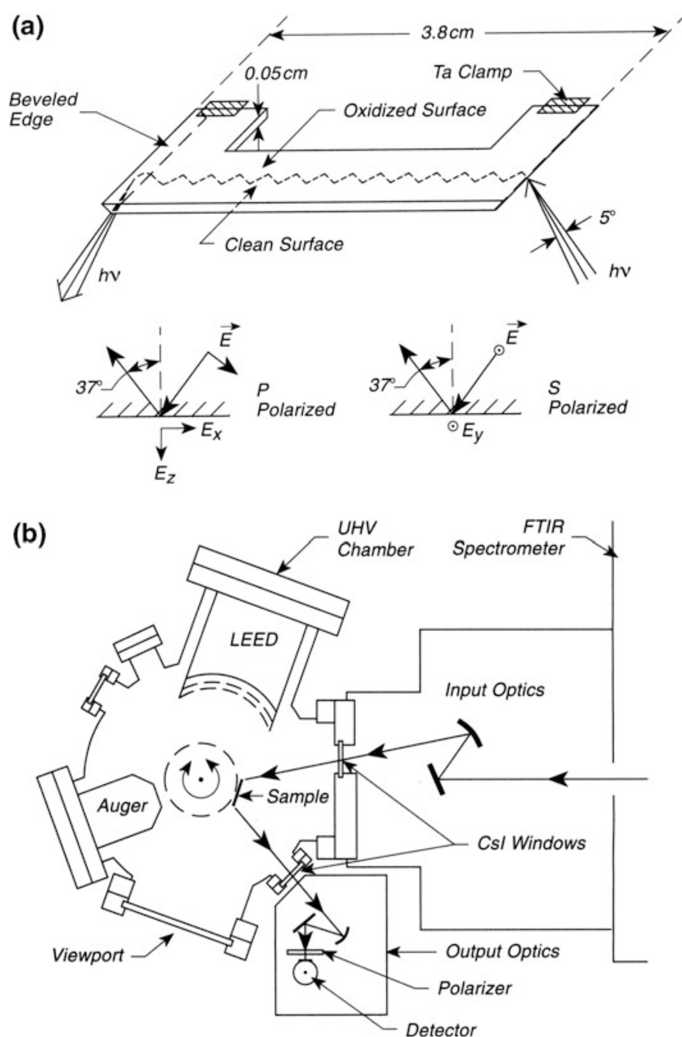

Fig. 30.3 Internal refection IR spectroscopy—semiconductors. **a** U-shaped Si single crystal plus vector diagram for *p*- and *s*-polarization. **b** UHV optical system

Figure 30.3a shows the geometrical arrangement used for holding a silicon single crystal on a manipulator and for making connections for electrical heating [18]. Here, Ta clips are attached to the top of the U-shaped crystal and the crystal may be heated by the passage of current. Conductive cooling to the clips causes a temperature gradient across the crystal (100 K at 1000 K), but in the portion probed by the IR beam, only a small gradient is observed. The edges of the crystal are beveled and polished for admittance of the focused IR beam. The vector diagram for *p*- and *s*-polarization is also shown in Fig. 30.3a. Oxidation of the top surface deactivates this surface for adsorption.

Figure 30.3b shows the UHV system and the associated optical system for use in the FTIR internal reflection measurements [19]. The U-shaped silicon crystal is mounted on a manipulator and may be rotated to an Auger spectrometer or to a LEED apparatus. In its position for internal reflection spectroscopy, the focused IR beam from the FTIR spectrometer passes through a CsI IR window (see p. 521) and enters the silicon sample at the proper incident angle. After many internal reflections, the exiting radiation passes through another CsI window and is focused by a mirror through a polarizer and onto the detector.

For silicon, the absorption of infrared light below about 1450 cm^{-1} prevents transmission with typical sample lengths of 3–5 cm.

Excellent reviews of this field, giving many other optical arrangements for doing IR surface spectroscopy on semiconductors, are available [20–25].

30.4 Internal Reflection IR Spectroscopy—Gallium Arsenide

The use of internal reflection IR spectroscopy for silicon single crystals has been discussed on p. 324. Different problems exist when the same measurement technique is applied to gallium arsenide. In order to permit IR transmission through GaAs, the carrier concentration needs to be kept below about $10^{16}/cm^3$ [26, 27]. GaAs with this level of carriers is commercially obtainable from one supplier, which produces 1 Ω-cm material [27]. Normally, wafer GaAs is sold with conductivities of about 10^6 Ω cm (semi-insulating), or about 10^{-2} Ω cm. While the semi-insulating material would be satisfactory for IR measurements, it cannot be conveniently heated by resistive heating; alternatively, the highly doped material can be heated electrically, but its resistance is so low that large currents are needed and temperature nonuniformities are produced [26]. This material is also opaque in the infrared [26].

The mounting of 1 Ω-cm material for internal reflection infrared spectroscopy is shown in Fig. 30.4. The infrared beam enters and exits through polished beveled edges. Heating current flows perpendicular to the IR beam direction, using Ta mounting clips on the top and bottom of the crystal. A thermocouple is conveniently glued to the crystal using a refractory cement, used also for thermocouple attachment to other semiconductor crystals such as SiC [28]. Welding the thermocouple first to a Ta foil square (1.2 mm × 1.2 mm) and then gluing this to the GaAs provides good agreement between the thermocouple and pyrometry [26]. The advantages of this mounting arrangement are that either surface can be studied, or if both are studied together a two-fold improvement in the signal strength in the FTIR measurement is obtained. The two sides of the crystal, if terminated by the same element, exhibit orthogonal orientation of the dangling bonds. Thus, using *s*- and *p*-polarized IR radiation, one can probe the adsorbate orientation [26]. A disadvantage of working with the 1 Ω-cm material is that the resistance becomes too great for

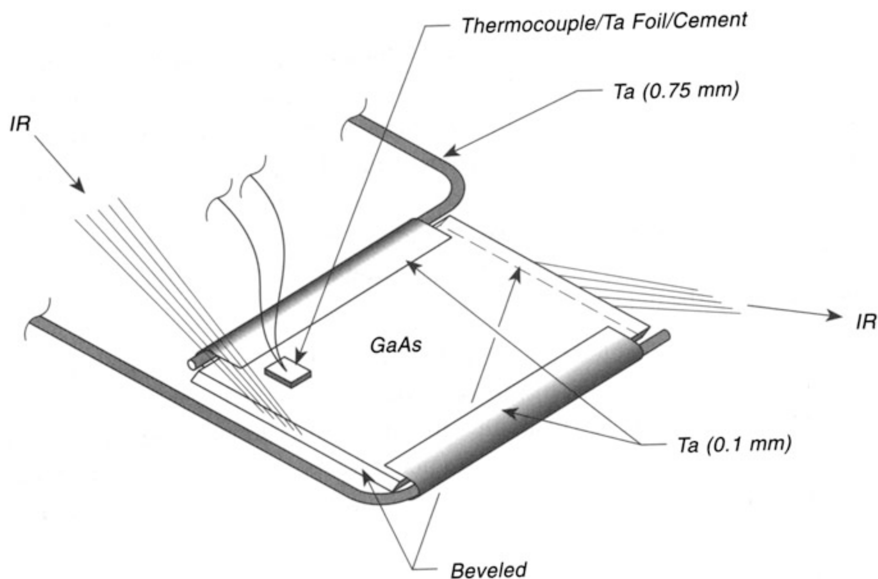

Fig. 30.4 GaAs—mounting for internal reflection IR spectroscopy gallium arsenide

electrical heating when the sample is cooled to 120 K. This problem can be alleviated by warming the sample slightly with a projector lamp (see p. 371) [26].

30.5 Infrared Spectroscopy—Continuous Pumping of Detector Dewar

InSb and HgCdTe infrared detectors are used in the mid-IR range (4000–500 cm^{-1}) for the study of adsorbed species on surfaces. The detector element is mounted on the end of a small metal Dewar which is kept filled with liquid nitrogen during operation, as shown in Fig. 30.5. The Dewar is often pumped on a separate vacuum system and then sealed with a Viton-sealed valve. In addition, the detector window is often sealed with a Viton O-ring. Thus, over time, slow permeation, outgassing, and leakage can be expected (see p. 108), and the condensation of water and other materials may occur on the detector surface, causing interference with infrared measurements. These problems can be prevented by using a small appendage ion pump to continuously pump the detector [29].

The IR detector is connected to a metal bellows-sealed valve and thence to a tee as shown in Fig. 30.5. One branch of the tee is connected to the ion pump via a 1.5-cm-diameter bellows that extends up to about a 30-cm length as it makes the transition from the detector to the ion pump. The second branch is temporarily connected to an oil diffusion pump (liquid nitrogen trapped) for preliminary pumping of the Dewar and the appendage pump.

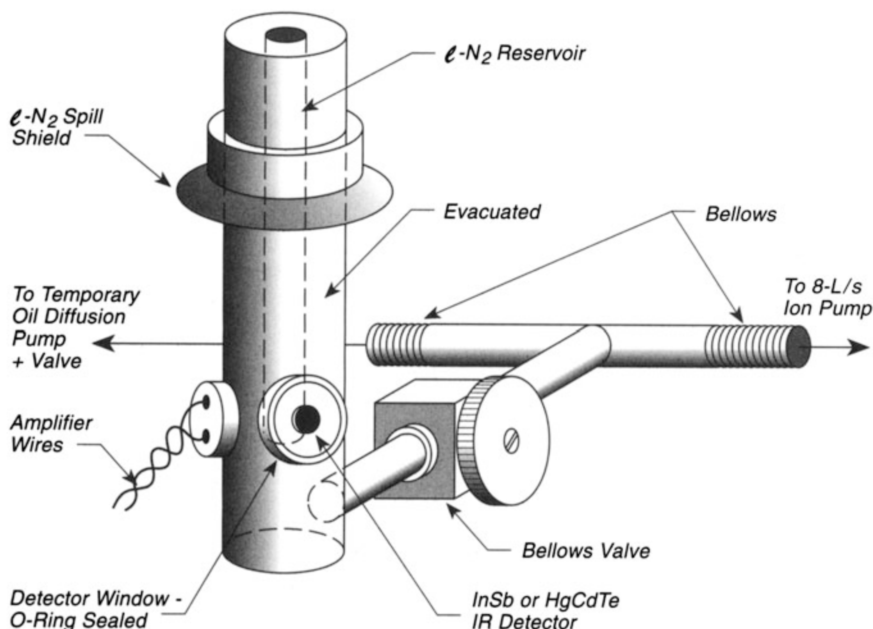

Fig. 30.5 Ion-pumped IR detector

Initially the entire system is pumped out by the diffusion pump. The valve on the detector is then closed and the ion pump (not operating) and the metal tubing are baked out with heating tape. When the pressure is low enough that the ion pump can be operated, the valve to the diffusion pump is closed and the diffusion pump is removed from the vacuum system. The heating is discontinued and when the line is cooled, the valve to the detector is opened. Under these conditions, the IR detector will be continuously pumped and condensation effects will be eliminated on the detector. It is wise to place a conical shield just below the top of the Dewar entrance to prevent liquid nitrogen from accidentally pouring over the detector window and the vacuum seal for the amplifier wires, since these vacuum seals may be broken by such accidental cooling [30].

30.6 Rapid IR Spectrometer Purge After Cell Transfer—Using Rubber Sleeves

Infrared spectrometers require that the optical path length be free of absorbing atmospheric gases. Both CO_2 and H_2O vapors must be removed by using either N_2(g) or specially-dried and CO_2-scrubbed compressed air. Some IR spectrometers have a sample compartment which is separately purged from the spectrometer

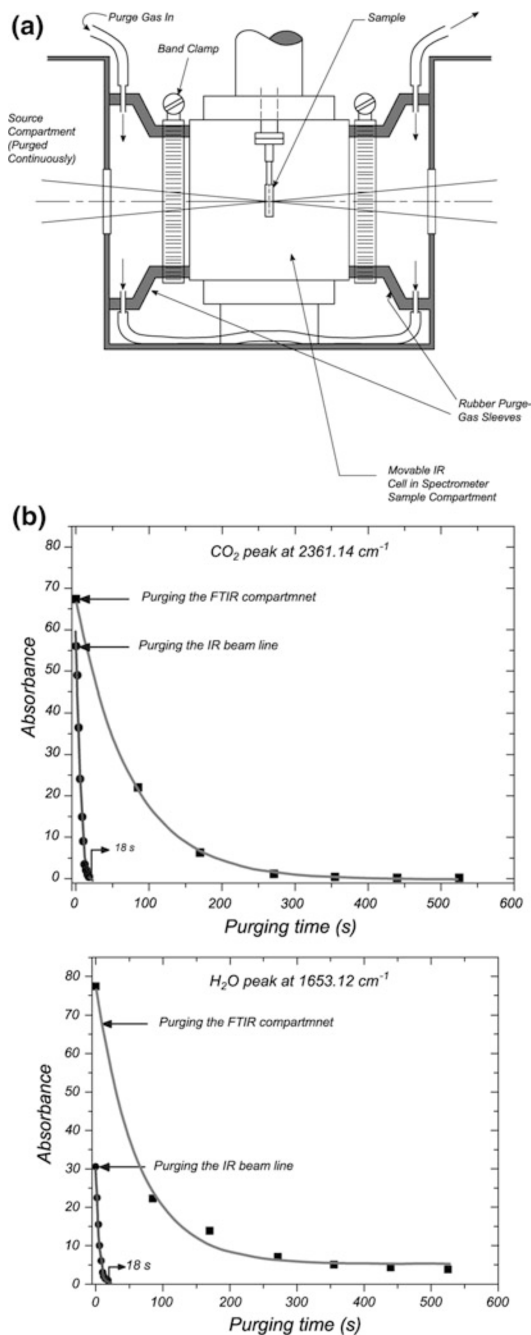

Fig. 30.6 Rapid IR spectrometer purge after cell transfer—using rubber sleeves. **a** Sample cell in IR spectrometer. **b** Purge performance—CO_2 and H_2O absorbance

source and detector compartments. The sample compartment is usually rather large to admit large IR cells. It usually contains a sample compartment lid which is opened and closed as the cell is transferred in and out. The cell and its connecting tubing and wiring will cause problems with compartment sealing, requiring cutting of the lid and unsatisfactory sealing with tape, etc. In Fig. 30.6a, an arrangement for a portable cell is shown in which custom-cut rubber purge gas sleeves are arranged to slide into the sample compartment under slight compression, thereby making a gas tight seal with the inner walls of the sample compartment and the inserted IR cell. The seals are held on the cell window flanges with band clamps. With this arrangement, the IR spectrometer remains purged always, and the small volume within the rubber sleeves is separately purged with great rapidity. Figure 30.6b shows a comparison of the purge rate for the sleeves, compared to the entire spectrometer, for CO_2 and H_2O. It is seen that the small-volume rubber sleeves are purged about 25 times more rapidly than the entire spectrometer sample compartment. In addition, complex gas-tight seals involving the compartment lid are avoided, and the lid may be removed permanently. Soft rubber sleeves may be obtained in several sizes from the plumbing department of a local hardware store, where they are sold as flexible couplings for sewer systems. To cut the length to fit, a mandrel is used on a lathe, and a smooth cut suitable for purge gas sealing at the wall is produced with a sharp blade. This apparatus was produced in [31].

References

1. J. Pritchard, M.L. Sims, Trans. Far. Soc. **66**, 427 (1970)
2. M.L. Kottke, R.G. Greenler, H.G. Tompkins, Surf. Sci. **32**, 231 (1972)
3. J.T. Yates Jr, R.G. Greenler, I. Ratajczykowa, D.A. King, Surf. Sci. **36**, 739 (1973)
4. B.E. Hayden, in *Vibrational Spectroscopy of Molecules on Surfaces*, eds. by J.T. Yates, Jr., T. E. Madey (Plenum, New York, 1987)
5. E. Schweizer, B.N.J. Persson, M. Tüshaus, D. Höge, A.M. Bradshaw, Surf. Sci. **213**, 49 (1989)
6. W. Erley, J. Electron Spectrosc. Related Phenom. **44**, 65 (1987)
7. W. Erley, Surf. Sci. **205**, L771 (1988)
8. D. Höge, M. Tüshaus, A.M. Bradshaw, Surf. Sci. **207**, L935 (1988)
9. T. Buffeteau, B. Desbat, J.-M. Turlet, Mikrochim. Acta (Wien) **II**, 23 (1988)
10. W.G. Golden, in *Fourier Transform Infrared Spectroscopy*, vol. 4, eds. by J.R. Ferraro, L. J. Basile (Academic, New York, 1985), p. 315
11. A.E. Dowrey, C. Marcott, Appl. Spectrosc. **36**, 414 (1982)
12. F.M. Hoffmann, Surf. Sci. Rep. **3**, 107 (1983)
13. Y.J. Chabal, Surf. Sci. Rep. **8**, 211 (1988)
14. Q. Wu, L. Hanley, J. Phys. Chem. **97**, 2677 (1993)
15. G. Zhuang, G. Chottiner, I.T. Bae, E. Hwang, D.A. Scherson, Rev. Sci. Instrum. **65**, 2494 (1994)
16. Z. Xu, J.T. Yates Jr, J. Vac. Sci. Technol. **A8**, 3666 (1990)
17. J. Yoshinobu, R. Zenobi, J. Xu, Z. Xu, J.T. Yates Jr, J. Chem. Phys. **95**, 9393 (1991)
18. Y.J. Chabal, Bell Laboratories, Lucent Technologies (personal communication). See Y. J. Chabal, Phys. Rev. Lett. **50**, 1850 (1983a).

19. Y.J. Chabal, Lucent, AT&T (personal communication). See Y.J. Chabal, E.E. Chaban, S.B. Christman, J. Electron Spect. Rel. Phenom. **29**, 35 (1983b)
20. N.J. Harrick, *Internal Reflection Spectroscopy* (Wiley, New York, 1967)
21. R.M. Mirabella, N.J. Harrick, *Internal Reflection Spectroscopy: Review and Supplement* (Harrick Scientific Corporation, Ossining, NY, 1985)
22. Y.J. Chabal, in *Semiconductor Interfaces: Formation and Properties*, eds. by G. LeLay, J. Derien, N. Boccara, Springer Proc. Phys. **22**, 301 (1987)
23. Y.J. Chabal, Surf. Sci. Rep. **8**, 211 (1988)
24. Y.J. Chabal, in *Internal Reflection Spectroscopy: Theory and Applications*, ed. by R.M. Mirabella, Jr. (Marcel Dekker, New York, 1993), printed in Practical Spectroscopy, 15, 191 (1993)
25. M. Katiyar, J.R. Abelson, J. Vac. Sci. Technol. **A13**, 2005 (1995)
26. Dr. J.R. Creighton, Dept. 1126, MS 0601, P.O. Box 5800, Sandia National Laboratories, Albuquerque, NM 87185-0601 (personal communication). J.R. Creighton, Appl. Surf. Sci. **82/83**, 171 (1994)
27. GaAs with no intentional dopants (HB material, about 1 Ω-cm) is available from Sumitomo Electric, 551 Madison Avenue, New York, NY 10022
28. F. Bozso, L. Muehlhoff, M. Trenary, W.J. Choyke, and J.T. Yates, Jr., J. Vac. Sci. Technol. **A2**, 1271 (1984). Aremco 516 ceramic cement is used. Obtainable from Aremco Products, Inc., P.O. Box 429, 23 Snowden Avenue, Ossining, NY 10562-0429; the cement should be preserved in the refrigerator and has a limited shelf life
29. Contributed by Dr. Victor M. Bermudez, Naval Research Laboratory, Code 6863, Washington, DC 20375-5347
30. Developed in author's laboratory
31. A. Stevanovic, M. Büttner, Z. Zhang, J.T. Yares Jr, J. Am. Chem. Soc. **134**, 324 (2012)

Chapter 31
Calorimetric Heats of Adsorption—Single Crystals

31.1 Measurement of the Calorimetric Heat of Adsorption on Ultrathin Metal Single Crystals

There are many methods for measuring the energy required for desorption of a molecule from a single crystal surface using either isosteric heat measurements under equilibrium conditions, or using desorption kinetic methods. The interpretation of the isosteric measurements requires perfect reversibility in adsorption and desorption, a condition not met when compound formation or dissolution of the adsorbate in the crystal occurs. The interpretation of the kinetic measurements are beset with difficulties having to do with the inability to write the desorption rate laws that apply with accuracy. The calorimetric method avoids these difficulties by directly measuring the heat evolved upon adsorption and by using only the first law of thermodynamics.

In order to employ a calorimetric device, the heat capacity of the calorimeter must be made very small in order for a measurable temperature rise to be produced. This has been cleverly done, using single crystal films of metals which are only 2000 Å in thickness [1], using apparatus as shown in Fig. 31.1. These films are grown epitaxially on an alkali halide crystal surface, and the continuous metal film is then lifted off of the salt crystal as it dissolves in water. The metal crystal film is transferred and attached to a ring, made of the same metal, and may be placed at the focus of a pulsed molecular beam of the adsorbate. The thin crystal may be cleaned in UHV by ion bombardment and by heating in vacuum or in reactive gases used for cleaning. Standard surface analysis and LEED studies are routinely performed on the thin crystal after cleaning. As the gas pulses arrive and are adsorbed on a 2-mm-diameter spot, the temperature of the thin crystal rises, and the pulsed emission of infrared radiation is measured from the rear of the crystal by focusing the radiation on a mercury cadmium telluride detector held at liquid nitrogen temperature. Temperature rises on the crystal per pulse are below 0.1 K for chemisorbing gases, where each pulse delivers about 0.01 mL of chemisorbed

© Springer International Publishing Switzerland 2015

J.T. Yates Jr., *Experimental Innovations in Surface Science*,
DOI 10.1007/978-3-319-17668-0_31

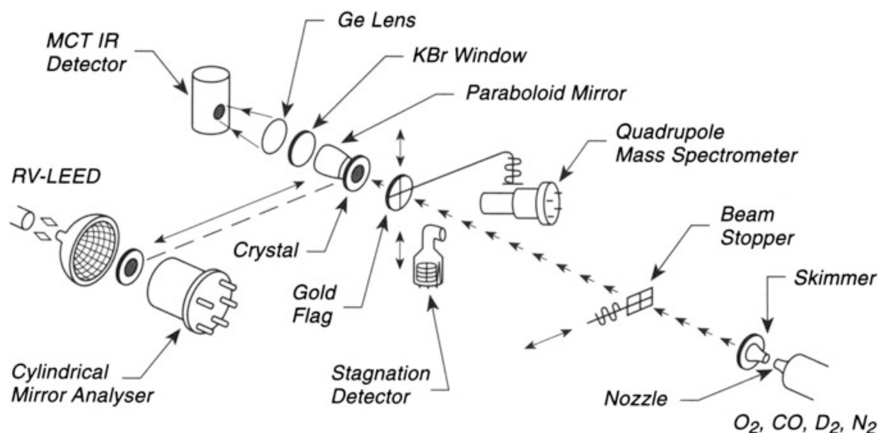

Fig. 31.1 Calorimetric adsorption heat—ultrathin metal films

species to the surface. The emissivity of the backside of the crystal is significantly enhanced by initially coating it with amorphous carbon from a candle flame. For calibration, a pulsed laser beam of known energy per pulse is used, and its reflectivity at near normal incidence is measured. The temporal character of the laser beam is matched to that of the pulsed molecular beam in the calibration measurements. The energy losses after each pulse are found to be due to radiation losses only.

In addition to the errors in measuring the small pulses of heat, errors in the coverage measurement (and the sticking coefficient) currently limit this method [1]. The sticking coefficient and absolute coverage are measured using the method of King and Wells [2], which measures the intensity of the reflected gas from the crystal during each pulse. A gold flag is employed in these measurements. A stagnation detector (see p. 429), which is a Bayard-Alpert gauge with a small aperture, is employed for measurements of the absolute beam flux, as discussed on p. 314.

31.2 Improved Adsorption Calorimeter for Single Crystals at 100–350 K

The pioneering development of single crystal adsorption calorimetry (SCAC) by the King group as documented in Sect. 31.1 has been markedly improved. A new heat detector principle has been developed by the Campbell group, and the latest stage of development is shown here [3]. A metal-coated pyroelectric polymer ribbon (uniaxially oriented β-polyvinylidene fluoride, β-PVDF) of 9 μm thickness and 4 mm width is employed as the detector, and electrical contact is made with the front and back surfaces using Al film contacts. These films, with Al coatings, are

available from Goodfellow. The PVDF detector is bent into an arch and gently pressed to the back of the crystal which has been thermally cleaned in UHV before contact. Pulses of adsorbent gas molecules, arriving at 0.5 Hz, cause temperature bursts due to the evolution of the adsorption energy. The transient rise of crystal temperature causes part of the PVDF detector to change its degree of polarization, releasing an electrical charge through an electronic circuit. The ease of using the PVDF detector compared to others allows the crystal to be cleaned at high temperatures and also allows calorimeter operation below 300 K. This permits a wide range of heat-of-adsorption experiments to be performed on thicker ($\sim$75 μm) single crystals than previously possible.

The latest advances in the technique are sketched in Fig. 31.2A–D. It has been found that noise, caused possibly by electrical leakage at the PVDF edges, can be reduced by etching the Al film coating away from the ribbon edge. Figure 31.2 A shows this: (a) indicates the aluminized PVDF film; (b) shows masking of the Al

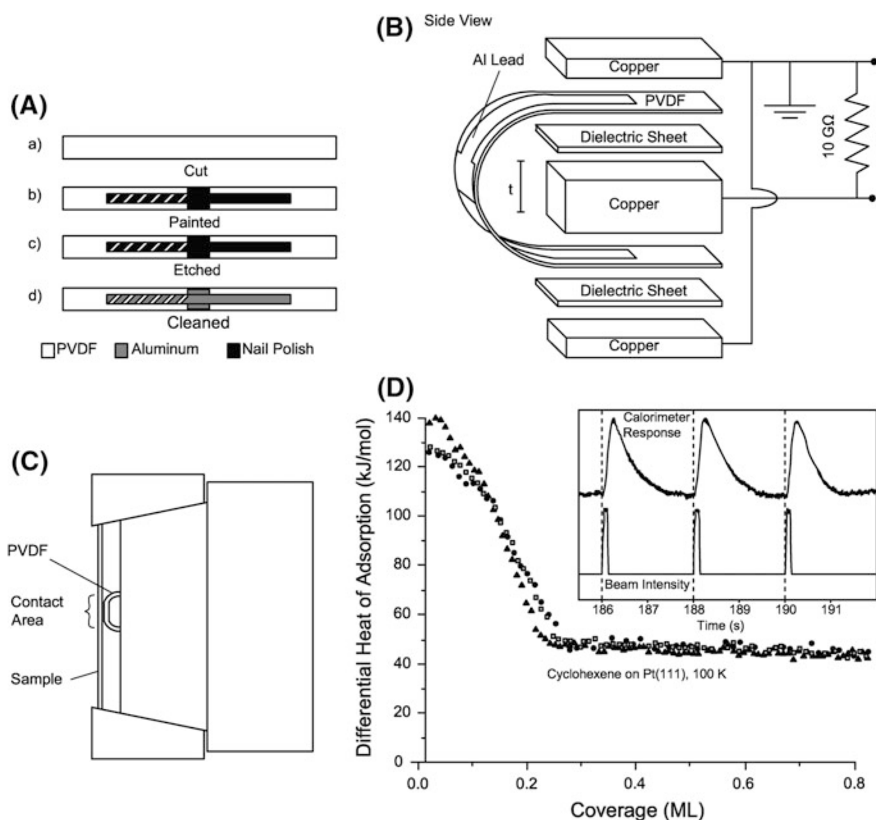

Fig. 31.2 Improved adsorption calorimeter for single crystals at 100–350 K. **A** Electrodes on PDVF front and back surfaces. **B** Bent PDVF sensor. **C** contact of sensor with thin sample. **D** Experimental adsorption measurement

film on front and back faces of the ribbon with nail polish; (c) shows the electrochemically-etched ribbon with preservation of Al only under the nail polish covering; (d) shows the final assembly with the removal of the nail polish with methanol.

Figure 31.2B shows a schematic of the assembly for holding the bent PVDF detector and for making electrical contact to both faces. A copper bar of thickness t, of the order of a few mm, is used to define the width of the arch and the projection of the arch. For contact with the crystal, the arch is compressed reproducibly by 0.5–1 mm.

Figure 31.2C shows a schematic of the design to compress the arch of the PVDF detector against the back of the sample. Self-aligning conical holders are driven into contact, and care in design prevents appreciable bending of the thin crystal sample.

Figure 31.2D shows a series of three experimental measurements of the heat evolution during the adsorption of cyclohexene on Pt(111). Pulses of gas, involving 1.1 % of a monolayer are incident. As the coverage increases for the chemisorbed cyclohexene, the heat of adsorption per pulse drops due to site blocking as well as other effects. At 0.25 mL, the monolayer is complete and second layer adsorption, with a constant heat of adsorption, takes place. The raw calorimetry data are shown in the inset, and repeated experiments show a pulse-to-pulse standard deviation of about 1.3 kJ/mol. The thermal energy released per pulse is 0.24 μJ which corresponds to a temperature rise in the adsorption spot on the crystal of ~7–8 mK. The detector temperature rises in each pulse by 0.3 mK. The use of a pulsed He–Ne laser on the crystal allows a calibration of the PVDF detector to give energy liberated at the crystal surface. The improvements shown here have yielded a ~ 40 fold improvement in the pulse-pulse standard deviation over earlier PVDF detectors. The paper [3] describes future developments to further enhance detection sensitivity.

References

1. C.E. Borroni-Bird, D.A. King, Rev. Sci. Instrum. **62**, 2177 (1991)
2. D.A. King, M.G. Wells, Surf. Sci. **29**, 454 (1972)
3. W. Lew, O. Lytken, J.A. Farmer, M.C. Crowe, C.T. Campbell, Rev. Sci. Instrum. **81**, 024102 (2010)

Chapter 32
Surface Debye Temperature

32.1 Measuring the Surface Debye Temperature of a Single Crystal

The Debye temperature of a bulk solid is a measure of the stiffness of the bonds within the crystal and is related to the Debye characteristic frequency, ν_D. This frequency corresponds to the highest allowed vibrational mode in the crystal in the distribution of frequencies following a mode frequency distribution function with a magnitude which is proportional to the square of the mode frequency. The Debye temperature is $\Theta_D = h\nu_D/k$, where k is Boltzmann's constant.

The Debye-Waller factor, *2M*, is connected to the Debye temperature through (32.1), and determines the intensity of scattering of an electron beam incident on the crystal through (32.2).

$$2M = 24m_e\left(E\cos^2\alpha + V_0\right)T/m_a k(\Theta_D)^2 \tag{32.1}$$

where m_a = mass of the atoms in the crystal, m_e = mass of the electron, α = the angle of incidence, V = the inner potential, and E is electron energy.

For an electron beam incident on a crystal, in the kinematic approximation,

$$I = I_0 e^{-2M} \tag{32.2}$$

where I_0 is the incident intensity and I is the diffracted intensity.

Figure 32.1a shows a four-grid LEED apparatus with a movable Faraday cup to intercept a selected diffraction beam [1]. The crystal surface in inclined by angle α from the incident beam, and the diffracted 0,0 beam is being collected in the drawing. As the crystal cools, the intensity of the diffracted beam increases as a result of the decrease in the vibrational motion of the atoms in the region of the solid surface being sampled by the incident electrons. As the energy of the incident electron beam is decreased in successive experiments, a lower sampling depth is

© Springer International Publishing Switzerland 2015
J.T. Yates Jr., *Experimental Innovations in Surface Science*,
DOI 10.1007/978-3-319-17668-0_32

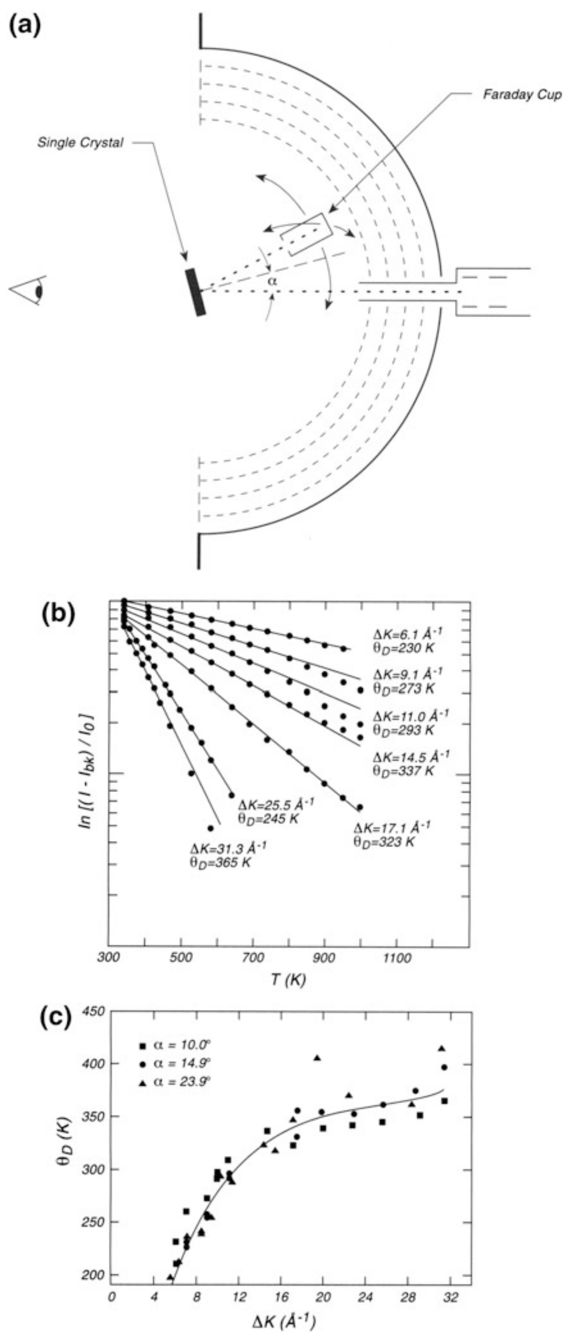

Fig. 32.1 Measuring the surface debye temperature of a single crystal. **a** LEED Apparatus with Faraday Cup. **b** 0,0 Beam Intensity, Rh (111). **c** Debye temperature, Θ_D(K)

involved in the diffraction process, and the measured Debye temperature decreases as a result of the looser binding of the crystal atoms near to the surface. Figure 32.1b shows a Debye-Waller plot of $\ln(I - I_{bk})/I_0$ versus temperature for various values of ΔK, the perpendicular component of the momentum transfer between the electron and the metal atoms in the crystal. Here, I_{bk} is a background scattering contribution which can either be measured in the vicinity of the 0,0 beam, or treated parametrically as a variable. In this case, for low angles of incidence, one can only measure an effective perpendicular Debye temperature as ΔK is varied [2].

Figure 32.1c shows typical behavior of the Debye temperature measurements for three angles of incidence on a Rh(111) crystal as a function of ΔK. It may be seen that all of the measurements show that as ΔK increases, and the depth of sampling of the crystal by the electron beam increases, the measured value of Θ_D increases to a plateau at $\Theta_D = 370$ K, which is characteristic of the bulk of the crystal. The lower limit of Θ_D is near 200 K, and is characteristic of the surface metal atoms.

These measurements were made with a LEED apparatus mounted between two pairs of Helmholtz coils to cancel the earth's magnetic field. The values of the diffracted beam intensity were measured as the crystal slowly cooled to avoid the serious influence of the magnetic field associated with the electrical heating current. The Faraday cup aperture subtended an angle of 4.6×10^{-3} steradians, and was large enough to collect the entire beam, I.

References

1. C.M. Chan, P.A. Thiel, J.T. Yates Jr., W.H. Weinberg, Surf. Sci. **76**, 296 (1978)
2. G.A. Somorjai, H.H. Farrell, Adv. Chem. Phys. **20**, 215 (1971)

Chapter 33
Friction and Fracture

33.1 UHV Tribometer for Measuring the Coefficient of Friction

Many technologies depend upon knowledge of the coefficient of friction between a surface and a probe that slides across the surface. Since the coefficient of friction $\mu = F_s/F_n$, where F_s is the shear force, and F_n is the normal force, a device that simultaneously measures both components of force during sliding is needed. In addition, such a device should be able to be applied to surfaces that are initially atomically clean, followed by studies on the surface which has a known coverage of lubricant. These research demands have resulted in the development of the UHV tribometer [1].

Figure 33.1a shows a schematic picture of the tribometer. A single crystal is mounted on two support wires that connect to a rigid frame. Behind the crystal is a coiled thermionic emitter used for heating the crystal to achieve a condition of atomic cleanliness.

The frame surrounding the sample is connected by means of two L-shaped Cu/Be alloy springs (0.006-in. thick by 0.25-in. wide) and each arm of the L is 0.5 in. in length. Glued to each of these springs are strain gauges (see p. 343) thermally matched to the Cu/Be alloy. A total of eight strain gauges are employed, connected to two Wheatstone bridges (normal; shear).

Measurements are made by bringing the sample in contact with the slider (also a single crystal) which is mounted on a manipulator which can be translated at constant speed, under an applied normal load. Figure 33.1b shows the displacement components, δ, produced by applying a normal load to the sample, and it can be seen that both normal displacements and shear displacements are sensed by the strain gauges. However, for a normal force applied, the shear displacements counterbalance, and are not measured by the Wheatstone bridges. In the same way, for shear forces the normal displacement is counterbalanced and not measured by

© Springer International Publishing Switzerland 2015
J.T. Yates Jr., *Experimental Innovations in Surface Science*,
DOI 10.1007/978-3-319-17668-0_33

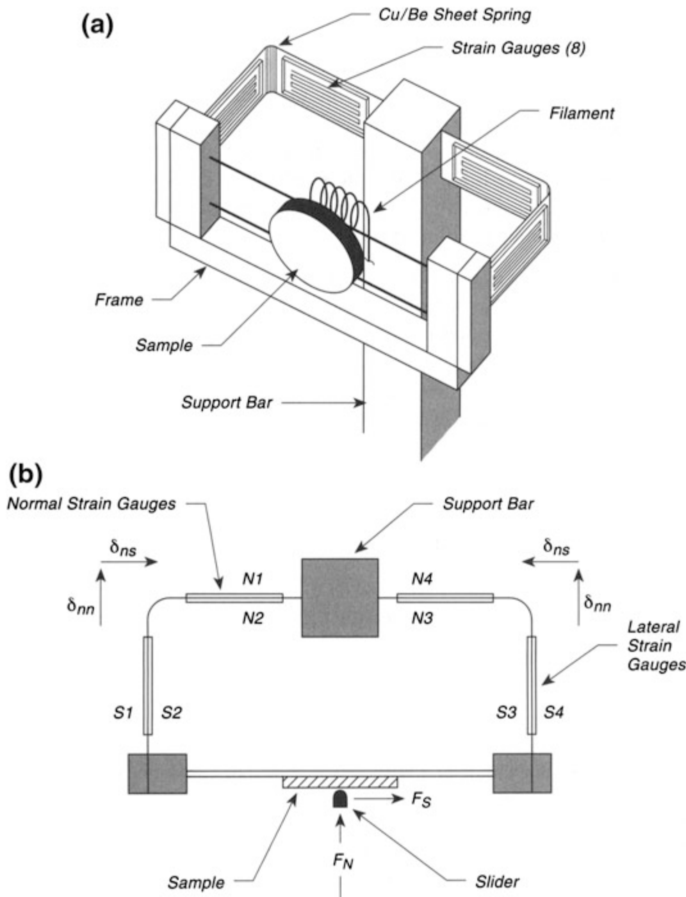

Fig. 33.1 UHV tribometer for measuring the coefficient of friction. **a** Strain gauge arrangement. **b** Forces at slider/sample interface and displacement components

the bridges. This arrangement therefore permits the coefficient of friction to be continuously measured during the sliding experiment.

It has been found on single crystal metal surfaces that a single monolayer of a low molecular weight molecule is effective in reducing the coefficient of friction. Three frictional regimes of increasing coverage of ethanol on an interface, a S-covered Ni(100) crystal surface, have been observed. Below a monolayer, sticking is observed; near a monolayer, stick-slip motion is observed; and above a monolayer, slip motion is observed [1].

Another tribometer design [2] is shown on p. 343.

33.2 Pin-on-Disk Measurement—UHV

The measurement of the coefficient of friction (see p. 341) is of importance in understanding lubrication. To do this without the influence of adsorption processes from the atmosphere, tribometers operating in ultrahigh vacuum have been devised. The device shown here has the ability to make friction coefficient measurements, as well as measuring the electrical resistivity of the interface between the pin and the disk. In addition, Auger spectroscopy measurements of the surface composition of the wear track can be made, using a scanning instrument [2].

Figure 33.2a shows an exploded view of the tribometer. The disk sample is mounted on a rotary platform that may be turned in UHV by an external motor. A pin sample bent in the form of a loop maybe pressed onto the disk sample by means of a spring tensioner that attaches to a cantilever beam. The cantilever beam is free to move in the z-direction on bearings in a trunnion that can be moved in the z-direction. Electrical contact is made to the pin for current and voltage measurements. Two brushes (Cu/Be alloy) make electrical contact with a commutator electrically connected to the sample; one of these is used for current, I, measurements, and the second for voltage, V, measurements. The lateral force, F, is measured by two semiconductor strain gauges [3] that are accurately and squarely mounted on a thinned section of the cantilever beam, using strain gauge cement [4]. The normal force, N, is adjusted by means of a screw adjuster on the spring tensioner. Figure 33.2b shows the vector forces and the electrical measurement method employed as the disk sample rotates. The entire pin-on-disk apparatus may be moved inside the vacuum system by means of internal x-, y-, and z-bearings; and rotary motion is provided by a rotary manipulator shaft.

The apparatus has been used to measure the effect of atmospheric gases on contact electrical alloys under wear conditions [5, 6].

33.3 UHV Fracture Stage for Surface Analysis After Fracture

The analysis of fracture surfaces is a significant feature of materials science, where often the weakening of a solid can be related to the accumulation of impurities at an internal interface. It is desirable to carry out the fracture and the surface analysis without exposure to the atmosphere to avoid surface contamination of the fresh fracture surface. Figure 33.3a shows an ultrahigh vacuum apparatus designed for this purpose. A specimen to be fractured is clamped in the jaws of a fracture stage which had been previously calibrated with a spring of known force constant. To measure the load under tension, a load cell (Fig. 33.3b) was used on a lower flange as shown, connected to the lower jaw by a stiff rod. This permits the force at the specimen to be measured as a function of the displacement, which is automatically measured at the stepper motor on top. To assure that the load cell does not experience a pressure

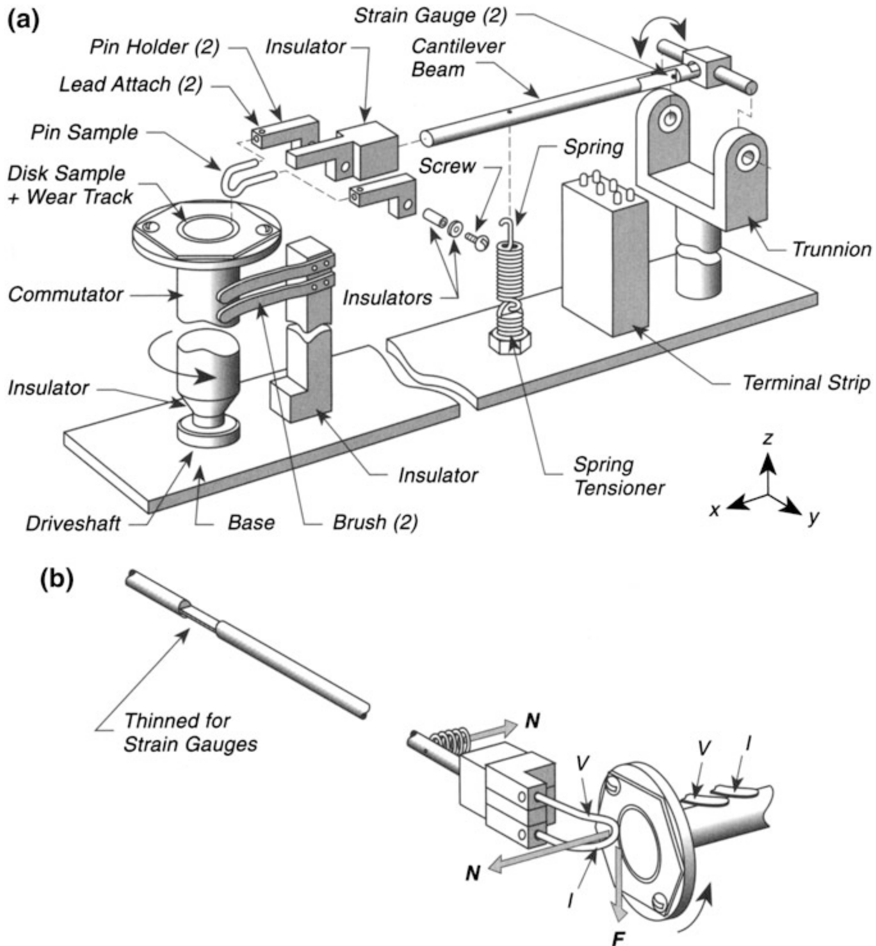

Fig. 33.2 Pin-on-disk measurements—UHV. **a** Exploded view. **b** Forces and electrical contacts

differential due to atmospheric pressure on the outside, it is capped with a Conflat flange which has a machined recess which is evacuated into the UHV system. Thus both the upper and lower diaphragms are uninfluenced by gas pressure. The load cell recorded force at 1 s intervals as the linear drive ran at a constant speed of 4 steps per second (2.5×10^{-6} ms^{-1}), giving force/displacement curves as shown in Fig. 33.3c. It is noted in the comparison that atmosphere influences the force/displacement curve. More force is required for fracture in the air, compared to fracture in UHV. After fracture the freshly exposed surfaces are subjected to surface analysis by vacuum transfer to a TOF-SIMS spectrometer [7, 8].

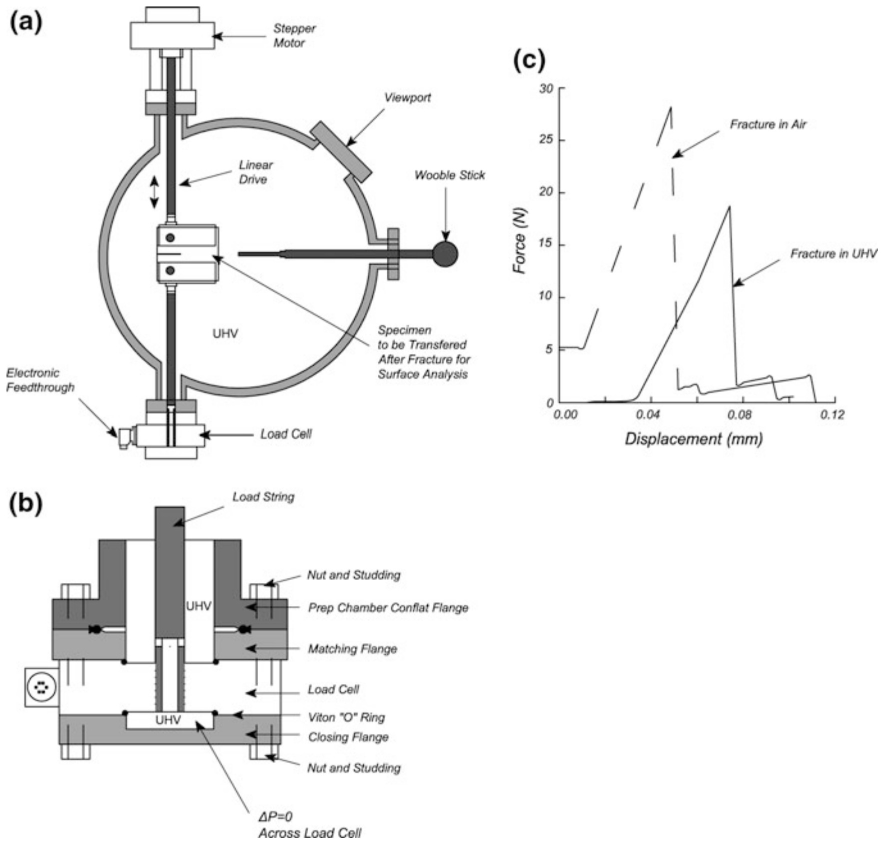

Fig. 33.3 UHV fracture stage for surface analysis after fracture. **a** UHV fracture device. **b** Load cell for accurate operation in UHV. **c** Force/displacement plots for polyester resin

References

1. A.J. Gellman, J. Vac. Sci. Technol. **A10**, 180 (1992)
2. T.G. McDonald, D.E. Peebles, L.E. Pope, H.C. Peebles, Rev. Sci. Instrum. **58**, 593 (1987)
3. P-doped U configuration, 350 Ω, 130 gauge factor, obtained from Kulite Semiconductor Products, Inc., 1 Willow Tree Road, Leonia, NJ 07605
4. M-Bond 610 Epoxy Adhesive
5. L.E. Pope, D.E. Peebles, J. Vac. Sci. Technol. **A4**, 1659 (1986)
6. L.E. Pope, D.E. Peebles, *Electrical Contacts-1986* (IEEE, New York, 1986), p. 65
7. A.R. Wood, N. Benedetto, N. Hooker, E. Scullion, P.A. Smith, J.F. Watts, Surf. Interface Anal. **40**, 1409 (2008)
8. A.R. Wood, M.-L. Abel, P.A. Smith, J.F. Watts, J. Adhes. Sci. Technol. **23**, 689 (2009)

Part IV
Thermal Control

Chapter 34
Heating Samples

34.1 Electronic Temperature Programmer—Metal Crystals

The accurate and reproducible programming of the temperature of metal single crystals is used for studies of temperature-programmed desorption (see Chap. 25, p. 273) as well as in many other applications. A review of the literature in this area to 1984 may be found in [1].

Figure 34.1a shows a block diagram of a temperature programmer design that has been thoroughly tested in many applications [1]. An input signal from the thermocouple, welded to a metal crystal, is fed into a thermocouple amplifier [2]. The input amplifier adds gain and offset to this signal, and delivers a 0 to +10 V signal to the process controller. The thermocouple amplifier protects the single crystal from being destroyed in the case of an open thermocouple circuit, which drives the output of the amplifier to a high positive level. An electronic thermocouple reference junction eliminates the need for an external reference and is routinely checked against a reference junction maintained at 77.3 or 273.2 K and connected temporarily to the input for calibration.

The ramp generator is programmed by the laboratory worker, as shown schematically in Fig. 34.1a. A more detailed block diagram of the ramp generator is shown in Fig. 34.1b. A fixed frequency oscillator drives the divider circuit that feeds a 12-bit binary counter. The 12-bit binary word is the input to a digital-to-analog converter, which with scaling and offset, delivers a 1–5-V signal to the process controller set point. The start point input presets the counter to a binary count specified by the operator. The end point input determines the temperature at which the ramp stops and holds constant temperature.

The power driver delivers up to 50 A with a burden voltage of 4 V. In addition, the crystal may be isolated and a DC voltage may be applied. A commercial 5-V DC supply was used, with a current regulator added to the output with appropriate

© Springer International Publishing Switzerland 2015

J.T. Yates Jr., *Experimental Innovations in Surface Science*,
DOI 10.1007/978-3-319-17668-0_34

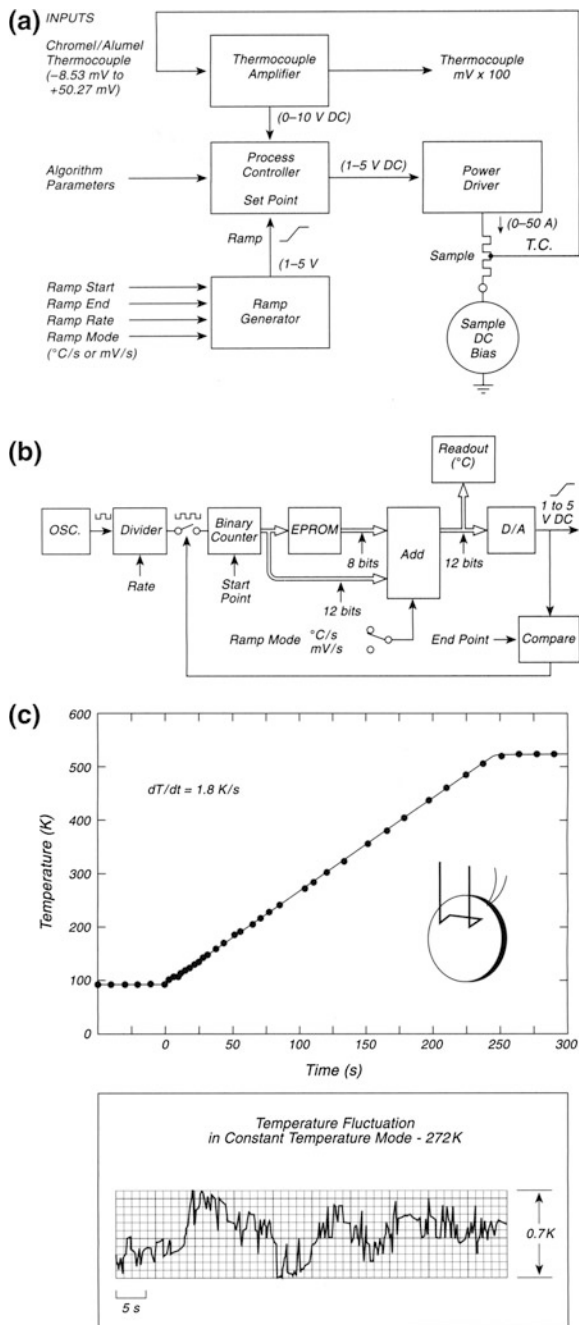

Fig. 34.1 Electronic temperature programmer—metal crystals. **a** Block diagram—temperature programmer. **b** Block diagram of ramp generator. **c** Performance of programmer

scaling and isolation to permit the process controller to control the power output. An input of 1–5-V DC produces a 0–50-A DC output.

The process controller [3] (Fig. 34.1a), was selected as the primary control device for the following reasons: (1) the ability to program the readouts in arbitrary units; (2) accuracy (±0.05 %, full scale); (3) speed (updates 3 times/s); (4) digital input of tuning parameters.

An illustration of the performance of the programmer is shown in Fig. 34.1c. The programmer tuning constants were adjusted to produce the linear temperature versus time performance from about 95–520 K as shown. The temperature stability at 272 K is shown, where fluctuations of only ±0.35 K were observed. Scan rates from about 2–8 K/s may be programmed into the controller.

In order to achieve optimum performance, appropriate values of the process controller constants (gain, rate, and integral time) need to be established. These three control constants are dependent on sample properties such as mass and resistivity and on the sample-mounting configuration. Initially the rate and integral time can be set to zero while an optimum gain is being established. An optimum gain value is one which minimizes oscillations in the sample temperature, both during the heating ramp and while the crystal is being maintained at constant temperature, and the optimum gain may differ slightly for the two operating conditions. It is also necessary to optimize the gain such that the difference between the ramp voltage and the measured thermocouple voltage is minimized during the heating ramp. The other control constants can then be adjusted to fine tune the operation of the controller. Tuning of the integral time is essential, particularly when trying to avoid an overshoot at the end of temperature ramp.

Another electronic controller, designed to correspond to the system's thermal response and capable of programming at 20 K/s without overshoot, has been described [4].

34.2 Temperature Programming of Metal and Semiconductor Crystals

Almost all of the studies of adsorption, desorption, and reactivity at surfaces involve control of the temperature of the surface as well as control of temperature programming. A traditional solution involves specialized controlling units, one of which is mentioned on p. 349. These controllers provide a technically simple but rigid solution for the temperature control. An alternative solution employs an acquisition board in a personal computer controlled by a program written in any programming language. This method provides great flexibility and can be used for any type of temperature sensor and any desired temperature program. A graphical programming language, LabVIEW [5], is especially appropriate for these tasks. It has a powerful graphical interface, a large library of subroutines for data acquisition, and a variety of mathematical operations. An example of a virtual instrument created by LabVIEW for temperature measurement and control of a silicon crystal is described below.

Figure 34.2a shows a block diagram of the measurement setup for a silicon crystal having a room temperature resistivity up to 100 Ω cm. The crystal temperature is measured by a thermocouple that has a known relationship to the true temperature (measured by pyrometer) as a function of temperature. A cold junction compensator [6] is used to establish, electronically, a reference voltage corresponding to the ice temperature, 273.2 K. The signal is fed to a separating amplifier and amplified by 50–100 times, which minimizes the noise level received at the acquisition board. A second purpose of the separating amplifier is the rejection of the DC offset caused by the potential applied to the crystal for heating. The acquisition board can only handle 10–20 V offsets, which would be normal for metal crystals because of their higher conductivity compared to a semiconductor crystal. The signal from the separating amplifier is fed to the acquisition board [7], which has an analog input/output with a maximum input and output voltage of 10 V. Two DC power supplies are needed, one to power the separating amplifier (±5 V) and a heating supply (60 W, 120 V, and a maximum current of 50 A).

Figure 34.2b shows a block diagram of the LabVIEW controlling program that controls the heating power supply according to a predetermined program. A sample of a complex heating/cooling program and the result is shown in Fig. 34.2c. This program provides the desired heating ramp from −200 up to 850 °C, and then cooling by various ramp functions, as shown on the front panel readout in Fig. 34.2c. The lower right-hand side of the front panel readout shows the actual program achieved compared to that desired.

Figure 34.2d shows a detailed view of the linearity of the heating ramp and the error that was measured. Here, P = 3 K/s, the linear ramp function. The lower difference plot shows the accuracy of this particular ramp and all of the data points fell in a 1.5 K noise range up to about 1000 K, where the mechanical contact (see p. 356) between the thermocouple and the Si crystal began to fail.

The ability to control the isothermal temperature of the crystal for long periods of time is also excellent, with better than 1 K temperature constancy and error spread. There is often an initial overshoot of the order of several K as one ramps up to a desired temperature, and this can be minimized by adjusting the proportional integrating differentiating (PID) parameters in the program, Fig. 34.2b.

The advantages of the LabVIEW approach to temperature programming are listed below:

1. Flexibility—the temperature profile can be changed as desired and nonlinear programs are possible. Any type of temperature sensor with a non-linear output can be used (see p. 405). Any type of correction for errors, such as the error in a thermocouple because of inefficient thermal contact (see p. 356), can be made.
2. High speed.
3. Universal interface—the acquisition board with multiple inputs and outputs coupled to the LabVIEW program, can be used for computer control of other instruments (e.g., a mass spectrometer). However, the interface cannot be used at the same time with another acquisition board driven by a program working in DOS.
4. Convenient graphical programming with a large library of subroutines.

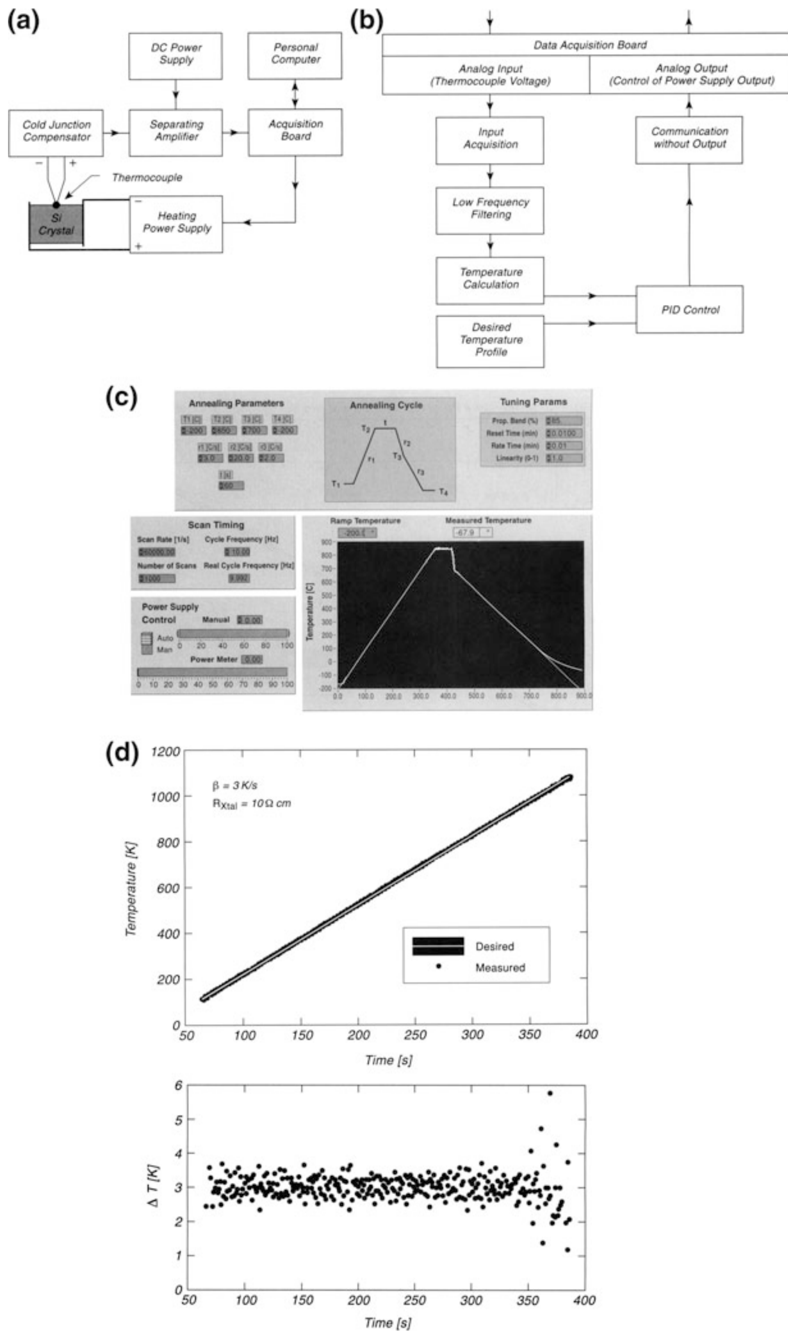

Fig. 34.2 Temperature programming of metal and semiconductor crystals. **a** Block diagram—resistive heating control. **b** Block diagram—LabVIEW controller logic. **c** Control parameters for temperature program. **d** Linearity and error in heating ramp

34.3 Mounting Nonweldable Crystals for Resistive Heating and Cooling

Crystals such as Ag, Al, Au, and Cu possess very high thermal conductivity and cannot easily be spot-welded to other metals because of the lack of melting at the low temperatures achieved at the junction during welding. The mounting of such crystals to heating/cooling wires requires a special method that will provide good mechanical, thermal, and electrical contact over many cycles of heating and cooling, and a design for this is shown in Fig. 34.3.

The crystal holder is fabricated out of OFHC copper, sapphire, and tungsten. These materials all possess optimum thermal conductivity properties below 100 K.

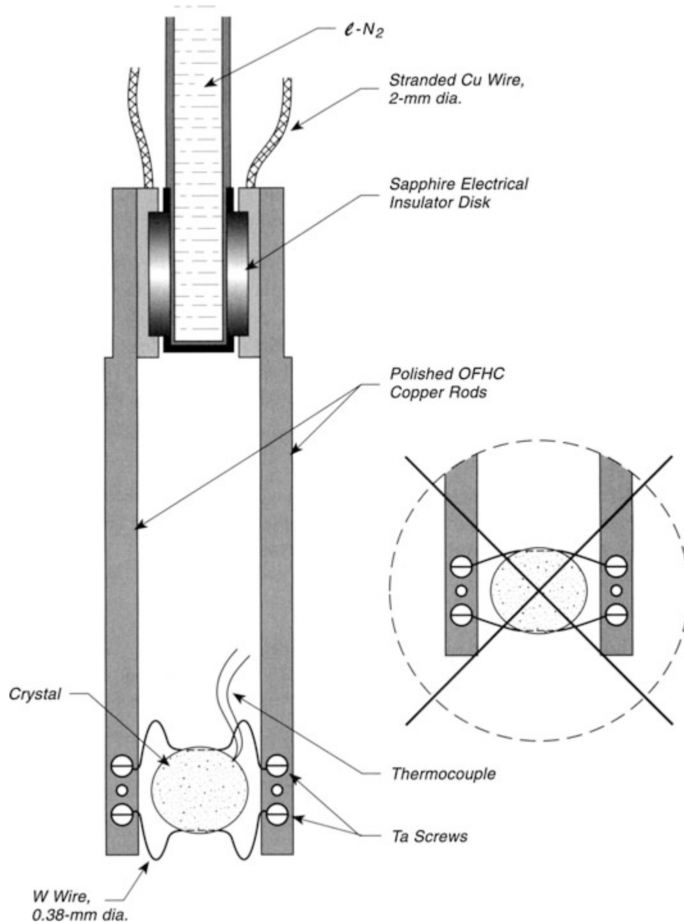

Fig. 34.3 Mounting nonweldable crystals for resistive heating and cooling

Figure 34.3 shows a scheme to mount such crystals. A slot is carefully cut into two opposite edges of the crystal. The slot makes a tight sliding fit for the tungsten wire heating lead, and the crystal should not be distorted to make this fit.

The tungsten heating/cooling leads are fabricated with a pair of U-loops that remove the effects of linear expansion that otherwise would push the wire from the slot. Thus, the crystal, incorrectly mounted as shown in the right-hand insert, is subject to variation in the cooling and electrical contact as the wire is heated and cooled owing to bowing of the wire in the slot. The looped wires on the other hand undergo thermal expansion effects which are almost counterbalanced on either arm of the U-loops.

Make the assembly as follows using gloved fingers:

1. Mount the preshaped W wire (0.38-mm diameter) on the lower set of Ta screws and tighten.
2. Fix the preshaped upper W wire on the right hand screw and do not tighten the screw.
3. Fix the crystal with its thermocouple (hole-mounted—details not shown) on the lower wire.
4. Rotate the upper wire counter clockwise until it fits into the slot and then tighten both screws carefully.

This mounting procedure produces a stable junction over many cycles that permits cooling of the crystal to about 32 K when liquid He is used in the reservoir intended for liquid nitrogen [8].

34.4 Strain-Free Single Crystal Mounting Azimuthal Motion

In certain applications, single crystals must be mounted in such a manner that during heating and cooling they are free from strain owing to expansion and contraction effects in the metal to which they are welded. This is particularly true in atom scattering experiments, where tilting of the crystal can cause significant problems.

The design shown in Fig. 34.4 eliminates this problem by allowing the conduction leads welded to the crystal to freely expand and contract [9]. This is facilitated by having one end of each lead free to slide. The square cross-section Ir rods (0.7×0.7 mm^2) are welded to Ta pads on the right-hand side, but are free to slide inside of sapphire bearing supports on the other end. The sapphire support bearings are held in place by Ta foils welded to the Ta support plates. Ta conductor leads (about 30-A capacity) are connected in pairs to the Ta support plates on the left, and current passes through these and the support plates to the Ir rods and thence through the crystal.

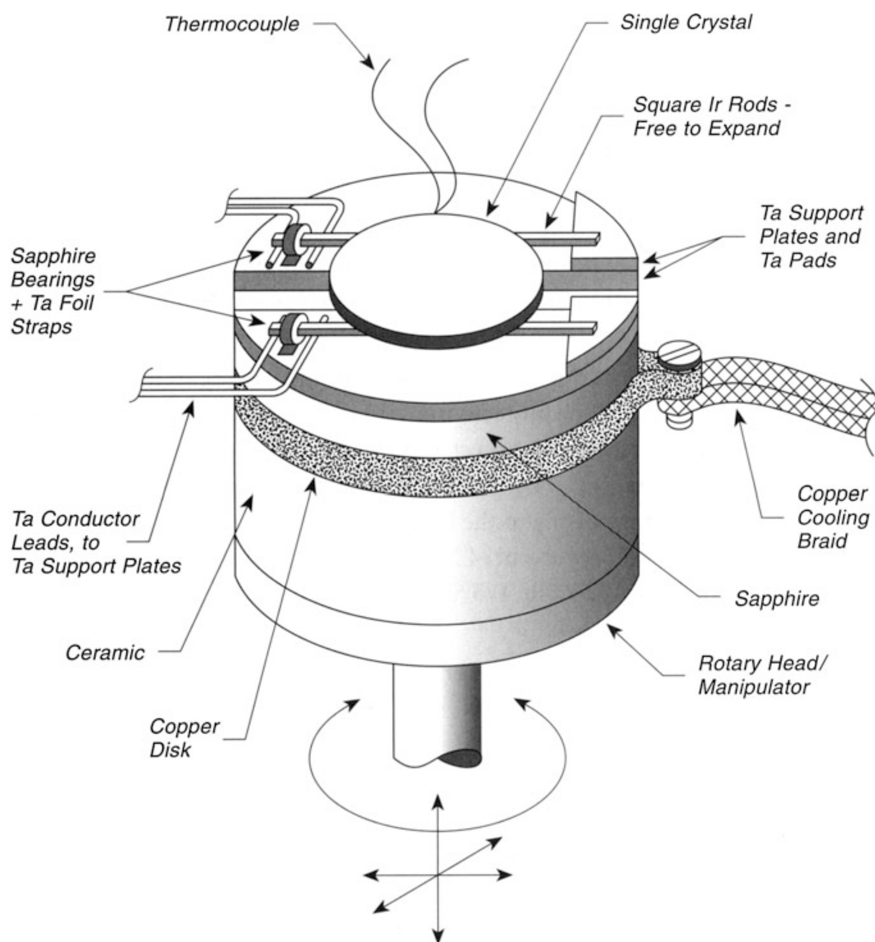

Fig. 34.4 Strain free single crystal mounting—azimuthal motion

With a Ru crystal, temperatures above 1600 K may be reached, and cooling to 95 or 50 K was achieved using liquid nitrogen or liquid helium, respectively. The Ru crystal was spot welded to the square Ir rods through a Ta sandwich foil.

34.5 Heating Silicon Crystals and Temperature Measurements

One of the most difficult tasks in the laboratory is uniformly heating silicon single crystals by resistive heating and measuring the temperature of the crystal. A variety of methods of making electrical contact to silicon crystals have been devised that

involve attachment to metal springs [10, 11] or elastic metal sheets [12, 13]. These contact methods often result in the formation of hot spots at certain regions of contact and can lead to nonuniform heating. Ta and Mo are used in these applications, since other metals can lead to metal contamination of the silicon crystal, either through metal diffusion through the bulk (Ni; Fe) or by transport by vaporization.

The attachment of thermocouples is also a difficult task owing to metal diffusion or metal vaporization. Here, too, Ta-protective envelopes must be used, as in the design of Bozack et al. [13], which employed Ta-protected W26 %Re/W5 %Re thermocouples inserted into slots cut into the crystal edge [13]. We have found that chromel-alumel (type K) thermocouples are unsatisfactory owing to the high vapor pressure of Ni (10^{-5}–10^{-4} Torr at 1450–1500 K) [14]. A few atomic percent of Ni produces, on Si(100), the well-known split-off dimer defects [15]. Thus, W26 % Re/W5 %Re thermocouples, shielded by Ta, have been used successfully in our own work.

Adhesive thermocouple contacts, such as zirconia-based Ultratem (Aremco), have been found to diffuse through Si above 1100 K. A Ta thermocouple tab contact, joined by a layer of Ge that alloys with both Ta and Si was proposed [11], but adhesion was lost on heating to high temperatures [16].

Figure 34.5a shows a design [17] that addresses the clamping of Si crystals to provide rather uniform electrical contact and temperature distribution. A Ta sheet ($20 \times 9 \times 0.125$ mm^3) is bent as shown in the diagram to form a bracket shape, which is then welded to a W rod (2-mm dia.), using a copper plate as an alignment jig, producing the structure shown in Fig. 34.5a(d). Four slips of Si wafer material are prepared ($4.5 \times 8.5 \times 0.4$ mm^3) and used to sandwich a Si wafer slice ($23 \times 8 \times 0.4$ mm^3) as shown in Fig. 34.5a(e). The entire sandwich structure is compressed by a flat U-shaped Ta spring that is wedged into the slot between the top Si slip and the top of the bracket, Fig. 34.5a(f). The fully assembled mounting is shown in Fig. 34.5a(g).

Figure 34.5b shows a method for attaching a W26 %Re/W5 %Re thermocouple (0.08-mm dia.) to the crystal by a U-shaped clip design [17]. To prevent direct contact of the ther-mocouple material to the crystal, it is shielded with a Ta tube (0.19-mm inner dia., 0.06-mm wall thickness, 5-mm length). The prewelded thermocouple is inserted into the Ta tube at the end, which has been previously cut off at an angle [Fig. 34.5b(a, b)], and the tube is flattened [Fig. 34.5b(b)], and formed into a bracket shape that tightly clips over the crystal edge [Fig. 34.5b(c)]. The thermocouple exits from the angled end and is bent upward as shown in Fig. 34.5b (c). The thermocouple voltage is converted to temperature using a calibration method similar to that of Smentkowski et al. [18], as discussed on p. 405. A cold junction compensator is used for the reference junction at 273 K.

Two designs for thermocouple attachment to Si crystals have been compared using a calibrated optical pyrometer. Figure 34.5c shows the two designs where the slotted crystal design from Bozack et al. [13] and the design shown here [17] are compared. The deviation for the slotted design is from 50 to 150 K, whereas the deviation of the U-shaped clip design is from 50 to 90 K over the same temperature range.

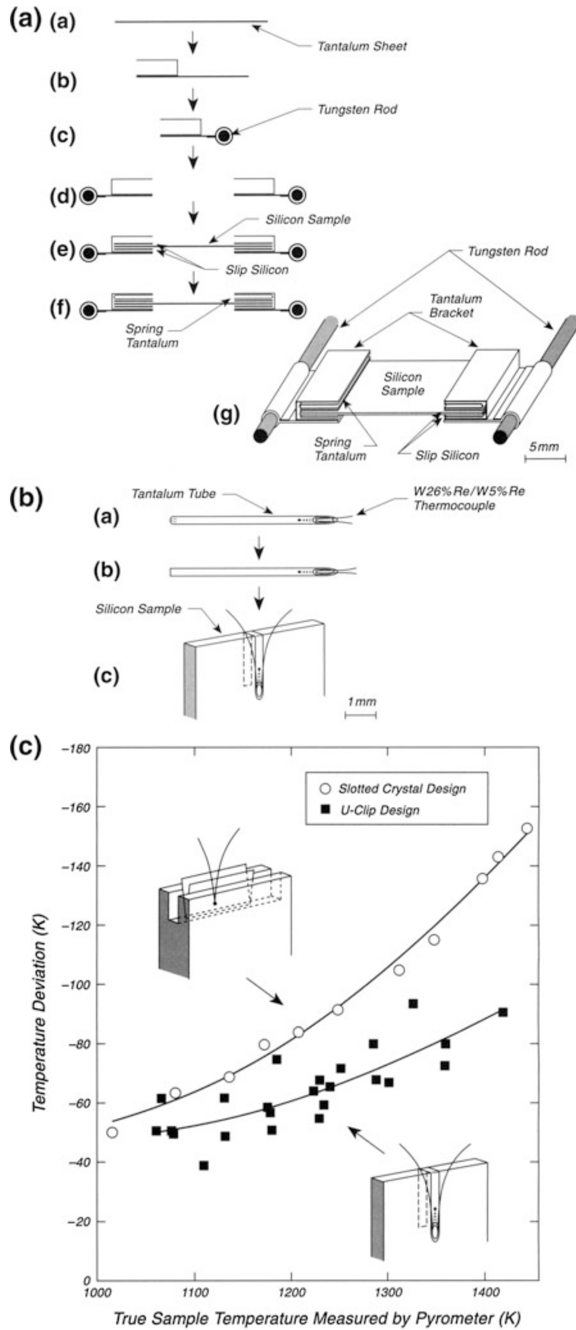

Fig. 34.5 Heating silicon crystals and temperature measurements. **a** Mounting design—Si sample. **b** Thermocouple attachment. **c** Temperature deviations—two thermocouple attachment methods

The uniformity of heating of the Si crystal with this mounting design is found to be ±15 K at 1400 K, as measured by an optical pyrometer. At temperatures above about 1100 K, temperature oscillations are sometimes observed with the U-shaped clip thermocouple.

Great care must be exercised in making the mount and the thermocouple clip. All Ta parts must be boiled in concentrated HCl solution to remove Ni contaminants [15]. All tools should be made of plastic to avoid metal contamination, and fabrication should be done under clean conditions without contact to metals other than cleaned Ta. In addition, Mo parts, which are more springy, may be substituted for Ta parts, although the HCl cleaning procedure followed by STM studies has not been done for crystals with Mo/Si contacts, as has been done for W/Ta contacts [15].

The use of interferometry for measuring the temperature changes in semiconductor crystals has been reported [19]. Here, both temperature dependent changes in the refractive index and in the thickness of the crystal wafer cause the optical path in the wafer to change in comparison to $\lambda/2n$, where λ = the laser radiation wavelength, and n = the refractive index. Temperature changes as small as 0.2 K have been detected, but one must start at some known temperature in order to make temperature measurements at other temperatures.

34.6 Avoiding Extraneous Electrical Effects Owing to Heating Crystals

Single crystals of metals may be heated in several ways for studies at constant temperatures. Unfortunately the presence of large AC or DC currents used for heating and the concomitant presence of stray electric and magnetic fields will be a severe disturbance to measurements involving electron currents to or from the crystal. A general method used to avoid this problem involves pulsing the heating current and making current measurements from the crystal during the time when the heating pulse is off.

Figure 34.6a shows a typical mounting for a metal single crystal on a manipulator using ohmic heating for the crystal. Large-diameter (1.0–1.5 mm) tungsten support leads are connected to current and cooling leads on the manipulator and conduct current to a pair of tungsten wires (0.3-mm diameter) welded to the back of the crystal. Tungsten is preferred to tantalum because of its higher coefficient of thermal conductivity at low temperatures. In this configuration the crystal is heated by thermal conduction from the hot wires rather than by ohmic heating of the crystal itself, and at incandescence, it will be seen that the parallel wires are comparatively bright in the region between the crystal and the support leads. The uniformity of welding to the crystal and the support leads can be judged by the relative brightness of the four intermediate regions. Poor welds will yield higher brightness and will possibly cause premature burnout. The thermocouple welded to the crystal edge is used to measure the crystal temperature.

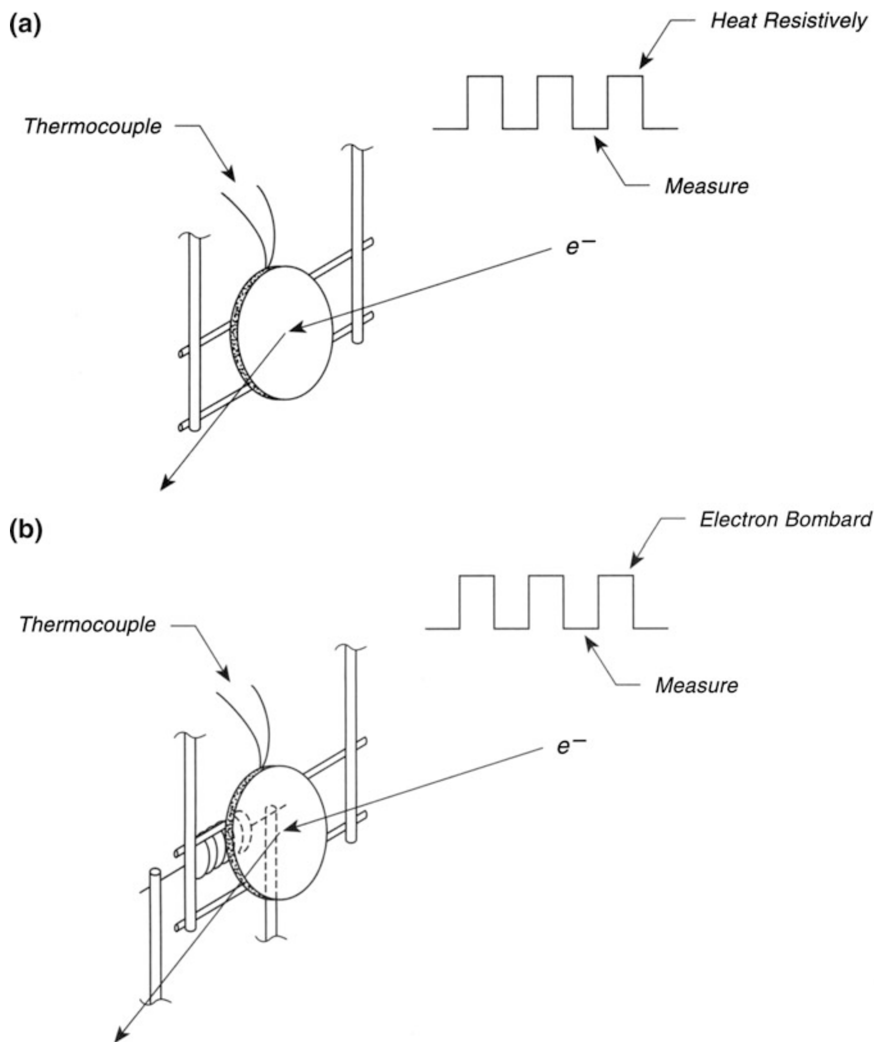

Fig. 34.6 Avoiding extraneous electrical effects owing to heating crystals. **a**. Interrupted ohmic heating. **b** Interrupted electron bombardment heating

Figure 34.6b shows a typical arrangement for heating by electron bombardment. The tungsten coil emitter located about 3–5 mm behind the crystal is kept at ground potential, and the crystal is biased positively (several hundred volts to 2 kV) (see p. 361). Thermionically emitted electrons are used for heating the crystal and any crystal can easily be melted accidentally with this method. In addition to electron bombardment heating, it is also possible to use radiation heating to achieve crystal temperatures approaching 1000 K. The upper temperature limits for radiation

heating depend upon the magnitude of the heat leakage to the support wires through the thinner wires welded to the crystal.

Three circuits for interrupted heating of single crystals have been reported in the literature [20–22]. For ohmic heating, at 1000 K, the temperature controller [20] required a duty cycle of 2/3. The switching rate was approximately 0.3 Hz, and the temperature regulation was ±15 K. Better control would be possible at higher switching rates [20]. For electron bombardment heating, a second circuit has been published in which a mechanical relay is used [21]. Here, bounce within the relay limits the time period for data acquisition to about 40 ms at 10 Hz. It is necessary to switch both the filament heater current and the bias voltage and since the power supplies are slow to recover from the switching, dummy loads are used in the off cycle. A difficulty reported for switching large currents and high voltages is that transients are produced that disturb electronic measuring equipment being used. Proper shielding of the elements of the circuit and the use of shielded cables eliminates these effects. A third circuit, which has shown favorable utilization in conjunction with LEED, Auger, and HREELS measurements is reported in [22].

The circuits shown in [20, 22] employ older electronic components, and the user should consult with an electronic specialist for designing similar circuits using modern components.

34.7 Electron Bombardment Crystal Heating

Electron bombardment heating of a metal crystal can often be used to bring the crystal to higher temperature than can be done conveniently by ohmic heating. Thus, for the highly refractory metals such as W, Ta, Mo, and Re, all of which require very high temperatures to remove impurities, electron bombardment is often used (see also p. 363.)

A typical design for electron bombardment heating, adapted from [23], is shown in Fig. 34.7. The crystal is supported on a manipulator by one or more welded wires that connect to a stub on the end of the manipulator. This stub is electrically isolated from the manipulator shaft by a high-voltage ceramic spacer that will work at positive bias potentials of several kilovolts. The high-voltage connection to the stub is provided by a well-insulated wire that passes through a ceramic sheath, and this sheathed wire is firmly attached to the manipulator shaft by means of a ceramic support designed to hold it tightly, and in isolation from the rotary manipulator shaft or any other grounded parts.

The very simple electron bombardment gun is made of a stainless steel tube with an aperture cap placed over the open end, and a custom made ceramic base to hold the heavy filament leads. Filament current is supplied through copper braid that is connected to the ceramic support, and thence to flexible power leads that connect to feedthroughs on the manipulator flange. The electron gun is mechanically connected to the ceramic support by a rod, as shown.

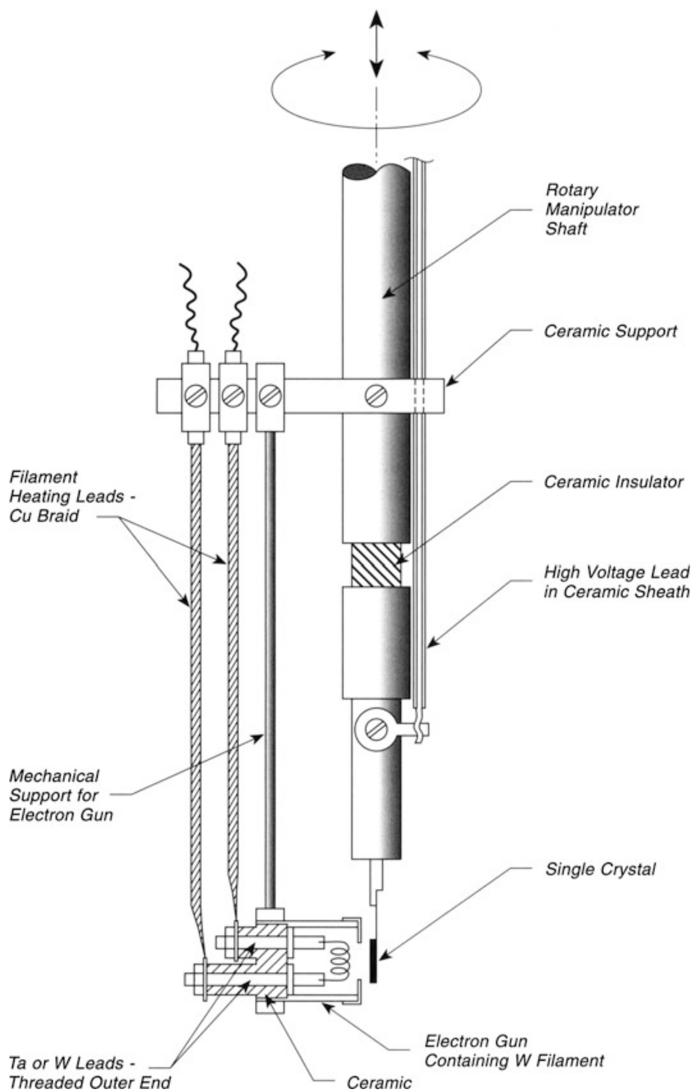

Fig. 34.7 Electron bombardment crystal heating

The filament for the electron gun can be made of pure W wire, or thoriated W wire (see p. 133). Emission currents of 10–50 mA with a positive bias of 1 kV on the crystal will supply 10–50 W, usually enough for heating to the desired temperature, depending on the thermal conductivity of the welded leads to the crystal and the radiation loss at the desired crystal temperature. For gentle heating, only radiation heating from the filament can be used, and in this case a non-thoriated W filament would be preferable. While the winding of W filaments is easily done,

professionally wound filaments of uniform shape may be purchased [24]. A very compact and tightly wound W filament can be obtained from a slide projector quartz-halogen lamp, and the quartz envelope can be cut off by a glassblower, leaving an accurately mounted W filament attached to the quartz base. The filament should not be removed from the lamp base as it will be difficult to reweld it to the leads without strain and subsequent distortion upon heating.

It is emphasized that the coiled W filament (typically wire diameter = 0.2 or 0.3 mm) should be welded to its supporting leads under conditions where there is no strain left in the coil after the second weld. Strain will result in extreme filament distortion upon heating to incandescence.

The temperature of the crystal can be measured with an optical pyrometer for adjustment (see p. 409). However, usually a thermocouple is employed for this, and one must remember that the thermocouple will also be biased at kilovolts when the crystal bias is on. Since these voltages are lethal, proper care must be taken in the insulation of the thermocouple leads, and in the isolation of the readout device connected to these leads.

One might consider reversing the bias and making the electron gun operate at a negative bias of a kilovolt or so, and grounding the crystal. This is not advised, since then electron bombardment will occur broadly to all regions at ground potential in the vicinity of the crystal, resulting in excessive outgassing and damage to devices and screens.

Even simplier electron guns may be constructed, the simplest being just an emitter filament supported a few mm from the back of the crystal.

34.8 Indirect Sample Heating

The use of indirect heating of samples is especially important for materials that are nonconductive and therefore cannot be heated by ohmic heating. However, indirect heating of conductor materials is also a favored method of heating, since excellent control of temperature can be achieved by indirect heating methods. Both heating by radiation and heating by electron bombardment are termed indirect heating, since neither method depends on the electrical resistance of the sample, as does direct ohmic heating.

Figure 34.8a shows a typical method for indirectly heating a sample using a button heater [25] that is supplied commercially [26]. The sample is held onto the top surface of the Mo cylindrical shell that surrounds the W heater wire. The W heater is immersed (potted) in an aluminum oxide powder. In the case shown here, the sample is held in place by means of a Mo sleeve that fits snugly over the Mo cylinder and has a lip that grips the front surface of the sample. This arrangement may be used up to about 1500 K without damage to the heater assembly. Since the heater wire is noninductively wound, electron spectroscopic measurements may be made with heating power on [25].

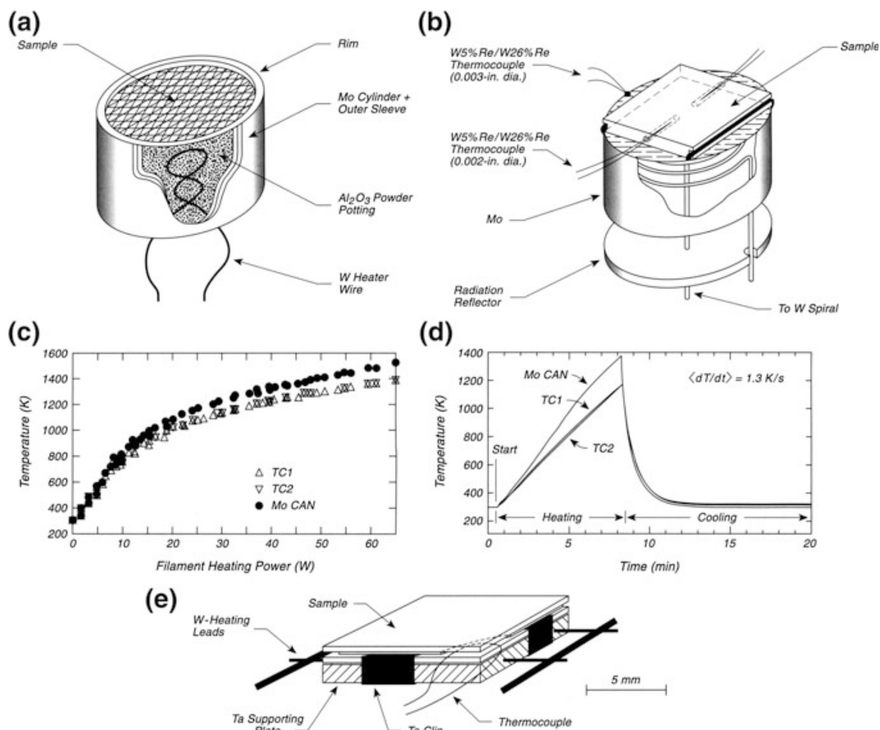

Fig. 34.8 Indirect sample heating. **a** Conduction heating (T ≤ 1500 K). **b** Radiation and e-bombardment heating (T ≥ 1500 K). **c** Static heating—config. B **d** Programmed heating and cooling—config. B. **e** Ohmic support heating

Figure 34.8b shows another arrangement that maybe used at temperatures above 1500 K, but which also is useful at lower temperatures [27]. A Mo cylindrical can is polished flat on its top surface, and the sample is placed in contact with the upper surface. In the case shown here, a single crystal of diamond is held by two tungsten or tungsten alloy wires by means of parallel slots in two opposing edges. The wires are spot-welded to the edges of the can and tightly bind the diamond to the polished top of the can. Inside the can is a flat W pancake spiral made by winding a W wire onto a mandrel into a watch spring configuration as a tight coil. No aluminum oxide potting powder is present, so that the Mo can is heated only by radiation from the W spiral, or by radiation plus electron bombardment if more power is needed. A reflective radiation shield behind the Mo can assists in increasing the efficiency of heating the Mo support by the incandescent filament. A more complex electron bombardment heating device involving a shielded thermionic emitter has been reported [28].

The performance of the heating assembly in Fig. 34.8b has been measured for a diamond single crystal [27], and the results are shown in Fig. 34.8c, d. In Fig. 34.8c the temperatures of two thermocouples, buried in laser-drilled holes in the edge of

the diamond crystal, are shown for static heating experiments, where the assembly is brought to steady temperature in ultrahigh vacuum. The two thermocouples differ by only 8 K in these experiments, indicating that the true temperature of the diamond is being measured. However, at a diamond temperature of 1400 K, the difference between the Mo support temperature and the diamond temperature amounts to 140 K. This difference decreases at lower temperatures. Since diamond is an excellent thermal conductor, it is likely that heat transfer from the Mo surface to the diamond back surface is the limiting factor in these experiments. Similar temperature differences between the temperature of a heated supporting surface and a contacting sample have been measured by others at about 10^{-3} Torr pressure. The sample was contacted to the supporting surface using a silver paint that worked up to 1073 K, where a 22 K temperature difference was measured [29].

Figure 34.8d shows the difference between the heating behavior of the diamond crystal and the Mo support can under conditions of temperature programming at a rate of 1.3 K/s. At a diamond temperature of 1150 K, a difference of temperature between the Mo support and the diamond of 225 K was noted (compared to only 90 K under static conditions as shown in Fig. 34.8c). The Mo can cools faster than the diamond when the heating is interrupted, as would be expected for cooling controlled by thermal conduction from the assembly.

The maximum filament heating power used to heat the diamond may be reduced by employing a mixture of radiation heating combined with electron bombardment heating. Thus, for example, a positive bias of 250 V produces thermionic heating of 12 W at a diamond temperature of 1273 K, whereas 47 W of filament heating power was needed under conditions of zero bias to achieve the same temperature.

A successful variation of this method, involving ohmic heating of the support assembly [29] is shown in Fig. 34.8e. Here, a polished Ta block of the same size as a TiO_2 single crystal is heated by means of W wires which pass through the body of the Ta. The temperature of the crystal is measured with an embedded thermocouple cemented [30–32] into a diagonal slot in the crystal corner, and programming of the heating power is controlled by this thermocouple which acts to supply a feedback signal. Somewhat similar methods for heating and cooling alkali halide crystals, and using an In metal film as a heat transfer medium have been reported [33].

34.9 Indirect Heating of Compound Semiconductors

A variety of indirect heating methods for semiconductors which cannot be heated by electrical conduction have been discussed on p. 363. GaAs is a special material because of its fragile mechanical properties and because many samples are of the incorrect conductivity for direct resistive heating (see p. 327). The method shown here is especially good for this type of material [34].

As shown in Fig. 34.9 the GaAs crystal is bonded to a sapphire plate using an indium film bond. The sapphire plate is coated on its back with a thin Ta film that is

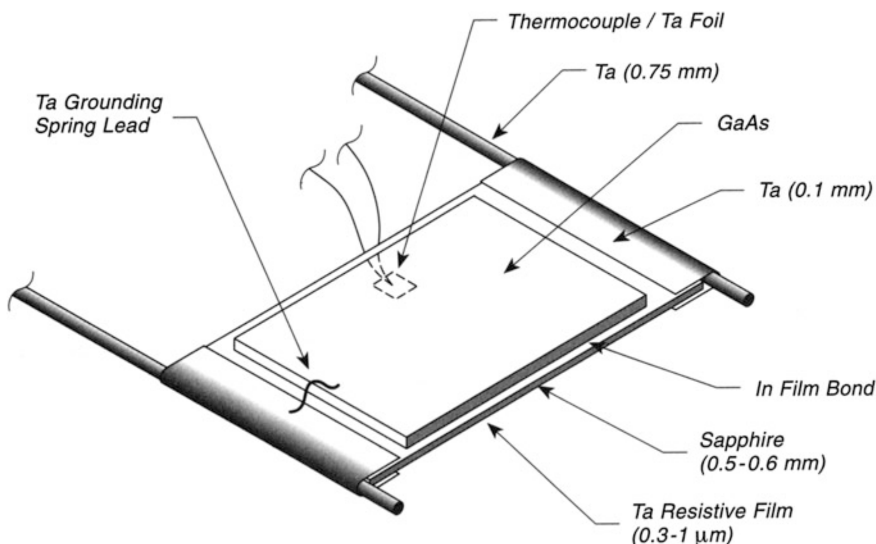

Fig. 34.9 GaAs—mounting for indirect heating

used for resistive heating. A thermocouple is attached to the Ta film for the measurement of the temperature.

The indium film is applied conservatively so as to not cause a short circuit between the Ta clip leads that support the sapphire plate on 0.75-mm Ta support leads. The indium film application may be easily done by using the Ta film resistor to raise the sapphire temperature above the melting point of In (157 °C). The Ta resistor film requires 1.5–2 A at 8–10 V to heat the unit to about 900 K. The GaAs sample is grounded by using a Ta spring contact that is welded to a Ta clip.

The disadvantages of this technique are that the In reacts slowly with GaAs, causing failure after long heating. This effect can be minimized by using only small amount of In. In addition, at high temperatures, the In has a significant vapor pressure (10^{-7} Torr at 833 K; 10^{-6} Torr at 895 K).

34.10 Heating Design—Insulator Crystals

A mounting design for electrically nonconducting crystals must provide a method for uniformly heating the crystal. When ohmic heating is to be used, various methods of placing the crystal on a heatable metal substrate have been described in other sections.

A method for making intimate contact between an insulator crystal and a metal [35] is shown in Fig. 34.10. The method involves first making a sputtered film of the metal on the back of the crystal, as shown in Fig. 34.10a. In the case of a MgO

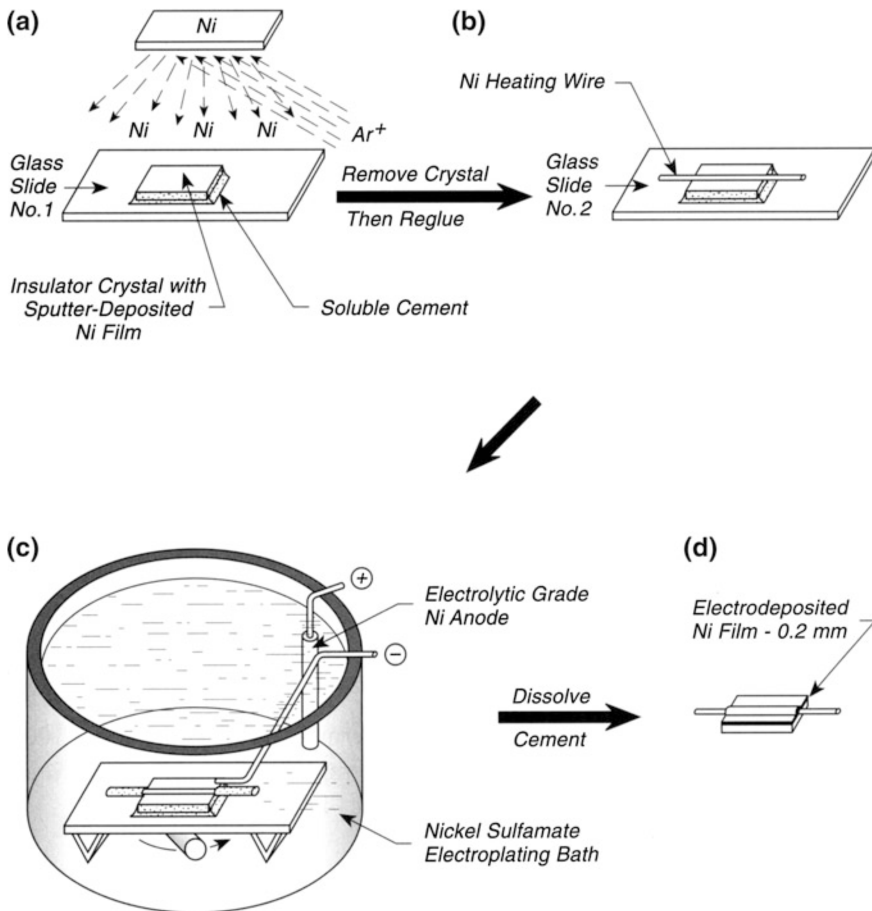

Fig. 34.10 Heating design—insulator crystals

crystal described here, about 1 μm of Ni was sputter deposited in a period of 30 min. This film provides an intimate contact to the back of the crystal while permitting the electrodeposition of a thicker metal film. Figure 34.10b shows the crystal with the sputter-deposited Ni film and with a Ni heating wire lying across the back. This assembly is placed into a vessel (Fig. 34.10c), and a thick coating of Ni is electrodeposited, making good contact with the underlying sputter-deposited Ni film as well as holding the heating wire in place. Between steps A and B, the cement used is removed and the crystal is placed on a new glass slide (No. 2) to remove the extraneous Ni film deposited on slide No. 1, which would also be electroplated.

The cement used in this procedure to mask the crystal edges is a commercial UHV leak sealer, Vacseal [36], and is acetone soluble. It is important to electroplate the thick Ni film without stress, and special procedures for doing this must be

followed. A nickel sulfamate plating solution (1 L volume) was employed containing nickel sulfamate (600 g/L), nickel bromide (45 g/L), boric acid (2 g/L), saccharin (0.5 g/L), and a surfactant X-100 (2 drops). The bath temperature is 40 °C, and its pH is 4.0 ± 0.1, which can be adjusted using sodium hydroxide solution. The approximate current density is 3.4 A/dm^2. The use of six to eight electrolytic grade Ni anodes [37] is important, only one of which is shown in Fig. 34.10c. Before use the electrolytic bath should be treated with 30 g of activated charcoal, filtered, and then plated onto a dummy anode for 2 h. Deposition rates on the back of the insulator crystal are typically 50 μm/h. The bath should be stirred with a magnetic stirring bar and final attachment of the Ni heating wire takes place as shown in Fig. 34.10d. To check on the stress in the Ni film being deposited, a thin strip of Cu ($1 \times 10 \times 0.05\ cm^3$) is used to receive the Ni film as a test. After plating for 30 min, the test strip should bend 1.5–2 mm toward the copper backside after the protective coating of lacquer is removed, indicating that the Ni film adheres well and is under slight compressive stress. The thermal expansion coefficient of the Ni, $13.3 \times 10^{-6}\ K^{-1}$, should match that of the crystal, as in the case of MgO ($13.5 \times 10^{-6}\ K^{-1}$). For a MgO crystal the Ni film could be cycled in vacuum many times to 1073 K without failure.

34.11 Cement Mounting—Semiconductor Crystals

A number of methods for mounting semiconductor crystals in ways where they can be electrically heated and cooled are discussed throughout this chapter beginning on p. 349. In the case of crystals which cannot be heated by electrical conduction, either because of unfavorable conductivity or because of unfavorable shape, it is possible to use a refractory cement that holds the crystal to a tungsten disk that is heated through welded contacts to refractory metal heating wires [38, 39].

In Fig. 34.11, an irregularly shaped SiC crystal has been cemented to a W disk using Aremco Ultratem 516 cement, which has a ZrO_2 base [40]. The W disk has previously been welded to a pair of Ta heating wires that pass current from the heavy W (1.5-mm-diameter) support leads. The cement is made electrically conductive by mixing with the appropriate amount of powdered graphite. This permits the electron spectroscopies to be used without sample charging.

A chromel-alumel thermocouple is connected to the back side of the SiC crystal by means of an alloy solder (90 % Au/10 % Ta) that anchors a tiny Ta tab to the crystal. The connection to the SiC crystal must be done in a preparative vacuum chamber to avoid gross oxidation of the crystal during induction heating.

Measurements with AES and XPS indicate that no migration of the ceramic cement occurs to the front of the SiC crystal up to 1400 K. The cement is adequate for mounting light crystals, but it is by no means robust.

At 1000 K, the temperature indicated by the thermocouple may be about 100 K too high compared to the true SiC temperature. The temperature range from 85 to 1400 K was employed, and minimal outgassing occurs at 1400 K [38].

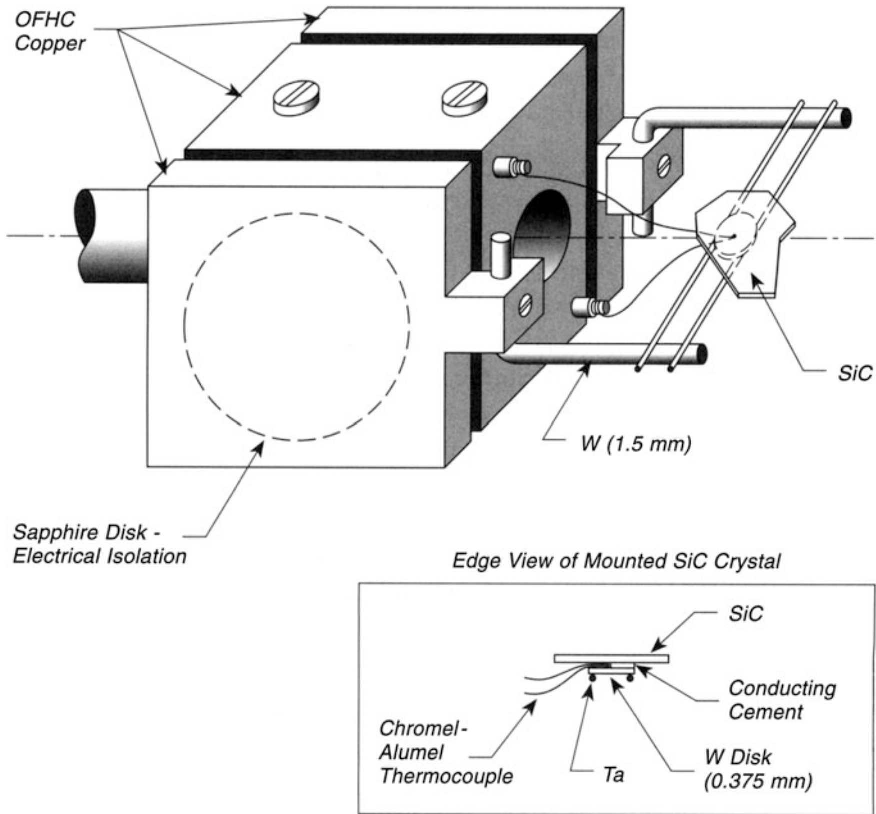

Fig. 34.11 Cement mounting—semiconductor crystals

34.12 Low-Stress Mount for Fragile Semiconductor Crystals

A system for mounting thin semiconductor crystals in an ultrahigh vacuum system for heating and cooling is described [41]. The method avoids stresses on the heated crystals, allowing them to remain flat at high temperatures. The method also allows a thermocouple to be mounted between two semiconductor samples, as shown in Fig. 34.12.

Two L-shaped copper electrical conductor bars are attached to coolable electrical feedthroughs that are in contact with a refrigerated Dewar tube. The Cu conductors are separated and aligned by a Macor spacer. On the front of the L-shaped conductor bars are tapped holes accommodating 0–80 stainless steel machine screws that have had their threads removed under their heads to avoid snagging on the semiconductor wafer samples. Chromel wire springs (0.016-in.-diameter wire, formed around an 0.0625-in.-diameter rod with 38 turns/in.) provide compression

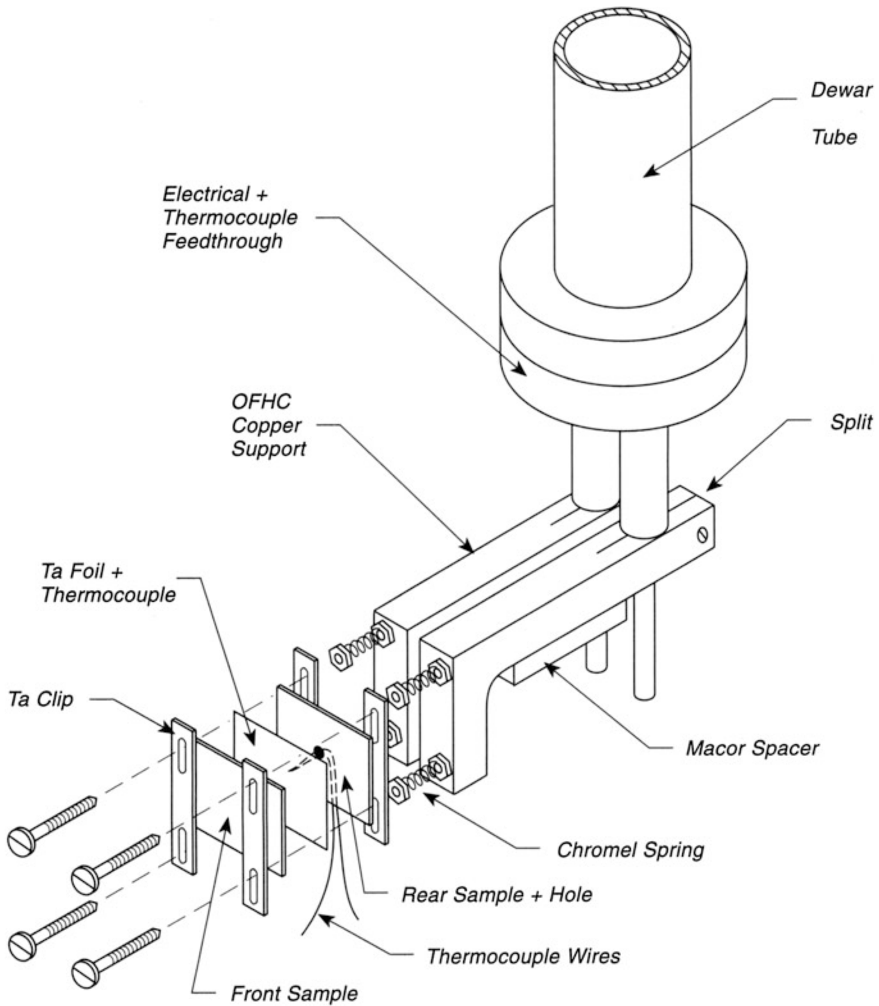

Fig. 34.12 Thin semiconductor crystal mounting—heating and cooling

force in the sandwich structure to be fabricated. A sandwich structure, consisting of two identical semiconductor samples, is placed between Ta clips (which have elongated holes allowing expansion to occur). Thermocouple wires are welded to the 0.005-in.-thick Ta foil that is sandwiched between the semiconductor samples. A hole drilled in the back semiconductor sample allows the thermocouple to extend back to its terminals on the manipulator feedthrough. The entire sandwich structure is compressed by turning and locking the nuts on the stainless steel machine screws. For two 0.014-in.-thick Ge samples, the compression in the chromel springs is typically 0.1 in.

This arrangement heats samples of Ge up to their melting point (1211 K) with virtually no temperature gradient across the samples. The thermocouple readings are within 2 K of pyrometer readings. By cooling the Dewar with liquid nitrogen, temperatures near 200 K are reached. The chromel springs lose their ability to compress the sample when long annealing near 1273 K is carried out.

The reader is warned that the stainless steel and type K thermocouple material used in this configuration is likely not to work for Si, which must be heated to much higher temperatures for cleaning. Both stainless steel and type K alloys will transfer Ni impurities to Si, giving unsatisfactory modifications of the Si surface structure and its surface properties (see p. 548).

34.13 Radiation Heating of Crystals Through Glass Windows

Single crystals may be heated by radiation from hot filaments mounted internally in the ultrahigh vacuum system, and this method possesses the best efficiency of coupling the radiant source (usually a hot W wire) to the crystal. For special cases, however, it may be preferable to employ radiation heating from external tungsten halogen lamp sources, which typically have maximum power limits in the 250–1000-W range. Usually the maximum temperature that can be reached with an external lamp is insufficient for cleaning the crystal and electron bombardment or ohmic heating methods must be employed for initial cleaning.

A very early use of external radiation heating for programming the temperature of semiconductor crystals can be found in the work of Palmberg and Peria [42]. In Fig. 34.13a, their glass ultrahigh vacuum apparatus is shown. A track allows the translation of the crystal, using a magnetic device, from location to location in the linear vacuum system. Shown is a 200-W halogen lamp inside a spherical reflector (silvered glass flask section). Figure 34.13b shows a variation on the design of Fig. 34.13a, where a commercial 750-W lamp (operating at reduced power) is housed in an ellipsoidal reflector, which has reflective aluminum focusing surfaces behind and in front of the lamp [43]. This arrangement permitted crystal temperatures near 1000 K to be achieved using the lamp alone, and cooling of the hemispherical glass surface was necessary to prevent damage to it by the lamp. A nonlinear heating rate was observed. The crystal was mounted on a 0.25-mm-diameter W support wire, which minimized cooling by conduction to the liquid-nitrogen-cooled support lead. A tungsten thermionic emitter is shown behind the crystal and this is used for electron bombardment cleaning at 2500 K, assisted by magnetic collimation. Figure 34.13c shows a lens arrangement for focusing light from a 900-W lamp [44]. The single-glass double-convex lens, f/1.32, has a magnification of unity. Lenses of this type are used as condenser lenses in photographic enlargers. The window is Pyrex glass with 95 % transmission in the near infrared, where the spectral radiancy is greatest for tungsten. A silicon crystal could

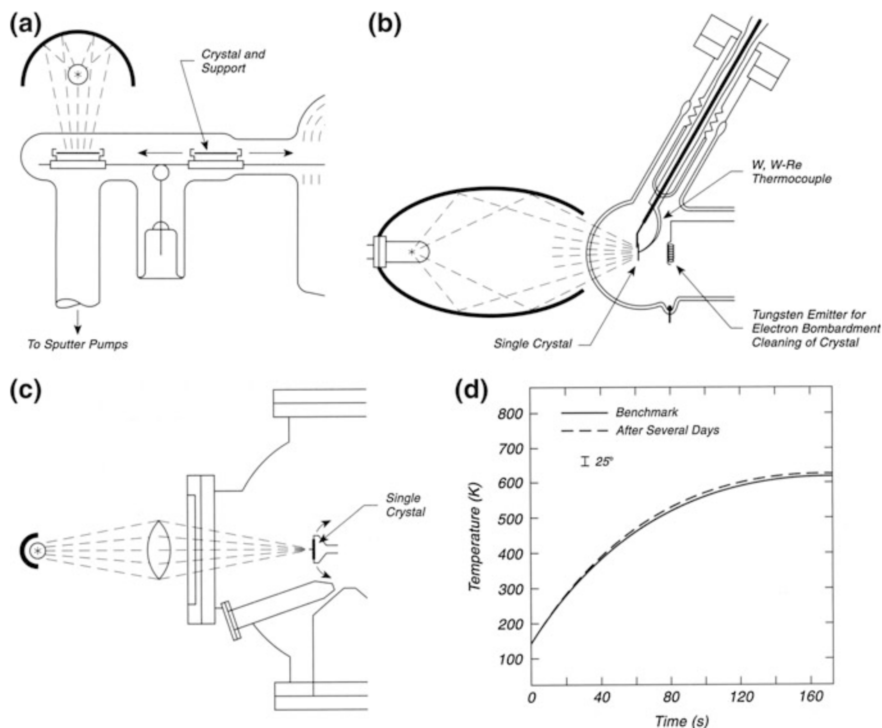

Fig. 34.13 Radiation heating of crystals through glass windows. **a** Hemispherical reflector. **b** Ellipsoidal reflector. **c** Lens + hemispherical reflector. **d** Temperature program for C

be raised to 900 K with this arrangement. The temperature program using the lamp in Fig. 34.13c is shown in Fig. 34.13d, and the reproducibility over a period of several days is within ±5 K.

34.14 Pyrolytic Graphite Heating Element for UHV

Heavy power deposition in an ultrahigh vacuum system can be achieved using electron bombardment, with the inherent possibility of burning out the emitter filament. The resistive heater described below avoids this problem.

The heater shown in Fig. 34.14a was constructed of chemical-vapor-deposited (CVD) pyrolytic graphite, which is highly anisotropic in its electrical conductivity [45]. The heater is fabricated from a slab of the graphite so that the current flow is in the C direction, which has a resistivity about 10^3 times higher than in the A or B directions. The width of the device in the C direction is governed by the thickness of the pyrolytic graphite supplied by the manufacturer [46], which is about 25 mm. The slab is cleaved along the A/B direction into slices 4–5 mm in thickness.

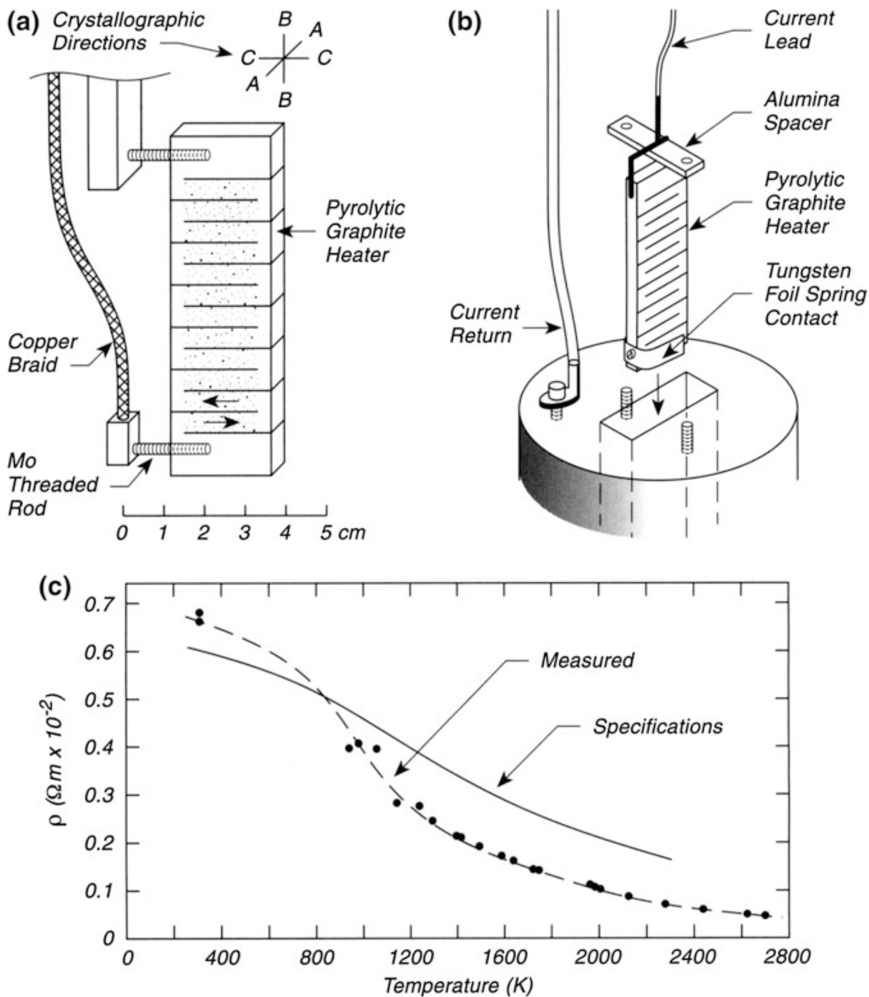

Fig. 34.14 Pyrolytic graphite heating elements. **a** Heater design—current flow in C direction. **b** Design for internal heating element—metal. **c** Resistivity in C direction

Resistive sections are separated from each other using a band saw or preferably a diamond saw wheel. Care must be taken not to fracture the graphite during sawing.

The heater is mounted on threaded Mo connection rods, as shown in Fig. 34.14a. These rods are not heated too much since the thermal conductivity along the C-direction is small compared to the other directions. When the temperature in the central region is in the 2000 K range ±30 K, typical power dissipation is about 2.0 kW for 155 V applied with 13.5-A current.

Figure 34.14b shows the heater used as in insertion device inside of a block to be heated to about 1200 K. The pyrolytic graphite heater was mounted in a rectangular

hole and was insulated from the metal by an alumina spacer. Electrical contact was made with a tungsten foil spring attached to the bottom of the heater as shown.

Although the heater is mechanically fragile, once in operation it may be repeatedly cycled in temperature without damage. The authors report that this design is compatible with ultrahigh vacuum.

The resistivity of the pyrolytic graphite heater was measured versus temperature, as shown in Fig. 34.14c. Relatively poor agreement was obtained compared to the manufacturer's specifications. This level of variation is typical for CVD pyrolytic graphite measured in the C-direction.

34.15 Heater—Paint-on Type

A simple resistance heater which can be painted on an insulating surface [47] may be useful in indirectly heating components in an ultrahigh vacuum system (as shown in Fig. 34.15). A thin layer of Aquadag [48], which is a colloidal graphite suspension, is painted onto a roughened quartz surface and outgassed for 0.5 h by baking in an oven at 300 °C, which is reported to be satisfactory for complete outgassing [48]. The graphite layer can then be smoothed with fine abrasive paper. Contact to the graphite layer is made using Ni or Pt strips, 0.1 mm thick, which are sandwiched between the graphite layer and a second quartz plate that is clamped to the first to assure good contact.

For a 27-mm-diameter plate, typical room temperature resistances are about 15 Ω. With a variable transformer, up to 20-V maximum, the heater could be used continuously for long periods at temperatures of 500 °C, and operation at higher temperatures may be possible. The application of these ideas to heating irregularly shaped surfaces is possible.

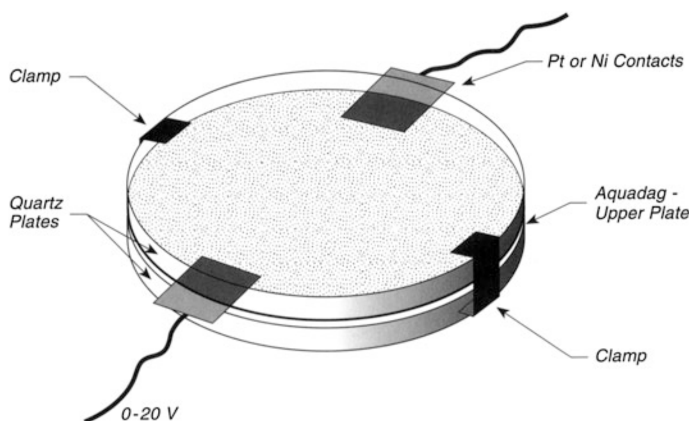

Fig. 34.15 Heater—paint-on type

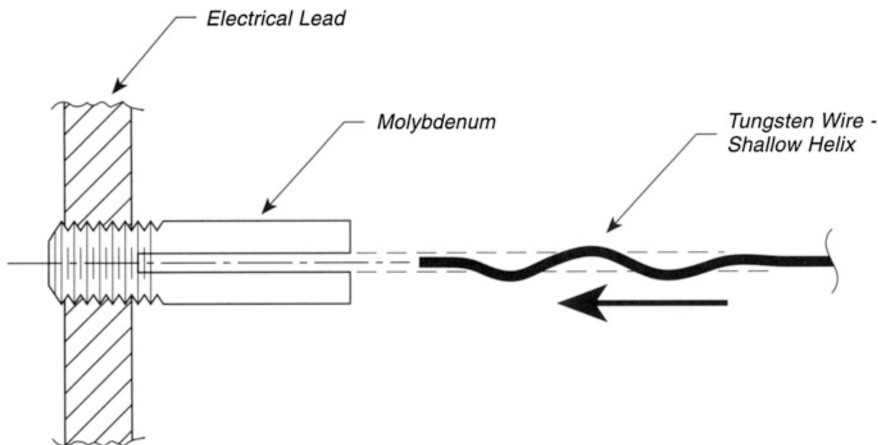

Fig. 34.16 Mounting of high-temperature tungsten filaments

34.16 Mounting High-Temperature Tungsten Filaments

The proper mounting of tungsten filaments so that operation at high temperatures does not melt or vaporize the filament mount is sometimes a problem in instrument design. A useful method of doing this without using complex screwing or clamping arrangements is shown in Fig. 34.16. A Mo rod, threaded to fit into an electrical mount, is drilled with an axial hole somewhat larger in diameter than the tungsten wire. The drilling process should be done slowly (1000 rpm) to avoid splitting the Mo rod [49]. The ends of the tungsten wire are then coiled by winding around a mandrel, followed by stretching, such that the helix formed makes a tight sliding fit into the hole in the Mo rod.

34.17 Rotatable Single Crystal

A cylindrical single crystal exposes different single crystal planes at different angles around its perimeter. Thus experiments which sample small areas may be carried out at different azimuthal angles, sampling different single crystal facets as well as at different atomic step geometries and densities on vicinal planes. The crystal geometry shown in Fig. 34.17a features a crystal shell with inside diameter of 14 mm and outside diameter of 20 mm, and involves a crystal length of 14 mm. The crystal is clamped to the bottom of a cryogenic reservoir containing liquid N_2, which with long cooling times can bring the crystal down to 89 K. The crystal may be heated for cleaning to above 900 K by radiation from the encased tungsten filament or by electron bombardment. Cooling occurs at an initial rate of $\sim$45 K min^{-1}, with the lowest temperature being achieved in about 60 min cooling

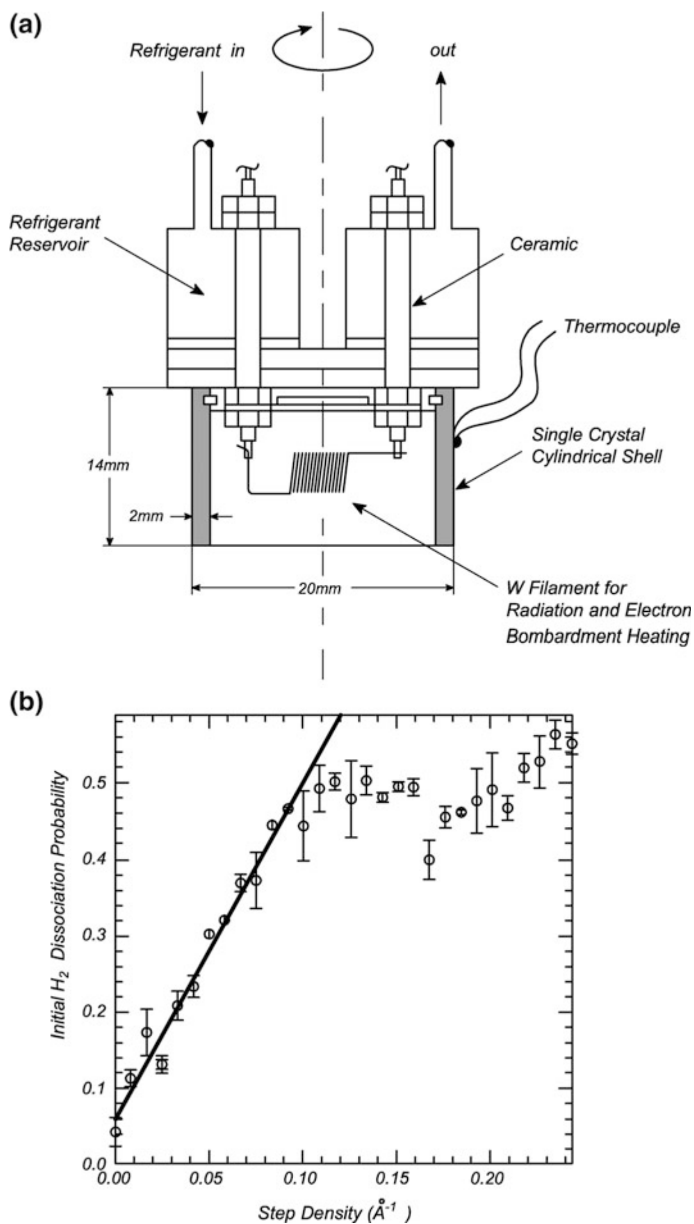

Fig. 34.17 Rotatable single crystal. **a** Structure of cylindrical single crystal. **b** H_2 dissociation probability versus atomic step density

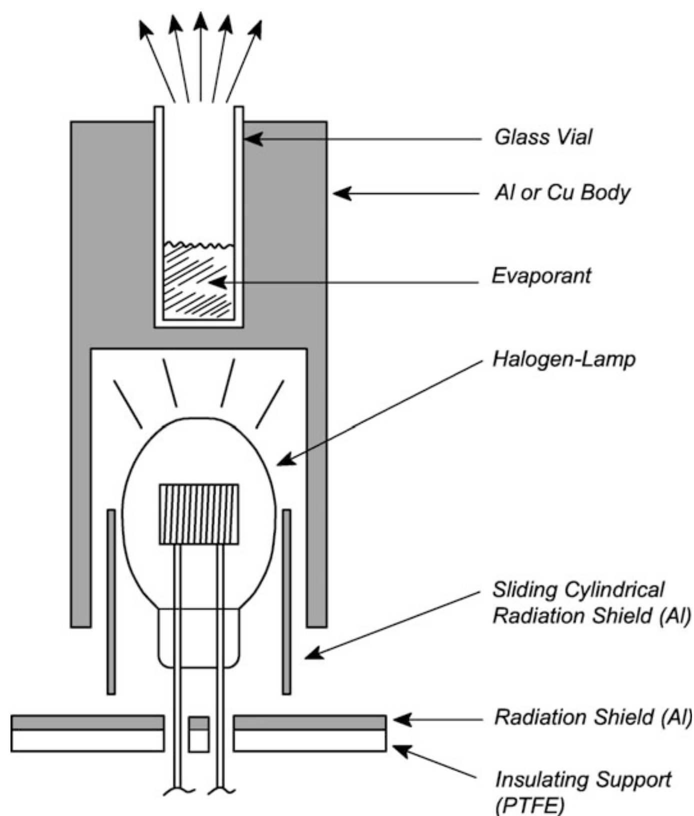

Fig. 34.18 Radiation-heated evaporator

time. The crystal may be programmed upwards in temperature at 1 K s^{-1} and thermal desorption is measured by an apertured and differentially-pumped mass spectrometer through a skimmer which is 6 mm wide and 1 mm high. Desorption spectra are obtained with an azimuthal angular resolution of 2°. The crystal is dosed by a molecular beam which produces a stripe on the crystal which is 6 mm wide and 0.3 mm high [50].

An example of the use of this approach involves measurements of the sticking coefficient of H_2 on the crystal at various positions involving different atomic step densities. Figure 34.17b shows this measurement, plotted versus the inverse distance between atomic steps which depends on the azimuthal angle setting of the crystal compared to the axis of the H_2 molecular beam. The sticking coefficient rises as the step density increases [50].

34.18 Radiation-Heated Evaporator

Tungsten lamps are excellent clean radiation sources for the interior of UHV systems. They may be of the quartz-halogen or quartz-Xenon type where the added gas prevents W evaporation on the inner surface of the quartz envelope. UHV compatibility is related to having only quartz and metal exposed to the vacuum system. Such bulbs are used in home lighting systems, auto headlamps, and projector lamps. They have the advantage of being able to operate at high power without filament burnout or W evaporation into the vacuum system. Also, there is no thermionic electron emission. Gases in the bulb will not escape into the vacuum system. These bulbs have been used also for passing focused radiation through windows for heating of samples in UHV (see Sect. 34.13).

A particular use of a lamp for heating an evaporant is shown in Fig. 34.18. An Al or Cu body, containing a glass vial with the evaporant, is heated from behind with a lamp encased in the body as shown. The lamp is carefully shielded by aluminum metal shields to prevent radiation heating of an insulating PTFE support or other parts of the support assembly. Thermocouple wires may be attached to the evaporator, but electrical pin contacts to thermocouple wires should be shielded from radiation to prevent heating of junctions which will supply spurious voltages. The design shown has been used up to 300 °C [51].

References

1. R.J. Muha, S.M. Gates, P. Basu, J.T. Yates Jr., Rev. Sci. Instrum. **56**, 613 (1985)
2. Model 2B50B, obtainable from Analog Devices, One Technology Way, Norwood, MA 02062-9106
3. Model UDC 500, obtainable from Honeywell, Micro Switch Division, 11 W. Spring Street, Freeport, IL 61032-4353. More advanced controllers are now available from Honeywell, such as the UDC 5000 ultrapro
4. M.A. DeAngelis, A.B. Anton, J. Vac. Sci. Technol. **A10**, 3507 (1992)
5. LabVIEW is available from National Instruments, 6504 Bridge Point Parkway, Austin, TX 78730-5039, USA
6. Type MJC-C, obtainable from Omega Engineering, Inc., P.O. Box 4047, Stamford, CT 06970, USA
7. Type Lab-PC+, obtainable from National Instruments, see Ref. [5]
8. J. Ahner, D. Mocuta, R.D. Ramsier, J.T. Yates Jr., J. Chem. Phys. **105**, 6553 (1996)
9. K.L. Rostov, Institute of General and Inorganic Chemistry, Bulgarian Academy of Sciences, 1113 Sofia, Bulgaria (private communication). This design is used in the laboratory of Professor Peter Toennies, Max Planck Institut, University of Göttingen, Stroemungsf, Bunsenstr. 20, D-37037 Göttingen, Germany
10. R.C. Henderson, R.F. Helm, Surf. Sci. **30**, 310 (1972)
11. J.A. Stroscio, W. Ho, Rev. Sci. Instrum. **55**, 1672 (1984)
12. K. Jacobi, W. Ranke, J. Electron. Spectrosc. Relat. Phenom. **8**, 225 (1976)
13. M.J. Bozack, L. Muehlhoff, J.N. Russell Jr., W.J. Choyke, J.T. Yates Jr., J. Vac. Sci. Technol. **A5**, 1 (1987)

14. Metal vapor pressures are listed and graphed, in *Handbook of Electron Tube and Vacuum Techniques*, ed. by F. Rosebury (American Institute of Physics, New York, NY, 1993), pp. 142–148
15. V.A. Ukraintsev, J.T. Yates Jr., Surf. Sci. **346**, 31 (1996)
16. W. Ho (private communication)
17. H. Nishino, W. Yang, Z. Dohnalek, V. Ukraintsev, J.T. Yates Jr., J. Vac. Sci. Technol. **A15**, 182 (1997)
18. V. Smentkowski, J.T. Yates Jr., J. Vac. Sci. Technol. **A14**, 260 (1996)
19. V.M. Donnelly, J.A. McCaulley, J. Vac. Sci. Technol. **A8**, 84 (1990)
20. G.E. Thomas, W.H. Weinberg, J. Vac. Sci. Technol. **16**, 87 (1979)
21. G.B. Hoflund, R.E. Gilbert, J. Vac. Sci. Technol. **18**, 56 (1981)
22. J.A. Stroscio, L.J. Richter, W. Ho, Rev. Sci. Instrum. **55**, 732 (1984)
23. J. Lecante, R. Riwan, C. Guillot, Surf. Sci. **35**, 271 (1973)
24. Standard and custom wound W filaments may be obtained from C.M. Furnaces, Inc., 103 Dewey Street, Bloomfield, NJ 07003
25. J. Klebanoff, V.H. Ritz, R.E. Thomas, J. Vac. Sci. Technol. **A2**, 1396 (1984)
26. Spectra-Mat Inc., 100 Westgate Drive, Watsonville, CA 95076
27. V.S. Smentkowski, J.T. Yates Jr., J. Vac. Sci. Technol. **A11**, 3002 (1993)
28. P.H. Holloway, J.B. Hudson, Rev. Sci. Instrum. **43**, 1045 (1972)
29. T.E. Jones, W.C. McGinnis, J.S. Briggs, Rev. Sci. Instrum. **65**, 977 (1994)
30. J.C.S. Wong, A. Linsebigler, G. Lu, J.-F. Fan, J.T. Yates Jr., J. Phys. Chem. **99**, 335 (1995)
31. F. Bozso, L. Muehlhoff, M. Trenary, W.J. Choyke, J.T. Yates Jr., J. Vac. Sci. Technol. **A2**, 1271 (1984). (Here the cement used was mixed with graphite in order to permit electrical conductivity for electron spectroscopy of a SiC single crystal)
32. A zirconia-based refractory cement was employed which matched the thermal expansion coefficient of TiO_2. This particular cement is Aremco 571. The address is Aremco, P.O. Box 429, Ossining, NY 10562-0429
33. E.P. Marsh, F.L. Tabares, G.A. Bach, J.P. Cowin, Rev. Sci. Instrum. **57**, 3134 (1986)
34. J.R. Creighton, Dept 1126, MS 0601, P.O. Box 5800, Sandia National Laboratories, Albuquerque, NM 87185-0601 (personal communication)
35. J.C. Burns, P.C. Stair, R. Haidle, J. Vac. Sci. Technol. **A8**, 3886 (1990)
36. Vacseal is made by Space Environment Laboratories, RO. Box 1061, Boulder, CO 80306
37. *Metal Finishing Guidebook and Directory* (Metals and Plastics, Hackensack, NJ, 1989), pp. 244–265
38. F. Bozso, L. Muehlhoff, M. Trenary, W.J. Choyke, J.T. Yates Jr., J. Vac. Sci. Technol. **A2**, 1271 (1984)
39. M.J. Bozack, L. Muehlhoff, J.N. Russell Jr., W.J. Choyke, J.T. Yates Jr., J. Vac. Sci. Technol. **A5**, 1 (1987)
40. Obtain from Aremco Products, Inc., P.O. Box 429, 23 Snowden Avenue, Ossining, NY 10562-0429; the cement should be preserved in the refrigerator and has a limited shelf life
41. K.A. Schultz, E.G. Seebauer, Rev. Sci. Instrum. **63**, 218 (1992)
42. R.W. Palmberg, W.T. Peria, Surf. Sci. **6**, 57 (1967)
43. T.E. Madey, J.T. Yates Jr., in *Structure et Proprietes des Surfaces des Solides*, No. 187 (Editions de Centre National de la Recherche Scientifique, Paris, 7–11 July 1969), p. 155
44. M.J. Bozack, L. Muehlhoff, J.N. Russell Jr., W.J. Choyke, J.T. Yates Jr., J. Vac. Sci. Technol. **A5**, 1 (1987)
45. C.S. Pitcher, P.C. Stangeby, G.E. Austin, G.M. McCracken, J. Vac. Sci. Technol. **A5**, 383 (1987)
46. Pfizer, Inc., 235 E. 42nd Street, New York, NY 10017
47. P. Winsemius, H.P. Lengkeek, Rev. Sci. Instrum. **44**, 229 (1973)

48. Obtain "Dag 660" from Acheson Colloids, 1607 Washington Avenue, P.O. Drawer 611747, Port Huron, MI 48061-1747
49. J.R. Conrad, S.F. Home, D.R. Pirkle, R.P. Torti, Rev. Sci. Instrum. **51**, 144 (1980)
50. C.L. Juurlink, C. Hahn (personal communication)
51. R.G. Jones (private communication)

Chapter 35
Cooling Samples

35.1 6 K—Cryogenic Crystal Holder

Cooling single crystal samples in ultrahigh vacuum below 77 K was at one time considered to be technically difficult because of the perceived need for cooled radiation shields for the structure holding the crystal. Recently, excellent cooling properties have been achieved without a radiation shield using a number of refinements that have permitted rapid cooling to 6 K, control of temperature to 30–70 mK at 10 K, and measurements with absolute temperature errors of about 0.7 K at 10 K and 1.5 K at 100 K [1].

Figure 35.1 shows the design for efficient cooling [1]. A liquid He cryostat [2] containing concentric ducts for liquid admission and gas transport away is mounted on a standard UHV manipulator. While the publication [1] shows the use of OFHC Cu cooling members, recent refinements have substituted highly polished Ag members for Cu primarily because the surface of Cu oxidizes slowly in use, giving a nonreflective surface that is not as efficient as the shiny Ag surface in reducing warming from the radiation fromthe surroundings [3]. All heat-conducting interfaces are made by pressing smooth surfaces together and not by welding, which produces poor thermal contact. A 10 × 10 × 55 mm^3 block of Ag is bolted to the bottom of the cryostat and holds two 1-mm-thick sapphire plates that are separated from each other by a gap. Three 2-mm-diameter screws, with ceramic isolation washers, apply force to hold two Ag electrical conduction leads in good contact with the sapphire plates. The screws pass through the lower Ag bar in large clearance holes that assure that no short circuits can occur. Each Ag bar is covered with a stainless steel force plate to avoid distortion of the Ag owing to the force of the screws. The two Ag conduction leads have 4-mm-diameter stainless steel power leads exiting from their back and passing up the cooled cryostat surface. These power leads are heat-stationed twice each, in series, to the cooled cryostat wall to reduce heat flow downward to the crystal assembly. The heat stations involve sapphire electrical isolation junctions, mounted 50 mm apart on the cryostat shield.

© Springer International Publishing Switzerland 2015

J.T. Yates Jr., *Experimental Innovations in Surface Science*,
DOI 10.1007/978-3-319-17668-0_35

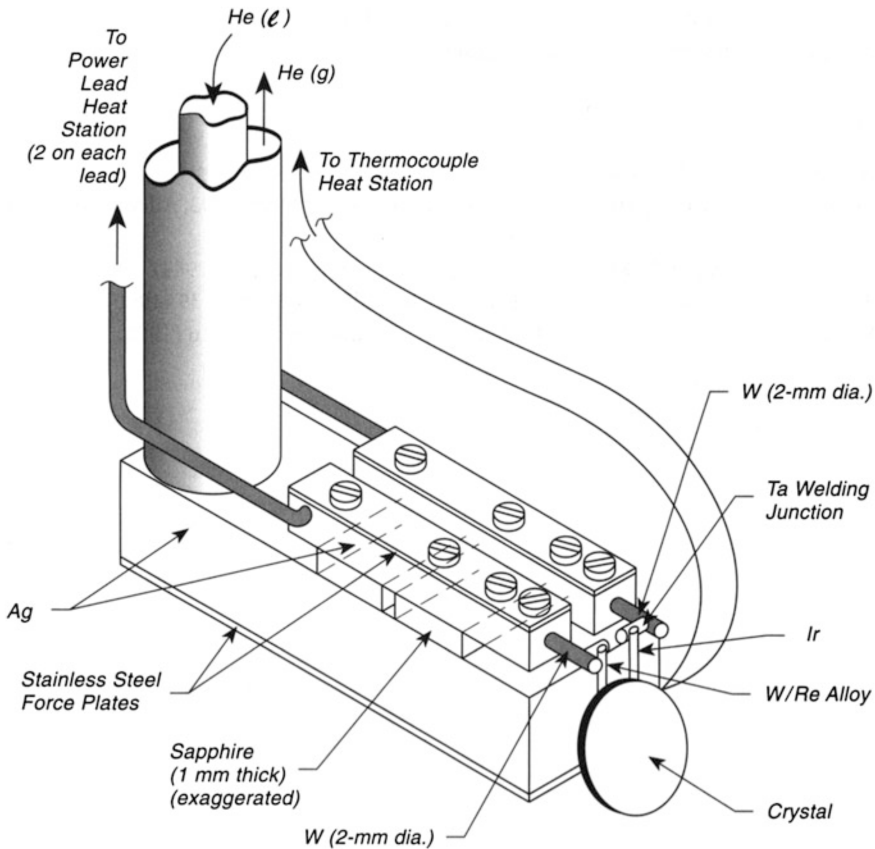

Fig. 35.1 6 K—cryogenic crystal holder radiation

The crystal is mounted on the Ag power leads using tungsten rods (5 mm long × 2 mm in diameter). These snugly fit into holes in the end of the Ag leads and are tightly connected, but not welded, to Ta stubs of about 2-mm length at right angles, as shown in Fig. 35.1. The crystal is mounted on two different contact leads (6 mm long) which consist of pairs of W/25 % Re wires of 0.5-mm diameter and two Ir wires of square cross section, 0.45 mm × 0.45 mm. The logic for this mounting structure is that at low temperatures pure metals do not have the needed resistivity for ohmic heating, and an alloy must be used for this purpose. Conversely, the Ir rod has good thermal conductivity at low temperatures. Unfortunately, the thermal expansion coefficient is different for the two wires, so that heating the crystal puts torque on the welds. To reduce this stress, the flexible Ta leads are incorporated, and the spacing between the W/Re and the Ir leads is kept small.

The thermocouple (in this case, type K) is welded to the back of the crystal and the leads pass upward after also being heat-stationed on the cryostat with isolation by sapphire. Heating rates from 0.01 to 100 K/s are possible. A heating current of 70 A DC at about 8 V is sufficient to bring the crystal to 1600 K. The cooling time between 650 and 6 K is 3 min.; from 1600 to 6.5 K the time is 5 min. At steady state, the consumption of liquid He is 4 L/hr. With the cryostat cool, the base pressure is below 10^{-11} mbar.

Reference [1] is highly instructive about the pitfalls of using cryogenic methods in ultrahigh vacuum applications.

Others have employed closed-loop He cryostats for cooling of crystals in UHV that do not achieve the very low temperatures described here [4–6].

35.2 Cooling Crystals by Contact with a Thermal Reservoir

One of the best ways to employ a low-temperature, closed-cycle cryogenic source with limited cooling capacity is to use a heat absorption reservoir that is continuously cooled, but only used periodically for cooling the sample. A design using this principle in shown in Fig. 35.2 [7], based on an earlier design [8].

The crystal and its mounting assembly, shown in Fig. 35.2a, is held on the end of a conventional manipulator, and it may be heated either by radiation from the W filament or by electron bombardment. The entire crystal and the heating assembly is electrically isolated from the manipulator by means of a machinable ceramic support. The sample may be contacted to the thermal reservoir by means of a conical thermal switch in order to initiate cooling. The stainless steel spring placed under compression when this contact is made to yield the best thermal contact possible between the two OFHC Cu components.

The cooling rate using this device is very impressive, and cooling from 1023 K to about 20 K occurs in 300 s, as may be seen in Fig. 35.2b.

A second design in which contact between the sample and the closed cycle refrigerator is maintained continuously is given in [9].

35.3 Cooling Samples on Manipulators—Thermal Conductivity Issues

A variety of designs for holding samples on manipulators is available in the literature, and most of these have a requirement that the crystal be isolated electrically from the manipulator, while being in contact thermally with a cryogenically cooled reservoir, usually made of oxygen-free high conductivity copper (OFHC Cu). Comparisons of cooling rates for different methods of electrical isolation have been made and are presented below [10].

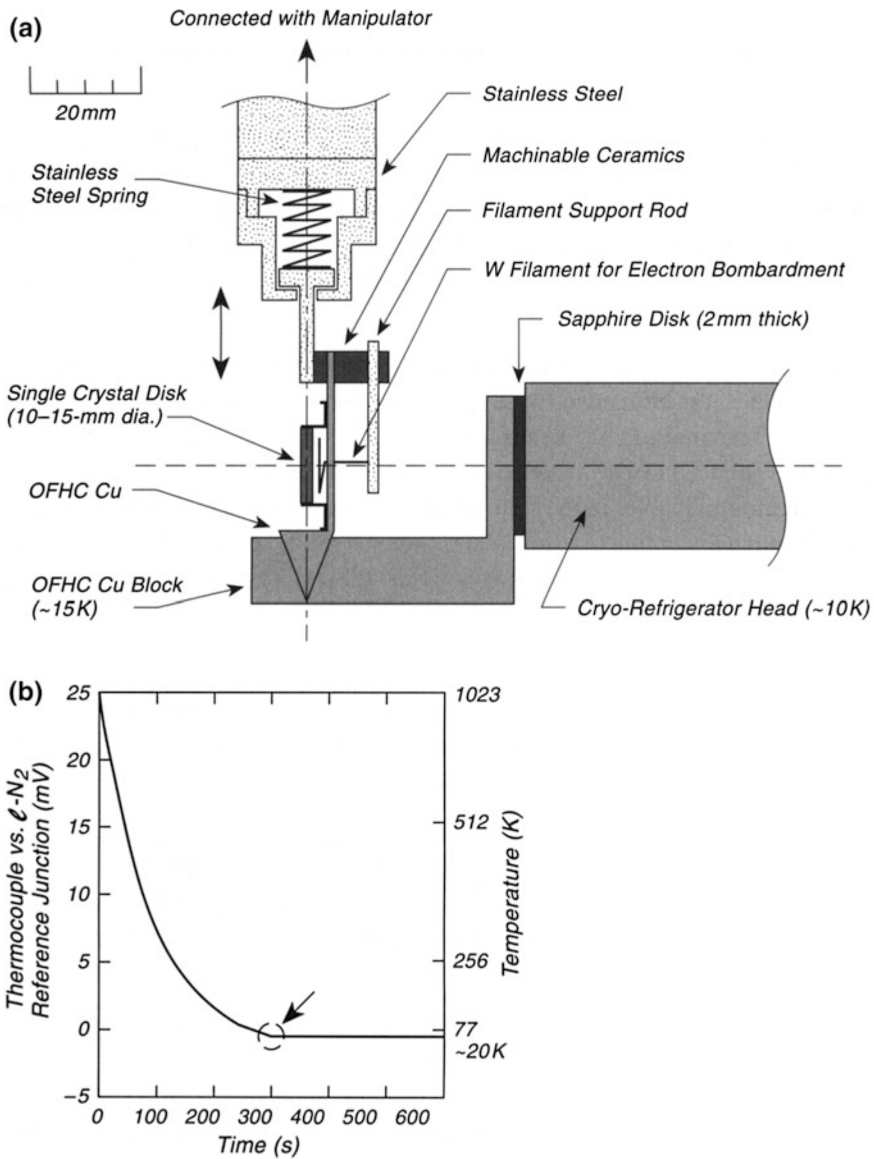

Fig. 35.2 Spring-loaded cooling by contact. **a** Side view of manipulator + thermal contact, **b** cooling curve

Figure 35.3a shows the experimental apparatus used in this work. A Cu reservoir with polished planar faces holds two Cu support bars that are clamped with equal force to the reservoir. The total contact area is 3.13 cm^2 for both support bars. The temperature of each bar (T_1 and T_2) can be measured during cooling, using type K

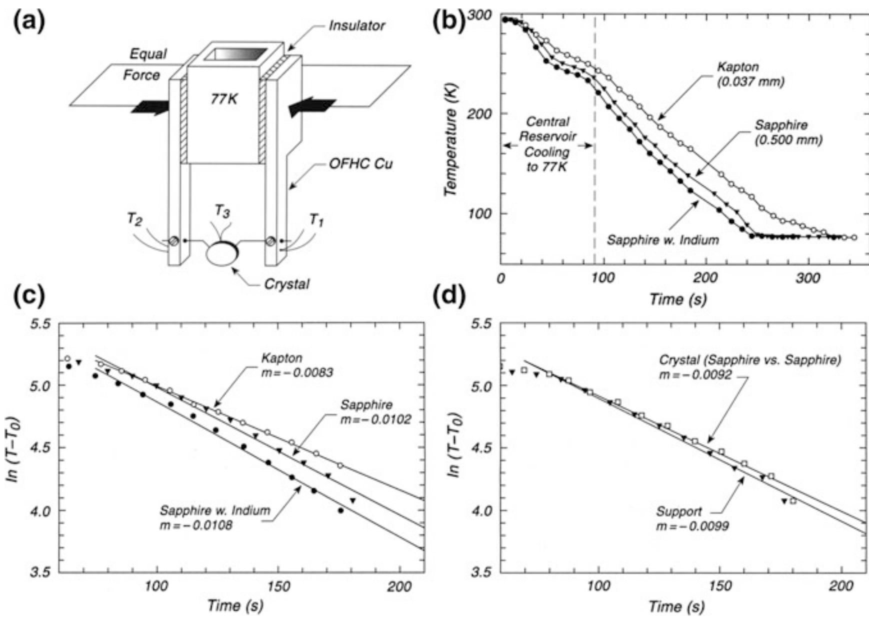

Fig. 35.3 Cooling samples on manipulators. **a** Manipulator cooling section. **b** Comparative cooling rates. **c** Comparison of cooling rates—various insulators. **d** Rate of crystal cooling versus support cooling

thermocouples that are wedged into small holes in the support bars. In addition, the crystal temperature can also be measured as cooling occurs to determine the influence of the 0.025-mm-diameter tungsten wire (and the associated spot welds) on the crystal cooling rate, compared to the support bar cooling rate.

Figure 35.3b shows cooling experiments comparing three different insulator materials. The slowest cooling rate of the support bars is achieved using Kapton films, 0.037 mm in thickness. Faster cooling of the support bars is achieved using 0.500-mm sapphire single crystal insulators. The fastest cooling is achieved when an indium film is used to join the sapphire to the cooling reservoir and the support bars. For cooling times up to 90 s, cooling of the central reservoir to 77 K is taking place, and the data in this time period are disregarded in the measurements.

Figure 35.3c shows semilogarithmic plots of the cooling rate after the reservoir has reached constant temperature. The slope of these plots is a measure of the rate of cooling through each insulator junction. It may be seen that the Kapton exhibits cooling at 81 % of the rate of the sapphire, and that the indium coating on the sapphire enhances its cooling rate by about 6 %.

Figure 35.3d shows a comparison of the cooling rate of the sapphire-insulated support, compared to the cooling rate of a metal single crystal. This comparison was carried out in order to test the effect of the thermal conductivity of the tungsten wire (and its spot-welds and screw pressure contact). The crystal was found to cool at a rate of 93 % of the cooling rate of the copper bar supports, indicating that this crystal support design is certainly satisfactory.

The differences in the sapphire- and Kapton-controlled cooling rates are in accordance with the measured thermal conductivity of these materials[1]. Thus, sapphire, or indium-coated sapphire, exhibit superior qualities compared to Kapton of the thickness employed here. Thinner Kapton is likely to be mechanically damaged when it is placed under pressure or baked out and may therefore exhibit electrical leakage.

35.4 Vacuum-Jacketed Cryogenic Manipulator Rod

Long manipulator rods filled with liquid nitrogen can act as cryogenic surfaces that can physisorb or condense gases used in surface science studies. As the liquid nitrogen level drops, reevolution of these gases can cause problems in experiments conducted under ultrahigh vacuum. The design shown in the Fig. 35.4a eliminates this problem by using a vacuum jacket to isolate the outer wall of the manipulator rod from the inner tube, which is cooled with liquid nitrogen [11].

A copper reservoir is supplied with liquid nitrogen through a 1/8-in. diameter stainless steel tube. The excess liquid and vapor exits through a 5/16-in.-diameter outer tube, which is concentric with a l/2-in.-diameter stainless tube welded to a Conflat flange. The outer tube is pumped and contains an adsorbent material for maintenance of the vacuum, as is sometimes used in metal Dewar flask vacuum jackets. The liquid nitrogen inlet and outlet tubes are able to rotate inside a compression fitting that contains a spring-loaded Teflon seal that allows the sample to be rotated while the nitrogen delivery tube and the outlet tube remain fixed. Liquid nitrogen is drawn through a latex rubber tube into the assembly from an unpressurized storage Dewar by means of a small carbon vane vacuum pump [12] attached to the outlet tube. A valve at the inlet of the pump is used to adjust the flow of liquid nitrogen. This pump is isolated from the liquid nitrogen reservoir by a length of copper tubing that permits the liquid nitrogen to convert to gaseous nitrogen before entering the pump. The length of the manipulator is 1.3 m below the Conflat flange.

Owing to thermal contraction, the inner tube will decrease in length upon cooling. Since this is fixed at only one end, it may contract and expand freely. The differential expansion of the outer two tubes is taken up by a formed bellows that is

[1]Tabulated values for thermal conductivity are sapphire, 41.90 J/s km at 273 K; 100 HN Kapton, 0.10-0.35 J/s km at 276 K. Goodfellow Catalog (Goodfellow Metals, 1995), p. 433; p. 501. In addition reference [10] gives information and references on thermal conductivities as a function of temperature. Sapphire exhibits a greatly enhanced thermal conductivity at 80 K of 960 J/sKm.

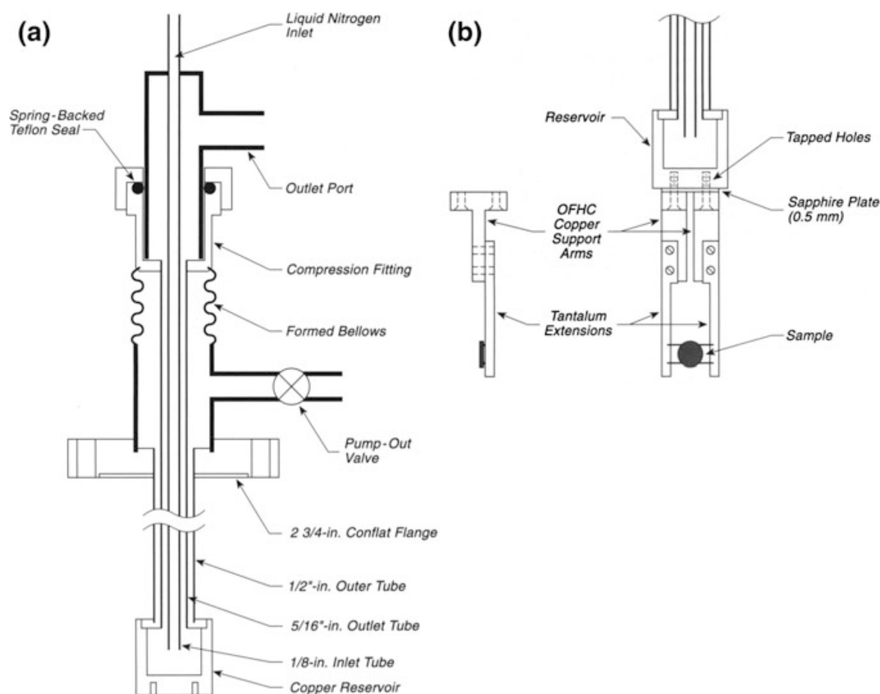

Fig. 35.4 Vacuum-jacketed cryogenic manipulator rod. **a** Vacuum-jacketed sample support tube. **b** Sample holder cryogenically coupled to copper reservoir

welded to the compression fitting. Some contraction and expansion of the outer tube still occurs as the inner tube changes temperature.

The sample holder shown in Fig. 35.4b is made of OFHC copper and is held on the base of the copper reservoir by four screws that pass through a 0.5-mm-thick sapphire plate that permits efficient cooling (see p. 383) as well as electrical isolation. A Ta support structure consisting of two arms for the sample is bolted to the copper support arms. Heating leads and thermocouple leads to the sample pass on the outside of the vacuum-jacketed manipulator rod and are heat-stationed on the lower cooled sections of the assembly.

In operation, the sample is cooled to 90 K when liquid nitrogen is the refrigerant. Measurements indicate that the outer tube slowly cools to about 200 K owing to cooling from its lower end, where it contacts the copper reservoir. This could be prevented by the installation of a small electrical heater on the outer tube.

Because of the length of the manipulator rod, a lower bearing is supplied in which the manipulator rod rotates. This prevents vibration of the sample inside the apparatus. Rotation and translation of the sample are supplied by a standard differentially pumped rotary seal (see p. 6) and a standard *x*-*y*-manipulator stage.

35.5 Manipulator Component with Cryogenic Azimuthal Rotation

A simple design [13], involving indirect heating of a sample that can be cooled to cryogenic temperatures and undergo limited azimuthal rotation, is shown in Fig. 35.5. The sample is mounted on a metal cap fixed to a sapphire cylinder that makes thermal contact with a Cu-Be cup through a novel ring of Cu-Be finger stock [14]. The Cu-Be cup is held by a hollow shaft that rotates in the Cu-Be block through

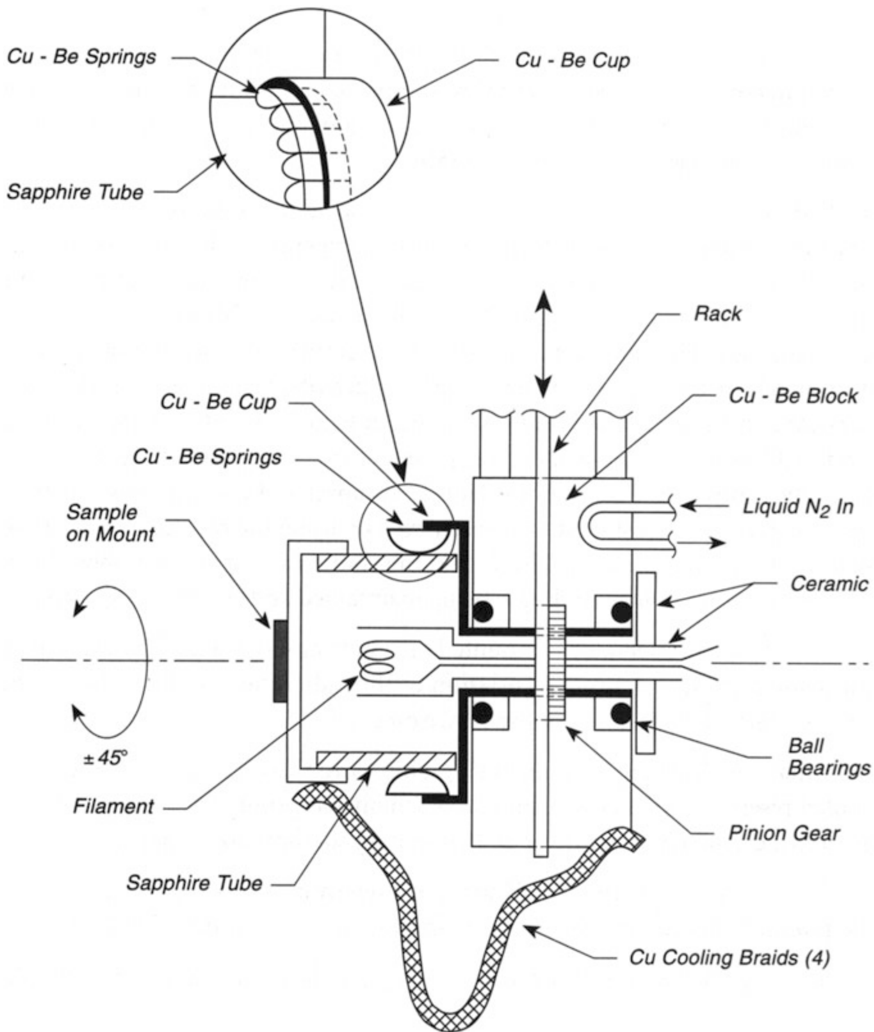

Fig. 35.5 Azimuthal rotation—cryogenic

stainless steel ball bearings that permit azimuthal rotation of the cup and the associated parts connected to the sample. The sapphire is a good thermal conductor but is an electrical insulator. In order to provide more cooling of the sample, four Cu braids are connected between the sample mount and the Cu-Be block, which contains internal pathways for flowing liquid nitrogen refrigerant. Azimuthal rotation is achieved using a rack and pinion connection allowing linear translation of the rack to produce rotation of the Cu-Be cup and the sample. An internal heater may be used for radiation heating or electron bombardment of the sample and its mount. It is electrically isolated and consists of a two-hole ceramic tube fixed in position with a ceramic collar so it does not rotate as the Cu-Be cup is rotated. The azimuthal freedom is ±45°, limited by the length of the copper cooling braids. The temperature range of the sample is from 130 to 1000 K, with cooling times of about 45 min.

35.6 Cooling Using Direct Contact

The use of cooling braids to supply flexibility in cooling of samples also causes a limitation in cooling rate owing to the low thermal conductivity associated with braids having a desired flexibility. Therefore, methods to cool movable samples by direct contact with a cold reservoir have been developed.

The first of the methods [15] to be described is shown in Fig. 35.6. Here a 200-g Cu tank is connected directly to a closed-cycle He refrigerator. The cold second stage is shielded from external radiation by a first stage shield as shown. The Cu tank contains a slot for the insertion of the sample holder containing a freshly cleaved semiconductor sample in this case. This sample holder makes contact with a droplet of molten Ga for the production of a metallic joint of high thermal conductivity. The Ga can be melted by radiation heating from an attached heater as shown in Fig. 35.6. The Cu tank can then be cooled to 20 K over a 140 min cooling period after starting the refrigerator. The long cooling time is probably a result of the large heat capacity of the massive Cu tank in this design. Temperature adjustment can be achieved by using the radiative heater in opposition to the He refrigeration unit. During heating, outgassing of the assembly with bursts of pressure is minimal since cooling is being maintained and slow heating occurs.

The closed cycle refrigerator is mounted on a bottom-entry manipulator permitting rotation and *x, y, z*-translation. Translation in the *z*-direction is especially important because of thermal contraction of the device on cooling.

A thermal switch arrangement involving a high area Cu-Cu contact between a liquid-He cooled reservoir and a crystal support assembly has produced a fast cooling performance and a crystal temperature of 20 K after long equilibration times [16].

A design of a highly efficient attachment of a removable closed-cycle refrigerator to a crystal mount has been described, with a limiting low temperature of 11 K [17].

Other arrangements for direct contact cooling are shown on p. 383 and 392.

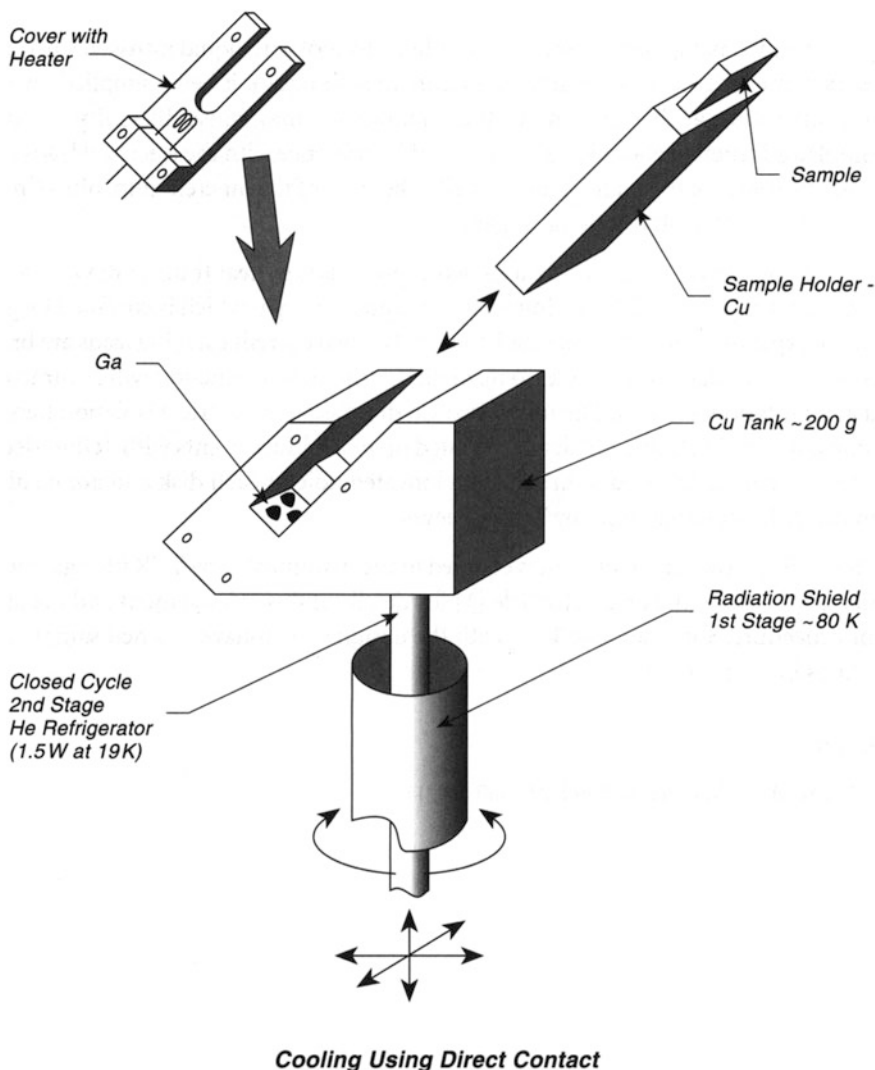

Fig. 35.6 Cooling without thermal braid

35.7 Cooling Reservoir—Horizontal Manipulator

A horizontal manipulator is inherently difficult to cool with liquid nitrogen since gravity may cause the refrigerant to drain from the tubing as it is being supplied. In addition, rubber seals at the inlet end of the manipulator may cause difficulty when the manipulator is rotated about its axis because of interference with the electrical leads passing into the center of the manipulator as well as because of the inherent difficulty of retention of refrigerant at all rotational angles.

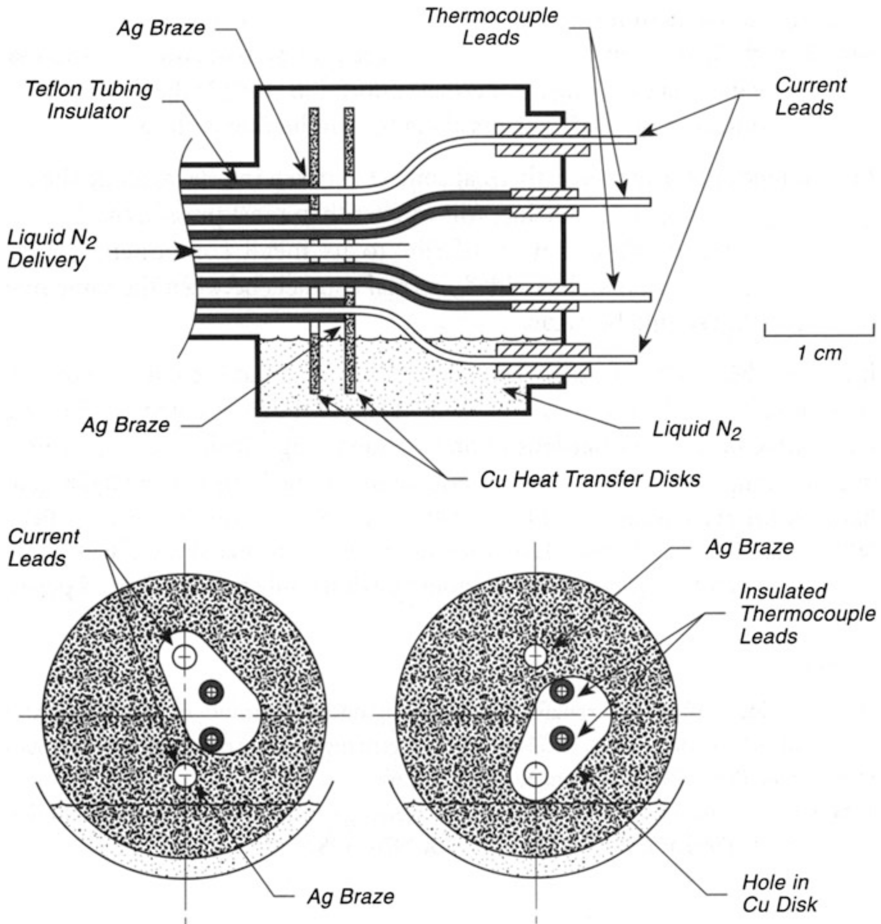

Fig. 35.7 Cooling reservoir—horizontal manipulator

The design shown in Fig. 35.7 uses two copper disks as heat transfer devices, and at all rotational angles the disks are immersed in liquid nitrogen which is confined by gravity in the expanded end of the manipulator [18]. The two current carrying leads are brazed into holes in alternate copper disks so that efficient thermal conduction will occur to each lead at all rotational angles. The use of two Cu disks assures electrical isolation between the current carrying leads, which are insulated up to the braze points with Teflon sleeves. The thermocouple leads pass through an elongated hole in each disk and are insulated from the disks and each other by Teflon sleeves.

The design shown in Fig. 35.7 is coupled to the manipulator by VCR fittings, and the reader is referred to the original article [18] for details of this arrangement and the alignment procedures for assembly. Tests with the design shown have reached sample temperatures in the range 103–123 K.

35.8 Cryogenic Connections

The design of efficient heat exchange methods that also permit motion of a cooled sample is made difficult by two factors: (1) the provision of sufficient thermal conductivity in the materials making the thermal connection, and (2) the provision of excellent thermal contacts between interfaces along the conduction pathway.

The best method for making a thermal contact between interfaces along the conduction path is by welding [19, 20]. Brazing, while better than most pressed mechanical connections, provides an alloy that is inferior to its metal components in thermal conductivity. Wherever possible, welded thermal contacts between the same materials (such as Cu or Ag) should be made.

Figure 35.8 shows a braid assembly made of OFHC Cu that is connected to a cryostat and to a Cu sample holder by means of welds at two of the three contact points. Because the Cu flexible braid work hardens upon extended usage, it should be considered an expendable component. The Cu heat conductivity can be improved by hydrogen firing at 1 bar pressure at a temperature of 600–800 °C for 3–5 min. Longer hydrogen firing may cause hydrogen embrittlement of the braid. The effect of limited hydrogen treatment is probably to remove copper oxide films that impede heat transfer at interfaces in the braid and on its connectors. Hydrogen firing should be done only by experienced persons!

35.9 Sample Cooling Using Thermal Braid

Many experiments require sample cooling below room temperature and below the temperature of liquid nitrogen. The use of copper thermal braid for this purpose provides flexibility in sample motion, and with proper design copper braid can be employed for efficient cooling.

In Fig. 35.9a, a copper braid is employed with a detachable thermal switch to provide intermittent cooling of a sample mounted on a movable manipulator [21].

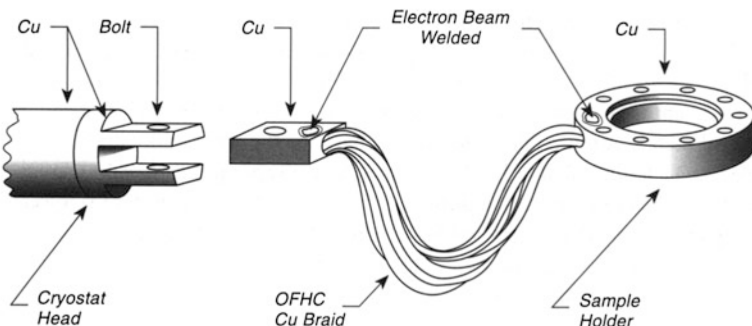

Fig. 35.8 Cryogenic connections

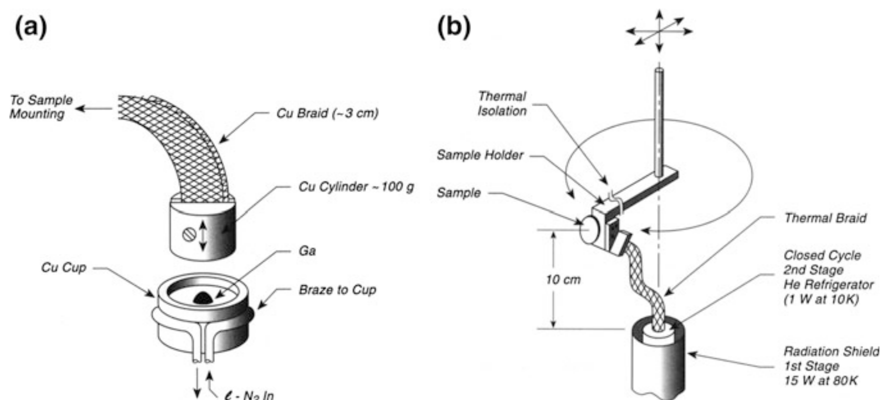

Fig. 35.9 Cooling using thermal braid. **a** Detachable cooling assembly. **b** Continuously Coupled cooling assembly

The braid is firmly connected to the sample mount by means of clamps made of Cu. The other end is connected to a solid Cu cylinder, weighing about 100 g which makes contact with a Cu cup. The Cu cup is cooled by flowing liquid nitrogen through a coil wrapped and brazed in place. The use of brazing is highly recommended, since the thermal conduction through a brazed joint is far superior to any other mechanical contact except for a weld between identical metals. A reversible metal contact between the Cu cylinder and the Cu cup is made using a liquid gallium droplet (mp = 32 °C at a vapor pressure of 10^{-14} Torr). Thus, to melt the Ga, hot air is passed through the coil on the cup; the weight is lowered into the cup by moving the sample holder to which it is attached, and subsequent cooling freezes the Ga, making a good thermal and mechanical contact. Sample cooling to 93 ± 10 K then occurs within about 200 s.

In Fig. 35.9b, a thermal braid is permanently attached to the sample holder [22]. The manipulator swings about a radius of 15 cm, and various degrees of freedom are present. The sample holder is thermally isolated from the manipulator shaft and most of the arm. The thermal braid is attached to a closed-cycle He refrigerator [23], which has two stages of cooling to 80 K (15 W) and to about 10 K (1 W). The 80-K stage provides cooling for a radiation shield that surrounds the low-temperature stage, as shown schematically in the Figure. Modeling of the energy transfer was done in order to compute the optimal dimensions for the sample holder and the braid. The minimization of thermal conduction to the sample holder makes thermal radiation the primary source of unwanted heat. Since the ratio of the surface area of the sample holder to that of the thermal braid is about 1:12, a cooled radiation shield around the sample is unnecessary in this design. It was calculated that the cross-sectional area of the Cu braid was 0.075 cm^2 on the basis of thermal conduction and thermal radiation considerations. It is of interest to note that this design achieved sample temperatures of 14–15 K routinely with only 1 W of cooling in the second stage of the closed-cycle refrigerator.

Copper braid should be made of oxygen-free, high-conductivity (OFHC) Cu for maximum efficiency. UHV-compatible closed-cycle refrigerators are commercially available [3]. It should be noted that efficient thermal connections to copper braid can be made by brazing the ends with silver solder, which can then be deformed by clamping. Procedures for achieving the same objective without brazing have been described [24].

35.10 Flexible Cooling Reservoir

The use of copper braid for cooling samples on a manipulator is widespread. This method of cooling avoids complex crystal motion devices that must also conduct heat efficiently, and mountings with six degrees of motional freedom are often built with braid cooling.

As the crystal and the manipulator shaft move, there will be the need for relief of the strain in the copper cooling braid. While a long braid may be used to give a sufficient degree of motion, this decreases the cooling efficiency of the system. It is also possible, however, to mount the cooling reservoir itself on a flexible mount as shown in Fig. 35.10 [25], thereby permitting a shorter braid to be used.

A mini-Conflat flange, mounted on the manipulator flange, is welded to a standard Swagelock Tee. A stainless tube enters the vacuum system through this flange and is connected to a very flexible bellows and then to a double kovar/glass seal, which acts as an insulating break, electrically isolating the cooled reservoir from the vacuum system and ground. An OFHC Cu reservoir is brazed to the end of the tube assembly, and contains a polished flat to which the copper braid and its copper lug are mounted (see p. 392). An indium foil gasket makes good thermal contact when compressed by a bolt that passes through the flat and is drawn down by a nut on the back side of the flat. The alternate use of threads in the soft copper flat is not recommended because of the possibility of stripping threads.

Liquid nitrogen is supplied to the copper reservoir by suction from a styrofoam cup or small Dewar through 1/8-in.-diameter Teflon tubing that can be sealed inside the Swagelock fittings. Sample temperatures below 100 K can easily be achieved.

35.11 Enhanced Cooling Using Liquid Nitrogen

A simple method [26] has been devised and tested for cooling below the temperature limit established by liquid nitrogen (77.3 K). The method involves bubbling He gas through the liquid nitrogen (transpiration); evaporation of liquid nitrogen

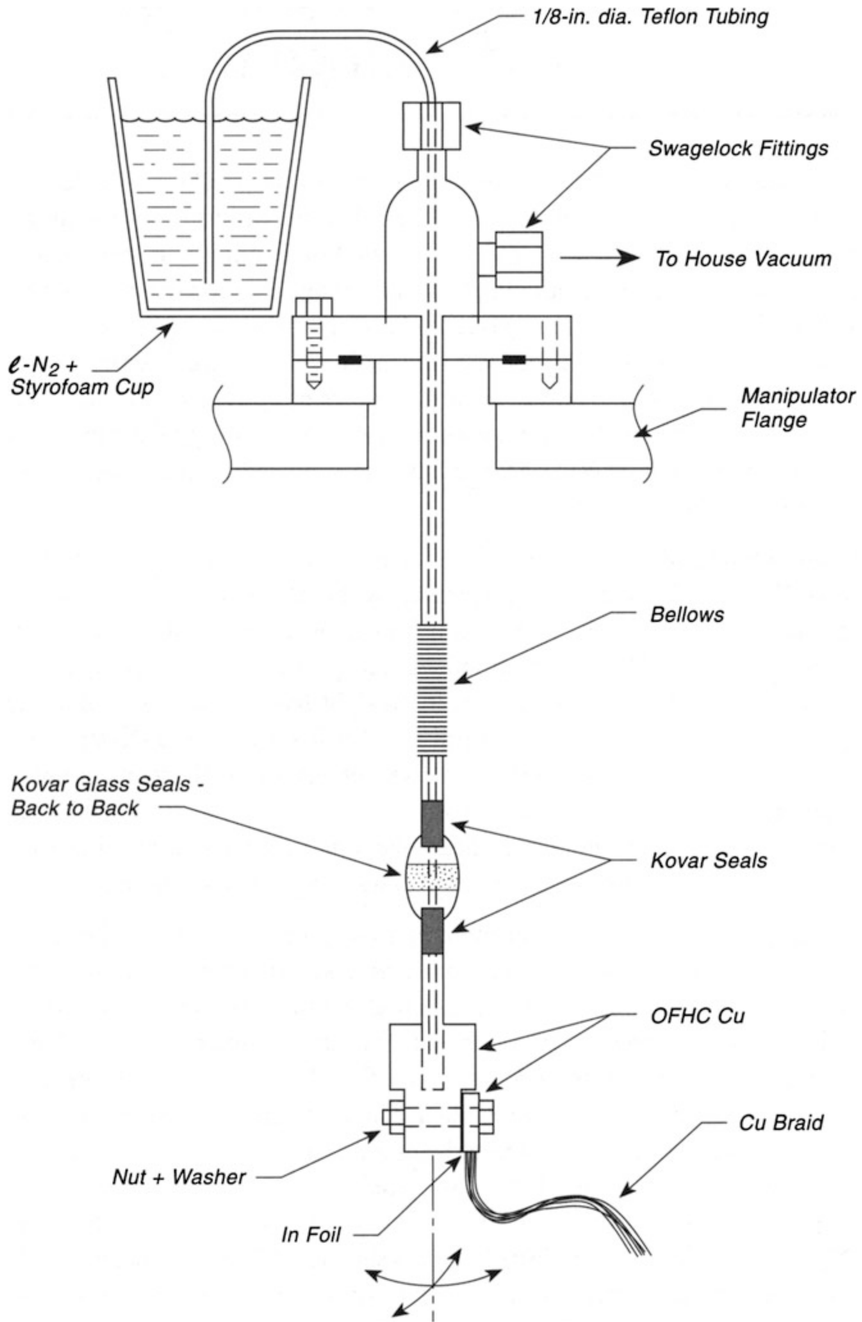

Fig. 35.10 Flexible cooling reservoir

requires heat absorption from the fluid itself, and the temperature falls as a consequence of the evaporation until the triple point (63.1 K) is reached. Thus, for work requiring temperatures slightly below that achieved using liquid nitrogen, this method is convenient. Compared to pumping liquid nitrogen to reduce its equilibrium vapor pressure and to achieve lower temperatures, this method offers the convenience of not requiring high-capacity pumps connected to manipulators by large flexible tubing, a procedure that is often mechanically complex and inconvenient.

A He bubble in equilibrium with $N_2(l)$ will contain both He and N_2, so that the partial pressure of N_2 will be less than the total pressure within the bubble. Thus as N_2 vaporizes within the bubbles, cooling will occur to reduce the temperature below the normal boiling point of $N_2(l)$. Figure 35.11a shows a demonstration apparatus where this experiment was carried out. A fritted disk bubbler was used in the right-hand Dewar flask, while the thermocouple reference junction was maintained at 77.3 K in the left-hand Dewar. After about 80 min of transpiration, solid nitrogen crystals were observed, and the temperature reached that of the triple point. When the He flow was stopped, the temperature remained stable for some minutes as the solid nitrogen melted at the triple point; heat leakage into the Dewar was responsible for this as well as for the gradual warming beyond 120 min.

Figure 35.11b shows a similar experiment in a 1.42-m column of liquid nitrogen that comprises the cooling reservoir of a reentrant stainless steel manipulator on an ultrahigh vacuum system. The temperature of a metal single crystal was measured as He bubbled into the bottom of the reservoir from the end of a 0.097-cm-diameter tube. The crystal temperature fell from 86.5 to 74 K during He flow. Stability of ±0.5 K was achieved, and excellent cooling control maybe maintained in this temperature range by adjustment of the He flow rate. Because of the limited amount of $N_2(s)$ produced at the bottom of the reservoir, interruption of the He flow produced an almost immediate rise in the crystal temperature as shown. Because of the length of the column of liquid N_2, additional liquid N_2 may be added without disturbance, as shown at the time indicated by the dots in Fig. 35.11b. This is a distinct advantage of using a long column of refrigerant where transpiration cooling occurs primarily at the bottom.

35.12 Level Alarm-Liquid Nitrogen

There are many designs for level alarms and controllers for liquid-nitrogen Dewars and Fig. 35.12 shows one of the simplest alarm devices for keeping a small supply Dewar filled [27]. A cork float senses the level of liquid nitrogen in the Dewar, and when the level drops to its lower limit, contact is made between a metal plate and an inverted metal cup at the top of the sealing cork lid. This completes the circuit, causing both an audio and a light signal to be emitted, alerting the operator to refill the Dewar through the refill funnel. The audio oscillator normally used to drive an Auger spectrometer employing a lock-in amplifier can be used.

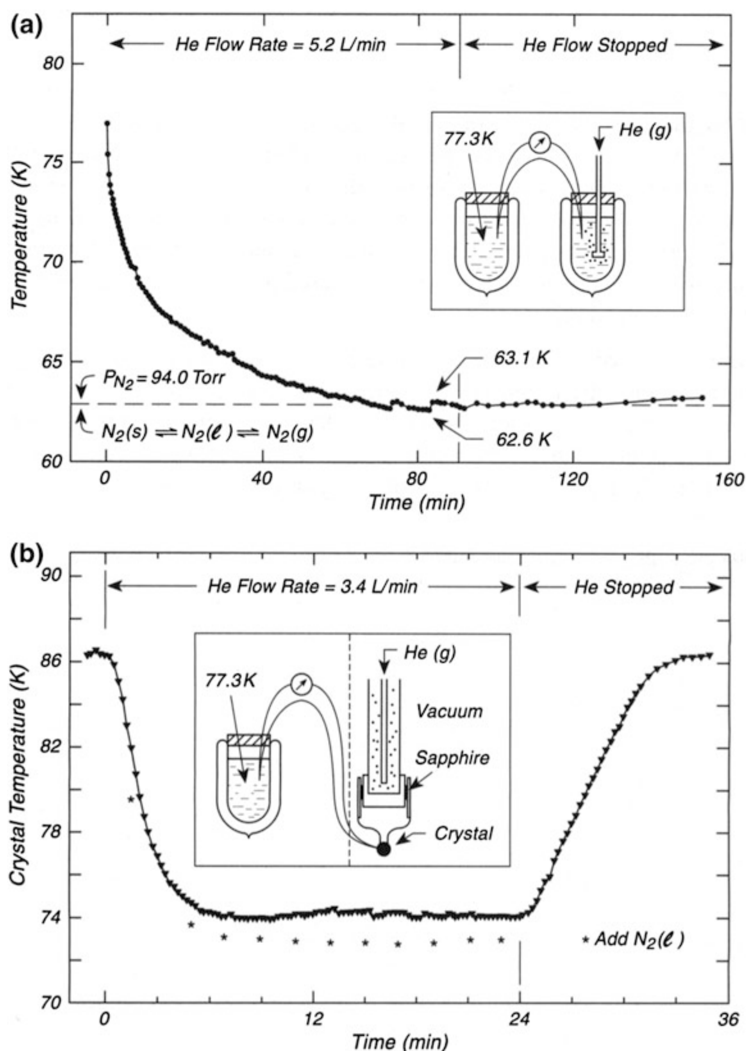

Fig. 35.11 Cryogenic trick for enhanced cooling with liquid N_2, **a** Attainment of N_2 triple point by He transpiration, **b** Cooling of metal crystal by he transpiration

The Dewar is sealed to the top of the entrance tube using cotton plus ice to make the seal. Simply wet the cotton from a plastic squeeze bottle, admit a little liquid nitrogen to freeze the water, and repair any leaks with more water on the cotton. This type of seal does not put any stress on the glass Dewar during warm-up in contrast to compression seals, which will allow the expanding metal to strain the glass Dewar bottom, sometimes resulting in breakage.

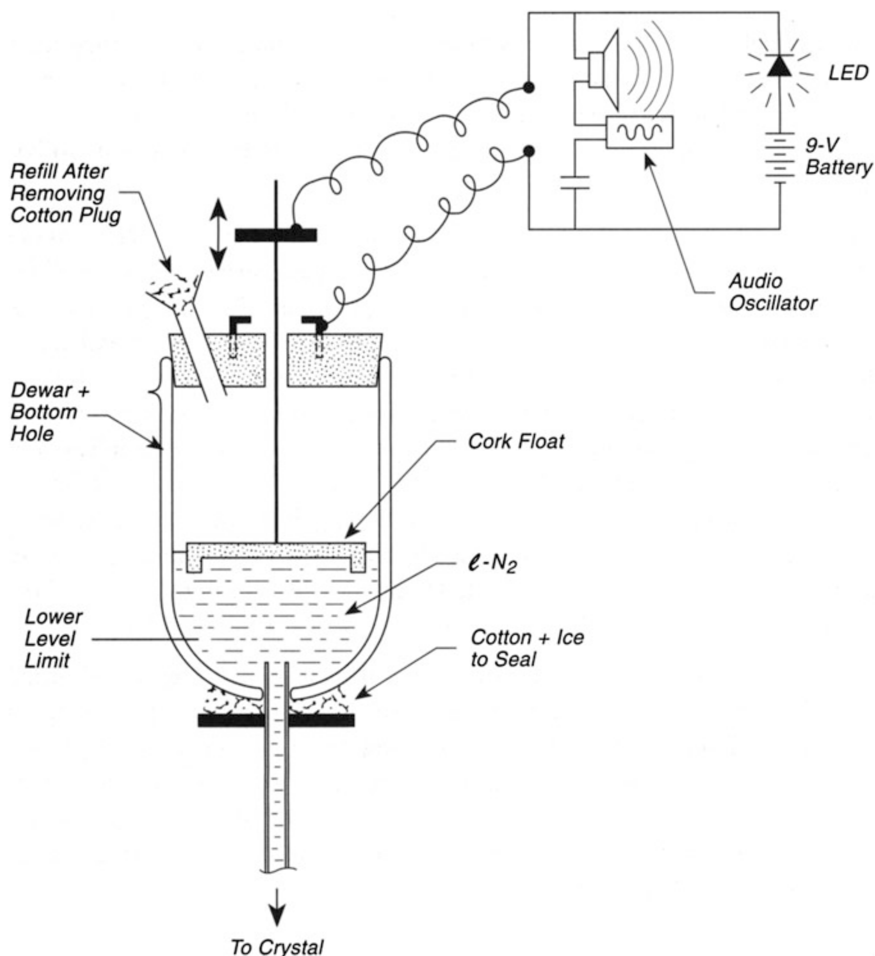

Fig. 35.12 Level alarm—liquid nitrogen

35.13 Liquid Nitrogen Reservoir—Non-leaking

For long term maintenance of liquid nitrogen in a cooled manipulator an external reservoir may be used. Shown in Fig. 35.13 is a design to attach a silvered Dewar flask to a central tube with a non-leaking seal. The central tube is evacuated through its connectivity to the vacuum system, and hence exhibits low thermal conductance to the outer wall. The Dewar is custom made to have a hole in its bottom, a few millimeters larger in diameter than the outside diameter of the central tube. Ordinary plumber's Teflon tape is generously wrapped in a conical shape around

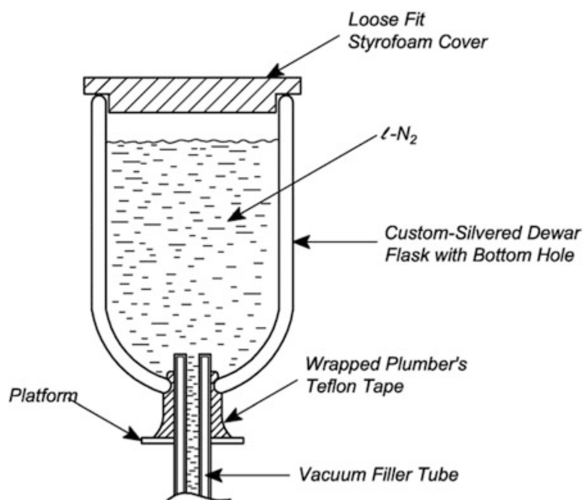

Fig. 35.13 Liquid nitrogen reservoir—non-leaking

the central tube and above the platform. The conical shape permits the Dewar to be tightly sealed to the central tube by forcing it to slightly compress the many layers of slippery Teflon tape. This makes a good seal for liquid-N_2 which normally has a low viscosity and tends to leak. Rubber seals become brittle in this application and will fail. The Dewar is fitted with a loose-fitting styrofoam cover to prevent excessive ice from forming. There may be condensation near the Teflon seal and this can be eliminated by using a small fan for drying.

35.14 Cryogenic Cooling to Below 4 K—Photon Stimulated Desorption of Adsorbed He

For studies of adsorbed He, it is necessary to cool below the boiling point of He. This is especially difficult because of the need to reduce radiation heating at the crystal to minimum values. The manipulator shown here achieves this with minimal use of liquid-He. It is designed to also raise the crystal temperature to more than 1570 K, and this has been demonstrated with Ru single crystal samples. The manipulator is immersed in a radiation shield in a liquid-N_2 bath which itself is cooled to below 77 K by pumping with a Roots blower. After heating the crystal to high temperature in UHV to clean it, liquid He is admitted to the central Dewar assembly and about 0.5 L accumulates. The inner He cryostat is then pumped with a Roots blower until the final temperature of ~ 1 K is reached, in an amazingly short time of about 20 min after the high temperature cleaning procedure. About 0.3 L of liquid He is consumed leaving 0.2 L for operation at the base temperature for about

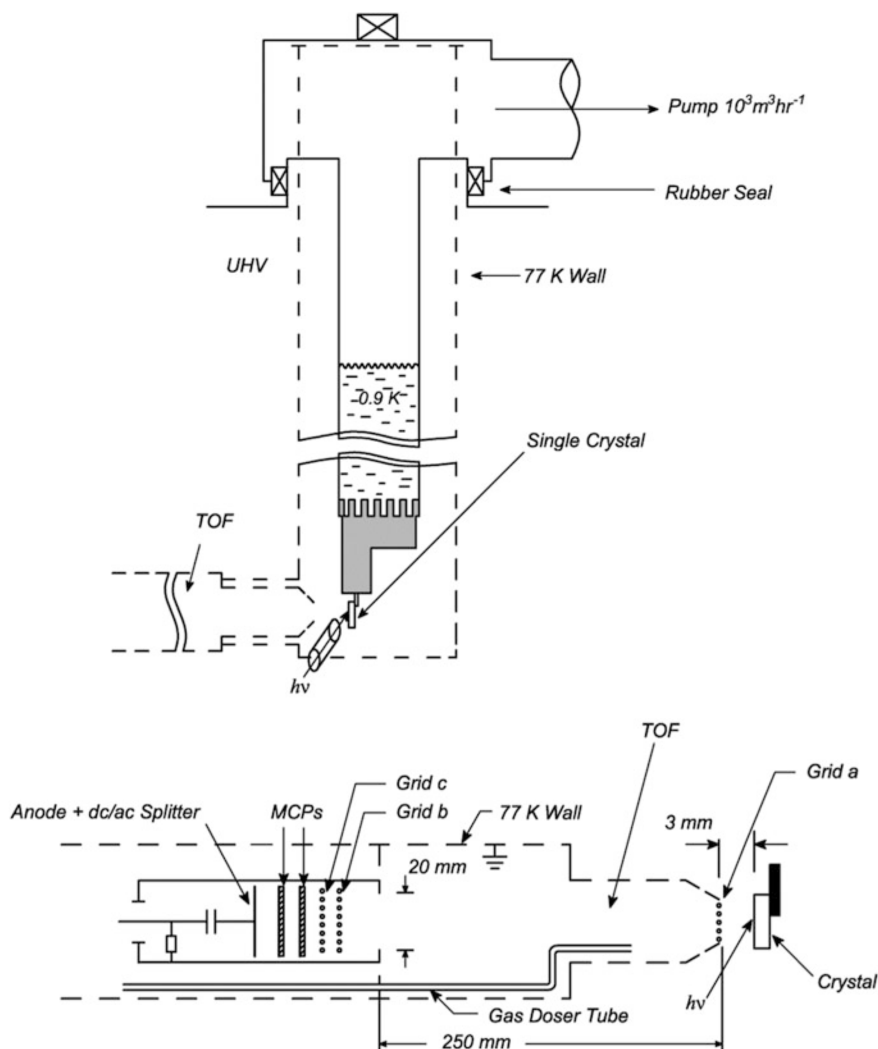

Fig. 35.14 Low temperature cryostat for He adsorption/photon desorption

4 h. Synchrotron radiation enters the cryoshield through a small aperture. Because adsorbed He on the crystal is removed by radiation from 300 K surfaces, it was necessary to design the TOF spectrometer for liquid-N_2 cooling also. The TOF spectrometer uses a pair of microchannel plates for amplification of the signal from desorbing ions and metastables, as well as for electrons emitted. It also contains a gas dosing tube for exposing the crystal to adsorbates [28] (Fig. 35.14).

35.15 Static Temperature Control by Mixing Gas Streams

Occasionally it is desirable to have accurate and steady temperature control below room temperature in an ultrahigh vacuum system, where bucking a cryogenic temperature against ohmic heating (as on a normal manipulator) is impossible. This objective can be achieved easily by having two temperature controlled gas steams which are mixed to achieve the desired intermediate temperature [29]. Using Dewar flasks filled with cryogenic fluids like liquid N_2 (77.3 K) and other systems such as dry ice/acetone (194.8 K), stable bath temperatures can be achieved. Flowing N_2 gas is brought to temperature using an immersed coiled tube in each temperature bath, T_1 and T_2. By adjusting the mixture using the two flow control valves, V_1 and V_2, stable intermediate temperatures may be achieved in a massive OFHC Cu thermal reservoir inside the UHV system through which the flowing gas circulates. To have the highest degree of fine control, gas leak valves like those used in UHV systems can be used to achieve stable gas flow conditions. Although it would be best to use cryogenic systems undergoing a phase transition for each bath to achieve the highest temperature stability, there are a number of fluid/refrigerant mixtures which are used for low temperature baths in the absence of phase transition [30] (Fig. 35.15).

35.16 Gas Thermal Switch

The ability to turn on and turn off cooling to a sample and its support may be useful in ultrahigh vacuum operations where condensation on the sample/support system must be avoided. This could be the case when the sample and its support are to be immersed in a high-pressure gas in a high-pressure vessel inside the UHV system. The design of a gas thermal switch to vary the cooling rate to a sample and its support is shown here [31].

The principle of the gas thermal switch is to use a heat transfer gas (He(g) is ideal) to conduct heat when cooling is needed, and then to evacuate the He(g) when cooling is not required. As shown in the exploded view of Fig. 35.16a, the OFHC copper cooling stage is maintained at the cryogenic temperature desired by means of contact with a reservoir of the cryogenic fluid (l-N_2 in this case). Brazed to this heat station is a concentric assembly of copper tubes. The cooling tubes nest into a set of concentric tubes connected to the OFHC copper sample holder that is thermally connected to the sample. Cooling is achieved by introducing about 0.5 Torr of He(g) into the 10-cm^3 volume containing the thermal switch. The cooling is interrupted by pumping the He(g) away. Given the geometry of the thermal switch (not exactly specified in the paper), the thermal conductivity varies between about

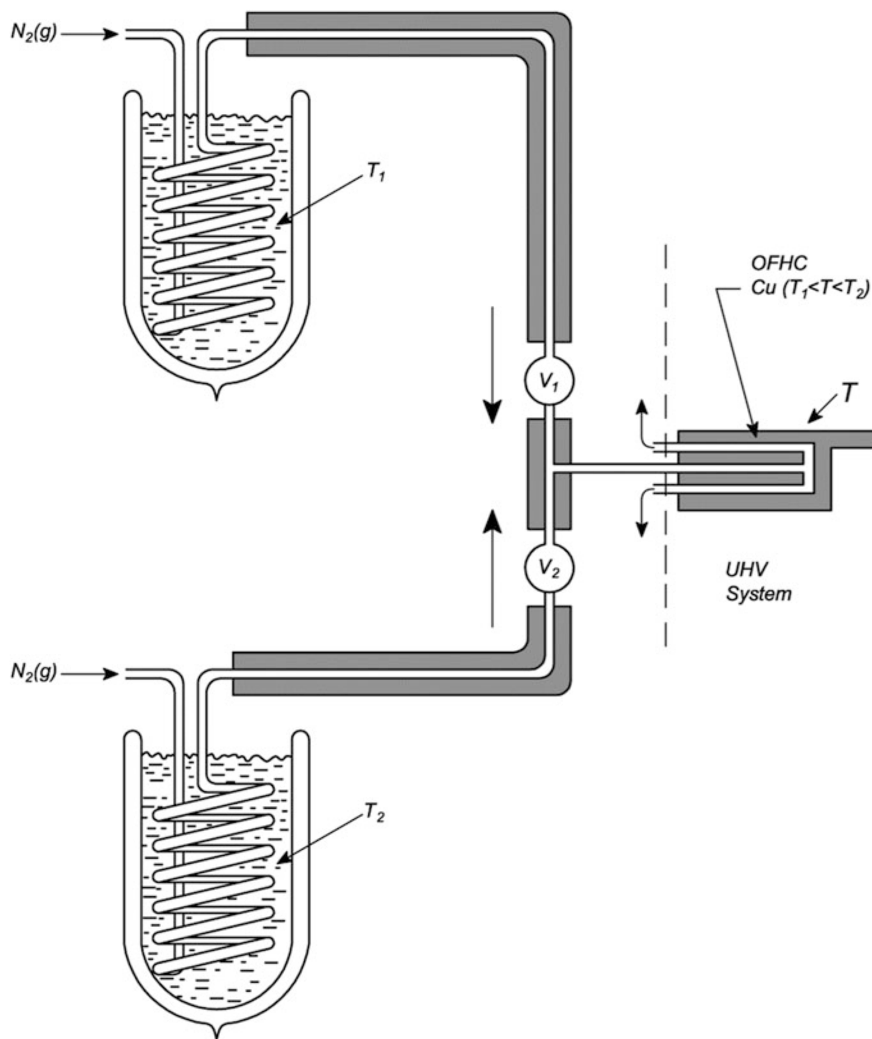

Fig. 35.15 Static temperature control by mixing gas streams

0.8 and 1.4 W/K with He(g) as a heat transfer medium to about 0.03 W/K with a vacuum of $<5 \times 10^{-3}$ Torr, which is achieved in 10-s pumping time.

Figure 35.16b shows the performance of the gas thermal switch. He(g) is admitted with the sample at 300 K and the cooling station at 100 K. Cooling starts immediately with a time constant of about 2 min; after some cooling, the He(g) is

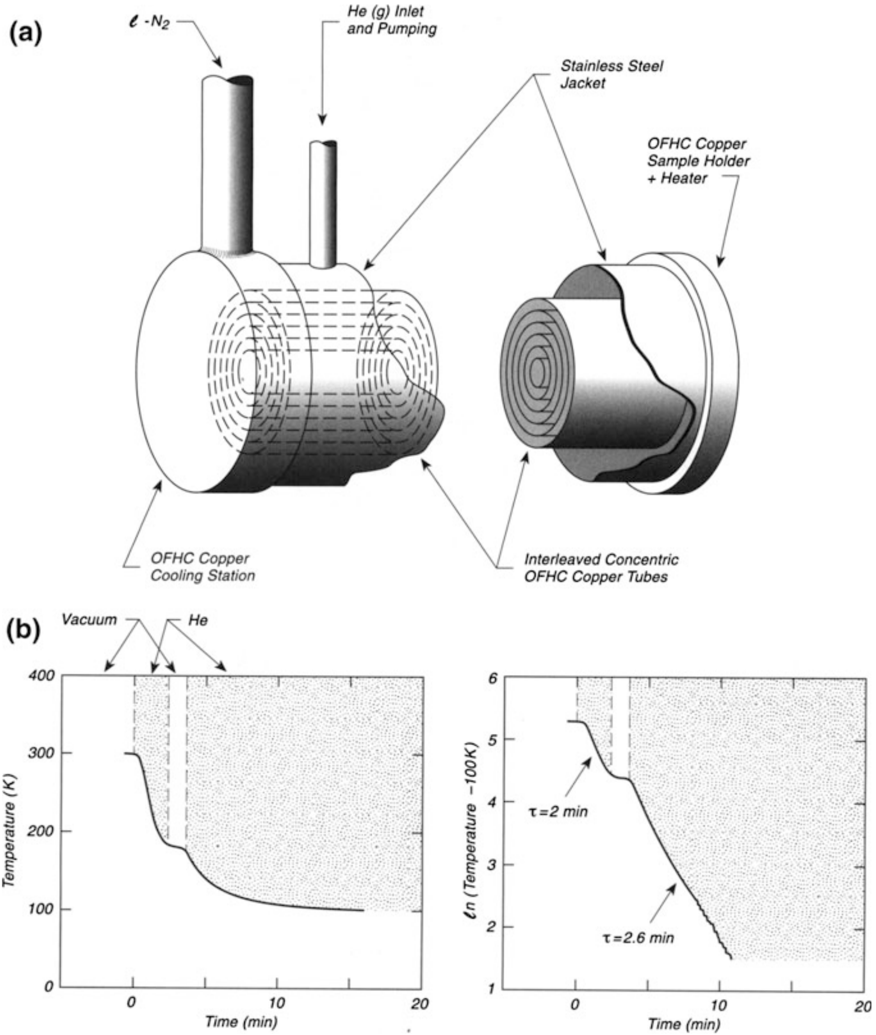

Fig. 35.16 Gas thermal switch. **a** Thermal switch—exploded view. **b** Cooling performance using vacuum and He(g)

evacuated, and cooling slows. Then He(g) is reintroduced, and cooling occurs with a time constant of about 2.6 min. The decrease in cooling rate in the second stage of cooling may be due to the decrease in the thermal conductivity of He as its temperature falls. Cooling to about 102 K is achieved in less than 10 min.

References

1. H. Schlichting, D. Menzel, Rev. Sci. Instrum. **64**, 2013 (1993)
2. Constant flow cryostat, Air Products, APD-Cryogenics, P.O. Box 2802, Allentown, PA 18105
3. H. Schlichting (private communication)
4. K. Wandelt, S. Daiser, R. Miranda, H.-J. Forth, J. Phys. **E17**, 22 (1984)
5. A. Winkler, M. Hausenblas, M. Leisch, K. Rendulic, Vacuum **40**, 39 (1990)
6. M. Milun, P. Pervan, T. Valla, P. Dukic, Rev. Sci. Instrum. **62**, 3116 (1991)
7. J. Yoshinobu, H. Ogasawara, M. Kawai, Surf. Sci. **360**, 234 (1996)
8. S. Masuda, Department of Chemistry, College of Arts and Sciences, The University of Tokyo, Komaba, Meguro-ku, Tokyo 153, Japan
9. A. Winkler, M. Hausenblas, M. Leisch, K.D. Rendulic, Vacuum **40**, 39 (1990)
10. C. Rusu, J.T. Yates Jr, J. Vac. Sci. Technol. **A15**, 436 (1997)
11. D.J. Frankel, B. Fruhberger, R.H. Jackson, D.J. Dwyer, Rev. Sci. Instrum. **64**, 2368 (1993)
12. Model 0522, Gast Manufacturing Corp., P.O. Box 97, Benton Harbor, MI 49023-0097
13. P.G. Strupp, P.C. Stair, J. Vac. Sci. Technol. **A9**, 2410 (1991)
14. Catalog No. 97-216. The springs are obtainable from Instrument Specialties Co., P.O. Box A, Delaware Water Gap, PA 18327. These springs make good mechanical and thermal contact and permit dimensional changes due to differing thermal expansion coefficients of the sapphire and the Cu-Be alloy
15. I.M. Vitomirov, C.M. Aldao, G.D. Waddill, J.H. Weaver, J. Vac. Sci. Technol. **A8**, 3368 (1990)
16. E.E. Chaban, Y.J. Chabal, Rev. Sci. Instrum. **54**, 1031 (1983)
17. G.L. Fowler, J. Vac. Sci. Technol. **A9**, 360 (1991)
18. A. Winkler, M. Hausenblas, M. Leisch, K.D. Rendulic, Vacuum **40**, 39 (1990)
19. Dr. R. David, Institut fur Grenzflächenforschung und Vakuumphysik, Forschungszentrum Jülich GmbH, Postfach 1913, D-52425 Jülich, Germany (private communication). See also R. David et al, Rev. of Sci. Instrum. **57**, 2771 (1986)
20. Detailed procedures for the preparation and welding of Cu braid are presented in the literature. See G.L. Fowler, J. Vac. Sci. Technol. **A5**, 2976 (1987)
21. E.E. Chaban, R.H. Citrin, F. Sette, J. Vac. Sci. Technol. **A6**, 3018 (1988)
22. V.K.F. Chia, D.K. Veirs, G.M. Rosenblatt, J. Vac. Sci. Technol. **A7**, 108 (1989)
23. Cryomech GB-220: Cryomech, Inc., 1630 Erie Boulevard E., Syracuse, NY 13210
24. G.L. Fowler, J. Vac. Sci. Technol. **A5**, 2976 (1987)
25. Dr. L.H. Dubois, DARPA/DSO, 3701 N. Fairfax Dr., Arlington, VA 22203-1714 (private communication)
26. J. Xu, H.J. Jansch, J.T. Yates Jr, J. Vac. Sci. Technol. **A11**, 726 (1993)
27. Dr. X.-C. Guo, Department of Chemical Engineering, Stanford University, Stanford, CA 94305-5025 (private communication)
28. P. Feulner, private communication from thesis of Sarah Kossler, U. Munich
29. W. Lew, O. Lytken, J.A. Farmer, M.C. Crowe, C.T. Campbell, Rev. Sci. Instrum. **81**, 024102 (2010)
30. A.J. Gordon, R.A. Ford, *The Chemist's Companion* (Wiley, New York, 1972), pp. 451–452
31. O. Sneh, S.M. George, J. Vac. Sci. Technol. **A13**, 493 (1995)

Chapter 36
Temperature Measurements

36.1 Tungsten-Rhenium Thermocouples—Calibration Over a Wide Temperature Range

Tungsten/rhenium thermocouples are often used in ultrahigh vacuum because this class of thermocouples can go to higher temperatures than all other thermocouple alloys [1]. Such thermocouples avoid sample contamination effects owing to metal vaporization, which is common for other thermocouples near the high-temperature end of their operating range. Unfortunately, a factory calibration of tungsten/rhenium thermocouples is not available below 255 K [1], although two calibrations in the range 77–300 K [2], and in the range 4–77 K [3] are published for W/5 % Re versus W/26 % Re thermocouples. The calibration data from the three sources have been brought together into a single master calibration that extends from either 4 or 32 to 2588 K [4]. The reader is referred to the original paper [4] for calibration tables and for full consideration of the errors present in the master calibration [4]. It should be noted that the variation of thermocouple alloy composition from batch to batch may cause larger errors in the temperature regions not covered by the factory calibration than in those temperature regions which are reported by the manufacturer.

Figure 36.1a shows the master calibration curve from 4 to 2588 K, using data from the three sources. This curve is not plotted at high enough resolution to be useful. A tenth-order polynomial function has been fitted to the data, and the function is given in [4], as well as at the end of this discussion. The difference between the calibration data and the tenth order function is plotted in Fig. 36.1b, showing that differences are always less than 7 K except for the very low

© Springer International Publishing Switzerland 2015

J.T. Yates Jr., *Experimental Innovations in Surface Science*,
DOI 10.1007/978-3-319-17668-0_36

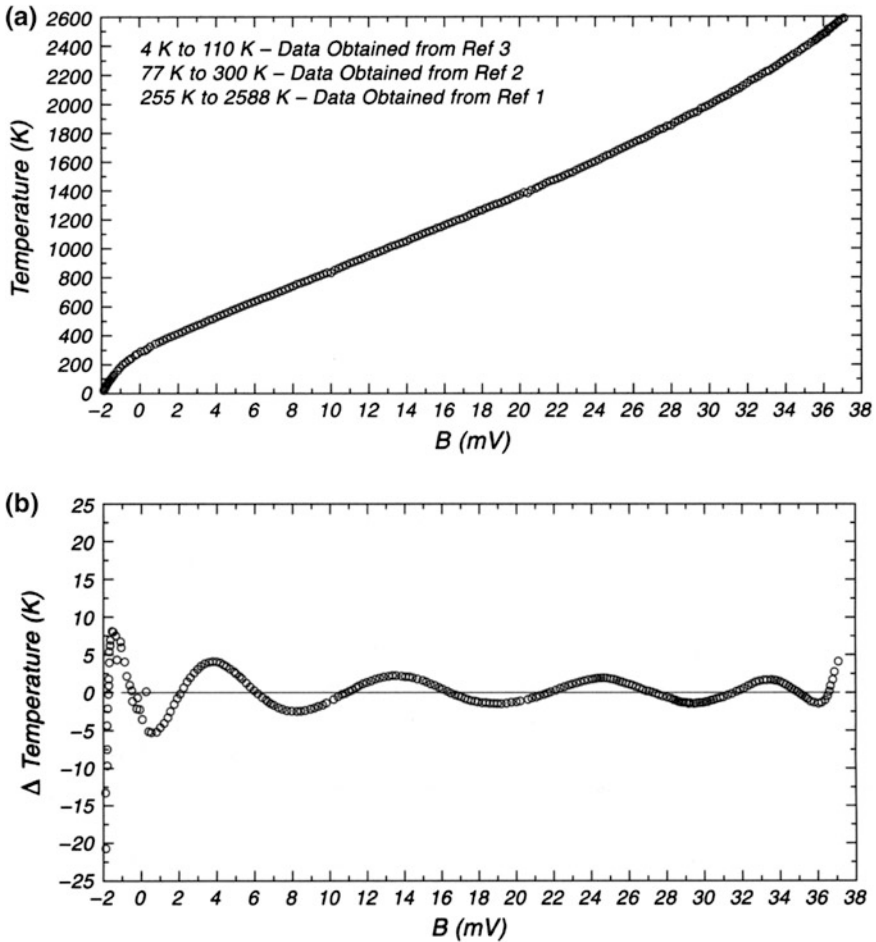

Fig. 36.1 Tungsten-rhenium thermocouples—calibration over a wide temperature range. **a** Temperature versus potential, W/26 % Re versus W/5 % Re Thermocouple. **b** Difference plot (Measured-Calculated) for thermocouple—4 to 2588 K

temperature region. The maximum difference above 800 K is near 2 K. For temperatures below 32 K, it is advisable to use the calibration in [3], which is exclusively concerned with this temperature range. The fitting curve of [3] cannot be extrapolated with accuracy above 32 K.

The power series for the range 4–2588 K is given below, and tabular solutions to this equation are given in [4] at intervals of 0.05 or 0.10 mV.

Table 36.1 Power series for the range 4–2588 K and solutions

$T = \Sigma C_n B^n$	
$C_0 = 276.5327901$	$C_6 = -4.147285358 \times 10^{-3}$
$C_1 = 83.31475475$	$C_7 = 1.529502993 \times 10^{-4}$
$C_2 = -15.19381797$	$C_8 = -3.422732361 \times 10^{-6}$
$C_3 = 4.431847913$	$C_9 = 4.253729476 \times 10^{-8}$
$C_4 = -0.7258516658$	$C_{10} = -2.351967817 \times 10^{-10}$
$C_5 = 0.06999557967$	

An extension of the calibration up to 3273 K has been reported [5].

36.2 Measuring Temperatures of Hot Filaments

The temperature of an electrically heated hot filament may be accurately measured by using it as a resistance thermometer. By determining its resistance compared to its resistance at a known temperature, quite accurate temperatures may be measured and maintained.

Figure 36.2a shows a metal filament containing potential leads across the central third of the filament. The filament is mounted on degassing loops to prevent outgassing effects during heating as described on p. 437. A known current, I, measured to about four significant figures with a digital ammeter, is passed through the filament using a current-regulated DC power supply. The electrical potential drop, V_c, across the central third of the filament, is simultaneously recorded to about four significant figures, using a digital voltmeter. The resistance of the central section of the filament is calculated from Ohm's law, $R_c = V_c/I$, and also the power dissipation from the central section of the filament is calculated, $P_c = IV_c$. If R_c is known at some standard temperature, T_s, and if the resistivity, ρ, of the filament material is known as a function of temperature (Tables for tungsten are readily available in handbooks), then the temperature of the center section of the filament maybe calculated from the ratio $R_c(T)/R_c(T_s) = \rho(T)/p(T_s)$, where T is the unknown. In practice, more accurate maintenance of temperature maybe achieved if P_c is monitored continuously rather than R_c. Typically, from day to day, P_c may be readjusted to match its previous values very accurately, assuring that the original temperature is reestablished. However, in practice, because of slow warming effects in the support system that have a minor effect on T_c, the measured value of P_c will drift slightly for some minutes until stability of the hot filament temperature is achieved.

There is one special point that must be emphasized for the most accurate measurements. The potential leads should conduct as little heat as possible away from the center section of the filament. To assure that this is the case, it is wise to etch the potential leads electrochemically to a diameter that is as small as possible, thereby limiting their thermal conductivity. For a well-made system, heating at

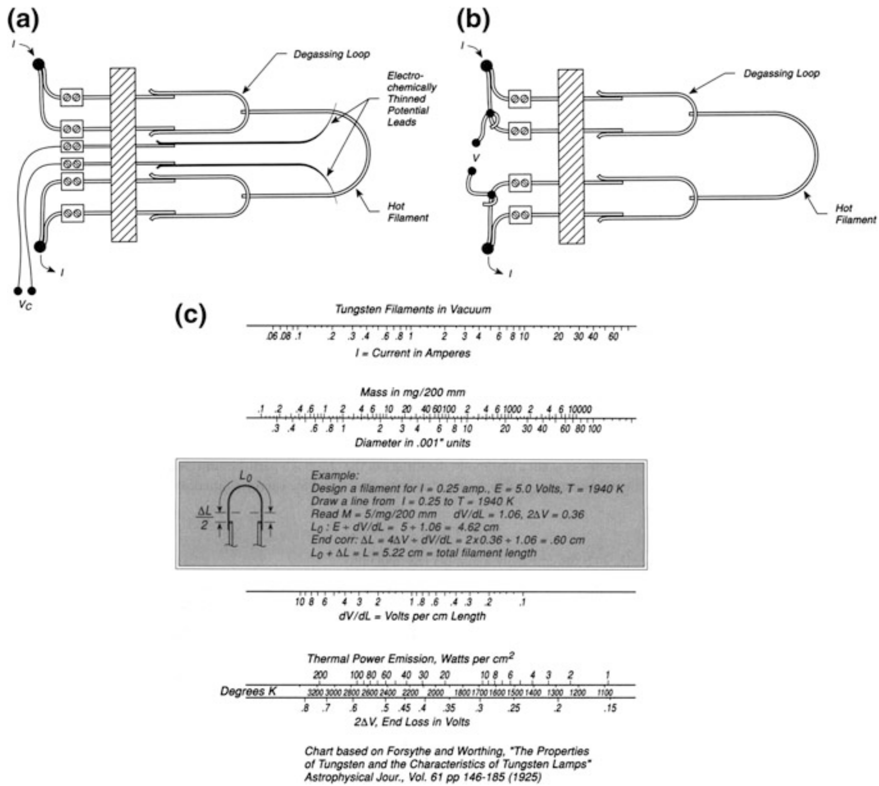

Fig. 36.2 Measuring temperatures of hot filaments. **a** Inner-potential leads. **b** Outer-potential leads. **c** Nomograph for design of tungsten wire heaters

incandescence will display no optically detectable temperature gradient in the vicinity of the welds of the thinned potential leads to the central section of the filament. However, there will be a gradient of temperature at the welds connecting the filament to the current leads, but the temperature measurement based on the central section of the filament is made far from this region.

For work that does not require extremely high accuracy or reproducibility, one may connect the potential leads outside the vacuum system, as in Fig. 36.2b, making similar measurements as described above. Here, the resistivity ratios will not accurately correspond to the filament temperature ratios because the filament temperature gradient, as well as the resistance of the mounting leads, is being sampled. In practice, measurements made in this fashion are best used to establish the same filament temperature from day to day, and this may be done with surprisingly high accuracy. The potential leads should be hard-soldered to the input current leads in order to avoid the effect of having variable contact points as would occur using clip leads.

One problem that can arise in the use of high-temperature filaments is the evaporation of the filament material, causing the diameter of the filament to decrease, upsetting the temperature calibrations. In addition, filaments containing attached pieces of evaporant material can change resistance over time due to this effect as well as to alloying effects.

A useful nomograph for estimating the power requirements needed to heat tungsten filaments of various diameters is shown in Fig. 36.2c. To determine heating parameters, a straight edge is used across the chart. The example shown in the center of Fig. 36.2c is a guide to tungsten wire heater design, including corrections for tungsten wire cooling at the ends welded to the feedthrough leads.

36.3 Pyrometric Measurement of Temperatures

The measurement of the brightness temperature of a hot object can be carried out with an optical pyrometer working at a particular wavelength, λ. Often optical filters in the pyrometer are used to define λ. Planck's law for a perfect blackbody emitting radiation energy, $W_b(\lambda, T)$, is

$$W_b(\lambda, T) = \left[2\pi hc^2/\lambda^5\right] / [\exp(hc/\lambda kT) - 1] \tag{36.1}$$

where T is the true temperature of the blackbody, c = speed of light, k = Boltzmann's constant, and h = Planck's constant. Since in (36.1), $hc/\lambda kT \gg 1$,

$$W_b(\lambda, T) = \left[2\pi hc^2/\lambda^5\right] \exp(-hc/\lambda kT) \tag{36.2}$$

When an object is not a blackbody, the surface of the object is a partial inward reflector of the radiant energy being emitted from the object, and the energy emitted, $W_n(\lambda, T)$, is

$$W_n(\lambda, T) = W_b(\lambda, T) \cdot \varepsilon(\lambda, T) \tag{36.3}$$

where $\varepsilon(\lambda, T)$ is the emissivity, a number less than unity.

In pyrometers of the disappearing-filament type, a tungsten filament, acting as a black-body, is compared with that of the hot sample by observing a superposition of the hot filament on the hot sample and then finding the pyrometer filament temperature where it becomes invisible against the image of the hot sample. This method is very sensitive, and a skilled operator, working in a darkened room with dark-adapted eyes, can make comparisons to within a few degrees K. Figure 36.3a shows the image seen through the eyepiece of a disappearing filament pyrometer. The equal-temperature point should be approached alternately from the low-temperature side and from the high-temperature side, and the readings from

both directions should be averaged to determine the brightness temperature of the sample.

In the case where the filament and sample brightness temperatures are identical, then

$$W_b(\lambda, T_{pyro}) = W_b(\lambda, T_{sample}) \cdot \varepsilon(\lambda, T) \cdot (1 - R)^2 \tag{36.4}$$

where R is the reflectivity of each surface of the window material through which the measurement is being made. R is given by

$$R = (n - 1)^2/(n + 1)^2 \tag{36.5}$$

where n = the refractive index of the window material at λ.

Using (36.2) and (36.3), and solving for T_{pyro}, one obtains

$$T_{pyro} = T_{sample} \Big/ \left\{ \left[1 - \lambda k T_{sample}/hc\right] \left[\ln \varepsilon (l - R)^2\right] \right\} \tag{36.6}$$

Both the emissivity, ε, and the window surface reflectivity, R, may be determined as correction factors for T_{sample}, as shown below.

For the emissivity, an experimentally determined number that is a specific property of the material being measured must be used. Tabulations of the emissivities for various metals are given in [6], as well as convenient correction plots to directly convert the brightness temperature to the true temperature for various emissivities.

For the particular case of Si at λ = 0.65 μm, the emissivity was measured separately by Allen [7] and by Sato [8]. Their data are fit by the following equation [9] in the temperature range 540–1700 K.

$$\varepsilon(0.65\,\mu\text{m}, T) = 0.4826 - 2.09 \times 10^{-5} T + 0.1583/\{1 + \exp[(T - 1410)/112.9]\} \tag{36.7}$$

Figure 36.3b shows the fit of the empirical (36.7) to the data. The relationship between T_{pyro} and $T_{silicon}$ can be calculated using (36.6) with values of R and ε(0.65 μm, T) calculated from (36.5) and (36.7), respectively. In the case of glass windows, the refractive index for 0.65 μm light is 1.46, and R = 0.035.

Figure 36.3c shows the deviation between the measured brightness temperature with the pyrometer at 0.65 μm, and the true temperature for Si, viewing through a glass window.

Similar considerations apply for pyrometric measurements made by electronic methods in the infrared region, as is common for studies of semiconductor materials, except that a specific emissivity will apply for the particular material and the wavelength of light employed.

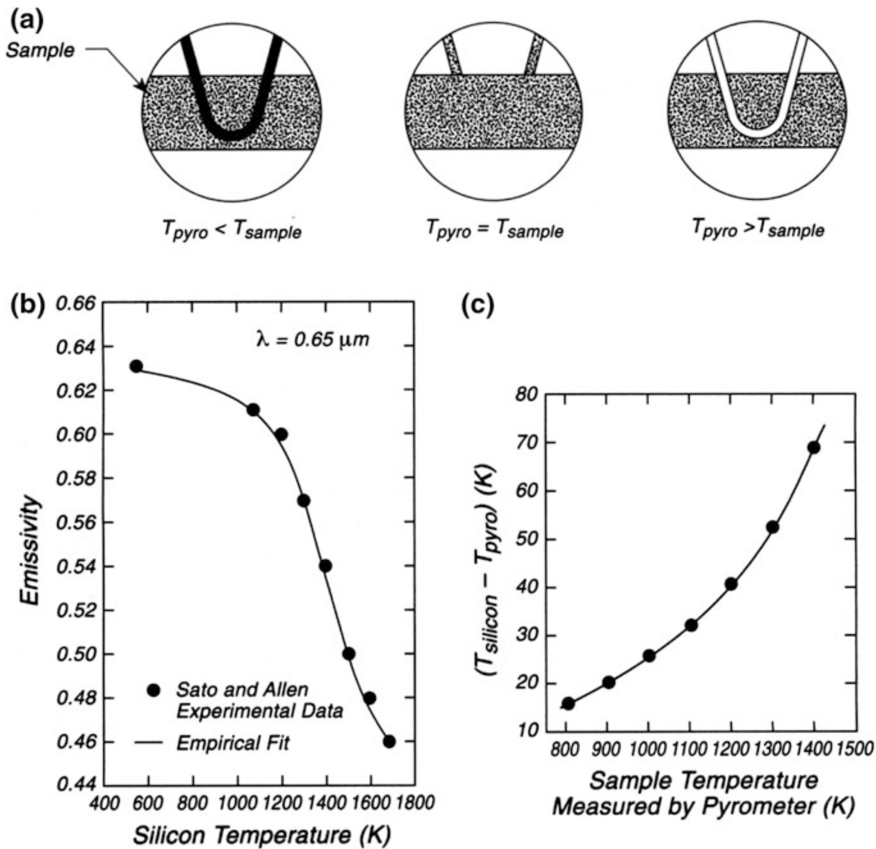

Fig. 36.3 Pyrometric measurement of temperatures. **a** Disappearing filament pyrometer—visual. **b** Si emissivity versus temperature. **c** Emissivity corrections to brightness temperature

36.4 Pyrometer Measurements Through Windows Coated Inadvertently with Variable-Thickness Thin Films

The deposition of a thin film on an optical window can cause a negative error in optical pyrometer readings, which will increase with the thickness of the deposited film. In order to avoid this effect, an empirical method has been developed and tested against thermocouple readings on a hot sample [1].

Figure 36.4a shows the basic principle of the method. A movable ionization gauge having an emission regulated thermionic emitter is used as a standard. The temperature of the emitter should remain constant in good vacuum for a standard constant emission current that is set into the controller. When the window is first installed, and when it is free of any thin film deposit, the brightness temperature of the thermionic emitter is measured as a function of the emissivity setting on the

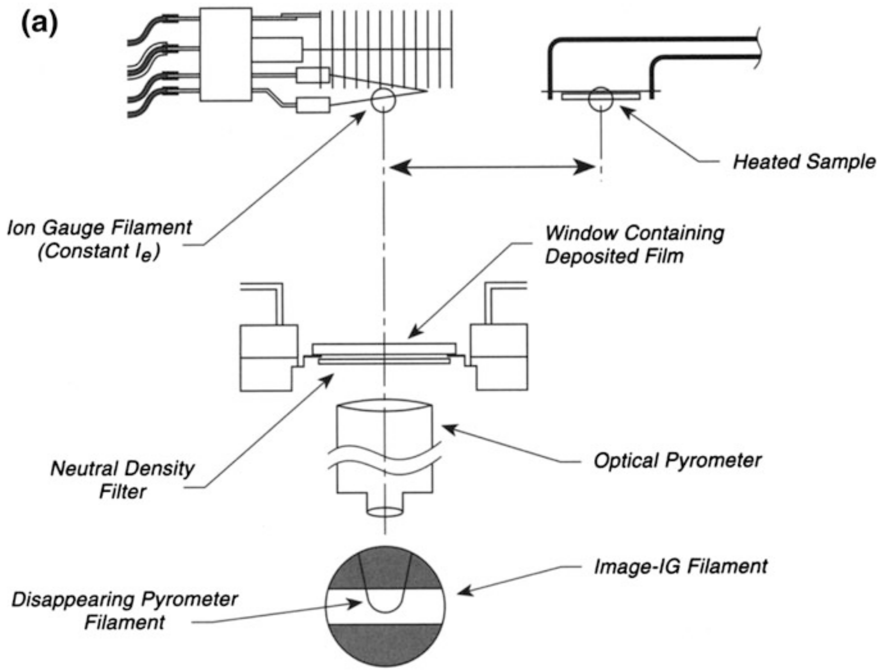

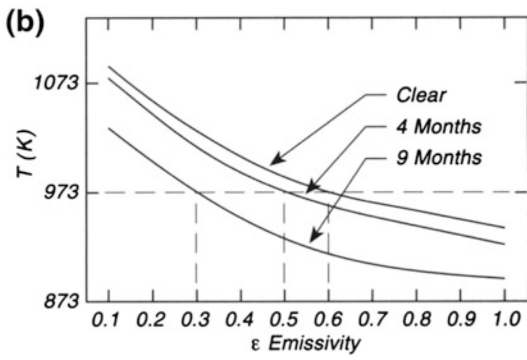

Fig. 36.4 Use of standard filament to calibrate pyrometer through film-coated windows. **a** Ion Gauge pyrometry standard. **b** Typical temperature versus emissivity setting for various window film deposits

pyrometer, and a curve like that of Fig. 36.4b (clear) is constructed. As the window becomes coated with an inadvertent thin film deposit, the brightness temperature of the thermionic emitter filament versus the emissivity setting will decrease, as shown for various time periods in Fig. 36.4b after the thin film has grown to various thicknesses. For any temperature, an emissivity setting returning the filament brightness temperature to the same value can be determined, as shown for example

for a brightness temperature of 973 K (dotted line), where emissivity settings of 0.6, 0.5, and 0.3 are needed to bring the pyrometer back to the standard temperature of 973 K. This same emissivity setting is then used when the sample temperature is being studied in the position of the thermionic emitter.

The pyrometer must, of course, be calibrated accurately in the absence of any thin film deposit. Both thermocouple and phase transformation information may be used for this purpose, or in the case of materials with known emissivities, tables of emissivity versus temperature may be used to make the correction from brightness temperature to true temperature. If the sample temperature is considerably lower than the ion gauge filament temperature, it will be necessary to employ an interposed neutral density filter for the thermionic emitter measurements, as shown in Fig. 36.4a. Because the thermionic emitter operates at about 1500 K, a neutral density filter is needed if measurements of sample temperatures considerably below this temperature are needed. In the example given, a neutral filter of optical density 2.0 (10^{-2} transmission) is needed to reduce the apparent filament temperature to about 1000 K for an emissivity setting of 0.6.

Separate calibrations using a clean window that did not become coated with the thin film verified that this procedure was accurate and that the thermionic emitter temperature was constant over a long time [1]. In the case shown here, an IRCON Model 2000 pyrometer, working in the range 0.7 mm–1.05 µm, was employed [10].

36.5 Calibration Point for Optical Pyrometer Used for Silicon

The provision of a calibration point for silicon at high temperatures for optical pyrometers may be useful in certain situations. A method developed for doing this in rapid wafer thermal processors [11] can be extended to other situations in the laboratory.

In Fig. 36.5, a silicon wafer, 0.3 mm thick, and covered by a 5000-Å-thick SiO_2 film, is coated with a 4000-Å Ge film, and then overcoated with a protective 1000-Å Si_3N_4 film. This sandwich structure serves as a useful calibration standard. The optical reflectivity of Ge at 0.6328 µm changes from 49 % just before semiconducting Ge melts to 72 % for melted Ge, which behaves with metallic properties. The melting point of Ge is 938 °C, and melting can be viewed through the Si_3N_4 overlayer. As shown in Fig. 36.5a, the sandwich test structure contains a K type thermocouple embedded in the backside of the silicon wafer, and an optical pyrometer to be calibrated at the melting point of Ge. A chopped laser beam is reflected off of the Ge sandwich face, and the reflectivity of the surface is measured as the temperature is raised, using external radiation for heating the wafer. Figure 36.5b shows the result. At a thermocouple temperature of 938 °C, a sharp

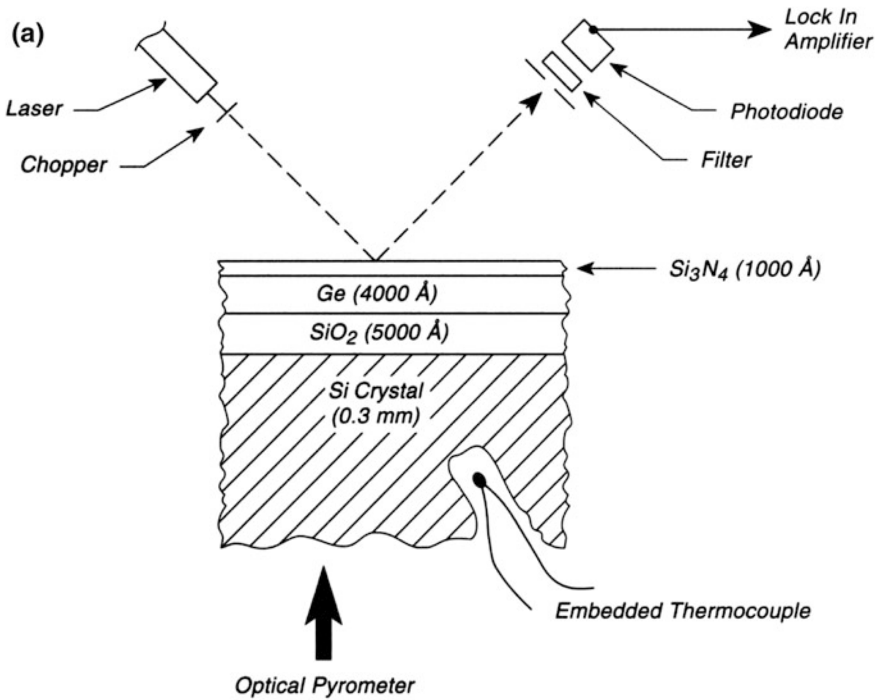

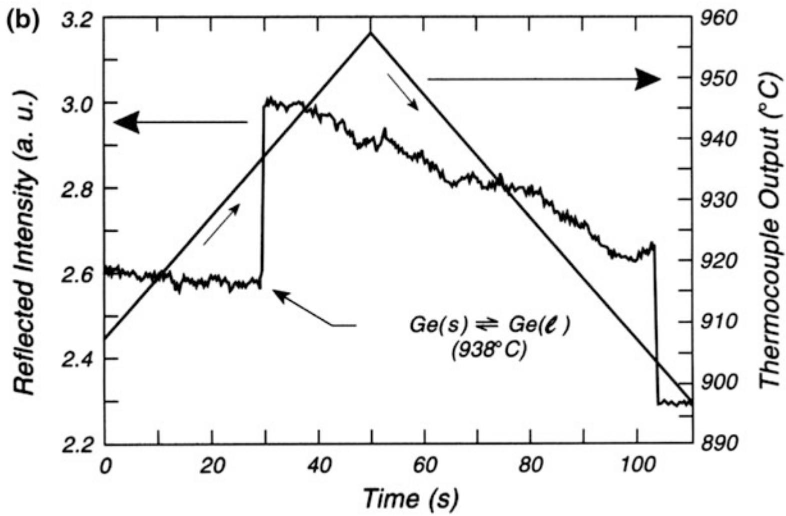

Fig. 36.5 Pyrometer calibration at fixed point for Silicon. **a** Ge/Si test structure. **b** Reflectivity changes at 0.6328 μm

increase in the reflectivity is observed, followed by a gradual decrease as the temperature continues to rise. On slowly cooling the wafer, the freezing point of the Ge is observed to be depressed to about 904 °C as a result of supercooling of the liquid Ge. The melting point of Ge was found to be reproducible to ±1° at 938 °C in ten measurements. It was shown that the thermal gradient through the Si crystal was about 2.5 °C/mm at the melting point of the Ge. These Ge sandwich structures can therefore be used periodically to calibrate the optical pyrometer emissivity setting (see p. 409).

36.6 Control of Silicon Temperature Using Resistivity

Both thermocouples and pyrometers are used to measure and control the temperature of silicon crystals during electrical heating. As discussed elsewhere (p. 548), the use of thermocouples for this purpose often produces metal contamination of the silicon crystal. A method is described here involving the measurement of the electrical resistance of the crystal during heating and cooling in order to determine and control the temperature. For purposes of evaluation of the resistance method, the crystal used in these measurements contains a W/26 % Re:W/5 % Re thermocouple which has a ball end buried inside a laser-drilled hole in the crystal and held in place with a MgO cement (Aremco 571P) [12].

The crystal is mounted on a Ta holder as shown in Fig. 34.5a, p. 358. The crystal dimensions are 9.5 × 3 × 0.3 mm^3. The silicon is P type, 100 Ω cm, boron doped. The resistance of the crystal was calculated using voltage and current measurements made during heating. Comparisons to the thermocouple and to an optical and an IR pyrometer are described in the original paper [12]. Figure 36.6a shows the dependence of the logarithm of the measured resistance versus 1/T. Above about 600 K, the expected linear relationship is observed, where the dominant intrinsic conductivity of the silicon exists. Below 600 K, the dominating conductivity is due to the dopants for this particular crystal. The slope in the linear region corresponds to the quantity $E_G/2k_BT$, and the best value of E_G (the silicon band gap) for this crystal was measured to be in the range 1.22 to 1.25 ± 0.05 eV, in good agreement with literature values of 1.170–1.205 eV [13–15].

Figure 36.6b shows the type of temperature control that may be achieved using the resistance and comparing to the temperature measured directly with the thermocouple. A programmed temperature ramp of 3 K/s, interrupted by a constant temperature period, and then a cooling ramp of −3 K/s are shown. The solid line represents the temperature measured with the thermocouple, and the dotted line with the silicon resistance. Good agreement is found with a maximum deviation of 20 at 1150 K. Control was carried out using LabVIEW [16], which is described on p. 351.

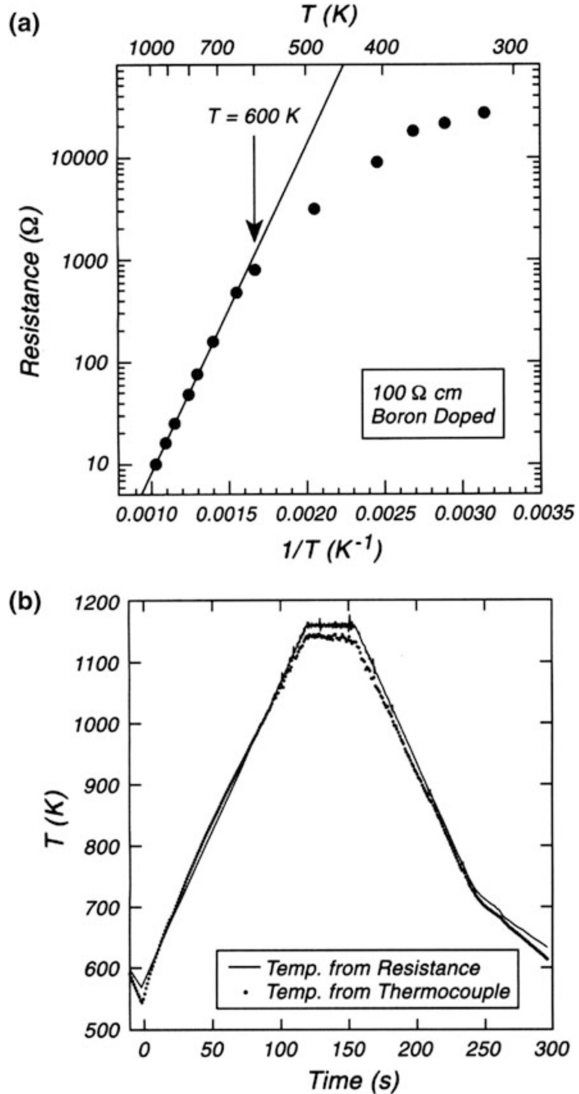

Fig. 36.6 Control of Silicon temperature using resistivity. **a** Dependence of Log R versus inverse temperature of Si(100) crystal. **b** Temperature programmed heating and cooling of Si (100)

The method must be calibrated against a standard at one or more points. This may be done best using a pyrometer and comparing the resistance with the corrected pyrometer reading (see p. 409). It would be better to do the calibration against the pyrometer at several points in the intrinsic region in order to make the best calibration, although the knowledge of the bandgap permits single point calibration [12].

References

1. *The Omega Complete Temperature Measurement Handbook and Encyclopedia* (Omega Engineering, Inc., Stamford, CT, 1989), pp. z8–z28
2. D.R. Sandstrom, S.P. Withrow, J. Vac. Sci. Technol. **14**, 748 (1977)
3. W.J. Mitchell, J. Xie, W.H. Weinberg, J. Vac. Sci. Technol. **A11**, 3133 (1993)
4. V.S. Smentkowski, J.T. Yates Jr, J. Vac. Sci. Technol. **A14**, 260 (1996)
5. R.R. Asamoto, P.E. Novak, Rev. Sci. Instrum. **38**, 1047 (1967)
6. C.J. Smithells, E.A. Brandes (eds.), *Metals Reference Book*, 7th edn (Butterworths, London and Boston, 1991)
7. E.G. Allen, J. Appl. Phys. **28**, 1510 (1957)
8. T. Sato, Jap. J. Appl. Phys. **6**, 339 (1967)
9. H. Nishino, W. Yang, Z. Dohnalek, V.A. Ukraintsev, W.J. Choyke, J.T. Yates Jr, J. Vac. Sci. Technol. **A15**, 182 (1997)
10. S.L. Wright, R.F. Marks, W.I. Wang, J. Vac. Sci. Technol. **B4**, 505 (1986)
11. J.-M. Dilhac, C. Ganibal, N. Nolhier, B. Rousset, Rev. Sci. Instrum. **63**, 188 (1992)
12. Z. Dohnálek, S. Mezhenny, I. Lyubinetsky, W.J. Choyke, J.T. Yates Jr, J. Vac. Sci. Technol. **A15**, 2766 (1997)
13. W. Bludau, J. Appl. Phys. **45**, 1846 (1974)
14. K.L. Shaklee, R.E. Nahory, Phys. Rev. Lett. **24**, 942 (1970)
15. H.D. Barber, Solid State Electron. **10**, 1039 (1967)
16. LabVIEW is sold by Analog Devices, One Technology Way, Norwood, MA 02062-9106

Part V
Delivery of Adsorbates to Surfaces

Chapter 37
Gases

37.1 Design and Performance of Microcapillary Array Beam Doser

Beam dosers for quantitative exposure of surfaces to gases have become widely used in surface science research. This is because of the disadvantages in filling an ultrahigh vacuum system with gas in order to study adsorption processes. These disadvantages relate to the large gas loads needed for system dosing as compared to beam dosing. Such large gas loads result in adsorption on the walls of the vacuum chamber, which then contributes to slow achievement of base pressure after adsorption by the sample surface is complete. In addition, large gas loads in a vacuum system can cause displacement effects from the system walls leading to impurity adsorption, as well as regurgitation effects from ion pumps in which impurity gases are produced (see p. 72). Also, the use of quantitative and absolute calibration procedures for the gas flux coming from a collimated doser is much superior to dosing with a system dose using an ionization gauge or a mass spectrometer, both of which have serious problems with absolute calibration.

Figure 37.1a shows a design for a microcapillary array beam doser [1]. A pinhole aperture made of stainless steel serves as a deformable gasket inside a Cajon vacuum fitting [2]. Typical aperture diameters are about 5 μm for convenient dosing fluxes for adsorption studies, as shown on p. 425, where calibration methods are described. The flux of gas issuing from the pinhole aperture travels into the doser body, where it strikes a baffle made of metal shim stock, held into place by springy arms that bend against the inside wall of the doser body. This baffle randomizes the gas molecules' motion inside the doser body and behind the microcapillary collimator plate. Collimation of the gas occurs in the high-density capillary array where parallel capillaries of 10 μm diameter and 500–1000 μm length are arranged in a hexagonal close packing arrangement [3]. The microcapillary array disk has a radius, R_S and should be purchased with the capillary axes perpendicular to the array surface, rather than inclined as in the chevron design

© Springer International Publishing Switzerland 2015

J.T. Yates Jr., *Experimental Innovations in Surface Science*,
DOI 10.1007/978-3-319-17668-0_37

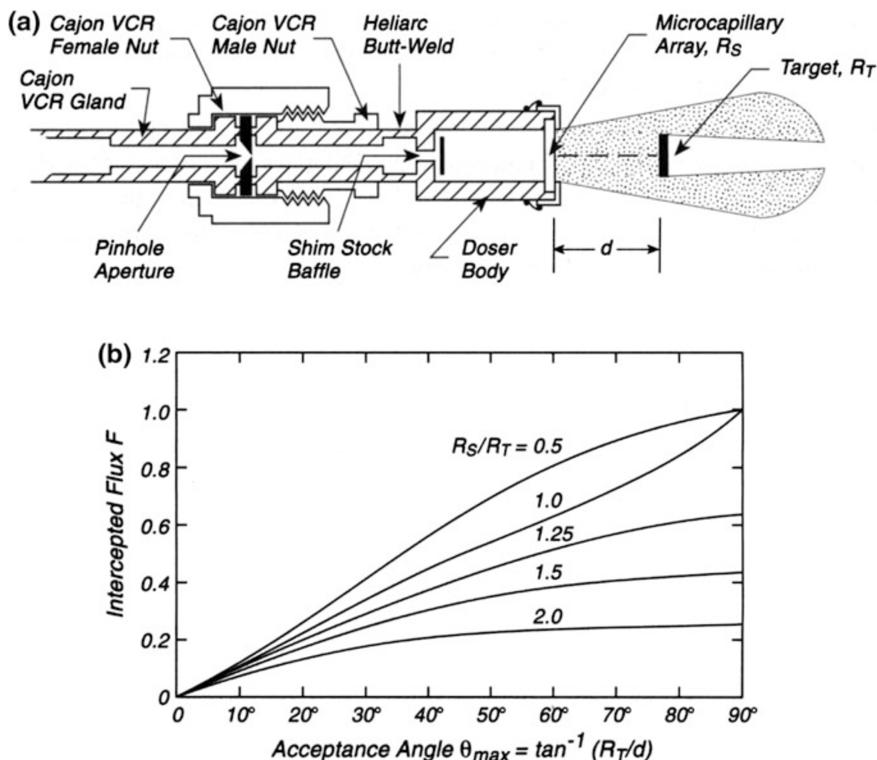

Fig. 37.1 Design and performance of microcapillary array doser, **a** Design of doser (R = radius), **b** Fractional interception by target

commonly manufactured [3]. The capillary array is held in place by a metal cap that, with a clearance of several micrometer, confines the edge of the array in a close-fitting groove on the end of the doser body. Care should be taken not to compress mechanically the very fragile glass capillary array during installation. The capillary array has a relatively high conductance for gases and acts mainly as a collimator in the gas doser.

Figure 37.1b shows the intercepted flux fraction from the array by the target of radius R_T for various geometries [4, 23]. The most uniform dosing over the target will take place with larger values of R_S/R_T but of course the fraction of the beam intercepted will decrease as shown in Fig. 37.1b. The assumptions used in deriving the functions shown in Fig. 37.1b assume that diffuse scattering occurs on the inside walls of the capillaries under molecular flow conditions where the mean free path is considerably longer than the diameter of the capillaries.

If the capillary array is too close to the target, reflected molecules from the target will have a finite probability of incidence on the crystal for a second encounter when they are reflected back by the capillary array surface.

There are precautionary measures to be considered with glass microcapillary array dosers. They are made of soft glass and therefore contain Si–OH groups on their surface. The hydrogen atoms are labile and will exchange with –OD groups in D_2O or in organic molecules such as CH_3OD [5]. In this case, isotopic exchange overnight can be carried out until the isotopic purity of the transmitted gas is not influenced by isotopic exchange on the inner walls of the capillaries. In addition, reactions of some molecules such as fluorinated ethers with acid sites on the silica surface have been reported [6]. Finally, certain unstable molecules such as $Fe(CO)_5$ have been shown to be reactive with the glass surface [7].

Recently, less finely packed array dosers made of metal have been used with success for uniform gas dosing in directions off the crystal normal [8].

For reactive gases, the use of an inert diluent gas has been described in [9] and also on p. 89.

Historically, collimated array gas dosers have been used since the 1970s, and some examples are given in [10–14].

A recent theoretical treatment of the transport of gases through microcapillary array dosers and other tubular devices is found in [15], which also contains a bibliography of earlier papers on this subject. A recent analysis of the flux distribution from a tube doser and a capillary array doser has been reported [16].

37.2 Gas Handling System for Array Beam Doser

The effective use of the microcapillary array beam doser shown on p. 421 requires a gas-handling system of appropriate design, as shown in Fig. 37.2 [17]. A stainless steel system, pumped by a turbopump, is designed to attach to several glass storage gas bulbs, using Cajon VCR fittings [17].

The storage of gases in glass bulbs at pressures near 1 atm prevents accidental over-pressurizing of the gas-handling system by compressed gases in cylinders. Also, during gas transfer to prebaked storage bulbs (for removal of adsorbed H_2O from the glass walls), one has the opportunity to use purification steps for gases such as the freeze-pump-thaw method commonly used to remove noncondensable impurities.

For calibration of the gas doser system, a test gas, such as N_2, is admitted to the gas-handling system to a few Torr pressure. The ballast bulb, of exactly known volume, is also filled with this gas. As will be shown on p. 425, the conductance of the pinhole aperture may be measured by measuring the time rate of change of pressure in the gas-handling system as the N_2 is slowly pumped through the pinhole aperture. To interrupt the flow from the array doser, Valve-1 is closed, and the region behind the doser is rapidly evacuated through Valve-2, keeping the gate valve to the UHV system closed.

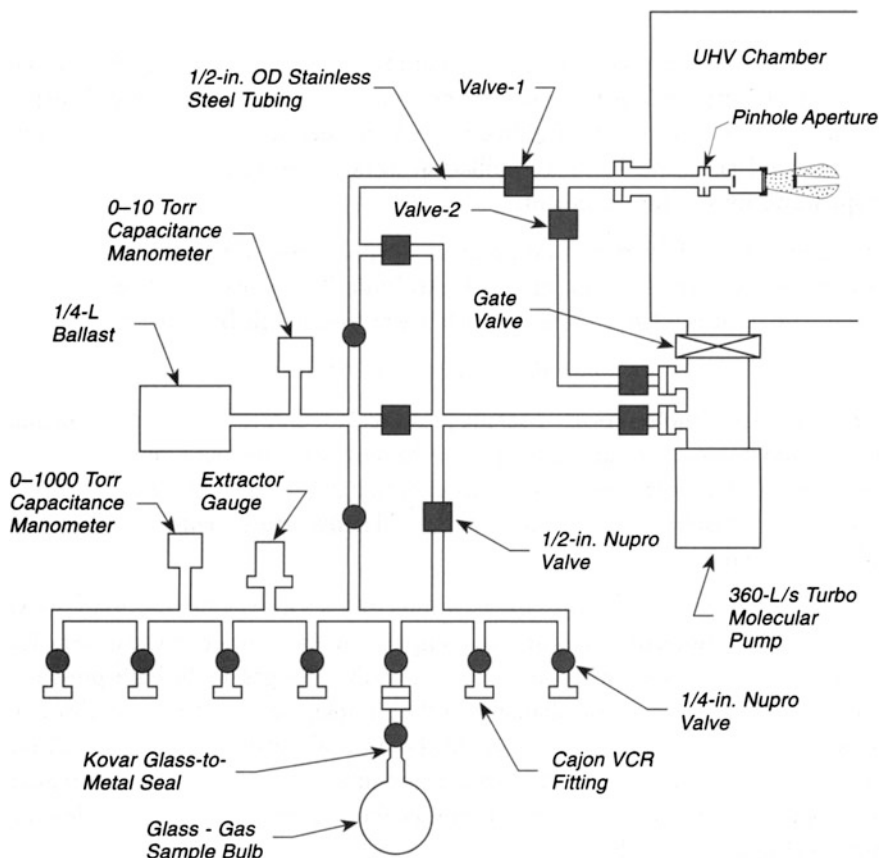

Fig. 37.2 Typical gas handling system—beam doser

Stainless steel systems such as this can be baked with heating tape to 150–200 °C while pumping with the turbopump. Because of the low pumping speed through the narrow tubing and the relatively high internal surface area compared to the volume, limiting pressures in the 10^{-8} Torr range are usually measured. For gases added to the Torr level, this background gas represents much less than 1 ppm of added impurity, which is usually superior to the initial purity of the gas being studied.

The internal surface of the stainless steel gas-handling system has a significant capacity to react with active gases such as Cl_2. Gases of this sort may often be used themselves to passify the stainless walls. This is done by storing the active gas at pressures of several Torr pressure overnight, and then pumping the gas away before adding fresh gas to the system [18]. It may be necessary to do this passivation treatment in several cycles. In other cases, treatment of the gas-handling system with oxygen gas to passivate the inner walls by oxidation has been found to be effective [19].

37.3 Calibration and Use of Array Beam Doser

Figure 37.3a shows a typical design for an ultrahigh vacuum system equipped to measure the kinetics of adsorption of a gas on an atomically clean crystal surface. A quadrupole mass spectrometer (QMS detector), shielded to receive only a random flux of background gases, and the microcapillary array doser are the principal components of the apparatus for this measurement.

The calibration of the doser was performed with N_2 over a period of about 10^5 s, as shown in Fig. 37.3b. The data, plotted logarithmically, against time, *t*, provide a linear curve whose slope is related to the conductance of the pinhole by (37.1).

$$dn/Pdt = -V/kT[d(InP/P_0)/dt] \quad (37.1)$$

where *n* number of molecules, P = backing pressure, V = storage volume, k = Boltzmann's constant, and T = temperature in Kelvin. For the most accurate measurement of the drop in pressure, the temperature-sensitive capacitance manometer in the gas storage region (see p. 423) must be thermally shielded to avoid temperature changes larger than a few tenths of a Kelvin.

Usually measurements of this type have a relative accuracy of better than 5 % when gases of various molecular weights are compared to each other in the doser

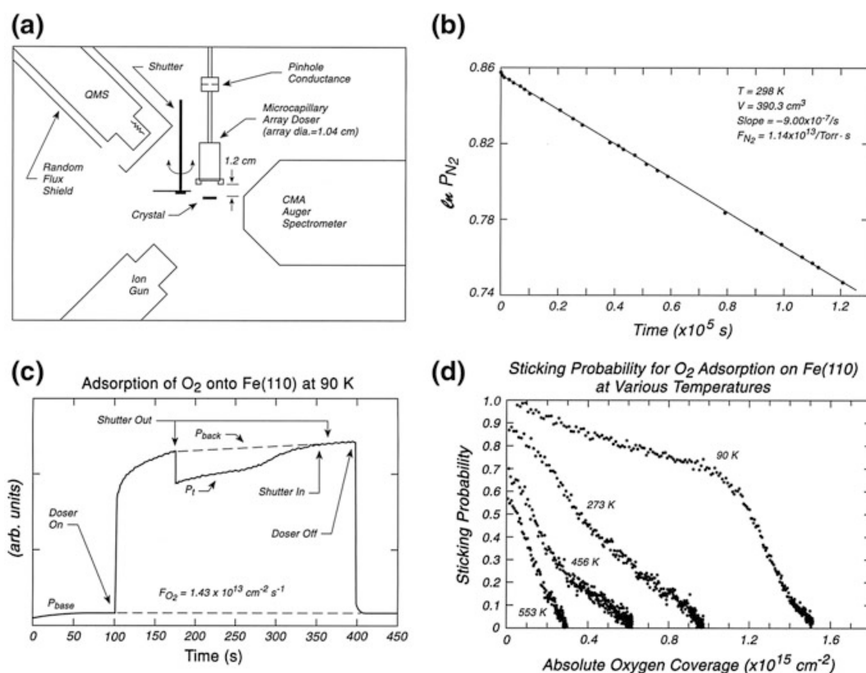

Fig. 37.3 Use of beam doser for kinetics and coverage measurements. **a** Typical apparatus—absolute coverage and sticking probability measurement, **b** Typical calibration curve—pinhole conductance. **c** Adsorption uptake curve. **d** Sticking probability versus absolute coverage

[20]. For molecular flow conditions, where the mean free path of the gas on the high-pressure side of the pinhole is larger than the diameter of the pinhole, the rate of effusion through the pinhole will be proportional to $M^{-1/2}$, where M = the molecular mass of the gas. This condition continues to be approximately true as one enters the transition region in gas density, at higher pressures, where viscous flow is beginning to occur in the pinhole aperture which has finite wall length.

Figure 37.3c shows measurements of the adsorption of O_2 on a Fe(110) surface at 90 K [21]. For this measurement, the shutter is placed between the doser and the crystal, and a steady base pressure of the order of 1×10^{-10} Torr or less is established, using the mass spectrometer tuned in this case to 32 amu. After steady conditions are achieved, the doser is turned on with the shutter still in place and the pressure measured by the mass spectrometer rises. Ideally the pressure should level out prior to opening the shutter to allow adsorption from the beam to occur, but since a small flux of random gas scattered from the back of the shutter is incident on the crystal, causing a slow increase in coverage, the waiting time is limited and a compromise must sometimes be reached in which "almost steady state" conditions for P_{back} are established, as shown here. At this point, the shutter is opened, and adsorption occurs until asymptotic behavior of the scattered flux of gas is observed. Then, when the sticking probability has fallen to a low value, placing the shutter into the beam causes no discontinuity to be observed in the mass spectrometer signal.

The data shown in Fig. 37.3c can be converted into sticking coefficient vs. absolute coverage, as shown in Fig. 37.3d, if the fractional interception of the doser beam is calculated (see p. 421) (or measured [20]). It is of interest to note that the entire measurement of sticking probability and absolute coverage are determined solely by the accuracy of the flux calibration and the accuracy of the fractional interception of the collimated gas beam by the crystal [22, 23]. The mass spectrometer does not have to be calibrated in any absolute sense.

This method is based upon earlier work with variations on the features of the apparatus and the measuring conditions [24–27].

37.4 Sticking Coefficient and Surface Reactivity

Measurements of the sticking coefficient and similar measurements of surface reactivity, all based on the original work of King and Wells[28], form a central core of modern studies of adsorption and reactivity on single crystals. This work is discussed in various other chapters of this book [see Sects. 24.7, 25.5, 37.1–37.3, 37.5]. The apparatus [29], shown in Fig. 37.4a, is very similar to that in Fig. 37.3. A collimated molecular beam of adsorbate is incident on a single crystal (CO + Pt (111)) maintained at constant temperature. A fraction of the incident beam is adsorbed with a particular coverage-dependent sticking coefficient and the remainder is scattered into the chamber, returning to the mass spectrometer after having been randomized in scattering direction by collisions with the chamber walls. By knowing the fractional interception of the crystal (see Sect. 37.1), the measurements permit

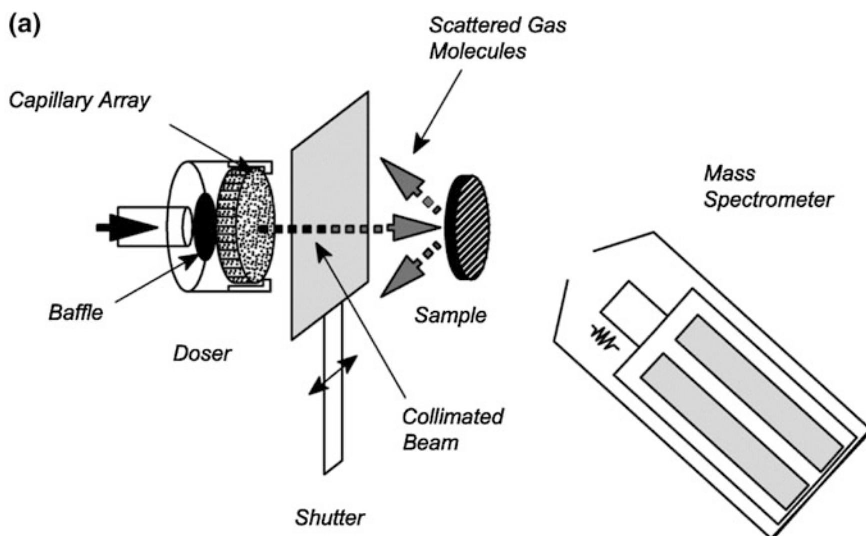

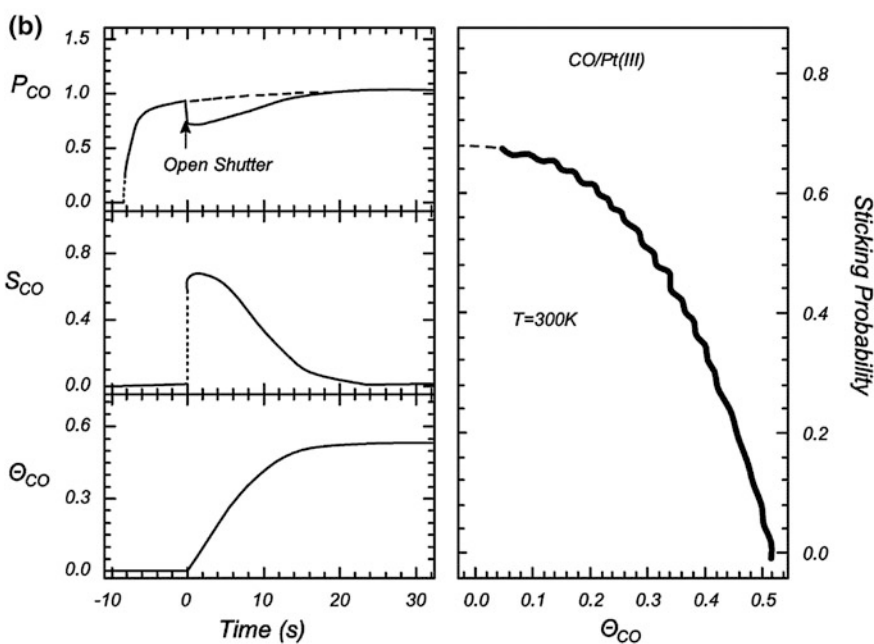

Fig. 37.4 Sticking coefficient and surface reactivity. **a** Sticking coefficient and surface reaction apparatus. **b** Typical uptake kinetics data

both the sticking coefficient to be measured as a function of absolute coverage and the absolute coverage to be measured as discussed in Sect. 37.3. Figure 37.4b shows the sticking coeffficient behavior of CO on Pt(111)at 300 K [2].

For a molecule which decomposes into fragments producing desorbing species, it is also possible with this apparatus to measure something of the chemical processes at work during adsorption under isothermal conditions. This is called scanning kinetic spectroscopy (SKS) and is shown in Sect. 25.5. The present work [28] also employs this method to observe the reaction of C_2H_4 on Pt(111), where ethane desorption and hydrogen desorption accompany C_2H_4 adsorption after a short delay time.

37.5 Beam Doser Shutoff—Condensable Gases

Very simple measures can sometimes be used to interrupt the flow of gases from a gas doser. As indicated on p. 430, the use of a small deadspace valve of special design is helpful in defining reproducible and absolute doses of gases into a collimated gas doser system. In some cases, where gases condensable in liquid nitrogen are being used with a gas doser, it is possible to interrupt the flow rapidly by using a cold trap as a pump. In Fig. 37.5, a cold trap made of Pyrex glass is immersed in a Dewar flask containing liquid nitrogen [30]. This cold trap is a very rapid pump for all gases that are condensable at 77 K. Flowing gas through the doser (see p. 423) may be turned off rapidly by closing the admission valve and then quickly opening

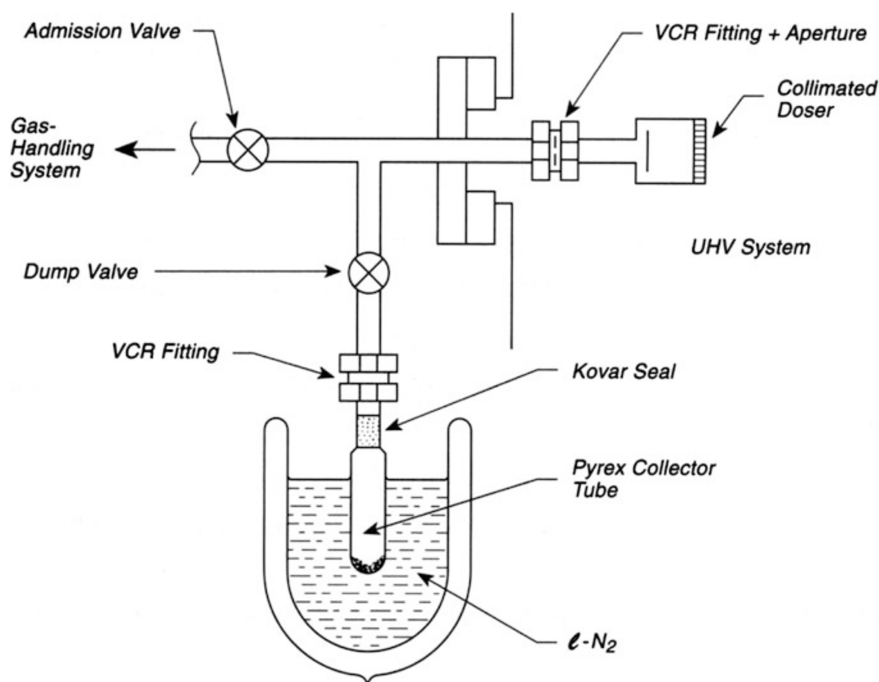

Fig. 37.5 Beam shutoff—condensable gases

the dump valve. This lowers the gas pressure very rapidly behind the conductance limiting aperture, and turns the doser off. Many doses of gas, and different condensable gases, may be trapped without cleaning the collector tube. For cleaning, the tube is disconnected from the doser line using the VCR fitting, cleaned with solvents, baked briefly in an oven, reconnected, and evacuated using the pump in the gas-handling system. This method is actually preferable to pumping corrosive gases from the trap, after each dose, through a turbopump because of possible failure of the turbopump after exposure over time to corrosive conditions.

37.6 Neutral Beam Intensity Measurement Using a Stagnation Detector

A stagnation detector may be used to determine the absolute intensity of a molecular beam. In Fig. 37.6, a portion of the beam (having a diameter larger than the orifice), enters a chamber containing an ionization gauge and a calibrated leak. After suitable corrections, the signal indicated by the ionization gauge can be related to the flux of gas in the beam [31].

Under conditions where the beam is shut off, the steady-state pressure, P, is

$$P_s = Q_o / C_{orf} \tag{37.2}$$

where Q_o is the net outgassing rate and C_{orf} is the conductance of the orifice.

When the valve to the calibrated leak is opened, the pressure increase will be

$$\Delta P_{leak} = Q_L / C_{orf} \tag{37.3}$$

where Q_L is the calibrated leak rate. The conductance of the orifice, which should be sharp-edged is, under molecular flow conditions

$$C_{orf} = 2.86(T/M)^{1/2} D^2 \mathrm{L/s} \tag{37.4}$$

where D is the orifice diameter in cm, T is the absolute temperature, and M is the molecular mass of the gas.

When the molecular beam passes through the calibrated orifice it will cause a pressure rise in the stagnation chamber given by

$$\Delta P_{beam} = Q_B / C_{orf} \tag{37.5}$$

The impingement rate, I_B, is related to ΔP_{beam} according to (37.6),

$$I_B = Q_B N_L / \pi D^2 = 0.91\, N_L (T/M)^{1/2} \Delta P_{beam} \tag{37.6}$$

where $N_L = 3.237 \times 10^{19}$ molecules/Torr-L at 298.15 K.

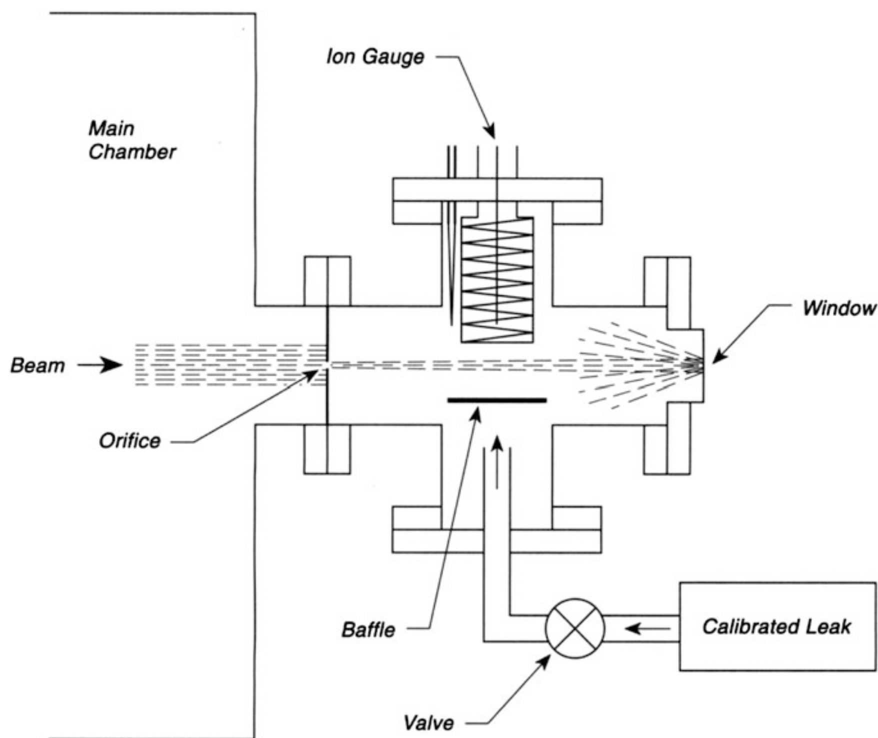

Fig. 37.6 Stagnation detector

It is important that the beam diameter be larger than the orifice and that the baffle inside the stagnation detector be arranged to prevent direct entry of the gas from the calibrated leak into the ionization gauge. For reactive gases such as oxygen, the operating temperature of the ionization gauge filament and the emission current should be reduced as much as possible to prevent pumping effects.

The intensity at a sample position that differs from the orifice position is related to the intensity at the orifice by the inverse square law for the distances involved. A good article detailing the many experimental aspects of the use of supersonic molecular beams in surface chemistry studies may be found in [32].

37.7 Low Deadspace Aperture Valve for Repetitive Gas Dosing

The use of gas dosers for adsorption experiments is highly recommended in order to avoid impurity effects from wall displacement and ion pump regurgitation processes as well as to have quantitative gas dosing capabilities, as discussed on pp. 421–428.

In the conventional gas dosing design, a rather large volume of gas is held in a storage section of the gas line, and to interrupt dosing, one must pump out this gas or some fraction of it held in a section of the gas storage line. For repetitive gas dosing, this is inconvenient, and in addition for expensive gases it is wasteful. The design shown here [33] avoids this effect by minimizing the deadspace volume so that only a few seconds of gas dosing occurs following closure of the valve. In addition, when a conductance-limiting aperture at the outlet to the small deadspace volume is used, quantitative gas dosing can be done when the valve is opened.

Figure 37.7a shows a view of the aperture valve assembly. The valve body of a stainless steel diaphragm ultrahigh vacuum valve (Nupro DL Series) is drilled and

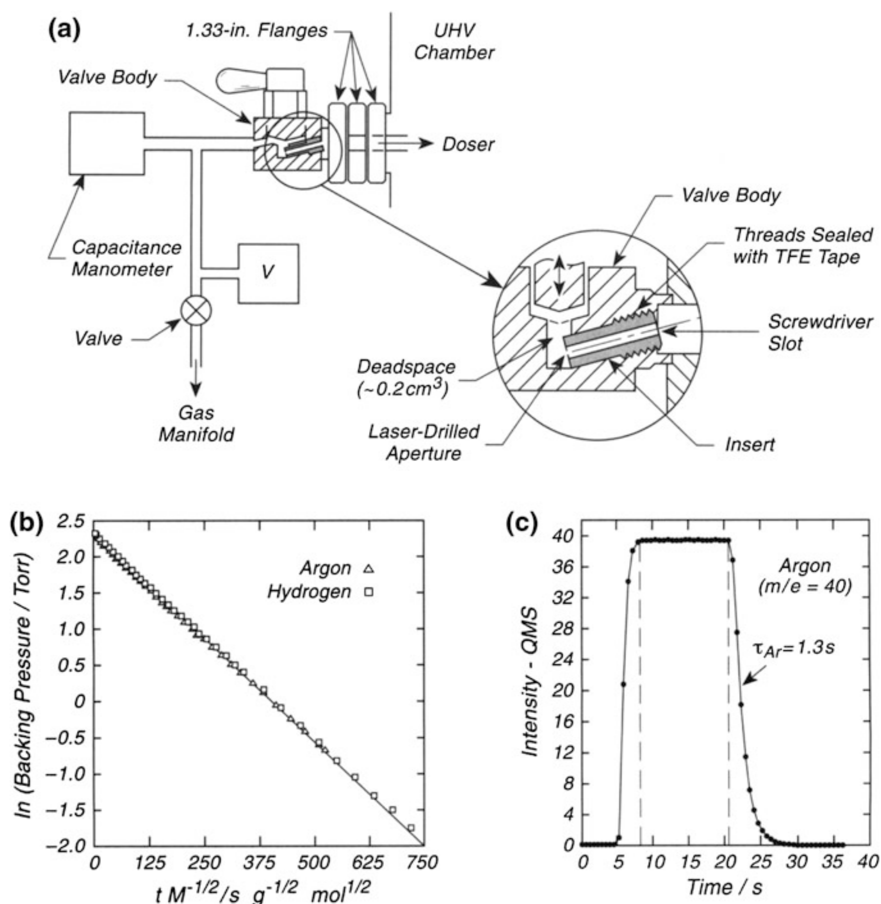

Fig. 37.7 Low deadspace aperture dosing valve. **a** Aperture valve assembly. **b** Pumping behavior—40 μm aperture. **c** Duty cycle—open and close

tapped with 1/16 NPT pipe threads to receive a stainless steel rod also threaded on the upper end. This is done at the correct angle inside the inlet side of the valve. This rod has a central hole, 2 mm in width, bored its length, except for an 0.003-in.-thick membrane at the inner end. The membrane is then laser-drilled with a nominal 60-μm-diameter conical hole [34]. The upper end of the insert contains a screwdriver slot for convenient insertion into the valve; Teflon tape is used to make a gas tight seal. The inlet to the valved assembly (originally the outlet) is connected to a conventional gas-handling system, containing pumping capabilities, a capacitance manometer, and a ballast volume, *V*, used for conductance calibration of the laser-drilled aperture. The outlet of the valve assembly is connected to a small flange that connects to a collimating gas doser (see p. 421) inside the ultrahigh vacuum system. With this arrangement, the deadspace when the valve is closed is about 0.2 cm^3. Thus, when the dosing is completed, and the valve is closed, evacuation of the deadspace into the ultrahigh vacuum system by way of the doser does not involve the flow of large amounts of gas, even when the backing pressure is near 0.1 Torr. Under these conditions, the number of molecules in the deadspace is about 4×10^{14}. If 20 % of these molecules strike the crystal and the sticking coefficient is 0.1, about 2 % of a monolayer will adsorb from the exhaust of the deadspace after the valve is closed.

Figure 37.7b shows a comparison of the pumping speed through the opened valve for both Ar and H_2, and may be used to measure the conductance of the laser-drilled aperture. It is noted that the effusion rate follows a semilogarithmic behavior from backing pressures of 10 Torr and lower, indicating that slight departures from molecular flow conditions do not sensibly disturb the conductance of the aperture from that predicted by the kinetic theory of gases for molecular flow. The superposition of points for the two gases on the curve gives further confidence in the notion that the behavior can be predicted from the molecular flow equations.

Figure 37.7c shows the response of a mass spectrometer in the vacuum system as the valve is opened and closed for one cycle. A total rise time of about 3 s is seen as the valve is opened. Constant Ar flux occurs beyond this time until the valve is closed, where the pumping out of the deadspace volume exhibits a time constant of 1.3 s. Even though these on-and-off periods give relatively slow response times, the doser may still be calibrated to give reproducible doses containing the on-off periods as well as the constant flux period. The use of a smaller laser-drilled aperture is possible, but the time constant for pumping will increase to unacceptable levels. A major feature of the apparatus is that the unit can deliver rather large fluxes at fairly low backing pressures and that it can be quickly cut off without wasting gas. Multiple exposures that are reproducible can be achieved.

A variation on this idea, involving a trapping volume of about 0.4 cm^3, has been employed to dump known quantities of gas onto a crystal by way of an effusive doser [35–37]. The trapping volume contains about 1.4×10^{16} molecules/Torr; and the repeatability of the dose, using a capacitance manometer for pressure measurements in the gas line feeding the doser volume, is estimated to be 0.5 % standard deviation.

37.8 Gas Flow Regulation—Squeeze Valve

A very simple method for regulating the flow of gases into an ultrahigh vacuum system with a minimum of contaminants involves the use of a brass squeezing device to restrict the flow through a thick-walled copper tube, as shown in Fig. 37.8a [38]. The copper tubing (3 mm OD × 1 mm ID) is annealed in a flame, then cleaned internally with nitric acid and rinsed with water and alcohol. The brass squeeze device is clamped to the tube, and the flow rate may be adjusted over a

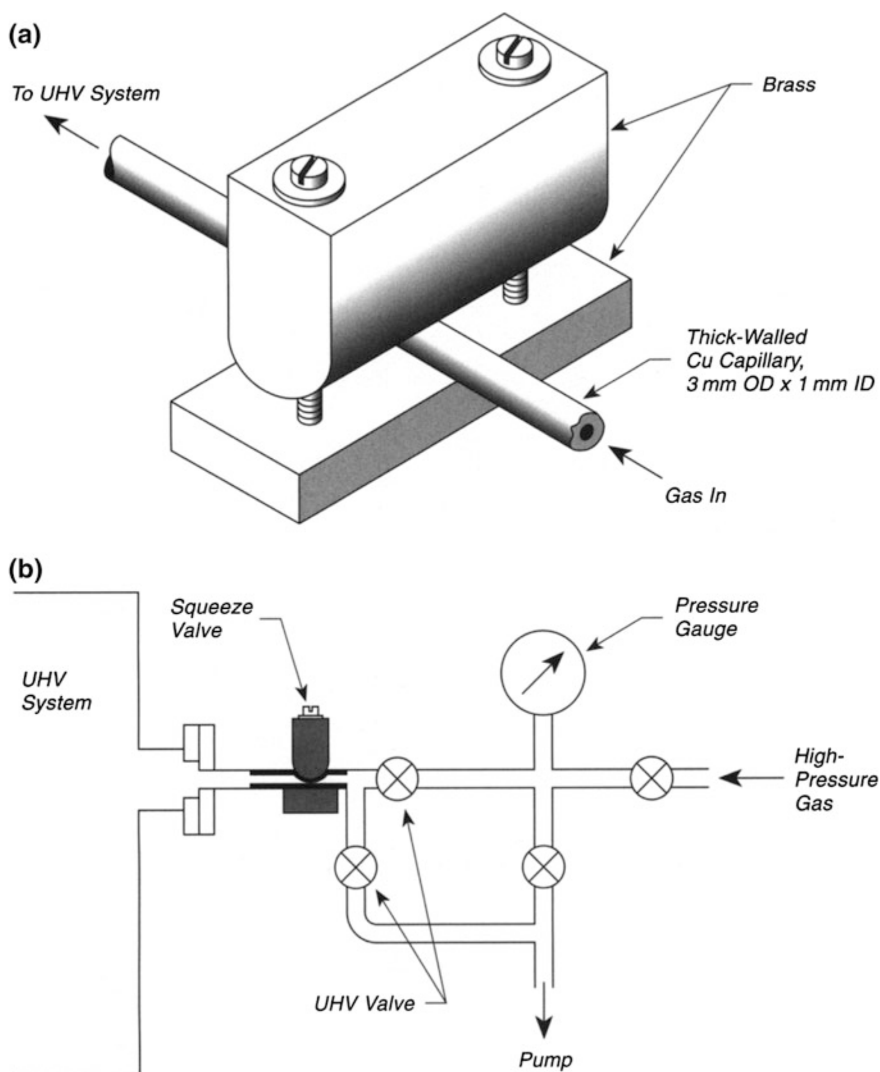

Fig. 37.8 Gas flow regulation—squeeze valve. **a** Squeeze valve. **b** Gas-handling system

wide range using the tightening screws. This action is reversible tens of times. The valve cannot be closed completely. To adjust the flow rate after the valve is set, the pressure in the high-pressure region is varied using the pressure gauge for measurement. To shut down the flow, the upper UHV valve is closed and the region between this valve and the squeeze valve is evacuated to the pump, as may be seen in Fig. 37.8b.

37.9 Retractable Beam Doser with Convenient On-Off Control

A convenient molecular beam doser which turns itself on or off upon retraction is shown in Fig. 37.9. A leak valve or a calibrated leak can be used to control gas flow. It is convenient to turn these dosers on or off by quickly pumping out the gas supply to the doser. In this case, a translational manipulator is used to move the doser in and out. When in the in position, the 4 holes in the doser tube between the

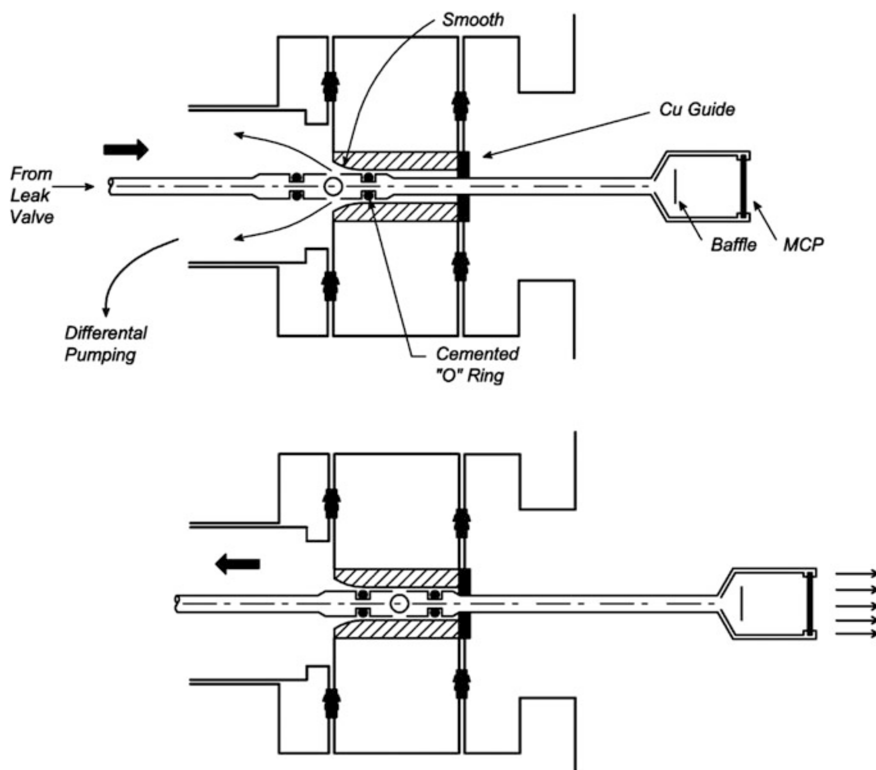

Fig. 37.9 Retractable molecular beam

two O-ring seals are isolated from differential pumping and the doser delivers gas at the established flow rate. When the doser is in the out position, the four pumping holes are exposed to differential pumping, turning the doser off. The O-rings are cemented into grooves machined in the on-off assembly. They slide into a polished cylindrical region with a slight taper on the left side for easy admission. The doser is guided by a Cu guide with a loose-fitting alignment hole. The doser contains a microchannel plate for gas collimation and a baffle to prevent beaming of the gas to the plate from the delivery tube, spoiling the collimation [39].

References

1. M. Bozack, L. Muehlhoff, J.N. Russell Jr, W.J. Choyke, J.T. Yates Jr, J. Vac. Sci. Technol. **A5**, 1 (1987)
2. P.L. Hagans, B.M. DeKoven, J.L. Womack, J. Vac. Sci. Technol. **A7**, 3375 (1989). Laser-drilled micron-size pinholes are produced in disks fitting VCR fittings by Precision Laser Services, 314 E. Wallace St., Ft. Wayne, IN 46803
3. Capillary array blanks, made without being coated with active surfaces for use as electron multipliers, are available from Galileo Electro-Optics Corporation, Galileo Park, P.O. Box 550, Sturbridge, MA 01518. Sizes up to 25-mm diameter are available
4. A. Winkler, J.T. Yates, Jr., J. Vac. Sci. and Technol. **A6**, 2929 (1988)
5. S.M. Gates, J.N. Russell Jr, J.T. Yates Jr, Surf. Sci. **146**, 199 (1984)
6. P.K. Leavitt, P.A. Thiel, J. Vac. Sci. Technol. **A8**, 148 (1990)
7. M. Henderson, R.D. Ramsier, J.T. Yates Jr, J. Vac. Sci. Technol. **A9**, 2785 (1991)
8. A.M. Glines, R.N. Carter, A.B. Anton, Rev. Sci. Instrum. **63**, 1826 (1992)
9. E.C. Henn, M.E. Bussell, C.T. Campbell, J. Vac. Sci. Technol. **A9**, 10 (1991)
10. D.W. Goodman, T.E. Madey, M. Ono, J.T. Yates Jr, J. Catalysis **50**, 279 (1977)
11. D.W. Goodman, J.T. Yates Jr, T.E. Madey, Chem. Phys. Lett. **53**, 479 (1978)
12. S.M. Gates, J.N. Russell Jr, J.T. Yates Jr, Surf. Sci. **159**, 233 (1985)
13. D.E. Ibbotson, T.S. Wittrig, W.H. Weinberg, Surf. Sci. **110**, 294 (1981)
14. J.E. Deffeyes, A.H. Smith, P.C. Stair, Surf. Sci. **163**, 79 (1985)
15. D.M. Murphy, J. Vac. Sci. Technol. **A7**, 3075 (1989)
16. D.E. Kuhl, R.G. Tobin, Rev. Sci. Instrum. **66**, 3016 (1995)
17. M.J. Bozack, L. Muehlhoff, J.N. Russell Jr, W.J. Choyke, J.T. Yates Jr, J. Vac. Sci. Technol. **A5**, 1 (1987)
18. A.L. Linsebigler, V.S. Smentkowski, M.D. Ellison, J.T. Yates Jr, J. Am. Chem. Soc. **114**, 465 (1992)
19. M.A. Henderson, R.D. Ramsier, J.T. Yates Jr, J. Vac. Sci. Technol. **A9**, 2785 (1991)
20. C.C. Cheng, R.M. Wallace, P.A. Taylor, W.J. Choyke, J.T. Yates Jr, J. Appl. Phys. **67**, 3693 (1990)
21. V.S. Smentkowski, J.T. Yates, Jr., J. Vac. Sci. Technol. A7, 3325 (1989); Surf. Sci. **232**, 113 (1990)
22. A. Winkler, J.T. Yates Jr, J. Vac. Sci. Technol. **A6**, 2929 (1988)
23. C.T. Campbell, S.M. Valone, J. Vac. Sci. Technol. **13**, 408 (1985)
24. D.A. King, M.B. Wells, Surf. Sci. **29**, 454 (1972)
25. T.E. Madey, Surf. Sci. **33**, 355 (1972)
26. A.A. Bell, R. Gomer, J. Chem. Phys. **44**, 1065 (1966)
27. C. Wang, R. Gomer, Surf. Sci. **84**, 329 (1979)
28. D.A. King, M.B. Wells, Surf. Sci. **33**, 355 (1972)
29. F. Zaera, Int. Rev. Phys. Chem. **21**, 433 (2002)

30. Author’s personal experience
31. W.G. Dorfeld, J.B. Hudson, R. Zuhr, Surf. Sci. **57**, 460 (1976)
32. S.T. Ceyer, D.J. Gladstone, M. McGonigal, M.T. Schulberg in *Investigations of Surfaces and Interfaces—Part A, Physical Methods of Chemistry Series*, 2nd Ed., Vol. IXA, edited by B.W. Rossiter and R.C. Baetzold (Wiley, New York, 1993)
33. S.M. Cohen, M.P. D’Evelyn, J. Vac. Sci. Technol. **A9**, 2414 (1991)
34. Lenox Laser, 1 Green Glade Ct., Phoenix, MD 21131
35. Dr. V.A. Ukrainsev, Texas Instruments, P.O. Box 655012, MS 461, Dallas, TX 75265 (private communication)
36. Y.A. Gelman, B.S. Podol’skii, V.A. Ukraintsev, Pribory I Tekhnika Experimenta **6**, 191 (1990)
37. I. Harrison, V.A. Ukraintsev, A.N., in *Artsyukhovich, SPIE Proceedings, Laser Techniques for Surface Science*, ed. by H.-L. Dai, S.J. Sibener, vol 2125, p. 285 (1994)
38. G. Scoles, Chemistry Department, Princeton University, Princeton, NJ 08544 (private communication). This method was devised at the FOM Laboratories in Amsterdam 40 years ago and is still in use
39. Michael Schmidt and Ulli Diebold, private communication

Chapter 38
Evaporation Sources

38.1 Degassing Evaporation Sources

The deposition of thin films by evaporation constitutes one of the main experimental procedures in surface and materials science. Indeed, the study of chemisorption on clean surfaces has as one of its origins the use of thin metal films as substrates in early studies done in the 1940s.

A major problem in making clean thin films originates from the outgassing of heated surfaces during evaporation, leading to contamination of the thin film by chemisorption from the background vacuum. This may be avoided by careful design in which prior out-gassing is achieved for components that will be heated during evaporation. Figure 38.1 illustrates how this is done, using two principles.

The first principle involves the use of degassing loops to support all filaments that will be heated [1]. In the center of the evaporation shield, the evaporation loop, containing welded pieces of the evaporant at its apex, is mounted on two degassing loops. Knowing the current (I_1) required to bring the evaporation loop to its desired temperature for evaporation of the evaporant, one passes current I_2 through the degassing loops prior to the evaporation step. The current I_2 should be somewhat larger than $I_1/2$ so as to bring the degassing loops to a higher temperature than they will ever attain during evaporation, and the two loops should be outgassed separately so as to avoid passing current through the evaporation loop during outgassing.

The second principle illustrated in Fig. 38.1 is the use of a shield-outgassing filament for heating the shield to temperatures higher than will be achieved while evaporation occurs from the evaporation loop [2]. This is achieved by radiation from the outer shield outgassing filament, where the shield thermocouple may be used to monitor the temperature achieved during outgassing compared to that during evaporation. Note that this shield outgassing filament is also mounted on degassing loops.

© Springer International Publishing Switzerland 2015

J.T. Yates Jr., *Experimental Innovations in Surface Science*,
DOI 10.1007/978-3-319-17668-0_38

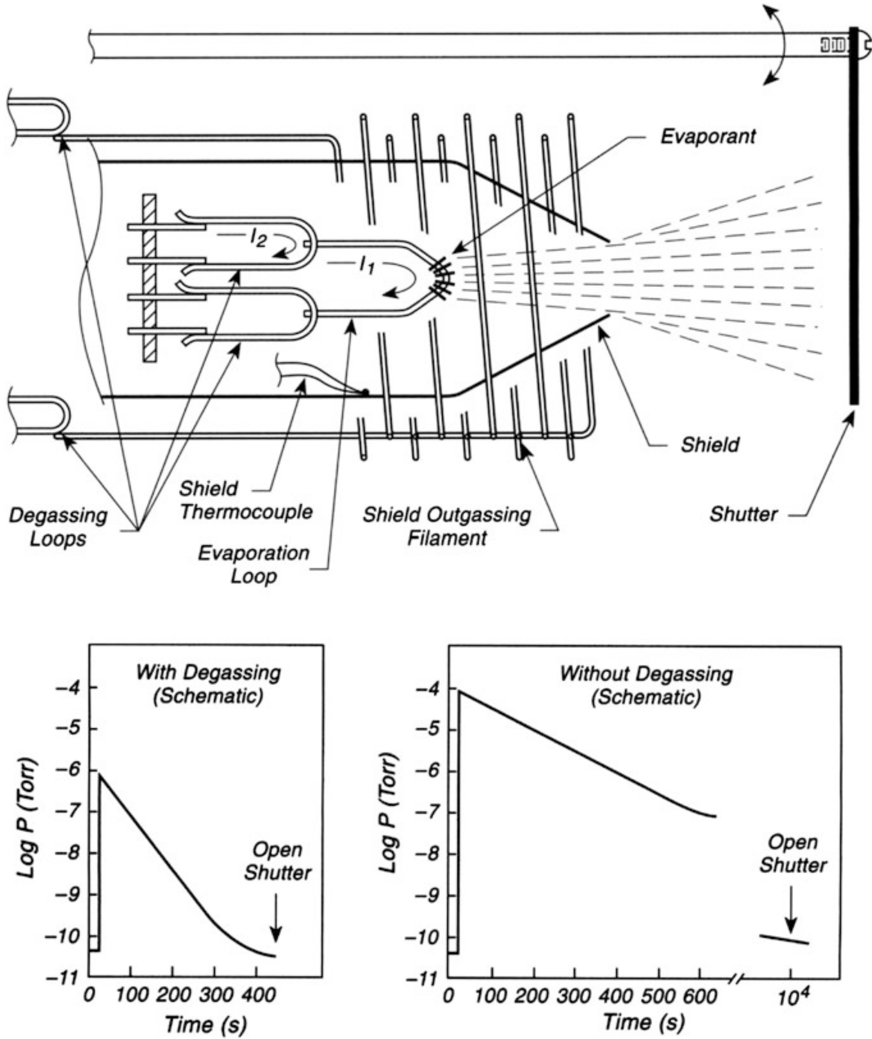

Fig. 38.1 Degassing evaporation sources

Schematic performance curves are shown in Fig. 38.1 to illustrate that extremely rapid employment of a properly outgassed evaporation source is possible compared to a poorly designed source that may outgas over days prior to being useful for evaporation under good vacuum conditions. The shutter should not be opened until an appropriate limiting pressure is achieved during evaporation.

Some evaporation sources will be subject to continual outgassing because of design limitations preventing the use of methods shown here. In that case, reduction of the unwanted gas fluence at the substrate may be achieved by differentially pumping the source and the substrate chambers that are connected by an aperture [3].

The monitoring of the temperature of the evaporation filament maybe achieved quite simply by the use of current and voltage drop measurements as described on p. 430.

A helpful word about the construction of welded assemblies involving refractory wires such as tungsten and tantalum will be useful. When these wires are fabricated from approximately 0.3-mm-diameter wire for the purposes described here, it is often found that upon heating to high temperatures, the wires will distort geometrically. This distortion is caused by mechanical strain present initially in the welded assembly if the welds and the wire are placed under strain during attempts to make additional welds on the same filament. To avoid this problem, all wires should be formed by bending over gently curved mandrels, and the welding of the preformed filaments should be carried out in such a way that no strain is placed on a weld when subsequent welds are made and that no distortion of the preformed filament shape occurs during final assembly by welding.

38.2 Metal Evaporation Sources for Downward Evaporation

Two oven designs for the downward evaporation of metals using radiative heating have been described that operate at very low outgassing rates [4]. The problem with most downward evaporation sources that involve melting of the evaporating metal is that gravity may cause molten metal to fall from the evaporator to the substrate.

The cylindrical oven body is made of tantalum foil, 0.05 mm thick, spot-welded into shape and containing end caps made of the same size material. The oven is then wrapped with several layers of 0.01-mm-thick Ta foil to provide substantial thermal shielding. This heat shielding is essential to permit good thermal efficiency and therefore low outgassing rates. Two 3-mm-diameter Mo rods are used to bring in power to a W coil filament, 1 mm in diameter and 250 mm long. The longer of the two rods is spot-welded to the inside of the Mo oven body to provide mechanical support for the assembly. The second passes through a hole in the top cap and is insulated by a thin tube of pyrolytic boron nitride, pBN. When the oven is operating the resistance of the W coil is about 0.5 Ω. A W25 %Re/W3 %Re thermocouple monitors the temperature of the top end cap, but does not necessarily read the correct temperature of the metal source.

Figure 38.2a shows the design for a nonmelting metal (3-mm slab) that is supported with thin W wires on the bottom of the oven. A W shield, placed on the top of the source material reduces upward evaporation, extending the life of the oven. This source has been used for Fe film deposition rates of between 5 and 30 Å/min at power levels of 90 W and above without melting. The oven-to-substrate distance is 10 cm in this case. Mn has also been evaporated with this design.

Figure 38.2b shows a modified design that permits evaporation of metals that must be melted to achieve the desired rate of film growth. A set of Ta rings

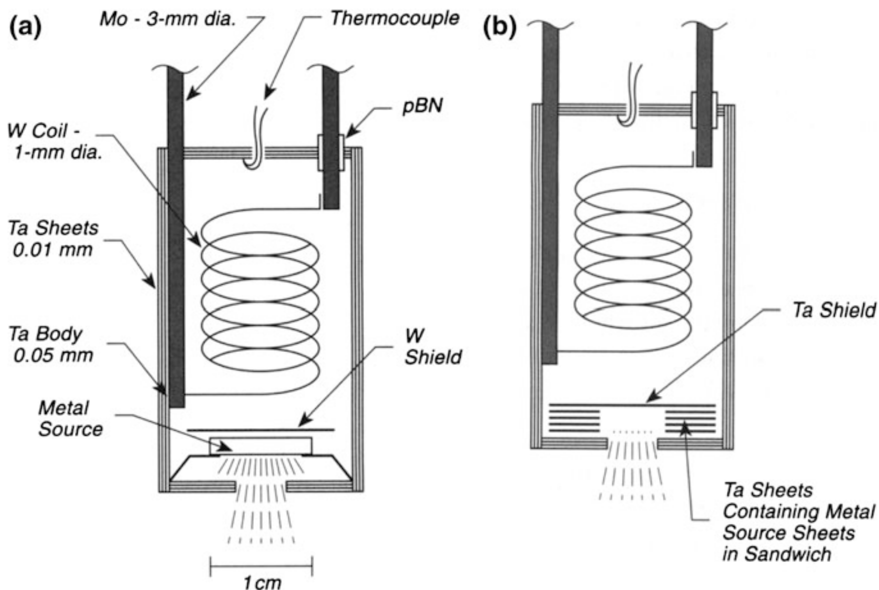

Fig. 38.2 Downward evaporation source, **a** nonmelting metal, **b** melting metal

(0.01 mm thick) alternate with rings of the evaporating metal (0.1 mm thick). The volume of the metal charge may approach 0.4 cm^3. A thicker Ta shield disk (0.05 mm thick) is placed above the stacked rings to direct the metal deposition downward and to shield the substrate from the radiation of the hot W filament. For Cu deposition, a power level of 95 W will give a deposition rate of 10 Å/min, and 145 W gives a rate of about 45 Å/min. The melted metal is held between the thin Ta rings by surface tension. Silver has also been evaporated successfully with this oven design. Metals that alloy with Ta may self-destruct the oven.

The ovens are surrounded by tightly coiled water-cooled Cu tubing that does not touch the oven and that extracts much radiant heat. It is reported that with this design, the total pressure rise is $<5 \times 10^{-11}$ Torr [4].

An excellent review of metal evaporation sources and materials compatibility at high temperatures is given in [5].

38.3 Ultralow Coverage Metal Evaporation

The use of a quartz thickness monitor (QTM) for absolute measurement of the thickness of deposited films has been discussed elsewhere (p. 309). The extension of this technique to very low coverages of deposited material has been made by Chin et al. [6]. Essentially they arrange for the rate of evaporation to be determined by a QTM placed rather close to the evaporation source (7.6 cm), while collecting

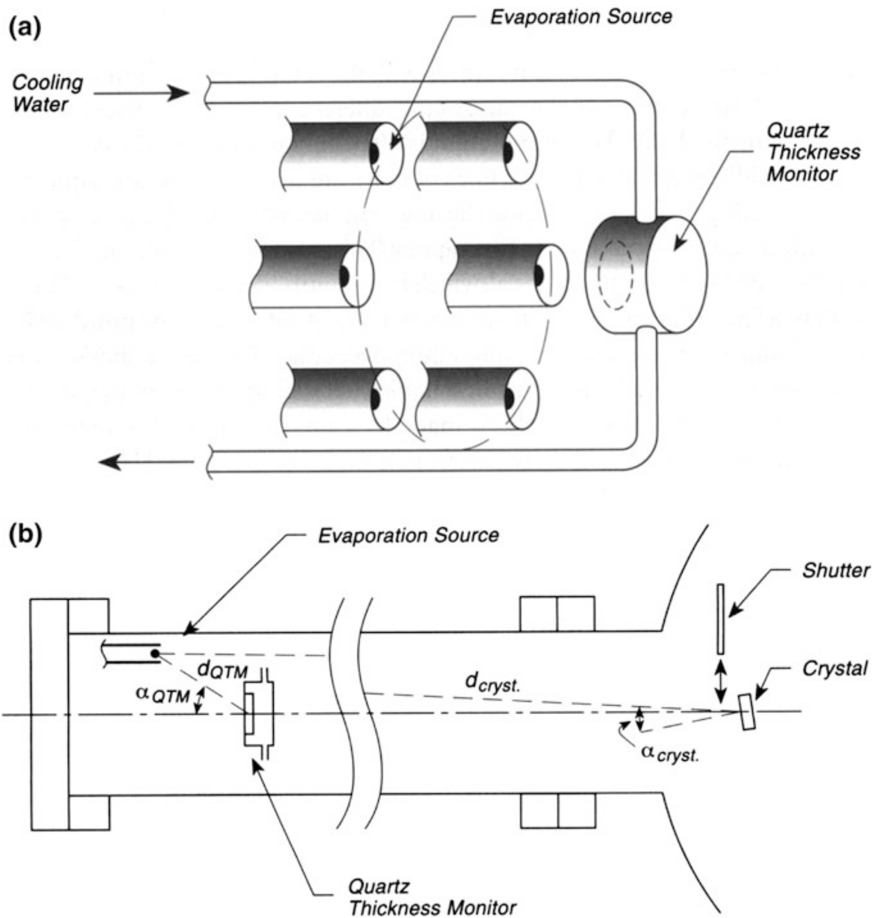

Fig. 38.3 Ultralow coverage metal evaporator, **a** multiple evaporator source, **b** sources mounted at long distance

the deposit on the crystal substrate at a much longer distance ($d_{crystal}$ = 112 cm). The apparatus shown in Fig. 38.3a consists of a set of multiple evaporation sources of similar geometry mounted at a distance, d_{QTM}, from the QTM, which is centrally located. The crystal substrate is mounted in an ultrahigh vacuum chamber facing the evaporation source, which is located far from the substrate in a long flight tube as shown in Fig. 38.3b. Considering both the distances and the angles between the normal to the QTM and the crystal, α_{QTM} and $\alpha_{cryst.}$, the equation for the relative rates of deposition is

$$R_{cryst.}/R_{QTM} = (d_{QTM})^2 \cos\alpha_{cryst.}/(dcryst.)^2 \cos\alpha_{QTM}$$

In the design and testing of this long-path evaporator, the effect of gravity on the evaporating beam was shown to be negligible as was the effect of beam scattering by residual gases at ultrahigh vacuum. For the geometry shown, it was calculated that because of the lower pumping speed at the evaporation source compared to that at the crystal, the pressure in the evaporator region would be about 40 % greater than in the ultrahigh vacuum chamber.

In order to obtain a calibration factor for the apparatus, a second QTM was placed at the crystal position and the ratio of the signals received during evaporation from each of the individual sources was measured. It was found that each of the evaporators gave the designed ratio of about 200 within a 20 % error range, whether the evaporator source material is in the form of a bead or a coil of wire. It was also shown that shadows cast by the QTM and its support structure were unimportant at the flight distances employed. Minimum deposition levels of the order of 10^{-4} ML are possible with this apparatus. An added advantage of the geometry used is that heating of the crystal substrate by radiation from the sources is negligible.

An excellent review of metal atom evaporation sources and materials compatibility at high temperatures is given in [7].

38.4 Congruent Evaporation of Multicomponent Materials

The evaporation of alloys and mixtures will almost always result in composition changes during evaporation because of the differences in vapor pressures of the different components. Thus, flash evaporation is often employed where the entire alloy or mixture is rapidly evaporated to yield films of more uniform composition, equivalent to that of the starting material. Often, the starting material is dispensed as a powder onto a heated surface where evaporation occurs rapidly. This procedure has certain deficiencies, such as the need to powder the material, which might introduce impurities, and the problem with blockage of tubes, etc., with powdered material. Often, too, the powdered material is mechanically ejected, causing film inhomogeneities. The device shown in Fig. 38.4 overcomes these problems by use of a liquid material for the dispenser device [8]. Films of InSb and As/Sb/Se have been made by a predecessor of the method to be described, and films of doped Se have been made by the new method [8].

A quartz capillary tube is partially immersed in a molten alloy of the desired composition, and the liquid is kept slightly above the melting temperature. The molten alloy is forced through the capillary tube by means of an inert gas with a pressure of the order of 10 Torr, and this pressure is dynamically regulated by means of pumping and a gas emission needle valve. The molten source material streams out of the capillary tube into an evaporator heated to a temperature that produces rapid evaporation from its inner surfaces, and is above the melting point of any congruent compound that might form. The evaporator is baffled so that direct

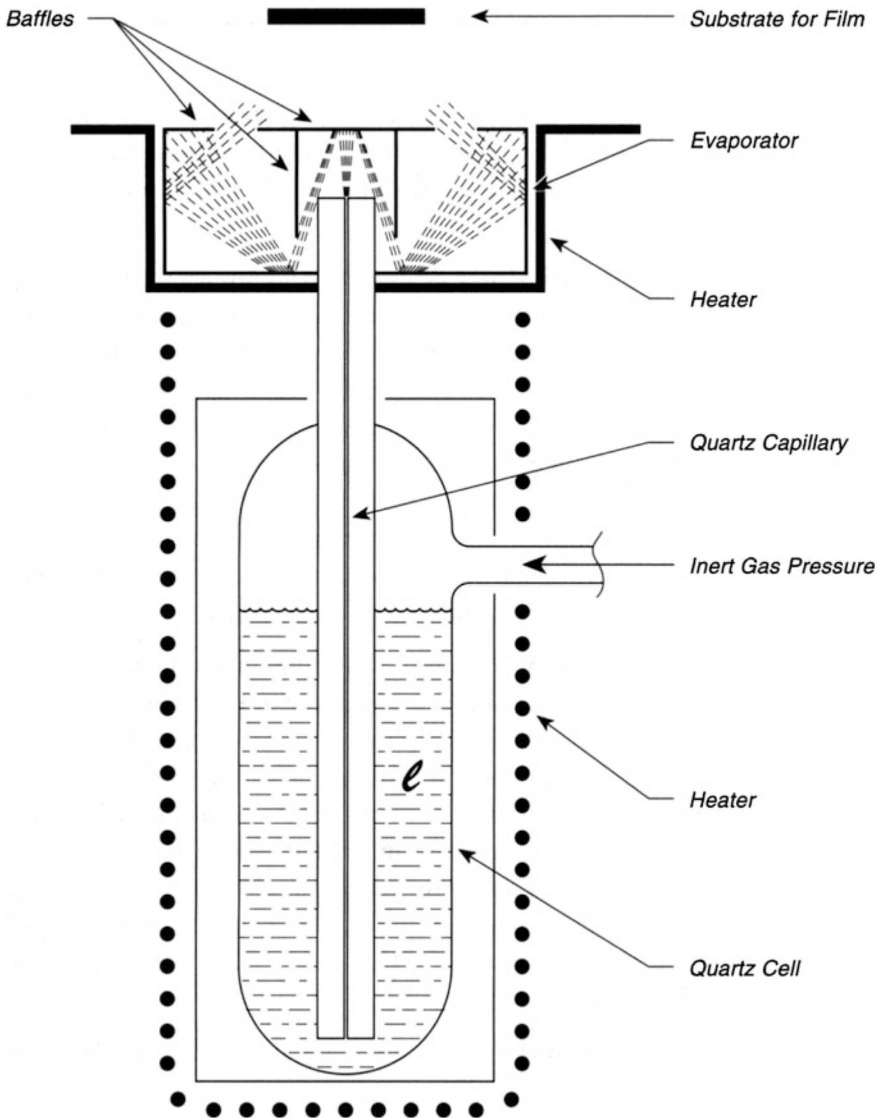

Fig. 38.4 Congruent evaporation source

line of sight between the capillary end and the substrate is not present. In this arrangement, the molten source material can be thoroughly outgassed prior to film deposition. It is advantageous to heat the top of the capillary and the evaporator to temperatures where the source material already starts to evaporate before leaving the capillary.

38.5 Evaporator for Eutectic-Forming Metals

Often, eutectic-forming metals are combined to form evaporation sources for the higher vapor pressure metal. However, at the temperature of vaporization, a lower-melting eutectic alloy may form, causing the mechanical failure of the evaporator device by melting.

A method to avoid this problem has been developed that prevents the formation of the eutectic in sufficient quantities to cause mechanical failure. In the case of a zirconium evaporator, this method has proved satisfactory [9]. Figure 38.5a shows the basic principle of the method. A tungsten rod serves as a mandrel for the evaporator coil, which consists of smaller-diameter W wire wound together with Zr wire. Ohmic heating of the assembly by passing current through the large Ta connector and support plates raises the Zr and W to the correct evaporation temperature (about 2300 K), using 38–40 A, and permits Zr decomposition at a rate of 0.25–0.35 ML/min on the sample located 3 cm from the evaporation source. A special outgassing procedure was employed for this source [9], which is gassy given the high operating temperature and the method of construction.

The principle of operation may be seen from considerations of Fig. 38.5b. Here, a lower melting eutectic mixture of Zr and W is produced at intermediate atomic fractions of W. In the case of the source described above, one avoids arriving at the eutectic region for a substantial part of the assembly by limiting the amount of Zr available compared to the amount of W. Thus, even if the eutectic forms in the immediate region of a Zr/W interface, diffusion of Zr from this region will of necessity bring one to the left-hand region of the phase diagram and into the composition range where extreme depression of the W melting point does not occur. This principle is often applied in designs for W/Ni and W/Al [10] evaporators where the same kind eutectic formation occurs, causing difficulties.

An excellent article describing metal evaporation methods and materials compatibility at high temperatures is available [11].

38.6 Simple Lithium Metal Evaporation Source

The use of alkali metals as adsorbed species and as modifiers of surfaces is well documented in the literature [12], and several alkali metal evaporation sources are used, as indicated on p. 483. A particularly nice source for Li has been described and is presented here [13, 14].

A binary alloy of Al and Li, containing 6.5 % Li, was used in the form of a disk, 10 mm in diameter and 1.5 mm thick [15]. The material was rinsed in acetone before use and is known to be covered with a thick oxide layer. Two 0.25-mm-diameter Ta wires were looped through two pairs of holes, and a fifth hole was used for attachment of a type K thermocouple, as shown in Fig. 38.6a. Although not used by the developers of this Li source [13, 14], the Ta heating wires

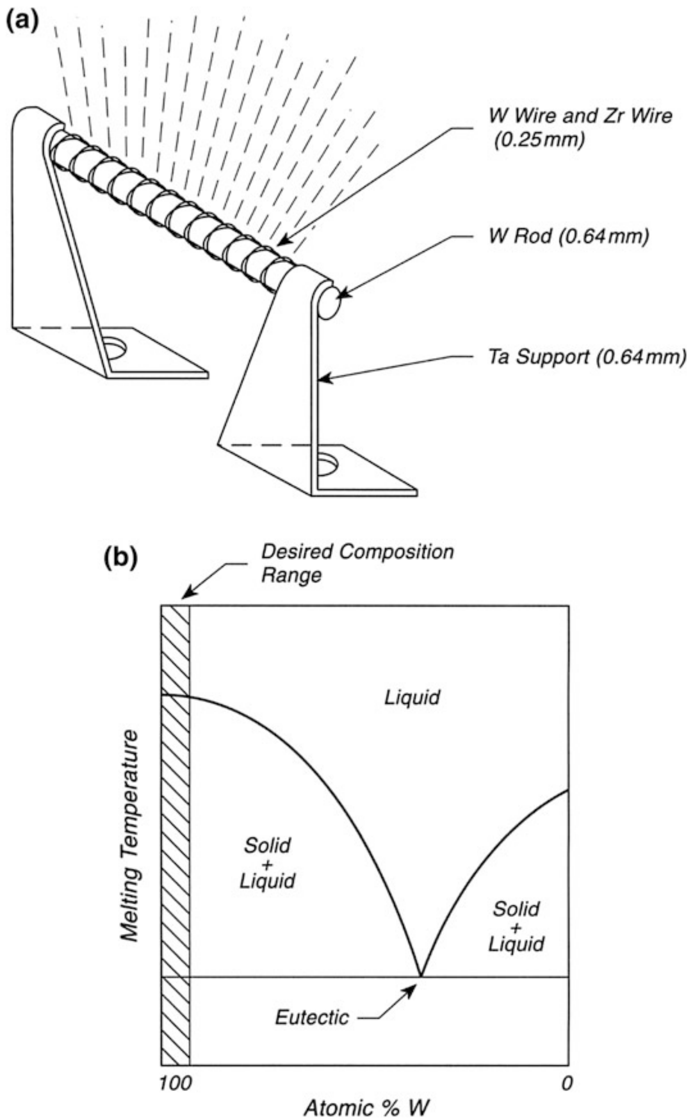

Fig. 38.5 Evaporator for eutectic-forming metals, **a** evaporator, **b** phase diagram

should be mounted on degassing loops (see p. 407 and 437) for maximum efficiency in outgassing the support. The evaporation source is surrounded by a stainless steel shield.

Li evolution from the source was monitored with a quadrupole mass spectrometer, and the temperature dependence of Li evolution is shown in Fig. 38.6b. For actual film deposition, a temperature of 695 K was employed, and Li was

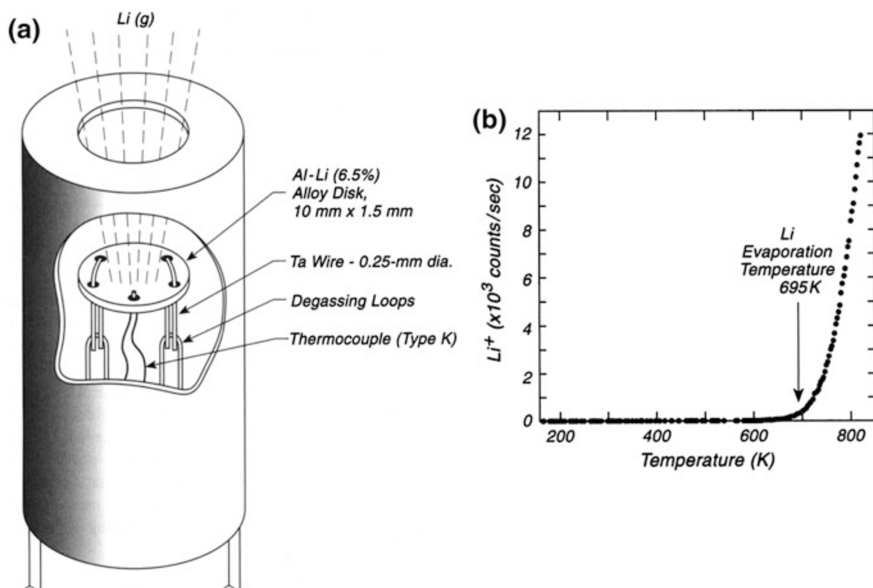

Fig. 38.6 Li thin film evaporation source, **a** Li evaporation source, **b** Li^+ mass spectrometer signal—T scan rate = 0.5 K/s

collected on an atomically clean Al(111) surface on which work-function and X-ray photoelectron spectroscopy measurements were made. From these measurements, it was estimated that approximately 1 ML/min was being deposited with the Al(111) face approximately 1 cm from the source. A 25-ML layer of Li showed no evidence for impurities by X-ray photoelectron spectroscopy. These results indicate that even with the oxide coating, the alloy can supply clean Li by evaporation. The pressure during deposition increased from 1.5×10^{-10} Torr to 3.5×10^{-10} Torr, and the evolved gas was mainly H_2, CO_2, and H_2O.

A more complex source involving Li/Al alloys is described in [16], and the spatial, time-dependent, and temperature-dependent characteristics of this source have been carefully evaluated.

38.7 Aluminum Evaporation Sources—Long Lived

The evaporation of aluminum in ultrahigh vacuum to yield a clean film requires special expertise. The most common design for an evaporator involves the use of W wire as a heater, with Al being evaporated while in contact with the hot W. This is a short-lived source because of alloy formation, producing a low-melting alloy that causes mechanical failure of the W wire. A clever method to avoid alloy formation has been devised, in which a film of Al is oxidized on the W wire to form a barrier

that retards alloy effects [17]. A variety of the most recent methods for evaporating Al have been reviewed in a paper which also presents a different solution to the lifetime problem [18].

The evaporation source is made of zero-porosity alumina tubing (DIN 40 685 type AL23-710) [19], 1.1 mm inner diameter and 1.7 mm outer diameter, 6 mm long. Into this was inserted a 6-mm piece of high-purity (99.999 %) Al wire, with a 1-mm diameter. A tungsten coil, made of 0.25-mm wire and wrapped around a 1.37-mm-diameter mandrel prior to use, was fastened tightly around the alumina tube by virtue of the size difference between the coil and the tube. This assembly was then spot-welded to two Mo rods of 2-mm diameter. The assembly was rigidly supported between the Mo rods using ceramic locating blocks, not shown in Fig. 38.7. The evaporation source was surrounded by a shield that was supported on the mounting flange, and that contained an 8-mm-diameter hole on the axis of the device. A rotatable shutter was used in front of the aperture to control the Al deposition time and to permit outgassing of the source without deposition.

The source was degassed for hours at a 60 % power level compared to the operating conditions used for evaporation. Typical operating conditions were achieved at 2.5 V, 1.4 A, and 3.5 W, under which conditions the alumina tube assembly glowed with a bright orange-yellow color. Final outgassing, with the shutter closed, was carried out for 30 s at the operating temperature. Operation could occur for 5–10 min before the pressure rose to 5×10^{-10} Torr. Under these conditions, deposition occurs at a rate of about 0.5 ML/min. Auger spectroscopy and X-ray photoelectron spectroscopy both indicated that impurities on the evaporated Al film were below the detection limit. The source could be operated reproducibly for several months before failure. Since Al melts at the operating temperature, the source should be mounted horizontally.

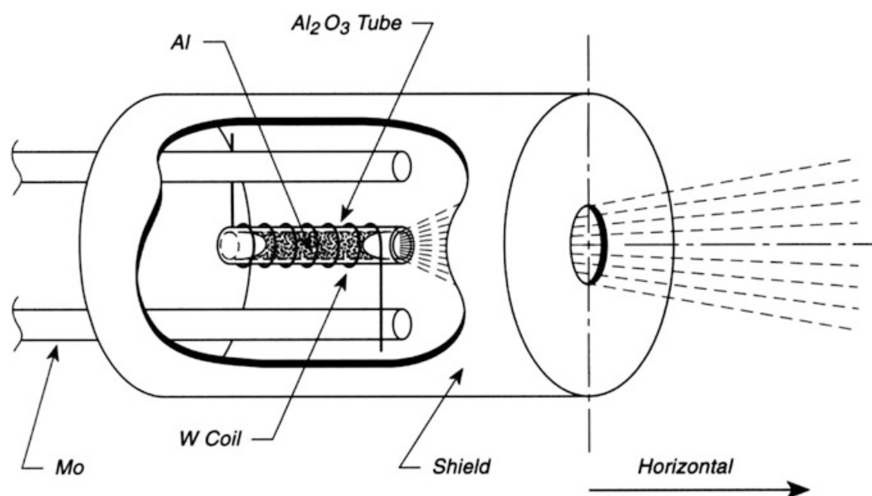

Fig. 38.7 Al evaporation source—long-lived

An improved design for this type of source has recently been reported [20]. Two improvements are incorporated to outgas the source and its supports more thoroughly. First, the heating leads wrapped around the Al_2O_3 are mounted on degassing loops as described on p. 407 and 437; secondly, the entire source is surrounded by a Ta radiation shield that can be separately degassed by means of electron bombardment from a W filament mounted inside the shield, somewhat as shown on p. 407. After degassing by these methods, the source could be operated for hours in the 10^{-11} mbar range [20]. In addition, the outside of the Al_2O_3 tube was modified by grinding a helical channel along its length. This reduced the mass of the tube and increased the thermal contact between the heater filament and the tube. Finally a Chromel-Alumel thermocouple was connected to a Pt sphere that itself was attached to the tube by melting a Pt wire with a hydrogen flame and observing that a portion of the molten Pt drops away while another portion wets the alumina [20]. The thermocouple reads a temperature hundreds of degrees Kelvin below the Al temperature but this may still be used to control the Al evaporation rate even when the thermal contact between the heating wire and the alumina tube varies [20].

38.8 Cr Evaporator Sources of Compact Design

Often the methods used for metal film evaporation require large, high-current evaporation devices that are incompatible with experimental apparatus designed to study the films themselves. Both heating and large outgassing effects are associated with many of the high-power evaporation devices. Therefore, very simple designs will often give better results in research experiments that do not require massive film deposition capabilities. The Cr evaporator discussed here is one example of ultimate simplicity which meets these requirements [21].

Two sizes of W wire loops, 0.25 and 0.5 mm in diameter, are used. These wires are cleaned with 600 grit sandpaper followed by ultrasonic cleaning in acetone and methanol, and then are bent into a hairpin shape as shown in Fig. 38.8. The hairpin filaments are suspended in an electroplating bath with about 2-mm submersion. The electroplating bath is of the following composition [22]:

100 ml H_2O, deionized
30 g CrO_3
5 g NaOH (add slowly)
0.6 g H_2SO_4
0.1 ml ethanol

Electroplating is carried out with a Pb anode. Currents of about 45 and 90 mA are used for the small and large filaments, respectively. The plating voltage is about 3 V. Electroplating for 18 h typically deposited 75 and 250 mg of Cr on the small and large loops, respectively. Before use, the filaments are rinsed in deionized water

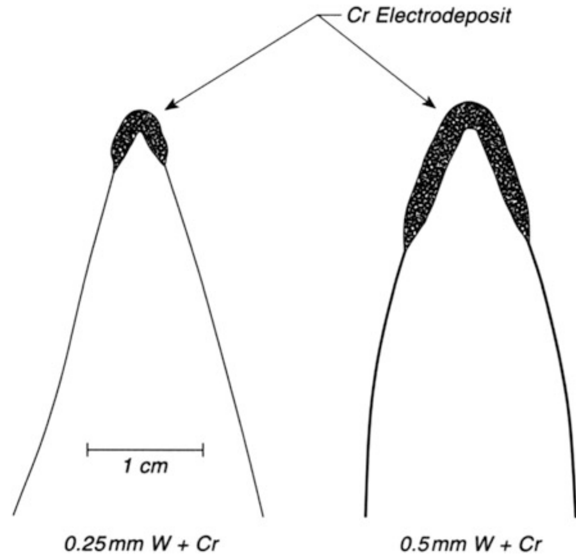

Fig. 38.8 Electrodeposited Cr on W wires for Cr thin film deposition

and methanol. After installation, degassing is done before bakeout at 5–6 A and 15–16 A for the small and large filaments, respectively. The filaments are outgassed a second time during chamber cooling after bakeout, and may then be used in ultrahigh vacuum without appreciable gas evolution in the 6×10^{-10} Torr range.

The small evaporators yielded Cr film growth rates of 4 Å/min at a current of 7 A for a distance of 5 cm. The larger evaporator yielded 4 Å/min at a 10 cm distance at 20-A heating current. These evaporation rates could be increased by a factor of 10–20 by working at higher filament currents. Both filaments produced about 4000 Å of total Cr film thickness before depletion. Auger spectroscopy showed that impurities were not present at the limit of Auger detection if the sources were thoroughly outgassed before use. For early stages of evaporation from a poorly outgassed filament, oxygen impurities were seen. The films produced are of sufficient purity to be used in studies of the magnetic properties of multilayer structures [23].

38.9 Electron Beam Evaporator for Refractory Materials

While many substances can be evaporated using ohmic heating of a filament or a crucible, the successful evaporation of highly refractory materials such as tungsten or molybdenum requires a more intense source of heat, which can be provided by using a high-energy electron beam. A serious problem with conventional electron

beam evaporation methods is the emission of both high- and low-energy stray electrons, which cause effects such as:

1. Electron stimulated desorption from walls and the cold shroud which may lead to film contamination.
2. Film damage.
3. Interference with current measuring instruments, such as ionization gauges, mass spectrometers and electron diffraction apparatus.

Of the two types of electron gun evaporators (magnetically and electrostatically focused instruments), the magnetically focused instruments are more susceptible to the difficulties mentioned above [24]. Figure 38.9a shows a schematic diagram of an electrostatically focused electron gun. A thoriated W filament of circular geometry is located between a shield and a cage, and both are biased at between −5 and −10 kV (−HV). The filament is heated by a 12-V, 30-A power supply. Electrons are emitted and follow trajectories to the grounded hearth containing the sample to be evaporated. A focusing mechanism (not shown) can change the relative position between the hearth and the rest of the components of the gun, permitting an exact focusing of the electron beam on the top of the molten metal in the hearth. A second degas mode involves keeping the filament at −3 kV and grounding the remaining components of the electron gun evaporator. Out-gassing was reduced by making all components out of refractory materials, such as W, Mo, and Ta. The shield and hearth were made of Mo; the cage was constructed of Ta mesh on a Mo frame with a W top cover containing a central hole. Using a Ta mesh cage prevents heat buildup, and radiation-induced heating of large surfaces leading to outgassing.

The secondary electrons produced in the gun cannot escape from the cage, which is biased at −HV. The high-energy electrons have a potential V in the range $-HV < V < -HV + V_f$, where V_f is the potential drop across the emitter filament due to its resistance. In addition, there are high-energy backscattered electrons, which mostly are at a potential of V or a slightly lower potential owing to energy loss upon scattering. Since the potential at the hole in the cage can be positive relative to $-HV$ by a few hundred volts, backscattered electrons will escape from it. To eliminate this problem, a tungsten mesh grid with 2-mm spacings was placed over the hole to retard electrons there. In addition, by biasing the filament at −9.9 kV, excellent focusing is achieved and stray electron currents are minimized, as depicted in Fig. 38.9b, where calculated trajectories for cylindrical symmetry are shown.

This evaporation source can operate for refractory metal evaporation at pressures $<2 \times 10^{-9}$ Torr [24]. A cryogenically shrouded source of somewhat similar design has been described [25]. A highly stable electron beam evaporation source has been described in [26]. A method involving the measurement of the ion current generated by ionization of evaporating metal atoms and relating this measurement to the rate of metal evaporation is described in [27].

An excellent review of metal evaporation methods and materials compatibility at high temperatures is available in [28].

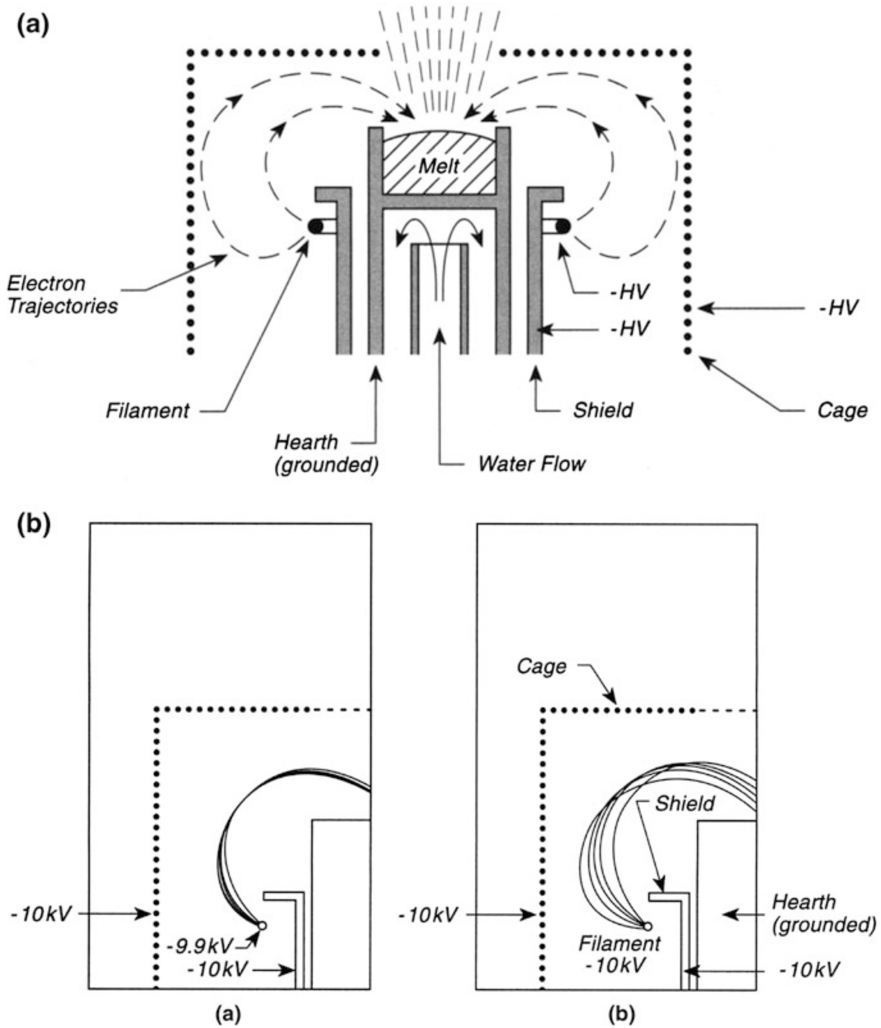

Fig. 38.9 Electron beam evaporation, **a** evaporator, **b** electron trajectories

38.10 Small Electron Beam Evaporator for Refractory Metals

As discussed previously (p. 449), electron beam evaporation is a desirable method for the deposition of thin films of refractory metals that does not involve the problems of ohmic heating of a filament to very high temperatures. The design shown in Fig. 38.10 incorporates simple features [29], combined with low mass components, eliminating problems with large surfaces outgassing during operation.

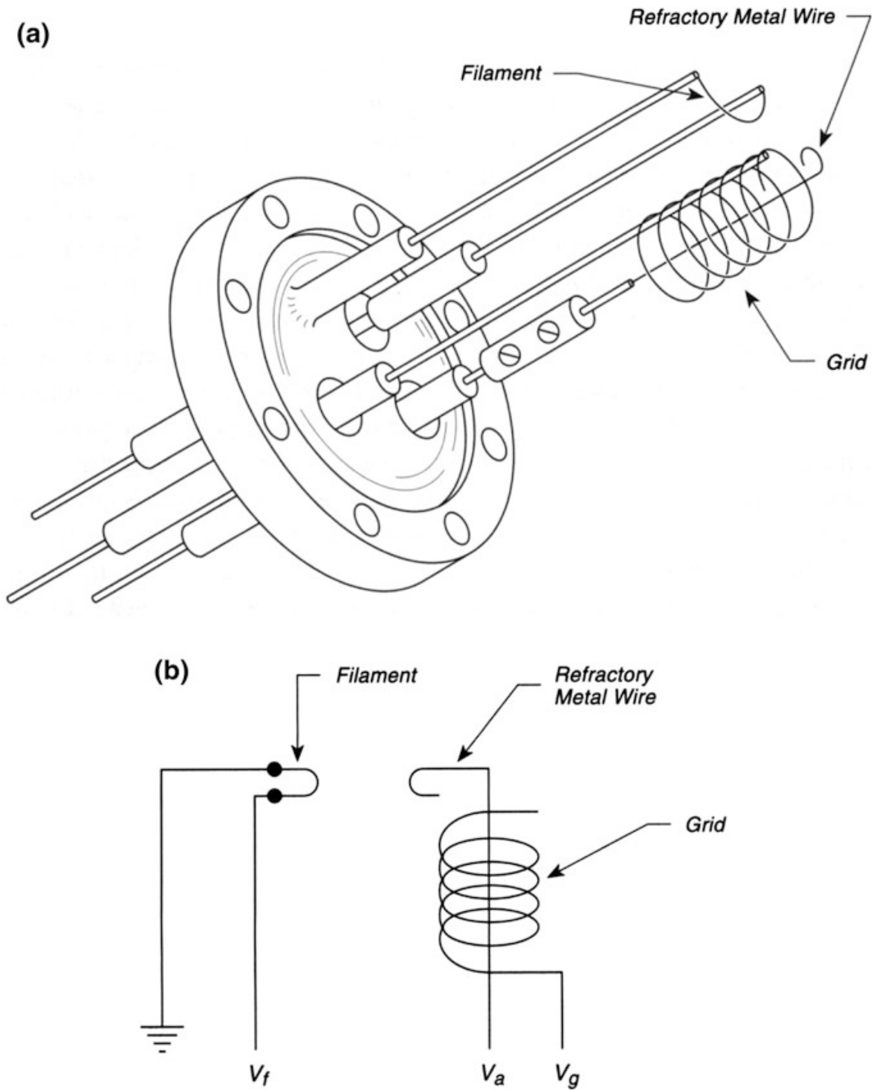

Fig. 38.10 Electron beam evaporation, **a** evaporator design, **b** circuit

The device is simple to build, does not require cooling water for its components, operates in the 10^{-9} Torr range, and produces clean films of refractory metals.

The evaporation device is mounted on a 2.75-in.-diameter flange containing high-voltage feedthroughs. A tungsten emitter filament, about 1 cm in length and 0.012 cm in diameter, is spot-welded on 0.1-cm-diameter Ni rods as shown. It is positioned 1–2 cm from the evaporation source. The source is a 6-cm wire (0.025-cm diameter) made of the refractory metal to be evaporated that is fashioned

into a loop on the outer end; the base of this wire is welded to a 0.1-cm-diameter Ni rod connected to a feedthrough pin by a set-screw contact for easy replacement. The source wire is placed on the axis of a Mo wire helix with a diameter of about 1.5 cm, made of 0.025-cm-diameter Mo wire.

For operation, the source wire is set at about +6 kV = V_a, and the grid is set at about −3 kV = V_g. The filament voltage, V_f, is slowly raised using a current supply until the collected current at the evaporator source is in the 5 to 20-mA range. Next the negative voltage on the grid is empirically adjusted until electron bombardment heating occurs only on the loop of the source wire. Overheating the loop can result in melting which is undesirable. Films with greater than 1000-Å thickness have been evaporated from W, Ta, and Ir at rates in the range 1–10 Å/min.

A variation on this source in which a small Mo crucible replaces the pendant droplet source described here has been designed and tested [30]. The mass of the crucible is kept to a minimum, and the emitter coil is wound so that it encircles the crucible edge and is slightly below the edge [30].

An excellent review of metal evaporation sources and materials compatibility at high temperatures is given in [31].

The cover of this second edition features this simple metal evaporator source because of its wide application.

38.11 Electron Beam Evaporator

A design [32] differing somewhat from those shown elsewhere in this section, which focuses a high-energy electron beam at a point on the end of a source wire for the purpose of evaporating a metal is shown in Fig. 38.11. The metal source wire is 1–2 mm in diameter, mounted on a high-voltage Cu feedthrough that can be translated in the vertical direction. In normal operation, a molten droplet of metal is produced on the end of the wire by electron bombardment. The circular electron emitter filament, made of 0.25-mm-diameter W wire, is looped over itself in a 15-mm diameter circle, and welded to two Ta wire leads (1-mm diameter), which are connected to vacuum feedthroughs as shown. The distance between the plane of the loop and the source tip is typically 6–9 mm. Nominal operating conditions are shown in Fig. 38.11. As the source wire is evaporated, the beam current decreases and may be restored by advancing the source to a position where the current returns to its original value. With a source-to-sample distance of 15 cm, several hundred Å of film may be deposited before source motion is necessary. The filament is shielded from the substrate receiving the evaporated film by the aperture plate, and this reduces radiative warming of the substrate. The source is readily outgassed behind a closed shutter by running with the cooling water removed and at a reduced voltage (0.5–1 kV). During normal operation, with water cooling, the pressure in the UHV system remains in the 1–4 × 10^{-10} Torr range. Impurity transport to the film has been measured for Fe and Co source wires using both Auger spectroscopy and X-ray

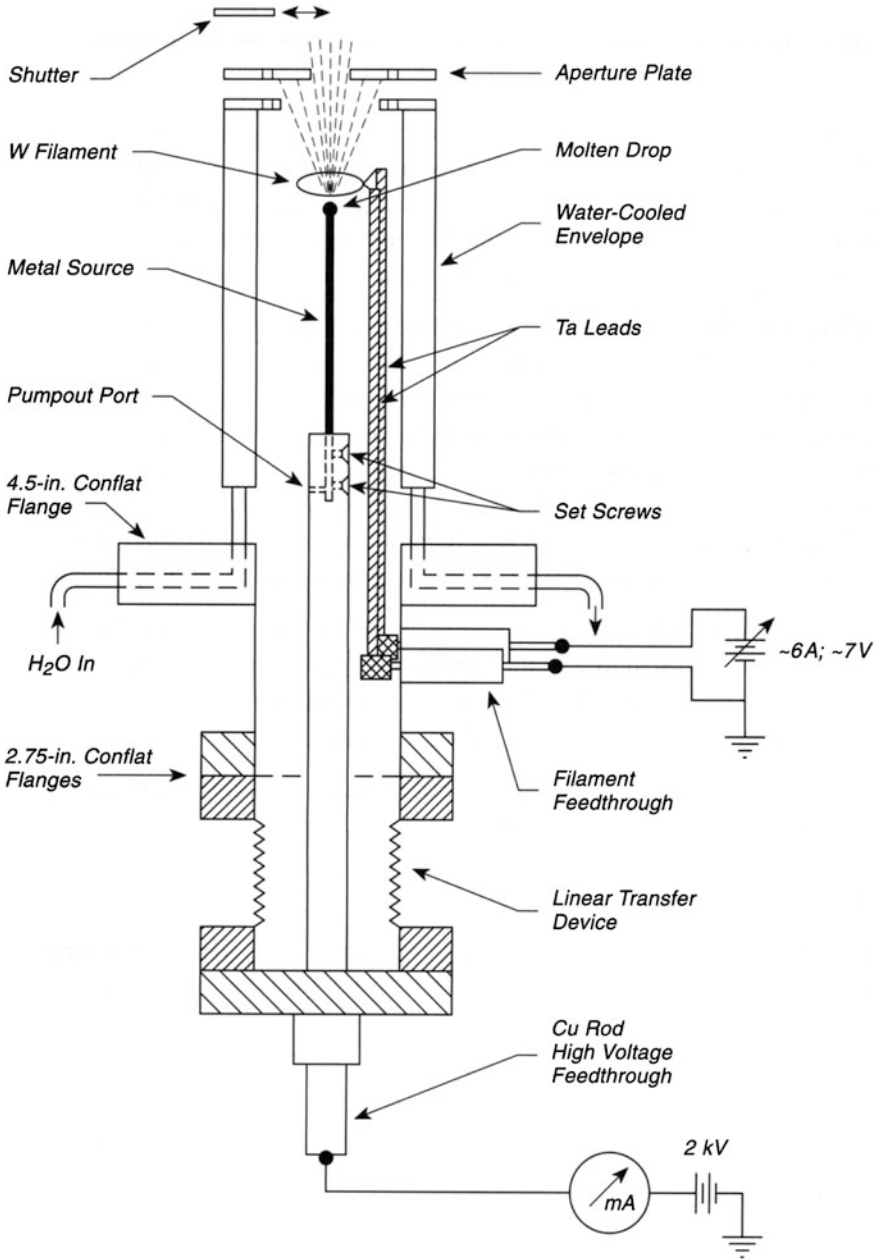

Fig. 38.11 Electron beam evaporator

photoelectron spectroscopy, and impurity levels below the detection limit were found.

A design similar to this, but using a very small Mo crucible in the position of the end of the source wire, has been described [33] for the evaporation of low-melting metals under conditions where the low outgassing qualities of this evaporator are retained.

A review of metal evaporation sources is contained in [34]. In addition, an excellent review of metal evaporation sources and materials compatibility at high temperatures is given in [35].

38.12 Break-Seal Ampoule Doser

Often low-vapor pressure compounds are used as precursors for the growth of compound semiconductor films on a substrate. Many of these compounds react with stainless steel and therefore cannot be transferred through heated tubing. This design places a glass ampoule of the compound close to the substrate so that the vapors do not come into contact with metal prior to deposition [36].

A glass ampoule is filled with the compound in a dry box under an inert atmosphere and the ampoule is sealed. The ampoule is rigidly attached to the end of a transfer rod inside a copper carrier assembly that fits the ampoule (Fig. 38.12). The copper assembly is wound with W wire, sheathed in fiberglass or quartz fiber sleeving, and a thermocouple is placed in contact with the copper carrier for temperature measurements during vaporization from the ampoule. The use of a bellows transfer device is superior to a magnetically driven device, since the heater

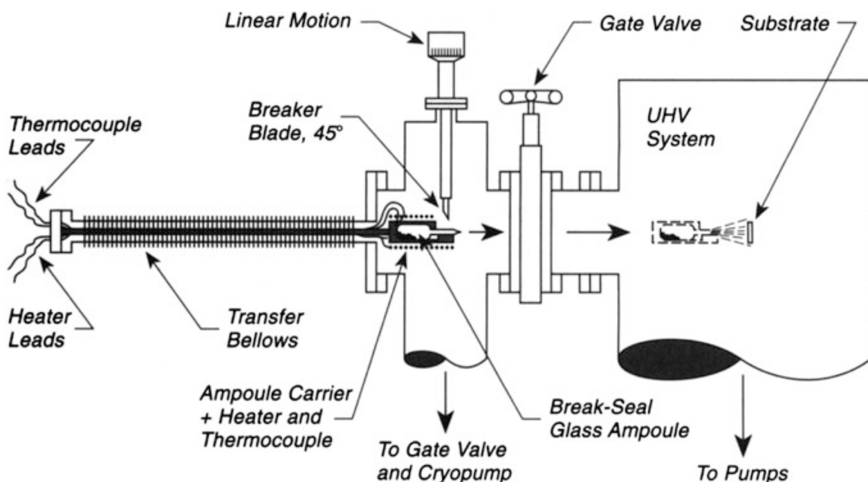

Fig. 38.12 Break-seal ampoule doser

and thermocouple wires are fixed along the transfer rod during motion and do not have to flex each time the ampoule is moved.

A linear motion device with a stainless steel blade is used to break off the neck of the ampoule when it is desired to start the vaporization process. Once the neck is broken, the ampoule can be moved into the UHV chamber through a gate valve, and the temperature of the doser can be adjusted to produce the desired rate of precursor vaporization.

A cryopump is chosen for the first chamber because it pumps water vapor efficiently and it is not impeded by glass fragments.

38.13 Cadmium Sulfide Evaporation Source

Thin films of CdS may be thermally evaporated from CdS powder. The apparatus shown in Fig. 38.13 is made entirely of tantalum, tungsten, and boron nitride [37]. A large area baffled aperture produces a uniform CdS deposit. In addition the baffle shields the substrate from radiation from the indirect heater. The baffle has a 3-mm-wide gap between its outer edge and the Ta shield.

The sublimation source is made of a Ta cup welded to a Ta tube. This slips over a cylindrical shield made of BN, which contains a rigid coil of fairly heavy wound W wire in three strands. The entire assembly may be unloaded by pulling upward on the handle, leaving the W wire exposed. In operation, the CdS nearest to the central heater sublimes first. The source temperature is measured with a Pt/PtRh 13 thermocouple welded to the baffle. At a temperature of 550 °C, CdS is deposited at a rate of 7 Å s^{-1} on the substrate at 120 °C and 24 cm distant. The operation time at this rate of evaporation is about 4 h before refilling is needed.

By choosing the correct evaporation and source temperatures, the resistivity of the deposited CdS film may be controlled.

A CdS evaporation source using elemental evaporation has been described [38].

38.14 Arsenic Atom Source

The use of elements from Groups II, III, IV, V, and VI in the production of semiconductor devices is widespread. Many of the elements sublime as atoms, but in Groups V and VI, sublimation as dimers and tetramers is commonly observed. It is advantageous—for example, in the growth of GaAs surfaces—to employ atomic As, which forms surfaces with fewer defect sites than surfaces grown from As_2 or As_4 species. The device shown in Fig. 38.14 permits the substantial atomization of As_2 and As_4 by use of a final heated atomizer stage [39]. The principles embodied here can also be used with other elements where atomization is desired. It should be remembered that the equilibrium between atomic species and higher molecular

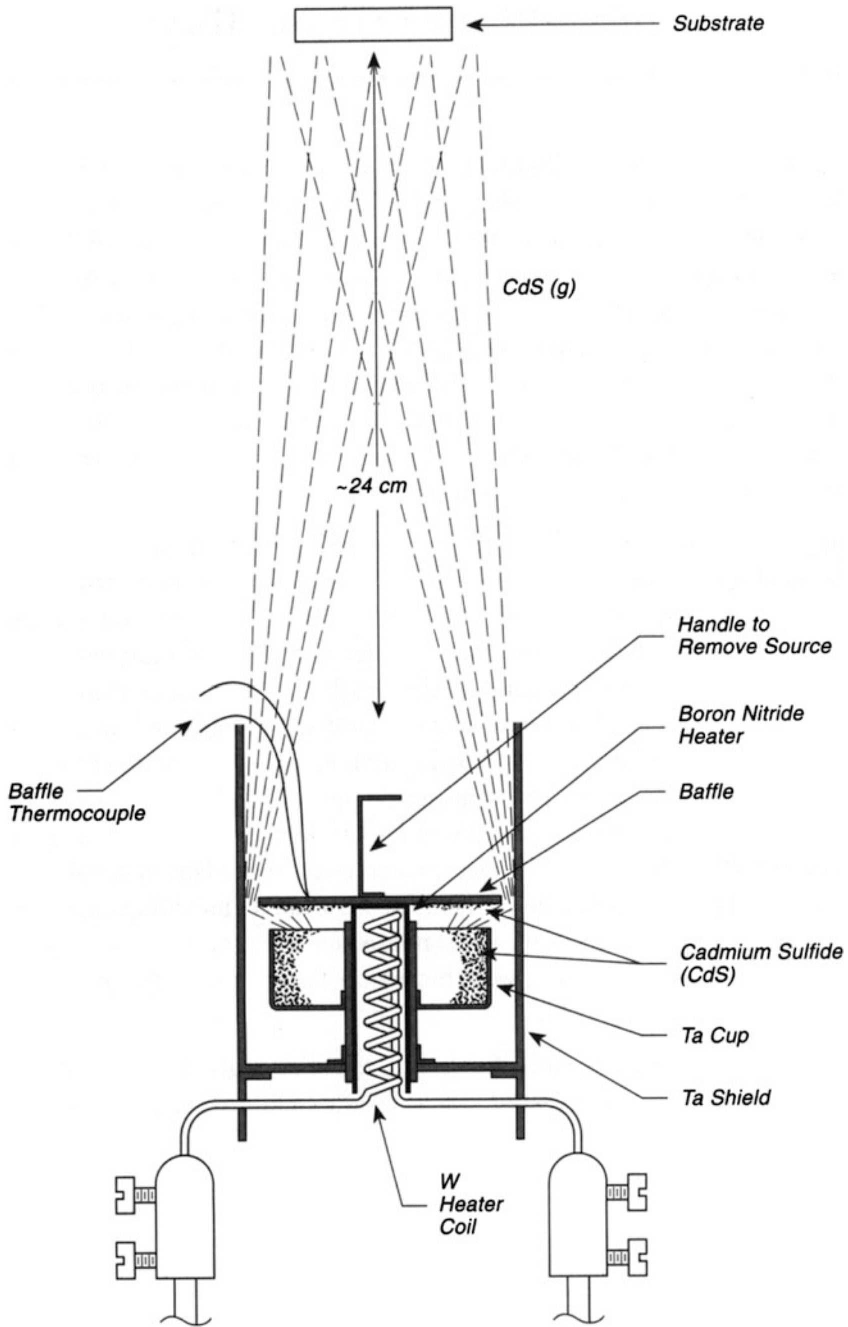

Fig. 38.13 Cadmium sulfide evaporation source

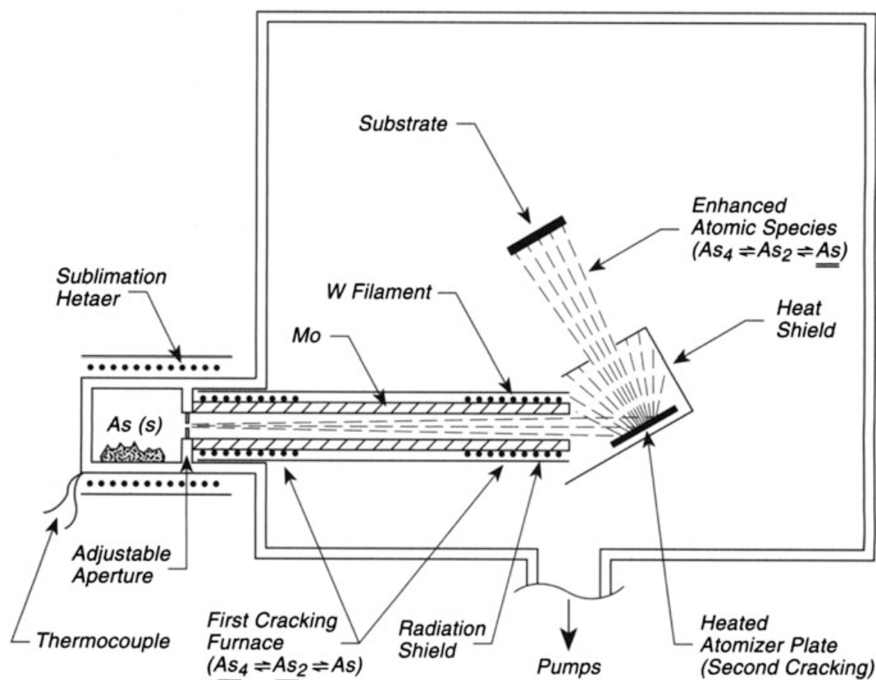

Fig. 38.14 Arsenic atom source

weight species is favored toward the atomic species by high temperatures and by low pressures.

Figure 38.14 shows, schematically, the device used to make atomic beams of As containing small fractions of As_2 and As_4. A sublimation source, loaded with As(s), is connected to a first-stage cracking furnace through an adjustable aperture. Adjustment of this aperture allows the beam pressure of As species to be controlled throughout the apparatus. The subliming species are conducted through the first stage cracking furnace and then exit to a heated plate that serves as the second-stage atomizer. The products from the second stage are significantly enriched in atomic As, and are emitted from a second aperture toward the substrate. The atomizer can be operated in the range above about 1200 K when the local pressure is below about 10^{-3} Torr; it can also be operated in the range above 1400 K when the local pressure is about 10^{-2} Torr. Many materials can be used for the atomizer plate with various elements to be atomized, including refractory metals such as W, La, Nb, Re, Mo, and Ta, and stainless steel, Ni, graphite, Pt, B, Si, ceramics, and BN. Compound formation between the material of the atomizer plate and the beam is to be avoided.

The preferred range of operation for various materials is given in Table 38.1, and substantial but not complete atomization will be produced under the listed conditions.

Table 38.1 Preferred range of operation—atom sources

Substance	Pressure at atomizer (Torr)	Temperature range (K)
As	$<10^{-2}$	>1400
	$<10^{-3}$	>1200
P	$<10^{-3}$	>2000
	$<10^{-5}$	>1800
Sb	$<10^{-2}$	>1400
	$<10^{-4}$	>1200
S	$<10^{-2}$	>2000
	$<10^{-4}$	>1700
Se	$<10^{-2}$	>1600
	$<10^{-4}$	>1300
Te	$<10^{-2}$	>1300
	$<10^{-4}$	>1100

38.15 Portable Microevaporator for Depositing Low Coverages of Single Atoms

Temperature programmed desorption from an adsorbed layer may be used to deposit small coverages of atoms or molecules onto surfaces and provides a method for the control of very small coverages on a collector surface [40, 41]. To do this a tungsten filament is first cleaned in ultrahigh vacuum by heating to high temperature, and is then covered with the desired adsorbate, such as an alkali metal (see Sect. 40.4) or another metal which is known to evaporate at a convenient filament temperature. The tungsten evaporator can be conveniently made by removing the quartz bulb of a halogen lamp and mounting the fused lamp base on a convenient support, here shown in Fig. 38.15 as molybdenum bars connected through a sapphire baseplate. Electrical contact to the filament can be made using two tungsten helices welded to the lamp leads (one shown) which permit the adjustment of the filament position up or down. The diameter of the wire in the helices should be large enough that the current needed for evaporation from the filament does not cause desorption from of residual gases from the helices (see Sect. 38.1). An evaporator of this type could be loaded with adsorbate at one position in the UHV chamber and then swung around to the position needed for deposition. It has been used to deposit Li, Pd and Au onto single crystals, and the observation of atomic dispersion of the evaporated material has been made with the STM.

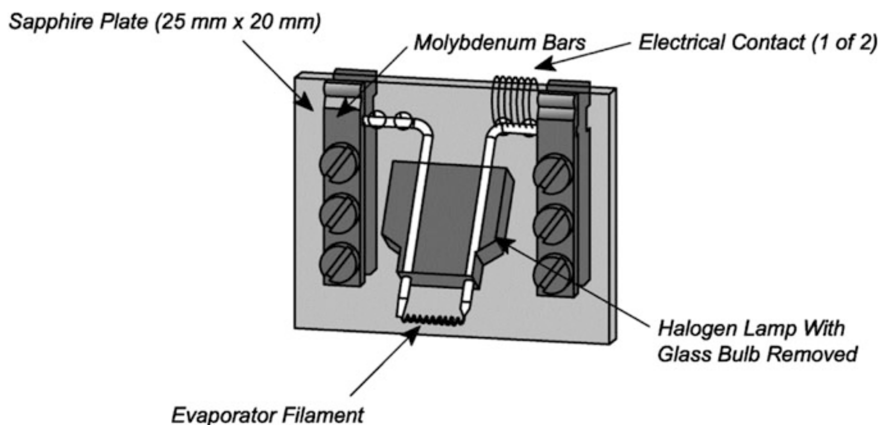

Fig. 38.15 Portable microevaporator for depositing low coverages of single atoms

38.16 Nanoscale Templating of Close-Packed C_{60} Nanostructures

Linear chains of fullerene molecules are of interest due to their one-dimensional architecture. The C_{60} molecule is a lively candidate for the building block for such linear structures. Figure 38.16a shows an STM image of partially oxidized Cu(110), where striped structures of ⋯Cu–O–Cu⋯ assemblies form during oxidation at 250 °C with a few monolayer dose of O_2. Oxidized stripes a few hundred nm in length form, separated by 0.76 nm wide gaps. Shown in Fig. 38.16b is a ball model of a portion of the striped structure with clean Cu regions of width of $3a_0$, where a_0 is the 0.25 nm interatomic spacing for Cu in the lateral direction. This 0.76 nm wide gap fits well a C_{60} molecule with a diameter of 0.73 nm.

The deposition of C_{60} from an evaporator source in UHV leads to the formation of long chains of C_{60} molecules as shown in Fig. 38.16c. which indicates that regular structures can be obtained by annealing at 250 °C. Wire lengths of C_{60} longer than 100 nm can be obtained by this procedure. In Fig. 38.16d a higher resolution image shows that the C_{60} chains consist of an ordered-pentamer and a disordered-hexamer units. Further details of the structures achieved and their electronic properties are given in [42].

38.17 Quantitative Molecular Beam Dosing of Slightly Volatile Organics

The field of surface science is increasing concerned with the study of larger molecules with low vapor pressures. While a number of types of heated dosers are described in this book none have the capability to deposit an accurately known flux

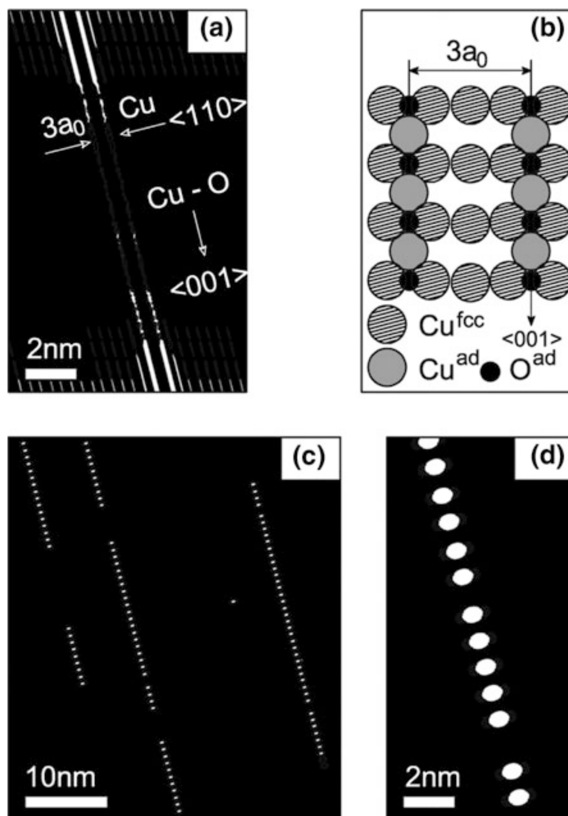

Fig. 38.16 Nanoscale templating of closed-packed C_{60} nanowires

of molecules. In the method described in Fig. 38.17, an oven containing an internal circulating fan is constructed around the source (sample) bulb to adjust the vapor pressure accurately and a heated delivery system, maintained above the vaporization temperature, conducts the vapor through a heated leak valve and into a heated doser tube [43].

Figure 38.17a shows the construction of the heated doser. All surfaces which contact the vapor are heated above the sublimation temperature, ensuring that condensation does not occur. To do this simply, the doser is made of OFHC copper to ensure maximum thermal conductivity, and a glass sleeve containing a wound tungsten heating wire is clamped on the doser just under the 2¾″ flange. Heating at this point, as measured by a thermocouple, can be used to adjust the temperature of the doser guide tube which faces the crystal to receive the organic adsorbate.

In Fig. 38.17b, a schematic of the high temperature vapor source and conduction system is given. Inside of the oven, maintained at a constant temperature to produce the desired vapor pressure, a Baratron capacitance manometer indicates the vapor pressure of the organic. The heated source may be pumped by a small turbopump which is connected through a cold trap to the sample bulb, 4. The heated source

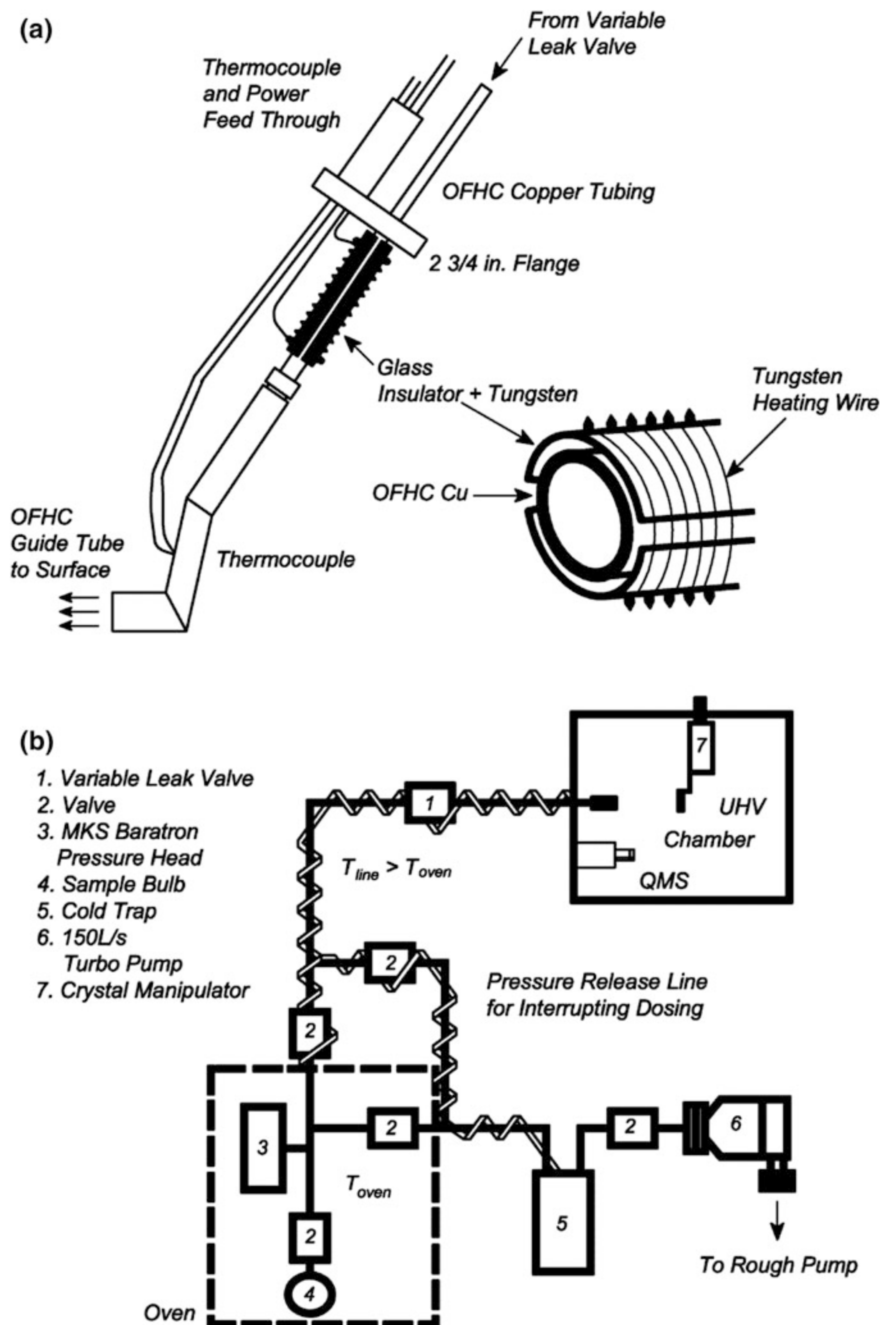

Fig. 38.17 Quantitative molecular beam dosing of slightly volatile organics, **a** heated gas doser, **b** vacuum system—heated, **c** reproducibility of vapor pressure measurements of naphthalene, **d** enthalpy of sublimation for naphthalene, **e** mass spectrometer for response in UHV chamber during dosing

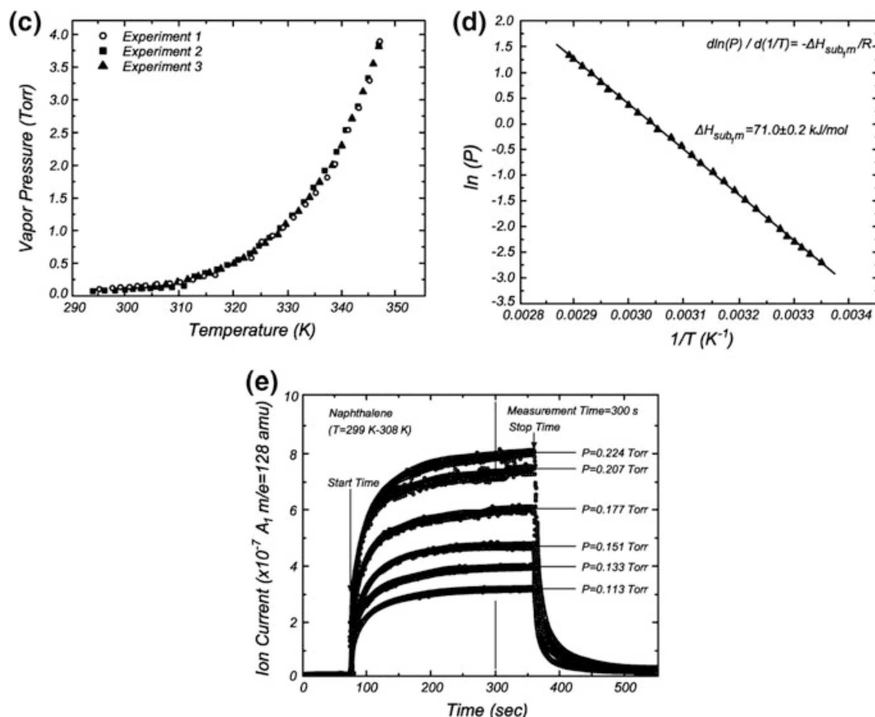

Fig. 38.17 (continued)

region is connected to the doser in the UHV system by a gas line which is heated about 20 K above the source temperature in the oven. Flow to the heated doser can be interrupted by pumping the source through the turbopump.

Figure 38.17c shows the measured vapor pressure of naphthalene in the temperature range 294–346 K. Three separate measurements agree well. Figure 38.17d shows a Clausius-Clapeyron plot of the vapor pressure; the slope yields the sublimation enthalpy of 71.0 ± 0.2 kJ/mole, which agrees well with the literature.

Figure 38.17e shows the behavior of the mass spectrometer in the vacuum system as naphthalene vapor is admitted at various vapor pressures through the heated doser system. The walls of the UHV system initially adsorb naphthalene molecules, and the mass spectrometer observes this wall-adsorption during the approach to steady state system pressure, which is achieved after about 400 s dosing. However, a crystal placed in the molecular beam will see an immediate steady flux of naphthalene and it was shown that the coverage increased in linear proportion to the pressure of naphthalene as measured in the oven source multiplied by the time of exposure [43].

A critical feature in the apparatus is a heated adjustable leak valve, 1, which is a Granville-Phillips (series 203) variable leak valve. In the different experiments, the leak valve is not adjusted to open or close it, since these valves are not reproducible

upon cycling open and closed. It serves therefore only to adjust the fraction of the incident vapor which passes. It can be adjusted initially to select the time required to achieve a desired coverage on the single crystal but is not adjusted further in quantitative dosing measurements. Its leak rate during our measurements was about 2×10^{14} molecules naphthalene/Torr s.

This doser method has been shown to work well using other low vapor pressure organics [43, 44].

38.18 Organic Doser

A simple doser for subliming volatile organic materials is made from a 1 in. ceramic standoff with vented screws mounted in both ends. The top screw covers a small reservoir containing the powdered material to be sublimed. The bottom reservoir is empty and also contains a vented screw through which a thermocouple is forced and spot welded. Heating is accomplished by passing current through 0.010″ W (3 %Re) wire, although ordinary W wire would certainly serve too. A shutter may be used to interrupt evaporation [45] (Fig. 38.18).

38.19 Vapor Deposition of Organic Thin Films

The evaporation of organic materials and higher-vapor-pressure inorganic materials into an ultrahigh vacuum system may be done with various heated sources. A difficulty arises with large Knudsen cells and metal boat evaporators in that they have a large heat capacity and are difficult therefore to bring to temperature rapidly; also, difficulties in controlling the temperature may be present. A small evaporation source eliminating these problems is shown in Fig. 38.19 [46]. While the device described in the literature was made from the cathode components of a commercial electron gun [46], the basic design principles shown here may be useful in devices built in many ways.

An indirectly heated cathode assembly in a ceramic base, and containing an alumina-coated W spiral heater assembly, is provided with a second closely fitting Ni tube to hold the organic material. In some cases, the organic material is held on a plug of fine quartz wool to prevent it from falling out or bumping during evaporation. A thermocouple is welded to the source tube to monitor the evaporation temperature. A few mm^3 of organic material is added, and the source is installed in the vacuum system. One must be careful to determine that the vapor pressure of the material at the base temperature of the vacuum system will not severely degrade the vacuum. Materials such as long chain alkanes, phthalocyanines, and some metal halides have been handled successfully at temperatures up to 500 °C. The film deposition rate, controlled by the temperature, ranged from 0.01 to 5 nm/s, typically 0.1 nm/s. The gun can be used for several years.

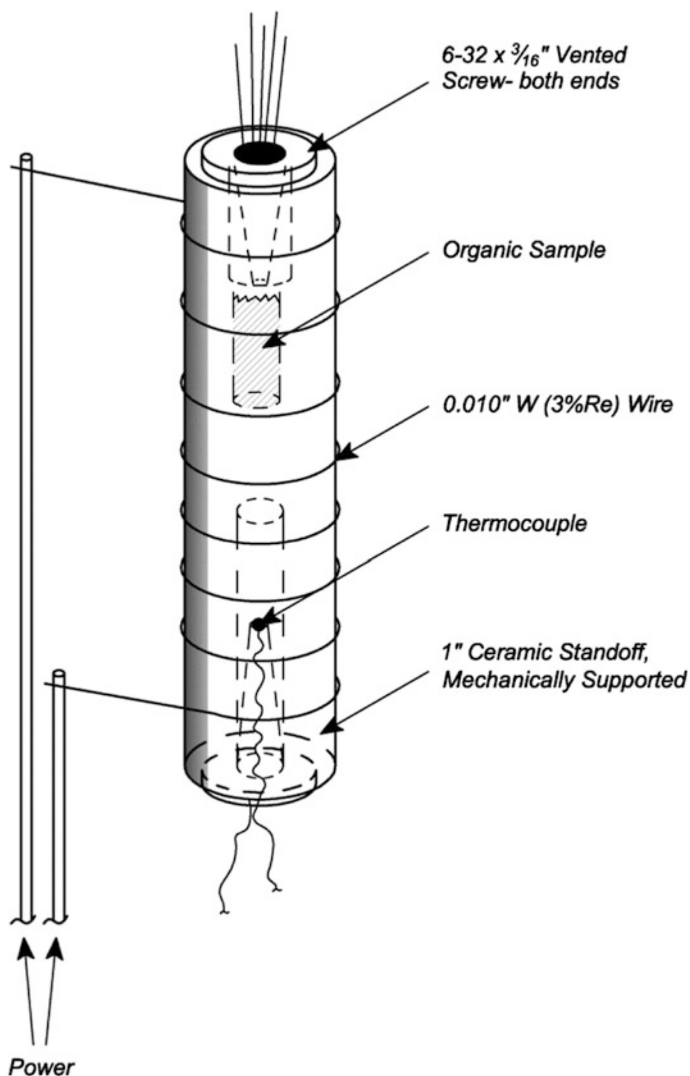

Fig. 38.18 Organic doser

38.20 Evaporator for Organic Film Deposition

Many evaporators for organic materials are made of ceramic crucibles (e.g. boron nitride) with ohmic heaters and thermocouples for achieving and measuring the evaporation temperature. At least 3 electric feedthroughs are necessary for each crucible if one leg of the ohmic heater is connected to ground. In this design, only a single feedthrough is needed as the ohmic heater is also used as a temperature

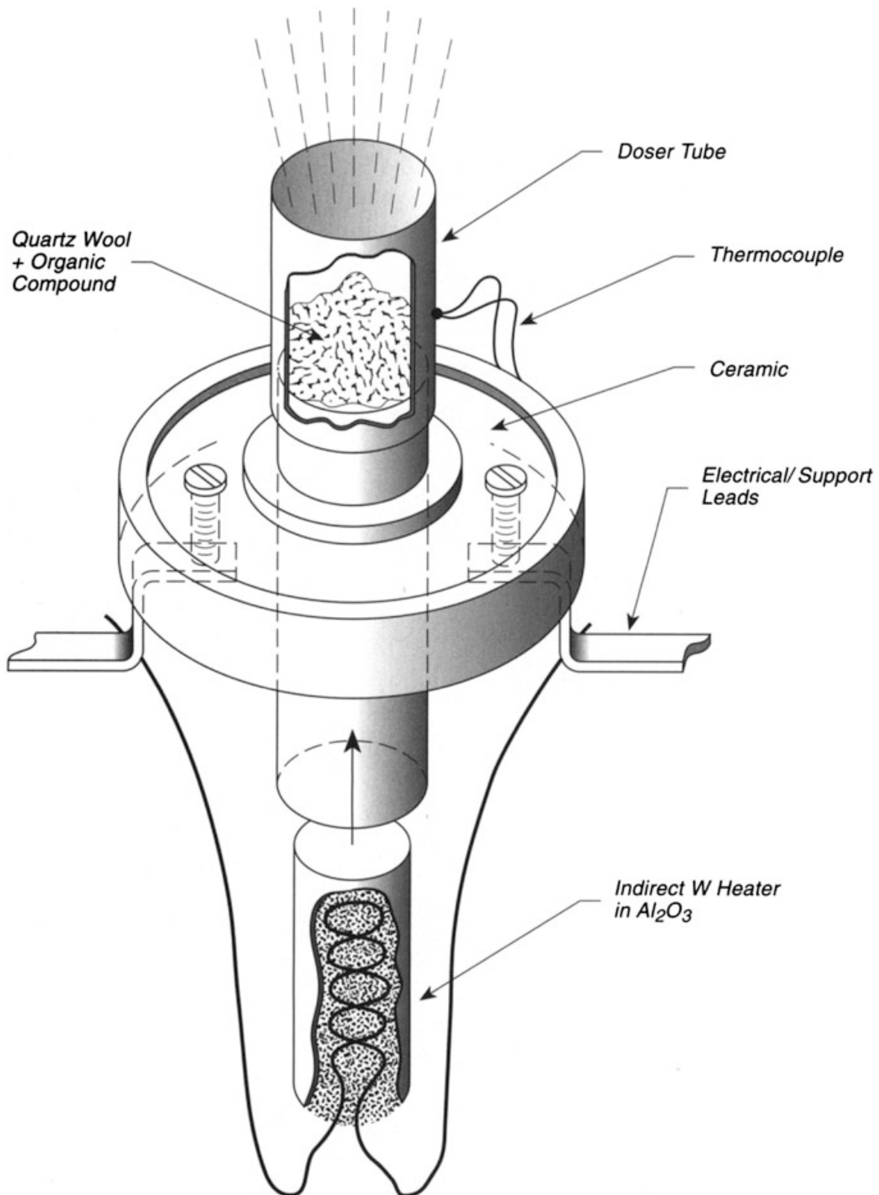

Fig. 38.19 Vapor deposition of organic thin films

sensor by means of measuring its electrical resistance during operation. A Pt heater wire is tightly wrapped around a grooved BN crucible and pressed into place by a mica sheet insulator and a Mo shield which is in two sections for clamping tightly. For measuring the temperature, a small current of order 0.1 A (I) is passed through

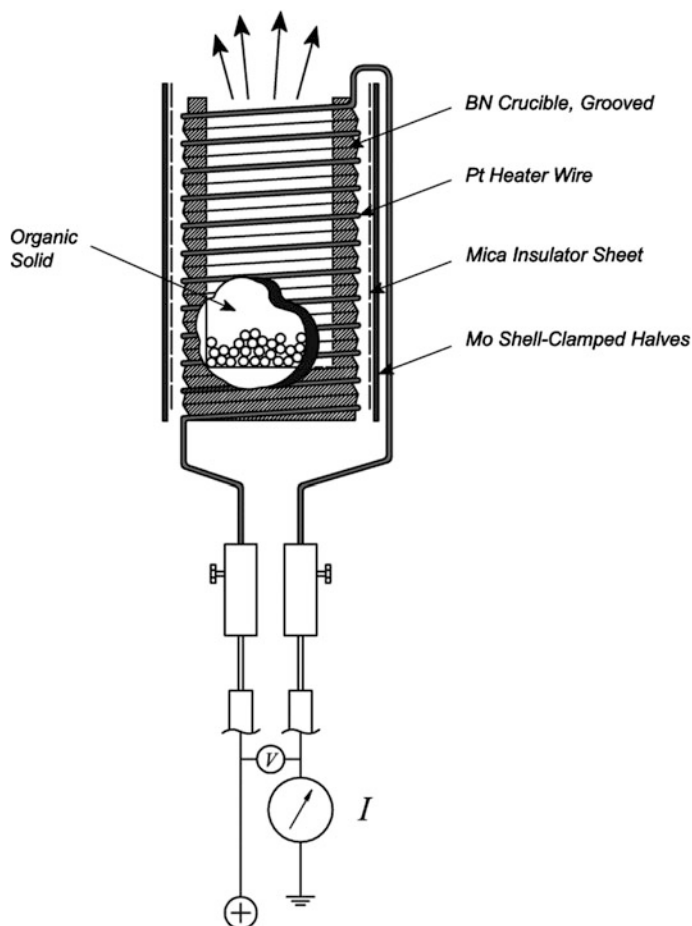

Fig. 38.20 Evaporator for organic film deposition

the Pt wire and the voltage drop (*V*) is measured. For the *I/V* ratio (*R*), the resistance is obtained and used as a measure of the temperature by using the well-documented polynomial of the Pt resistance versus *T*. For pulsed evaporation, the current is increased using simple electronics, keeping the crucible at preset temperatures before and after evaporation. The accuracy of the measurement of *R* and *T* can be increased by using larger diameter Pt lead wires welded to the end of the resistance wire, minimizing effects on the total circuit resistance by heating of the Pt lead wires [47] (Fig. 38.20).

References

1. The use of degassing loops originates from the thin film community but the historical origin of this useful method is not known
2. Professor R.J. Behm (personal communication)
3. W.F. Leonard, Rev. Sci. Instrum. **40**, 187 (1969)
4. D.A. Steigerwald, W.F. Egelhoff Jr, J. Vac. Sci. Technol. **A7**, 3123 (1989)
5. K.J. Ross, B. Sonntag, Rev. Sci. Instrum. **66**, 4409 (1995)
6. K.K. Chin, P. McKernan, I. Lindau, J. Vac. Sci. Technol. **A4**, 1949 (1986). This paper contains references to tests of this device as well as to related devices
7. K.J. Ross, B. Sonntag, Rev. Sci. Instrum. **66**, 4409 (1995)
8. F. Jansen, J. Vac. Sci. Technol. **21**, 106 (1982)
9. P.R. Davis, H.R. Poppa, J. Vac. Sci. Technol. **15**, 1771 (1978)
10. P.J. Chen, M.L. Colaianni, J.T. Yates Jr, Phys. Rev. B **41**, 8025 (1990)
11. K.J. Ross, B. Sonntag, Rev. Sci. Instrum. **66**, 4409 (1995)
12. H.P. Bonzel, A.M. Bradshaw, G. Ertl (ed.), *Physics and Chemistry of Alkali Adsorption* (Amsterdam, Elsevier, 1989)
13. F.J. Esposto, K. Griffiths, P.R. Norton, R.S. Timsit, J. Vac. Sci. Technol. **A12**, 3245 (1994); for details of the surface behavior of Li/Al alloys
14. F.J. Esposto, C.-S. Zhang, P.R. Norton, R.S. Timsit, Surf. Sci. **290**, 93 (1993)
15. Supplied by Alcan, International, Ltd. It is rumored that Canadian beer cans are made of this alloy (personal communication, P.R. Norton)
16. R.P. Schorn, E. Hintz, S. Musso, B. Schweer, Rev. Sci. Instrum. **60**, 3275 (1989)
17. G. Polanski, J.P. Toennies, Surf. Sci. **260**, 250 (1992)
18. W.J. Wytenburg, R.M. Lambert, J. Vac. Sci. Technol. **A10**, 3597 (1992)
19. Degussa Limited, Wilmslow, Cheshire, England
20. H.-G. Keck, E. Kopatzki, and R.J. Behm (private communication)
21. J.J. McClelland, J. Unguris, R.E. Scholten, D.T. Pierce, J. Vac. Sci. Technol. **A11**, 2863 (1993)
22. H.F. Mar et al. (eds.), *Encyclopedia of Chemical Technology* (Wiley, New York, 1979), vol. 6, p. 104
23. J. Unguris, R.J. Celotta, D.T. Pierce, Phys. Rev. Lett. **67**, 140 (1991)
24. M. Heilblum, J. Bloch, J.J. O'Sullivan, J. Vac. Sci. Technol. **A3**, 1885 (1985)
25. L. Ramberg, E. Flemming, T.G. Andersson, J. Vac. Sci. Technol. **A4**, 141 (1986)
26. Y.W. Beag, K. Egawa, R. Shimizu, Rev. Sci. Instrum. **64**, 3647 (1993)
27. T. Jones, J. Sawler, D. Venus, Rev. Sci. Instrum. **64**, 2008 (1993)
28. K.J. Ross, B. Sonntag, Rev. Sci. Instrum. **66**, 4409 (1995)
29. J.R. Waldrop, R.W. Grant, J. Vac. Sci. Technol. **A1**, 1553 (1983)
30. J. Araya-Pochet, G.A. Mulhollan, J.L. Erskine, Rev. Sci. Instrum. **62**, 2288 (1991)
31. K.J. Ross, B. Sonntag, Rev. Sci. Instrum. **66**, 4409 (1995)
32. B.T. Jonker, J. Vac. Sci. Technol. **A8**, 3883 (1990)
33. J. Araya-Pochet, G.A. Mulhollan, J.L. Erskine, Rev. Sci. Instrum. **62**, 2288 (1991)
34. L.I. Maissel, R. Glang, *Handbook of Thin Film Technology* (McGraw Hill, NY, 1970), pp. 1–51
35. K.J. Ross, B. Sonntag, Rev. Sci. Instrum. **66**, 4409 (1995)
36. Dr. M.S. Jackson, J.G. Ekerdt, *Department of Chemical Engineering* (The University of Texas at Austin, Austin, TX 78712-1062) (private communication)
37. R.T. Galla, Rev. Sci. Instrum. **36**, 403 (1965)
38. D. Beecham, Rev. Sci. Instrum. **41**, 1654 (1970)
39. Professor Stephen R. Leone, University of Colorado at Boulder, Joint Institute for Laboratory Astrophysics, Boulder, CO 80309-0440 (private communication). U.S. Patent No. 5,541,407 Arsenic Atom Source, S.R. Leone, A.L. Alstrin, P.G. Strupp, A.K. Kunz, S.M. Casey, and R.V. Smilgys

40. H.-P. Rust, T. Konig, G.H. Simon, M. Nowicki, V. Simic-Milosevic, G. Thielsch, M. Heyde, H.J. Freund, Rev. Sci. Instrum. **80**, 113705 (2009)
41. K. Lammle, A. Schwarz, R. Wiesendanger, Rev. Sci. Instrum. **81**, 053902 (2010)
42. M. Feng, J. Lee, J. Zhao, J.T. Yates Jr, H. Petek, J. Am. Chem. Soc. **129**, 12394 (2007)
43. L. Thompson, J.-G. Lee, P. Maksymovych, J. Ahner, J.T. Yates Jr, J. Vac. Sci. Technol. **A21**, 491 (2003)
44. J. Lee, O. Kuzmych, J.T. Yates Jr, Surf. Sci. **582**, 117 (2005)
45. K. Vijalakshmi, R.A. Rosenberg, private communication
46. N. Sato, K. Seki, H. Inokuchi, Rev. Sci. Instrum. **58**, 1112 (1987)
47. P. Feulner, private communication

Chapter 39
Ions

39.1 Solid State Cesium Ion Gun Source

The use of Cs as an adsorbate of interest on metals and semiconductors extends back to the early work of Langmuir in this area. Several types of sources have been used, including sources that use elemental liquid Cs [1–4], and Cs^+ surface ionization sources [5, 6]. One type of Cs^+ source uses Cs vapor that feeds a porous W plug from behind, producing high current density and low beam temperature. This type of source suffers from the need for differential pumping, and the porous W can also clog when the system is vented to air [5, 6]. A second type of surface ionization source consists of an aluminosilicate powder deposited on a tungsten base. Cs^+ ions are stored in the aluminosilicate and are thermionically emitted [7]. This source requires no differential pumping, but because of the variation in surface potential across its surface, there is a large energy spread of the emitted ions. The source to be described here combines the best features of both of these types of surface ionization sources [7]. Depending upon the energy of the ions desired, different extraction geometries are employed [7].

Figure 39.1a shows a cross-sectional view of the Cs^+ source. A pellet of Cs-M zeolite (cesium mordenite) is made by ion exchange with Na-M zeolite in aqueous solution [8]. Successive exchanges of the Na^+ for Cs^+ must be carried out, and one must use specially purified CsCl salt (reduced Rb impurity levels) to avoid the incorporation of Rb into the source [9, 10]. By heating the exchanged mordenite zeolite to 1050 °C, a phase transition from Na-M to Cs-M structure occurs. The powder is then ground to a particle size of 1 μm, placed in a cylindrical die, and heated to 1350 °C for 3 h, producing a hard pellet that may be machined slightly with a grinding wheel. The emitting surface of the pellet is then coated with a W film, which provides the surface ionization, as well as a surface of constant potential. The back side of the pellet is coated with a Pt film for electrical contact. When the pellet is heated, the flux of Cs toward the grounded W film can be controlled by the applied bias potential across the pellet. A total charge of 10 C can

© Springer International Publishing Switzerland 2015

J.T. Yates Jr., *Experimental Innovations in Surface Science*,
DOI 10.1007/978-3-319-17668-0_39

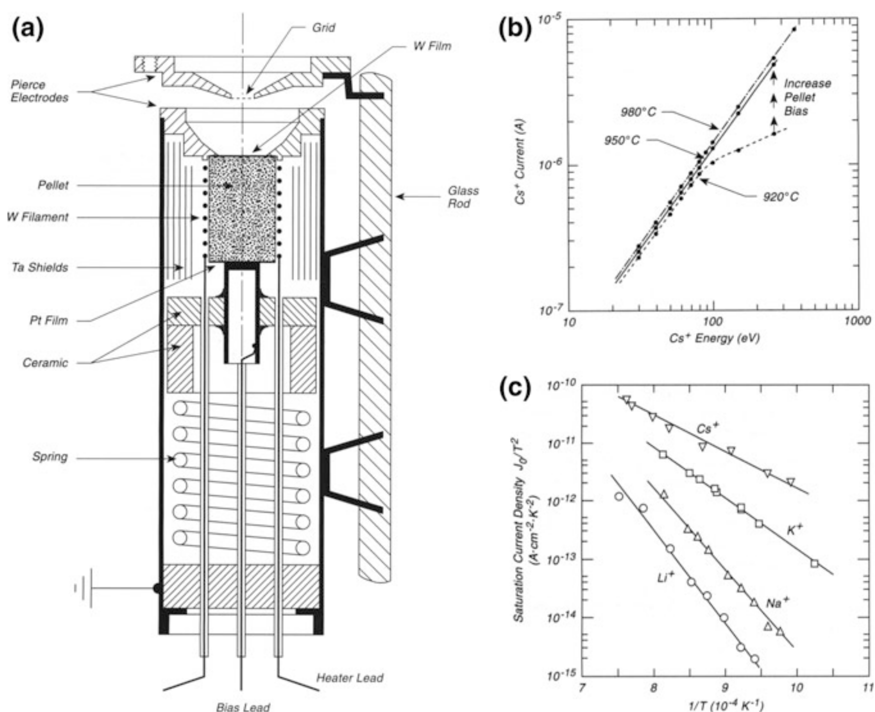

Fig. 39.1 Solid state Cs^+ ion gun + other alkalis. **a** Ion gun design. **b** Performance. **c** Zeolite source Performance for various alkalis

be extracted from a pellet 0.5 cm in diameter and 1 cm long. Current densities up to 30 mA/cm^2 have been extracted.

The time needed to degas the source for operation at less than 10^{-10} Torr is about 1 day at 1100 °C. When not being used, the source is kept at about 500 °C to avoid the need for further outgassing. The advantage of this source is that only Cs^+ is emitted, so that measurements of the collected charge can be converted into absolute coverage [7].

In Fig. 39.1a, the W film on the pellet is pressed against an aperture by a spring, and a bias electrode presses against the Pt film on the back of the pellet. Heating by radiation occurs from a 0.25 mm diameter W coil filament, which is coated with alumina powder. Coaxial Ta foils are used as internal shields to reduce the power loss, and 15–18 W brings the pellet to operating temperature (about 1000 °C). In this particular design, a Pierce electrode arrangement is used to control the ion focusing for ions in the range 50–500 eV [7]. For ion energies in the range 5–50 eV, a planar diode extraction geometry is used [7], and for ion energies above 500 eV, the Pierce gun is mated to a column containing two Einzel lenses [7]. The performance of the different gun designs is given in the original reference [7], and one example of the Pierce gun performance is shown in Fig. 39.1b. Here, the space

charge limitation governs the $V^{3/2}$-dependence of emitted Cs^+ current, where V is the ion energy. However, at 920 °C, the supply of Cs^+ falls near an ion energy of 100 eV, and a larger bias across the pellet restores the performance to that of a space charge limited source.

It has been reported [11] that alkali ion sources involving aluminosilicates in contact with tungsten metal must be "burned in" in ultrahigh vacuum for hours in order to remove the impurity alkalis. Thus, alkalis with low ionization potential will dominate in the ionization process at first, and trace quantities of these impurity alkali atoms will result in a large fractional contamination during first operation of the source. If the source is burned in and then allowed to stand for months in UHV, the impurity ions may reappear in substantial quantity [11]. Thus, it is always wise to use a mass spectrometer for analysis of the alkali ion product from these sources [11]. The application of SIMION ion optical calculations [12] to a large-capacity alkali ion gun has been reported [13].

A careful study of the relative efficiency of zeolite A ion sources for Li^+, Na^+, K^+, and Cs^+ has been published [14] and this report contains details of the preparation and evaluation of the various sources. Figure 39.1c shows the saturation current density for the four zeolite emitters coated on Pt surfaces as a function of emitter temperature, measured in a simple diode arrangement in which the ion emission extrapolated to zero bias was evaluated. An approximately 0.5-cm^2 area of Pt mesh emitter was used. A Rb^+ ion source, operating with a mixture of Rb^+-substituted aluminosilicate zeolite and powdered Mo has been described. Here too a Pierce-type electrostatic focusing structure was used [15].

The investigation of the Cs^+ purity from various composition aluminosilicates has been reported [16].

The design of a high-quality ion gun for delivering Li^+ ions in the energy range 1–100 eV with an energy spread of only 0.22 eV has been published [17].

39.2 Alkaline Earth Metal Ion Sources

Although high-temperature sources for production of the alkalis are well known, the use of similar alkaline earth sources is less well established. Recently, a study of the oxides MgO, CaO, SrO, and BaO has been made, and the purity of the emitted Mg^+, Ca^+, Sr^+, and Ba^+ ions have been investigated [18].

Filaments (0.25-mm diameter) of either W or Ta were used to support the oxides in front of a quadrupole mass spectrometer as shown in Fig. 39.2a. This was done by making a slurry of the powdered oxide in distilled water and transferring powder to the metal coil. Tungsten wire was used for CaO and MgO, and Ta wire was used for the other oxides, including MgO in later studies, since it was found that MgO reacted with W. Measurements were made of the total ion emission as well as the purity of the emitted ions as a function of the temperature. Temperature measurements were made with a pyrometer.

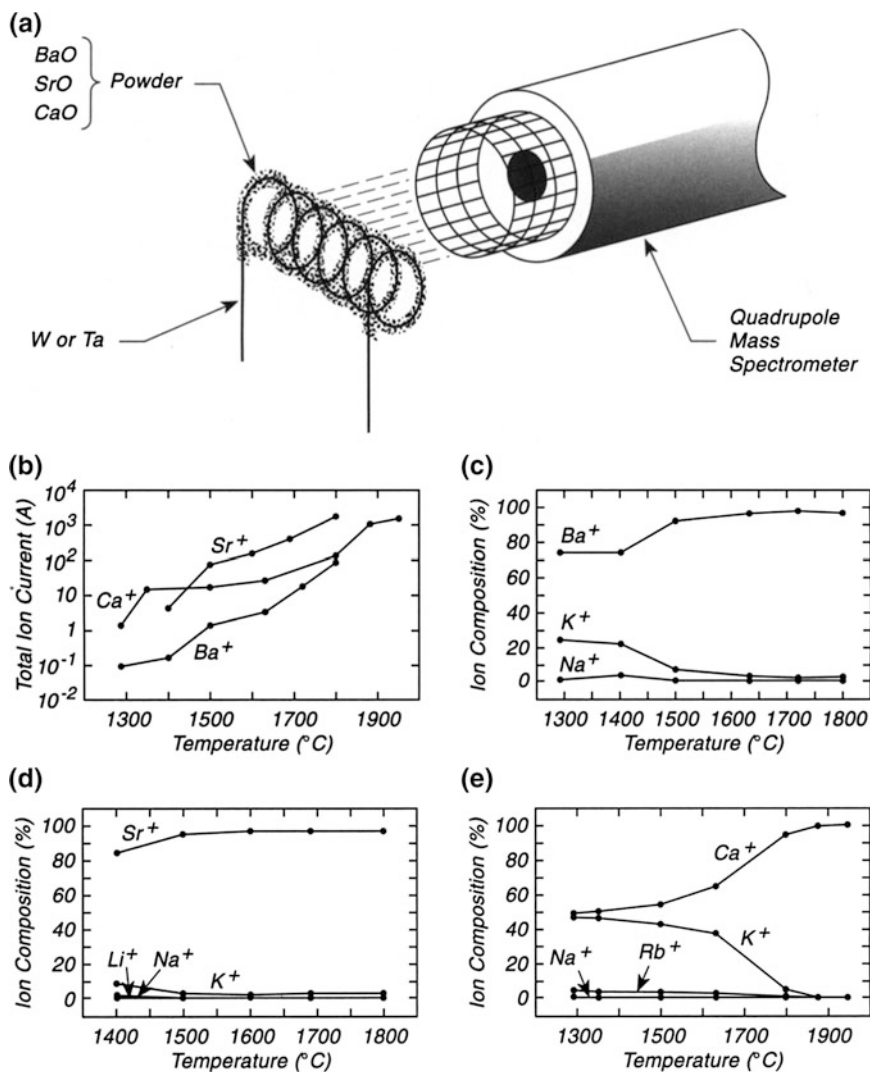

Fig. 39.2 Alkaline earth ion sources. **a** Ion detection by mass spectrometer. **b** Ion current versus T. **c** BaO/Ta. **d** SrO/Ta. **e** CaO/W

Figure 39.2b shows the ion current measured for three of the filaments as the temperature is raised. Currents as high as 1 μA are observed at elevated temperatures, but failure of the filaments occurs rather rapidly at extreme temperatures owing to the reaction of the metal oxide with the refractory metal filament. Figure 39.2c–e show the impurity behavior for BaO, SrO, and CaO as a function of the temperature. In all cases, alkali metal ion impurities are observed, even though the oxides were of purity of 99.9 % or better. This is due to the highly preferred

surface ionization of the alkalis as a result of their low first ionization energy. As the filaments are heated to higher temperatures, the alkali ion impurities decrease in yield and rather pure Ba^+, Sr^+, and Ca^+ ions are liberated. The purity of Mg^+ from MgO coatings was less than 50 % at all temperatures, and this would therefore be an unsuitable source for Mg^+.

References

1. J.-L. Desplat, C.A. Papageorgopoulos, Surf. Sci. **92**, 97 (1980)
2. G.S. Tompa, J.L. Lopes, G. Wohlrab, Rev. Sci. Instrum. **58**, 1536 (1987)
3. T. Castro, R. Reifenberger, Rev. Sci. Instrum. **58**, 289 (1987)
4. R.D. Swenumson, U. Even, Rev. Sci. Instrum. **52**, 559 (1981)
5. D.G. Welkie, in *Secondary Ion Mass Spectrometry SIMS V*, ed. by A. Benninghoven et al. (Springer, New York, 1986), p. 146
6. G.R. Brewer, *Ion Propulsion* (Gordon and Breach, New York, 1970), Chap. 4
7. A.E. Souzis, W.E. Carr, S.I. Kim, and M. Seidl, Rev. Sci, Instrum. **61**, 788 (1990)
8. D.W. Breck, *Zeolite Molecular Sieves* (Wiley, New York, 1977), Chap. 7
9. R.E. Weber, L.F. Cordes, Rev. Sci. Instrum. **37**, 112 (1966)
10. T.E. Madey, J.T. Yates Jr., J. Vac. Sci. Technol. **8**, 39 (1971)
11. M.J. Hogan, P.P. Ong, Rev. Sci. Instrum. **61**, 1338 (1990)
12. D.A. Dahl, J.E. Delmore, *The SIMION PC/PS2 User's Manual*, *Version 3.1*, Informal Report, EGG-CS-7233, Rev. 2 (November 1987). Program available from Idaho National Engineering Laboratory, EG&G Idaho, Inc., P.O. Box 1625, Idaho Falls, ID 83415
13. S.T. Beck, D.W. Warner, B.A. Garland, F.V. Wells, Rev. Sci. Instrum. **60**, 2653 (1989)
14. Y. Satoh, M. Takebe, K. Linuma, Rev. Sci. Instrum. **58**, 138 (1987)
15. D.W. Hughes, R.K. Feeney, D.N. Hill, Rev. Sci. Instrum. **51**, 1471 (1980)
16. P.P. Ong, T.L. Tan, Rev. Sci. Instrum. **65**, 3729 (1994)
17. H.B. Haskell, O. Heinz, D.C. Lorents, Rev. Sci. Instrum. **37**, 607 (1966)
18. T.L. Tan, Z.L. Zhou, P.P. Ong, Rev. Sci. Instrum. **66**, 2879 (1995)

Chapter 40
Active Gases and Species

40.1 High Flux Atomic Hydrogen Sources—Thermal

Atomic hydrogen is employed for research in the surface science field as a reagent for rapidly producing chemisorbed hydrogen on semiconductor surfaces and also on metal surfaces that do not readily dissociate molecular H_2. The surface chemistry of atomic hydrogen has been investigated as early as the work of Langmuir [1, 2] who first produced it on a hot tungsten filament. The production of atomic hydrogen has been investigated by a number of workers [3–5]. It has been found that the efficiency of H atom production is proportional to $(P_{H2})^{1/2}$ at H_2 pressures above about 10^{-6} Torr where pseudoequilibrium conditions exist. At lower H_2 pressures, the rate is proportional to P_{H2}. Under these conditions, the reported efficiency of H_2 dissociation is about 0.3 per H_2 collision with the tungsten surface at temperatures above 2500 K [3]. It has been observed that the efficiency of dissociation is decreased by impurities often present on a tungsten filament [4].

Two sources that place a relatively high H_2 gas density near a heated tungsten surface have recently been described [6, 7]. Both of these sources produce large fluxes of atomic hydrogen compared to a bare tungsten filament operating in the vacuum system, if comparisons are made at the same gas throughput to the system's pumps. In Fig. 40.1a a tungsten capillary (0.6-mm ID, 1.6-mm OD) is electron bombarded from a tungsten filament so that the end of the capillary is heated to 1800–1815 K over a 4-mm length. An acceleration voltage of +560 V on the capillary (HV) and a 30 mA emission current achieve this condition. A Cu shield, with a conical hole drilled on axis, serves as a radiation shield. It is cooled by a water circulation tube that is butt-brazed to the solid Cu shield. The sample is placed 10 mm in front of the shield, or 20 mm from the end of the W capillary. The back end of the W capillary is snugly fitted into a ceramic sleeve, which also connects to a 4-mm-diameter stainless tube that delivers H_2 gas to the atomizer. Since the gas density is low during operation, no need exists for vacuum tight seals, and the adapter uses only friction fits to the capillary and the tube. The working H_2

© Springer International Publishing Switzerland 2015

J.T. Yates Jr., *Experimental Innovations in Surface Science*,
DOI 10.1007/978-3-319-17668-0_40

pressure at the entrance to the W capillary is about 10^{-2} Torr. In order to change the position of the H atom doser, it is mounted on a translational device. It is reported that a total atomic H flow of about 3×10^{14}/s may be achieved under these conditions. The degree of dissociation approaches 50 %. Therefore the total gas influx is small, minimizing the background H_2 pressure. It is estimated that about 20 % of the H atoms are emitted in a central portion of the beam with a cone angle of ±15° [8, 9].

In Fig. 40.1b, a spiral W filament (1.5-cm diameter, 0.025-cm-diameter wire, 14.5-cm length) [10] is located within a cup-shaped stainless steel doser having a perforated array in its central portion [7]. Hydrogen gas flows into this doser through a tube that is connected to a calibrated conductance aperture (see pp. 89–91; 421–428), and the flow rate is adjusted using a capacitance manometer on the high-pressure side of the aperture. A typical flow rate of about 2×10^{16} H_2/s is employed, at a system pressure of 2×10^{-7} Torr. The incoming H_2 encounters a deflector baffle that produces a random flux on the back of the perforated array. The sample is shielded from radiation by the wall of the doser body. In order to reflect the H atoms to the sample (avoiding radiation heating of the sample as well as possible impurities from the hot filament) a cooled Pyrex plate at 120 K is located close to the outlet of the atomic hydrogen source. This reflects atomic H with high efficiency [11, 12]. The Pyrex is held onto a stainless steel cooling reservoir with metal clips and is thermally connected to the l–N_2 reservoir with a film of In metal.

In studies of the efficiency of the doser [7], it was found that a reduction in efficiency of a factor of 4.8 occurred using the reflector source compared to a line-of-sight geometry. However, experiments working at the same system gas throughput indicate that the doser produces about 50 times more atomic hydrogen than a bare W filament, operating without a doser geometry. Thus, even the factor of 4.8 reduction in efficiency owing to the reflector is compensated by the higher atomic H production rate achieved at the high gas densities in the doser. This source is therefore about a factor of 10 more efficient than a bare W wire in delivering atomic H to the sample for identical H_2 gas loads. A monolayer of H atoms (about 4×10^{14}/cm^2) was adsorbed by a Si(100) surface at 400 K when 4×10^{18} H_2 molecules had passed through the doser with the W filament operating at 2000 K.

Figure 40.1c shows the relative efficiency of atomic H production plotted versus the reciprocal temperature (K^{-1}). The source produces atomic H at a rate which reaches a maximum near 2000 K. Similar results were reported by George et al. [13].

An interesting study, comparing the pumping speed of atomic H with that of H_2 during adsorption on engineering surfaces in the range 2.5–4.3 K, has been published [14]. Interestingly, the pumping speed for H_2 is between a factor of 3 and 40 above that of atomic H. This difference in either condensation or adsorption is attributed to the higher internal energy of the atomic H compared to H_2.

A hydrogen atom source involving a design similar to that of [6] has been carefully evaluated to determine the efficiency of atomic H production [15]. A second similar source has also been evaluated by mass spectrometric methods

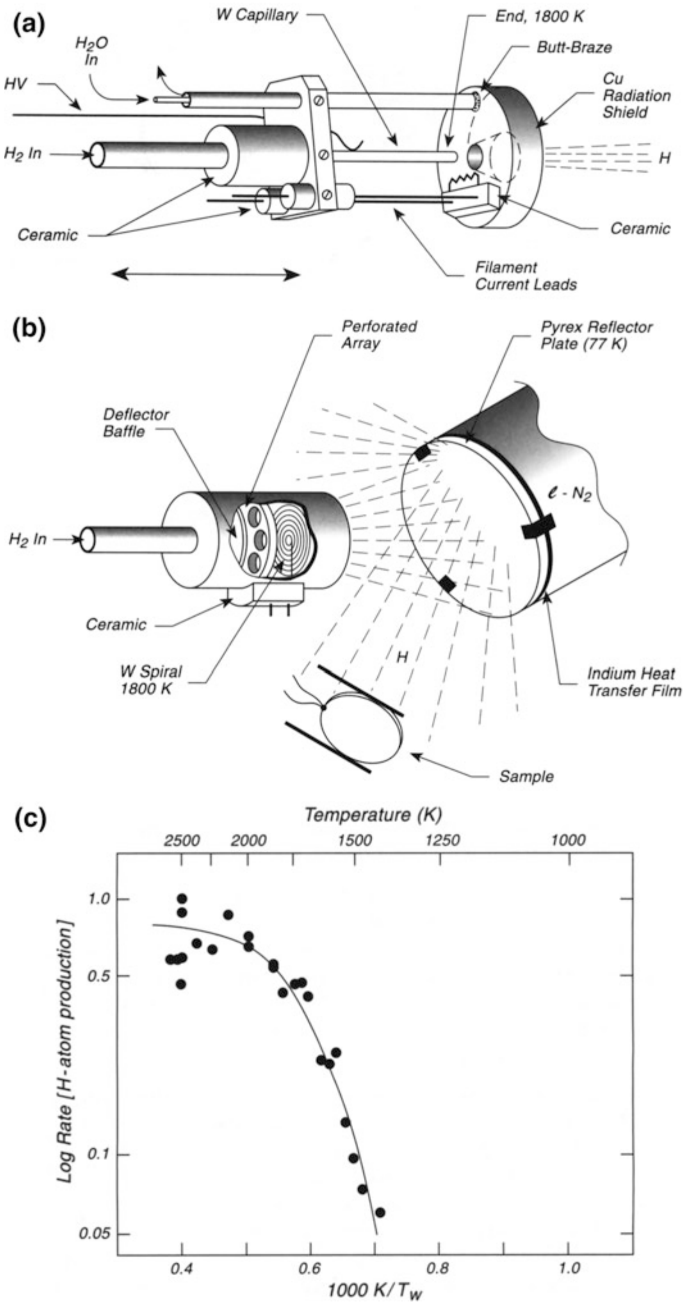

Fig. 40.1 High flux atomic H sources. **a** H atom source—hot tube design. **b** H atom source—spiral filament design. **c** Efficiency of design B for H-atom formation

[16]. In addition, atomic H beams, cooled by collision with surfaces near 6 K, have been produced [17].

A number of detectors for atomic H have been devised and are reviewed briefly in [18]. One of these [18] involves the use of a thermistor (primarily NiO) for measurement of an atomic H flux. Electrical conductivity changes, measured with a Wheatstone bridge and phase-sensitive detection, were used for the evaluation of the flux of atomic H made in a microwave discharge. Control experiments eliminated the possibility of effects owing to the influence of heating and radiation on the detector. The mode of operation of the detector is unknown and could be due to local heating as a result of H atom recombination or to electronic surface effects. The lower limit of sensitivity is estimated to be 10^{11} H/cm^2 s.

An atomic H source involving the use of a W/26 % Re alloy tube ohmically heated to 2400 K has been described. The W/26 % Re alloy does not have the brittle properties of pure W [19].

Many interesting uses for atomic H have been described in the literature and are beyond the scope of this book.

40.2 Atomic Hydrogen Beam Source—Radio Frequency Driven

The use of thermal sources for the production of atomic H has been described on p. 477. It is also possible to produce beams of atomic H using microwave discharge sources. These sources are convenient to utilize but one must be cautious that impurities and radiation from the discharge region do not affect the experiments. There are many different RF discharge sources available, as described in [20]. A typical source not unlike others that have been made [20] is described below.

Figure 40.2 shows a diagram of a Pyrex glass source of simple design. It is capable of producing atomic H with up to 95 % dissociation of H_2(g). The density of atomic H ranges from 5×10^{11} to 2×10^{13} H/cm^3. The tube is 18-mm inside diameter and 240 mm long. It is terminated at each end by a 1-mm-ID capillary to prevent the discharge from spreading outside the source, and it is cooled by a water

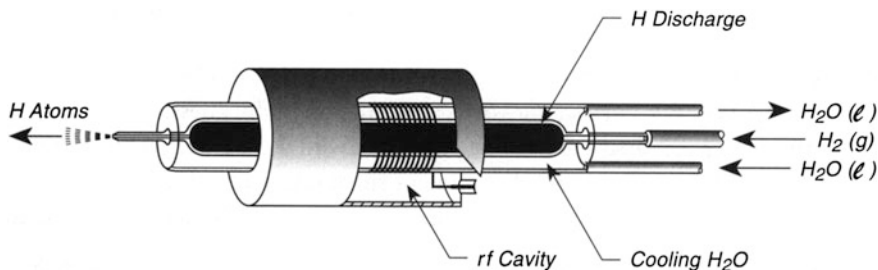

Fig. 40.2 H atom source

jacket to reduce the temperature and to reduce H atom recombination on the inner walls [21]. This may be responsible for the long life and stability of this design.

The discharge is excited by about 25 W of RF power into a coaxial cavity resonant at 35 MHz. The cavity consists of a copper cylinder, surrounding the discharge tube, and a 12-turn helix of constant pitch. Power is coupled via a single-turn link coupling. Details of cavity design and cavity dimensions have been published [22]. The coaxial cavity is properly impedance-matched to the generator to insure 90 % power absorption into the cavity. The RF generator is properly designed to prevent the propagation of unwanted RF signals. The RF oscillator and driver stages are housed within individual screened compartments. The amplifying stages are narrow band with sharply tuned filters in each stage, eliminating harmonics. Notch filters are used in the power input to prevent RF propagation into the laboratory AC supply. Low noise was achieved in auxiliary instruments when the RF supply was operating.

A hydrogen pressure of about 0.15 Torr was used in the source. Great care was taken to clean the discharge tube before use, successively washing with hot chromic acid (in sulfuric acid), water, acetone, HF(aq), and distilled water. A palladium leak (see p. 511) was used to purify the H_2 before use and back diffusion of contaminants was avoided. The tube operated for about 5000 h without trouble.

40.3 Atomic Fluorine Source

The delivery of reactive atomic species in high purity to surfaces poses one of the difficult experimental problems in adsorption and surface reaction studies. Species such at atomic F are particularly difficult to prepare and transfer without secondary reactions on the walls of the source. An excellent design [23], probably applicable in general to producing a number of reactive species, is shown in Fig. 40.3.

A low pressure 10 %F_2/90 % He mixture is flowed through an alumina tube which passes through an Evanson-type microwave discharge cavity, and the products are then pumped through the apparatus using a rotary pump which is corrosion resistant. The microwave discharge products are admitted to the preparation chamber through a 25-μm-diameter orifice mounted on the end of the outer stainless steel tube. The orifice was laser-drilled (see p. 421) in a stainless steel sheet of 25 μm thickness. The alumina tubing inside the source is thought to become passivated with the formation of a nonvolatile layer of AlF_3, and is superior to a tube made of silica [23, 24]. The microwave discharge source [25] is operated at 30–60 W of power in the total pressure range of 0.05-10 Torr.

The species emitted from the orifice were studied with a modulated quadrupole mass spectrometer, which measured the consumption of F_2 (38 amu). The results show that essentially complete dissociation occurs below a total pressure of 2 Torr, as shown in Fig. 40.3b. When working in the molecular flow regime below a pressure of 5.7 Torr, the angular distribution is described as having a $\cos^2$ distribution, and for sample sizes of the order of 0.5 cm at source-to-sample distances of

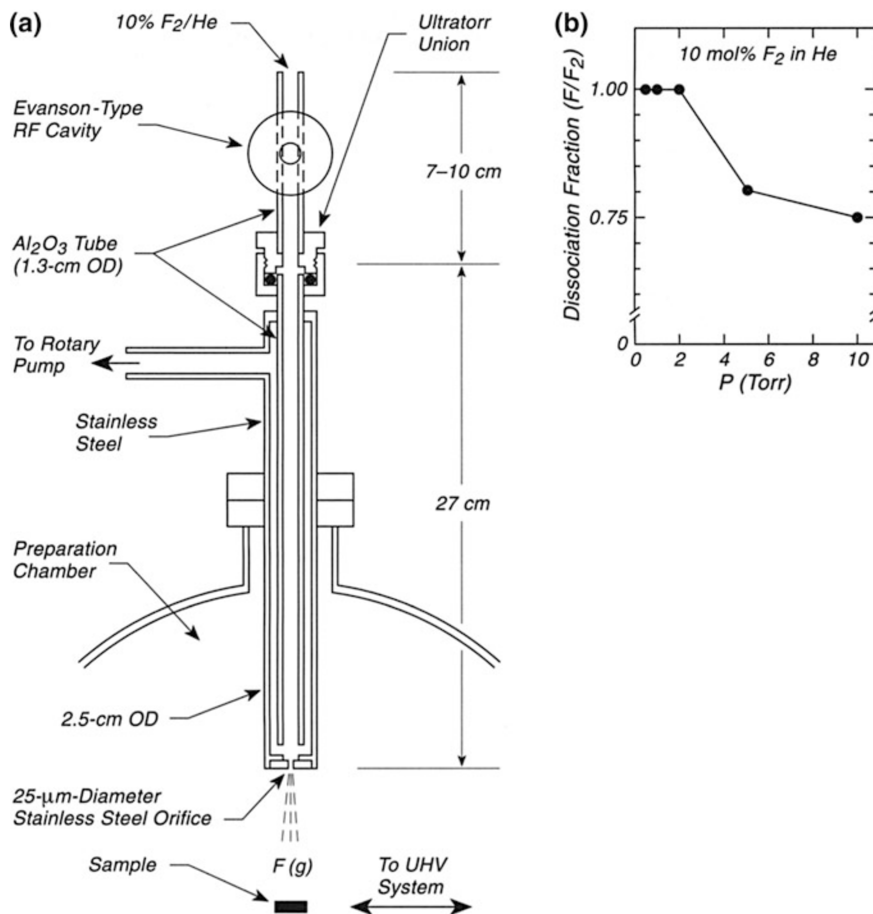

Fig. 40.3 Microwave source of F atoms. **a** Source, **b** performance versus pressure

about 1 cm, the fluence is rather uniform. It is calculated that at a total pressure of 0.7 Torr, the source delivers F atoms at a flux of about $1 \times 10^{14}/cm^2$ s in the beam with a random flux from the source and the chamber being at about 5 % of this beam flux.

Microwave sources are widely used in molecular beam studies [24, 26], but this source is one of the first such sources to be successfully employed in surface studies [27–29]. It is also useful for generating chlorine atoms. For chlorine, a quartz tube may be used instead of an alumina tube [30, 31].

It should be noted that large gas loads accompany the use of this source, and that a rapidly pumped preparation chamber, isolated from the ultrahigh vacuum surface analysis chamber, is one way to reduce the gas load in the analysis chamber when the source is being used.

40.4 Alkali Metal Sources

The alkali metals form one of the most interesting class of adsorbates on the surfaces of both metals and semiconductors [30]. As a result they have been widely studied since the pioneering work of Langmuir in the 1930s [32]. The alkali metals are also used in the production of low-work-function photocathode surfaces, and in other applications in the field of physical electronics. As a result, excellent commercial sources of alkalis for research are available from SAES getters [33].

Figure 40.4a shows a view of a typical SAES alkali getter source; these are available to deliver Li, Na, K, Rb, and Cs. A powdered mixture of the alkali metal chromate, M_2CrO_4, and a reducing agent (St 101 alloy—84 % Zr and 16 % Al) is held in a nichrome boat with a very narrow slit running along its length, as shown. A nichrome retaining wire is squeezed along the backside of the slit to prevent powdered material from being ejected from the slit. Butting pieces of two designs are described, which block the ends of the boat and which serve as connectors for electrical heating. As current is passed, the temperature rises into the 550—850 °C region, as indicated in Fig. 40.4b, and the solid state reduction reaction liberates the alkali metal which escapes from the slit. The Zr also acts as a getter for impurity gases such as H_2 and CO. The typical operating temperature for deposition must be adjusted on the basis of experience, but it is usually preferable to use lower rates for controlled deposition experiments. The typical amount of H_2 emitted from one of the sources is about 1 Torr-cm^3 per cm of getter length, and degassing is achieved by initially working at 500 °C. Various geometrical shapes and sizes are available.

The solid state oxidation-reduction reaction between the reducing agents, Zr and Al in the metal alloy reactant can be written as shown in Fig. 40.4c, but the exact details of the reaction are probably not well worked out. An excess of the Zr-Al St 101 alloy is employed so as to have material for the gettering of active gases during the reaction.

In addition to alkali metal getters, SAES also makes alkaline-earth Ba getter sources of a different configuration from the alkali metal sources (Type St 15A/20HY/400 and St 15/20KLS/200). The reactant consists of 45 % $BaAl_4$ alloy mixed with 55 % Ni powder. This composition, on being heated to about 850 °C, reacts exothermically instantaneously releasing about 25–30 % of its Ba. Continued heating by RF methods releases the remainder of the Ba. These sources are used to process vacuum tubes by throwing a heavy getter film of Ba, which is active for CO [34], H_2 and other gas adsorption. An SAES source of Ba geometrically similar to the alkali sources is the type St 14/Fr, which can be ohmically heated as is done with the alkali sources.

A description of an alternate design for a Cs ion source, involving diffusion of Cs through a heated porous W plug, is given in [35].

Alkali metal sources may also be based on the direct evaporation of the metal, and many such sources have been described. A novel source, which delivers large quantities of Na as an atomic beam, has been described; it employs a metal mesh wick to return excess Na to the evaporator section. This source also works under

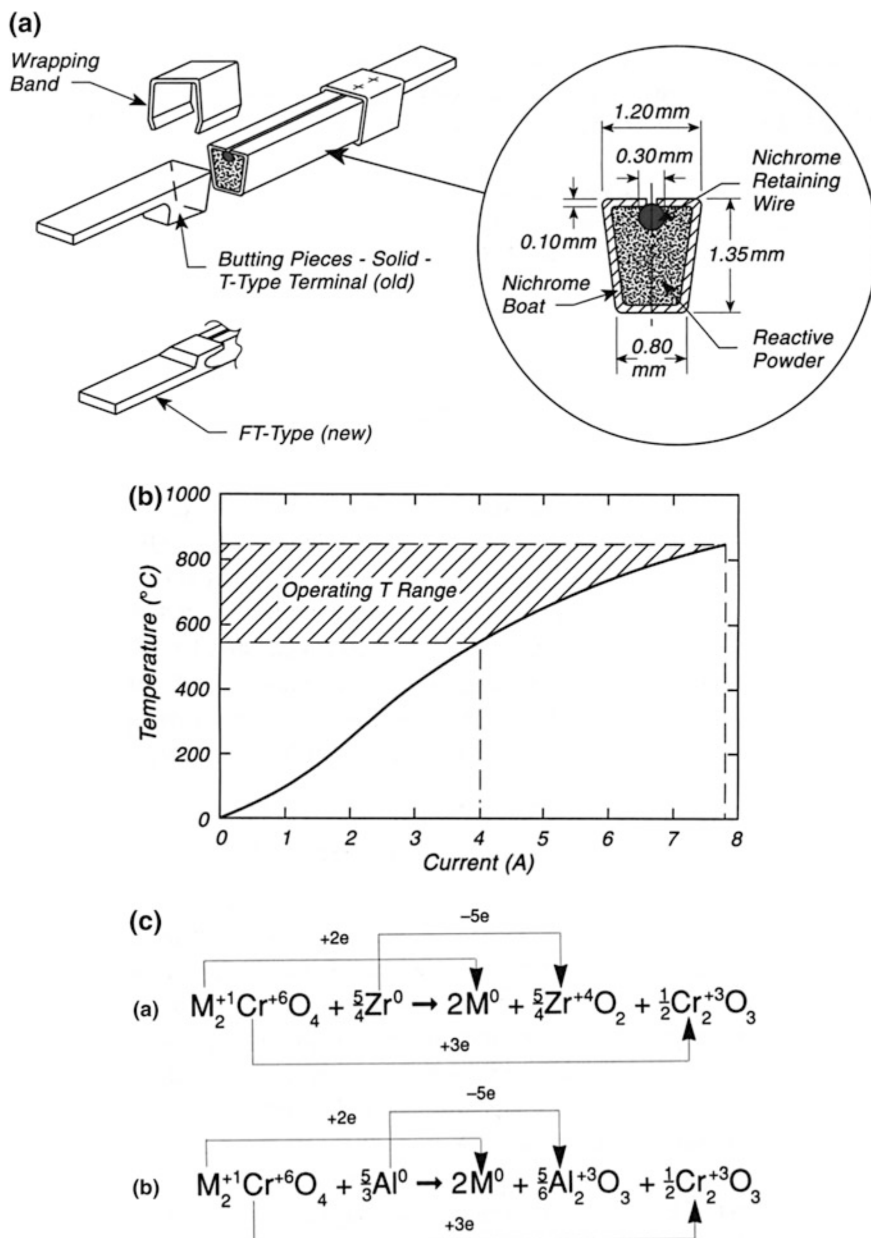

Fig. 40.4 Alkali metal sources, **a** Structure of SAES alkali metal dispenser. **b** Typical temperature-current performance. **c** Solid state reaction—using Zr or Al

ultrahigh vacuum conditions [36]. In addition, zeolite sources containing alkalis are often employed, and one of these is discussed on p. 471.

40.5 Thermal Source of Methyl Free Radicals

The involvement of methyl radicals in the surface chemistry of hydrocarbon reactions is often encountered. However, because of the difficulty of producing clean sources of CH_3, this radical species has been neglected in adsorption studies. Pyrolysis of molecules containing methyl groups has been the preferred method for the generation of methyl radicals [37–41], but most methods also generate other reactive species that can cause interference in studies of the methyl radical surface chemistry. The source described here avoids this problem by using dimethyldiazine as the source of the CH_3 and by working at molecular flow conditions where high pressure gas phase processes to produce other highly reactive molecules are avoided to a high degree [42]. The pyrolysis reaction

$$CH_3NNCH_3 \rightarrow 2CH_3 + N_2 \quad (40.1)$$

is a fairly clean reaction, and if gas phase reactions of the methyl radicals are avoided, then only surface reactions in the source can contribute impurities.

Figure 40.5 shows a schematic design of the pyrolysis apparatus. Dimethyldiazine is allowed to pass through a quartz tube that has its central section heated by means of a closely wound Ta wire, 0.25-mm diameter, which is cemented to the outside of the pyrolysis tube using a ceramic cement (Aremco Type 576). The quartz tube is connected to the source of dimethyldiazine using a graphite ferrule [43] in a swagelock reducing union. The thermocouple embedded into the heating section allows the temperature to be adjusted to the optimum one for complete conversion of dimethyldiazine to pyrolysis products, which occurs near 1200 K. A cooling section beyond the pyrolysis region allows the CH_3 radicals to become accommodated at a lower temperature than their production temperature. Various lengths of the three zones shown in Fig. 40.5b were studied [42]. A typical mass spectrum for dimethyldiazine and for the completely pyrolyzed product is shown in Fig. 40.5c. In addition to CH_3, measurable fractions of CH_4, C_2H_6, and H_2 are produced along with N_2 at 1173 K and a chamber pressure of 5×10^{-7} Torr.

The dimethyldiazine was synthesized using the method of Renaud and Leitch [44] and was stored in a stainless steel container over a period of several months without decomposition. Ar was mixed with the dimethyldiazine as an internal standard for quantitative flow measurements [42]. A quadrupole mass spectrometer was used to acquire the mass spectra shown, working inside a stainless steel chamber pumped by a turbomolecular pump [42].

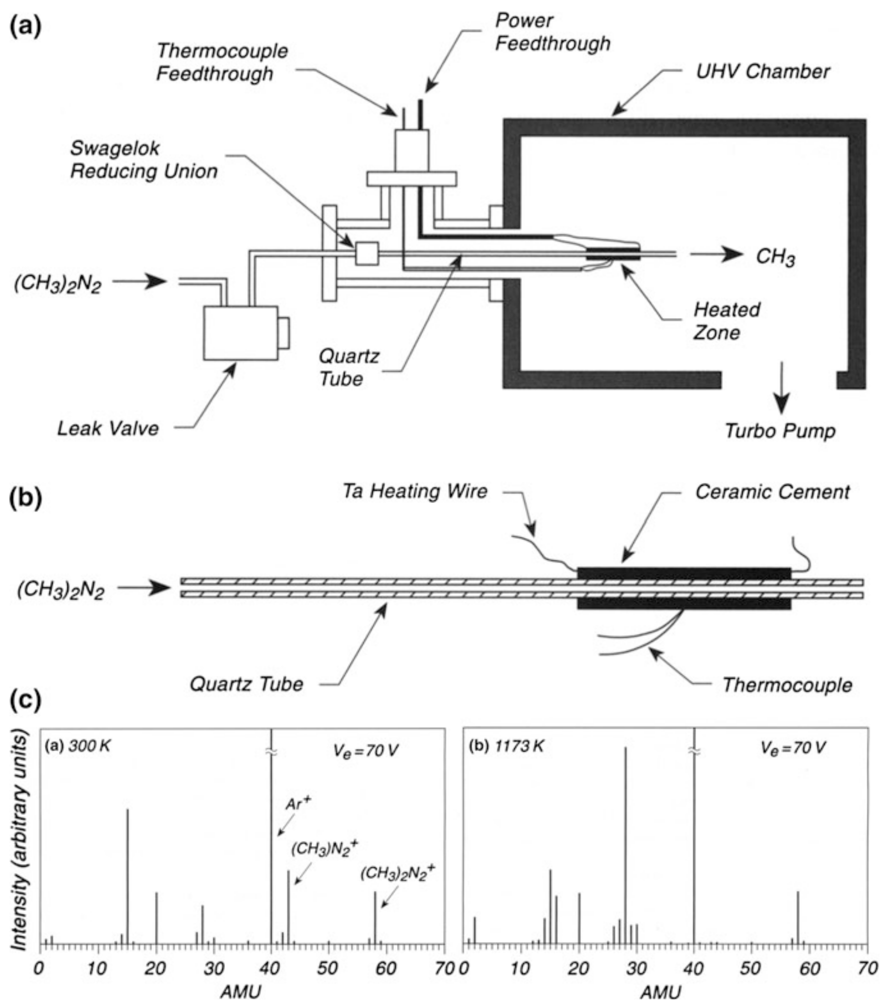

Fig. 40.5 Methyl radical sources. **a** Methyl radical source. **b** Pyrolysis tube. **c** Mass spectrum of gas from source

40.6 Production, Storage, and Use of Ozone

The ozone molecule, O_3, is a powerful oxidizer, useful in situations where oxidation of surfaces is needed under mild conditions. It has been used, for example, in the growth of $Ba_2YCu_3O_{7-\delta}$ thin films [45, 46]. However, when stored as the liquid at cryogenic temperatures, O_3 is dangerous and may explode. The apparatus described here avoids this problem by storing O_3 by adsorption in the pores of silica gel at temperatures slightly above its boiling point [47, 48]. The rate of decomposition under these storage conditions is about 5 % per week.

Ozone is toxic at a concentration of around 1 ppm by volume. The odor threshold in air is about 0.01–0.02 ppm. The threshold limit value (TLV) is 0.1 ppm, which is above the odor threshold. The use of ozone must involve safe storage, use of inert surfaces such as passivated stainless steel, quartz, Pyrex glass, Teflon, or passivated aluminum, and constant monitoring with an ozone detector [49].

Figure 40.6 shows an oxygen cylinder containing dry oxygen that feeds a commercial ozone generator (which produces a corona discharge). The rate of production of O_3 is such that a concentration of O_3 of 8 weight % is produced steadily at 1 atm with an O_2 feed rate of 1.7 L atm/min. This corresponds to the production of about 11 g of O_3/h. The O_3 is trapped at 195 K on 300 g of silica gel [50] up to levels of about 7 weight %, so that in 2 h of operation this limit will be reached. Excess oxygen is vented to the atmosphere with Valve A open and all other valves (B-D) closed. The gel should display a deep blue color at this loading level. To transfer small quantities of O_3 into the vacuum chamber, Valve A is closed, and Valves B and C are opened. Under these conditions, a steady pressure of O_3 will be evolved and pumped into the rotary pump, with a pressure of about 10^{-2} Torr, as monitored by the capacitance manometer. Valve D may then be opened to admit O_3 to the vacuum chamber. This procedure has the advantage that the flowing O_3 is continuously produced by vaporization from the silica gel, maintaining purity during the exposure of samples in the vacuum system to the tiny fraction of O_3 that arrives through the doser tube, compared to that which is exhausted.

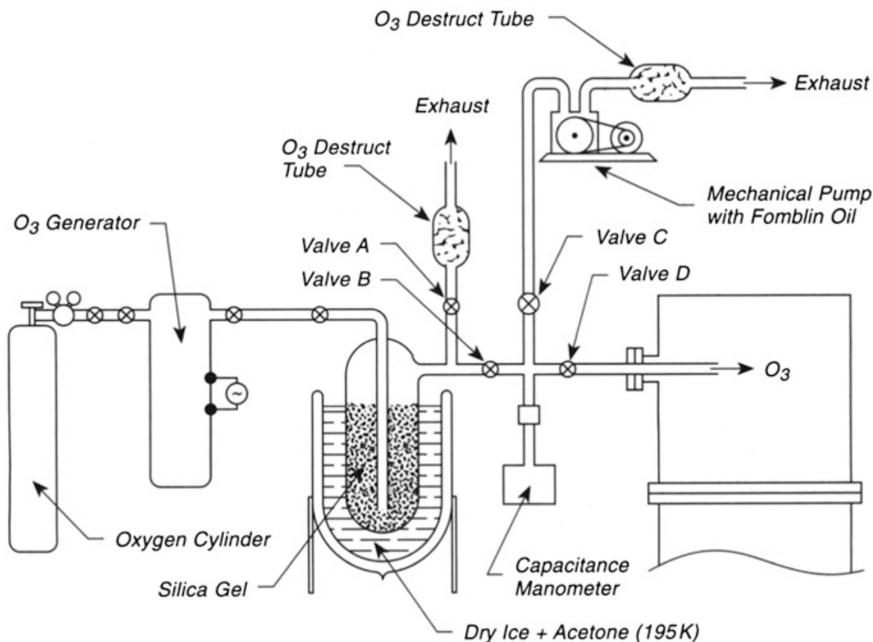

Fig. 40.6 System for production, storage, and use of ozone

The system is equipped with O_3 destruct tubes containing copper sponge that catalytically decomposes O_3. These are also available commercially. The rotary pump oil should be non-hydrocarbon-based, using either Fomblin [51] or Krytox [52]. Teflon O-rings should be used in all locations, and not rubber O-rings, since ozone is well known to destroy rubber by attacking carbon-carbon double bonds. Extreme care should be taken to keep the dry ice + acetone trap cold at all times when O_3 is trapped on the silica gel.

An alternate method [53] employs a cryopump controlled by a thermocouple feedback to boil off O_3 from liquid O_3 at a precisely controlled temperature. The O_3 is condensed in a vacuum-jacketed reservoir whose temperature is precisely adjustable through the operation of a cryopump. These authors provide a rupture disk for this O_3 storage system in case of an explosion, which is a possibility for liquid O_3 stored in this manner.

A simple electrical discharge apparatus for producing 100 % pure O_3 in a nonflow system, and for continued repurification, has been described. Less than 100 cm^3 of pure oxygen at atmospheric pressure is converted in a batch operation, and purification occurs by pumping traces of residual O_2 away at 77 K [54].

The calibration of a mass spectrometer for O_3 and the measurement of its cracking pattern in a magnetic mass spectrometer has been carried out carefully, using a 5.3-L storage volume (Teflon coated) to receive the O_3 from a cold trap after pumping off impurity O_2, etc. The storage volume was the source for a molecular beam of O_3 that entered the ionizer of the mass spectrometer. It was found that the half-life of O_3 at a pressure of 0.1 Torr in the storage volume was about 12 h at room temperature [55].

40.7 Ozone Generator and Molecular Beam Doser Source

Ozone is widely used in surface chemistry and materials chemistry as a high power oxidizing agent. In Sect 40.6, we show how to make relatively large quantities of very pure laboratory ozone and how to quantitatively dose it into an ultrahigh vacuum system. For occasions where small quantities of ozone are needed in an ultrahigh vacuum system, a simpler doser working on a different principle [56] may suffice as shown in Fig. 40.7.

Oxygen gas at a pressure less than about 100 Torr is admitted into a glass tube specially constructed for the preparation of O_3 and for the removal of excess O_2. The glass reservoir is immersed deeply in a liquid nitrogen bath and a Tesla coil is used to convert O_2 to O_3. A dark blue liquid O_3 will be seen to form on the inner walls and to flow to the bottom of the reservoir. Several doses of O_2 may be used to build up the quantity of collected O_3. The conversion process is aided by the presence of a small amount of Cu wool in the neck of the preparation/storage reservoir and the discharge from the Tesla discharge is directed into the gas by the Cu. The discharge should be done through the liquid nitrogen in the bath. Following partial conversion of O_2 to O_3, the excess of O_2 is distilled away at liquid

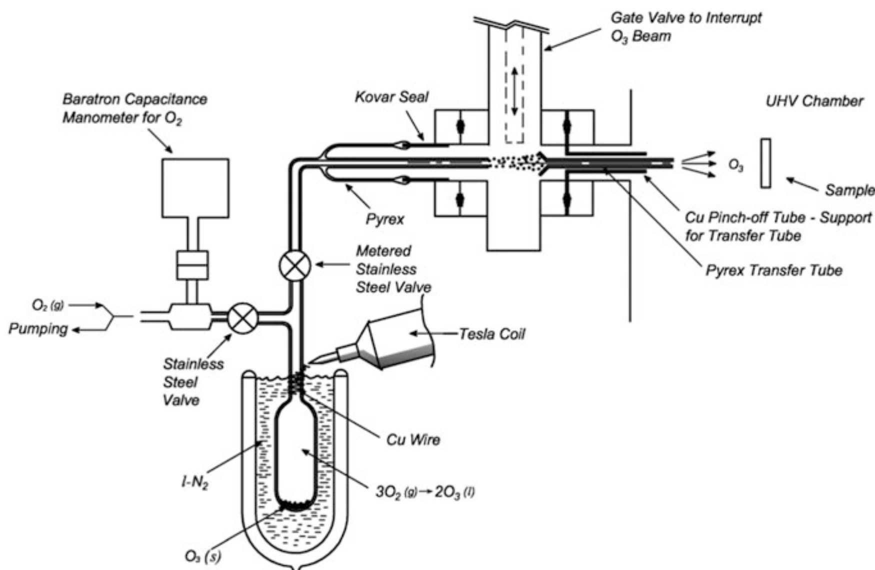

Fig. 40.7 Ozone generator and molecular beam doser source

nitrogen temperature being aware that liquid O_3 has an appreciable vapor pressure of a few Torr at 77 K and will also be removed slowly. The pump used for distillation should not contain any oxidizable oil.

Admission of the O_3 to the doser is accomplished by using a stainless steel metering valve which allows the stored O_3 to slowly leak into the glass beam doser assembly and into the UHV system. The use of glass between the storage reservoir and the Pyrex transfer tube assures minimal wall decomposition of the O_3 by collision with metal surfaces. Passivation by exposure to O_3 will deactivate the small amount of metal exposed. It will be found that even the Pyrex walls act initially to decompose the O_3 to some degree (see Sect. 40.6), and only by passivation in O_3 will the rate of wall decomposition approach zero. To shut off the doser beam at the UHV system, a small gate valve is placed into the middle of the two section-glass doser assembly. Since it will be useful to have a way to monitor the rate of flow of O_3 into the ultrahigh vacuum system it is suggested that one uses the response of the ion gauge in the UHV system to the flow of O_3 to be monitored. The O_3 which is not adsorbed on the sample becomes randomized by collision with the walls of the stainless steel system and will all decompose to O_2 and the ion gauge therefore measures an increase in O_2 pressure which is proportional to the beam flux of O_3.

40.8 Detection of Ozone or Atomic Oxygen by Oxidation of Silver Films

Silver reacts only slowly with molecular oxygen, while its reactivity with O_3 is very rapid. In the apparatus shown in Fig. 40.8a, O_3, originating from liquid O_3 vaporization in an O_3 cryogenic storage system, is incident on a Ag film (500 Å thickness) evaporated onto a quartz crystal microbalance [57] (see p. 486 and 309). The rate of increase of mass is proportional to the O_3 flux in the initial stages of oxidation, and then falls off to a lower rate as bulk diffusion effects begin to control the growth kinetics as shown in Fig. 40.8b. The O_3 angular distribution from the delivery tube (stainless steel) was also measured by moving the detector off axis, maintaining a constant tube-to-detector distance of 6.3 cm, and a constant O_3 flow rate of 1.9 standard $cm^3\ s^{-1}$. The profile of O_3 is Gaussian (Fig. 40.8c), and when Ar diluent was used, the flux of O_3 decreased and the angular profile was broadened somewhat. It was estimated that the detection efficiency of the Ag film was 26 % for O_3, assuming that one O atom from O_3 oxidizes the Ag, and that molecular O_2 is evolved. This efficiency assumes that the O_3 is 100 % pure when it exits the delivery tube, and if this is not so, then the detection efficiency is higher. The near 100 % purity of the distilled O_3 was chemically checked using reaction with KI solution [58], and also by its vapor pressure. O_3 fluxes in the range 10^{14} to $10^{16}\ cm^{-2}\ s^{-1}$ were measured.

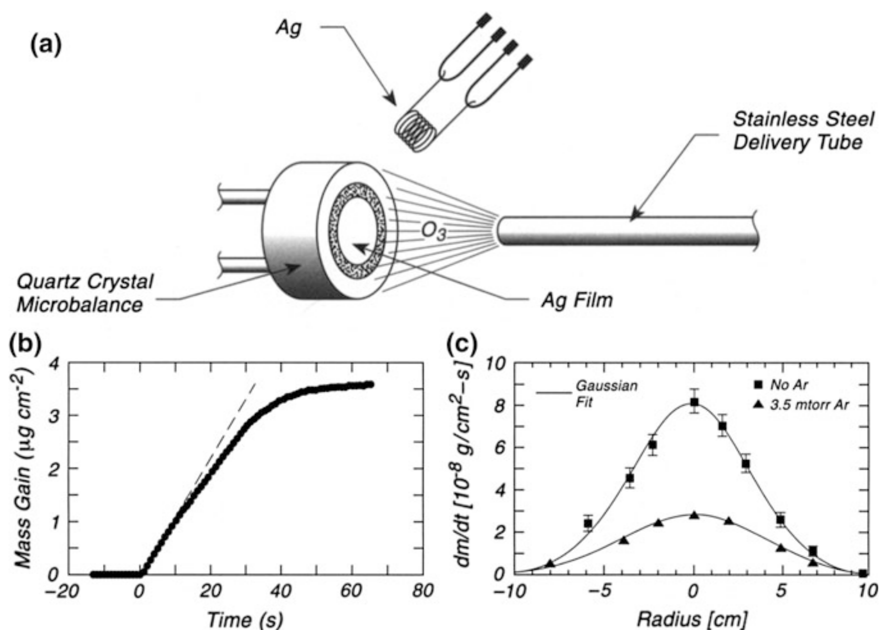

Fig. 40.8 Detection of ozone or atomic oxygen. **a** Geometry for O_3 detection. **b** Mass change during O_3 + Ag reaction. **c** Angular distribution of O_3

The fate of the O_3 in the film growth system was studied by placing O_3 detectors in various positions outside the beam. It was found that almost no O_3 was detected, suggesting that efficient wall decomposition reactions occur, converting O_3 to O_2.

A similar study, involving atomic O made in an RF discharge, was made using Ag films on a quartz crystal microbalance [59].

40.9 Purity of Ir and Pt Hot Filament Sources for Atomic Oxygen Production

A number of reports have been made of the use of hot Ir and Pt filaments, operating in an oxygen atmosphere, for the production of atomic oxygen, . Usually the atomic oxygen is delivered directly to a surface by line-of-sight transmission from the filament to the surface. The work to be described here has used mass spectrometry of the gas phase above hot Ir and Pt filaments and Auger spectroscopy measurements of the composition of an atomically clean Au surface to investigate exactly what is evolved from the Ir and Pt surfaces [56, 60]. Unfortunately, it is found that atomic oxygen is not cleanly produced and that the transport of Ir and Pt oxides also occurs making suspect any use of this method to produce pure atomic O.

Figure 40.9a shows line-of-sight mass spectroscopy of an Ir filament operating in 1.8×10^{-5} Torr of O_2. The detection of the Ir oxides is shown as the Ir filament temperature is raised. It was shown that the Ir signal corresponds mainly to Ir(g) production which occurs also in the oxygen atmosphere. Figure 40.9b shows the Auger spectrum of a Au surface after long exposure to a hot Ir filament at 2096 K, operating in ultrahigh vacuum. It is seen that even at this low temperature (compare to Fig. 40.9a), over long times, the Au Auger spectrum is modified by the deposition of Ir. An Auger ratio, A/B, may be used to deduce the magnitude of the Ir coverage. In Fig. 40.9c, this ratio maximizes after about 100 h of exposure to Ir at 2096 K, meaning that the Au Auger signal has been obscured by several monolayers of Ir which have been deposited. In Fig. 40.9d, the same experiment, done in O_2(g), shows that Ir is detected by Auger spectroscopy on the Au substrate even at $\sim$1600 K, whereas atomic O (or Ir oxides) are not detected until 1760 K. Thus atomic oxygen, transport to Au does not occur in the absence of Ir transport meaning that Ir should not be used as a source of pure atomic O [60].

A similar set of experiments were performed with Pt. As shown in Fig. 40.9e, the low energy Auger spectrum of the Au is altered by the deposition of Pt at 1683 K in ultrahigh vacuum. In 137 min of deposition the, Au 69 eV feature is extinguished, meaning that several ML of Pt have deposited. In Fig. 40.9f, the development of the O-Auger intensity and the Pt coverage, as measured by an Auger ratio, are compared. It may be seen by a careful comparison of the two panels that Pt transport is observed prior to atomic O (or Pt oxides) transport to the Au surface [61].

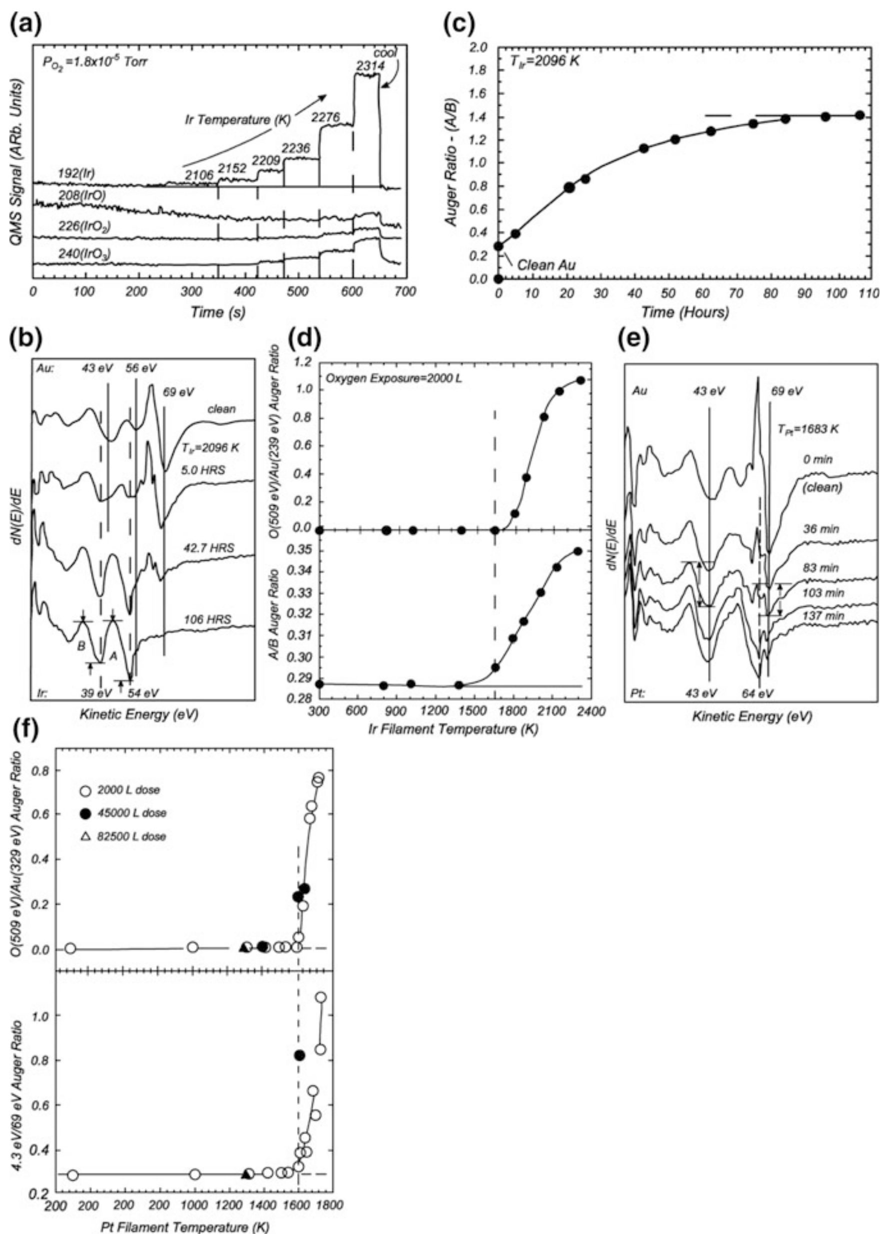

Fig. 40.9 Purity of Ir and Pt hot filament sources for atomic O production. **a** Line-of-sight mass spectrometry—Ir + O_2, **b** Auger ratios—Ir deposition in vacuum on Au (2096 K = T_{Ir}), **c** Ir/Vacuum—2096 K—on Au, **d** Deposition of O and Ir in O_2 on Au versus T, **e** Auger ratios—Pt in vacuum on Au (1683 K = T_{Pt}), **f** Deposition of O and Pt in O_2 on Au versus T

Both of these experiments indicate that neither Ir nor Pt hot filaments, operating in an oxygen atmosphere, can be trusted to deliver pure atomic O to an exposed surface.

40.10 Pure Hydrogen Peroxide Doser for Ultrahigh Vacuum

Hydrogen peroxide, H_2O_2, is a strong oxidizer, often used in aqueous solution for oxidizing inorganic or organic substances. It works by a chemical reduction process involving the oxygen, where the oxidation number of the peroxide ion (O^{1-}) changes to O^{2-} in water product. A balanced equation for its use as an oxidizer is

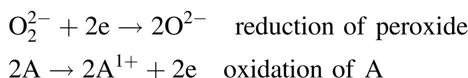

$$O_2^{2-} + 2e \rightarrow 2O^{2-} \quad \text{reduction of peroxide}$$
$$2A \rightarrow 2A^{1+} + 2e \quad \text{oxidation of A}$$

Usually H_2O_2 is sold by chemical suppliers in a 30 % aqueous solution, which, when diluted 10 fold becomes the 3 % solution used as a medical antibiotic solution. Pure H_2O_2 may be made by vacuum evaporation [62] of 30 % H_2O_2 solution, where the water component of the solution exhibits a higher vapor pressure than the H_2O_2. Pure hydrogen peroxide is a faint blue syrupy liquid which freezes at −0.4 °C [62].

The purification of H_2O_2 by vacuum distillation has been described in a careful study [63], where the reflection IR spectrum of a thin film of H_2O_2 was measured as it evaporated in ultrahigh vacuum from a reflective quartz microbalance surface, and where in the final stages of evaporation a hydrogen peroxide dehydrate phase was removed, leaving the least volatile pure H_2O_2 phase.

An apparatus to purify 30 % H_2O_2 and then to deliver pure H_2O_2 vapor into an ultrahigh vacuum system is shown in Fig. 40.10. The micrometer leak valve connects the purification system with the UHV system. The H_2O_2 30 % solution is added through a PTFE (Teflon)-glass stopcock (lubricated only with a halocarbon grease on the O-ring seals) and this solution is vapor distilled into a scroll pump containing no organics. Following removal of the major fraction of the liquid by distillation, pure liquid H_2O_2 is left in the bulb. The vapor pressure of the H_2O_2 is about 0.76 Torr at 13 °C to 7.6 Torr at 45 °C [64]. At these pressures, H_2O_2(g) can be easily transported to the UHV chamber using the leak valve.

Because H_2O_2 readily oxidizes organic compounds, the entire apparatus shown in Fig. 40.10 should be cleaned initially with the boiling 30 % solution for complete organic removal [63]. H_2O_2 taken from a 30 % aqueous solution without vacuum distillation has been used to grow high quality ZnO epitaxial films [65].

The 30 % H_2O_2 solution is a strong oxidizer which will cause burns to the skin, the respiratory tract and to the eyes. The heat of reaction with oxidizable materials may cause ignition.

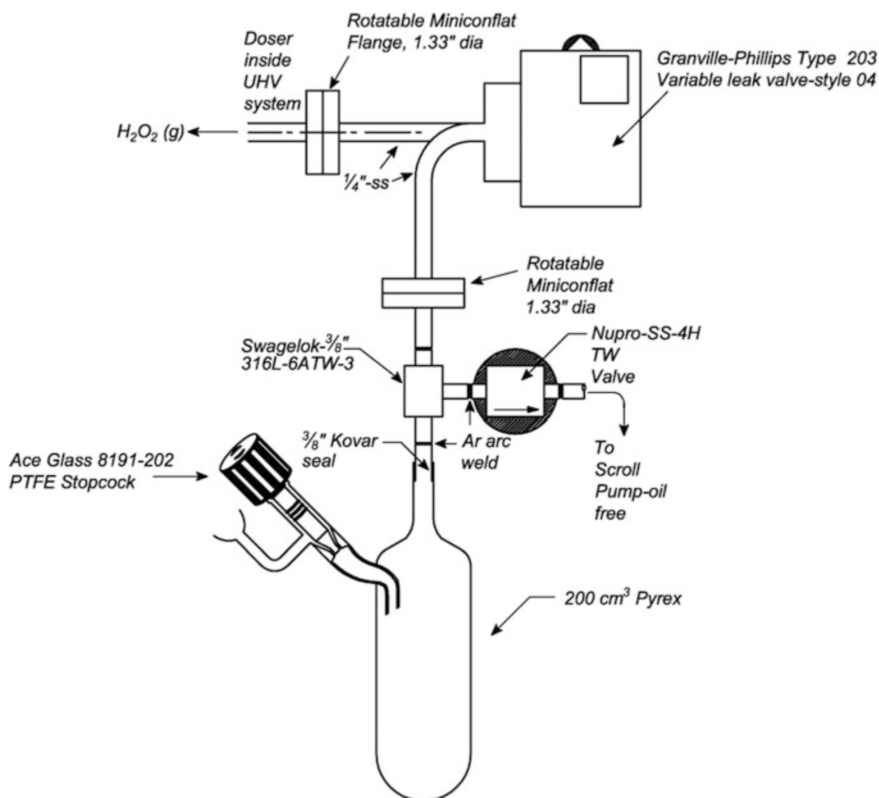

Fig. 40.10 Hydrogen peroxide purifier and gas source

References

1. I. Langmuir, J. Am. Chem. Soc. **34**, 1310 (1912)
2. I. Langmuir, J. Am. Chem. Soc. **37**, 417 (1915)
3. J.N. Smith Jr, W.L. Fite, J. Chem. Phys. **37**, 898 (1962)
4. D. Brennan, P.C. Fletcher, Proc. Roy. Soc. London Ser. A **250**, 389 (1959)
5. T.W. Hickmott, J. Chem. Phys. **32**, 810 (1960)
6. U. Bischler and E. Bertel, J. Vac. Sci. Technol. **A11**, 458 (1993). W capillary for this source may be obtained from Metallwerke Plansee GmbH, A-6600 Reutte/Tirol, Austria, Tele: 43 5672 70 0; FAX: 43 5672 70 500. The entire source is available from Physikalisches Buro Stein-muller GmbH, Rinnerstr. 16d, A-6074 Rinn/Aldrans, Austria
7. K.H. Bornscheuer, S.R. Lucas, W.J. Choyke, W.D. Partlow, J.T. Yates Jr, J. Vac. Sci. Technol. **A11**, 2822 (1993)
8. B.A. Von Gottwald, Vakuum Tech. **22**, 106 (1973)
9. C.T. Campbell, S.M. Valone, J. Vac. Sci. Technol. **A3**, 408 (1985)
10. Spiral W filaments in standard or special dimensions may be obtained from CM Furnaces Inc., 103 Dewey Street, Bloomfield, NJ 07003
11. H. Wise, B.J. Wood, Adv. At. Mol. Phys. **3**, 291 (1967)
12. J.P. Toennies, W. Welz, G. Wolf, J. Chem. Phys. **71**, 614 (1979)

13. B.E. Koehler, C.H. Mak, D.A. Arthur, P.A. Coon, S.M. George, J. Chem. Phys. **89**, 1709 (1988)
14. V.G. Luppov, M. Mertig, T. Roser, B.S. van Guilder, B. Vuaridel, YuM Melnik, A.F. Prudkoglyad, Rev. Sci. Instrum. **62**, 2738 (1991)
15. B. Van Zyl, M.W. Gealy, Rev. Sci. Instrum. **57**, 359 (1986). It is interesting to note that in these studies, the maximum in H_2 dissociation probability is not reached until tungsten temperatures above 2400 K are employed. This may be due to the presence of gas phase collisions here, where collisionless conditions generally apply in sources used for surface studies in ultrahigh vacuum
16. H. Koschmieder, V. Raible, Rev. Sci. Instrum. **46**, 536 (1975)
17. A. Hershcovitch, A. Kponou, and TO. Niinikoski, Rev. Sci. Instrum. **58**, 547 (1987)
18. K.C. Harvey, C. Fehrenbach Jr, Rev. Sci. Instrum. **54**, 1117 (1983)
19. M. Eisenstadt, Rev. Sci. Instrum. **36**, 1878 (1965)
20. J. Slevin, W. Stirling, Rev. Sci. Instrum. **52**, 1780 (1981)
21. B.J. Wood, H. Wise, J. Phys. Chem. **66**, 1049 (1962)
22. W.W. MacAlpine, R.O. Schildknecht, in *Proceedings of IRE*, 2099 (1959)
23. C.D. Stinespring, A. Freedman, C.E. Colb, J. Vac. Sci. Technol. **A4**, 1946 (1986)
24. C.E. Kolb, M. Kaufman, J. Phys. Chem. **76**, 947 (1972)
25. Microwave sources are available from Opthos Instruments, Inc., 17805 Caddy Drive, Rockville, MD 20855
26. S. Sibener, R.J. Buss, C.Y. Ng, Y.T. Lee, Rev. Sci. Instrum. **51**, 167 (1980)
27. C.D. Stinespring, A. Freedman, Appl. Phys. Lett. **48**, 718 (1986)
28. A. Freedman, J. Appl. Phys. **75**, 3112 (1994)
29. G.N. Robinson, A. Freedman, R.L. Graham, Langmuir **11**, 2600 (1995)
30. A. Freedman, C.D. Stinespring, J. Phys. Chem. **96**, 2253 (1992)
31. H. Bonzel, A.M. Bradshaw, G. Ertl, *Physics and Chemistry of Alkali Metal Adsorption* (Elsevier, Amsterdam, 1989)
32. J.B. Taylor, I. Langmuir, Phys. Rev. **44**, 423 (1933)
33. Getter sources may be obtained from SAES Getters S.p.A., Head Office, Via Gallarate, 215, 20151 Milano, Italy. USA Offices: SAES Getters/U.S.A. Inc., 1122 E. Cheyenne Mtn. Blvd., Colorado Springs, CO 80906
34. F. Ricca, P. Delia, Porta. Vacuum **10**, 215 (1960)
35. D.L. Schaefer, Rev. Sci. Instrum. **41**, 274 (1970)
36. L.V. Hau, J.A. Golovchenko, M.M. Burns, Rev. Sci. Instrum. **65**, 3746 (1994)
37. F. Kalos, A.E. Grosser, Rev. Sci. Instrum. **40**, 804 (1969)
38. K.N. Walzl, C.F. Koerting, I.M. Xavier, A. Kuppermann, J. Chem. Phys. **86**, 88 (1987)
39. F.A. Elder, C. Giese, B. Steiner, M. Inghram, J. Chem. Phys. **36**, 3292 (1962)
40. P. Chen, S.D. Colson, W.A. Chupta, J.A. Berson, J. Phys. Chem. **90**, 2319 (1986)
41. J. Dyke, N. Jonathan, E. Lee, A. Morris, J. Chem. Soc., Faraday II **72**,1385 (1976)
42. X.-D. Peng, R. Viswanathan, G.H. Smudde Jr, P.C. Stair, Rev. Sci. Instrum. **63**, 3930 (1992)
43. Alltech Assoc., Inc. 2051 Waukegan Rd., Deerfield, IL 60015
44. R. Renaud, L.C. Leitch, Can. J. Chem. **32**, 545 (1954). Proper caution should be employed working with dimethyldiazine as it is a carcinogenic agent
45. D.D. Berkley, A.M. Goldman, I. Maps, B.R. Johnson, J. Morton, T. Wang, Rev. Sci. Instrum. **60**, 3769 (1989)
46. D.D. Berkley, B.R. Johnson, N. Anand, K.M. Beauchamp, L.E. Conroy, A.M. Goldman, K. Mauersberger, M.L. Mecartney, J. Morton, M. Tuominen, Y.-J. Zhang, Appl. Phys. Lett. **53**, 1973 (1988)
47. E. Coleman, T. Siegrist, D.A. Mixon, P.L. Trevor, D.J. Trevor, J. Vac. Sci. Technol. **A9**, 2408 (1991)
48. G.A. Cook, A.D. Kiffer, C.V. Klumpp, A.H. Malik, L.A. Spence, *Advances in Chemistry Series 21* (American Chemical Society, Washington, DC, 1959), p. 44
49. *Matheson Gas Data Book*, 6th ed. (Matheson Gas Products, Secaucus, NJ, 1980), pp. 574–577

50. Aldrich #24,982-3; CAS (7631-86-9). Sold by Aldrich Chemical Co., P.O. Box 2060, Milwaukee, WI 53201
51. Fomblin is a registered trademark of Montedison Specialty Chemicals, Milano, Italy
52. Krytox is a registered trademark of E.I. dupont De Nemours and Co., Inc., Wilmington, DE
53. S. Hosokawa, S. Ichimura, Rev. Sci. Instrum. **62**, 1614 (1991)
54. M. Griggs, S. Kaye, Rev. Sci. Instrum. **39**, 1685 (1968)
55. S. Anderson, K. Mauersberger, Rev. Sci. Instrum. **52**, 1025 (1981)
56. L. Andrews, R.C. Spiker Jr, J. Phys. Chem. **76**, 3208 (1972)
57. J.T. Kucera, J.D. Perkins, K. Uwai, J.M. Graybeal, T.P. Orlando, Rev. Sci. Instrum. **62**, 1630 (1991)
58. D.H. Byers, B.E. Saltzman, *Advances in Chemistry Series*, vol. 21 (American Chemical Society, Washington, DC, 1959), p. 93
59. V. Matijasevic, E.L. Garwin, R.H. Hammond, Rev. Sci. Instrum. **61**, 1747 (1990)
60. V.S. Smentkowski, J.T. Yates Jr, J. Vac. Sci. Technol., A **12**, 219 (1994)
61. V.S. Smentkowski, J.T. Yates Jr, J. Vac. Sci. Technol., A **12**, 224 (1994)
62. W.T. Foley, P.A. Giguere, Hydrogen Peroxide and its analogues II. Phase equilibrium in the system hydrogen peroxide-water. Can. J. Chem. **29**, 123 (1951)
63. M.J. Loeffler, B.D. Teolis, R.A. Baragiola, J. Phys. Chem. B **110**, 6911 (2006)
64. *CRC Handbook of Chemistry and Physics*, 84th edn. (CRC Press, Boca Raton, 2003–2004), Section 6-71
65. N. Izyumskaya, V. Avrutin, W. Schoch, A. El-Shaer, F. Reuβ, Th. Gruber, A. Waag, J. Crystal Growth, **269**, 356 (2004)

Chapter 41
Electrochemical Sources and Devices

41.1 Electrochemical Sulfur Source

A solid-state electrochemical cell is especially convenient as a source for sulfur vapor deposition in surface science experiments. The cell was originally designed by Wagner [1] in the 1950s, and variations on its design have been in use since [2–7]. In Fig. 41.1a, a cross-sectional view of the cell is shown. It consists of a glass tube, 2.6 mm in inside diameter at the outlet on the top, which has been made by a glassblower to have a slightly larger diameter on its bottom end. The waist joint in the center serves as a stop to hold the contents under compressive force, as will be described. A pellet of AgI fits tightly into the glass tube and is contacted by a silver foil cathode electrode on its bottom that is welded to a Pt wire. The Pt wire is directed through the center of a glass capillary piston and through a spring device that exerts a compression force on the piston from the bottom. Above the AgI pellet is a Ag_2S pellet, compressed against a Pt ring that is welded to a Pt wire anode that passes up through the collimating tube. The assembly is contained inside a metal tube that may be heated by ohmic heating from a resistance wire insulated from the metal tube and wrapped around it. At a cell temperature of 485 K and a potential drop of 0.15 V, a maximum flux of 4–5 × 10^{12} S_2 molecules/s was generated. The literature indicates that S_2 is the major gas species generated under these conditions [5, 6].

The measured angular distribution of S on a Pt crystal is shown in Fig. 41.1b, but unfortunately the doser-crystal distance was not reported for these measurements [2]. A Gaussian distribution is observed with Auger spectroscopy, where data measured in both the *x*- and *y*-direction are superimposed on the same graph.

The electrochemical cell operates in ultrahigh vacuum with minimal outgassing and may be operated with pressures being maintained in the 10^{-10}-Torr range.

© Springer International Publishing Switzerland 2015

J.T. Yates Jr., *Experimental Innovations in Surface Science*,
DOI 10.1007/978-3-319-17668-0_41

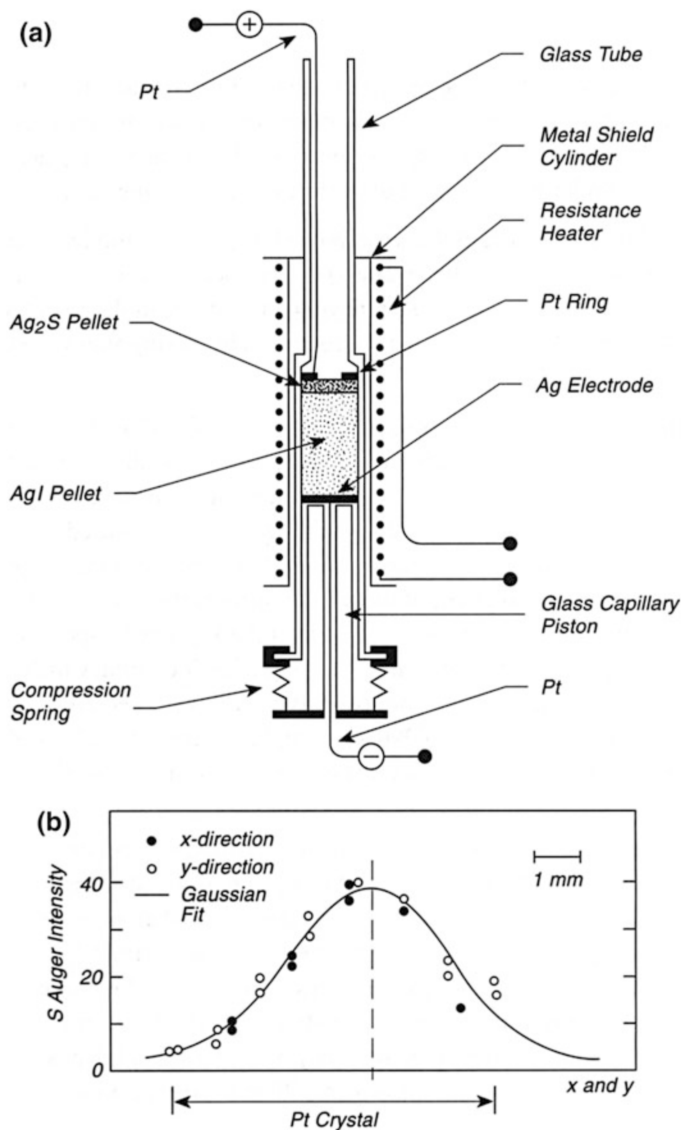

Fig. 41.1 Electrochemical S source. **a** Electrochemical cell. **b** Spatial S distribution

41.2 Electrochemical Halogen Sources

Halogens are important surface species in surface chemistry and their delivery to surfaces in a controlled manner forms an important research technology. This discussion concerns the delivery of iodine gas by means of electrochemical

generation [8], but others have used similar methods for both chlorine and bromine [7, 9, 10].

The source shown in Fig. 41.2a is a silver iodide pellet. At moderate temperatures, an electrochemical reaction, $2AgI(s) \rightarrow 2Ag(s) + I_2(g)$, occurs in the pellet as a result of a potential applied between two electrodes, relying on the ionic mobility in the heated pellet. The mobile defect concentration may be increased by mixing about 5 % CdI_2 with the AgI before casting the pellet.

The current flow through the heated pellet can be regulated using a constant current DC source, and a voltage of about 25 V will cause a current of about 25 μA to flow without external heating. The cells display extremely non-ohmic behavior, especially during start-up. In order to increase the efficiency of the source, it is housed in a Pyrex heater tube coated on the outside with a semiconducting SnO_2 thin film (see p. 123) having a resistance of about 10–100 Ω/cm of tube. Alternatively, the Pyrex tube can be heated using a spiral nichrome wire wrapped around the tube [11]. The temperature of the tube and the pellet is adjusted by passing current through the SnO_2 film, which has a band of Aquadag colloidal graphite on each end to act as a contact between the conductive film and two clamps. At a temperature of 390 K, an applied voltage of 20 V produces a stable cell current of about 100 μA. The cell walls may adsorb I_2 during initial operation, but then stable operating conditions are achieved. Faraday's laws may be used to roughly estimate the flux of iodine from the source.

Figure 41.2b shows the output of the electrochemical cell as a function of the current as measured with a quadrupole mass spectrometer in line of sight, and on axis with the source. The system pressure was simultaneously measured with an ionization gauge that did not have line of sight to the source, and it is believed that it measures mainly I_2 gas. The mass spectrum indicates that I^+ at 127 amu and I_2^+ at 254 amu are the main ions generated in the mass spectrometer from $I_2(g)$, although some H_2 and Cl_2 are also produced. If the pellet is heated to higher temperatures, near 430 K, the conductivity may be increased to give higher I_2 fluxes, but deposition of CdI_2 also occurs slowly. It is also reported that a baffle at room temperature may be used to avoid deposition of undesirable substances, and that gaseous iodine can still be deposited on the sample with this arrangement.

To make the AgI/CdI_2 button, 7 g of the mixed salt is melted and poured onto the Pt/Rh mesh that is held on a glass plate under a cylindrical mold made of Pyrex. The Ag coil is inserted into the top of the melt before solidification. If the Pt/Rh mesh is heated to redness in a Bunsen burner flame prior to being covered with the liquid melt, and if it is held flat on the plate, the melt will cover only the exposed wire and will not submerge the electrode. Alternatively, red-hot Pt/Rh can be fused into the cold pellet [7]. The pellet can easily be removed from the Pyrex mold after cooling for insertion into the long support-heater tubing, which acts as a beam collimator in use.

Similar devices have been made for producing all of the halogens [7], and their performance is similar to that reported here. It is reported that after many hours of operation, a dead short often occurs through the pellet. This indicates that a metallic Ag dendrite has grown inside the pellet; brief passage of a high current through the

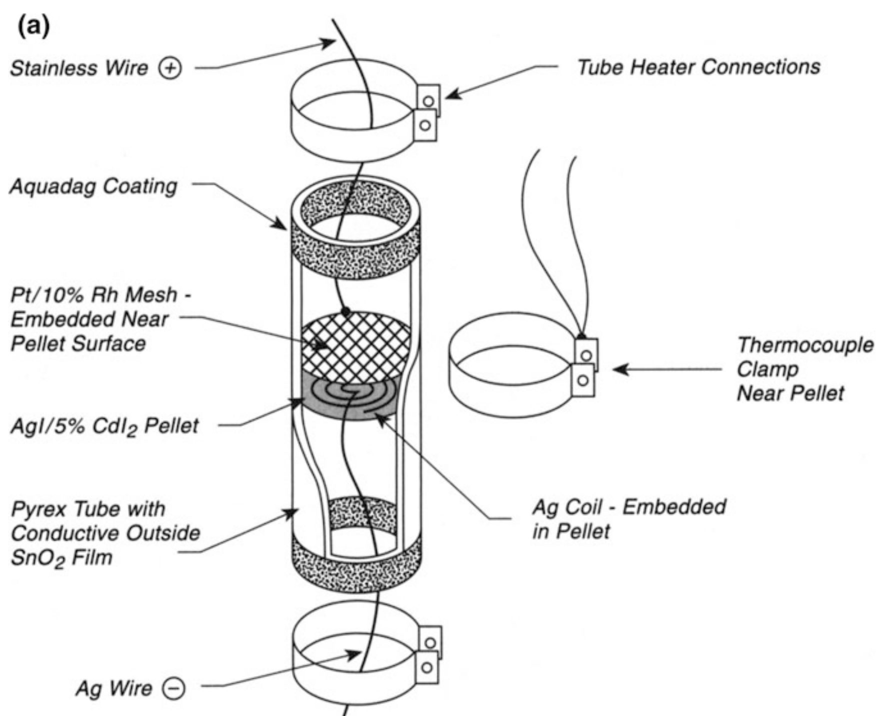

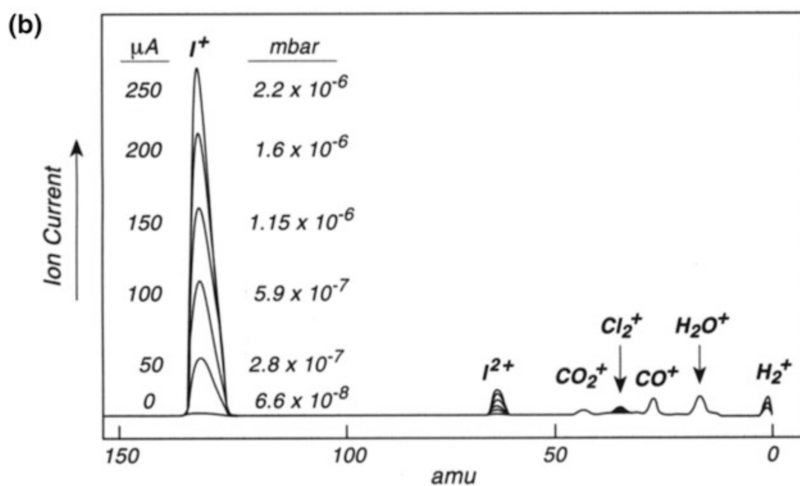

Fig. 41.2 Typical electrochemical halogen source. **a** Cell. **b** Mass spectrum at 150 °C

heated pellet may break the dendrite. In addition, for the Cl_2 cell used at excessive temperatures (>420 K) significant AgCl(g) was evolved. The halogen sources may be voltage modulated in the frequency range of 0.5–22.5 Hz, and the modulated halogen beam produced can then be used in kinetic studies on single crystal surfaces [9], and useful waveforms may be employed.

The production of pure F_2 by electrochemical means has been partially successful [10], although the high reactivity of fluorine with materials has caused problems. A CaF_2 pellet, held by springy contacts between a Pt plate and a Pt gauze, was employed for electrochemical generation at temperatures of 420–450 K. The gas evolved at the anode was focused onto the sample with a short tube, coated with CaF_2. Small amounts of SiF_4 were detected if glass tubing was used. The source delivers small amounts of platinum fluorides and HF. Studies with this source of the adsorption of F_2 on Pt showed that PtF_2 is evolved above about 500 K from Pt at low coverages, and that PtF_4 is evolved at high coverages, in addition to F(g) at 890 K [12]. The HF yield from the electrochemical cell may be reduced to a few percent of the F_2 yield by outgassing and electrolysis. Currents between 2 and 50 μA were used. During F_2 dosing, the total pressure of the vacuum system was below 1×10^{-9} mbar.

Halogen atom sources have been described and one example is a pulsed source involving Cl_2 dissociation in a microwave cavity. One interesting feature of this work is the study of $2P_{3/2}$- and $2P_{1/2}$-Cl atom losses on Teflon walls [13].

A source of halogen ions produced by surface ionization on a LaB_6 surface of low work function has been described [14].

41.3 Electrochemical I_2 Doser

Halogen dosers, based on electrochemical generation are popular and have been treated in Sect. 41.2 of this book. Recently an I_2 doser working at low temperature has been developed which adds to the technology described previously (Fig. 41.3). Previous dosers required high temperatures to achieve electrical conductivity in the solid state electrolyte. By using the compound Ag_4RbI_5, high ionic conductivity is achieved near room temperature. Ag_4RbI_5 is prepared and about 0.5 g is compressed into a disk of 2 mm thickness and 7.5 mm width using a hydraulic press at 600 MPa, for 5 min. The disk is made with Pt mesh on the anode side. The disk is placed between two stainless electrodes and the application of a voltage causes current to flow with the production of I_2(g). The cell had an operating resistance of about 2.5 kΩ and operates at about 200 μA when dosing. The collimator directs the I_2 flow to the sample. The Ag_4RbI_5 is stable up to 500 K allowing mild vacuum system bakeout to be used. The design cannot be extended to similar compounds of Cl and Br because these mixed salts have insufficient conductivity. Outgassing at 100 μA is recommended prior to opening the shutter for dosing [15].

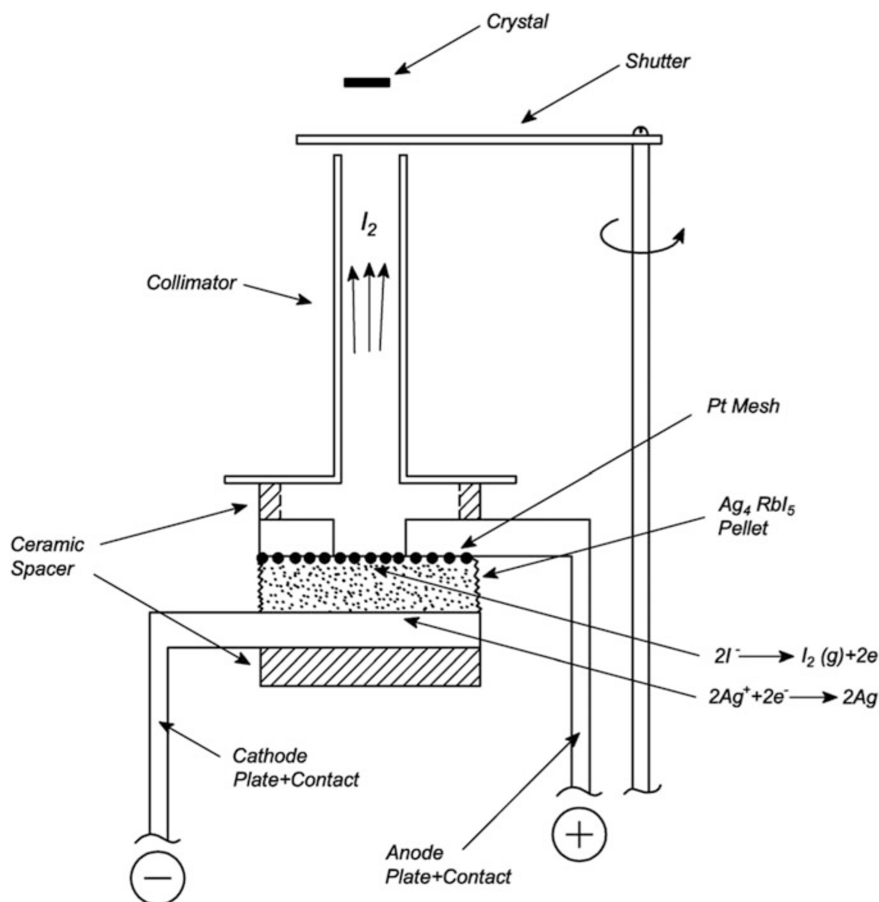

Fig. 41.3 I_2 electrochemical doser

41.4 Electrochemical Device Working in UHV

The application of UHV surface analysis methods to working solid state electrochemical devices is of widespread interest. To study working devices, it is necessary to carry out electrochemical redox processes involving gases, and to control electrical potentials in the device. In addition, since ion mobilities govern device performance, one must be able to control the device temperature during operation. Figure 41.4a shows a top view of a working device, with a Ni-film deposited working electrode. The device is mounted on a base plate which is transferrable to one or more manipulators and which connects to an external potentiostat/galvanostat used for impedance spectroscopy. Three springy electrodes mounted around the device exterior make contact at various points, as shown in Fig. 41.4b. The small contact area of the probes minimizes heat transfer from the heated device. Device

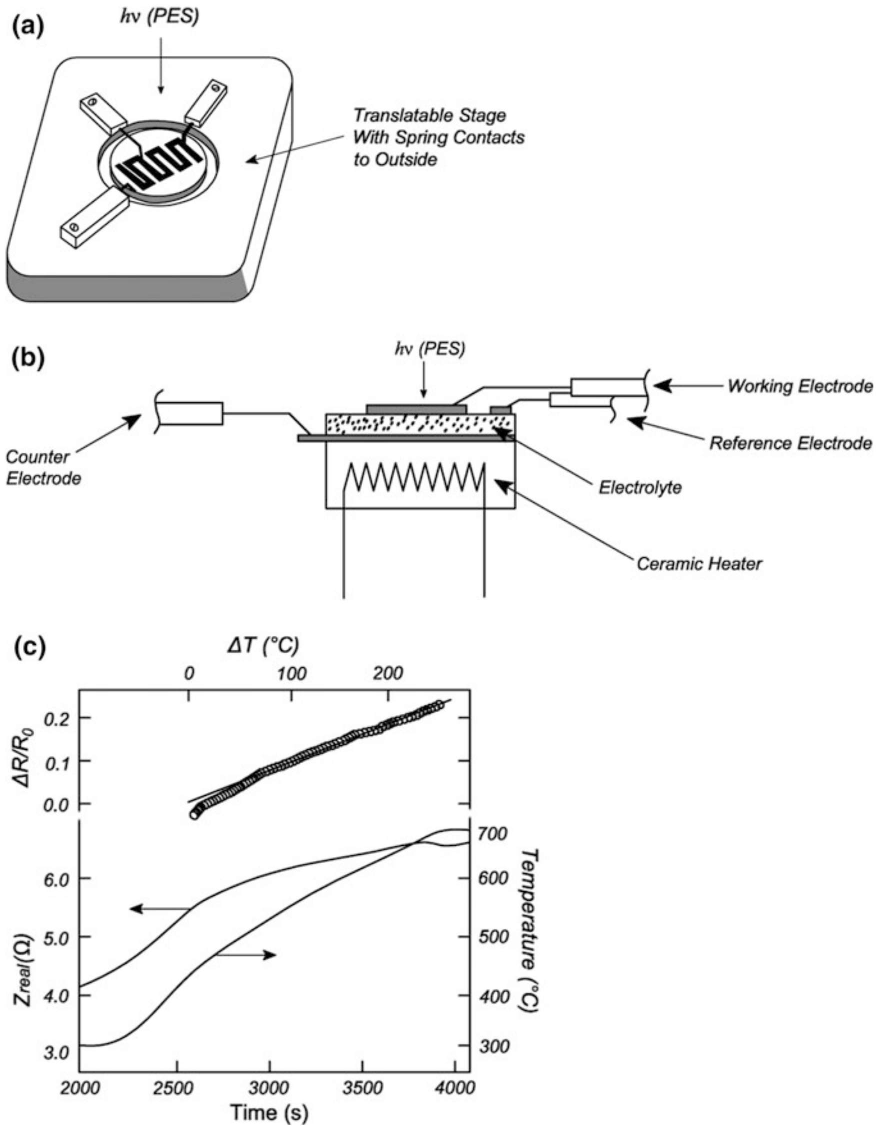

Fig. 41.4 Electrochemical device working in UHV. **a** Top view. **b** Side view. **c** Thermal behavior

heating is achieved by means of ceramic heater button with an embedded resistor. In Fig. 41.4c, the real component of the device impedance is plotted versus temperature measured with a pyrometer, and the relative resistance is also shown during heating. These plots show that good contact is being made over the temperature range studied and the temperature dependence of the resistance measured is consistent with that of a Ni film used in the device as the upper electrode, indicating that most of the impedance is in the film [16].

References

1. C. Wagner, J. Chem. Phys. **21**, 1819 (1953)
2. W. Heegemann, K.H. Meister, E. Bechtold, K. Hayek, Surf. Sci. **49**, 161 (1975)
3. T.E. Gallon, I.G. Higginbotham, M. Prutton, H. Tokutaka, Surf. Sci. **21**, 224 (1970)
4. H. Tokutaka, M. Prutton, I.G. Higginbotham, T.E. Gallon, Surf. Sci. **21**, 233 (1970)
5. J.C. Greenbank, B.B. Argent, Trans. Far. Soc. **61**, 655 (1965)
6. D. Detry, J. Drowart, P. Goldfinger, H. Keller, H. Rickert, Z. Physik, Chem. NF **55**, 314 (1967)
7. N.D. Spencer, P.J. Goddard, P.W. Davies, M. Kitson, R.M. Lambert, J. Vac. Sci. Technol. **A1**, 1554 (1983). (This paper contains references to a number of arrangements to the electrochemical generation of halogens, etc)
8. A. Mowbray, R.G. Jones, J. Vac. Sci. Technol. **A7**, 3373 (1989)
9. W.T. Tysoe, N.D. Spencer, R.M. Lambert, Surf. Sci. **120**, 413 (1982)
10. R.G. Jones, Prog. Surf. Sci. **27**, 25 (1988). (A general review of halogen adsorption on surfaces)
11. Professor Philip R. Watson, Department of Chemistry, Oregon State University, Corvallis, Oregon 97331-4003 (Private communication)
12. E. Bechtold, Appl. Surf. Sci. **7**, 231 (1981)
13. W. Müller-Markgraf, M.J. Rossi, Rev. Sci. Instrum. **61**, 1217 (1990)
14. N. Kashihira, E. Vietzke, G. Zellermann, Rev. Sci. Instrum. **48**, 171 (1977)
15. S.A. Furman, D.A. Harrington, J. Vac. Sci. Technol. **A 14**, 256 (1996)
16. J.A. Whaley, A.H. McDaniel, F. El Gabaly, R.L. Farrow, M.E. Grass, Z. Hussain, Z. Liu, M.A. Linne, H. Bluhm, K.F. McCarty, Rev. Sci. Instrum. **81**, 086104 (2010)

Chapter 42
Gas Purification

42.1 Gas Purification for Experiments at High Pressures

The use of high-pressure gases for experiments involving single crystal surfaces always involves the problem of the preferential adsorption on the crystal of trace impurities present in the gas. At high pressures, even 1 ppm of adsorbable impurity can result in the selective adsorption of a monolayer or more of impurity. This problem maybe eliminated by several methods, depending upon the gases and the impurities involved.

For gases with low condensation temperatures, storage over previously baked (573 K) zeolite pellets [1] at liquid nitrogen temperature is a favored method for the adsorption of trace impurities with high condensation temperatures [2]. This is a favored method for the additional purification of 99.9999 % pure methane, for example [2]. In addition, carbon monoxide almost always contains traces of $Ni(CO)_4$ and $Fe(CO)_5$ as impurities produced within the storage cylinder or in the stainless steel gas handling system, and these metal carbonyls can be removed by storage of the CO over a wide pore zeolite at liquid nitrogen temperature. See p. 509 for a discussion of the use of cryogenic storage and distillation at liquid hydrogen temperature. Alternatively, metal carbonyls can be removed by passing CO through a copper coil heated to 100 °C, which is sufficient to decompose the carbonyls, and then through a trap cooled with liquid nitrogen. It is important to avoid the use of stainless steel tubing following the purification of the CO [3].

Adsorption of active chemisorbing gases in the presence of inactive gas is often effectively carried out by means of a Ti getter film which is freshly deposited inside a storage vessel under vacuum [3–5]. See p. 507 for the use of a Ti getter film for the final stages of purification of He(g) [5]. An apparatus involving the use of zeolite trapping followed by storage over a Ti film is shown in Fig. 42.1a. A commercial titanium sublimation pump cartridge is employed in a stainless steel storage vessel, and gas storage takes place at 77 K.

© Springer International Publishing Switzerland 2015

J.T. Yates Jr., *Experimental Innovations in Surface Science*,
DOI 10.1007/978-3-319-17668-0_42

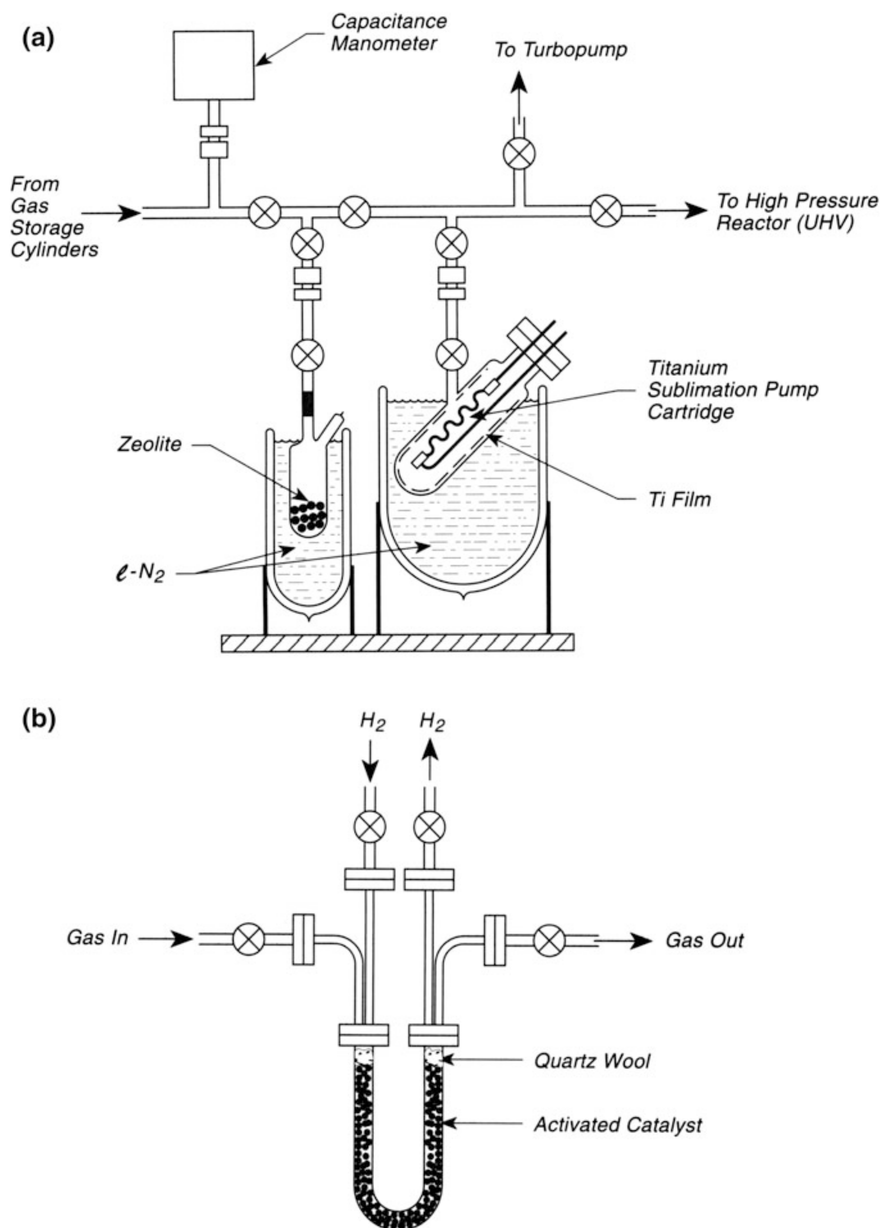

Fig. 42.1 Gas purification for experiments at high pressure. **a** Gas purification by adsorption. **b** Gas purification over catalyst (high area)

Catalytic chemists have for years used a method involving gas exposure to a high area catalyst prior to admission to the reactor chamber. This method has also been applied to Ni single crystals being studied under high pressures of methane [6, 7]. Figure 42.1b shows the configuration of the gas purification apparatus used in these studies. A U-tube is filled with a Ni catalyst (in this case), which consists of Ni particles supported on a high surface area oxide support. The particle size ranges from 0.3 to 0.8 mm diameter. Both ends of the U-tube are plugged with quartz wool to prevent transfer of dust away from the catalyst. The catalyst is activated by reduction in flowing H_2 at 800 K, and then is evacuated at 800 K to remove H_2. Either methane or nitrogen may be cleaned of impurities such as CO, O_2, CO_2, and hydrocarbons (excluding CH_4) using this apparatus.

The cleanup of H_2 maybe achieved using a supported Cu catalyst in the same manner. The chemisorption of H_2 by Cu is suppressed by working at liquid nitrogen temperature. The activation of the Cu catalyst is first carried out using H_2, and one must be careful to initially use a low pressure of H_2, since the exothermic reduction of copper oxides may cause a runaway condition. Reduction temperatures of 650 K are recommended [8, 9].

42.2 Production and Purity Measurement for Extremely Pure He

The production of He with extremely high purity for use in ultrahigh vacuum systems is a challenge requiring special gas handling techniques. It must be remembered that hydrogen is a major impurity in stainless steel ultrahigh vacuum systems, and that to avoid hydrogen impurities, glass vacuum systems must therefore be employed. The bakeout treatment of a glass vacuum system differs from a metal system, and bakeout temperatures of the order of 600 K must be used [10].

A number of methods for producing pure He have been reported in the literature. The use of superfluid He leaks [11] and diffusion through Vycor glass [12, 13] have been used by others, but the diffusion rate for H_2 through hot Vycor is about 0.1 of that for He [11], so that other methods must be used to achieve large factor reductions in the hydrogen impurity level.

The apparatus [14] shown in Fig. 42.2 was mainly constructed of Pyrex glass with bakeable metal valves, and it was processed by bakeout to achieve a base pressure of 1×10^{-10} Torr. The pumping speed in this apparatus is only about 2 L/s. Operation of the purification system begins with the deposition of Ti getter films on the inner walls of the two bulbs, G_1 and G_2, by heating W loops to which Ti wire segments have been spot welded. The surface area of these films is each about 300 cm^2. The Vycor leak is outgassed at 1025 K until the outgassing cannot be detected using the Bayard-Alpert gauge at 1×10^{-10} Torr pressure. Valve V_4 is then closed and He is effused through the Vycor leak at 975 K. The He used on the high

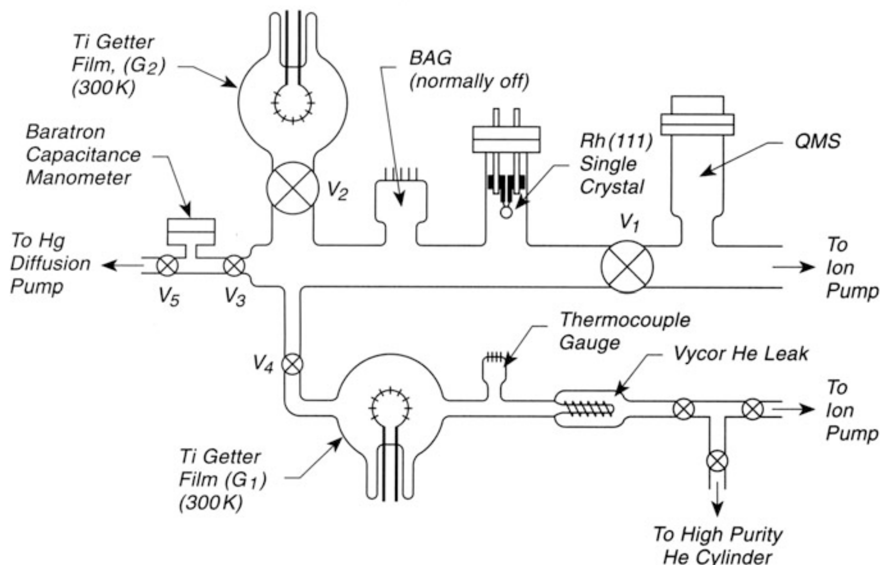

Fig. 42.2 Production and purity measurement for extremely pure He

pressure side of the Vycor leak is specified to be 99.999 % pure, and it is admitted to approximately 1 atm pressure, into a gas handling system initially at 10^{-7} or 10^{-8} Torr. Typical He effusion rates are approximately 6 × 10^{14} He atoms/s. Storage of He takes place overnight at several Torr pressure in the closed system over the freshly evaporated Ti getter film, G_1.

The Rh(111) single crystal was used as an integrating detector of H_2 in the purified He, using temperature-programmed desorption (TPD) with the mass spectrometer (QMS) as the detector. Purified He was admitted to less than 1 Torr pressure, with Valve V_2 open to the system, and with a freshly deposited Ti film in getter bulb, G_2, in order to continue getter purification of the He during exposure to the clean Rh(111) single crystal. An exposure of 1000 s was used in the He purity test, leading to exposures of from 100 to 900 Torr s to the He. Following pumping with the Hg diffusion pump, followed by use of the ion pump, TPD of both H_2 and CO was carried out, and compared to blank experiments without He. A least squares fit to the data gave 5.4 × 10^{10} H/cm^2-Torr s (He) for the contamination rate with the CO contamination rate about an order of magnitude smaller. It was shown that the rate of H_2 adsorption was not limited by gas diffusion kinetics at the He pressures used. Assuming a sticking coefficient of unity for the H_2, these measurements indicate that $P(H_2)/P(He) = 1.9 \times 10^{-11}$, which is a factor of about 10^6 improvement over the original high purity He [14]. Flowing He has been similarly purified using hot Ti sponge in the flow lines [15].

Superleaks for the control of He flow into a vacuum system have been described [16]. They are made of porous Vycor glass [17] with approximately 40-Å-diameter

pores occupying about 30 % of the volume. By using various diameters of the Vycor, the He leak rate can be adjusted. A leak made of 1-mm-diameter porous Vycor, 8 mm long, exhibits a leak rate for He of 4×10^{-6} std. cm^3/s at 300 K at 1 atm presure. The leaks may be used also by immersion in liquid He [16].

42.3 Purification of Gases by Cryogenic or Gettering Methods

The production of high-purity gases for laboratory use in ultrahigh vacuum applications has been discussed previously in the case of He (see p. 507). Here we present other methods for the purification of gases such as He, H_2, Ar, N_2, and O_2 [18].

As shown in Fig. 42.3a, a combination of zeolite adsorption and cryogenic impurity condensation was employed for both He and H_2 purification. The apparatus, made of glass, consists of a conventional gas handling system connected to a cryogenic purification unit. The zeolite trap and the glass wool trap, along with the collection tube and associated glass lines, were baked out to achieve ultrahigh vacuum. The cryostat was then filled with either *l*-H_2 or *l*-He, which causes the pressure in the tube to drop to $<10^{-12}$ Torr. Gas from the gas handling system was then slowly admitted to the cold system, and condensation of highly pure gas was observed to occur, drop by drop, off of a tungsten field emission tip located in the collection tube, which was also a field emission microscope. This indicates that the glass wool section of the apparatus was condensing impurities preferentially from the incoming H_2 or He gas, and that gas phase transport of purified gas occurred from the glass wool section to the collection tube. The purity of the collected gas was measured by evaporation of the liquified gas, which filled the collection tube, and observing that the W field emission tip was still clean after immersion and reevacuation. Concentrations of chemisorbing impurities were estimated to be $<5 \times 10^{12}/cm^3$ of liquid, considering the diffusion lengths in the liquid. This corresponds to an atomic fraction of impurities of the order of 10^{-14} in the purified gas.

In the case of Ar, N_2, and O_2 that cannot be purified by the method shown in Fig. 42.3a, because of the high freezing point of these gases, a second method of purification was devised, as shown in Fig. 42.3b [18]. Here, the glass vacuum system was baked to 430 °C to achieve ultrahigh vacuum, and a Ta or Ni film was evaporated on the walls of the 2-L vessel, after seal-off from the high vacuum line using a torch seal-off. Ar or N_2 was then admitted into the system, and condensed into the trap at *l*-H_2 temperature, after which the connection to the gas source was sealed off. Then the condensed gas was allowed to evaporate and condense several times to facilitate gas contact with the getter film, since diffusion through the gas will be slow at the $\sim$ 1 atm pressure employed. The gas could be condensed into the collection tube using liquid N_2-O_2 mixtures whose temperature could be adjusted by using different compositions, and monitored with an immersed

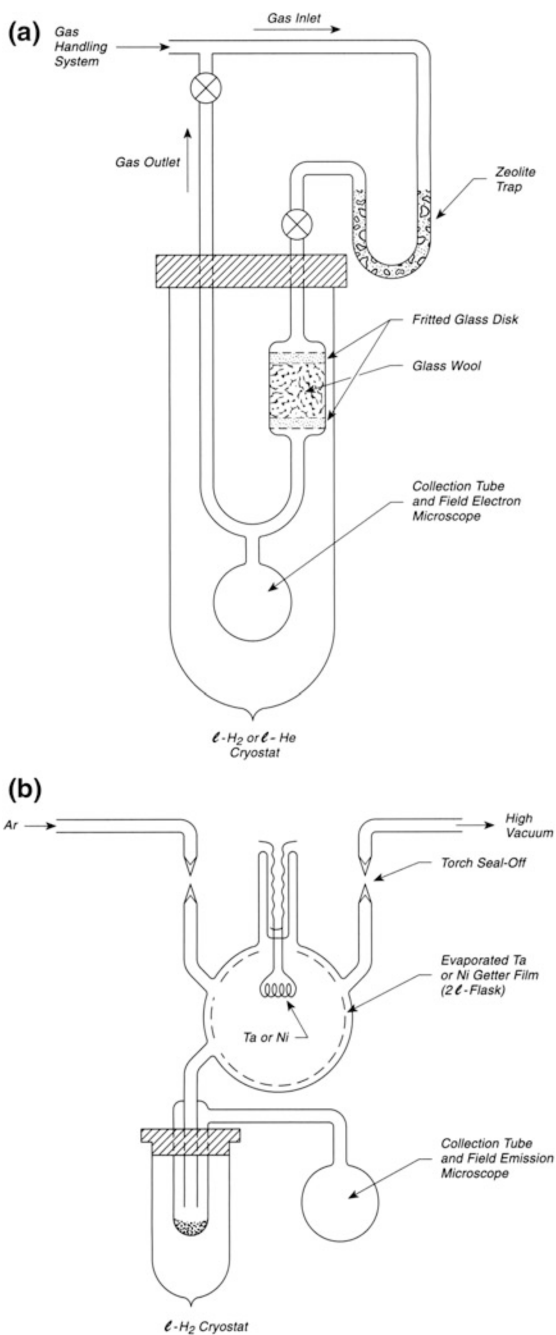

Fig. 42.3 Gas purification apparatus. **a** He and H_2 purification. **b** Ar and N_2 purification

thermocouple. By reestablishing ultrahigh vacuum by condensing the gas into the trap within the cryostat, field emission measurements showed that no detectable adsorption had occurred on the field emission tip for the case of Ar. For N_2 purification, a Ni getter film was employed, but irreversible chemisorption of N_2 prevented the use of field emission to detect impurities. For O_2, admission of tank gas through l-N_2 traps was used without a getter film, and field emission measurements were also not possible because of oxygen chemisorptions.

The power of metal getter films for maintaining very low vacuum conditions in sealed-off glass vacuum systems is clear from observations made with field emission tips sealed off in the presence of getter films. In one instance, almost no contamination of the tip was observed in one year, indicating a pressure of the order of 10^{-16} Torr or lower [19].

42.4 Gas Purification by Permeation Through Metals

For some applications the supply of extremely pure gases into a vacuum system is needed, and conventional cylinder sources are inadequately pure for this purpose. Thus, for years, chemists have used permeation through high-temperature membranes for the removal of impurities from the gas. In addition to supplying pure gas, the permeation technique also affords easy control of flow rate by the adjustment of the temperature.

In Fig. 42.4a, either hydrogen or oxygen permeation sources are shown [20]. For hydrogen, pure Ni permeation tubing is used [21]; for oxygen, pure silver permeation tubing is used [21]. The permeation tubes are 10–13 cm in length. The thin permeation tubes are silver brazed (in hydrogen) to the ends of 0.25-in.-diameter copper tubes mounted on ceramic insulator feedthroughs welded into a flange. Passing current through the device provides the heating necessary to allow gas permeation to occur. The purity of gases produced in this manner has been studied by Whetten and Young [22], Young [23], and comparisons are made in the book by Redhead [24]. The worker should remember that while high gas purity can be achieved by permeation methods, it is also likely that the gas in a UHV system will become impure owing to displacement from the walls of the chamber or by interaction with hot filaments [24]. Studies of Ag permeation sources for the production of pure O_2 have shown that long periods of operation of the source must occur before gases like H_2S, SO_2, CO, and CO_2 are eliminated to the percent level [25, 26]. It may be best to condition a Ag source on a separate vacuum system to avoid the evolution of the gases into the main system [25, 26].

In Fig. 42.4b, a glass device involving a permeation thimble is shown. For hydrogen, both pure Ni thimbles and pure Pd thimbles have been used. For oxygen, pure silver thimbles are employed. The thimble, brazed to a Kovar seal, is centrally mounted in a glass envelope containing a helical refractory metal heating filament that heats the thimble by radiation. Permeation of purified gas from the outer

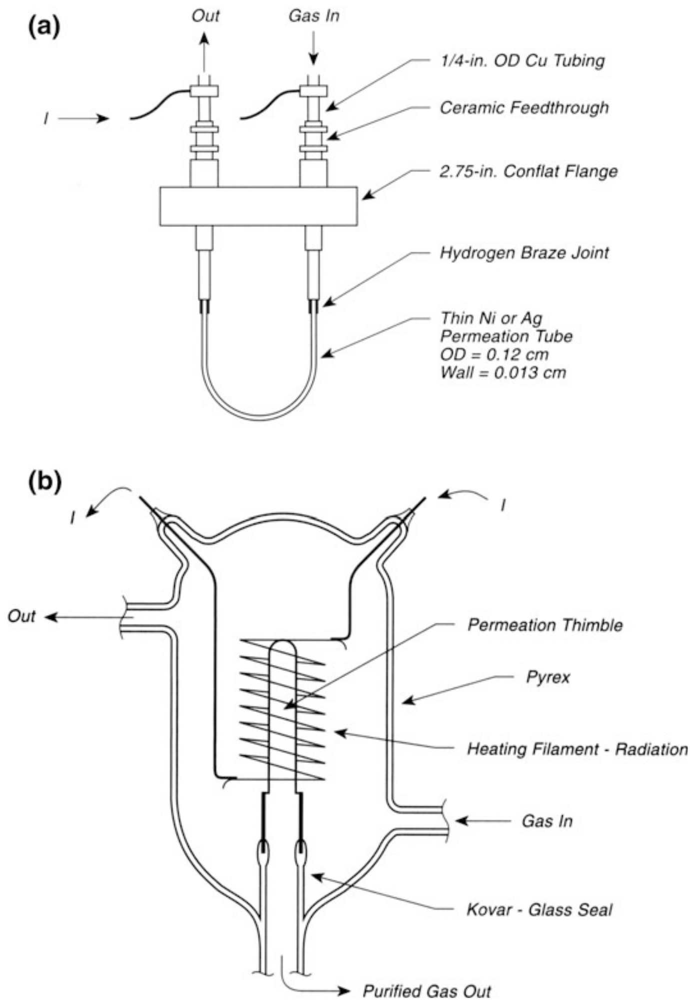

Fig. 42.4 Gas purification by permeation through metals. **a** H_2 or O_2 permeation source—ohmic heating. **b** permeation thimble—radiation heating

envelope to the inside of the thimble takes place. In both experimental arrangements, shown in Fig. 42.4a, b, it is appropriate to flow the source gas slowly through the apparatus to replenish gas at the source.

A solid state source of oxygen, followed by permeation through a Ag tube wall, is described on p. 513.

The use of a pure iron permeation source for purification of hydrogen and deuterium has been reported in [27–29].

42.5 O_2 Source—Solid State

Various permeation sources, in which gaseous O_2 is purified by diffusion through a selective metal, are described on p. 511. These sources all involve the use of oxygen gas, supplied as a gas, to drive the diffusion/purification process. A clever modification of this idea involves the use of a solid that liberates O_2 at the diffusion/purification temperature, supplying a long-lived source of purified oxygen without the need for a vacuum system to introduce O_2 gas into the permeation source [30].

Figure 42.5 shows a Ag tube device packed with MnO_2 powder. The tube is sealed by electron beam welding and then welded to two Ag tabs as shown. The electron beam welding, being done under vacuum, automatically removes most of the entrained air in the powdered MnO_2.

Passing electrical current through the Ag tube raises its temperature first to a degassing temperature of about 450 °C; when the source is resistively heated to about 550 °C, the MnO_2 begins to decompose, liberating O_2 inside the tube that then diffuses through the Ag, becoming highly purified. The rate of production of purified O_2 increases as the temperature is raised, and gas pressures from about 10^{-9} to 10^{-2} Torr can be sustained in pumped UHV systems using this source.

42.6 Reusable Sample Holder for Hydrogen Permeation Studies

The permeation of hydrogen gas through pure metals and alloys is of technological and scientific interest. One of the methods used to make permeation measurements is to electron-beam-weld the metal sample diaphragm to a cylindrical tube end [31]. Another method is to use a sample with machined knife edges that contact a deformable gasket [32]. Elastomer gasket or O-ring sealing is only useful at room

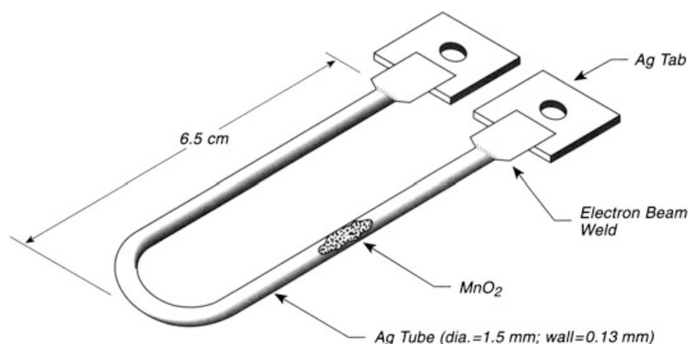

Fig. 42.5 O_2 source—solid state

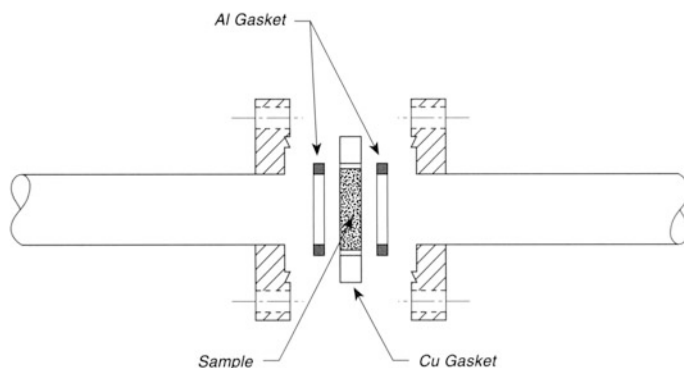

Fig. 42.6 Reusable sample holder—hydrogen permeation

temperature. The method to be described here differs from the earlier methods, is simple, and the apparatus is reusable [33].

Two standard Conflat flanges with a standard Cu gasket are used. The sample, in the form of a circular disk, is mounted inside the Cu gasket, and two Al gaskets are placed on either side of the sample. The Cu gasket, when bolted in place, protects the sample from the outside environment. The Al gaskets are plastically deformed between the sample and the inner region of the flanges, and their thickness should be properly adjusted to a dimension leading to compression and sealing. In cases where an incomplete seal at the Al gasket was found, this was attributed to work hardening of the gasket during manufacture. This could be corrected by annealing the assembled sample holder for 1–3 h at 573 K, then retightening the bolts. The sample holder was used up to 623 K, and is shown in Fig. 42.6.

An entirely different method for measuring hydrogen diffusivity in metals, involving electrical measurements as hydrogen diffuses along the length of a foil, is described in [33].

References

1. One may use Varian Vacsorb molecular sieve, catalog No. 944-0000, obtainable from Varian Vacuum Products, 121 Hartwell Avenue, Lexington, MA 02173
2. T.P. Beebe, D.W. Goodman, B.D. Kay, J.T. Yates Jr, J. Chem. Phys. **87**, 2305 (1987)
3. Dr. J. Wambach, Danish Technical University, Department of Physics, Building 307, DK-2800 Lyngby, Denmark (private communication)
4. L. Hanley, Z. Xu, J.T. Yates Jr, Surf. Sci. **248**, 265 (1991)
5. J.T. Yates Jr, J.J. Zinck, W.H. Weinberg, Rev. Sci. Inst. **50**, 132 (1979)
6. I. Chorkendorff, Technical University of Denmark, Building 307, DK-2800, Lyngby, Denmark (private communication)
7. I. Chorkendorff, I. Alstrup, S. Ullmann, Surf. Sci. **227**, 291 (1990)
8. P.A. Taylor, P.B. Rasmussen, C.V. Ovesen, P. Stoltze, I. Chorkendorff, Surf. Sci. **261**, 191 (1992)

9. P.B. Rasmussen, M. Kazuta, I. Chorkendorff, Surf. Sci. **318**, 267 (1994)
10. P.A. Redhead, J.P. Hobson, E.V. Kornelsen, *The Physical Basis of Ultrahigh Vacuum* (American Institute of Physics, New York, NY, 1993), pp. 417–430
11. M.A. Biondi, Rev. Sci. Instrum. **22**, 535 (1951)
12. F.J. Norton, J. Appl. Phys. **28**, 34 (1957)
13. J.R. Young, N.R. Whetten, in *Transactions of 8th Vacuum Symposium and 2nd International Congress* (American Vacuum Society, New York, NY, 1961), p. 625
14. J.T. Yates Jr, J.J. Zinck, W.H. Weinberg, Rev. Sci. Instrum. **50**, 132 (1979)
15. G.B. Hoflund, R.P. Merrill, J. Vac. Sci. Technol. **A1**, 1560 (1983)
16. M.F. Wilson, D.O. Edwards, J.T. Tough, Rev. Sci. Instrum. **39**, 134 (1968)
17. Vycor glass is made by Leaching Pyrex glass in alkali solution. It is available from major scientific glass manufacturers
18. B. Halpern, R. Gomer, J. Chem. Phys. **51**, 1031 (1969)
19. Personal observations
20. L.C. Burton, J. Vac. Sci. Technol. **8**, 758 (1971)
21. Type "A" Ni tubing was used; fine (99.99 %) silver tubing was used. Uniform Tubes, Inc., 7th Avenue, Collegeville, PA 19426
22. N.R. Whetten, J.R. Young, Rev. Sci. Instrum. **30**, 472 (1959)
23. J.R. Young, Rev. Sci. Instrum. **34**, 891 (1963)
24. P.A. Redhead, J.P. Hobson, E.V. Kornelsen, *The Physical Basis of Ultrahigh Vacuum* (originally published by Chapman and Hall, 1968; reprinted American Institute of Physics, New York, 1993)
25. L.C. Beavis, Rev. Sci. Instrum. **43**, 122 (1972)
26. E.G. Burroughs, Rev. Sci. Instrum. **40**, 33 (1969)
27. M. Arbab, J.B. Hudson, Appl. Surf. Sci. **29**, 1 (1987)
28. M. Arbab, J.B. Hudson, Surf. Sci. **206**, 317 (1988)
29. M. Arbab, J.B. Hudson, Surf. Sci. **209**, 183 (1989)
30. D.L. Schaefer, Rev. Sci. Instrum. **41**, 274 (1970)
31. M. Kanno, M. Yamawaki, T. Namba, in *Proceedings of the 2nd Japan Institute of Metals International Symposium, Hydrogen in Metals*, Supplement to Trans. JIM 21,105 (1980)
32. E.H. Van Deventer, V.A. Maroni, J. Nucl. Mater. **113**, 65 (1983)
33. D.J. Pine, R.M. Cotts, Rev. Sci. Instrum. **55**, 614 (1984)

Chapter 43
Liquid Handling in UHV

43.1 Adding Liquid to Atomically Clean Surfaces

As surface chemistry deals with more and more complex systems it has become necessary to work at high gas pressures as described elsewhere in this book. In addition, examples are available where work under liquids has been done while maintaining clean surfaces. The simple addition of a drop of liquid water to an atomically clean TiO_2 single crystal was found to be very difficult when pure water injection with a syringe through a rubber septum was attempted. Large quantities of silicon were found on the crystal following injection and evaporation of the water droplet, and this was thought to be due to silicones present in the rubber seal. Therefore, a syringe-injection procedure using only a tiny stainless guide tube for the syringe needle was employed as shown in Fig. 43.1a. The wetting chamber was baked to achieve ultrahigh vacuum with the syringe seal closed. Upon establishing an atmospheric pressure of very pure flowing O_2 gas (<0.05 ppm hydrocarbons) (plus a few extra Torr to cause outward atmospheric flow), it was found that ultrapure water could be injected into the stainless guide tube while O_2 gas constantly flowed from the inside to the outside along the loose fit between the hypodermic syringe and the guide tube wall. Following droplet evaporation on the atomically clean TiO_2 crystal inside the chamber (achieved by reducing the relative humidity of the flowing gas), and evacuation, the crystal was withdrawn into the analytical chamber and an Auger analysis was performed. Figure 43.1b shows the Auger spectrum after a wetting/evaporation cycle. The C Auger signal, compared to the TiO_2 Auger features, showed that less than 0.05 ML of carbon remained after evaporation. The lower limit of carbon for the cleaned crystal was about 0.005 ML. The syringe needle and the syringe were treated in boiling H_2O_2 (aq) for several hours to remove hydrocarbons prior to the water deposition experiments [1].

© Springer International Publishing Switzerland 2015
J.T. Yates Jr., *Experimental Innovations in Surface Science*,
DOI 10.1007/978-3-319-17668-0_43

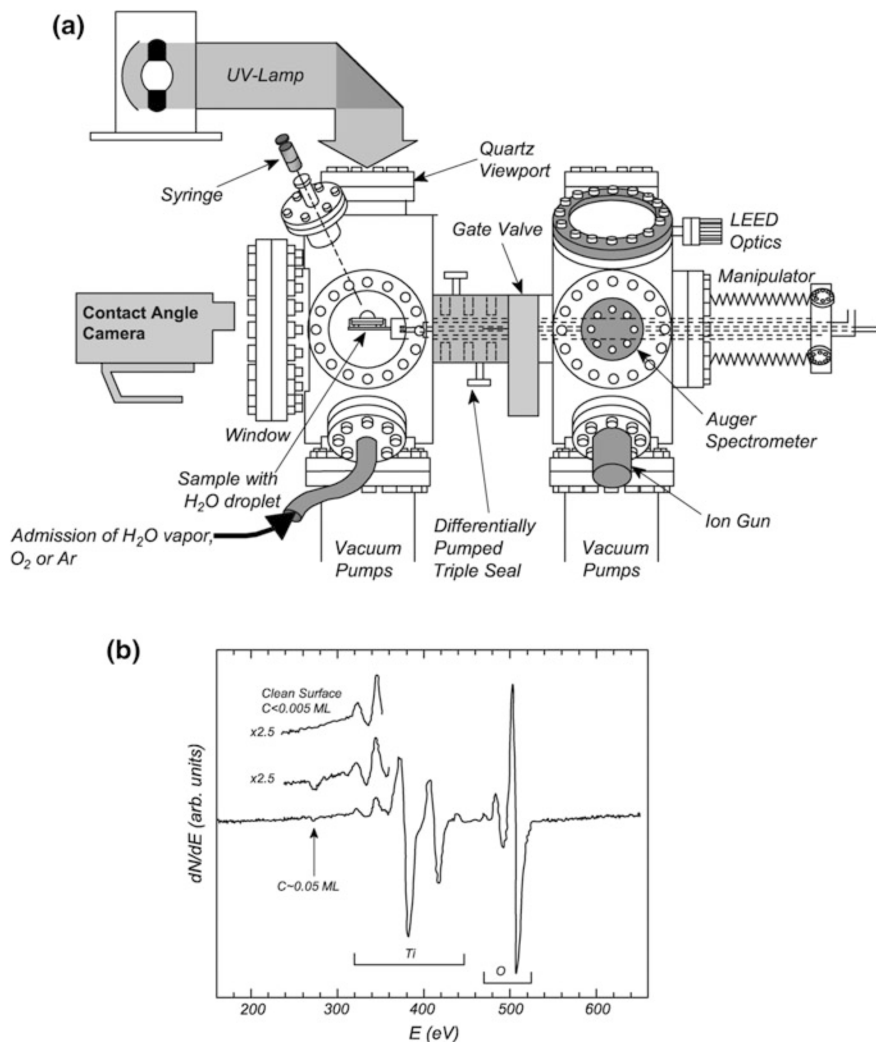

Fig. 43.1 Adding liquid to atomically clean surfaces. **a** Apparatus for wetting studies of ultrahigh-vacuum-prepared TiO_2 surfaces. **b** Proof of surface cleanliness by auger spectroscopy

Reference

1. T. Zubkov, D. Stahl, T.L. Thompson, D. Panayotov, O. Diwald, J.T. Yates Jr, J. Phys. Chem. B **109**, 15454 (2005)

Part VI
UHV Windows

Chapter 44
Spectroscopic Windows

44.1 Mounting Infrared Windows on UHV Systems

For the transmission of infrared radiation to and from an ultrahigh vacuum system for the purpose of carrying out infrared spectroscopic measurements, it is essential to employ windows that are highly transparent in the desired spectral region. Often, alkali halide crystals are used for this purpose. Alkali halides have a small linear thermal expansion coefficient relative to metals (about 0.1 of the metal) and thus undergo high stresses under elevated temperature conditions when rigid contact is made between the window material and the metal. Several window-mounting designs that place elastomer seals between the window and the metal have been reported [1–5]. In each of these designs the elastomer yields by means of shear strains during bakeout relieving the strain in the alkali halide window and thereby avoiding fracture. The common elastomer in all of the designs is Viton (see p. 108 for studies of gas diffusion through Viton), and this material will stand repeated bakeout at 200 °C. Two of the designs, shown in Fig. 44.1a, b, involve differential pumping to avoid leakage and/or diffusion of atmospheric gases through the Viton seals. The designs shown in Fig. 44.1c, d do not employ differential pumping. The design of Fig. 44.1c places an Al gasket between two Viton O-rings, eliminating leakage or diffusion through the outer O-ring. The design of Fig. 44.1d eliminates differential pumping or seals between the Viton gaskets.

Figure 44.1a is the original differentially pumped design by Hollins and Pritchard [1], and has proven effective in many different laboratories [2]. The NaCl or KBr window is retained in a stainless steel flange by an outer clamping flange. The inner space between the Viton O-rings is differentially pumped to pressures of the order of 0.1 Torr by a rotary pump, and it is reported that this pumping is essential for the best system pressure. On the ultrahigh vacuum side of the window, the O-ring is compressed outside of a loosely fitting retainer ring that keeps it from

© Springer International Publishing Switzerland 2015
J.T. Yates Jr., *Experimental Innovations in Surface Science*,
DOI 10.1007/978-3-319-17668-0_44

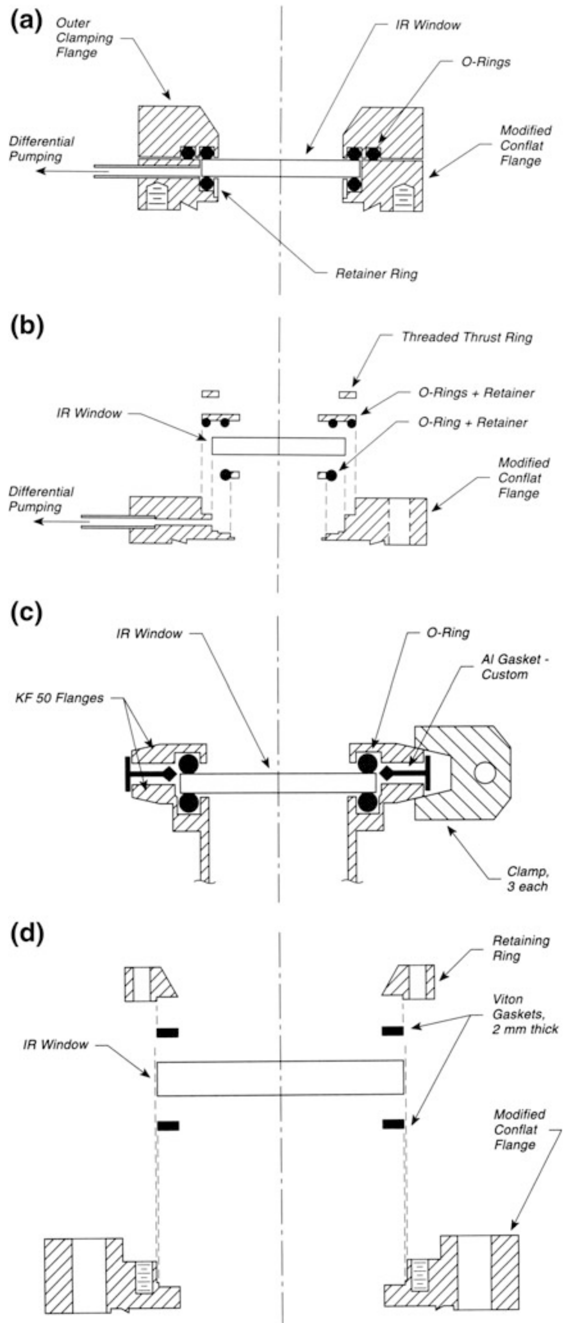

Fig. 44.1 Infrared spectroscopy Windows Mounting. **a** Original design—outer clamping flange. **b** Modified flange design—zero profile. **c** Modified design—no differential pumping. **d** Viton gasket design—no differential Pumping

moving inward and also avoids local trapping of gas introduced during assembly. If the differentially pumped space is let up to air before bakeout, the system pressure responds immediately; however, after bakeout, the O-ring seals mate more effectively to the metal and window, and only a small degradation of vacuum occurs if air is introduced into the differential volume. The indicated base pressure after bakeout is about 5×10^{-11} Torr.

Figure 44.1b shows a modification of the original design in which no extension beyond the system outer flange occurs (zero profile) [3]. Here, a modified Conflat flange, equipped with differential pumping, receives an O-ring plus a metal ring retainer to hold the O-ring in a circular geometry. An IR window is seated on this O-ring, and a double O-ring plus retainer ring is compressed on the outside of the window by a threaded thrust ring that screws into the flange opening. The inner O-ring (1/16-in.) of the pair seals against the window, while a slightly larger diameter 1/16-in. O-ring seals against a ledge in the flange. The atmospheric pressure forces the inner O-ring against the outer rim of its groove in the retainer ring. This device has been employed with KRS-5 and Csl window material, and is routinely baked at 100–110 °C. Once the seal is made, no effect of pumping out the differential space is observed, and pressures of the order of 5×10^{-11} Torr are reported.

Figure 44.1c shows a third method for sealing IR windows to an ultrahigh vacuum system [4]. The components are constructed of KF 50 flanges, which are commercially available. The outer section has its groove widened in order to hold the O-ring. The inner section has been modified by welding tubulation containing an O-ring groove into a hole cut into the KF 50 flange. A specially designed Al gasket is placed between the inner and outer flanges before assembly. An IR window is then pressed between the inner and outer O-ring seals and compression by three separate clamps results in gasket deformation, leading to a vacuum-tight seal between the two O-rings, and removing the need for differential pumping. Bakeout of the window was limited to 150 °C and the O-rings were observed not to stick to the sealing surfaces. The leak rate was estimated to be smaller than 1×10^{-12} Pa m^3 s^{-1}.

Figure 44.1d shows a double seal made of two flat Viton gaskets that seal against the IR window [5]. A special thrust ring is bolted onto a modified Conflat flange using six bolts and a small volume at the edge of the IR window is captured by both gaskets. Bake-out temperatures up to 150 °C have been used, and the base pressure is reported to be 2×10^{-10} mbar.

All four of these designs must be carefully made to avoid metal contact with the brittle window material upon compression of the O-ring seals.

A design similar to that of Fig. 44.1a, b has been reported [6] for sealing IR windows to a glass system.

For some applications, CaF_2 single crystal windows[1] [7–10] and MgO windows[2] [11, 12] may be attached to flanges for IR studies, and these seals require neither differential pumping nor O-ring-sealing technology. A review of this method may be found in [13], and an RF heating method for making these seals is given in [14]. Irtran 4 windows (ZnSe, polycrystalline) have been sealed to Voscovit 501 alloy using Pyroceram 7575 sealant [15].

The use of a lead gasket in conjunction with sealing a NaCl window to a stainless steel flange has been reported to be successful for ultrahigh vacuum applications. A specially shaped flange sealing surface and a series of conical washers acting as compression springs are involved to compensate for differential thermal expansion. These windows assemblies are bakable to 275 °C, and exhibit a leak plus outgas rate of $<3 \times 10^{-10}$ atm cm^3/s [16].

A simple method involving the sealing of Irtran 2 and Irtran 6 [17] into rotatable Conflat flanges has been given in [18]. Here, a silicone cement (Gevac [19]) is used to seal the window to the rotatable insert, and a ring of Al is placed between the outer flange and the insert in order to apply pressure directly over the underlying knife edge to prevent flexure of the flange during tightening. This design is superior to that of [20], which involves flexure of the nonrotatable flange employed.

44.2 Windows for Vacuum UV Transmission into Ultrahigh Vacuum Systems

The Viton O-ring technology for sealing windows such as KBr, CaF_2, and MgO to ultrahigh vacuum systems involve severe limitations on the bakeout temperatures that may be employed (see p. 521). Other sealing methods involving, for example, fused AgCl cements, are susceptible to leak formation upon exposure to ultraviolet light, and also are incompatible with many metals because of corrosion effects. A new method, which works for both CaF_2 and MgF_2 windows, is described below [21].

Figure 44.2 shows a stainless steel window flange welded to a tubulation that connects to the ultrahigh vacuum system. A 0.65-cm-wide step is provided to support the window, which is 1 mm smaller in diameter than the outer diameter of

---

[1] CaF_2 windows, sealed directly to Conflat flanges through a thin silver/silver chloride intermediate sealing assembly, may be obtained commercially from Harshaw Crystal and Electronic Products, Solon Technologies, 6801 Cochran Road, Solon, OH 44139. These windows are unsatisfactory for use with ultraviolet light because of the sensitivity of the AgCl cement to photodecomposition. A description of the sealing process is given in [7–10].

[2] MgO windows have been sealed to Pyrex glass sleeves using gold/silver chloride sealing with the Pyrex being sealed by a Kovar graded seal to stainless steel flanges. For a diagram of this method, see [11, 12].

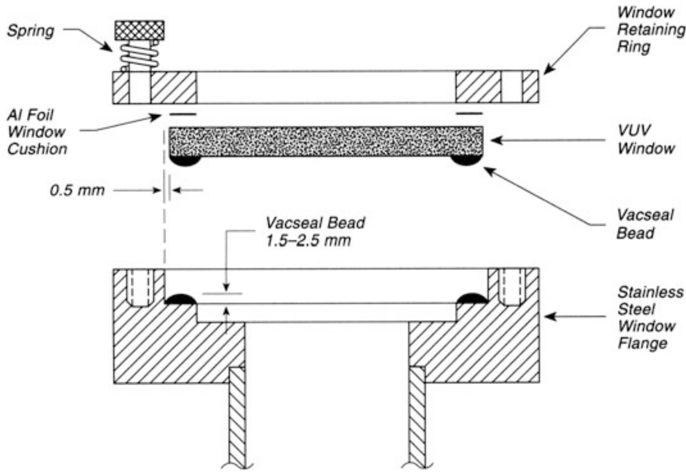

Fig. 44.2 Vacuum UV Window—UHV

the step. An outer window retaining ring presses the window against the seal, and the pressure at the seal can be adjusted using bolts which compress springs around the perimeter. A soft aluminum foil cushion is used between the retaining ring and the outer part of the window.

The vacuum seal is made by building up a Vacseal [22] bead on both the window and the step surface of the flange as shown in Fig. 44.2. The Vacseal bead is not considered to be a leak sealer between the window and the flange, but a deformable gasket material. The following recipe is recommended for the production of a high temperature seal which is He leak tight:

1. Clean and degrease the window and the flange.
2. Apply Vacseal as shown to the step and window surfaces as shown, keeping both surfaces horizontal. A 1.5-2.5-mm-thick bead is formed on each surface.
3. Place flange and window into an oven at room temperature and heat to 125 °C for 5 h. Then, following this precuring procedure, allow to cool to room temperature. There should be no bubbles in the beads.
4. Invert window and carefully place on the flange. The two beads should coalesce into a single seal about 2–2.5 mm in thickness without voids or bubbles.
5. Gently tighten the retainer ring but do not displace the Vacseal sealing material.
6. Cure at 150 °C for 15 h. Cool to room temperature and inspect for cracks or voids. The sealant should be amber in color. The spring-loaded bolts may be tightened slightly in this step.
7. Place the seal into the oven at 200 °C for 8 h. Cool and leak check.

If voids or cracks appear during the above procedure, start over. Methyl ethyl ketone (MEK) may be used to dissolve the cured Vacseal. Ethyl alcohol will not dissolve the seal and may be used to clean the window without causing a leak to form. One must be careful to not apply mechanical stresses to the cured window assembly. The seals are bakeable to 330–400 °C and are leak-tight for periods in excess of 6 months [21]. This sealing technique has been used on windows of 7.5-cm diameter [21]. The optical distortion of the widows is small, and thermal cycling may be carried out.

Another method, useful for mounting quartz windows on Al flanges, has been reported [23]. Here, an indium seal is employed and the window may be baked to 120 °C, which is the bakeout temperature needed for Al ultrahigh vacuum systems.

44.3 Construction of Be Windows for Ultrahigh Vacuum Use

Thin Be windows are often employed for transmission of X-rays into UHV systems. Although electron-beam-welded windows are commercially available [24], brazing onto stainless steel Conflat flanges is sometimes used [25, 26]. The procedure for doing this is reported here [26].

Figure 44.3a schematically shows the mechanical procedure employed for making an ultrahigh vacuum brazed seal to type 304 stainless steel. Beryllium foil, 0.25–0.50 mm thick, must be specified to be of vacuum quality [27]. Such foils may be used for spans up to 20 cm in length. The stainless steel surface is abraded with 250 grit sandpaper, and all sharp edges on the vacuum side are rounded. A brazed region 6–9 mm wide is employed. The Be foil is shaped in exterior dimensions by etching, using common fingernail polish to protect the regions to be preserved. The protective layer can later be removed using acetone solvent. The acid etching mixture is specified in Table 44.1. The braze material is 99.99 % Ag foil of 0.075-mm thickness, cut into a ring. The silver should be cleaned with silver polish or by means of a chemical bath specified in Table 44.2, in which metallic Al is used to reduce oxidized and sulfided Ag layers. The cleaned components are loaded into a stainless steel cylinder and the lower flange is tack welded to the cylinder. The stacked assembly is covered with quartz cloth and loaded with a weight as shown in Fig. 44.3a. The assembly is fired in a vacuum furnace according to the procedure outlined in Table 44.3.

He leak detection indicates no leaks at the sensitivity of the detector, 10^{-11} mbar L s^{-1}.

The transmission of X-rays through Be foils of different thicknesses is shown in Fig. 44.3b.

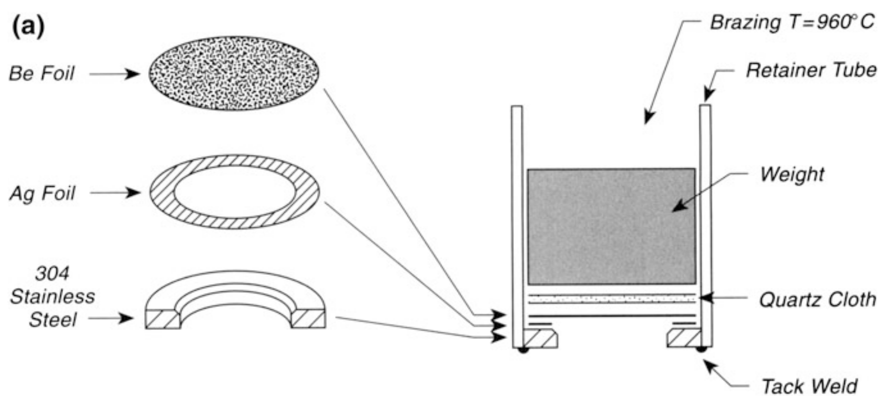

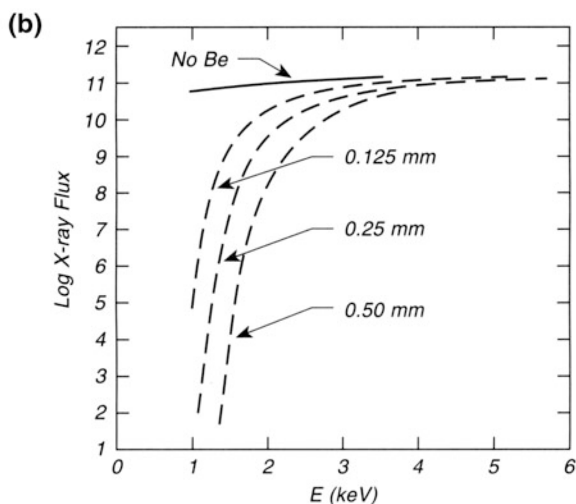

Fig. 44.3 Beryllium Window Fabrication. **a** Brazing Be windows to stainless steel. **b** X-ray transmission through Be

Table 44.1 Be etching solution (0.5 mm/min)

HNO_3	2 % by volume
H_2SO_4	2 % by volume
HF (aq)	2 % by volume
H_2O	Balance

Table 44.2 Silver cleaning

H_2O	1 L, boiling in beaker
$NaHCO_3$	15 cm^3 of powder
NaCl	15 cm^3 of powder
Add large piece of Al foil	
Add Ag ring—boil 1–2 min	
Remove Ag ring—clean in H_2O	

Table 44.3 Brazing procedure

Evacuate to 10^{-4} Torr
Preheat to 850 °C, 45 min
Stabilize at 900 °C, 25 min
Braze at 960 °C, 10 min
Cool
Vent furnace, leak check Be seal

44.4 Bakeable Aluminum Ultrahigh Vacuum Window

Low atomic number elements are often used for windows to transmit X-rays or high-energy particle beams. A very simple bakeable aluminum foil window mounting design is shown in Fig. 44.4 [28]. The Al foil window, cut into a circle, is mounted between two Cu gaskets that are used to make vacuum seals to two Conflat flanges. The window material is Alcoa 3003 aluminum with an H19 temper. The only special machining required is to put a radius, *R*, onto the inside edge of the Cu gasket placed on the vacuum side of the window. The radius *R* should equal the thickness of the window material, *T*.

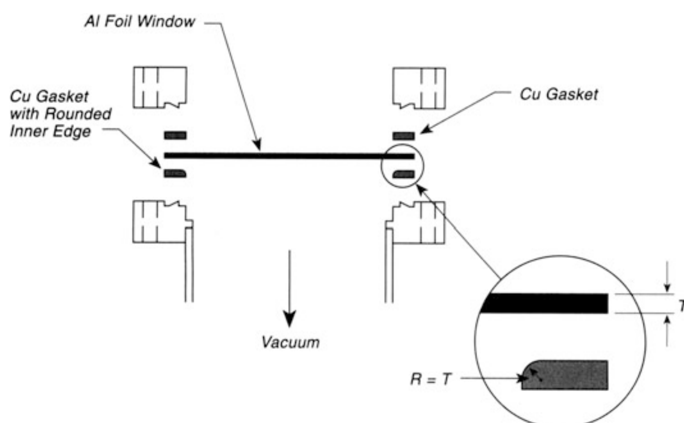

Fig. 44.4 Conflat Flange seal for Al foil window

Both 0.05- and 0.13-mm Al foil of 3.81-cm diameter and 10-cm diameter exhibit a leak rate for He of $<5 \times 10^{-10}$ std. $cm^3\ s^{-1}$. Foils of 0.13-mm thickness have been baked at 260 °C overnight with one side at atmospheric pressure without developing leaks; foils of 0.05-mm thickness have been baked at 180 °C overnight without developing leaks. This sealing technique has been shown to be unsuccessful with Be windows.

44.5 Metal Thin Foil Windows—Welding

Very thin metal foils may be welded to a stainless steel flange using electron beam welding in vacuum. However, there is danger of damaging the foil because of the lack of heat conduction away from the fusion region. A method [29] for successful welding is shown in Fig. 44.5.

The foil, which may be of Cu, Ni, or stainless steel, is several microns in thickness. It is placed on the flange and a backup washer of 304 stainless steel (0.05–0.13 mm thick, made by photoetching from sheet material) is placed on top of the foil, as shown. A hold-down fixture and clamps are used. The electron beam (120 kV, 250 μA, 0.13-mm diameter) is directed as shown in Fig. 44.5, and the foil is fused to the flange, after which the washer may be removed. A rotating table, with a velocity of 76 cm/min at the weld point is used.

If the foil initially contains wrinkles, it will flatten as a result of welding at the circumference. This is thought to be due to radial forces exerted at the circumference during cooling of the weld puddle.

44.6 Preparation of Large-Area Si Single Crystal Windows

The preparation of large windows of uniform thickness made of single crystal silicon could be useful in many ways, for example, in X-ray lithography, in energy-loss particle detectors, in Schottky diodes, and Josephson junctions, in ion beam analysis, and in in situ transmission electron microscopy. A variety of thinning methods have been used [30], and the description here is concerned with preparing such windows in a thickness range from 1000 to 20,000 Å [30]. The method has been demonstrated for crystals of (100), (111), and (110) orientation [30].

Figure 44.6a shows the basic sequence of steps employed. Device-grade silicon wafers with a high-quality surface finish (e.g., Syton polish), of either p-type or n-type with 1–10 Ω-cm resistivity are subjected to boron diffusion in a furnace operating at 1050 °C with a planar BN diffusion source and nitrogen gas as the carrier gas. Roughly speaking, a diffusion time of 15 min will give a B penetration

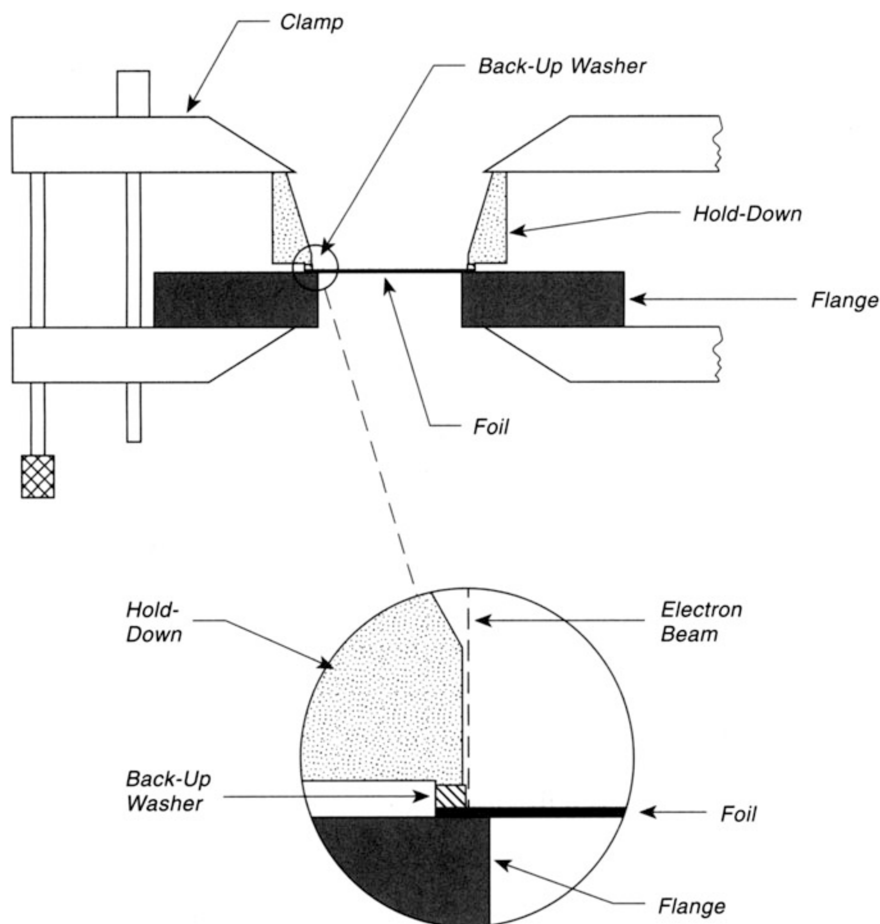

Fig. 44.5 Metal thin film window—welding

depth that is appropriate for making a window of 2000–2500-Å thickness. The diffusion time increases quadratically as the desired window thickness. The boron glass deposited on the surface is later removed by dipping into boiling HNO_3 (aq) followed by HF (aq), causing controlled crystal thinning. The silicon wafer is then cleaved into smaller pieces by a diamond scriber. Flat quartz discs are then used to support the wafer sections, using a paraffin dam around the perimeter of the Si sample. The wafer with the polished side down is then placed on the dam, and sealed on the edge by pressing down a piece of Teflon tape [31] onto the top of the wafer. The tape has a hole cut into it for the window etch. This protects the shielded regions of the wafer from etch solutions, as shown in Fig. 44.6b.

Two etch procedures are used. A preetch, which is fast, removes the majority of the silicon, at a rate of 25 μm/min. This consists of a mixture of the following

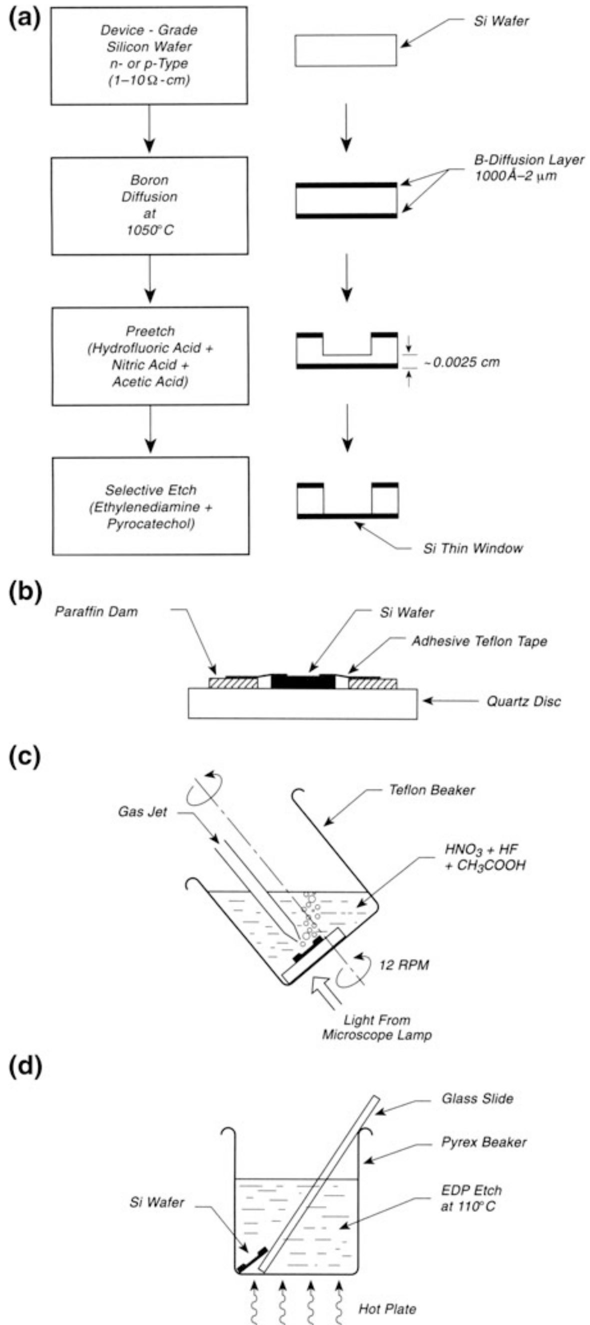

Fig. 44.6 Making thin Si windows by etching. **a** Sequence of steps—schematic. **b** Structure before preetch. **c** Preetch. **d** Selective etch

solutions: HF(aq) (48 % concentration); HNO_3 (70.4 % concentration), and glacial acetic acid, CH_3COOH (100 % concentration) in the volumetric ratio of 2:5:2. The etch rate can be increased or decreased by adjusting the HF concentration.

For the preetch procedure, as shown in Fig. 44.6c, the quartz-Si assembly is placed in a Teflon or polypropylene beaker (250 ml), which may be rotated and which contains a gas jet bubbler (plastic) supplying oxygen or nitrogen gas for agitation. The rotation of the beaker plus agitation by bubbling often gives uniform etching conditions, and also detaches bubbles that may form on the Si surface. Thinning to about 0.0025-cm thickness leads to a transparent film that will appear to be reddish by light transmission, indicating that the preetching should be immediately stopped. The Teflon tape is then carefully removed using a razor blade working from the outside, or using boiling trichloroethylene to dissolve the adhesive on the tape. Care must be taken not to disturb the fragile Si window.

The selective, slow etching procedure is done with a mixture of pyrocatechol ($C_6H_4(OH)_2$), ethylene diamine ($NH_2(CH_2)_2NH_2$)-(EDA), and water in the ratio 3 g:17 ml:8 ml. This etching solution does not attack Si if the B doping exceeds $7 \times 10^{19}/cm^3$. Etching rates for Si(111), Si(100), and Si(110) are found to be 3, 50, and 30 μm/h, respectively. The selective etch is carried out as shown in Fig. 44.6d, by leaning the quartz-Si assembly against a glass slide and operating at 110 °C. A curved glass cover (watch glass) should be placed over the boiling solution to condense the distillate and return it to the main etch solution. The EDA is the etching agent.

With Si(111) crystals, the EDA etching rate is slow, and lateral etching around the edge of the crystal will dominate, giving a noncircular boundary. This can be prevented by arranging in the preetch to have nonuniform etching by lowering the gas flow rate which leads to preferential etching in the middle of the window. Under these conditions, the EDA etching will start at the thinnest central region and will proceed laterally toward the edge, etching the non-(l 11) planes which exist there. The etching is stopped before the etching reaches the window boundary. This process leads to oval/round etched shapes which are mechanically more stable than etch configurations with sharp corners.

Modification of the highly doped windows is possible after etching. The B concentration may be lowered [32], and the window may probably be used as a seed to grow Si layers by CVD processes [30]. The thin Si windows can be made amorphous by ion implantation up to 1/3 of the thickness [30]. The window can be heated to 1000 °C without breaking. Layers of SiO_2 and metal silicides can also be grown at temperatures up to 850 °C [33, 34].

44.7 Strain-Free Optical Window Mounting

The effect of birefringence in strained optical windows can be a significant perturbation in ellipsometric measurements made inside of an ultrahigh vacuum system. This strain can be caused by the distortion of a flange during tightening of the

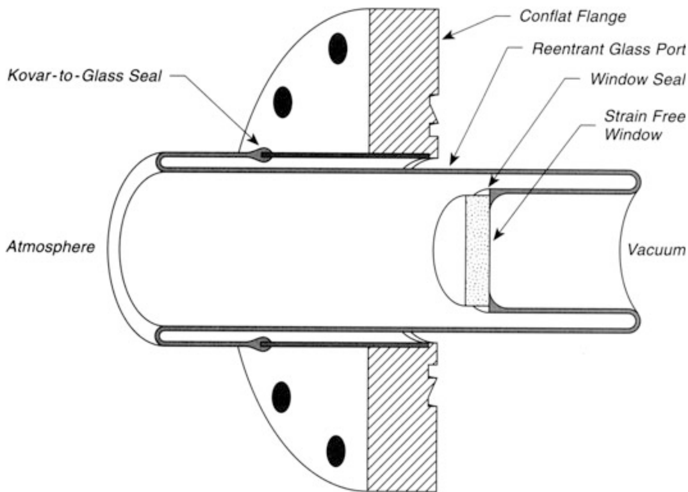

Fig. 44.7 Strain-free optical window mounting-section

mounting bolts that can be transmitted to the window. A re-entrant design such as that shown in Fig. 44.7 can eliminate this type of strain [35].

To construct this mounting, the glassblower will start with a Kovar-to-glass seal that has been welded into the flange. This seal first has glass matched to the thermal expansion coefficient of Kovar alloy, and then a graded seal leading to Pyrex on the outer end of the seal. The Pyrex is fashioned into an S-shaped reentrant seal, with the window mounting flared and polished flat to receive the window and its sealant. The length of glass in the S-section is sufficient to eliminate the transmission of stress to the window when the flange is tightened.

Glass-to-metal seals other than Kovar are sometimes used in these applications[3] [36, 37].

References

1. P. Hollins, J. Pritchard, J. Vac. Sci. Technol. **17**, 665 (1980) (this report also contains references to earlier window sealing methods)
2. Z. Xu, J.T. Yates Jr, J. Vac. Sci. Technol. **A8**, 3666 (1990)
3. R.G. Tobin, C. Chung, J.S. Luo, J. Vac. Sci. Technol. **A12**, 264 (1994)
4. C. Damerow, W. Erley, J. Vac. Sci. Technol. **A5**, 2974 (1987)
5. A. Bradshaw, private communication. The gaskets may be obtained from Busak and Sham-ban GmbH & Co., Handwerkstr. 5–7, 70565 Stuttgart, Germany
6. R. Raval, S. Munro, A. Coats, G. Beange, J. Vac. Sci. Technol. **A10**, 3593 (1992)
7. D.D. Berger, Rev. Sci. Instrum. **53**, 1619 (1982)

[3]Glass-to-metal sealing methods are described in [36, 37].

8. R.W. Roberts, J.F. Harrod, H.A. Poran, Rev. Sci. Instrum. **38**, 1105 (1967)
9. B. Caras, Rev. Sci. Instrum. **39**, 1441 (1968)
10. Y.-C. Chiu, Rev. Sci. Instrum. **41**, 639 (1970)
11. J.T. Yates Jr, D.A. King, Surf. Sci. **30**, 601 (1972)
12. R.W. Roberts, J.F. Harrod, H.A. Poran, Rev. Sci. Instrum. **38**, 1105 (1967)
13. Y.-C. Chiu, Rev. Sci. Instrum. **41**, 639 (1970)
14. M. Aslam, Rev. Sci. Instrum. **42**, 1892 (1971)
15. P.E. Wierenga, G.J. Mollenhorst, A.T.B. Wikkerink, Rev. Sci. Instrum. **49**, 408 (1978)
16. T.J. Manuccia, J.R. Peele, C.E. Geosling, Rev. Sci. Instrum. **52**, 1857 (1981)
17. Irtran optics are available from Eastman Kodak Co., 5/81 RC MC 02010, Rochester, NY 14650-2010
18. M. Kottke, R.G. Greenler, Rev. Sci. Instrum. **42**, 1235 (1971)
19. A silicon resin, type KL5, like that used in Ref. [14] can be obtained from Kurt J. Lesker Company, 1515 Worthington Avenue, Clairton, PA 15025-9911
20. L.J. Schkolnick, Rev. Sci. Instrum. **39**, 122 (1968)
21. C.H. Muller III, M.W. Barrett, D.D. Lowenthal, Rev. Sci. Instrum. **59**, 1425 (1988)
22. Vacseal is sold as a viscous liquid in 3 oz. bottles. Space Environment Laboratories, Box 1061, Boulder, CO 80306
23. H. Saeki, J. Ikeda, H. Ishimaru, Vacuum **39**, 563 (1989)
24. Electrofusion Corp., 34325 Ardenwood Blvd., Fremont, CA 94536
25. P.L. Hartman, Rev. Sci. Instrum. **57**, 2564 (1986)
26. G. Navrotski, J. Vac. Sci. Technol **A12**, 262 (1994)
27. Brush-Wellman, Elmore, OH 43416
28. J. Edgecumbe, Rev. Sci. Instrum. **37**, 1419 (1966)
29. P. Fowler, J.V. Minges, Rev. Sci. Instrum. **40**, 841 (1969)
30. N.W. Cheung, Rev. Sci. Instrum. **51**, 1212 (1980)
31. Obtained from Connecticut Hard Rubber Co., P.O. Box 2560, Meriden, CT 06450
32. C.L. Huang, T. van Duzer, IEEE Trans. Electron Devices **ED-23**, 579 (1976)
33. N.W. Cheung, L.C. Feldman, P.J. Silverman, I. Stensgaard, Appl. Phys. Lett. **35**, 859 (1979)
34. N.W. Cheung, M.-A. Nicolet, J.W. Mayer, in *Proceedings of the Symposium on Thin Film Phenomena- Interfaces and Interactions*, vol. 80.2, ed. by J.E.E. Baglin, J.M. Poare (The Electrochemical Society, Princeton, 1980)
35. Professor David Waldeck, Department of Chemistry, University of Pittsburgh, Pittsburgh, PA 15260 (private communication). The design originated with Professor C.B. Harris' group at the University of California, Berkeley, CA
36. E.L. Wheeler, *Scientific Glassblowing* (Wiley Interscience, NY, 1958), p. 157
37. W.E. Barr, V.J. Anhorn, *Scientific and Industrial Glass Blowing and Laboratory Techniques* (Instrument Publishing Co., Pittsburgh, 1947), p. 116

Chapter 45
Observation Windows

45.1 Shielded Observation Window

In ultrahigh vacuum evaporation of materials to produce thin films, the accumulation of deposits on observation windows can be detrimental to temperature measurements using an optical pyrometer. A calibration procedure using a constant temperature internal source has been described earlier (see p. 411), and this method will work for thin film deposits. However, a preferable procedure involves shuttering the window so that short observations can be made; then the window can be protected during most of the evaporation period. An internal rotatable shutter provides one way to do this, and the design shown in Fig. 45.1 shows another method [1].

A Pyrex window is sealed onto a glass-metal seal that involves either Kovar alloy or stainless steel tubing mated to the glass. The tubing is welded to a formed metal bellows connected to a flange as shown. A retention mechanism, held in place by a wing nut, allows the bellows to be bent so that the window is out of line of sight from the evaporation source during most of the evaporation period. For observation, the retention mechanism is removed and the window then aligns with the source. One should use formed bellows, not welded bellows, for constructing this device.

Alternatively, a disposable window, inserted into the chamber, can be used to protect observation windows [2].

© Springer International Publishing Switzerland 2015

J.T. Yates Jr., *Experimental Innovations in Surface Science*,
DOI 10.1007/978-3-319-17668-0_45

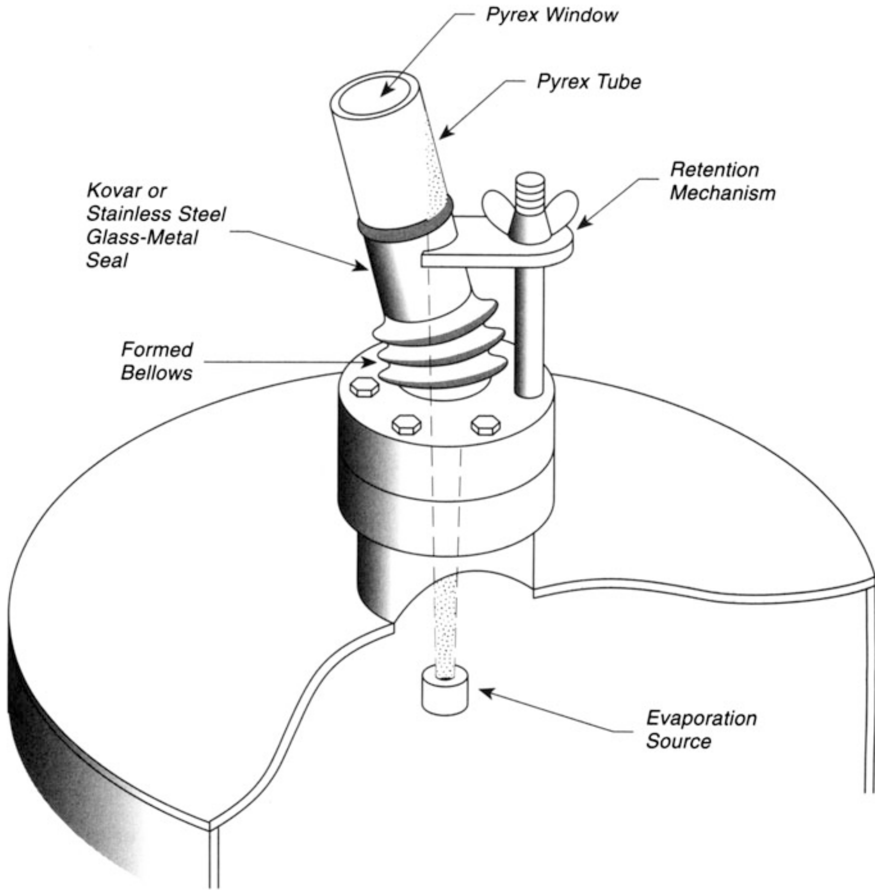

Fig. 45.1 Shielded observation window

45.2 Heated Internal Window for Prevention of Film Deposition

External windows used for observation of evaporation sources may be protected from film deposition internally by using a heated window to intercept the evaporating material. If the temperature of the internal window is sufficiently high to cause evaporation, optical measurements maybe made through the two windows without interference from film deposition.

Figure 45.2 shows schematically an arrangement for heating a quartz internal window to temperatures sufficiently high the prevent As deposition during MBE growth of GaAs, for example [3]. The inner quartz window is heated ohmically through a Ti film deposited around the edge of the quartz disk on both faces to a thickness of about 1.5 μm. The electrical resistance of the film, when contacted at

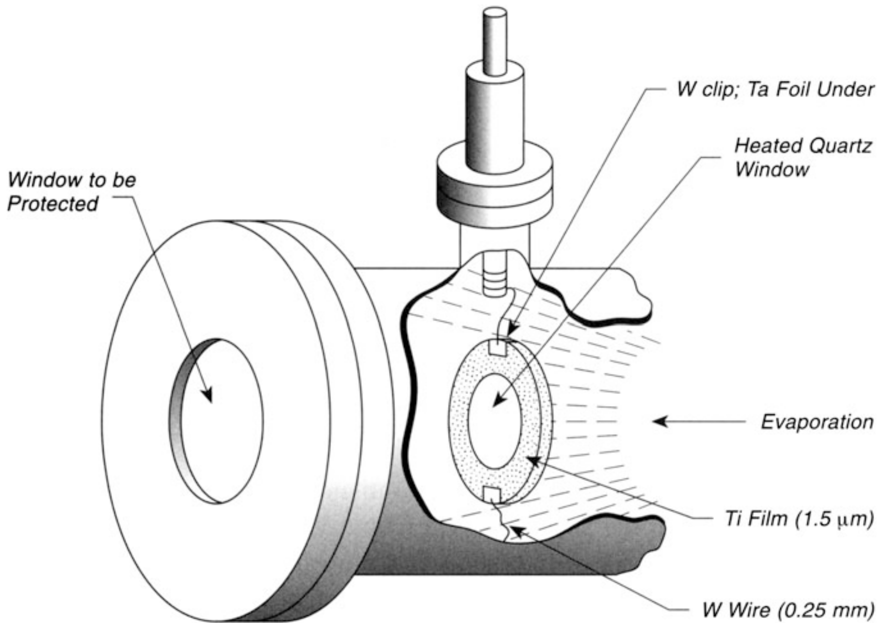

Fig. 45.2 Windows heated windows

points opposite each other, is about 2 Ω at room temperature and about 10 Ω at the operating temperature. Electrical contact to the Ti film is made using W clips made from 0.25-mm-diameter wire and protective Ta foil pads prevent abrasion of the Ti film by the W clips. Electrical heating at a power level of about 20 W maintains the temperature around the edge of the quartz window at 550–600 °C, and the temperature in the center is estimated to be 350–400 °C, based on a calculation for radial heat transfer [4]. It was reported that evaporation of over 1000 g of As over 1 year was carried out using one protective quartz window, and it was found that the optical transmission of the internal window only decreased by 5 %, corresponding to a temperature error of only 2° for pyrometry measurements at 600 °C. For GaAs deposition, it was found that the heated window did not introduce impurities into the films produced by molecular beam epitaxy.

Alternatively, the use of disposable internal glass windows has been employed successfully for this purpose [5].

45.3 UHV Glass Window Seal—Low Optical Distortion

Glass seals in Conflat flanges are generally made by a brazing technique that distorts the window, limiting its usage for certain optical studies. In addition, when optical coatings are applied to flange-sealed glass windows, the high temperature of

the coating process may further distort the window. A number of alternative window seals have been described [6–10] but often require considerable modification of the standard flanges.

In Fig. 45.3, a modified Conflat flange and gasket are employed to seal BK 7 [11] glass into an ultrahigh vacuum chamber [12]. The window material can range from high precision optical flats to window glass. These glass blanks can be optically coated if desired. A commercial OFHC Cu gasket is machined to have its own knife edge. The window seals the gasket by deforming the Cu knife edge. The dimensions shown are somewhat arbitrary. Pressure is applied to the window seal using a rotatable bolt ring which may be modified to increase the area which applies force to the window. Twenty sheets of 0.001-in.-thick Al foil are used as a cushion between the retaining ring and the glass. Alternatively either Cu or Pb wire may be used for the cushion.

The bolts are tightened uniformly and slowly until no leak is observed with a He leak detector. For a 4.5-in.-diameter flange, torques of about 3 ft. lb/bolt are employed for sealing. The technique forms seals with less than 10^{-10} atm cm^3 s^{-1}

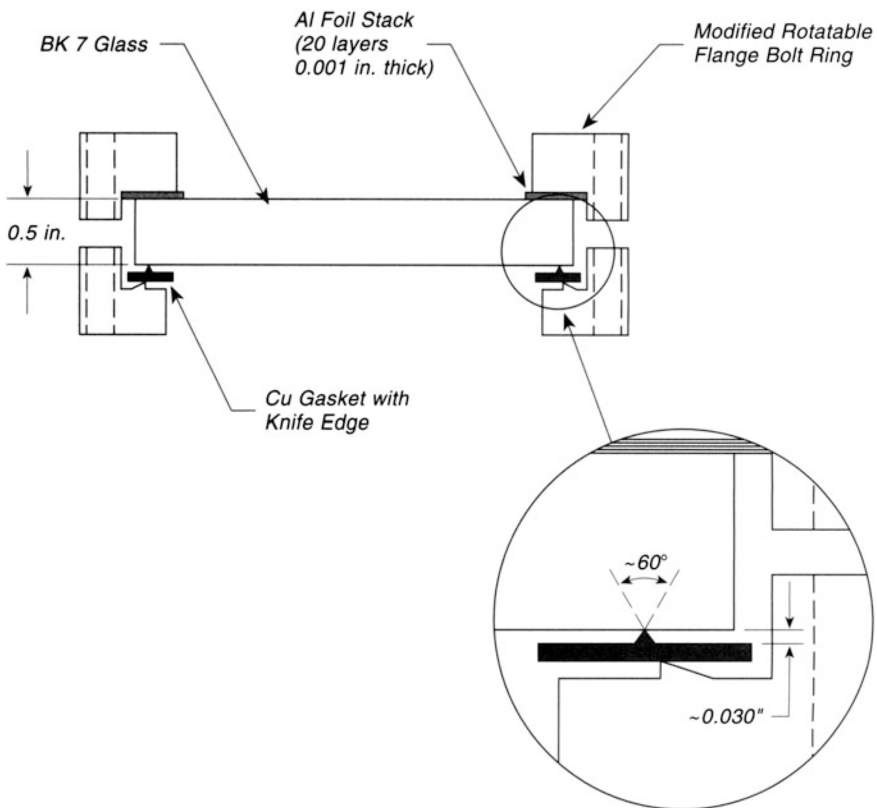

Fig. 45.3 Windows UHV glass window seal—low optical distortion

He leak rates. Baking to 250 °C may open leaks, and these can be eliminated by retightening the flange bolts. A test for stress-induced birefringence showed that only 0.01 % of 851-nm light passed through two crossed linear polarizers with a window mounted between them.

It is important to keep the Cu knife edge at least 0.1 in. from the edge of the glass to prevent breakage, and this may necessitate offsetting the Cu knife edge from the underlying stainless steel knife edge, as shown in Fig. 45.3 [12].

45.4 Zero-Length Window Assembly

Several methods for mounting windows on ultrahigh vacuum systems are available, but the method shown here is the most simple, requiring only standard components. As shown in Fig. 45.4, a window is retained between two Viton O-ring seals, using a rotatable outer flange without its normal insert [13]. The assembly is mounted onto a normal Conflat flange attached to the vacuum system. The inner seal may be

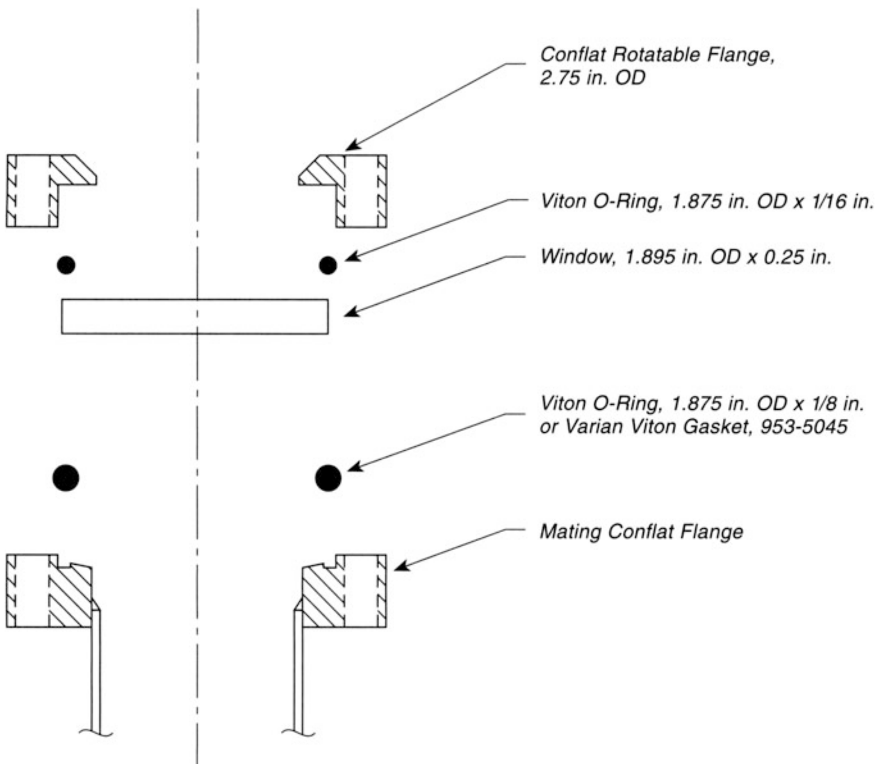

Fig. 45.4 Zero length window

either a O-ring or a special Viton gasket manufactured by Varian for use in place of copper gaskets. The upper bakeout temperature for the Viton is 150 °C. The general design is also applicable to larger flanges.

References

1. A. Chambers, J. Vac. Sci. Technol. **A7**, 259 (1989)
2. Dr. W.A. Egelhoff, National Institute of Standards and Technology, Gaithersburg, MD 20899-0001 (private communication)
3. D.E. Mars, J.N. Miller, J. Vac. Sci. Technol. **B7**, 682 (1989)
4. D.E. Mars, J.N. Miller, J. Vac. Sci. Technol. **B4**, 571 (1986)
5. Dr. W.F. Egelhoff, National Institute of Standards and Technology, Gaithersburg, MD 20899-0001 (private communication)
6. T.J. Manuccia, J.R. Peele, C.E. Geosling, Rev. Sci. Instrum. **52**, 1857 (1981)
7. C. Damerow, W. Erley, J. Vac. Sci. Technol. **A5**, 2974 (1987)
8. C.H. Muller III, M.W. Barrett, D.D. Lowenthal, Rev. Sci. Instrum. **59**, 1425 (1988)
9. H. Saeki, J. Ikeda, H. Ishimru, Vacuum **6**, 563 (1989)
10. M.T. Duignan, D.J. Garhardt, W.T. Whitney, Rev. Sci. Instrum. **60**, 3537 (1989)
11. BK 7 blanks are supplied by Newport Optical Glass Inc., Costa Mesa, CA, and by Glassfab Inc., P.O. Box 1880, Rochester, NY 14603
12. A. Noble, M. Kasevich, Rev. Sci. Instrum. **65**, 3042 (1994)
13. L.A. Biagi, J. Vac. Sci. Technol. **8**, 464 (1971)

Part VII
Surface Preparation Methods

Chapter 46
Cleaning Metal and Semiconductor Crystals—Examples

46.1 Surface Segregation and the Cleaning of Metal Single Crystals

The preparation of clean single crystals of the metals is fundamentally important in surface science research, since surface properties are often highly dependent on poisons and promoters that are present. It is commonly known that bulk impurities present in zone-refined single crystals at the ppm level can often segregate to the surface upon heating. Based on the phase diagram of two component alloys, Burton and Machlin [1] gave an easy method to predict whether a solute would segregate to the surface upon heating, as described below.

In Fig. 46.1a, two typical phase diagrams are shown for alloys, where the region between the solidus (dashed curve) and the liquidus (solid curve) is a two-phase region. In phase diagram (a), at some constant % solute, if the solid is warmed to the melting point on the dashed curve, a liquid depleted in solute will be formed. In contrast, in phase diagram (b), melting of the alloy solid will produce a liquid phase that is enriched in solute. The authors point out that many of those qualities that distinguish a liquid from a solid—namely, lower symmetry and lower coordination—also distinguish the surface from the bulk, so that the tendency for the liquid to be enriched or depleted of the solute on warming may apply also to the surface of an alloy. This expectation was confirmed for 16 alloys, where alloys with almost coincident liquidus and solidus curves were categorized as type (b′), and behaved as type (a) systems, and exhibited no surface segregation.

If methods can be found to stabilize a solute on a surface by reaction to form a stable compound or to remove the solute from the surface as a volatile species, then it is possible to deplete the bulk phase of this solute. This is commonly achieved by using oxygen as a reactant, producing a volatile oxide that enhances the concentration gradient of the solute, allowing more solute to diffuse to the surface where it is removed by reaction. In combination with sputtering, surface segregation is

© Springer International Publishing Switzerland 2015

J.T. Yates Jr., *Experimental Innovations in Surface Science*,
DOI 10.1007/978-3-319-17668-0_46

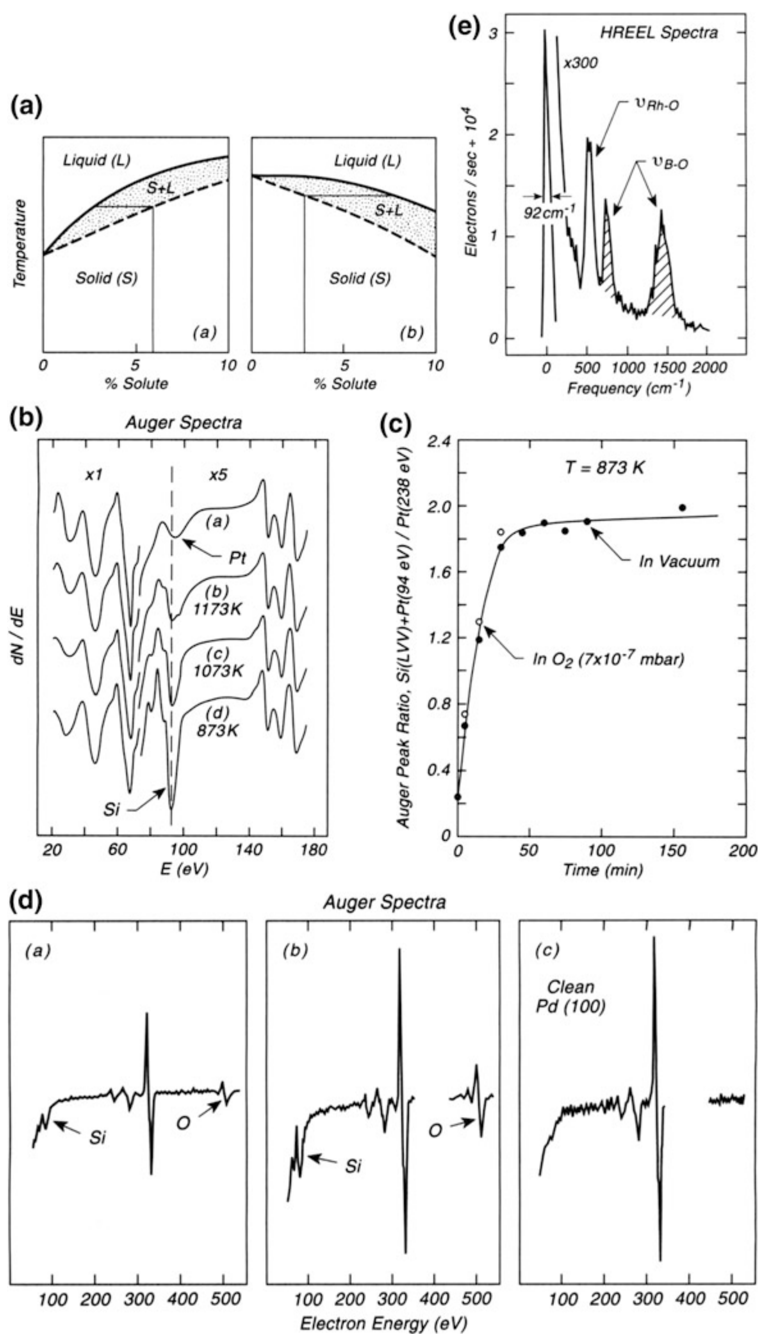

Fig. 46.1 Surface segregation and cleaning of metal surfaces chemically. **a** Typical phase diagram for alloys. **b** Si segregation on Pt. **c** Si segregation in vacuum and in O_2 on Pt. **d** Silicon segregation on Pd. **e** B-O vibrational modes on Rh(111) after reaction at 970 K in O_2

effective in purifying the bulk (or at least the near surface region) so that bulk impurities are not available at the surface during an experiment.

A description of the surface cleaning methods employed for a total of 74 elements has been given in a very useful review by Musket et al. [2].

Several examples of the use of chemical methods for cleaning surfaces in this manner are presented below to illustrate the general principles involved and the types of measurements used to follow the cleaning process.

Platinum

Elements such as Si, Ca, Al, S, C, and P are often found in zone-refined Pt crystals, and an excellent review of and insight into this problem has been provided in the work of Bonzel et al. [3–5][1]. Si segregates strongly to the surface of Pt, but this was not appreciated until the early 1980s because the prominent Si (92 eV) feature is almost coincident with a Pt(94 eV) feature. This may be seen in Auger spectra in Fig. 46.1b, where heavy Si segregation is observed under equilibrium conditions at 873 K, and less heavy segregation is observed at higher temperatures. Spectrum (a) is of the freshly sputtered surface (Si free) and the small Pt Auger feature at about 94 eV is evident. Studies of the effect of O_2 on the rate of Si segregation to the surface show that at 10^{-7} mbar and at Pt temperatures of 873 K, no enhancement of the Si segregation occurs in the presence of O_2, as shown in Fig. 46.1c. Studies at higher temperature [3–5] indicate that bulk SiO_2 will form for $T > 1000$ K. It is pointed out that the Auger intensity of the O(KLL) feature, associated with Si atoms, is the best monitor of the amount of Si present after oxidation. Platinum oxides are thermodynamically unstable in vacuum at the temperatures discussed here. The properties of the oxide on silicon-contaminated Pt first led investigators to postulate the presence of a "platinum oxide" with unexpected thermodynamic stability on Pt surfaces [3–5].

Palladium

Similar results to those found for Pt are reported for Pd [6]. Here, too, Si-stabilized oxides are formed under conditions where PdO would be thermodynamically unstable, as shown in Fig. 46.1d. The oxidation occurred at 1073–1273 K in 10^{-6} mbar O_2 for spectra (a) and (b). Argon ion sputtering was used prior to acquiring spectrum (c).

Rhodium

A common impurity in single crystal Rh is boron, which is difficult to remove by sputtering [7, 8]. It has been found that heavy oxidation is effective in removing boron by the formation of a boron oxide species that is best detected by high-resolution electron spectroscopy (HREELS) [9]. The interference between Rh and B Auger spectral features makes Auger spectroscopy impractical for seeing small amounts of B on Rh. Figure 46.1e shows an HREELS spectrum of the B-O vibrational modes obtained when Auger spectroscopy was ineffective in detecting B.

---

[1]Earlier important studies of this problem include [4].

46.2 Chemical Method to Measure and Remove Carbon from Pd

The high thermodynamic energy of NO compared to O_2 may be used to oxidize impurities from single crystal surfaces as well as from the walls of ultrahigh vacuum systems as was described on p. 87.

In a special case, involving carbon impurities purposely introduced to a Pd single crystal, this effect was employed not only to clean the Pd crystal of carbon but also to provide a rather sensitive method for showing that carbon had been removed [10]. Carbon on Pd is difficult to measure by Auger spectroscopy because of the overlap of the C(KLL) Auger line with the Pd(MNN) line. Figure 46.2a shows a series of Auger spectra for increasing exposure to C_2H_4 using quantitative exposure conditions. A careful examination of the Auger spectra shows that small changes occur, and a ratio measurement shown in Fig. 46.2b indicates that the (C + Pd)/Pd Auger ratio does increase slightly following C_2H_4 exposure, but the poor signal-to-noise ratio on this number makes a quantitative measurement impossible.

The carbon may be quantitatively reacted away using NO as an oxidizing agent in much the same fashion as was done by others using O_2 [11] to oxidize the C as well as to measure the presence of C using measurements of the CO and CO_2 formation in thermal desorption. In the case of the NO being employed as an oxidizing agent, using isotopically labeled ^{15}NO permits the discrimination of $^{15}N_2$ (30 amu) product from CO (28 amu product) and hence to supply a quantitative basis for measuring the coverage of carbon from the $^{15}N_2$ formation. Figure 46.2c shows the thermal desorption spectra for 30 amu species produced after treating carbon-covered Pd with ^{15}NO. Successive experiments were done with higher levels of carbon, deposited by quantitative doses of C_2H_4. The cross-hatched portion of the thermal desorption spectra is due to $^{15}N_2$ from the reaction 2C (a) + 2NO(a) → 2CO + N_2. The sensitivity of the method for low carbon levels may be judged by the fact that C_2H_4 exposures much less that 1×10^{14} cm^{-2} give measurable $^{15}N_2$ yields in the high-temperature peak. The low-temperature desorption peak, also from $^{15}N_2$, originates from the normal dissociation of NO on the Pd surface.

Using this measurement method for determining the presence of small amounts of carbon on Pd, a cleaning procedure involving exposure to 3×10^{16} NO cm^{-2} at 510 K followed by heating in vacuum to 850 K was devised. This method gave reproducibly clean Pd, which yielded the three overlapping $^{15}N_2$ desorption curves shown at the bottom of Fig. 46.2c for three sequential ^{15}NO adsorption experiments on the carbon-free crystal.

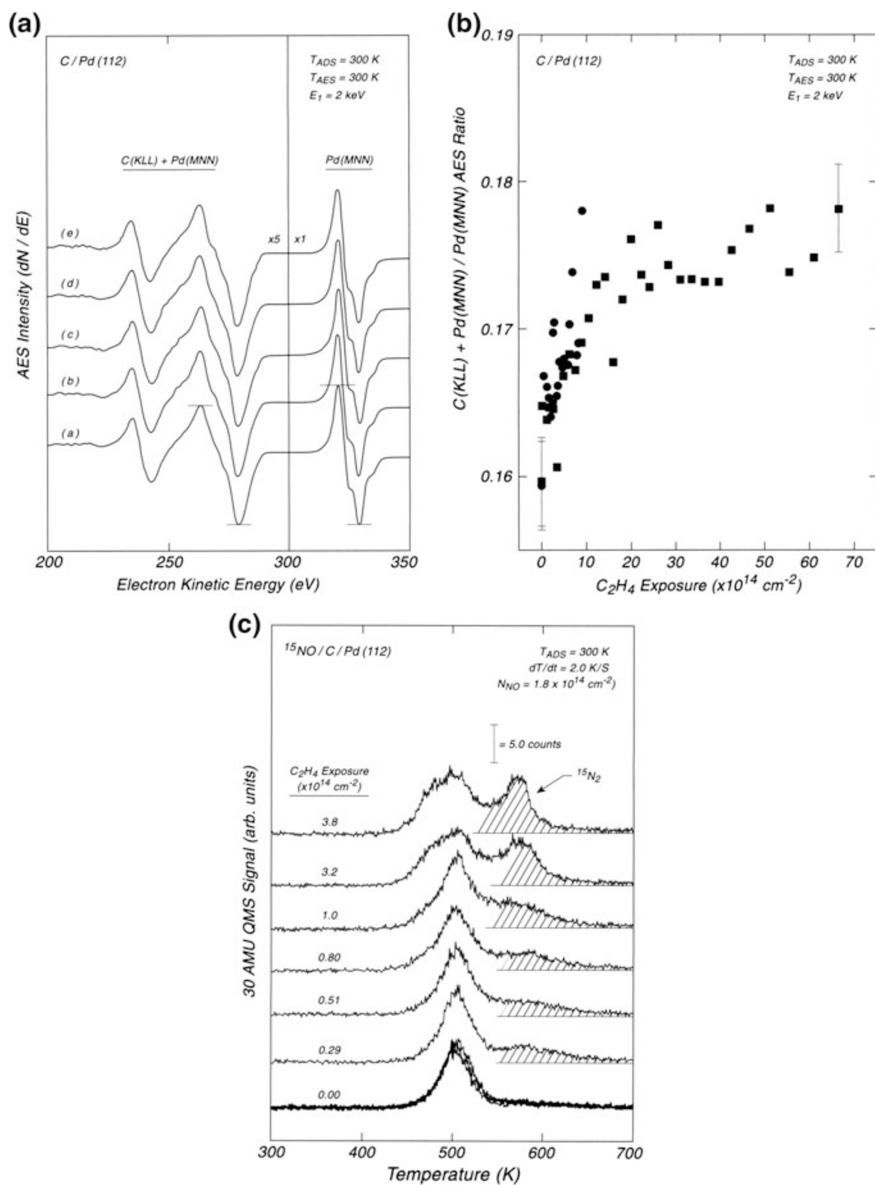

Fig. 46.2 Chemical method to measure and remove C from Pd. **a** Pd auger spectra for increasing C coverage. **b** Auger ratio for increasing C coverage. **c** 2C + 2 $^{15}NO(a) \rightarrow {}^{15}N_2 + 2CO$

46.3 Surface Cleaning Procedures—Silicon

The production of metal-free silicon surfaces is a common starting point in much surface science work dealing with this element. The metals nickel and iron are common impurities originating from the vacuum system environment owing to various types of sources. Their presence causes significant reconstruction effects on Si(100) [12–14] and on Si(111) [12, 15, 16]. The STM permits the observation of reconstruction effects at high sensitivity [17], and recently STM has been used to compare the statistical distribution of defects with the measured Auger intensity from impurity Ni in the surface region [17]. The transport of Ni through the silicon lattice is extremely rapid [18], causing Ni contamination effects to spread throughout the crystal from their origin during ordinary thermal processing.

The fundamental unit of the reconstructed Si(100) surface owing to very low levels of Ni contamination is the "split-off-dimer" structure, shown in Fig. 46.3a. Four silicon dimer sites are affected and produce a characteristic STM image of two neighboring dark dimer sites, a neighbor bright dimer site, and a neighbor dark dimer site. From detailed Auger spectroscopy studies, about one-half of the detected Ni atoms are responsible for the split-off dimer sites [17]. As the concentration of impurity Ni increases, the split-off dimer structures organize themselves to produce vacancy channels having ($2 \times n$) overlayer periodicities. Ultimately, high corrugation levels of Si(100) with 50-Å roughness are produced. Figure 46.3b shows the correlation between the statistical counting of split-off-dimer structures and other methods of surface analysis. A linear relationship is observed between the density of the defects and the surface analysis for Ni.

The origin of the Ni impurities may be from several sources listed below:

1. Ni bulk contamination in Ta used in contact with silicon: The bulk analysis of high-purity Ta may give 3 ppm of Ni. The typical amount of Ta in the vicinity of the Si could therefore supply hundreds of monolayers of Ni to the Si.
2. Ni surface contamination of Ta following machining: The transfer of Ni from alloy tools used to manufacture Ta parts may be a source of significant Ni levels.
3. Ni contamination from thermocouple alloys: Alloys such as chromel-alumel (type K) are about 90 % Ni. At temperatures of 1450–1500 K, the vapor pressure of Ni will be in the 10^{-4}–10^{-5} Torr range, and even protection of the Si by Ta foil envelopes surrounding the thermocouple junction will not prevent Ni contamination from this source. It is recommended that Ta-protected tungsten/rhenium thermocouples be used.
4. Metals deposited by sputtering. Almost all workers using the STM as a detector of surface cleanliness and structure on Si(100) have discarded the use of ion bombardment as a way of cleaning the surface. Metal atoms produced from sputtering effects inside the ion gun, or from sputtering of metal structures in the neighborhood of the Si sample, are probably transferred to the Si surface.

A simple method that seems to eliminate Ni contamination in Ta components consists of boiling for 5–10 min in concentrated HC1 (<5 ppb Ni), and then boiling

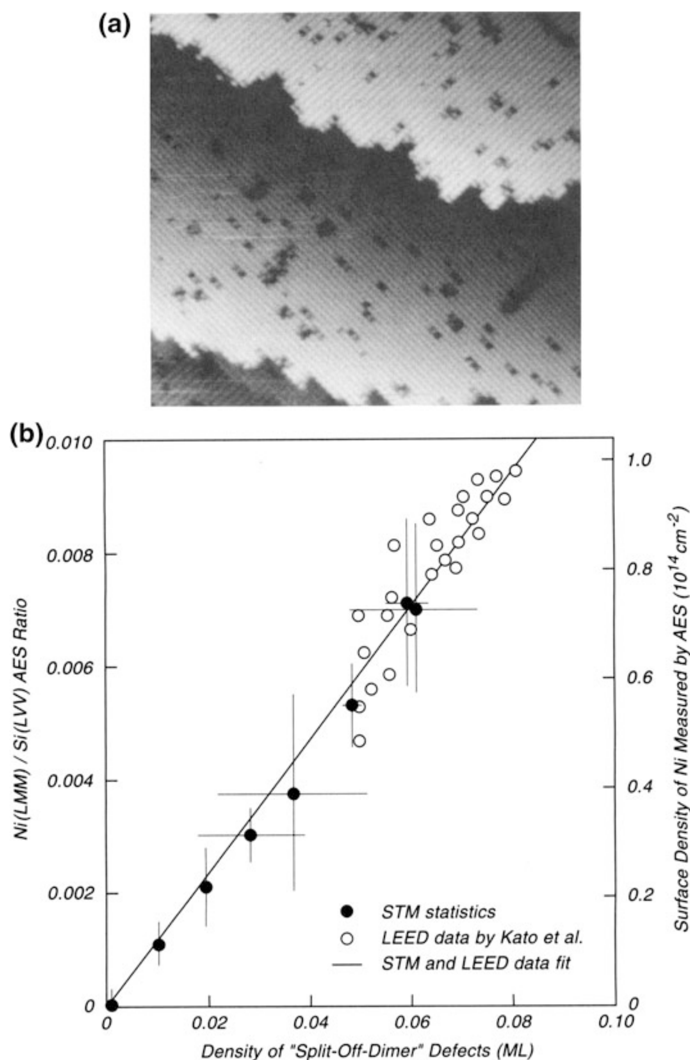

Fig. 46.3 Surface cleaning procedure—Silicon. **a** STM image of Si(100) showing "Split-Off-Dimer" defects. **b** Correlation of STM defect and AES and LEED measurements

in deionized water. This procedure has been shown to reduce the Ni concentration in the Si surface to below the Auger sensitivity (signal to noise = 0.0003) level, giving Si crystals that are long-lived and almost Ni-free as measured by STM [17].

The cleaning procedure for Si(100) wafer strips is then to heat to 900–950 K overnight to outgas and then to anneal to 1420–1450 K for 30–60 s, cool quickly to 1000–1100 K, hold at temperature to 120 s, and finally cool down to 300 K at a slow rate of 2 K/s. Alternating current heating is used.

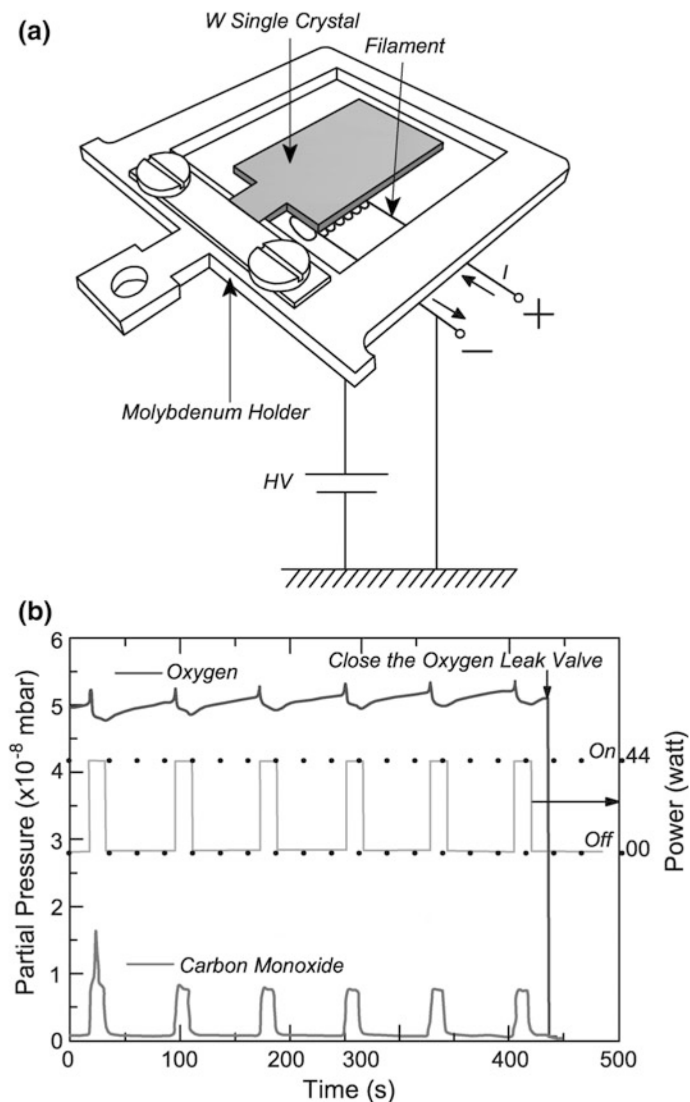

Fig. 46.4 Preparation of clean tungsten single crystals. **a** Sample holder and flashing geometry. **b** Thermal desorption spectra of W(110) crystal behavior at 6×10^{-8} mbar O_2 pressure. Both CO and O_2 partial pressures are monitored

46.4 Preparation of Atomically Clean Tungsten Single Crystals

Tungsten and some of the other refractory transition metals are easily contaminated in ultrahigh vacuum as a result of hydrocarbon adsorption and decomposition to make a metal carbide film. This film can be oxidized in vacuum to make a very stable molecule, CO, which desorbs, leaving pure clean metal behind. The surface cleaning procedure occurs in two steps: (1). Cycles of low power flashes ($T \sim 1200$ K) in $P(O_2) = 6 \times 10^{-8}$ mbar; and (2). a single high desorption pressure flash ($T = 2200$ K) in vacuum to remove the oxide layer produced in the first stage of treatment. The loss of oxide at high pressure leaves a clean surface. In the case of tungsten wire, the loss of tungsten oxides has been carefully studied [19–21]. Figure 46.4a shows a typical W single crystal held in a molybdenum holder and a spiral W heater filament. Figure 46.4b shows the typical oxygen, carbon monoxide and power in the cleaning of the carbon from the crystal surface. It may be seen in Fig. 46.4b that CO desorption reaches a constant behavior during heating more than once. The first CO desorption differs from later stages, indicating that most CO is lost in the first cycle under oxygen [22].

References

1. J.J. Burton, E.S. Machlin, Phys. Rev. Lett. **37**, 1433 (1976)
2. R.G. Musket, W. McLean, C.A. Colmenares, D.M. Makowiecki, W.J. Siekhaus, Appl. Surf. Sci. **10**, 143 (1982)
3. H.P. Bonzel, A.M. Franken, G. Pirug, Surf. Sci. **104**, 625 (1981)
4. M.J. Cardillo, G.E. Becker, Surf. Sci. **99**, 269 (1980)
5. H. Niehus, G. Comsa, Surf. Sci. **102**, L14 (1981)
6. S.D. Bader, L. Richter, T.W. Orent, Surf. Sci. **115**, 501 (1982)
7. D.G. Castner, G.A. Somorjai, Appl. Surf. Sci. **6**, 29 (1980)
8. P.A. Thiel, J.T. Yates Jr, W.H. Weinberg, Surf. Sci. **82**, 22 (1979)
9. S. Semancik, G.L. Haller, J.T. Yates Jr, Appl. Surf. Sci. **10**, 546 (1982)
10. R.D. Ramsier, K.-W. Lee, J.T. Yates Jr, J. Vac. Sci. Technol. **A13**, 188 (1995)
11. H. Conrad, G. Ertl, J. Küppers, E.E. Latta, Surf. Sci. **65**, 235 (1977); ibid 245 (1977)
12. K. Kato, T. Ide, S. Miura, A. Tamura, T. Ichinokawa, Surf. Sci. **194**, L87 (1988)
13. H. Niehus, U.K. Kohler, M. Copel, J.E. Demuth, J. Microscopy **152**, 735 (1988)
14. X.F. Lin, K.J. Wan, J. Nogami, Phys. Rev. B **47**, 13491 (1993)
15. A.E. Dolbak, B.Z. Olshanetsky, S.I. Stenin, S.A. Teys, T.A. Gavrilova, Surf. Sci. **218**, 37 (1989)
16. R.M. Wallace, C.C. Cheng, P.A. Taylor, W.J. Choyke, J.T. Yates Jr, Appl. Surf. Sci. **45**, 201 (1990)
17. V. Ukrainsev, J.T. Yates Jr, Surf. Sci. **346**, 31 (1996)
18. E.R. Weber, N. Wiehl, Mat. Res. Soc. Symp. Proc. **14**, 19 (1983)
19. D.A. King, T.E. Madey, J.T. Yates Jr, J. Chem. Phys. **55**, 3236 (1971)
20. D.A. King, T.E. Madey, J.T. Yates Jr, J. Chem. Phys. **55**, 3247 (1971)
21. D.A. King, T.E. Madey, J.T. Yates Jr, J. Chem. Soc. Faraday Trans. **1**(68), 1347 (1972)
22. Kh Zakeri, T.R.F. Peixoto, Y. Zhang, J. Prokop, J. Kirschner, Surf. Sci. **604**, L1 (2010)

Part VIII
High-Area Solids

Chapter 47
Infrared Cells

47.1 Infrared Cell for Adsorption Studies on Supported Catalysts

The study of supported catalysts using transmission IR spectroscopy is a well-established technique employed widely throughout the field. Over 50 cell designs have been devised and reported in the literature [1]. The cell described in Fig. 47.1 has special features of importance for some types of applications, especially where a simple design for use at cryogenic temperatures is desired. A unique feature of this cell is the capability to study the adsorption of gases on the support and on the support plus the active catalytic material in the same experiments [2].

The cell consists of two 2.75-in. diameter Conflat flanges containing IR transparent (down to 1000 cm^{-1}) windows made of CaF_2 single crystals, and joined to the flange through semiflexible Ag mounting rings, using fused AgCl cement. These window flanges are sealed with Cu gaskets to a double-sided central flange that contains the support for the sample. The sample support is a Cu ring (OFHC Cu) that is brazed with Ag braze (no Cd alloy) to a thin stainless steel tube that exits through two thin-walled support tubes at the edge of the central flange. A mixture of liquid nitrogen and nitrogen gas is passed through the supporting tubes to cool the sample to near 100 K, and the temperature of the support ring is monitored by a thermocouple entering the central flange at another position. Temperature control may be achieved in the low-temperature region by control of the flow rate of the refrigerant, and at high temperatures electrical heating by an external resistive heater may be controlled. The cell is evacuated through a stainless steel valve that leads to the gas-handling and vacuum system. Temperature gradients across the CaF_2 sample holding disk (to be described below) that is mounted in the Cu ring are negligible, as shown by experiments with multiple thermocouples cemented to the CaF_2 plate [3].

The sample of a high area oxide support containing metal particles is prepared by spraying a slurry of the support material and a salt of the metal onto a CaF_2

© Springer International Publishing Switzerland 2015

J.T. Yates Jr., *Experimental Innovations in Surface Science*,
DOI 10.1007/978-3-319-17668-0_47

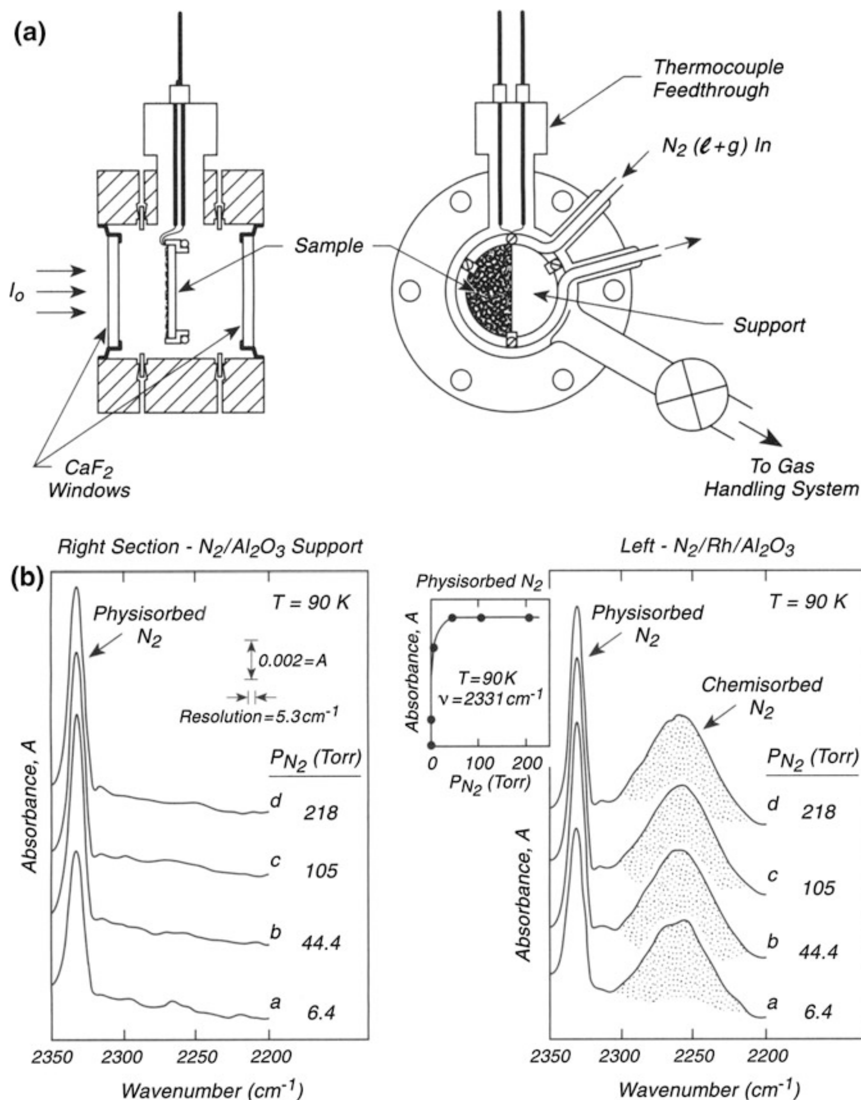

Fig. 47.1 IR cell for adsorption studies on supported catalysts. **a** IR cell. **b**. Transmission IR spectra

single crystal disk held on a hot plate at about 70 °C. Here a 9:1 acetone:water solution is the solvent for the metal salt and a carrier for the oxide support. Flash evaporation of the solvent occurs during the spraying, and the oxide sticks to the disk and retains the ions from the salt. In some cases it will be necessary to lightly abrade the CaF_2 disk to permit better adhesion. The disk is masked so that one-half is sprayed with the catalyst/support mixture while the other half is sprayed with the

support alone. This permits adsorption processes on the support to be studied independently under the identical conditions present at the supported catalyst. Typical deposited surface densities are at the 0.01 g/cm^2 level. The disk containing the adjacent sprayed sections is transferred to the cell and clipped into the Cu ring, and the cell is assembled, using annealed Cu gaskets (see p. 99) and gently tightening alternate bolts a little at a time to prevent excessive flexure of the window flanges and fracture of the CaF_2 windows. The catalyst is then prepared for study by appropriate heating and reduction conditions using hydrogen, and heating the cell in a small oven that surrounds it. The CaF_2 windows should be carefully protected against thermal shock in use.

After reduction and evacuation to remove hydrogen, the sample is ready for chemisorption experiments. Figure 47.1b shows an example of the chemisorption of N_2 on Rh metal that is supported on $A1_2O_3$. At the temperature of the experiment, N_2 is also physically adsorbed on the $A1_2O_3$. The spectrum on the left was measured on the right-hand side of the sample and shows only physisorbed N_2. The spectrum on the right, measured on the left-hand side of the cell, shows the presence of both physisorbed N_2 on the $A1_2O_3$ support and chemisorbed N_2 on the metallic Rh catalyst surface. The cell is translated from side to side inside the spectrometer using a simple linear bearing track arrangement in order to measure each half of the sample.

This cell has been used extensively where a simple design was satisfactory. A more complex design, having additional capabilities, is shown in [1] and discussed on p. 557. The CaF_2 windows mounted in Conflat flanges are commercially available [4].

47.2 Wide-Temperature-Range IR Cell for High-Area Solids

Over 50 cell designs for use in the study of high area surfaces by infrared spectroscopy have been reported since 1967, as reviewed in [1]. The cell shown in Fig. 47.2 possesses unique features, which, in combination, are not found in other designs reported. These features include ultrahigh vacuum operation, wide temperature range extending from about 100 K to above 1500 K without use of an external furnace, accurate temperature control to 1 K, linear temperature programmability up to 8 K/s, and very rapid sample cooling rates [1].

The cell design in Fig. 47.2a comprises a six-way stainless cube to which windows and gas delivery and pumping tubes may be attached by means of 2.75-in. Conflat flanges. The sample itself is held on a tungsten grid that is clamped between high thermal conductivity Ni clamps [5], mounted on an electrical feedthrough that exits from the bottom of a reentrant Dewar made of stainless steel. The feedthrough also contains matched thermocouple leads that are attached to a thermocouple welded to the top center of the grid. The entire assembly is oriented using a

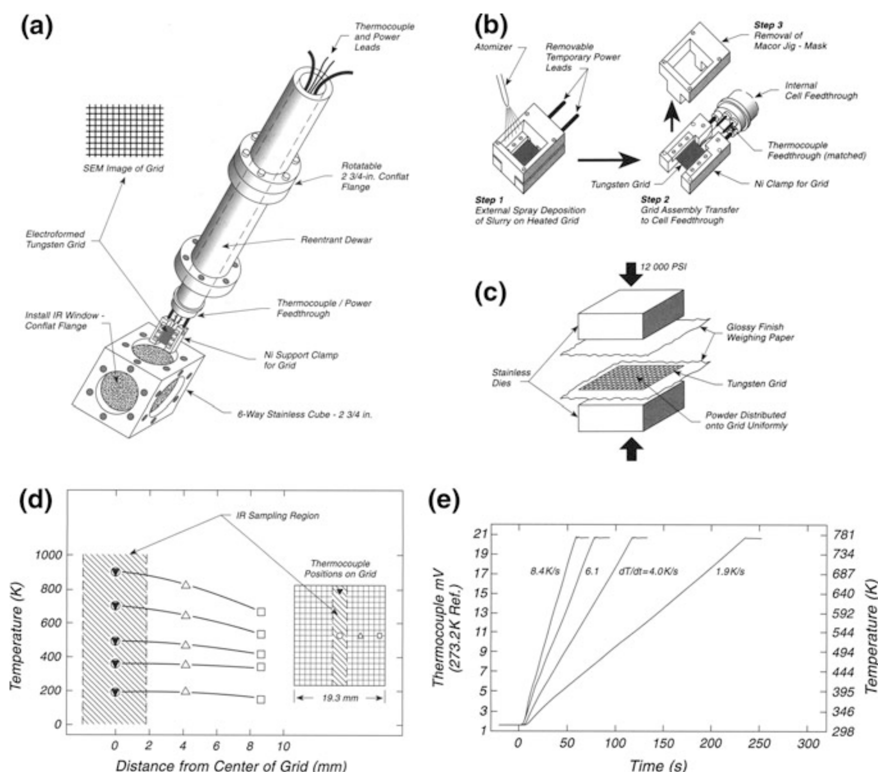

Fig. 47.2 Wide-temperature-range IR cell for high area solids. **a** Cell + sample holder. **b** Spraying technique for sample preparation. **c** Hydraulic pressing technique. **d** Grid temperature distribution at steady state. **e** Temperature programming grid

rotatable flange and is inserted into the six-way cube, along with other desired attachments.

The grid material is made of thin tungsten foil that has precise square holes photo-etched in 0.0125–0.05-mm-thick material and exhibiting 58 % optical transparency in the IR [1]. Each of the square holes is 0.22 mm in width, surrounded by 0.05-mm boundaries. The uniform geometry is advantageous in controlling the uniformity of powder deposition, as will be shown below. Gold grids of the same geometry have also been employed in this cell.

Two methods may be used for the deposition of high-area solids on the W grid. As shown in Fig. 47.2b, Step 1, a spraying technique [1] like that described on p. 123 may be used in which the powdered solid is suspended in a volatile solvent and sprayed onto the heated grid. Heating to about 70 °C is achieved using temporary power leads to the grid and its Ni clamp support, causing flash evaporation of the solvent. The grid is rigidly held in a T-shaped Macor jig-mask that is designed to maintain correct spacing between the Ni clamps so that they may be slid over the power feedthrough leads on the bottom of the reentrant Dewar without

flexure of the grid containing the powder deposit as shown in Step 2. The Macor jig is then removed, as shown in Step 3. The powder first sticks to the boundaries of the 0.22-mm-wide openings and then as the deposition continues, the powder uniformly fills the holes. Oxide powder densities up to about 0.01 g/cm^2 may be achieved in the grid openings.

A second method for placing powder into the grid openings is shown in Fig. 47.2c [6]. Here, the unmounted grid is held between two sheets of glossy weighing paper and an excess of powder is sprinkled over the grid. Two stainless steel dies are used to sandwich the grid and its protective paper, and hydraulic pressure of about 12,000 psi is applied. This causes the powder to enter the grid openings and to be rigidly held there. Upon removal of the glossy paper, a razor blade is used to scrape off the excess powder from the top of the grid, and the grid is then mounted in the Ni clamps for loading into the IR cell. The powder material in the grid openings will withstand gentle bending of the grid. Powder densities of the order of 0.004 g/cm^2 may be achieved. The spectroscopic, gas transport, and thermal behavior of the pressed powders is very similar to that of the sprayed deposits [6].

The thermal properties of the grid during electrical heating to a stable temperature by a feedback controller have been characterized as shown in Fig. 47.2d, e [1]. In Fig. 47.2d, four thermocouples were attached as shown in the diagram. The open circle and black triangle points were used to measure temperature gradients along a vertical line in the center of the grid. The three open point measurements were made to determine the temperature gradient along a horizontal line through the center of the grid. In the central 4-mm-wide region of the grid that is sampled by the IR beam, no vertical gradient in temperature is observed. A small dropoff in temperature is seen in the central region as one moves horizontally owing to heat conduction away from the grid by the Ni clamps. The ability to temperature-program the grid and the supported powder to elevated temperatures is illustrated in Fig. 47.2e. Here, almost linear heating rates between 1.9 and 8.4 K/s are demonstrated, with the controller being programmed to stop the heating ramp at about 750 K in this case. Rapid cooling in 10–20 s from 900 K to the base temperature of 325 or 150 K maybe achieved [1].

Other cells for heating catalysts to high temperatures and cooling to low temperatures have been described. One of these is used for EXAFS measurements and works in a range from about 77 to 700 K [7]. Another, involving the use of a pressed sample in a copper grid, has been described and characterized for thermal behavior [8].

Cells in which the sample can be heated provide an ideal situation for the study of infrared emission spectroscopy. While many IR emission studies have been done on planar surfaces containing coatings, a few studies of high area surfaces as IR emission sources have been carried out too [9, 10]. One must be careful to rule out artifacts in this type of measurement [10].

47.3 Measurements of Diffusion Through Powders Using Transmission Infrared Spectroscopy

Measuring the activated diffusion of adsorbed molecules through powdered adsorbents may be carried out by using transmission IR spectroscopy to monitor either the adsorbate average concentration or the surface coverage of markers on the adsorbent surface which are modified by the arrival of an adsorbate molecule [11–15]. These measurements are carried out isothermally in the type of IR cell shown in Sect. 47.2. In this cell, a thin sample of the powder is held inside of the openings in a tungsten support mesh, and as isothermal diffusion occurs, the absorbance is used to follow the migration process. Two methods have been used successfully: (1) An ice layer of the adsorbate is warmed and its inward diffusion is monitored by its arrival at –OH sites which are modified upon hydrogen bonding to the adsorbate molecule [11, 12]; (2) A fully covered layer is monitored during isothermal desorption outward [13–15]. These two methods are schematically shown in Fig. 47.3a, b, where cross sections through the powder depth are shown before and after diffusion.

Figure 47.3c shows the schematic potential energy profile for a diffusing molecule. Initially, when localized by chemisorption on its adsorption site, the potential energy will be minimized. Lateral motion occurs when the molecule is promoted to the mobile precursor state [16], where it is held by weaker van der Waals forces and is able to transport along the surface over low barriers. This process takes place within the pore structure of the powder. Should the molecule be considered free of the surface in the pore, the process would be called Knudsen diffusion [17, 18], but it is believed that the mobile precursor model is more applicable since adsorption processes on well defined single crystal surfaces often proceed by the mobile precursor process [16]. At the end of the transport along a pore, desorption will occur into vacuum from the mobile precursor state. Within the framework of the mobile precursor state model, the activation energy for surface diffusion is given by the height of the escape barrier as shown in Fig. 47.3c. As the molecule moves laterally, it may frequently encounter an open chemisorption (trap) site and return to a lower potential energy.

Figure 47.3d shows four surface diffusion experiments for an organic molecule diffusing on an oxide surface from 260 to 290 K [15]. The curves are fits to a two process model, where slower diffusion amongst strong binding sites is mixed with faster diffusion on weaker binding sites. Figure 47.3e shows the Arrhenius plots for the two processes. Molecules moving in the faster process deplete first from the surface. Often, the IR spectrum of the diffusing molecule changes a little in moving from the mixed diffusion process to the slower process as surface coverage is depleted.

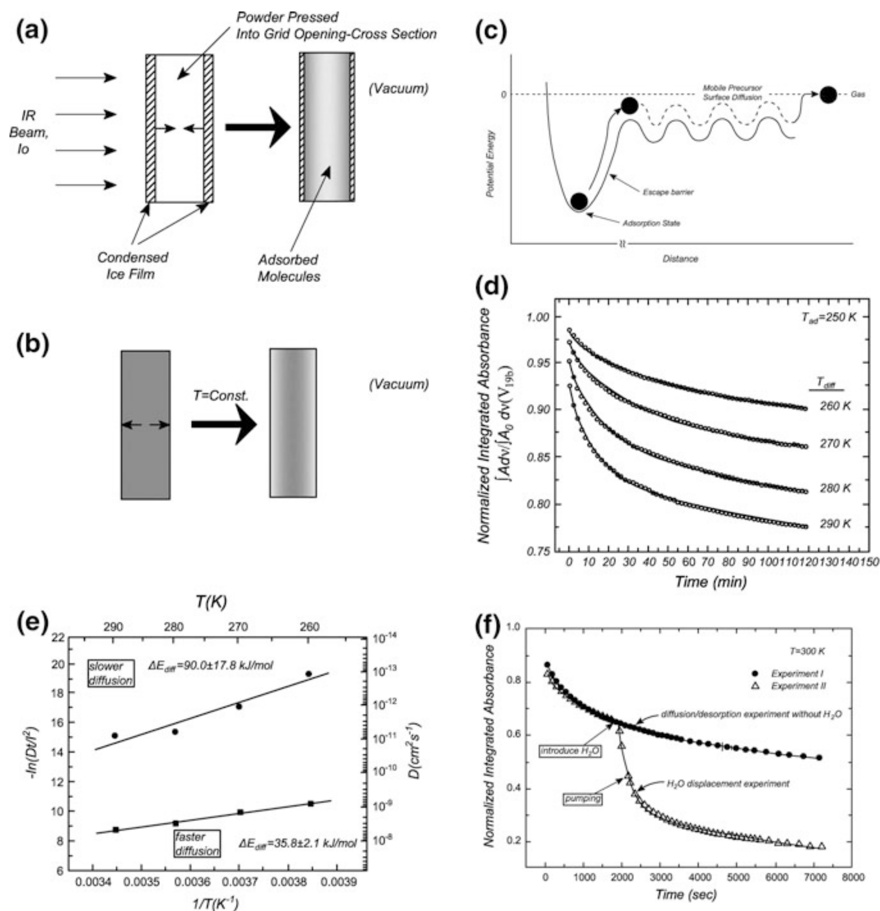

Fig. 47.3 Measurement of diffusion through powders using transmission IR spectroscopy. **a** Diffusion from condensed ice film. **b** Diffusion from adsorbed monolayer. **c** Potential energy profile during diffusion. **d** Normalized integrated absorbance from adsorbed molecules diffusion into vacuum. **e** Activation energy for parallel diffusion processes. **f** Effect of $H_2O(g)$ injection on diffusion organic molecules

In Fig. 47.3e, a diffusion experiment was carried out in which a non-hydroxylated oxide was employed [14]. As diffusion progressed, water vapor was injected and then pumped away. This caused the diffusing organic molecule to more quickly depopulate due to its weaker bonding to surface –OH groups compared to clean oxide surface sites. The hydroxyl groups promote rapid surface diffusion.

47.4 Using Transmission Infrared Spectroscopy to Witness Diffusion into Core-Shell Structures

Core-shell structures are sometimes able to transport adsorbed molecules from the outside to the inside. Since the transporting of adsorbed molecules undergoes different interactions with the shell surfaces and the core surface, its frequency is an excellent indicator of its progress through the shell to the core. Figure 47.4a shows a core-shell structure which has been investigated in this manner. A $\sim$10 nm diameter CoO shell has been prepared around a $\sim$2 nm diameter Pt particle [19]. Carbon monoxide has been added and the temperature has been raised while recording transmission IR spectra. CO is postulated not to transport by a gas phase route through pores in the CoO shell; however CO does transport as an adsorbed species across CoO surfaces which surround the pores in the shell structure. Eventually the diffusing CO reaches the Pt core and chemisorbs, giving a characteristic vibrational spectrum for CO/Pt. Figure 47.4b shows the intensity of the CO/CoO and CO/Pt spectral features as a function of temperature when the sample is placed under 2 Torr of CO at 110 K and then warmed. Initially, no spectral features are resolved, as the CO has not entered the shell structure. At about 150 K, CO/CoO appears and increases in coverage as CO enters into the CoO pores. At about 200 K, CO transport through the shell structure carries it to Pt sites on the core, and CO/Pt spectral features begin to develop. Figure 47.4c shows the spectral measurements as a function of temperature. This is a modification of the method discussed in Sect. 47.3 where adsorbates are observed to transport through macroscopic distances into the depth of a packed bed of a high surface area adsorbent—but here the transport distances involved are in the nanometer regime.

47.5 Diffusion in Powders as Measured by Transmission IR Spectroscopy

The understanding of transport processes by diffusion through powdered adsorbents is a key to the production of efficient technological sorbents and for efficient transport of reactants to catalytic sites dispersed on high surface area material. Transmission IR spectroscopy offers a method to measure the rate of diffusion of molecules through such materials. One has a choice of monitoring molecular diffusion into a powder from an outer layer of the ice form of the molecule [12, 20] or monitoring the diffusion outward from a saturated layer preadsorbed on the high area material [13–15, 21]. A technique involving pressed powder samples, held under temperature-controlled conditions in a W-grid in an IR cell, is used. The cell and the methods of using it are described in Sects. 47.2–47.4.

In the case of inward diffusion from the condensed ice on the outer geometrical surface of the powder, it is important to measure the arrival of molecules at interior sites in the powder bed. One of the best ways to do this for oxide surfaces is to

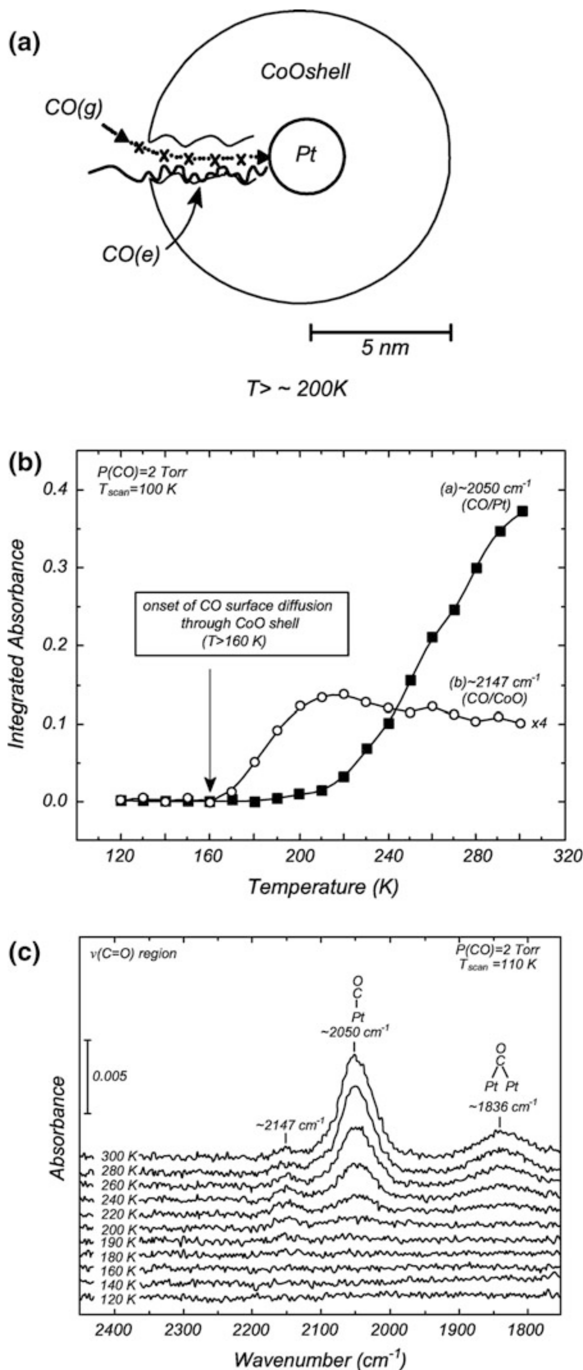

Fig. 47.4 Using transmission infrared spectroscopy to witness diffusion into core-shell structures. **a** Schematic of CO diffusion through a CoO shell in Pt@CoO. **b** Integrated absorbance during CO diffusion in CoO@Pt. **c** Difference spectra for CO transport through Pt@CoO

monitor the free hydroxyl groups as they slowly become complexed with the adsorbing molecules. Usually isolated M–OH groups will shift downward in frequency when hydrogen bonded to adsorbed molecules, producing M–OH···X species. This includes the Xe molecule [20] as well as many types of organic molecules which sense the strong dipole of the M–OH group. Figure 47.5a shows the cross section of a pressed powder involved in this inward-diffusion experiment. It is important in such an experiment to be certain that the source of the diffusing molecules, the ice, is not depleted as this would change the boundary condition for the diffusion process. Figure 47.5b shows the drop in absorbance of isolated Al–OH species and the production of complexed species as diffusion inward occurs. The drop in normalized integrated Al–OH absorbance is shown versus time as diffusion occurs and using Fick's second law of diffusion, the diffusion coefficient can be extracted from these data [12].

In the case of outward diffusion, shown schematically in Fig. 47.5c, molecules become mobile inside the pore structure of the powdered adsorbent, which has been saturated with adsorbate, and eventually desorb, causing the integrated absorbance to fall. Figure 47.5d shows a fitted kinetic plot for the diffusion where two activated diffusion processes were found, leading to slower and faster diffusion, as shown by the Arrhenius plot [13]. Defect sites on the oxide surface are thought to be responsible for the slow rate of diffusion over these sites. The value of the diffusion coefficient is derivable from these data where the boundary condition of zero coverage applies to the outer geometrical surface [13]. The outward diffusion is sometimes accompanied by small changes in the IR spectrum as the adsorbed molecules leave, since one preferentially samples the more strongly-bound species as the diffusion/desorption process proceeds [13–15]. The outward diffusion method more readily lends itself to studies of temperature dependence since in the inward process one must remain below the melting temperature of the ice. Recently, diffusion studies through a metal catalyst supported on an oxide were able to detect the separate transport of an adsorbed molecule from metal- to- metal site as well as transport across the oxide sites [21].

47.6 Transmission IR Spectroscopy Through Opaque Materials

The adsorption of gases on high surface area solid surfaces is of interest technologically. Transmission IR spectroscopy can be applied to such materials (see Sect. 47.2) if they possess sufficient optical transparency. If the materials are opaque, they may be studied by DRIFTS (Diffuse Reflection Infrared Fourier Transform Spectroscopy) [22–25]. However, even opaque materials may be studied by transmission IR spectroscopy, where transmission occurs by light scattering through the powdered material and the adsorbed species are located along scattering

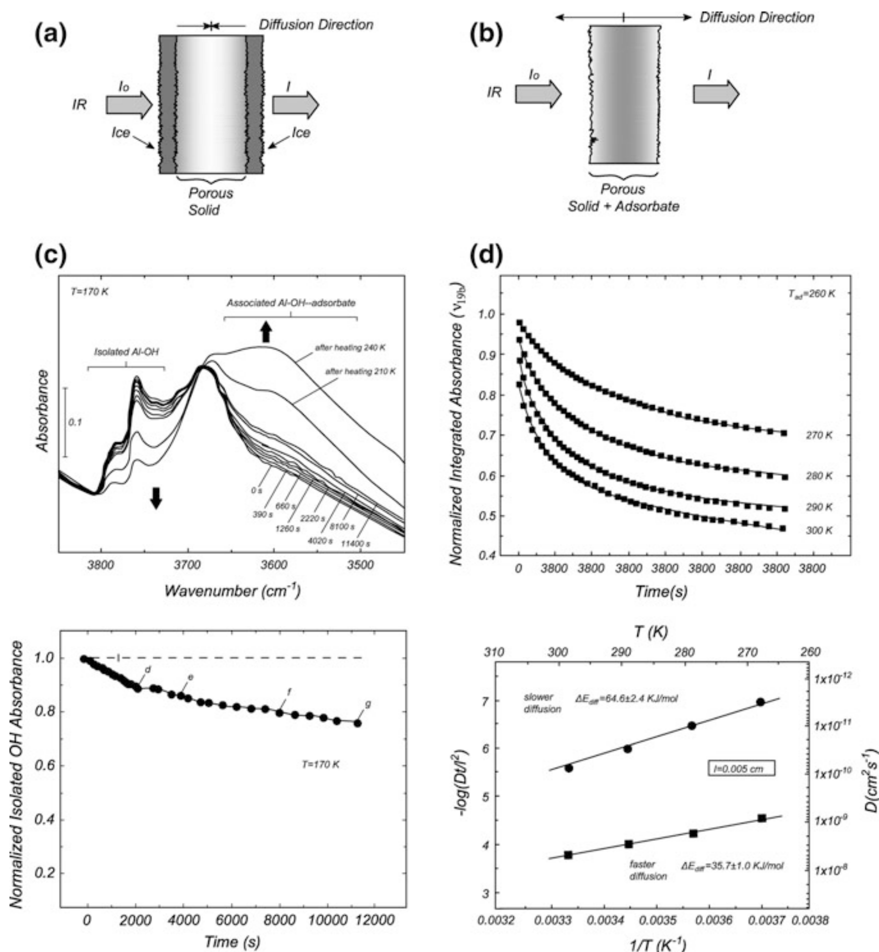

Fig. 47.5 Diffusion in powders as measured by transmission IR spectroscopy. **a** Molecular diffusion from ice overlayer—cross section through compresses sample. **b** Molecular diffusion from saturated monolayer—cross section through compresses sample. **c** Typical spectroscopic data showing molecular capture by Al–OH groups and kinetics of diffusion from ice. **d** Typical spectroscopic data showing diffusion/desorption from MgO powder and arrhenius behavior for two processes

pathways [26]. Much of the history of the use of transmission IR spectroscopy for studying adsorption on powdered materials is contained in [27–29].

For the study of opaque materials it is well known that suspending the opaque particles in an optically transparent matrix (the famous pressed disk method) is useful. Figure 47.6a shows a hydraulic pressing die which may be used for making 6 different samples on a single tungsten grid support as described in Sect. 47.2. Figure 47.6b shows a schematic of carbon particles suspended in pressed KBr,

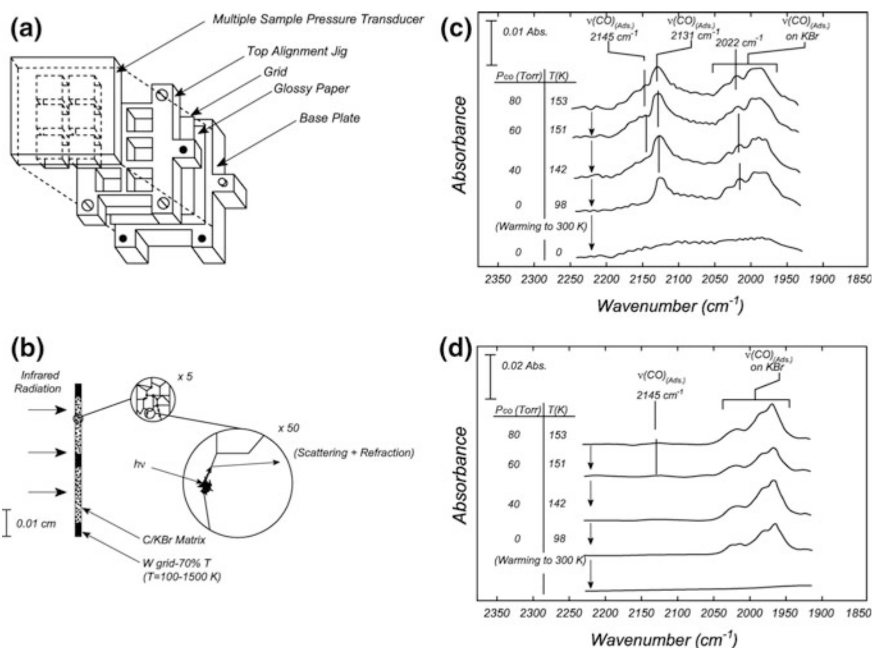

Fig. 47.6 Transmission IR spectroscopy through opaque materials. **a** Hydraulic pressing die—6 samples. **b** Cross section through grid + KBr/C sample. **c** Transmission IR—CO/C/KBr. **d** Transmission IR—CO/KBr

where the carbon particles are stored at KBr grain boundaries in the pressed sample. The individual square openings in the grid are 0.22 mm^2 in area, separated by W grid elements. The pressed samples are 0.051 mm in thickness. Light scattered through the KBr matrix interacts with the adsorbed species on the suspended carbon particles.

Figure 47.6c shows the IR spectrum for a high area C/KBr sample when adsorbed CO is in equilibrium with the gas at the cryogenic temperatures shown in the figure legend. Two regions of IR absorption are seen. At 2145 and 2131 cm^{-1}, CO on the carbon surface is detected; at lower CO frequencies, adsorption on the KBr surfaces is detected. For a KBr matrix alone, Fig. 47.6d shows only the low frequency CO species as strong bands, accompanied by very low coverage species with a frequency of 2145 cm^{-1}, close to that of gas phase CO. It is noted that for many molecules adsorbed on surfaces, there is a matrix shift of a few cm^{-1} due to the dual interaction of the molecule with its adsorbent, coupled with interactions with the surrounding KBr matrix [30].

References

1. P. Basu, T. Ballinger, J.T. Yates Jr, Rev. Sci. Instrum. **59**, 1321 (1988)
2. H.P. Wang, J.T. Yates Jr, J. Phys. Chem. **88**, 852 (1984)
3. T.P. Beebe, P. Gelin, J.T. Yates Jr, Surface Sci. **148**, 526 (1984)
4. Windows of CaF_2 Single Crystal Mounted in Conflat Flanges may be Obtained from Harshaw Crystal and Electronic Products. Solon Technologies, 6801 Cochran Rd., Solon, OH, 44139
5. Custom Fabricated Grids made of W or Other Metals are Available from Buckbee Mears, 245 E. Sixth Street, St. Paul, MN 55101
6. T.H. Ballinger, J.C.S. Wong, J.T. Yates Jr, Langmuir **8**, 1676 (1992)
7. F.W.H. Kampers, T.M.J. Maas, J. van Grondelle, P. Brinkgreve, D.C. Konigsberger, Rev. Sci. Instrum. **60**, 2635 (1989)
8. M. Hughes, L. Bourget, R.G. Greenler, J. Cat. **139**, 691 (1933)
9. D. Kember, D.H. Chenery, N. Sheppard, J. Fell, Spectrochim. Acta **35A**, 455 (1979)
10. D. Kember, N. Sheppard, J. Chem. Soc., Faraday Trans. **2**(77), 1321 (1981)
11. D.B. Mawhinney, J.A. Rossin, K. Gerhart, J.T. Yates Jr, Langmuir **16**, 2237 (2000)
12. S. Kim, O. Byl, J.-C. Liu, J.K. Johnson, J.T. Yates Jr, J. Phys. Chem. B **110**, 9204 (2006)
13. S. Kim, X. Wang, C. Buda, M. Neurock, O.B. Koper, J.T. Yates Jr, J. Phys. Chem. C **113**, 2219 (2009)
14. X. Wang, S. Kim, C. Buda, M. Neurock, O.B. Koper, J.T. Yates Jr, J. Phys. Chem. C **113**, 2228 (2009)
15. I.X. Green, C. Buda, Z. Zhang, M. Neurock, J.T. Yates Jr, J. Phys. Chem. C **114**, 16649 (2010)
16. W.H. Weinberg, in *Kinetics of Interface Reactions*, eds. by M. Grunze, H.-J. Kreuzer (Springer, New York, London, 1986)
17. J.H. de Boer, *The Dynamical Character of Adsorption* (Oxford University Press, London, 1968)
18. D.D. Do, *Adsorption Analysis Equilibria and Kinetics* (Imperial College Press, London, 1998)
19. S. Kim, Y. Yin, A.P. Alivisatos, G.A. Somorjai, J.T. Yates Jr, J. Am. Chem. Soc. **129**, 9510 (2007)
20. T.H. Ballinger, P. Basu, J.T. Yates Jr, J. Phys. Chem. **93**, 6758 (1989)
21. I. Green, W. Tang, M. Neurock, J.T. Yates Jr, Science **333**, 736 (2011)
22. J.T. Yates Jr, T.E. Madey (eds.), *Vibrational Spectroscopy of Molecules on Surfaces* (Plenum, NY, 1987)
23. P.E. Fanning, M.A. Vannice, Carbon **31**, 721 (1993)
24. B.J. Meldrum, C.H. Rochester, J. Chem. Soc. Faraday Trans. **86**, 861 (1990)
25. M.B. Mitchell, V.N. Sheinker, E.A. Mintz, J. Phys. Chem. B **101**, 11192 (1997)
26. A.T. Bell, M.L. Hair, *Vibrational Spectroscopies for Adsorbed Species* (American Chemical Society, Washington, DC, 1980)
27. M.L. Hair, *Infrared Spectroscopy in Surface Chemistry* (Dekker, New York, 1967)
28. L.H. Little, *Infrared Spectra of Adsorbed Species* (Academic Press, New York, 1966)
29. A.V. Kiszelev, V.I. Lygin, *Infrared Spectra of Surface Compounds* (Wiley, New York, 1975)
30. D.B. Mawhinney, J.A. Rossin, K. Gerhart, J.T. Yates Jr, Langmuir **15**, 4617 (1999)

Chapter 48
Adsorption/Desorption—Thermal

48.1 Adsorption and Desorption from High-Area Solids

The study of the surface behavior of high area solids can be carried out using extensions of the fundamental measurement methods developed for studies of low area single crystal surfaces. Among the most widely used methods in single crystal studies is temperature-programmed desorption (TPD), often called thermal desorption spectroscopy (TDS) [1]. The TPD method, with appropriate calibration, can be used to measure absolute surface coverages as well as the kinetics of desorption as a function of surface coverage on both single crystals and high-area solids.

Figure 48.1a shows a thermal desorption spectrometer that was used for the study of ethylene adsorption on a high-area (423 m^2/g) NaX zeolite [2]. The sample, of mass 10 μg, was deposited on a Ta disk by use of a micropipet that deposited known volumes of a slurry containing the suspended zeolite in suspension. Upon evaporation of the solvent, it was found that the zeolite particles were separated from each other as they adhered to the Ta surface. Thus, interparticle diffusion effects during adsorption and desorption were eliminated by the high particle dispersion, although pore diffusion in the zeolite particles was clearly evident in the measurements [2].

The high-area sample is first cleaned by heating in vacuum using a temperature programmer that operates in a feedback circuit involving the thermocouple. Gases are adsorbed in the pumped system, or for high exposures, with the gate valve closed.

The sample is held in front of a 2-μm sampling aperture that may be opened and closed using an O-ring seal on the end of a linear motion device. With the gate valve closed, this permits the sampling of gases near the sample surface at high pressures as would be necessary for the study of catalytic reactions. However, with the gate valve open after adsorption, sampling of desorbing gas from the powdered sample is possible in the pumped system through direct transmission from the

© Springer International Publishing Switzerland 2015

J.T. Yates Jr., *Experimental Innovations in Surface Science*,
DOI 10.1007/978-3-319-17668-0_48

Fig. 48.1 Adsorption/Desorption on powdered solids. **a** Thermal desorption mass spectrometer. **b** Typical Adsorptionuptake data

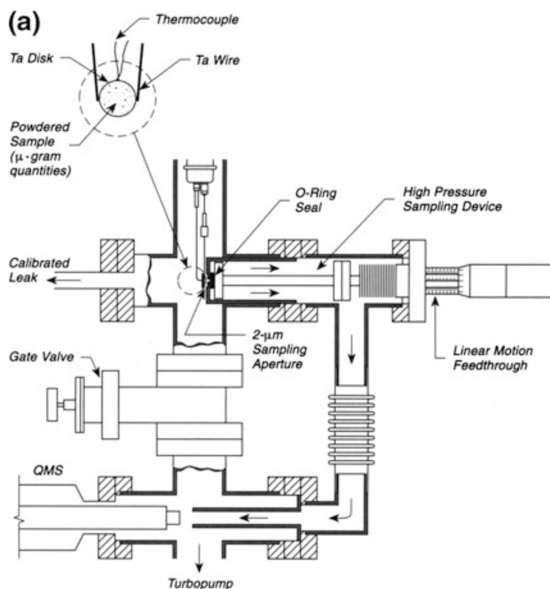

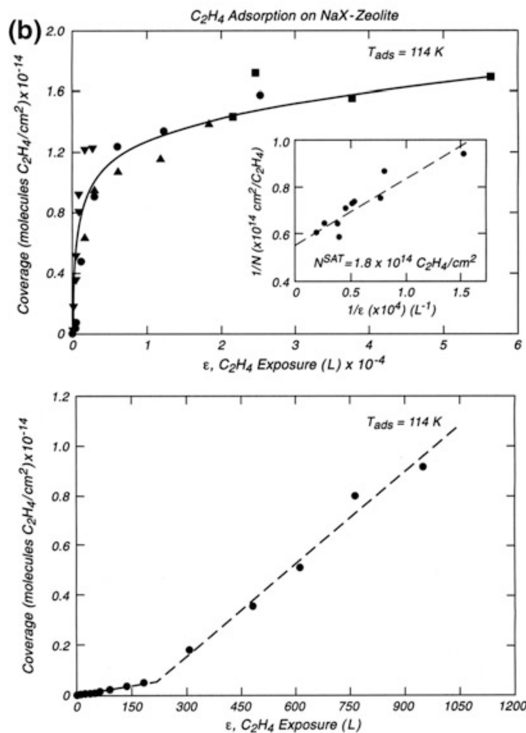

sample to the mass spectrometer. The mass spectrometer and pumping speed of the system may be separately calibrated using an absolute flow of gas into the pumped system through a calibrated leak (see p. 425). Knowing the mass of the sample and its surface area per unit mass, the absolute coverage of adsorbate may be determined by thermal desorption measurements, integrating the pressure signal over the time duration of the desorption peak.

Figure 48.1b shows an example of the uptake of ethylene versus exposure on NaX zeolite at 114 K. At low exposures, adsorption is postulated to occur on the outer surfaces of the isolated zeolite particles [2, 3]; at exposures above about 200 L (1 L = 1×10^{-6} Torr s), adsorption occurs into the pores of the zeolite, and the efficiency of adsorption increases significantly as indicated by the lower curve of Fig. 48.1b. Over the entire upper range of exposures, a typical sigmoid uptake curve is found, as shown in the upper curve of Fig. 48.1b. The inset shows an analysis that may be used to predict the saturation coverage of the adsorbate, which occurs in the limit of $1/\varepsilon = 0$, where ε is the gas exposure.

Extensive work on the analysis of TPD spectra from high-area solids has been reported and appropriate references are listed in [2]. Noteworthy is a study by Demmin and Gorte [4]. A major consideration is the effect of interparticle diffusion on the observed desorption kinetics, and the method shown here, involving very high particle dispersion, avoids this effect, while also offering sensitivity at the 10^{-4} ML level for powders with very high specific surface areas. Small corrections for the adsorption on the Ta support may be easily applied.

Similar methods have been applied to larger samples (0.1 g) of powdered material in the form of compressed pellets, but the influence of interparticle diffusion is not eliminated in these studies [5].

A recent review of temperature-programmed desorption from high area solids maybe found in [6].

48.2 Thermal Desorption from High Area Materials

The extension of temperature programmed desorption (TPD) to high area materials has occurred. A common problem is that the surfaces studied have such a wide range of adsorption sites that clear kinetic resolution of desorption from these sites is not possible. Also, because high area powdered materials which have been packed into a powder bed will mix gas desorption processes with surface diffusion processes, the resolution of desorption states into separate processes is virtually impossible. Early studies on zeolites were able to separate the external surface sites from interior sites using temperature programmed desorption [7]. Transmission IR studies (see Sects. 47.3–47.5) are also able to observe surface diffusion processes [8–10] as well as the adsorption sites in core shell structures [11].

One class of high area material which displays well defined adsorption sites is carbon single walled nanotubes (C-SWNTs) and the successful discrimination of these sites has been achieved by TPD methods [12–16]. In Fig. 48.2a, the UHV

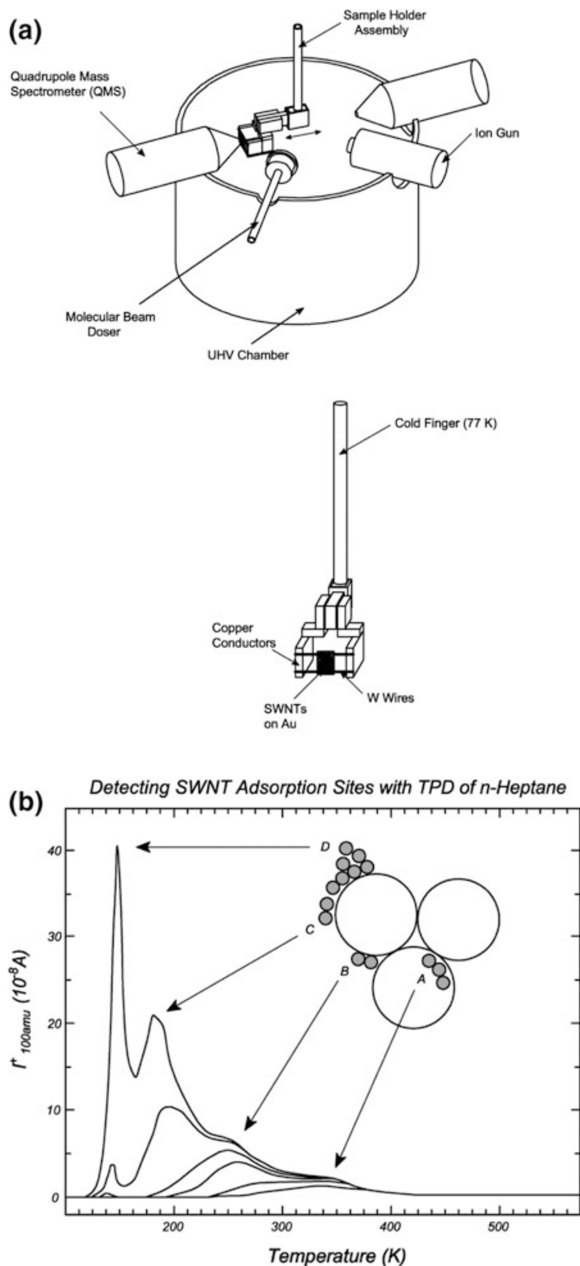

Fig. 48.2 Thermal desorption from high area materials. **a** Thermal desorption apparatus. **b**. n-Heptane thermal desorption from SWNT. **c** Experimental detection of different SWNT binding sites for several n-Alkanes. **d** Graphite versus single walled nanotubes—n-Heptane desorption

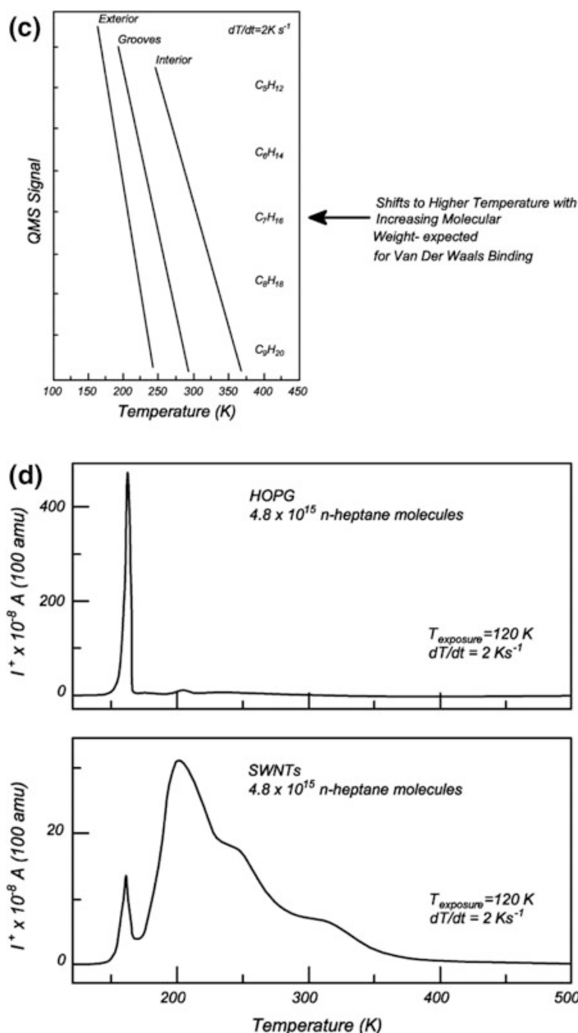

Fig. 48.2 (continued)

apparatus, involving an apertured mass spectrometer is shown [16]. The SWNTs are delivered in solvent to a Au platelet which can be programmed upwards in temperature. Because of their high specific surface area a few μg are all that is needed to obtain strong desorption signals. In the figure a molecular beam doser is shown which is used for quantitative delivery of adsorbate to the sample. We find in control experiments that desorption from the support is of order of 1 % of that from the SWNT sample. Figure 48.2b shows the desorption spectra of n-heptane from an opened SWNT sample [15]. The sequential depopulation of various desorption states, assigned as shown in the schematic to various classes of sites, is easily

observed. The desorption begins, at high enough coverage, by depopulating multilayer n-heptane, followed by desorption from the external first layer sites, the groove sites and finally the internal sites [14]. The desorption kinetics from these sites have been modeled. Figure 48.2c shows the behavior for a series of linear alkanes and it may be seen that the temperatures of desorption from the various states monotonically increase with increasing chain length and adsorption energy [17]. Finally, in Fig. 48.2d, we see desorption of n-heptane from graphite compared to nanotubes. While graphite exhibits an adsorption state which evolves at higher temperature than the multilayer n-heptane, the various sites on SWNTs are not observed [18]. The method has also been applied for the study of confined chemical reactions in the nanotubes [19], where surface defect sites have been found to be important.

48.3 Microcalorimetric Studies of Adsorption Heat on Powders

The direct measurement of the energy released during chemisorption provides a measurement of the binding energy of adsorbed molecules that depends only of the first law of thermodynamics. A method for making these measurements on thin single crystal surfaces has been given on p. 333.

In Fig. 48.3a, the cell used for calorimetric measurement on high-area metal catalysts is shown [20]. A metallic Ni catalyst, prepared from $Ni(II)(NO_3)_2 \cdot 6H_2O$ powder by reduction in H_2 at 623 K, is stored under He in a sealed-off Pyrex NMR tube, and this tube is located in one arm of the calorimeter cell. The metal weighs between 0.5 and 1.0 g and has a surface area of 1.7 m^2/g and a CO capacity of 22 μmol/g. The leak rate of the closed cell was measured to be about 10^{-6} μmol/min in a 70-cm^3 volume.

Calorimetric measurements are made on the catalyst by first breaking the glass NMR tube using the linear motion feedthrough that presses down on the inner tube. Then small amounts of CO (or other gases) are admitted and the thermal response of the calorimeter is measured, comparing the sample cell to the reference cell in two identical calorimeters. The uptake of gas is measured using standard volumetric techniques and a capacitance manometer with a sensitivity of 0.5×10^{-4} Torr.

The calorimeter is a commercial device, a Setaram C-80 heat-flux calorimeter.

Typical results are shown in Fig. 48.3b, and are compared with measurements made on a Ni(100) single crystal [21]. The coverage scales are normalized to the saturation coverage in both cases. It may be seen that the agreement is excellent, especially for the heat of adsorption at zero coverage. These results suggest that the chemical reduction technique used for preparation of the powdered Ni results is a clean surface that behaves in a fashion similar to atomically clean Ni surfaces. In [21], the range of the initial adsorption heat was 8 %, comparing three low index planes of Ni.

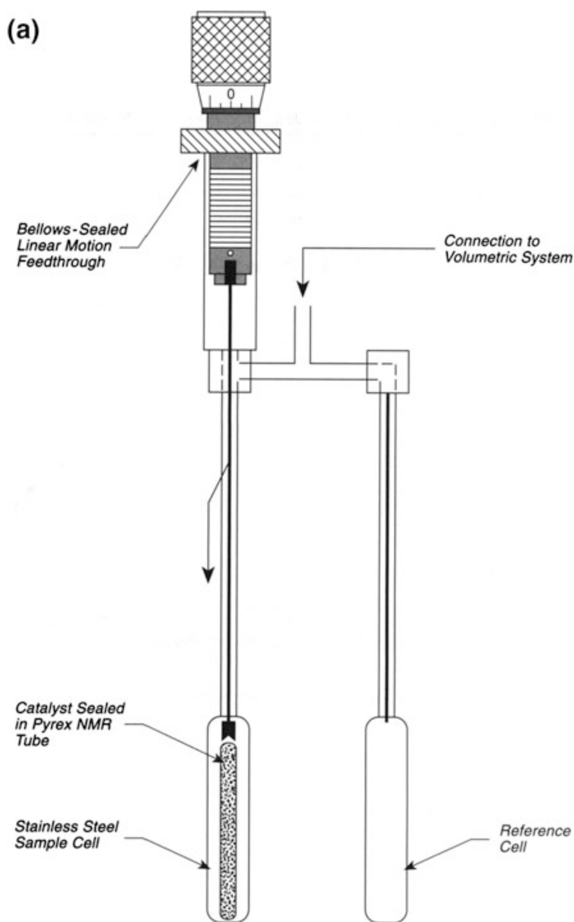

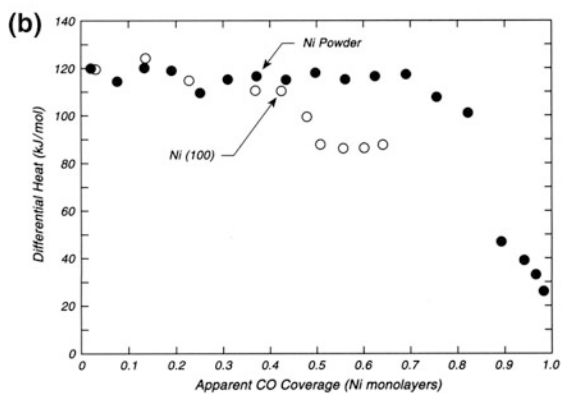

Fig. 48.3 Microcalorimetric studies microcalorimeter—adsorption heats on powders. **a** Calorimeter cells. **b** CO chemisorption on Ni

A second example of the use of microcalorimetry for powdered samples may be found in [22–24]. Here, the sample, weighing about 0.5 g, is spread over the flat bottom of the calorimeter (6.3-cm^2 geometrical area). This permits rapid equilibration between the gas and the adsorbed layer, and also rapid thermal equilibrium.

48.4 Chemical Vapor Synthesis of Oxide Nanoparticles

Chemical vapor synthesis (CVS) is well suited for the production of alkaline earth oxide nanoparticles (MgO, CaO, SrO, and BaO) and mixed oxides such as $Ca_xMg_{1-x}O$. Due to the absence of solvents, the vapor synthesis can yield clean material and controlled particle size. The reactor is shown in Fig. 48.4a, allowing controlled oxidation of metal vapors under reduced pressure [25]. Concentric quartz tubes are placed in a furnace with good temperature control. The inner tube contains two ceramic boats containing several

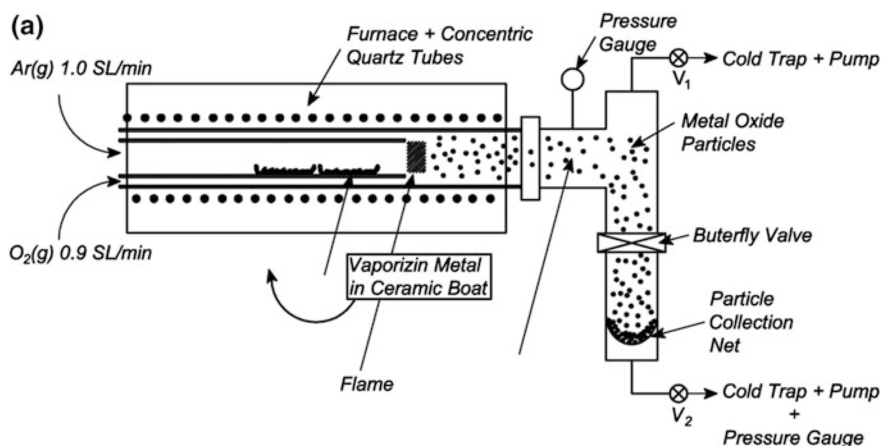

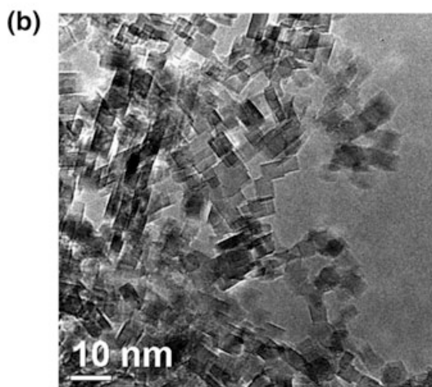

Fig. 48.4 Chemical vapor synthesis of oxide nanoparticles. **a** CVS reactor. **b** TEM image of MgO nanocubes

grams of metal and the temperature is adjusted under Ar flow to produce sufficient metal vapor pressure. The inert Ar carries the metal vapor to the end of the inner tube where it meets flowing oxygen. The exothermic oxidation reaction produces a bright stable flame at the end of the inner tube and alkaline earth oxide nanoparticles are produced as a result of homogeneous nucleation in the gas phase. Due to continuous pumping, the residence time of the oxide nuclei within the flame remains short enough to prevent substantial coarsening and coalescence. A by-pass system (Valve V_1) allows one to avoid particle collection during uncontrolled process conditions during initial heating. Following particle synthesis and collection in the particle collection net, the furnace is rapidly cooled by flowing air through the region surrounding the outer quartz tube. The oxide nanoparticles may be transferred in air to other instruments for study, and cleaning procedures in vacuum should be used to remove contaminants adsorbed on the nanoparticles during transfer. An electron micrograph of nanometer sized MgO nanocubes, exposing MgO (100) faces is shown in Fig. 48.4b.

References

1. J.T. Yates Jr, Meth. Exp. Phys. **22**, 425 (1985)
2. P. Basu, J.T. Yates Jr., Surf. Sci. **177**, 291 (1986). U.S. Patents 4,877,584 and 4,663,297
3. M. Kiskinova, G.L. Griffin, J.T. Yates Jr, J. Catal. **71**, 278 (1981)
4. R.A. Demmin, R. Gorte, J. Catal. **90**, 32 (1984)
5. G.D. Moggridge, J.P.-S. Badyal, R.M. Lambert, J. Vac. Sci. Technol. **A8**, 3874 (1990)
6. R.J. Gorte, Catal. Today **28**, 405 (1996)
7. P. Basu, J.T. Yates Jr, Surf. Sci. **177**, 291 (1986)
8. S. Kim, O. Byl, J.-C. Liu, J.K. Johnson, J.T. Yates Jr, J. Phys. Chem. B **110**, 9204 (2006)
9. S. Kim, X. Wang, C. Buda, M. Neurock, O. Koper, J.T. Yates, Jr. J. Phys. Chem. C **113**, 2219 (2009)
10. X. Wang, S. Kim, C. Buda, M. Neurock, O. Koper, J.T. Yates Jr, J. Phys. Chem. C **113**, 2228 (2009)
11. S. Kim, Y. Yang, A.P. Alivisatos, G.A. Somorjai, J.T. Yates Jr, J. Am. Chem. Soc. **129**, 9510 (2007)
12. P. Kondratyuk, J.T. Yates Jr, Chem. Phys. Lett. **383**, 314 (2004)
13. P. Kondratyuk, J.T. Yates Jr, Chem. Phys. Lett. **410**, 324 (2005)
14. P. Kondratyuk, Y. Wang, J.K. Johnson, J.T. Yates Jr, J. Phys. Chem. B **109**, 20999 (2005)
15. P. Kondratyuk, Y. Wang, J. Liu, J.K. Johnson, J.T. Yates Jr, J. Phys. Chem. C **111**, 4578 (2007)
16. P. Kondratyuk, J.T. Yates Jr, J. Am. Chem. Soc. **129**, 8736 (2007)
17. P. Kondratyuk, J.T. Yates Jr, Acc. Chem. Res. **40**, 995 (2007)
18. L. Mandeltort, J.T. Yates Jr (private communication)
19. L. Mandeltort, M. Buettner, J.T. Yates Jr, P. Choudhury, L. Xiao, J.K. Johnson, J. Phys. Chem. C **114**, 17148 (2010)
20. B.E. Spiewak, P. Livin, R.D. Cartright, J.A. Dumesic, J. Phys. Chem. **100**, 17260 (1996)
21. J.T. Stuckless, N. Al-Sarraf, C. Wartnaby, D.A. King, J. Chem. Phys. **99**, 2202 (1993)
22. D.J. Parrillo, C. Lee, R.J. Gorte, App. Catal. A: General **110**, 67 (1994)
23. D.J. Parrillo, R.J. Gorte, Catal. Lett. **17**, 16 (1992)
24. D.J. Parrillo, R.J. Gorte, J. Phys. Chem. **97**, 8786 (1993)
25. O. Diwald, Institute of Particle Technology, University Erlangen-Nuremberg (private communication)

Part IX
Safety

Chapter 49
Protecting the Vacuum System

49.1 Delay Circuit for Turbopumping Protection Against Vacuum Loss from Power Interruptions

Power interruptions can play havoc with UHV systems operating with a turbopump, and particularly when these systems are being baked out. A power failure has the effect of venting a turbopump, using the commercial vent valve designed to prevent oil back-streaming from the forepump into the turbopump and the vacuum chamber during a power interruption. A partial solution to avoid massive air entry into the UHV system is to employ a pneumatic gate valve between the turbopump and the vacuum system. However, there are two defects in this protection system: (1) the time of closure of the gate valve is too long to prevent at least partial loss of vacuum in the chamber; and, (2) when the power returns, the gate valve will quickly open, exposing the chamber to a turbopump which is at or near atmospheric pressure. A circuit to prevent these effects is described below [1]. There is a commercial device that will do almost the same thing electrically [2], and a pneumatic device also for the same purpose [3].

The first problem mentioned above is solved by venting the turbopump only after the gate valve is completely closed. This is done by supplying short-term emergency power to the turbopump vent valve for the necessary period of time (approximately 8 s is used). The second problem is solved by controlling the pneumatic gate valve with a relay [4] that latches in the off position upon power failure. This prevents the valve from reopening when the power returns until the relay is overridden.

Figure 49.1 shows the circuit, costing less than $100, which accomplishes both objectives. The nondelayed socket supplies power to the gate valve relay. A line switch between the nondelayed socket and the gate valve supplies manual control of the gate valve. The nondelayed socket power is designed to latch in the off position in the case of a power interruption, and pushing the reset button reactivates power at this socket when the main power is restored.

© Springer International Publishing Switzerland 2015

J.T. Yates Jr., *Experimental Innovations in Surface Science*,
DOI 10.1007/978-3-319-17668-0_49

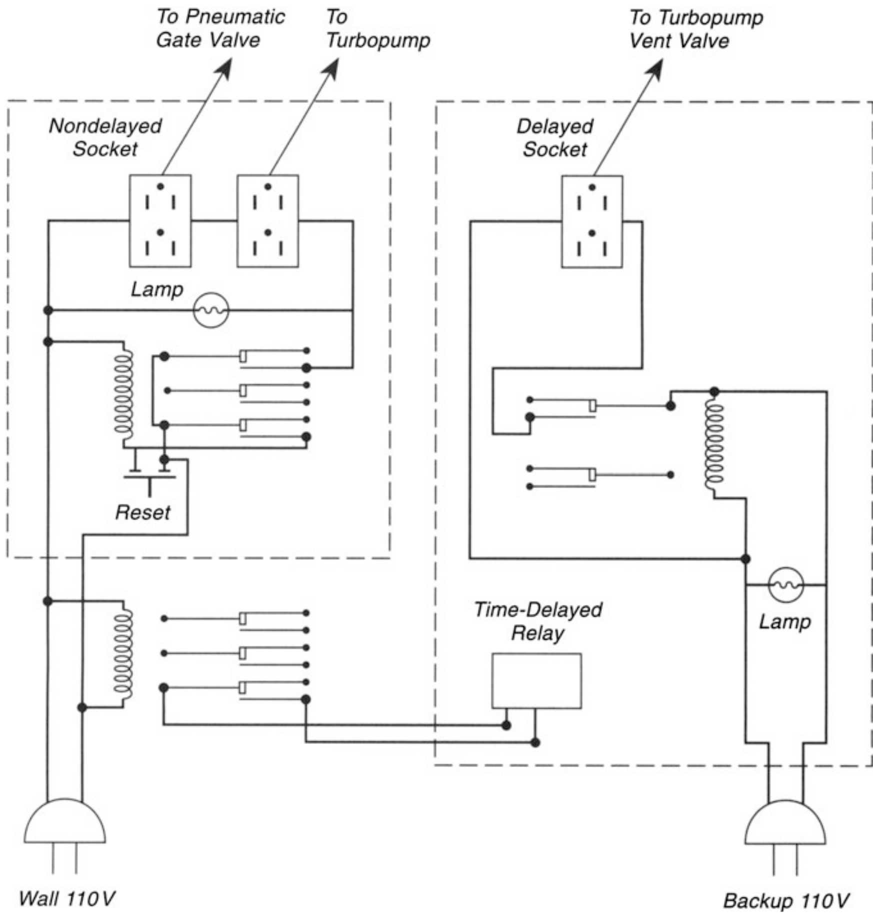

Fig. 49.1 Delay circuit for turbopumping protection against vacuum loss from power interruption

The delayed socket supplies emergency power to the turbopump vent valve. It is powered by a battery-driven backup AC power supply [5]. When main power is interrupted, emergency power is supplied and then shuts off, venting the turbopump. For momentary main power interruptions lasting less than 8 s, the turbopump vent valve will not open because power is supplied from the backup supply.

The control system does not assume that when power returns the turbopump restarts and can be automatically opened to the vacuum system, unlike other systems [2, 3]. It is deemed best to leave the system shut down after power interruptions, awaiting manual restarting.

49.2 Fast-Closing Beam Valve for UHV Chamber Protection

It is often necessary to protect an ultrahigh vacuum system from vacuum failure in an auxiliary system, such as an attached beam source system. In this particular case, since the beam is of small cross section, the valve can be very small. The valve must be electrically actuated by relays connected to pressure gauges in both systems.

Figure 49.2 shows a modified solenoid actuated valve [6] that is inexpensive, fast, and ultrahigh-vacuum-compatible. The solenoid driving the valve is encased in a housing that is sealed by O-rings so that gas evolution from the heated coil will

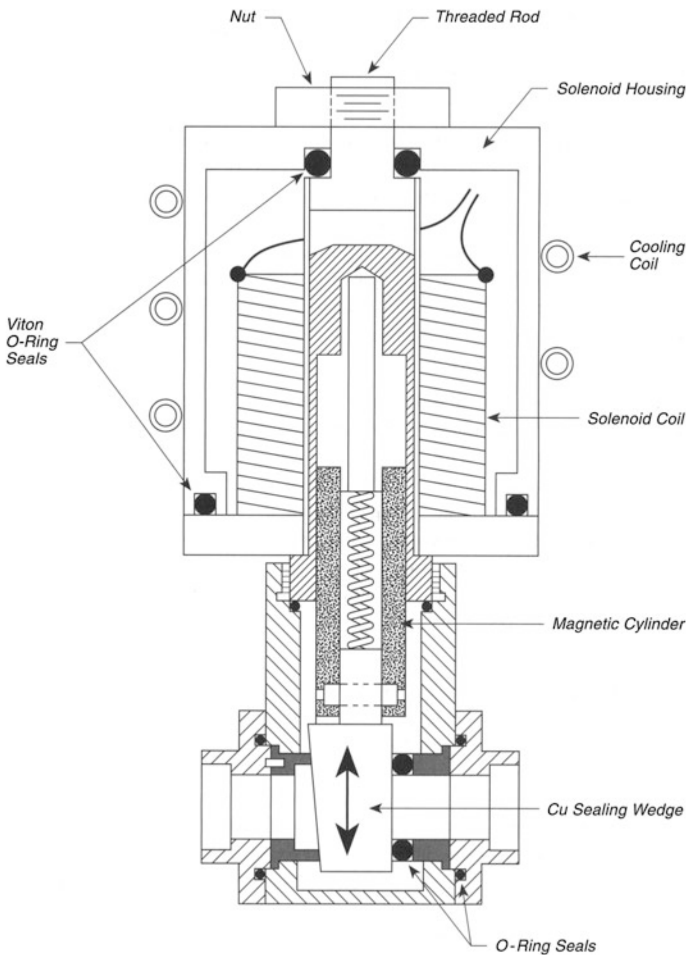

Fig. 49.2 Fast closing beam valve—UHV chamber

not degrade the vacuum. The housing is tightened into place by using a nut that engages a threaded rod at the top of the assembly.

When the current is on, the wedged-shaped Cu seal is drawn up into the solenoid; interruption of vacuum results in turning the solenoid off, and the Cu seal is dropped into the sealing position, where it is held in place by a spring and by gravity. The seal is made against a Viton O-ring in the lower portion of the valve. Copper cooling coils are used to dissipate heat from the solenoid. Electrical connections are brought out from the solenoid housing through a Conflat flange, not shown.

The leak rate through the closed valve is 4×10^{-5} Torr L/s, and is too large to be used to protect an ultrahigh vacuum system without a pumping section between the valve and the system. In the case of the use of this valve, a differentially pumped chopper region is present and serves this purpose [7].

A similar principle has been used to insert a large gate valve into an ultrahigh vacuum system [8].

49.3 Safety System for Oil Diffusion-Pumped UHV Systems

Modern oil diffusion pumps are now used to achieve ultrahigh vacuum, and these pumps exhibit some advantages over more expensive ion pumps or turbomolecular pumps. Among the advantages are lower cost, the ability to pump all gases, the absence of magnetic fields, and the absence of vibrations. Among the disadvantages are the possibilities of system contamination if failure of various components occurs [9]. The failure items are loss of vacuum, loss of power, loss of cooling water, and loss of liquid nitrogen cooling in the ultrahigh vacuum trap. A pneumatically actuated valve between the pumps and the ultrahigh vacuum system is the key element that closes to protect the system if some failure should occur.

A schematic drawing of an oil diffusion pumped ultrahigh vacuum system is shown in Fig. 49.3a. It consists of a standard bakeable chamber with an ionization gauge and a titanium sublimation pump (TSP). The pneumatically actuated gate valve separates the system from the external diffusion pump and liquid nitrogen trap. The oil diffusion pump contains special perfluoro polyether pump oil (Fomblin type) or polyphenyl ether (Santovac-5) pump oil used for achieving the best pressure. Silicone diffusion pump oils should be avoided in all UHV apparatus. The oil diffusion pump is protected from the oils of the mechanical pump by a bakeable molecular sieve trap, and the foreline pressure is monitored by a thermocouple gauge or other pressure gauge.

The simple relay circuit shown in Fig. 49.3b is designed to protect the system from the various failure possibilities [9]. Digital electronic components were avoided to reduce the circuit sensitivity to electrical noise. The control items in the vacuum system are: (1) foreline thermocouple gauge maximum pressure set point—

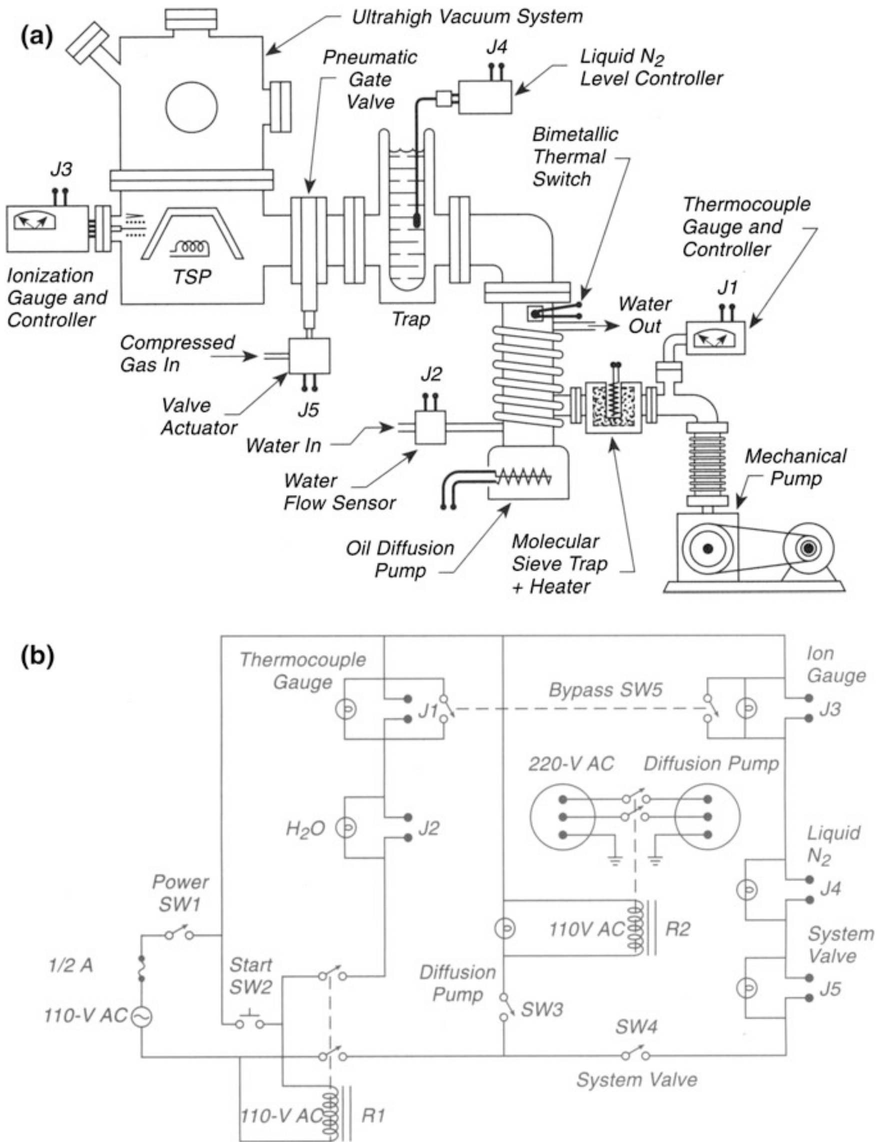

Fig. 49.3 Safety system for oil-diffusion-pumped UHV systems. **a** Schematic oil diffusion pumped UHV system. **b** Safety system schematic

to J1; (2) water flow sensor—to J2; (3) ionization gauge maximum pressure setpoint —to J3; (4) liquid nitrogen filler with low level sensor—to J4; (5) pneumatically actuated system valve—to J5. The relay, Rl, is a double-pole, single-throw relay and is turned on by closing the power switch, SW1, and then depressing the momentary contact switch, SW2. This sets R1 if the fore-line pressure is below the

Table 49.1 Interlock response to failure conditions

Failure	Diffusion pump power	System valve
Chamber pressure too high	On	Closed
Liquid N_2 level too low	On	Closed
Foreline pressure too high	Off	Closed
Water failure[a]	Off	Closed
Electrical failure	Off	Closed

[a]An additional bimetallic thermal switch control is available on most diffusion pumps that interrupts the heating power if the water goes off

thermocouple gauge set point and if there is sufficient water flowing through the diffusion pump, closing J2. The switch SW3, which controls the relay, R2, may then be used to switch on the diffusion pump. The system valve, SW4, can then be actuated if continuity exists through the right-hand side of the circuit, meaning that the liquid nitrogen trap and the ion gauge are operating in the proper range. If one is in the initial pumpdown period, the pressure will be too high at the ionization gauge, and this gauge and the thermocouple gauge can be bypassed temporarily by closing switch SW5.

Table 49.1 shows the various failure conditions and the components' condition when these failures occur.

49.4 Folding Linear Magnetic Translator

Rather long linear and rotary magnetic translators are often used in ultrahigh vacuum systems, and these are always in danger of being hit by laboratory personnel as they pass by. The design shown in Fig. 49.4 prevents this by folding the device housing containing the retracted magnetic translator/rotor.

Figure 49.4a shows a side view of the device. The welded bellows is folded upward through a 90° angle by a hinge and locked into place. In the horizontal position the bellows is held in a slightly compressed configuration by the gimbal subassembly. The outer end of the outer cylinder of the translator has a threaded rod attached on axis and this is retained in a "scissors" subassembly that permits accurate vertical positioning of the end of the translator. The bench holding the device is attached to the system lower flange by a rigid yoke assembly.

Figure 49.4b shows the gimbal subassembly and the two rotational adjustments that are possible as well as a lateral translation for alignment. A double-sided flange is used in order to be able to disassemble either the bellows or the translator section independently. Washers, used as spacers under the gimbal, permit vertical adjustment.

A critical design consideration is the appropriate size of the welded bellows. Figure 49.4c shows the dimensional parameters associated with a welded bellows-namely, the relaxed or free length (FL) at one atmosphere, the extended

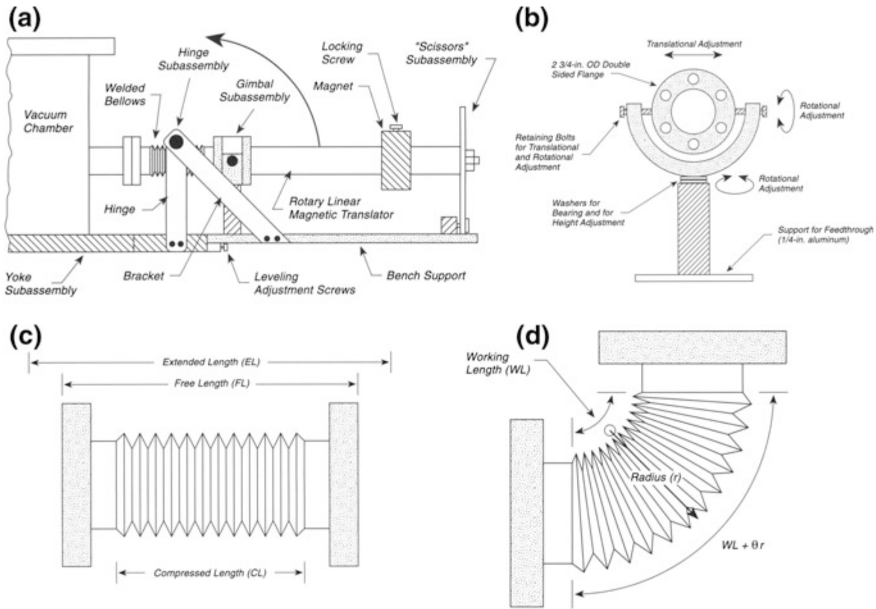

Fig. 49.4 Folding linear magnetic translator. **a** Side view. **b** Gimball subassembly. **c** Welded bellows—dimensional definitions. **d** Bellows in bent configuration

length (EL), and the compressed length (CL). These parameters are specified by the bellows manufacturer. In the bent condition, the inner radius of the bellows is defined as the working length (WL) in Fig. 49.4d. The outer length of the bent bellows is therefore WL + θr, and the condition in (49.1) must be met:

$$\mathrm{WL} + \theta \mathrm{r} < \mathrm{EL} \tag{49.1}$$

In order to achieve the condition in (49.1), the bellows must be compressed during installation by using the gimbal's subassembly, such that WL < FL. Note that welded bellows must be used for this device, since preformed bellows will not have the range of extension or the flexibility needed.

References

1. J.A. Polta, P.A. Thiel, J. Vac. Sci. Technol. **A5**, 386 (1987)
2. Balzers Part No. TCV 102. Obtained from Balzers, 8 Sagamore Park, Hudson, NH 03051
3. J.P. Saint-Germain, G. Abel, B.L. Stansfield, J. Vac. Sci. Technol. **A4**, 2391 (1986)
4. Time delay CNS-35-76 from Newark Electronics, 4801 N. Ravenswood Avenue, Chicago, IL 60640-4496
5. Available from Tripp Lite, 500 N. Orleans Street, Chicago, IL 60610

6. Vacoa model SOV-050-00-SS, Vacuum Accessories Corporation of America, 390 Central Avenue, Bohemia, NY 11716
7. T. Engel, D.N. Braid, Rev. Sci. Instrum. **57**, 301 (1986)
8. J.J. Zinck, W.H. Weinberg, Rev. Sci. Instrum. **55**, 810 (1984)
9. L.H. Dubois, J. Vac. Sci. Technol. **A6**, 162 (1988)
10. J.T. Fitch, J.J. Sumakeris, G. Lucovsky, J. Vac. Sci. Technol. **A11**, 2871 (1993)

Chapter 50
Protecting Personnel

50.1 Electrical Shocks in the Laboratory

The quantitative effects of electrical current flowing through the human body are listed in the Table 50.1 [1]. It is the current flow through the body that is the fundamental parameter involved in electrical shock, and the level of danger with a high-voltage power supply is related to the current rating of the supply. Safety with electrical devices involves minimizing accidental current flow through the body, especially through the heart. One may have to work with one hand in a pocket when there is danger of shock from high-voltage wires, but of course this is not an adequate protection against shock. Electrical shielding of leads and terminals is an obvious precaution that must be taken.

The avoidance of electrical shocks in the laboratory is carried out with an understanding of the meaning of the electrical ground and how to connect electrical equipment to ground. Figure 50.1a shows a three-wire wall outlet and a polarized male plug. The green ground wire is a non-current-carrying voltage reference line that is connected to the earth somewhere near the laboratory building. The white wire, which is neutral, is connected to the ground wire in the vicinity of the wall outlet. At the point of connection, the electrical potential of the white wire will also be at ground potential. However, as one moves from this connection point, there will be a change in the potential of the white wire owing to the IR drop caused by the current flow through the white wire. One should avoid connecting the white wire to the ground wire in the laboratory. The black wire is the hot wire, and it remains isolated from both the ground and the neutral wire. The wall outlet contains three contacts—the large slot for the neutral wire, the small slot for the hot wire, and the larger hole for the ground connection.

© Springer International Publishing Switzerland 2015

J.T. Yates Jr., *Experimental Innovations in Surface Science*,
DOI 10.1007/978-3-319-17668-0_50

Table 50.1 Quantitative effects of electric current on man

Effect	DC		AC—60 Hz		AC—10,000 Hz	
	Men (mA)	Women (mA)	Men (mA)	Women (mA)	Men (mA)	Women (mA)
Slight sensation on hand	1	0.6	0.4	0.3	7	5
Perception threshold	5.2	3.5	1.1	0.7	12	8
Nonpainful shock—muscular control not lost	9	6	1.8	1.2	17	11
Painful shock—muscular control not lost	62	41	9	6	55	37
Painful shock—let-go control threshold	76	51	16	10.5	75	50
Painful and severe shock—muscular contractions; breathing difficult	90	60	23	15	94	63
Possible ventricular fibrillation						
3-s shocks	500	500	100	100		
T-s shocks			$165T^{-1/2}$		$165T^{-1/2}$	

Figure 50.1b shows two electronic units connected to AC power through three-wire power leads. Usually the chassis of each of the units will be grounded internally to the green grounding wire. However, to make doubly sure that the chassis of each is grounded, it is good practice to connect each chassis to a separate external ground buss by means of the chassis ground connection on each unit. The reason for this is that if the hot wire or any internal high-voltage source should accidentally touch the chassis from the inside, the grounding of the chassis will protect the laboratory worker from accidentally contacting a high electrical potential.

50.2 Accidental Electrical Charging from Ionization Gauge

Accidental activation of the electron bombardment degassing capability of an ionization gauge in the presence of gas pressures that will support an electrical discharge can lead to potentially lethal electrostatic potentials on isolated components of an ultrahigh vacuum system. Figure 50.2 shows a schematic diagram of an ionization gauge operating at pressures in the 10^{-3} Torr range. A plasma is produced when the gauge is accidentally switched to the degas mode as a positive

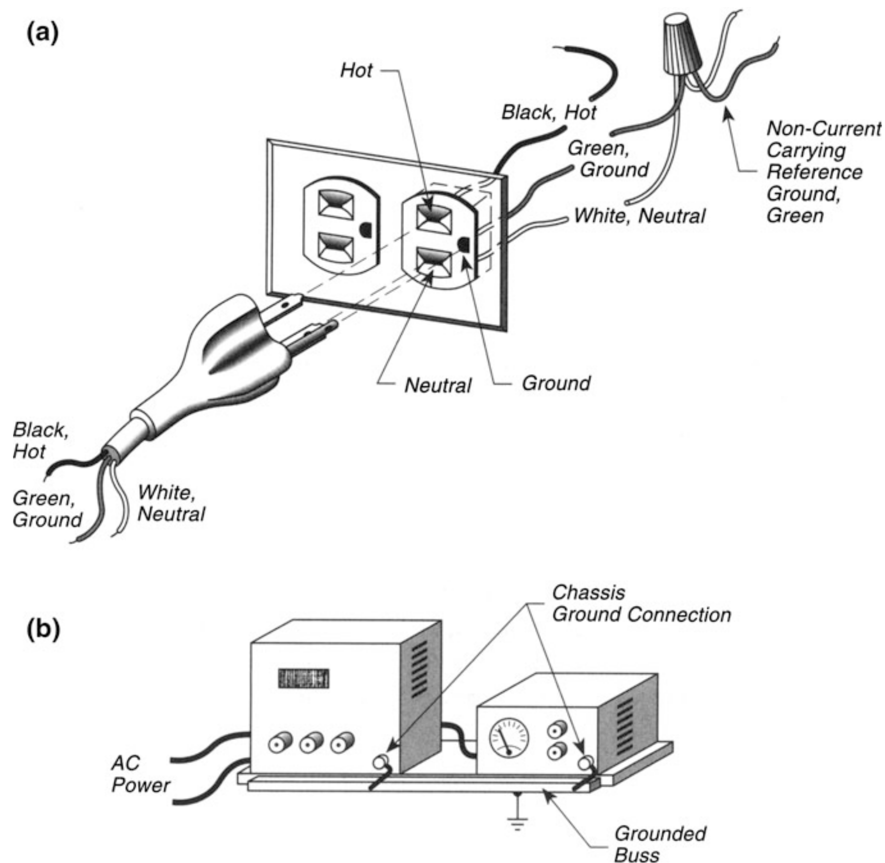

Fig. 50.1 Electrical shocks in the laboratory. **a** 110 V AC wall outlet + polarized plug. **b** Coupled chassis ground

potential in the kilovolt range is applied to the grid for normal electron bombardment cleaning. An electrically isolated feedthrough inside the vacuum system is immersed in the plasma and comes to the plasma potential which is near the potential of the grid. Contact with this feedthrough electrode external to the vacuum system can result in exposure to high electrical potentials, and one example of this

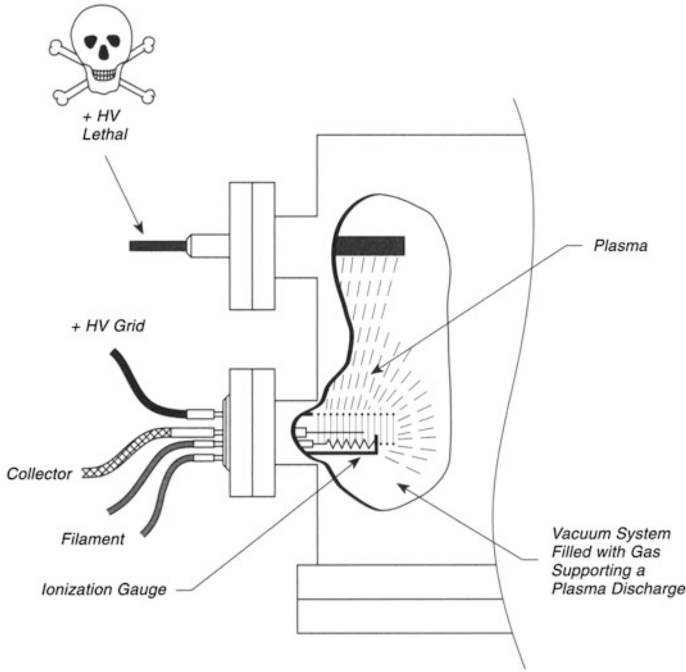

Fig. 50.2 Accidental electrical charging from ionization gauge

effect leading to death has been reported. A safe operating procedure to avoid this type of effect is never to attempt to outgas an ionization gauge when the pressure is high, which would be a pointless thing to do anyway.

Reference

1. W.T. Peria, Department of Electrical Engineering, Institute of Technology, 4-174 EE/CSci Building, 200 Union Street S.E., Minneapolis, MN 55455 (private communication). The table is taken from the Physical Electronics Laboratory Manual, ca. 1965

Appendix A

Useful Books—Experimental Surface Science Methods

Anderson, R.L., *Revealing Microstructures in Metals*, Scientific Paper 425-C000-P2 (West-inghouse Research Laboratories, Pittsburgh, PA, 1961).

Baria, D.N. and Bautista, R.G., *Compilation of Experimental Work on Thermal Emittances of Materials, Part I—Metals; Part II—Non-Metals; Part III—Alloys* (Ames Laboratory, USAEC, Iowa State University, Ames, IA 50010, 1974). Available from National Technical Information Service, Dept. A, Springfield, VA 22151.

Barr, W.E. and Anhorn, V.J., *Scientific and Industrial Glassblowing and Laboratory Techniques* (Instrument Publishing Co., Pittsburgh, PA, 1947).

Beavis, L.C., Harwood, V.J. and Thomas, M.T., *Vacuum Hazards Manual*, AVS Monograph Series M-l, 2nd Ed. (American Vacuum Society, New York, NY 10017, 1979).

Berman, A., *Total Pressure Measurements in Vacuum Technology* (Academic, New York, 1985).

Braker, W. and Mossman, A.L., *Matheson Gas Data Book* (Matheson Gas Products, Secau-cas, NJ 07094, 1980).

Breck, D.W., *Zeolite Molecular Sieves* (Wiley, New York, NY, 1977).

Bunshah, R.F., Ed., *Handbook of Deposition Technologies for Films and Coatings*, 2nd Ed. (Noyes, Park Ridge, NJ, 1994).

Dawson, P.H., *Quadrupole Mass Spectrometry and Its Applications* (American Institute of Physics, New York, NY 10017-3483, 1995).

Drinkwine, M.S. and Lichtman, D., *Partial Pressure Analyzers and Analysis*, AVS Monograph Series, M-3 (American Vacuum Society, New York, NY 10017,1979).

Dushman, S., *Scientific Foundation of Vacuum Technique*, 2nd Ed. (Wiley, New York, NY, 1962).

Ertl, G. and Küppers, J., *Low Energy Electrons and Surface Chemistry*, 1st Ed., (Verlag Chemie, Weinheim, 1974); 2nd Ed., completely revised (VCH Verlagsgesellschaft, mbH, Weinheim, 1985).

Fomenko, V.S., *Handbook of Thermionic Properties* (Translated), Edited by Samsonov, G.V. (Plenum, New York, NY, 1966).

© Springer International Publishing Switzerland 2015

J.T. Yates Jr., *Experimental Innovations in Surface Science*,
DOI 10.1007/978-3-319-17668-0

French, T.E. (Revised by Vierck, C.J.), *A Manual of Engineering Drawing*, 7th Ed. (McGraw Hill, New York, NY, 1947).
Gomer, R., *Field Emission and Field Ionization* (American Institute of Physics, New York, NY 10017-3483, 1993).
Gordon, A. J. and Ford, R.A., *The Chemist's Companion—A Handbook of Data, Techniques, and References* (Wiley, New York, NY, 1972).
Hablanian, M.H., *Diffusion Pumps*, AVS Monograph Series, M-5 (American Vacuum Society, New York, NY 10017, 1983).
Kennard, E.H., *Kinetic Theory of Gases* (McGraw-Hill, New York, NY, 1938).
Kohl, W.H., *Handbook of Materials and Techniques for Vacuum Devices* (American Institute of Physics, New York, NY 10017-3483, 1995).
Leco Corporation, *Metal Etching and Polishing* (St. Joseph, MI 49085, 1977).
Leybold-Heraeus, *Vacuum Technology Its Foundations, Formulae, and Tables* (Leybold-Heraeus, Pittsburgh, PA 15632).
Loeb, L.B., *The Kinetic Theory of Gases*, 3rd Ed., (Dover, NY, 1961).
Lunn, G. and Sansone, E.B., *Destruction of Hazardous Materials in the Laboratory* (Wiley, New York, NY, 1990).
Madey, T.E., Ed., *Vacuum Science and Technology, History of Vacuum Science and Technology*, Vol. 1 (American Vacuum Society, AIP Press, New York, NY, 1984).
Maissei, L.I. and Glong, R., *Handbook of Thin Film Technology* (McGraw-Hill, New York, NY, 1970).
Mark, H.F., Ed., et al., *Encyclopedia of Chemical Technology* (Wiley, New York, NY, 1979).
Moore, J.H., Davis, C.C. and Coplan, M.A., *Building Scientific Apparatus* (Addison-Wesley Reading, MA, 1983).
Müller, E.W. and Tsong, T.T., *Field Ion Microscopy* (Elsevier, New York, NY, 1969).
O'Hanlon, J.F., *A User's Guide to Vacuum Technology* (Wiley, New York, NY, 1980).
The Omega Complete Temperature Measurement Handbook and Encyclopedia, Omega Engineering, Inc., P.O. Box 4047, One Omega Drive, Stamford, CT 06907.
Pierce, J.R., *Theory and Design of Electron Beams* (D. van Nostrand Co., Inc., New York, NY, 1949); 2nd Ed. (1954).
Redhead, P.A., Hobson, J.P. and Kornelsen, E.V., *The Physical Basis of Ultrahigh Vacuum* (American Institute of Physics, New York, NY 10017-3483, 1993).
Redhead, P.A., Ed., Vacuum *Science and Technology, History of Vacuum Science and Technology*, Vol. 2 (American Vacuum Society, AIP Press, New York, NY, 1994).
Roberts, R.W. and Vanderslice, T.A., *Ultrahigh Vacuum and Its Applications* (Prentice-Hall, Engelwood Cliffs, NJ, 1963).
Robinson, N.W., *The Physical Principles of Ultrahigh Vacuum Systems and Equipment* (Chapman and Hall, London, 1968).
Rosebury, F., *Handbook of Electron Tube and Vacuum Techniques* (AIP, American Institute of Physics, New York, NY, 1993).

Roth, A., *Vacuum Sealing Techniques* (Pergamon, Oxford, UK, 1966).
Roth, A., *Vacuum Technology*, 2nd Ed. (North Holland, Amsterdam, 1982).
Sala, A., *Radiant Properties of Materials* (Elsevier, Amsterdam, 1986).
Smithells, C.J. and Brandes, E.A., Eds., *Metals Reference Book*, 7th Ed. (Butterworths, Lon-don and Boston, 1991).
Spangenberg, K.R., *Vacuum Tubes* (McGraw-Hill, New York, NY, 1948).
Strong, J., Neher, H.V., Whitford, A.E., Cartwright, CH. and Hayward, R., *Procedures in Experimental Physics* (Prentice-Hall, New York, NY, 1946).
Thompkins, H.G., *The Fundamentals of Vacuum Technology*, AVS Monograph Series, M-6 (American Vacuum Society, New York, NY 10017,1991).
Thompkins, H.G., *Pumps Used in Vacuum Technology*, AVS Monograph Series, M-9 (American Vacuum Society, New York, NY 10017,1991).
Thompkins, H.G., *Vacuum Gauging and Control*, AVS Monograph Series, M-12 (American Vacuum Society, New York, NY 10017,1994).
Wheeler, E.L., *Scientific Glassblowing* (Wiley, New York, NY, 1958).
Wilson, E.B., *An Introduction to Scientific Research*, 1st Ed. (McGraw-Hill, New York, NY, 1952).
Wilson, N.G. and Beavis, L.C., *Handbook of Vacuum Leak Detection*, AVS Monograph Series, M-2 (American Vacuum Society, New York, NY 10017, 1979).
Wood, E.A., *Crystal Orientation Manual* (Columbia University Press, New York, NY, 1963).
Wutz, M., Adam, H. Walcher, W., *Theory and Practice of Vacuum Technology* (Friedr. Vieweg und Sohn, Braunschweig/Wiesbaden, Germany, 1989).

Appendix B

Manufacturers

See Tables B.1, B.2 and B.3.

Table B.1 United States, UK, and Canadian manufacturers

Company	Products
12R PO Box 159 Cheltenham, PA 19012 Tel: 215-379-3333 Fax: 215-663-8847	Tools for scientists
II-VI 375 Saxonburg Blvd. Saxonburg, PA 16056 Tel: 412-352-4455 Fax: 412-352-4980	Infrared materials
Accuratus RD4 Brass Castle Rd. Washington, NJ 07882 Tel: 908-689-0880 Fax: 908-689-8796	Macor machineable glass; ceramics
Ace Glass, Inc. 1430 Northwest Blvd. PO Box 688 Vineland, NJ 08360 Tel: 800-223-4524 Fax: 800-543-6752 or 63941 S. Hancock St. PO Box 996 Louisville, KY 40201 Tel: 800-626-5381 Fax: 800-635-4698	Glass products

(continued)

© Springer International Publishing Switzerland 2015

J.T. Yates Jr., *Experimental Innovations in Surface Science*,
DOI 10.1007/978-3-319-17668-0

Table B.1 (continued)

Company	Products
Ace Plastic Co. 494 Wortman Ave. Brooklyn, NY 11208-5428 Tel: 212-523-5500 Fax: 407-659-3816	Plastic balls for crystal models
ACF Metals 2239 E. Kleindale Rd. Tucson AZ 85719-2440 Tel: 520-325-9557 Fax: 520-32509493	Metal foils, carbon foils
Acheson Colloids 1607 Washington Ave. PO Drawer 611747 Port Huron, MI 48061-1747 Tel: 800-255-1908 Fax: 313-984-1446	Aquadag—colloidal graphite
Ad-Vance Magnetics, Inc. 625 Monroe St. PO Box 69 Rochester IN 46975 Tel: 219-223-3158 Fax: 219-223-2524	Magnetic shields
Advanced Ceramics Corp. P.O. Box 94924 Cleveland, OH 44101-4924 or 11907 Madison Ave. Lakewood,OH 44107-5026 Tel: 800-822-4322 Fax: 216-529-3954	Graphite monochromators
Advent Associates, Ltd. 6663 Woodwell St. Pittsburgh, PA 15217 Tel: 412-422-8100 Fax: 412-422-8101	Ion guns, vacuum components
Advent Research Materials LTD Blyth Road Industrial Estate Halesworth Suffolk England 1P19 8DD Tel: 44 1986 874555 Fax: 44 1986874557	Metals, alloys, foils, sheets, wires, rods, tubes
AESAR Johnson Matthey, Inc. PO Box 1087 Seabrook, NH 03874 Tel: 1-800-343-1990	Single crystals

(continued)

Table B.1 (continued)

Company	Products
AIRCO Lansbrook Rd. Acton, MA 01720 Tel: 508-263-7769 Fax: 508-263-6014	Specialty gases
Aithaca 50 Charles Lindbergh Blvd. Suite 400 Uniondale, NY 11553 Tel: 516-229-2330 Fax: 516-227-2350	Single crystals
Alberox Industrial Park New Bedford, MA 02745-1289 Tel: 508-995-1725 Fax: 508-995-6954	Feedthroughs
Alcatel Phil Danielson Danielson Associates, Inc. PO Box 157 51471/2 Main St. Donners Grove, IL 60515 Tel: 612-370-1279	Pumps, mechanical
Aldrich Chemical Co. PO Box 2060 Milwaukee, WI 53201 Tel: 414-273-3850 Fax: 414-273-4979	Chemicals
Alfa Johnson Matthey 30 Bond St. Ward Hill, MA 01835-8099 Tel: 800-343-0660 Fax: 800-322-4757	Chemicals, high purity electronic grade
Allen Datagraph, Inc. Industrial Way Salem, NH 03079 Tel: 800-258-6360 Fax: 603-893-9042	X-Y recorders/plotters
Alltech Assoc. Inc. 2051 Waukegan Rd. Deerfield, IL 60015 Tel: 800-255-8324 Fax: 708-948-1078	Graphite fittings for Swagelok fittings
American Laboratory PO Box 3220 Lowell, MA 01853-9878	Annual buyer’s edition

(continued)

Table B.1 (continued)

Company	Products
Analog Devices One Technology Way Norwood, MA 02062-9106 Tel: 617-329-4700 Fax: 617-326-8703	Computer chips and boards
APD Cryogenics, Inc. 1833 Vultee St. Allentown, PA 18103-4783 Tel: 610-791-6700 Fax: 610-791-0440	Cryopumps; Helitron He coolers
Aremco 23 Snowden Ave. PO Box 429 Ossining,NY 10562-0429 Tel: 914-762-0685 Fax: 914-762-1663	Single crystals
Automation Gages, Inc. 850 Hudson Ave. Rochester, NY 14621 Tel: 1-800-922-0329 Fax: 716-338-7370	Translation stages
Baikowski International Corp. 6006 Old Pineville Rd. Charlotte, NC 28210 Tel: 704-523-1707	Alumina polishing powder
Baker Process Equipment PO Box 898 308-Moon Clinton Rd. Coraopolis, PA 15108 Tel: 412-264-8271 Fax: 412-264-8758	Filters, dryers, purifiers
Balzers 8 Sayamore Park Rd. Hudson, NH 03051 Tel: 603-595-3250 Fax: 603-595-3200	Mass spectrometers
Barnes/Spectra Tech. 652 Glenbrook Rd. Stamford, CT 06906 Tel: 800-243-9186	IR spectrometers
Bearings, Inc. 5536 Baum Blvd. Pittsburgh, PA 15232 Tel: 412-681-4900	Ball bearing power transmission units
Berghof/America PO Box 6029 Concord, CA 94524 Tel: 800-544-5004 Fax: 510-827-1189	Teflon products

(continued)

Table B.1 (continued)

Company	Products
Bertan 121 New South Rd. Hicksville, NY 11801 Tel: 516-433-3110 Fax: 516-935-1766	High-voltage power supplies
Bid Service PO Box 128 Bradley Beach, NJ 07720 Tel: 908-775-8300 Fax: 908-774-1443	Surplus vacuum and semiconductor processing equipment
Blake Industries, Inc. 660 Jerusalem Rd. Scotch Plains, NJ 07076 Tel: 908-233-7240	X-ray instruments
Bomco Inc. 125 Gloucester Ave. Gloucester, MA 01930-2294 Tel: 508-283-9000 Fax: 508-283-2882	Quartz-Mo seals
Bristol Organics LTD Sharpness Docks Berkeley Glos GL 13 9UG UK Tel: 0453-811400	Fluorine compounds (organic)
Brush-Wellman Elmore, OH 43416 Tel: 419-862-2745	Beryllium
Buckbee Mears Corp. 245 East 6th St. St. Paul, MN 55101-1959 Tel: 612-228-6400 Fax: 612-228-6572	Photolithography W grid
Buehler Analyst 41 Waukegan Rd. PO Box 1 Lake Bluff, IL 60044 Tel: 847-295-6500 Fax: 847-295-7979	Crystal cutting, polishing, fiber optics, optical instrumentation
C&H Sales 2176 E. Colorado Blvd. PO Box 5356 Pasadena, CA 91117-9988 Tel: 800-325-9465 Fax: 818-796-4875	Surplus equipment
C.M. Furnaces, Inc. 103 Dewey St. Bloomfield, NJ 07003 Tel: 201-338-6500 Fax: 201-338-1625	Evaporation sources, filaments

(continued)

Table B.1 (continued)

Company	Products
California Fine Wire Co. PO Box 446 Grover, CA 93483-0446 Tel: 805-489-5144 Fax: 805-489-5352	Wire, thermocouple wire, fine wire
Cambridge Isotopes 50 Frontage Rd. Andover, MA 01810-5413 Tel: 800-322-1174 Fax: 508-749-2768	Isotopes, stable
Canberra Industries, Inc. Nuclear Products Group 800 Research Pkwy. Meriden, CT 06450 Tel: 203-238-2351 Fax: 203-235-1347	Counting electronic
Ceramaseal PO Box 260, Rte. 20 New Lebanon, NY 12125 Tel: 518-794-7800 Fax: 518-794-8080	Feedthroughs
Cercoa ECS Co. 55 Webster Ave. New Rochelle, NY 10801 Tel: 914-636-4325 Fax: 914-636-3701	Ceramic materials
Chemvac Associates 808 High Point Ave. Virginia Beach, VA 23451 Tel: 804-422-9823	Vacuum joints
Chromalox 641 Alpha Dr. Pittsburgh, PA 15238 Tel: 800-443-2640 Fax: 412-967-5148	Heaters
Cliftronics, Inc. 2 South St. Clifton Springs, NY 14432 Tel: 315-462-9471	Electronics equipment and supplies, electron guns
Cole-Palmer 7425 North Oak Park Ave. Chicago, IL 60648 Tel: 800-323-4340	Laboratory supplies-general
Comstock 1005 Alvin Weinberg Dr. Oak Ridge, TN 37830 Tel: 615-483-7690 Fax: 615-481-3884	Electron energy analyzers, electron guns

(continued)

Table B.1 (continued)

Company	Products
Connecticut Hard Rubber Co. PO Box 2560 Meriden, CT 06450 Tel: 203-634-0555	Teflon tape
Connecticut Technology PO Box 524 Stratford, CT 06497 Tel: 203-375-5015 Fax: 203-375-0541	Langmuir-Blodgett film deposition
Cooke Vacuum Products 13 Merritt St. South Norwalk, CT 06854 Tel: 203-853-9500 Fax: 203-858-9553	Vacuum components
Copper & Brass Sales 17401 Ten Mile East Detroit, MI 48021 Tel: 800-926-2600 Fax: 313-775-5078	UHV soft aluminized bronze
Cory Lab Inc. 823 5th St. Menominee, MI 49858 Tel: 906-863-9336	Sapphire/metal feedthroughs
Cotronics 3379 Shore Pkwy. Brooklyn, NY 11235 Tel: 718-646-7996 Fax: 718-646-3028	Ceramic materials
CREE 2810 Meridian Pkwy. Durham, NC 27713 Tel: 919-361-5709 Fax: 919-361-4630	Silicon carbide
Cryofab PO Box 485 540 N. Michigan Ave. Kenilworth, NJ 07033 Tel: 207-686-3636 Fax: 908-686-9536	Cryogenic equipment, dewars, etc.
Cryomech Inc. 1630 Erie Blvd. E. Syracuse, NY 13210 Tel: 315-475-9692 Fax: 315-422-1202	Cryogenic equipment

(continued)

Table B.1 (continued)

Company	Products
Custom Cable Corp. 242 Butler St. PO Box 1050 Westbury NY 11590-3193 Tel: 800-242-2253 Fax: 516-334-3989	Eletric equipment and supplies, coaxial cable
CVC 525 Lee Rd. PO Box 1886 Rochester, NY 14603 Tel: 716-458-2550	Vacuum products
CVT Engineering Ltd. 110 Shawmut Rd. Canton, MA 02021	Vacuum transfer devices
Dabilier 207 Radley Rd. Abingdon Oxon OX14 3XA England Tel: 0235-28271	Ion sources
Daedal, Inc. 1140 Sandy Hill Rd. Harrison City, PA 15636 Tel: 800-245-6903 Fax: 412-861-3330	Positioning equipment
DEI 2301 Research Blvd. Suite 105 Fort Collins, CO 80526 Tel: 970-493-1901 Fax: 970-493-1903	Pulse generators (high voltage)
DoAll Northern IL. Co. 236 Laurel Ave. Des Plaines, IL 60016 Tel: 800-955-8191 Fax: 708-824-4340	Machine tools, precision gauges, cutting tools
Dow Corning PO Box 0994 Midland, MI 48640-0994 Tel: 517-496-4000	Silicon products
Duniway Stockroom Corp. 1600 N. Shoreline Blvd. Mountain View, CA 94043 Tel: 800-446-8811 Fax: 415-965-0764	Rebuilt ion pumps and vacuum components
Dupont 1007 Market St. N-2426-A Wilmington, DE 19898 Tel: 800-527-2601 Fax: 302-773-2291	Polymers

(continued)

Table B.1 (continued)

Company	Products
E. McGrath, Inc. 35 Osborne St. Salem, MA 01970-2599 Tel: 508-744-3546 Fax: 508-741-4020	Used and new surplus equipment
Ealing Corp. 89 Doug Brown Way Holliston, MA 01746 Tel: 800-343-4912 Fax: 508-429-7893	Optical components
East Coast Sales 11 Business Park Dr. Armonk, NY 10504 Tel: 914-273-1400 Fax: 914-273-5866	Tools-semiconductors
Eastman Kodak Co. 5/81 RC MC 02010 Rochester, NY 14650-2010 Tel: 716-722-4385 ext. 1704 Fax: 716-477-4947	Irtran optics
Edmond Scientific A-415 Edscorp. Bldg. Barrington, NJ 08007 Tel: 609-573-6250 Fax: 609-573-6295	Optics, etc.
Edwards High Vacuum 301 Ballardvale St. Wilmington, MA 01887 Tel: 508-658-5410 Fax: 508-658-7969	Vacuum components
Electrofusion Corp. 34325 Ardenwood Blvd. Fremont, CA 94536 Tel: 415-795-1100	Beryllium windows
Electronic Space Products International 1050 Bensen Way Ashland, OR 97520 Tel: 800-638-2581	
Energy Beam Sciences 11 Bowles Rd. PO Box 468 Agawam MA 01001 Tel: 800-992-9037 Fax: 413-789-2786	LaB_6 cathodes

(continued)

Table B.1 (continued)

Company	Products
Energy Research & Generation, Inc. 900 Stanford Ave. Oakland, CA 94608 Tel: 510-658-9785 Fax: 510-658-7428	Aluminum foams
Engelhard Industries Division Engelhard Corp. Electronic Materials Systems 1 West Central Ave. East Newark, NJ 07029 Tel: 201-268-7800	Liquid bright gold
EPI MBE Products Group 1290 Hammond Rd. St. Paul, MN 55110 Tel: 612-653-0488 Fax: 612-653-0725	MBE products
Esco 171 Oakridge Rd. Oakridge, NJ 07438 Tel: 800-327-1399 Fax: 201-697-3011	Optical materials-sapphire
Extrel Products 575 Epsilon Dr. Box 11512 Pittsburgh, PA 15238-2838 Tel: 412-963-7530 Fax: 412-963-6578	Quadrupole mass spectrometers
Fairfield Synthesis PO Box 20 Blythewood, SC 29016 Tel: 803-754-3856 Fax: 803-754-8833	Custom organic synthesis
Farchan 2603 NW 74th Place Gainesville, FL 32653 Tel: 352-378-5864	Organic chemicals
FEI PO Box 654 McMinnville, OR 97128 Tel: 503-648-7075	Electron guns
Fil-Tech 1143 Diamond St. San Francisco, CA 94114	Vacuum supply filaments

(continued)

Table B.1 (continued)

Company	Products
Fine Science Tools 373 Vintage Park Dr. Foster City, CA 94404 Tel: 800-521-2109 Fax: 415-349-3729 e-mail: info@finescience. com	Surgical tools
Fluorocarbon Corp. 10871 Kyle St. PO Box 520 Los Alamitas, CA 90720 Tel: 213-594-0941	Teflon
Fluorochem Ltd. Wesley St. Old Glossop Derbyshire SK13 9RY England Tel: 04574-68921	Molecular formular index
Fluoroware 102 Jonathan Blvd. N. Chaska, MN 55318 Tel: 612-448-3131 Fax: 612-448-5576	Teflon-semiconductor tools, handling equipment
Foametal, Inc. 37645 Vine St. Willoughby, OH 44904 Tel: 216-951-9081 Fax: 216-951-9360	Metal foams
Friedfich & Diownick, Inc. 2127 Wheaton Ave. PO Box 230 Millville, NJ 08332 Tel: 609-825-0305 Fax: 609-327-4299	Glass capillary
Furon 4402 Corporate Center Dr. Los Alamitos, CA 90720 Tel: 714-995-1818 Fax: 714-761-1270	Gaskets, seals
Fyrepel PO Box 518 Newark, OH 43055 Tel: 614-344-0391 Fax: 614-344-6025	Aluminized fiberglass sheet
Galileo Galileo Park PO Box 550 Sturbridge, MA 01566 Tel: 800-648-1800 Fax: 508-347-9191	Channeltron and chaneel plate multipliers

(continued)

Table B.1 (continued)

Company	Products
Gallard/Schlesinger 584 Mineola Ave. Carle Place, NY 11514 Tel: 516-333-5600 Fax: 516-333-5628	Chemicals, metals
Gast Manufacturing Corp. 2300 NM 63 #139 Benton Harbor, MI 49022 Tel: 616-926-6171	Industrial equipment and supplies, carbon vane vacuum pump
Glassfab, Inc. PO Box 1880 Rochester, NY 14603 Tel: 716-262-4000 Fax: 716-454-4305	
Goodfellow Metals 800 Lancaster Ave. Berwyn, PA 19302-1780 Tel: 610-640-1612 Fax: 800-283-2020	Metal foils
Hamamatsu 420 South Ave. Middlesex, NJ 08846 Tel: 908-469-6640	Photomultipliers
Hamilton Technology, Inc. 101 N. Queen St. PO Box 4787 Lancaster, PA 17604 Tel: 717-299-2581 Fax: 717-397-8510	HAVAR foil
Hanovia Division of Engelhard Industries 1 West Central Ave. East Newark, NJ 07029 Tel: 201-268-7800	Organometallic paints
Hansen R.G. & Associates 631 Chapala St. Santa Barbara, CA 93101 Tel: 805-564-3388 Fax: 805-963-0733	Laboratory cryogenic systems and components
Harrick Scientific Corp. Croton Dam Rd. Box 867 Ossining, NY 10562 Tel: 914-762-0020	IR-VIS-UV accessories, spectrometers

(continued)

Table B.1 (continued)

Company	Products
Harshaw Optical 6801 Cochran Rd. Solon, OH 44139 Tel: 800-472-5656 Fax: 216-349-6581	IR and UV windows
Helicoflex 400 Myrtle Ave. Boonton, NJ 07005 Tel: 201-334-8100	Vacuum fittings
Helicoflex Co. 118W. 12th St. Parkerburg, WV 26101 Tel: 304-428-1644 Fax: 304-428-3490 e-mail: hxrpvseals@aol.com	Seals
Helicoflex Co. PO Box 9889 Columbia, SC 29290 Tel: 803-783-1880 Fax: 803-783-4279	Seals
Hex Metal Specialties Inc. 515 Commerce Dr. Fairfield, CT 06430 Tel: 203-384-0331 Fax: 203-368-4082	Single crystals
High Vacuum Apparatus 7055 Engle Rd. Suite 6-607 Middleburg Hts., OH 44130 Tel: 216-826-0559 Fax: 216-826-1171	Gate valves
Honeywell Industrial Automation & Controls 1100 Virginia Dr. Washington, PA 19034	Electronics
Honeywell Micro Switch Div. 11 W. Spring St. Freeport, IL 61032-4353 Tel: 800-537-6945 Fax: 815-235-5574	Electronics
IBM Instruments, Inc. Orchard Park PO Box 332 Danbury, CT 06810	FTIR spectrometers

(continued)

Table B.1 (continued)

Company	Products
ICON 19 Ox Bow Ln. Summit, NJ 07901 Tel: 908-273-0449 Fax: 908-273-0449	Isotopes
Indium Corporation of America PO Box 269 1676 Lincoln Ave. Utica, NY 13503-0269 Tel: 800-448-9240 Fax: 800-221-5759	Indium
Infrared Laboratories, Inc. 1808 E. 17th St. Tucson, AZ 85719-6505 Tel: 520-622-7074 Fax: 520-623-0765	Dewars, He detectors
Insaco 1365 Canary Rd. PO Box 9006 Quakertown, PA 18951-9006 Tel: 215-536-3500 Fax: 215-536-7750	Sapphire fabrications
Instrument Specialties Co. PO Box A Delaware Water Gap, PA 18327 Tel: 717-424-8510 Fax: 717-424-6213	Springs
Instruments SA, Inc. 3880 Park Ave. Edison, NJ 08820-3097 Tel: 800-438-7739 Fax: 908-549-5125	Monochromators, optical
Insulator Seal, Inc. 23874-B Cabot Blvd. Hayward, CA 94545-1661 Tel: 800-548-9509 Fax: 510-887-7475 e-mail: sales@isi-seal.com	Feedthroughs-ceramic/metal
Intek Services, Inc. 7 McMillan Way Suite 101 Newark, DE 19713 Tel: 302-366-8530	Teflon suspension

(continued)

Table B.1 (continued)

Company	Products
International Crystal Lab 11 Erie St. Garfield, NJ 07026 Tel: 201-478-8944 Fax: 201-478-4201	IR accessories
IonSpec One Longstreet Irvine, CA 92714 Tel: 714-857-0793	Fourier transform mass spectrometry
Isotec, Inc. 3858 Benner Rd. Miamisburg, OH 45432-4304 Tel: 513-859-1808 Fax: 513-859-4878 e-mail: isosales@isotec.com	Isotopic gases
Israelachvili Instrument 2233 Foothill Ln. Santa Barbara, CA 93105 Tel: 805-899-9292 Fax: 805-899-9190	Surface force intrument
J&H Berge, Inc. 4111 S.Clinton Ave. So. Plainfield, NJ 07080-0310 Tel: 1-800-684-1234	Ball bearings, ultrasonic (nalgene) cleaners
Jensen Tools 7815 S. 46th St. Phoenix, AZ 85044-5399 Tel: 800-426-1194 Fax: 800-366-9662	Tools
JML Direct 690 Portland Ave. Rochester, NY 14621-5196 Tel: 716-342-9482 Fax: 716-342-6125	Optical components
Keithley 28775 Aurora Rd. Cleveland, OH 44139-1891 Tel: 216-248-0400 Fax: 216-248-6168	Electronics-measurement
Kepco 131-38 Sanford Ave. Flushing, NY 11352 Tel: 718-461-7000 Fax: 718-767-1102	Power supplies

(continued)

Table B.1 (continued)

Company	Products
Kimball Physics Inc. 311 Kimball Hill Rd. Wilton, NH 03086 Tel: 603-878-1616 Fax: 603-878-3700	Electron and ion guns, LaB_6 emitters
Kulite Semiconductor Products, Inc. 1 Willow Tree Rd. Leonia, NJ 07605 Tel: 201-461-0900 Fax: 201-461-0990	Strain gauge
Lab Safety Supply PO Box 1368 Janesville, WI 53547-1368 Tel: 800-356-0783 Fax: 800-543-9910	Safety lab equipment
Lake Shore Cryotonics, Inc. 64 Walnut St. Westerville, OH 43081-2399 Tel: 614-891-2243 Fax: 614-891-1392	Cryogenics, cryogenic thermometry
Lamba 515 Broad Hollow Rd. Melville, NY 11747-3700 Tel: 516-694-4200	Power supplies
Lasertechnics 5500 Wilshire Ave., NE Albuquerque, NM 87113 Tel: 505-822-1123 Fax: 505-821-2213	Pulsed valve
LDS Vacuum Products, Inc. 980 Sunshine Ln. Aitamonte Springs, FL 32714 Tel: 407-862-4643 Fax: 407-862-8723	Vacuum supplies
Lebow Co. 5960 Mandarin Ave. Goleta, CA 93117 Tel: 805-964-7117 Fax: 805-964-7117	
Leisk Albert Dr., Burgess Hill West Sussex, RH15 9NX England Tel: 044-46-45821 2	Flanges and gaskets

(continued)

Table B.1 (continued)

Company	Products
Lenox Laser 1 Green Glade St. Phoenix, MD 21131 Tel: 301-592-3106	Laser beam machining, laser repair
Lesker, Kurt J. Co. 1515 Worthington Ave. Clairton, PA 15025 Tel: 412-233-4200 Fax: 412-233-4275	Vacuum components
Linseis PO Box 666 Princeton, NJ 08550 Tel: 609-799-6282 Fax: 209-799-7739	X-Y recorders
Love Controls Corp. 475 Wheeling Rd. Wheeling, IL 60090 Tel: 800-828-4588 Fax: 708-541-7366	Temperature controllers
M-G Industries 175 Meister Ave. PO Box 5328 North Branch, NJ 08876 Tel: 610-695-7400 Fax: 610-695-7600	Gases
Magnetic Shielding Corp. 750 N. Thomas Dr. Bensenville, IL 60106 Tel: 708-766-7800 Fax: 708-766-2813	Magnetic shields
Mark V Laboratory 18 Kripes Rd. East Granby, CT 06026 Tel: 800-243-9776 Fax: 203-653-4087	Metallographic equipment
Markson PO Box 1359 Hillsboro, OR 97123-9981 Tel: 800-528-5114 Fax: 800-858-2243	Lboratory supplies/general
Materials Research Corp. 542 Rte. 303 Orangeburg, NY 10962 Tel: 914-359-4200 Fax: 914-359-3453	High-purity materials for thin film deposition
McAllister W.280-T Prairie Ave. Cover D'Alend, ID 83814 Tel: 208-772-9527	STM, Kelvin probe, vacuum components

(continued)

Table B.1 (continued)

Company	Products
MDC 2384 Cabot Blvd. Hayward, CA 94545-1651 Tel: 800-443-8817 Fax: 510-887-0626	Vacuum components
Melles Grot 1770 Kettering St. Irvine, CA 92714 Tel: 800-835-2626 Fax 714-261-7589	Optical items
Metal Bellows 1075 Providence Highway Sharon, MA 02067 Tel: 617-784-1400 Fax: 617-784-1405	Bellows, etc.
Metal Crystals & Oxides, Ltd. Button End, Harston CB2 5WX Cambridge, England Tel: 0223-872022	Metals (pure), metal foils, single crytstal metals
Metaleurop 111 Richmond St. West Suite 418 Toronto, Ontario Canada Tel: 416-366-3954 Fax: 416-366-0586	Single crystals
Meyer Tool & Mfg., Inc. 4601 Southwest Highway Oak Lawn, IL 60453 Tel: 708-425-9080 Fax: 708-425-2612	Vacuum chambers-fabrication
Micromeritics One Micrometitics Dr. Norcross, GA 30093-1877 Tel: 770-662-3633 Fax: 770-662-3696	Particle size and surface area measurement instruments
Midac 17911 Fifth Ave. Irvine, CA 92714 Tel: 714-660-8558 Fax: 714-660-9334	IR emission
Miller-Stephenson Chemical Co. Beckus Ave. Danbury, CT 06810 Tel: 203-743-4447 Fax: 203-791-8702	Fluorocarbon lubricants

(continued)

Table B.1 (continued)

Company	Products
Minnesota Valley Engineering, Inc. 407 Seventh St. NW New Prague, MN 56071 Tel: 612-758-4484	Vacuum insulated piping systems
MKS Six Shattuch Rd. Andover, MA 01810-2449 Tel: 800-227-8766 Fax: 508-975-0093	Capacitance manometers
MMR Technologies 1400 N. Shoreline Blvd. A5 Mountain View, CA 94043-1312 Tel: 415-962-9620 Fax: 415-962-9647	Cryogenic-closed cycle refrigerators
Monocrystals 24400 Highland Rd. Richmond Heights, OH 44143 Tel: 216-531-9820 Fax: 216-531-9789	Single crystals
MSA PO Box 426 Pittsburgh, PA 15230 Tel: 800-672-2222 Fax: 412-967-3451	Air pollution sensors
MSC 151 Sunnyside Blvd. Plainview, NY 11803 Tel: 800-753-7937 Fax: 516-349-0265	Machinist's tools
MTS Systems Corp. Box 24012 Minneapolis, MN 55424 Tel: 612-937-4000 Fax: 612-937-4515	
Munns Mfg., Inc. 5885 La Ribera St. Livermore.CA 94550 Tel: 510-447-0310 Fax: 510-447-0110	Vacuum equipment (UHV)
MVE 8011 34th Ave., S. Bloomington, MN 55425-1636 Tel: 800-247-4446 Fax: 612-853-9661	Vacuum-insulated products

(continued)

Table B.1 (continued)

Company	Products
National Instruments 6504 Bridge Point Pkwy. Austin, TX 78730-5039 Tel: 512-794-0100 Fax: 512-794-8411 Website: www.natinst.com	LabVIEW, other instrumentation for data analyses and acquistion
Neslab Instruments PO Box 1178 Portsmouth, NH 03802-1178 Tel: 603-436-9444 Fax: 603-436-8411	Cooling units
New Focus, Inc. 340 Pioneer Way Mountain View, CA 94041 Tel: 415-961-2108 Fax: 415-961-6072	Optical components
Newark Electronics 4801 N. Ravenswood Ave. Chicago, IL 60640-4496 Tel: 312-784-5100 Fax: 312-907-5217	Electronics distributor
Newport Corp. 1791 Deere Ave. Irvine, CA 92714 Tel: 800-222-6440 Fax: 714-253-1680	Pulsed valves, laser optical supports
Newport Optical Costa Mesa, CA	Optical components
Nolan Supply PO Box 6289 111-115 Leo Ave. Syracuse, NY 13217 Tel: 800-736-2204 Fax: 315-463-0316	Tools
Omega PO Box 4047 One Omega Dr. Stamford, CT 06907 Tel: 800-826-6342 Fax: 203-359-7700	Thermocouples, etc.
Opthos Instruments Inc. 17805 Caddy Dr. Rockville, MD 20855 Tel: 301-926-0589 Fax: 301-963-3060	RF sources

(continued)

Table B.1 (continued)

Company	Products
Oriel 250 Long Beach Blvd. PO Box 872 Stratford, CT 06497-0872 Tel: 203-377-8282 Fax: 203-378-2457	Micrometer positioners
Ortec PO Box 1397 Easley, SC 29640 Tel: 803-859-1471 Fax: 803-859-8580	Electronics
Osaka Vacuum 5547 Beacon St. Pittsburgh, PA 15217 Tel: 412-422-8100 Fax: 412-422-8101	Turbo pumps
Park Scientific Instruments 1171 Borregas Ave. Sunnyvale, CA 94089-1304 Tel: 800-776-1602 Fax: 408-747-1601	STM
PCR PO Box 14166 Gainesville, FL 32802 Tel: 904-376-8246 Fax: 904-371-6246	Fluorinated compoundsm silicanes
Perkin Elmer 6509 Flying Cloud Dr. Eden Prairie, MN 55344 Tel: 800-237-3603 Fax: 612-828-6322	Vacuum equipment and electron spectrometers
Petrarch Systems Inc. Bartram Rd. Bristol, PA 19007 Tel: 215-781-9255	Silicon compounds
Pfizer, Inc. 235 E. 42nd St. New York, NY 10017 Tel: 212-573-2323 Fax: 212-573-1166	Chemicals, pyrolytic graphite
Phoenix Equipment Co. 100 Fernwood Ave. Rochester, NY 14621-5684 Tel: 716-266-5550 Fax: 716-266-1598	Used equipment-scientific

(continued)

Table B.1 (continued)

Company	Products
PIC Design PO Box 1004 Benson Rd. Middlebury, CT 06762 Tel: 800-243-6125 Fax: 203-758-8271	Gears
Pittsburgh Corning 800 Presque Isle Dr. Pittsburgh, PA 15239 Tel: 412-327-6100 Fax: 412-327-5890	Insulation/fiberglass
Polysciences 400 Valley Rd. Warrington, PA 18976-2590 Tel: 800-523-2575 Fax: 800-343-3291 e-mail: polysci@tiggar.jvnc. com	Metals
Polytec PI Inc. 3001 Redhill Ave. Costa Mesa, CA 92626 Tel: 714-850-1835 Fax: 714-850-1831	Piezoelectric translators
Praxair 3101 Preble Ave, NE Pittsburgh, PA 15233 Tel: 412-766-6900 Fax: 412-766-9532	Specialty gases
Precision Laser Services Inc. 314 E. Wallace Fort Wayne, IN 46803 Tel: 219-744-4375 Fax: 219-744-5666	Drilling, welding, cutting
Progressive Technology Inc. 12122 Dry Creek Rd. #1021 Auburn, CA 45602 Tel: 916-823-5047 Fax: 916-823-3275	Ceramic tubing, washers, bolts, nuts, and balls
Pyrometer Instrument Co. 234 Industrial Pkwy. PO Box 70 Northvale, NJ 07647 Tel: 201-768-2000 Fax: 201-768-2570 e-mail: pyroinfo@pyrometer.com	Optical pyrometers

(continued)

Table B.1 (continued)

Company	Products
Qualitech Gas Products, Inc. 110 Nichol Ave. McKees Rocks, PA 15136 Tel: 412-771-7660	Gases
Quantar Technology, Inc. 3004 Mission St. Santa Cruz, CA 95060-5700 Tel: 408-429-5227 Fax: 408-429-5131	
Queensgate Instruments, Inc. Suite 600 90 Merrick Ave. East Meadow, NY 11554 Tel: 516-357-3900 Fax: 516-357-9686	Nano positioning systems
R.G. Hansen & Associates 631 Chapala St. Santa Barbara, CA 93101 Tel: 805-564-3388 Fax: 805-963-0733	Cryogenic equipment
R.M. Jordan Co. 990 Golden Gate Terrace Grass Valley, CA 95945 Tel: 916-272-4580 Fax: 916-272-2955	Reconditioned quadrupole mass spectrometers, etc.
Rama Corporation 600 W. Esplanade Ave. San Jacinto, CA 92583 Tel: 909-654-7351 Fax: 909-654-3748	Heaters-bakeout
Raychem 300 Constitution Dr. Menlo Park, CA 94025 Tel: 415-361-3860	Electronic equipment and supplies, SME alloys
RHK Technology 209 Voorheis Rd. Pontiac, MI 48053 Tel: 313-858-8958	High-resolution electron energy loss spectrometer
S&J Trading, Inc. PO Box 337 Glenoaks, NY 11004	Mica
SAES Getters, Inc. 1122 East Cheyenne Mountain Blvd. Colorado Springs, CO 80906 Tel: 719-576-3200 Fax: 719-576-5025	Alkali getters

(continued)

Table B.1 (continued)

Company	Products
Sargeant-Welch PO Box 5229 Buffalo Grove, IL 60089-5229 Tel: 800-727-4368 Fax: 800-676-2540 e-mail: sarwel@sargentwelch.com	Vacuum components
Saville & Co. 414 Rodi Rd. PO Box 27286 Pittsburgh, PA 15235 Tel: 412-731-6401 Fax: 412-731-4098	Shim stock
Scientific Gas Products 2330 Hamilton Blvd. S. Plainfield, NJ 07080-9986 Tel: 201-754-7700	Gases
Scientific Instrumentation Services, Inc. 1027 Old York Rd. Ringoes, NJ 08551-1039 Tel: 908-788-5550 Fax: 908-806-6631	
Scientific Instruments Rd. 3, Box 593 Ringoes, NJ 08551-9675 Tel: 908-788-5550	Cryogenics, closed cycle refrigerators, low temperature thermocouples (Cr/Fe:Au)
Scott Specialty Gases 6141 Easton Rd. PO Box 310 Plumsteadville, PA 18949-0310 Tel: 800-220-4436 Fax: 215-766-0320	Gases
Sensote, Inc. 1202 Chesapeake Ave. Columbus, OH 43212 Tel: 800-848-6564 x880 Fax: 614-486-0506	
Setra 45 Nagog Park Acton, MA 01720 Tel: 508-263-1400 or 800-257-3872 Fax: 508-264-0292	Pressure gauge, digital capacitance manometers

(continued)

Table B.1 (continued)

Company	Products
Shipley Company, Inc. 2300 Washington St. Newton, MA 02162 Tel: 617-969-5500	Photo resist coating materials
Sigmund Cohn Corp. 121 S. Columbus Ave. Mt. Vernon, NY 10553 Tel: 914-664-5300 Fax: 914-664-5377	Very fine wire, precision fabricated metals
Small Parts 13980 NW 58th Ct. Box 4650 Miami Lakes, FL 33014-0650 Tel: 800-220-4242 Fax: 800-423-9009	Parts, small nut, bolts, gears, washers, miscellaneous parts-stainless steel PO mechanical components
South Bay Technology 1120 Via Callejon San Clemente, CA 92672 Tel: 714-492-2600 Fax: 714-492-1499	Crystal cutting equipment
Space Environment Laboratories Box 1061 Boulder, CO 80306 Tel: 303-443-4090	Vacseal leak sealer
Specialty Minerals, Inc. 640 N. 13th St. Eastern, PA 18042 Tel: 610-250-3321 Fax: 610-250-3325	Pyrolytic graphite
Spectra Tech 2 Res. Dr. PO Box 869 Shelton, CT 06484-0869 Tel: 800-243-9186 Fax: 203-926-8909	Ion sources, heaters
Spectra-Mat, Inc. 100 Westgate Dr. Watsonville, CA 95076 Tel: 408-722-4116 Fax: 408-722-4172	Ion sources
Starrett 29 McKean St. Pittsburgh, PA 15219 Tel: 412-431-8700 Fax: 412-431-5150	Tool chests, precision tools

(continued)

Table B.1 (continued)

Company	Products
Stavac Associates 114 Black Thorn Dr. Butler, PA 16001 Tel: 412-586-2100 Fax: 412-586-5927	Ion sources
Strem 7 Mulken Way Dexter Industrial Park Newburyport, MA 01950-4098 Tel: 508-462-3191 Fax: 508-465-3104	Chemicals, custom synthesis
Sumitomo Electric 551 Madison Ave. New York, NY 10022 Tel: 212-308-6444	GaAs
Surface Interface, Inc. 110 Pioneer Way Suite Mountain View, CA 94041 Tel: 415-965-8205 Fax: 415-965-8207	Manipulators, UHV banana plugs
Swagelok 31400 Aurora Rd. Solon, OH 44139 Tel: 216-439-5934 Fax: 216-349-5843	Vacuum fittings
Swiss Jewel Co. 613 Lafayette Bldg. Philadelphia, PA 19106 Tel: 215-925-2867 Fax: 215-922-3055	Sapphire-fabricated barings, etc.
T.E. Brown & Co. Button End Harston Cambridge England Tel: 0223-872072	Spark cutter
Technical Devices, Inc. 5721 Prescott Rd. Prescott, AZ 86301 Tel: 602-772-7500	Wire bonding tool
Technitool 5 Apollo Rd. Box 368 Plymouth Meeting, PA 19462 Tel: 610-941-2400	Tools, specialized

(continued)

Table B.1 (continued)

Company	Products
Fax: 610-828-5623	
Terranova 5841 Bell Rd. Auburn, CA 95602 Tel: 800-519-2634 Fax: 916-269-2877	Pressure measurement, vacuum valves
Test Lab Co. 1066 Linda Vista Ave. Mountain View, CA 94043 Tel: 800-42-5835	Reconditioned test equipment
Thermionics 22815 Sutro St. PO Box 3711 Hayward, CA 94540 Tel: 510-538-3304 Fax: 510-538-2889	UHV apparatus and accessories
Thorlabs Inc. 435 Rte. 206 Newton, NJ 07860-0366 Tel: 201-579-7227 Fax: 201-383-8406	Optical components
Time Motion Tools 12778 Brookprinter PI. Poway, CA 92064 Tel: 619-679-0303	Tools
Topac, Inc. 99 Derby St. Suite 303 Hingham, MA 02043 Tel: 617-740-8778 Fax: 617-740-8779 e-mail: topac@wing.net	Channel multipliers
Tripp Lite 500 N. Orleans St. Chicago, IL 60610 Tel: 312-329-1777 Fax: 312-644-6505	Electronics
Tube Sales Interstate Industrial Park Bellmaur, NJ 08031 Tel: 215-923-5176	Stainless steel tubing
Tucker Electronic PO Box 551419 Dallas, TX 75355-1419 Tel: 800-527-4642 Fax: 214-348-0367 e-mail: sales@tucker.com	Electronics

(continued)

Table B.1 (continued)

Company	Products
Tylan General 1110 Shepard Dr. Blue Bell, PA 19422 Tel: 610-272-1933 Fax: 603-894-4909	Vacuum components
U-C Components, Inc. 410 Logue Ave. Mountain View, CA 94043-4019 Tel: 415-964-3827 Fax: 415-964-0216	Vented screws
Uniform Tubes, Inc. 7th Ave. Collegeville, PA 19426 Tel: 215-539-0700	Metal tubing, specialty
Unimetrics Corp. 501 Earl Rd. Shorewood, IL 60436 Tel: 800-854-6931 Fax: 815-741-0799	Micro syringes and accessories
Unique Wire Weaving Co., Inc. 762 Ramsey Ave. Hillside, NJ 07205-1094 Tel: 800-445-6912 Fax: 908-688-4601	Stainless mesh
United Chemical Technologies, Inc. 2731 Bartram Rd. Bristol, PA 19007 Tel: 215-781-9255 Fax: 215-785-1226	Silanes and silicones
United Detector 12515 Chadron Ave. Hawthorne, CA 90250 Tel: 310-978-1150 Fax: 310-644-1727	Electronic equipment and supplies
UTI 1313 Fifth St. SE Suite 130 Minneapolis, MN 55414 Tel: 612-378-1393 Fax: 612-378-2287	Mass spectrometers

(continued)

Table B.1 (continued)

Company	Products
Vacoa 10-7 Technology Dr. E. Setauket, NY 11733 Tel: 516-751-7115 Fax: 516-751-7154	Vacuum valves and accessories
Vacuum General 9577 Chesapeake Dr. San Diego, CA 92123 Tel: 619-571-1222 Fax: 619-576-1703	Capacitance gauges
Vacuum Science Workshop, Ltd. 5045 N. 30th St. Colorado Springs, CO 80919 Tel: 719-531-7711 Fax: 719-531-7714	Electron spectrometers
Varflex 512 W.Court St. Rome, NY 13440 Tel: 315-336-4400 Fax: 315-336-0005	Glass braid
Varian 121 Hartwell Ave. Lexington, MA 02173-3133 Tel: 1-800-882-7426 Fax: 617-860-5437	Turbopumps, vacuum products, feedthroughs
Vat 600 West Cummings Park Woburn, MA 01801 Tel: 617-935-1446 Fax: 617-935-3940	Gate valves
Velmex, Inc. 7550 State Routes 5 & 20 Bloomfield, NY 14469-9389 Tel: 800-642-6446 Fax: 716-657-6153	Unislide assemblies
Victor Equipment Co. 101 S. Hanley Rd. St. Louis, MO 63105 Tel: 314-721-5573 Fax: 314-721-4822	Gas apparatus
Virginia Semiconductor, Inc. 1501 Powhatan St. Fredericksburg, VA 22401 Tel: 540-373-2900 Fax: 540-371-0371	Silicon membranes, silicon crystals

(continued)

Table B.1 (continued)

Company	Products
Voltaix PO Box 5357 197 Meister Ave. North Branch, NJ 08876 Tel: 908-231-9060 Fax: 908-231-9063	Gases-semiconductor process
W.R. Grace 7221 W. Parkland Court Milwaukee, WI 53223 Tel: 414-354-4400 Fax: 414-354-5088	Silica, powdered; silica, gel
Watlow 2987 Babcock Blvd. Pittsburgh, PA 15237 Tel: 412-311-5004 Fax: 412-322-1322	Heating elements-bakeout
Wavemat 44191 Plymouth Oaks Blvd. Suite 100 Plymounth, MI 48170	Microwave plasma sources
Wiley 1245 South Sixth St. Coshocton, OH 43812 Tel: 614-622-0755 Fax: 614-622-3231	Organic chemicals
Wilmad Glass Co. Rt. 40 & Oak Rd. Buena, NJ 08310 Tel: 800-297-8165 Fax: 800-297-8174	Glass tubing-capillary
Winfred M. Berg Inc. 499 Ocean Ave. East Rockaway, NY 11518 Tel: 516-599-5010	Precision mechanical components
YSI Yellow Springs Instrument Co., Inc. 1725 Branum Ln. Yellow Springs, OH 45387 Tel: 513-767-7241 Fax: 513-767-9353	Temperature measurement

Table B.2 German and European manufacturers

Company	Products
Advent Research Materials Ltd Blyth Road Industrial Estate Halesworth, Suffolk England IP 19 8DD Tel: 44-1986 874555 Fax: 44-1986-874557	Pure materials, metals, foils, wires, powders
Alcatel Hochvakuumtechnik GmbH Am Kreuzeck 10 D-97877 Wertheim Tel: 09342-8700 Fax: 09342-87030	Vacuum components, quadrupole mass spectrometer, pumps
Alfa Produkte Zeppelinstr. 7 D-76185 Karlsruhe Tel: 0721-853061 Fax: 0721-849674	Pure metals, metal products, noble metal technology, single crystals, wires, foils, powder
Araldit AtI Ciba-Geigy GmbH Oeflinger Str. D-79664 Wehr (Boswn) Germany	
Aurel GmbH Malteser Str. 443C D-86899 Landsberg	Si-crystals
Balzers Hochvakuum GmbH Otto-von-Guericke-Ring 7 D-65205 Wiesbaden Tel: 06122-706-0 Fax: 06122-70610	Vacuum components
Bender & Hobein GmbH Fraunhofer Str. 7 D-85737 Ismaning Tel: 089-9965480 Fax: 089-9965490	"Surfrasi" silconizing agent, glass coating
Berger Lahr GmbH Breslauer Str. 7 D-77933 Lahr Tel: 07821-5820 Fax: 07821-582313 or Zuständiger Kundendienst SIG Positec GmbH Büro Mitte Maybachstr. 14 D-63456 Hanau Tel: 06181-66580 Fax: 06181-665818	Synchronous and step motors of all sizes, positioning systems

(continued)

Table B.2 (continued)

Company	Products
Best Ventil & Fitting GmbH Robert-Bosch-Str. 20 D-63477 Maintal-Dörnigheim Tel: 06181-46041 Fax: 06181-432161	Swagelok, Whitey, Cajon, Nupro, Snotrik, valves, glass-metal connections
Busak & Shamban GmbH & Co. Handwerkstr. 5-7 D-70565 Stuttgart 80 Tel: 0711 7864-0 Fax: 0711-7803171	Gaskets
Caburn-MDC Ostendstr. 1 D-12459 Berlin Tel: 030-6953-9840 Fax: 030-635-3786	UHV components, feedthroughs, coaxial cables
Caddock Europe Leopoldstr. 28a/2 D-80802 München Tel: 089-390799 Fax: 089-391230 or Caddock Electronics Inc. 1717 Chicago Ave. Riverside, CA 92507-2364 Tel: 001-714-788-1700 Fax: 001-714-369-1151	High precision resistors, high voltage resistors up to 10000 MOhm
Carl Roth GmbH+Co Postfach 21 11 62 D-76161 Karlsruhe Tel: 0721-56060 Fax: 0721-560649	Chemicals, laboratory equipment
CETEC Spezialarmaturen Ernst H.F. Hiller Vahrer Str. 248 d D-28329 Bremen Tel: 0421-461855 Fax: 0421-462385	UHV components
CKL Vacuumtechnik Vertriebs GmbH Unterfeldring 17 D-85256 Vierkirchen Tel: 08139-890 Fax: 08139-8943	UHV components, pumps, sputter guns
CompoTherm Oberflächentechnik GmbH Siemenstr. 16-18 D-28857 Syke Tel: 04242-593-12 Fax: 04242-593-13	High-speed pyrometers

(continued)

Table B.2 (continued)

Company	Products
Conatex Postfach 1220 D-66592 St. Wendel/Saar Tel: 06851-2071 Fax: 06851-2076	Technical equipment for scientists: thermometers, thermocouples
Cryo Vac Dr. Johannes Klug, Handelsvertretung Hasbacher Str. la D-51503 Rösrath Tel: 02205-85454 Fax: 02205-5797	Cryo technology, cryo component and materials, insulation, low temperature glue
Cryophysics Landwehrstr. 48 D-64293 Darmstadt Tel: 06151-86281 Fax: 06151-84481	Modulators, crystals, harmonic generating, polarizers, Q-Switches, lasermetrics, LN_2 cryostats, super insulation
Cryoson GmbH Postfach 1104 D-63821 Schöllkrippen Tel: 06024-1233 Fax: 06024-7879	Steel dewars, LN_2-containers
Deutsche Air Liquide—Kryotechnik König-Adolf-Str. 3 D-65191 Wiesbaden Tel: 0611-543048 Fax: 0611-547264	LN_2 dewars, cryo technology, LHe containers
Dr. Sjuts Optotechnik Max-Planck-Str. 1 D-37191 Katlenburg-Lindau Tel: 05556-1011 Fax: 05556-4587	Electro multipliers, channeltrons
EA-Elektro-Automatik Helmholtzstr. 33-35 D-31747 Viersen Tel: 02162-3785-0 Fax: 02162-16230	High current power supplies
EBARA Germany GmbH Donaustr. 7 D-63452 Hanau Tel: 06181-1876-0 Fax: 06181-1876-40	Turbo and cryo pumps
EMCO Elektronik GmbH Einsteinstr. 35 D-82152 Martibsried Fax: 089-85-97785	RF power amplifiers, micro wave components

(continued)

Table B.2 (continued)

Company	Products
EMV Elektronische Meβgeräte Vertriebs GmbH Wallbergstr. 7 D-82024 Taufkirchen Tel: 089-6128054 Fax: 089-6128593	Electronic measuring instruments
ENI Germany A Division of Aster Germany GmbH Holderäckerstr. 15 D-70839 Gerlingen Tel: 07156-21095 Fax: 07156-49372	RF amplifiers, power amplifiers
Epoxy Produkte GmbH Guntherstr. 31 Postfach 1207 D-64658 Fürth/Odenwald Tel: 06253-4546 Fax: 06253-21687	Solvent free epoxy products conducting cement (for $LiTaO_3$ contacts)
Farnell Advance Electronic GmbH Dieselstr. 21 D-63533 Mainhausen Tel: 06182-21091-93 Fax: 06182-28819	Power supplies, measuring instruments
FAST Comtec GmbH Grünwalder Weg 28a D-82041 Obserhaching Tel: 089-613-1081 Fax: 089-613-6171	Transient recorder, PC-boards, NIM boards, multichannel scaler, discriminators, time-counters
FHR Anlagenbau, GmbH Bergener Ring 41 D-01458 Ottendorf-Okrilla/Dresden Tel: 089-613-1081 Fax: 089-613-6171	UHV, HV, sputter instruments and supplies, pure gases, valves
FISONS Instruments Vertriebs-GmbH peter-Sander-Str. 43 D-55252 mainz-Kastel Fax: 06134-289904	UHV components, surface science, analysis instruments
FOM Kruislan 407 1098 SJ Amsterdam The Netherlands Tel: 31-20-6081301 Fax: 31-20-6684106	Single crystal preparation
Friatec (ehemals Friedrichsfeld GmbH) Postfach: 710261 D-68222 Mannheim Tel: 0621-4860 Fax: 0621-477999	Ceramic parts, UHV feedthroughs

(continued)

Table B.2 (continued)

Company	Products
Fritz Eichenauer GmbH Industriestr. 1 D-76770 Hatzenbühl Tel: 07275-7020 Fax: 07275-702200	Heating Elements
FuG Elektronik GmbH Florianstr. 2 D-83024 Rosenheim Tel: 08031-81093 Fax: 08031-81099	High-precision power supplies, high-voltage power supplies and resistors
General Scanning GmbH Münchener Str. 2 D-82152 Planegg Tel: 089-8595031 Fax: 089-8599487	Galvo drives, scanners
Goodfellow GmbH Postfach 5427 D-65729 Eschborn Tel: 06196-703441 Fax: 06196-482954	Metals in all forms: foils, crystals, tubes, powder
Gossen GmbH Mess- und Regeltechnik Postfach 1780 D-91007 Erlangen Tel: 09131-8271 Fax: 09131-28895	General measuring instruments, controlling instruments
Gräff Bonner Str. 54 D-53842 Troisdorf Tel: 02241-41031 Fax: 02241-404002	High-precision thermometers, thermocouple instruments
Hahn & Bischof Donarweg 3 D-81739 München Tel: 089-601-4409 Fax: 089-601-2748	UHV-, MBE-instruments, analysis instruments, nano crystal fabrication
Hameg Instruments Kelsterbacher Str. 17 D-60528 Frankfurt Tel: 069-67805-0 Fax: 069-67805-13	Oscilloscopes, signal generators, multimeters
Hela GmbH Postfach 411011 D-12120 Berlin Tel: 030-7927080	Electrical wires, polymide cables, kapton wire

(continued)

Table B.2 (continued)

Company	Products
Heraeus Sensor GmbH Im Stift 6-8 D-58119 Hagen Tel: 02334-8040 Fax: 02334-80432	Temperature measuring program, thermocouples, high-precision resistors, temperature probes
Heraeus Wittmann GmbH Englerstr. 11 D-69126 Heidelberg Tel: 06221-30430	Silicon-heating elements, heating ribbons
Hiden Analytical Vertretung für Deutschland VACUA GmbH Niedmannweg 13 D-82431 Ried/Kochel Tel: 088-57693010 Fax: 088-579771	Quadrupole mass spectrometer, ion sources for surface analysis
HMS-Electronik Hans M Strassner GmbH Am Arenzberg 42 D-51381 Leverkusen Tel: 02171-3814 Fax: 02171-33852	Extremely low-noise pre-amplifiers, lock-in amplifiers
Hoke GmbH Hanauer Landstr. 11-13 D-60134 Frankfurt Tel: 069-4050090 Fax: 069-4050094	Pure gases and gas handling supply
Hositrad/Holland P.O.B. 114 3870 CC Hoevelaken The Netherlands Tel: 03495-37210 Fax: 03495-35274	CVD, UHV parts, manipulators, loadlocks, Ti Pumps. Repair of ion pumps (Varian and Leybold)
Hositrad/Deutschland Lindnergasse 2 D-93074 Regensburg Tel: 0941-55827 Fax: 0941-562296	
HP Hewlett-Packard GmbH Vertriebszentrum Bad Homburg Hewlett-Packard-Str. D-61352 Bad Homburg v.d.H. Tel: 06172-16-0 Fax: 06172-16-1309	Synthesizer, function generators, oscilloscopes, RF components, multimeters, power supplies
HP Direct Dornierstr. 7 D-71034 Böblingen Tel: 07031-140 Fax: 07031-142100	

(continued)

Table B.2 (continued)

Company	Products
Ina Wälzlager Schaeffler KG Industriestr. 1-3 D-91074 Herzogenaurach Tel: 09132-820 Fax: 09242-5349	Needle bearings, linear bearings, linear motions, planetary gearings
Intervac Henning GmbH Gemeindedingerstr. 7 D-97892 Kreuzwertheim Tel: 09342-22417 Fax: 09342-7058	Vacuum components supply
Isopad GmbH Engelerstr. 11 D-69126 Heidelberg Tel: 06221-30430 Fax: 06221-304343	Heating supplies: heating ribbons, collars, tubes, etc
Joachim Schwarz Hindenburgstr. 12 D-76332 Bad Herrenalb Tel: 07083-51833 Fax: 07083-51925	UHV components
Joisten & Kettenbaum Asselborner Weg 14-16 D-51429 Bergisch Gladbach Tel: 02204-839-0 Fax: 02204-839-60	Tools for surface treatment, polishing supply, diamond paste
JUST Vakuum Technik Lehnstr. 34 D-66869 Kusel Tel: 06381-6060 Fax: 06381-6040	Vacuum components, pumps, quadrupole mass spectrometers
Karlsruher Glastechnisches Werk Schieder GmbH Spezialfabrik für Isoliergefäβe Gablonzer Str. 6 D-76185 Karlsruhe Tel: 0721-95897-0 Fax: 0721-95897-77	Glass instruments, cryostats for LN_2 and LHe. Specialize in insulation dewars
Keithley Instruments GmbH Landsberger Str. 65 D-82110 Germering Tel: 089-8493070 Fax: 089-84930759	High precision measuring instruments
Klaus Schaefer GmbH Postfach 1660 D-63206 Langen Tel: 06103-79085 Fax: 06103-71799	Marketing of products: Crowcon, Extrel, General Vacuum, Walker Scientific, Ceramaseal, Cryomagnetics, Leak Sealant, IMAG

(continued)

Table B.2 (continued)

Company	Products
KMF Laborchemie GmbH Postfach 900129 D-51111 Köln Tel: 02241-96850 Fax: 02241-67353	"Surfrasil" siliconizing agent, glass coating
Knuerr-Heinzinger Elecronic GmbH Anto-Jakob-Str. 4 D-83026 Rosenheim Tel: 08031-44040 Fax: 08031-440444	High-precision power supplies. High voltage and high-current power supplies
Kristallhandel Kelpin Im Schilling 18 D-69181 Leimen Tel: 06224-72558 Fax: 06224-77189	Metal single crystals, electro-optical and acusto-optical crystals
Kurt J. Lesker Company Karl-Heinz-Beckurts-Str. 13 D-52428 Jülich Tel: 0130-812843 Fax: 0130-812842	Vacuum components
LeCroy GmbH Mannheimer Str. 177 D-69123 Heidelberg Tel: 06221-831001 Fax: 06221-834655	Digital oscilloscopes, CAMAC modules, transient recorders
Leybold Vakuum GmbH Bonner Str. 498 D-50968 Köln Tel: 0221-347-0 Fax: 0221-347-1250 or Postfach 510760 D-50943 Köln	Ultra high vacuum parts and analysis instruments
Linde AG Kostheimer Landstrae 25 D-55246 Mainz-Kostheim Tel: 06134-208-31 Fax: 06134-208-25	Gases and gas handling supplies
M.K. Juchheim GmbH Moltkestr. 13-31 D-36039 Fulda Tel: 0661-60030 Fax: 0661-6003-500	Thermometer, process controlling, thermocouples, time switches
MaTecK Material-Technologie & Kristalle Dr. H. Schlich Karl-Heinz-Beckurts-Str. 13 D-52428 Jülich Tel: 02461-690740 Fax: 02461-690749	Single crystals, wafers, pure materials and alloys, high-precision polishing service

(continued)

Table B.2 (continued)

Company	Products
Mawi-therm Temperatur-Prozeβtechnik Hofstr. 23 D-40789 Monheim Tel: 02173-51094 Fax: 02173-58623	Thermometer, temperature controller infrared thermometer, pyrometer, thermoelements
Melja Diagnostik GmbH Lilienthalstr. 7-25 D-34123 Kassel Tel: 0561-57-15-77 Fax: 0561-57-16-36	"Surfrasil" siliconizing agent, glass coating
Menz & Könecke GmbH D-41379 Brüggen Tel: 02163-5940 Fax: 02163-5210	Electrical heating supplies for baking out
Merck Frankfurterstr. 250 D-64271 Darmstadt Tel: 06151-723368 Fax: 06151-722000	Chemicals and metals. Also inexpensive vacuum parts and lubricants of different companies: Alcatel, Busch, Kinney, Tietschle, CTI, Edwards, Leybold, Welch, Sargent, Stokes, Balzers, etc. Precision Plus Vacuum Parts, Inc.
Messer Griesheim GmbH Postfach 210553 In der Steinwiese 5 D-57074 Siegen Tel; 0271-69040 Fax: 0271-6904160	Gases and gas handling supply, liquid nitrogen and helium
Metal Crystals & Oxides LTD Unit B5 Button End Industrial Estate Harston Cambridge England CB2 5NX Tel: 1223-872072 Fax: 1223-872517	Single crystals, special materials
Metrofunk Kabel-Union GmbH Postfach 410109 D-12111 Berlin Tel: 030-8314052 Fax: 030-7925343	Electrical wires, polymide cables, kapton wire
MKS Instruments Deutschland GmbH Schatzbogen 43 D-81829 München Tel: 089-420008-0 Fax: 089-424106	Vacuum components, gas analyzer, capacitance manometer, gas flow controllers

(continued)

Table B.2 (continued)

Company	Products
Moorfield Associates Moorfield House Plumley Moor Rd. Plumley CheshierWA 16 9RS UK Tel: 0565-722609	VSW instruments, HREELS IB200 spectrometer. Used UHV analysis instruments
Niederlassung Hanau Wilhelm-Rohn-Str. 25 D-63405 Hanau Tel: 06181-34-1202 Fax: 06181-34-1212	
neoLAB Rischerstr. 7 D-69123 Heidelberg Tel: 06221-844219 Fax: 06221-844233	General laboratory equipment
Normag Labor- und Verfahrenstechnik GmbH Postfach 1269 Feldstr. 1 D-65719 Hofheim a.Ts. Tel: 06192-2099-0 Fax: 06192-209939	Special glass instruments, glass grinding spindle valves
Omicron Vakuumphysik GmbH Idsteiner Str. 78 D-62232 Taunusstein Tel: 06128-73044 Fax: 06128-73596	Rear view LEED, STM, AFM, UPS He-source, evaporation sources
Oxford Instruments Kreuzberger Ring 36 D-65205 Wiesbaden Tel: 0611-7640 Fax: 0611-764175	High precision superconducting magnets, cryotechnology, low temperature STM
Paskovsky Meβelektronik GmbH Postfach 1259 D-63502 Langenselbold Tel: 06184-3042 Fax: 06184-62610	Amplifier and linearization modules for thermocouples
Perkin Elmer Bruckmannring 40 D-85764 Oberschleissheim Tel: 089-315-717-0 Fax: 089-315-3117	UHV surface analysis equipment: XPS, AES, ESCA, UPS, ISS, SAM, SIMS, LEED, HEED, electron, photon, and ion sources, hemispherical or cylindrical analyzers, manipulators
Phytron-Elektronik GmbH Industriestr. 14 D-82194 Gröbenzell Tel: 08142-503-0 Fax: 08142-503-190	Step motors, special clutches

(continued)

Table B.2 (continued)

Company	Products
Piezosystem Jena Wildenbruchstr. 15 D-07745 Jena Tel: 03641-675-390 Fax: 03641-675-393	Piezo, high-precision positioning systems
Pink Vakuumtechnik Am Kessler 6 Postfach 1509 D-97877 Wertheim Tel: 09342-872-0 Fax: 09342-872-20	Vacuum systems, special manufacturing
Polytec GmbH Polytec Platz 5-7 D-76337 Waldbronn Tel: 07243-6040 Fax: 07243-69944	Inorganic high-temperature cements
Rohde und Schwarz Vertriebs-GmbH Mühldofst.r 15 D-81671 München Tel: 089-41290 Fax: 089-41293208	Synthesizer, function generators, signal generators, RF components, oscilloscopes
Rolf Müller Juethorn Str. 72 D-22043 Hamburg Tel: 040-652-65602 Fax: 040-570-3000	Thermo electrical components, thermocouples, miniaturized welding tools
Rosenkranz Elektronik Gro-Gerauer Weg 55 D-64295 Darmstadt Tel: 06151-3998-0 Fax: 06151-399818	Used electronic instruments, oscilloscopes, function generators multimeters
SAES GETTERS Postfach 420552 Gerolsteiner Str. 1 D-50899 Köln Tel: 021-443086 Fax: 0221-441095	Alkali-metal dispensers, NEG pumps, getter material
SASKIA Hochvakuum—und Labortechnik Am Vogelherd 3 D-98693 Ilmenau Tel: 03677-6040 Fax: 03677-604110	Vacuum systems, pumps, gauges

(continued)

Table B.2 (continued)

Company	Products
Scandivac Nordic Vacuum Engineering AB Industrivägen 16 S-59041 Rimforsa Sweden Tel: 46-494-20530 Fax: 46-494-21197	Thermionics vacuum parts, UHV-rotation tables for manipulators, electron guns, pumps, valves
Schlumberger Technologie GmbH Ingolstädter Str. 62a D-80939-München Tel: 089-318890 Fax: 089-35908	CAMAC and NIM modules, crates, Si-detectors, digital voltmeters
Schulz-Electronic GmbH Postfach 11 01 18 D-76486 Baden-Baden Tel: 07223-58054 Fax: 07223-58093	Power supplies
SI Spectroscopy Instruments GmbH Rudolf-Diesel-Str. 7a Postfach 1326 D-82239 Gilching Tel: 08105-5011 Fax: 08105-5577	SRS Stanford Research Systems: lock-in amplifier, signal generators, timer counter, boxcar averager, chopper
Sigma-Aldrich Chemie GmbH Postfach D-82039 Steinheim Tel: 0130-5155 Fax: 0130-6490	Chemical materials and equipment, glass instruments
Specs GmbH Volastr. 5 D-13355 Berlin Tel: 030-4633031 Fax: 030-4642083	Surface science analysis instruments, electron, photon and ion sources
Struck Bäckerbarg 6 D-22889 Tangsted/Hamburg Tel: 04109-55-0 Fax: 04109-5533	Transient recorders, CAMAC modules
Struers GmbH Albert Einstein Str. 5 D-40699 Erkrath Tel: 0211-20030 Fax: 0211-200399	Metallographic products, grinding and polishing machines, polishing supplies, diamond paste
tectra GmbH Reuterweg 65 D-60323 Frankfurt/M Tel: 069-720040 Fax: 069-720400	Vacuum components, all kinds of surface science equipment and analysis instruments

(continued)

Table B.2 (continued)

Company	Products
Tektronix GmbH Sedanstr. 13-17 D-50668 Köln Tel: 0221-72220 Fax: 0221-722362	Digital and analog oscilloscopes, spectrum analyzers
Telemeter Electronic Posthof 4 D-86609 Donauwörth Tel: 0906-706-930 Fax: 0906-21706	RF amplifier, signal generators, microwave components
Thermal Quarz-Schmeize GmbH Vor dem Haβel 8 D-21438 Brackel Tel: 04185-4035 Fax: 04185-5309	Various products made of glass
VAB Vakuum Anlagen Bau GmBH Sandhöhe 11 D-25337 Elmshorn Tel: 04121-73095	UHV systems and components, Ti sublimation pumps, valves, manipulators
Vacom Leutragraben 8a D-07743 Jena Tel: 03641-443994 Fax: 03641-443993	Vacuum components, pumps, valves, gauges, feed throughs
Vakuumschmelze GmbH Grüner Weg 37 Postfach 2253 D-63456 Hanau Tel: 06181-380 Fax: 06181-382645	Permanent magnets
Varian GmbH-Vacuum Products Kuehnstr. 71d D-22045 Hamburg Tel: 040-6696031 Fax: 040-6682282	Vacuum components, electron guns, surface science analysis instruments
VAT Bretonischer Ring 7 D-85630 Grasbrunn-Neukeferloh Tel: 089-465015 Fax: 089-463765	Valves, bellows, vacuum parts
Victoreen Inc. 6000 Cochran Rd. Cleveland, OH 44139 Tel: 001-216-248-9300 Fax: 001-216-248-9301 or Compotron Geretsrieder Str. 4 D-84478 Waldkraiburg Tel: 08638-3051 Fax: 08638-2781	High-precision, high-voltage resistors

(continued)

Table B.2 (continued)

Company	Products
VSE Vakuumtechnik GmbH Rottmosserstr. 16 D-83543 Rott a. Inn Tel: 08039-4454 Fax: 08039-4457	Metal valves, leak valves, vacuum components
VSI Vakuum Science Instruments GmbH Bahnhofstr. 2 D-65307 Bad Schwalbach Tel: 06124-70830 Fax: 06124-708333	Analyzer for UPS, AES, ISS, HREELS-spectrometer Video-LEED, electron guns, vacuum components
Wacker-Chemie GmbH Hans-Seidel-Platz 4 D-81737 München Tel: 089-627901 Fax: 089-62791770	Si-single crystals
Wallace & Tiernan Postfach 1563 D-89305 Günzburg Tel: 08221-904-0 Fax: 08221-904-203	Pennwalt manometer, aneroid-absolute manometer
Wavetek Electronics GmbH Freisinger Str. 34 D-85737 Ismaning Tel: 089-9609490 Fax: 089-967170	Function generators, pulse generators, microwave components
Well-Diamantdrahtsägen Oppauerstr. 37 D-68305 Mannheim Tel: 0621-741990 Fax: 0621-745897	Diamond wire saws, crystal cutting tools
Witzenmann GmbH Östliche Karl-Friedrich-Str. 134 D-75175 Pforzheim Tel: 07231-5810 Fax: 07231-581820	Bellows, diaphragm bellows
Zinsser Analytical GmbH Eschborner Landstr. 135 D-60489 Frankfurt Tel: 069-7891060 Fax: 069-78910680	Pure metals, alloys, chemicals

All addresses with D postal codes are located in Germany

Table B.3 Japanese manufacturers

Company	Products
Anelva 5-8-1 Yotsuya Fuchu-city Tokyo 183 Japan Tel: 31423 34 0221 Fax: 81 423 60 2277	Gauges, ion pumps, mechanical pumps, vacuum flanges, valves, etc.
Daikin 2-4-12 Nakazaki-Nishi Kita-ku Osaka 530 Japan Tel: 81 6 374 9306 Fax: 81 6 374 9296	Cryopumps, cryo-refrigerator
Denka 141 Yurakucho Chiyoda-ku Tokyo 100 Japan Tel: 81 3 3507 5257 Fax: 81 3 3507 5078	Ceramics, LaB_6 cathodes
Hamamatsu Photonics 8-21 Toranomon Minato-ku Tokyo 105 Japan Tel: 81 3 3436 0491 Fax: 81 3 3433 6997 or 314-5 Toyooka-mura Iwata-gun Shizuoka 438-01 Japan Tel: 81 539 62 5245 Fax: 81 539 62 2205	CCD camera, microchannel plate, multi-capillary plate, etc
Irie Kiken Co., Ltd. 11-7 Ginza Chuou-ku Tokyo 104 Japan Tel: 81 3 3542 4692 Fax: 81 3 5565 7064	Flexible tubes, quick-coupling (NW) components

Index

Note: Page numbers followed by ‘f’ denotes Figure and ‘n’ denotes Footnote

A
Absolute adsorption
  coverage measurement, 253–255
  King and Wells method, 253, 334, 426
  TPD method, 569, 571
Absoulte coverage, 253, 255, 309
Absolute sticking coefficient, 256
  at desorption temperature, 256
  measurement, 253–255
Adsorption
  gas purification and, 506*f*
  metal fatigue and, 95
  powders, 576
  supported catalysts, 555
Adsorption/desorption from high area solids, 569–571
Alkali metal source, 483–484
Aperture, adjustable iris, 30–31
Aquadag, 11, 47, 120, 123, 196, 374, 499
Argon purification, 510*f*
Atomic arsenic, 456–458
Atomic fluorine, 481–482
Atomic hydrogen
  detectors, 480
  high-flux thermal source, 477–480
  radiofrequency driven source, 480–481
Atomic oxygen detection, 490–491
Atomic oxygen production and purity, 491–492
Atomization
  arsenic, 456
  fluorine, 481
  hydrogen, 477, 481
Au
  evaporation source, 313
  single crystal, Au(111), 155
Au UPS spectrum, 236*f*
Auger electron spectroscopy (AES), 196
  calibration with quartz microbalance, 312
  lubrication and, 343
Azimuthal sample motion, 3, 4*f*
  cyrogenic manipulators for, 388–389
  strain-free mounting for, 355, 356*f*

B
Bakeout
  eliminated, 45
  glass systems, 506
  heaters for, 83
  in metal UHV systems, 83–85
  to UHV condition, 69
  viton seal and, 109
  wall oxidation and, 87
Bayard-Alpert gauge
  contamination of, 135
  corrections for external radiation and external electron flux effects, 142–143
  filament replacement in, 145
  high sensitivity of, 262
  ion gun based on, 215–216
Bearings
  high-speed rotary shafts, 29–30
  internal ball, 10
  lifetime, 25
  rotation translation, 27*f*
  self lubricating, 26–27
  steel ball, 29
  teflon, 29
  tungsten carbide ball, 27
  vacuum ball, 11
Bellows, 109
  folding, 587
  hypalon/nylon, 52
  temporary leak sealing of, 108
Beryllium window construction, 526
Birefringence, 532
Bond-Barrel holder, 156, 158–159
Books, experimental methods, 593

© Springer International Publishing Switzerland 2015
J.T. Yates Jr., *Experimental Innovations in Surface Science*,
DOI 10.1007/978-3-319-17668-0

Boron as impurity, 545
Boron nitride
- crucible, 467
- diffusion, 529
- lubricant, 26
- shield, 456

Brightness temperature, 409

C

C60 evaporation, nanoscale templating, 460
Calibrated effusive molecular beam measurements, 253–255
Calorimetric heats of adsorption, 333–336, 574–575
Calorimter, Setaram C-80, 575*f*
Capacitance
- crystal positioning using, 11
- measuring circuit, 12*f*

Capacitance manometer, 425, 432, 461, 478, 486, 574
Capillaries, cleaning, 89–91
Carbon monoxide. *See* CO
Cataphoretic desorption
- of LaB_6, 136
- of ThO_2, 133

Cathodes
- ThO_2/LaB_6 coated, 133, 135, 187
- CeB_6 coated, 139
- ThO_2coated Ir, 219

CEMA. *See* Chevron electron multichannel plate array
Cement
- AgCl, 525, 555
- MgO (Armeco 517P), 415
- semiconductor crystal mounting, 368, 369*f*
- vacseal, 367, 525
- ZrO_2 (aremco Ultratem 516), 368

Ceramic insulator deterioration, 64
Cesium ion gun design, 471–473
Channeltron detector, 262–264
Charged particle oscillator, He(I) and He(II) ultraviolet source, 236
Chemical actinometer, 245–246
Chemisorption
- CO and Ni, 574, 575*f*
- CO and Pt, 426, 427*f*
- cyclohexene on Pt, 335
- IR transmission spectra, 556*f*
- N_2on Rh, 557
- O_2 on Pd, 238–242

Chevron electron multichannel plate array (CEMA) detector, 232
Cleaning crystals
- metal, 543
- palladium, 546
- silicon, 548
- tungsten, 551

CMA auger spectrometer, 310
- photoelectron spectrum measurement, 236
- Pt deposition measurement, 309, 310, 312

CO, carbon monoxide
- desorption form polycrystalline W, 259
- purification, 503
- tungsten single crystal, 551

Coefficient of friction, 341–344
Conductiver coatings, 123–124
Conflat flange
- aluminum, 101
- for Al foil window, 528*f*
- sexless, 99

Cooling reservoir, 385, 390
- flexible, 394, 395*f*
- for horizontal manipulator, 390, 391*f*

Cooling samples
- by mixing gas streams, 401
- contact with thermal reservoir, 383
- crystal holder for, 381–383
- gas thermal switch, 401–402
- on manipulators, thermal conductivity issues, 383, 385–386
- using direct contact, 389
- variable rate, 401–403

Cryogenic connections, 392
Crystal cleaving, 93–94
Crystal heating
- electron bombardment, 361–363
- interrupted ohmic heating, 359–361

Crystal manipulator, 3–5
Crystal mounting
- non-weldable, 354, 355*f*
- strain free for azimuthal motion, 355–356

Crystal positioning, 11–12
Crystal temperature measurement, 362
Cu, copper
- braid, 54, 305, 392
- C_{60} on Cu(110), 460
- for cooling tank, 389
- gasket removal device, 102–103
- improved heat conductivity, 392
- oxidation of, 381
- reservoir, 386, 387*f*, 389

Cu, copper, 381. *See also* OFHC Cu
Cu-Be cup, 388

D

Dark current, 262
Debye temperature, 337–339
Desorption kinetics

angular resolved, 273–275
from single crystal faces, 259
Detectors
InSb infrared, 328
ion-pumped infrared, 329f
MCP-type, 227, 229
MgCdTe (MCT) infrared, 321, 328, 334 f
PVDF thermal, 335
resistive anode, 225, 227
silicon surface barrier, 305, 306
stagnation, 334, 429
Deuterium kinetic isotope effect, 282
Diamond, heating behavior, 364, 365f
Diamondlike carbon coating, 101
Differential pumping method, 6–11
Dimethyldiazine
carcinogenic agent, 495
methyl radical source, 485
Diode ion pump performance in He pumping, 75–76
Dynode multiplier, regeneration of, 263
Dynode rejuvenation, 205–206

E
EDA. *See* Ethylene diamine
Einzel lens, 187, 220, 472
Electrical conductivity, TiO_2 single crystal, 200–201
Electrical connections
band clamp, 67
cold-formed wire connector, 64
leakage, 64
phosphor bronze spring, 66
sliding metal contact, 66
tungsten-to-tungsten wrap, 61
ultrahigh resistance vacuum feedthroughs, 64–65
Electrical isolation of UHV components, 151
Electrical shock
avoidance, 591
effect on man, 589
from ionization gauge, 590
Electrochemical device, UHV, 500, 501f
Electrodeposition, Cr on W wire, 448–449
Electron beam
angular divergence measurement, 198–199
damage from stray electrons, 260
evaporator, 450f
point focused, 453
position monitor, 224
small evaporator design, 451–453
Electron bombardment heating, experimental difficulties, 277
Electron energy analyzers, 191, 194–196
Electron gun
beam properties, 188
cathode, 141
design and behavior, 187–189
electrostatically focused, 450, 451f
emission current regulation, 189
low-energy design, 192f
low energy/broad beam, 189–192
pulsed, 189, 227, 228f, 231, 231f
work function measurement, 291–292
Electron multipliers
channeltron-type, 262–264
Cu/Be-type rejuvenation, 206
Electron reflection coefficient measurement, 293–294
Electron scattering, single and multiple processes, 205
Electron spectrometer calibration, 196–197
Electrons, specularly reflected, 202
Electroplating, 120, 367, 448
Emissivity, 410
Epoxy adhesive, 179, 343
ESDIAD
benzoate on Cu(110), 227, 228f
pattern for CO on Cu(110), 225, 226f
planar grid apparatus, 227
pulse counting analyzer, 225–227
see. LEED
time-of-flight, 226–228
Etching
large thin window fabrication procedure, 529, 531–532
STM tips, 168–172
Ethylene adsorption/desorption study, zeolitesurface, 569–571
Ethylene dimaine (EDA) etching agent, 532
Eutectics, Zr and W, 444–445
Evanston-type microwave discharge cavity, 480
Evaporation source
aluminum, 446–448
cadmium sulfide, 456
congruent, 442, 444–446
gold, 310–313
lithium, 444–446
see. Metal evaporation
EXAFS measurement, 559

F
Faraday cup, 162
absolute detection efficiency using, 226
modified for electron current measurement, 202–203
movable, 218–219

multiple, 188, 198–199
$Fe(CO)_5$ decomposition, 89
Feedthrough
high-speed rotary, 25
ultrahigh resistance sapphire-metal, 64
Fermi level determination, 197
Filament power supply tester, 141
Filament temperature measurements, 407–409
W filament nomograph, 408
Films
BeO on dynodes, 205
electrically conductive SnO2, 123
for O_2 and O_3 detection, 490
Si_3N_4, 413
thickness measurements, 315
Flanges
Conflat, 6
KF, 523
Formic acid, isotopically labeled, 271
Fracture stage, 343, 345*f*
Friction measurement, 341–343

G

GaAs, gallium arsenide
indirect heating of, 365–366
internal reflection IR spectroscopy and, 326–327
MBE growth of, 536
surface oxidation, 247, 249*f*
Ga, gallium, metallic joint, 389, 393
Galling
prevention, 47
protection against, 29
Gas chromatography sensitivity enhancement, 287–288
Gas doser, 422
Gas dosers, 89–90, 422–426, 428–430, 432
designs, 90*f*
repetitive dosing, 430
retractable, 434–435
Gas flow regulation, 433
Gas purification
apparatus, 510*f*
at high pressure, 505–507
cryogenic or gettering method, 509–511
extremely pure He, 507–509
metal permeation method, 511–512
nitrogen, 509
Gaskets, 99, 101–104
annealed copper, 99
copper, 50, 56
cryogenic, 101–102
deformable, 513, 525
gold wire, 100, 101*f*
OFHC Cu type, 104
removal device, 102–103
silver-plated copper, 100
titanium nitride-coated copper, 100
see. Seals
Gas thermal switch, 401–403
$Gd_2(MoO)_4$. *See* GMO
Ge, germanium, optical pyrometer calibration, 413
Geiger Müller counter
for ^{14}C on Pt(111), 305
for inverse photoemission intensity, 207
Getter films
He storage, 505
maintaining vacuum and, 511
Ti, 273, 505
TSP pump, 72
GMO [$Gd_2(MoO_4)_3$], in measuring ion-beam size, 223*f*
Graphite, electron spectrometer calibration, 196
Grazing incidence X-ray photoemission spectroscopy (GIXPS), 247
Grids
conical grid fabrication, 121–122
hemispherical, 119–120, 227
in electron gun, 189
IR cell sample support, 557–559
large flat mesh, 120–121
tungsten, 244*f*, 557, 558*f*

H

Halogens
electrochemical source, 497–498
microwave discharge source, 480, 501
Heaters
button type, 363–365
halogen lamp, 378
paint-on type, 374, 374*f*
pyrolytic graphite, 372–373
tungsten filaments, 375, 375*f*
Heating
compound semiconductors , 365
conduction, 364*f*
design for insulator crystals, 366–368
indirect, 363–365
irregular shapes paint-on type , 374
Ohmic, 50, 55, 364*f*
radiation and electron bombardment, 277, 362*f*, 364*f*, 377*f*
silicon crystals, 356–359
temperature programmed, 277, 349–353, 415–416
He(I)/He(II)

photoemission source, 235–236
UV resonance line source, 236–238
He helium
adsorbed He, 399–400
below 4K, 399–400
cryocooler, 93, 399
extremely pure, 507–509
leak detection probe, 107
leaktight seal , 525
production and purity of, 507–509
pumping test , 75
purification apparatus, 510*f*
transpiration used for lowering *l*-N_2 temperature, 394–396
High area solids
adsorption and desorption on, 569–572
core-shell structures, 562–563
diffusion IR study, 560–566
IR cell for, 557–559
microcalorimetric studies , 574
opaque materials, 564–566
High-pressure reactor
gold-plated pan bronze , 41
sampling with gas chromatography , 287
High-pressure sample transfer cell, 50–51
Hot filament resistance thermometer , 265, 407
HREELS high-resolution electron energy loss pectroscopy, 196, 205, 361
for boron detection on Rh, 545
Hydrogen
as impurity, 507
atomic, 477–480
desorption form Ni(111), 273, 274*f*
dissolved in stainless steel , 87
permeation studies, 513–514
purification, 505–507
Hydrogen peroxide doser, 493–494

I

Infrared cells
adsorption studies, 555
high surface area study, 558
wide temperature range, 558, 559*f*
Infrared reflection-absorption spectroscopy (IRAS), 321–325
Fourier transform spectrometers (FTIR) and, 321, 323, 327
measurement at high pressure, 323–325
Infrared spectroscopy
continuously pumped detector, 328–329
differential pumping widow seals and, 522*f*
diffusion into core-shell structures, 562–564
diffusion through powders, 560–561
rapid purge using rubber sleeves, 329–330
opaque materials, 564–566
sealing windows to glass, 523
semiconductors and, 324
window mounting, 521–523
Insulators, electrical
Al_2O_3, 64
kapton, 11, 151, 385
macor, 207
sapphire, 64, 381, 385
Internal reflection IR spectroscopy, 328
gallium arsenide, 327
p and s polarization vector diagram, 326*f*
silicon and, 324–326
UHV optical system, 326*f*
Inverse photoemission, 206–207
Iodine (I_2) source, 499–501
Ion beam
angular distribution, 225, 226, 230
polishing, 160
STM tip sharpening, 173
time-of-flight separation, 227, 228*f*
with kinetic energy and mass resolution, 229
Ion beam sources
axial magnetic field and, 218*f*
Colutron GD-2, 220
low energy, magnetic focused, 220–221
measuring beam dimensions, 223
Ion bombardment
evaporation, 317–318
neutrals desorbed by, 221
sources, 213–214
Ionization gauge
corrections for external radiation and external electron flux effects, 142
electrical shock from, 591
filament replacement, 145*f*, 145–146
geometry in evaporation rate measurement, 314
metal film evaporation rate measurement, 314–315
movable, 411
Ion gun
based on Bayard-Alpert gauge, 214, 215
cesium, 471
cold cathode, 216–218
design of, 472, 473
low energy, 220, 222*f*
low gas emission, 211–212
modified, 212, 220, 221
pierce, 472–473
pulsed, 232
Ion pumps
cleaning by chemical etching, 78

methane liberation form, 72
Ion sources
alkali, 473
alkaline earth, 474
broad beam, 218–219
IRAS. *See* Infrared reflection-absorptionspectroscopy
IrO_2cathode insulating layer, 218
Isosteric heat measurements, 325*f*, 333

J
JASON program linear Poisson equation, magnetic shielding, 149
Joule-Thompson refrigerator, 115

K
Kapton insulator, 11, 151
Kapton/sapphire, comparative cooling rates, 385–386
Kaufman ion sources, 218
Kelvin probe
Au electrode, 299
effect of stray capacitance in, 297
electromagnetic driven, 298*f*
high-temperature flow reactor, 299, 300*f*
piezodriven, 296*f*, 297
reproducibility, 299
thermal desorption spectroscopy and, 297
work function in semiconductors, 295
Kinetic isotope effect, 282
for deuterium, 280
Kinetics of adsorption, 253, 255
Knudsen cell, 464

L
LaB_6 thermionic emitter material, 137
LabVIEW program, 277, 351, 415
controller logic, 353*f*
Laser-induced fluorescence (LIF), 231
Laser-ionized neutrals time of flight detection, 231–232
Leaks
calibrated, 571
check groove, 102, 103*f*
detection probe, 107–108
liquid sealers, 108
temporary sealing of bellows, 108–109
LEED/ESDIAD analyzer, 225–227
LIF. *See* Laser-induced fluorescence
Linear
of translating Auger spectrometer, 17
Linear motion
actuator for, 15*f*
inexpensive device for, 15–16
of translating Auger spectrometer, 16
platform (LMP), 32
solenoid driven, 15
Liquid adding to atomically clean surfaces, 517
Liquid nitrogen
enhanced cooling of, 394
level alarm, 396, 398*f*
non-leaking, 398, 399*f*
trap, 79
triple point, 396
Low-energy electron diffraction. *See* LEED
Low energy electron diffraction (LEED)
angle of incidence measurement in, 162–163
beam intensity measurement, 201
Kr isotherms using, 94*f*
movable Faraday cup in, 337, 338*f*
pattern, for Cu(110), 225, 226*f*
retarding diode method and, 289
XLEED, 302
Lubricants
aquadag, 123. *See also* Aquadag
boron nitride, 26
degradation, 29
fluorocarbon, 179
for heavy sliding loads, 27–28
graphite, 8, 100
molybdenum sulfide, 9, 31
Santovac 5 pump oil, 8
TiC/Ag, 28
Lubrication
coefficient of friction and, 341
of metal/metal interface, 27

M
Macor insulator, 140, 206
Magnetic eddy current drive, 22
Manipulator
cooling samples on, 383–386
horizontal cooling of, 389
multiple motion, 3–5, 18
rotary high precision, 13
vacuum-jacketed cryogenic, 386
Manufacturers, equipment and components, 597
Mass spectrometers
calibration, 270, 271*f*
differentially pumped, 72
enhanced sensitivity, 267–268
magic angle thermal desorption, 275–276
sensitivity comparison with bare ion gauge, 260
sensitivity ratios for, 270

Ta filament mass scale calibration, 266, 267*f*
thermal desorption, 571*f*
unshielded, 275
UTI-100C, 270
see. Quadrupole mass spectrometers
Mass spectrometry, 259–271
MCP. *See* Microchannel plate detector
Mechanical action on samples
crystal cleaver, 93–95
fatigue of Al(111) crystal, 95
mica cleavage device, 95
piezoelectric fatigue apparatus, 95–96
tungsten carbide blade, 93
Metal evaporation
alloys and mixtures, 440
chromium evaporator, 448
degassing, 437
downward evaporation, 439
eutectic mixtures, 444
flash evaporation, 442
low coverages of single atoms, 459
measurement of rate, 314
multiple evaporator, 441*f*
portable microevaporator, 459
ultralow coverage, 440
Metal fatigue, 95
Metal foam, vaccum applications, 75–77
Metal foil
aluminum, 528
beryllium, 526
HAVAR, 179
stretching, 179–180
tantalum/platinum sandwich weld, 175, 176*f*
wrinkle free, 179
Metal single crystal cleaning, 543–551
Methanol
reducing agent in spotwelding, 175, 176*f*
reaction on Ni(111), 280–282
Methyl chloride thermal desorption spectra, 72
Methyl radical source, 485
Microcalorimetric studies, 574
Microcapillary array beam doser, 421–429
calibration and use of, 425–426
design, 421, 422*f*
fractional interception, 426
gas handling for, 423, 424*f*
glass, 89
kinetic studies, 500, 501*f*
precautions, 423
retractable, 435
shutoff with condensable gas, 428
Micorchannel plate detector (MCP), 225–227
Motional freedom
cooling braid and, 392, 393*f*
cryogenic manipulator, 386
shape memory effect and, 20–22
six degrees of, 3
see. Rotary motion
Motion in vacuum, 3–36
Motors
high speed, 25–26
stepper motors, automated TPD, 278
very high speed, 26*f*
Mu metal, 297
Multicapillary array collimator, 211

N

N_2, nitrogen, polarizability form work function measurement, 291
Naphthalene dosing, 463, 464*f*
Neutral beam intensity measurement, 429
Ni permeation source, hydrogen purification, 511
NO, nitric oxide
impurity oxidation, 546
oxidative wall passivation, 87–88

O

Observation windows
film deposition prevention, 536–537
low optical distortion glass, 538
shielded, 535–536
strain-free mounting, 533
zero length assembly, 539
OFHC Cu, oxygen free high conductivity copper, 104
cooling braid, 392, 497
cooling reservoir, 394
crystal holder, 355
heated doser, 460–464
hollow bolt seal, 104*f*
sample cooling, 383
thermal shield, 34
Optical pyrometer
calibration point for silicon, 413, 415
disappearing filament type, 409–411, 412*f*
measurement through coated window, 411
radiant energy equation, 409
Optical windows. *See* Observation windows
Organic doser
BN crucible, 466
ceramic standoff, 464
volatile organics, 460–464
Outgassing
degassing loops, 313, 407–409
from motors, 24

Outgassing (*cont.*)
prevention, 407
studies, 110
Oxygen
atomic oxygen production, 491–493
chemisorbed, 238, 240, 241*f*
detection of atomic oxygen, 490
MnO_2solid state source, 513
purification, 505
Ozone
detection of, 490
generator, 488–489, 489*f*
mass spectrometer cracking pattern, 487, 488
molecular beam doser, 488–489
production, storage, use, 487–488

P
Palladium
carbon removal from, 546–547
surface segregation and, 545
Palladium leak, hydrogen purification with, 481
Palladium permeation source, hydrogen purification, 511
Pancake radiation heater, 47
Passivation, surface
oxidative, 424
teflon coating, 91
Permeation
atmospheric, 109
gas purification by, 511–512
reusable samples, 513–514
Phosphor screen
beam dimension measurement, 198
CEMA detector and, 231*f*, 232
dusting method for coating, 129–130
electrostatic deposition of, 129, 130
LEED apparatus, 123, 226
sedimentation deposition of, 127–129
spot photometer and, 202
Photochemical surface processes, 238–243
Photochemistry
of chemisorbed O_2, 238, 239*f*, 241*f*
photoreduction of Ag, 242
polarized UV light in, 240–242
Photoemission studies, hollow cathode resonance lamp for, 235–236
Photon stimulated desorption, 232, 399
Pierce ion gun, 472
Piezoceramic foil, in Kelvin probe, 295–297
Piezoelctric actuators
drive, 34, 95
fatigue on polycrystalline Ag, 95, 96*f*
Kelvin probe actuator, 299
Tube, 34
Planck's law, 409
Polarized UV light for photochemistry, 240–242
Polarizer-compensator-sample-analyzer (PCSA), 302, 303*f*
Polycrystalline metals
Ag, 95
Ni, 295, 297*f*
W, 259
Pulse counting, 225–229
Pump oil
Fomblin, 488, 584
Santovac-5, 584
Pumping
differential, 6, 7, 9, 41, 235, 237*f*, 435, 471, 521
getter film, 72, 273, 483, 505
parallel, 72
pressure equalizing device, 72–74
tests, 76*f*
two-stage differential, 237*f*
vibration-free ballast-type, 71
Pumps
aspirator/sorption, 69–70
diode ion, 72, 75–76
ion, 8, 56, 69, 71, 72, 75, 211, 236, 327
oil contamination elimination, 69
oil diffusion, 237
regurgitation effect, 72
safety system, 584–586
see. Titanium sublimation pump
triode ion, 75
turbomolecular, 41, 237
zeolite sorption, 69, 115
Pyrolytic graphite
chemical vapor deposited, 372
paint-on heater, 374
Pyrometer. *See* Optical pyrometer

Q
QTM. *See* Quartz thickness monitor
Quadrupole mass spectrometers (QMS)
channeltron detector, 262–264
enhanced sensitivity, 267
enhanced signal-to-noise ratio in, 262–264
floating grid, 265, 266*f*
line-of-sight for thermal desorption, 269–270
see. Mass spectrometers
modulated ion source, 267–268
ozone and atomic oxygen detection, 490
shielded, 259–262, 425

spurious electron emission elimination, 265–266
Quartz crystals
oscillator, 321
thin film measurement on, 314–315
see. Quartz thickness monitor
Quartz flat partial reflector, 238
Quartz microbalance. *See* Quartz thickness monitor
Quartz prism UV polarizer, 238, 240
Quartz thickness monitor (QTM), 309–312, 314–315
calibration of, 309
magnetic drive, 24
very low coverage measurement, 440

R
Radiation damage reduction, 243
Radioactive adsorbates, 305–307
Rapid wafer thermal processors, 413
Re ribbon, ThO_2 deposition on, 136
Resonance enhanced multiphoton ionization (REMPI), 231
Retarding diode method, 289–291
RHEED intensity measurement, 313
Richardson equation, 133
Rotary motion, 3–14
arcsec resolution, 13–14
axial, 6
bearings, 29
cryogenic azimuthal, 388–389
electrical readout, 10
fine angular adjustment of, 14*f*
heavy-duty turntable, 20
high-speed feedthrough, 25–26
magnetic shutter, 23–24
optimization of angular resolution, 20
rapid, 10
through small angles, 18–19
turntable, 20
two-axis device, 19*f*
ultrahigh vacuum, 6–11

S
SAES alkali metal sources, 483
Safety, 589–592
Sample cooling, 392–394
Sample transfer, 39–49, 51–57
at low temperature, 45, 47, 48
from high pressure to UHV, 39–41, 44
from UHV to external cell, 45, 46
high-pressure cell, 49–52
internal cup high-pressure cell, 49–50
Lebold-Heraeus device, 41
longitudinal with disconnect, 53*f*
magnetic rod, 52
mirror port, for enhanced sample transfer, 56, 57*f*
movable crystal, 41*f*
rod-through-chamber, 42, 43*f*, 44 *f*
rotation to multiple ports, 45
transfer rod, 47
translatable reactor cup, 40*f*
vibration-free, 56
with trolley system, 33
Sample transfer with disconnect
inexpensive, 54, 55*f*
in standard UHV system, 52
in STM systems, 54
Sapphire
crystal holder, 354
electrical leakage prevention, 64–65
rod, 299, 300*f*
support bearing, 355
thermal conductivity of, 386
UV grade window, 238
Scanning kinetic spectroscopy (SKS), 280–282
Scanning tunneling microscopy (STM), 54, 155, 168, 299, 459, 548
repeatable sample positioning, 34–35
Scanning tunneling microscopy. *See* STM
Scanning tunneling spectroscopy (STS), 299–300
Sealants, use of, 24, 108, 523, 525, 533
Seals
compression, 103–105
doubly differentially pumped, 45, 322
for infrared windows, 521
gold wire cryogenic-type, 99–102
helicoflex O-ring, 113
high force, 43
high temperature, 6, 524
indium, 526
kovar glass, 394, 533
metal to Teflon, 43
rotary design, 7*f*, 8*f*
sliding rod, 42*f*
spring-loaded Teflon, 9, 52, 56
UHV glass window, strain-free, 533
vacseal leak sealer, windows sealer, 367, 525
Wilson type, 6
see. Gaskets
Semiconductor crystals
cement mounting for, 368–369
cleaning, 548–549
interferometry and temperature measurement, 359

Semiconductor crystals (*cont.*)
 low stress mount for heating/cooling, 369–371
 SiC, 327
Shape memory effect (SME)
 Clamp, 22*f*
 NiTi alloy, 21
 shutter, 22*f*
 small motions with, 21–22
Shelton diode for work function measurement, 293–294
Shielding, 149–150
 ad-mu 80, 150
 electrical, 151–152
 magnetic in UHV, 149–150
Shutter device, rotatable, 22–23
Silica gel
 Davisil, 131*n*
 ozone storage, 486
Silicon
 crystal heating, 361–363
 crystal mounting, 358*f*
 emissivity of, 409–410
 etching, 530
 split-off-dimer defects, Ni induced, 549*f*
 surface cleaning, 548–549
 temperature control using resistivity, 415
Silver films, for ozone and atomic oxygen detection, 490
Silver permeation source, oxygen purification, 511
SIMION electrostatic lens and analysis program, 189
 ion optical calculations, 473
Single crystals
 alignment, 156–159
 anisotropy of electrical conductivity, 200–201
 Bond-Barrel holder, 156, 158*f*
 CaF_2disk, 557
 calorimetry, 333, 334
 curvature of, in grinding and polishing, 157
 cutting goniometer, 159
 cylindrical, 375–377
 desorption kinetics on, 259
 electron beam angle of incidence on, 163, 164*f*
 fabrication, 155–160
 ion beam polishing, 160
 orientation, grinding and polishing, 156–159
 photochemical processes on, 238
 radiation heating of through glass windows, 371–372
 reconstruction effects, 548
 see. Metal single crystals
 use as calorimeter, 240, 241*f*
 UV irradiation of, 238
SKS. *See* Scanning kinetic spectroscopy
SME. *See* Shape memory effect
Single crystal surface
 Au(111), fabrication, 155, 156*f*
 chemisorption and reaction on, 305
 Kelvin probe desorption measurement, 295
 kinetics on, 284
 synthesis reactions on, 284
 tungsten, atomically clean, 550–551
Sources
 alkali metal, 483
 alkaline earth ion, 474
 atomic arsenic, 456
 atomic fluorine, 481–482
 BN diffusion, 529
 cesium, 471–473
 electrochemical cell, 497, 498*f*
 He(I), He(II), 238*f*
 high-flux atomic hydrogen, 477–480
 hydrogen peroxide, 493–494
 I_2, 499–501
 ion bombardment, 213–214
 Kaufman ion source, 218
 Lyman-α, 245–247
 methyl free radicals, 485
 pulsed vacuum UV, 247–248
 UV from high-pressure Hg arc, 238
 see. Atomic hydrogen; Thermionicemitters; Vacuum ultraviolet sources
Spot photometer construction and use, 201–202
Spot-welding
 difficult junctions, 175–177
 see. Welding
 slotted crystals, 177
Springs
 chromel wire, 369
 Cu-Be, 68, 388
 phosphor bronze, 66
 Ta wire, 67
Sputtering
 axial, to sharpen tips, 173
 cleaning by, 213
 coating tube inner walls, 314
 contamination effects, 213
 crystal polishing, 160
 deposition rates, 216
 for hybrid thin film deposition, 314–315
 ion gun for, 211–221
 neutral species, 275

TiN, 99
Stagnation detector, 429
Sticking coefficient, 270, 377
measurement, 330–331, 366
Sticking probability versus absolute coverage, 426f
equation, 255
STM tip, 171
approach mechanism for, 31
density of states, 299
etching for field ion microscopy, 169f
fabrication, 167–173
outgassing, tip flasher, 170
reproducible etching, 168–169
sharpening, 170, 173
single crystal metal, 173
Strain gauges, 337, 341
Sulfur source, 497
Supersonic
molecular beams, 429
nozzles, 180–181
Supported catalysts, 555
Surface barrier detector, 302–303
Surface contaminants, 265
Surface Debye temperature, 334–336
Surface poisoning, 280
Surface reaction kinetics at high pressure, 44
Surface reaction processes, 280
Surface segregation, 545
Surface studies
electrochemistry apparatus, 115f
ellipsometry for studying adsorption, 300
enhanced surface sensitivity, 247
radiotracer techniques for, 302–303
Syringe, adding liquid, 517, 518f

T

Tantalum (Ta) plasma, 247
Tantalum tube, hydrogen embrittlement prevention, 215
TDS. *See* Thermal desorption spectroscopy
Teflon
compression fitting, 115
impurities from, 50
liners, 42
Temperature measurement
hot filaments, 407–409
pyrometric, 409, 410
thermocouples, 349–351
W filament nomograph, 408
Temperature-programmed desorption (TPD), 259–262, 266, 278–280, 283, 284
Temperature-programmed reaction spectroscopy (TPRS), 280, 282–284
Temperature programming
metal crystals, 349–351
metal and semiconductor crystals, 351–353
Tesla coil, 91, 206, 488
Thermal braid cooling, 389, 392–394
Thermal desorption, 273–280
angular distribution, 273–275
apparatus for, 274f
apparatus for automated TPD, 278–280
azimuthal angular resolution on a cylindrical single crystal, 376–377
CO on Ru(001), 298, 299f
H_2on Ni(111), 273, 274f
line-of-sight, 269–270
Thermal desorption spectroscopy (TDS), 259, 267–268, 275–276. *See also* TPD
Thermionic emitters
brightness temperature, 409, 411
carburization, 136
cathode design, 142f
electron gun, 187
emitter evaporation rates, 138f, 139
filament replacement in, 145–146
high-temperature operation, 141–142
LaB_6 coated, 136, 137f
lanthanum hexaboride, 135–136
low work function coatings, 137
mounting, 139–140
shielded, 215
shielded and open emitters, 140f
spiral, 139
thoriated, 133–135
Thermocouple gauge, sealing, 104, 105f
Thermocouples
attachment, 357, 358
avoiding excess local heating, 275
calibration, 349, 405–407
cemented, 365
chromel-alumel, 357, 448
contamination, 357
welding to metal single crystal, 175
Thin film deposition, 309–319
absolute surface coverages, 305–307
hybrid methods, 317–318
measurement, thickness limitations, 313
on tube inner walls, 314–315
organic vapor deposition cell, 464, 466f
stable/metastable films, 314
Tilt motion, 3, 5f
Titanium sublimation pump (TSP), 72, 84, 115, 211, 247, 259, 505, 584

Topping model, 291, 292f
Temperature-programmed desorption (TPD), 259, 275–276, 508, 569–571
TPRS. *See* Temperature-programmed reaction
Translator, folding linear magnetic, 586
Traps
  liquid nitrogen, 79–80
  metal foam, 75–77
  water-cooled Cu, 235
  zeolite, 235
Tribology, review, 29
Tribometer, 341–343
TSP. *See* Titanium sublimation pump
Tungsten
  coils, 62
  crystal holder, 354
  grid, 244f, 557, 558f
  hairpin filament, 309
  high-temperature operation, 375
  single crystal, atomically clean, 550–551
  wire, fabrication, 62
  wire heaters, nomograph for design, 409f
Tungsten ribbon attachment to power leads, 61–62
Turbopump power interrupt protection, 581–582

U
Ultra high vacuum systems (UHV)
  access port, 56–57
  adding liquid to surfaces, 517–518
  aluminum, 113–114
  bakeout, 83
  chamber protection, 583
  common impurities in, 548
  differential pumping in, 8
  electrochemical device, 502–503
  grating rotation, 19–20
  fracture stage for surface analysis, 343–344
  stainless steel wall passivation, 87–88
  surface electrochemistry apparatus, 114–116
  trolley transport system, 33
Ultrathin metal single crystals, 333, 334f
Ultraviolet light (UV)
  lamp for photochemistry on surfaces, 238
  Lyman-α, 245–247
  polarized, 240
Ultraviolet photoelectron spectroscopy (UPS), 196
  gold (Au) spectrum, 236

V
Vacuum ultraviolet sources (VUV), 235–240, 247–248
Valves
  fast closing, 583–584
  low deadspace aperture, 430, 431f
  polyfluoroalkoxy (PFA), 89
  small gate, 45
  squeeze, 433–434
  straight through, 47, 235
Variable aperture, flange mounted, 30–31
Variable aperture, organics, 464
Viton
  atmospheric permeation, 108, 110
  bakeout limitation, 524
  outgassing, 40, 323
Vycor permeation source, helium purification, 507

W
Wagner electrochemical cell, 497
Wall passivation, 87–91
Wall reactions
  minimization, 89–91
  reduction with gold film, 39
Wehnelt cylinder, 187
Welding
  for thermal contact, 392
  metal foil window, 529
  sandwich weld, 175, 176f
  see. Spot-welding
Wien filter, 220
Wilson seal, 6
Wilson differential pumping method, 6
Windows
  alkali halide, 521
  bakeable aluminum, 528
  bakeout limitations, 525
  beryllium, 526, 527f
  CaF_2, 207, 323, 523, 524, 557
  disposable, 535
  for vacuum UV transmission, 525–526
  glass seals for, 537–538
  heated, 536–537
  IR transparent, 321, 557
  Itran, 524
  large-area Si crystal preparation, 529
  metal thin foil welding, 529
  mounting, 521
  SrF_2 , 207
  thin film coated, 411

UV grade sapphire, 238
UV transparent, 207
X-ray transmission, 526–529
zero length assembly, 539
see. Observation windows
Wire
ceramic-bead insulated, 66
gold wire, 155
polycrystalline, 174
Pt heater wire, 466, 467*f*
single crystal, 163
straightening and braiding, 182–183
tantalum, 50, 266
tungsten, 50, 62, 408*f*
Work function
changes, retarding diode method, 287–288
difference for two surfaces, 291
electron gun measurement, 289–291
electron reflection coefficient measurements, 291–292
measurement, 297
minimization of differences along a surface, 189
SnO_2, 123
tungsten, 133

X
Xe/Ag(111), 302
X-ray photoemission spectroscopy, grazing incidence, (GIXPS), 247
X-ray standing wave spectroscopy (XSW), 13

Z
Zeolite
ethylene adsorption study on, 569
for gas storage, 505
trap, 77*f*, 509
Zone electropolishing, 167–168